Universität Hamburg
DER FORSCHUNG | DER LEHRE | DER BILDUNG

Electrophysiology of human induced pluripotent stem cell-derived neurons cultivated on micro- and nanostructured substrates

Dissertation

zur Erlangung des Doktorgrades
an der Fakultät für Mathematik, Informatik
und Naturwissenschaften
Fachbereich Physik der Universität Hamburg

Center for Hybrid Nanostructures
Institut für Nanostruktur- und Festkörperphysik

Vorgelegt von

Jann Immo Harberts

— Hamburg, 2022 —

GUTACHTER DER DISSERTATION:

    Prof. Dr. Robert H. Blick

    Prof. Dr. Wolfgang J. Parak

    Prof. Dr. John A. Rogers

ZUSAMMENSETZUNG DER PRÜFUNGSKOMMISSION:

    Prof. Dr. Robert H. Blick

    Prof. Dr. Wolfgang J. Parak

    Prof. Dr. Jochen Liske

    Prof. Dr. Viacheslav Nikolaev

    Prof. Dr. Gabriel Bester

VORSITZENDER DER PRÜFUNGSKOMMISSION:

    Prof. Dr. Jochen Liske

DATUM DER DISPUTATION:

    13.09.2022

VORSITZENDER FACH-PROMOTIONSAUSSCHUSS PHYSIK:

    Prof. Dr. Wolfgang J. Parak

LEITER DES FACHBEREICHS PHYSIK:

    Prof. Dr. Günter H. W. Sigl

DEKAN DER FAKULTÄT MIN:

    Prof. Dr.-Ing. Norbert Ritter

Abstract

Merging human induced pluripotent stem cell (iPSC)-derived neurons with the advantages of functionalized micro- and nanostructured cell culture substrates might open up new pathways for, e.g., bioengineering and regenerative medicine. This advanced type of cells, however, is exceptionally difficult to cultivate making the feasibility of such a unique combination uncertain.

In this thesis, the cultivation of human iPSC-derived neurons was thus investigated on a selection of micro- and nanostructured substrates to identify potential challenges such as an altered differentiation outcome of the Petri dish-established culturing protocols due to the modified growth environment. Specifically, the neuronal differentiation while being cultured on nanowire (NW) arrays as well as the formation of neuronal networks inside 3D-printed microscaffolds were tested and verified. Both types of substrates are of keen interest in stem cell culture: on the one hand, NW arrays are able to facilitate, for example, the delivery of biological payloads, or to enhance the electrochemical coupling to the substrate for superior sensing/stimulation. On the other hand, 3D-printed microscaffolds allow for establishing defined neuronal networks and improved resemblance of the three-dimensional nature of the human brain for brain-on-a-chip (BoC) applications. The functionality of the neurons, i.e., the quality of the generated cells, and the neuronal networks were analyzed using electrophysiological patch clamp measurements. Immunocytochemistry (ICC) served to substantiate the neuronal characterization. The interactions of the cells with the substrates were analyzed using confocal laser scanning microscopy (CLSM) and cross-sectional scanning electron microscopy (SEM) prepared by focused ion beam (FIB) milling. One key result of this work is the demonstration of equal neuronal differentiation on several types of NW arrays featuring substantially diverse substrate geometries such as altered NW lengths, array pitches, and NW diameters compared to planar controls. The positive outcome of the extensive study suggests that prospectively, the well-established applications of NW arrays, which have so far only been demonstrated on basic cell lines and primary cells from animals, might be applicable to human iPSC-derived neurons. Another major achievement of this thesis is the generation of defined neuronal networks inside the 3D-printed microscaffolds in which the human iPSC-derived neurons showed spontaneous excitatory postsynaptic currents (sEPSCs) indicating functional network activity. Here, the versatility of the two-photon polymerization (2PP) direct laser writing (DLW) technique employed to prepare the 3D scaffolds enables the fabrication of scaffolds with arbitrarily complex network topologies which might then enhance, for instance, brain organoid cultivation and BoC applications.

Concludingly, both types of the utilized hybrid systems might in the future set new standards in life sciences and biotechnology by facilitating unconventional approaches for, e.g., personalized high-throughput drug screenings and neurodegenerative disease studies.

Inhaltsangabe

Die experimentelle Verknüpfung von humanen induzierten pluripotenten Stammzell (iPSC)-abgeleiteten Neuronen mit den Vorzügen von funktionalisierten mikro- und nanostrukturierten Zellkultursubstraten könnte elementare Fortschritte in Forschungsfeldern wie z.B. der regenerativen Medizin liefern. Allerdings ist die Kultivierung solch fortschrittlicher Zellen ausgesprochen anspruchsvoll, sodass eine erfolgreiche Umsetzung dieser besonderen Vereinigung nicht zwingerdermaßen trivial ist.

In dieser Arbeit wurde deshalb die Kultivierung von humanen iPSC-abgeleiteten Neuronen auf einer breiten Auswahl an mikro- und nanostrukturierten Substraten getestet. Ein fundamentales Ziel war die Prüfung eines potentiellen Einflusses der neuen Zellkulturumgebung auf die Entwicklung der Neurone gegenüber herkömmlichen Petrischalen, sowie die Identifizierung von ggf. einhergehenden neuronalen Veränderungen wie z.B. einer reduzierten Funktionalität. In diesem Kontext wurden insbesondere sowohl die neuronale Ableitung auf Nanodrahtanordnungen (NW arrays) als auch die Bildung von biologischen neuronalen Netzwerken in 3D-gedruckten Mikrogerüsten (3D microscaffolds) untersucht. Beide Substrattypen sind von besonderem Interesse für die Kultivierung von Stammzellen: Die NW arrays können beispielsweise für eine verbesserte intrazelluläre Anlieferung von biologischen Nutzlasten sorgen oder die elektrochemische Ankopplung der Zellmembran an das Substrat, welche z.B. für weitere Messungen und Stimulierungen relevant ist, stärken. Die 3D microscaffolds erlauben die Herstellung von definierten neuronalen Netzwerken für eine sinnmäßigere Nachbildung der dreidimensionalen Struktur des menschlichen Gehirns für sogenannte brain-on-a-chip (BoC) Anwendungen. Sowohl die Funktionalität der Neurone—m.a.W. die Qualität der generierten Zellen—als auch die neuronalen Netzwerke wurden vornehmlich mittels der Patch-Clamp-Technik untersucht. Des Weiteren wurden die Zellen durch immunzytochemische (ICC) Färbungen charakterisiert. Die Interaktion der Zellen mit den Substraten wurde durch querschnittsbildgebende Verfahren wie Konfokal- (CLSM) und Rasterelektronenmikroskopie (SEM) untersucht, wobei letzteres durch Materialabtragung mittels fokussiertem Ionenstrahl (FIB milling) ermöglicht wurde. Ein wesentliches Ergebnis dieser Thesis ist die Darlegung einer zu planaren Substraten gleichwertigen neuronalen Ableitung auf diversen Typen von NW arrays dessen geometrische Charakteristiken wie z.B. die NW Längen, die array Schrittweiten und die NW Durchmesser fundamental variiert wurden. Dieses positive Resultat der umfassenden Untersuchung legt nahe, dass in Zukunft die etablierten Anwendungen von NA arrays, welche bisher lediglich mit herkömmlichen Zellenlinien oder primären Tierzellen gezeigt wurden, auch auf humane iPSC-abgeleitete Neurone anwendbar sind. Ein weiteres Kernresultat dieser Arbeit ist die definierte Herstellung von neuronalen Netzwerken innerhalb der 3D-gedruckten microscaffolds, wobei die humanen iPSC-abgeleiteten Neurone spontane stimulierende postsynaptische Ströme (sEPSCs), die auf eine Netzwerkaktivität hinweisen, zeigten. Die Vielseitigkeit des für die Herstellung der microscaffolds verwendeten Zwei-Photonen-Lithographie (2PP) 3D-Druckverfahrens (DLW) erlaubt es dabei Strukturen mit beliebig komplexen Netzwerktopologien herzustellen von denen zukünftig z.B. das Heranziehen von cerebralen Organoiden oder die Durchführung von BoC-Applikationen profitieren könnten.

Zusammenfassend setzen die beiden verwendeten Hybridsysteme möglicherweise in der Zukunft neue Maßstäbe in den Biowissenschaften durch die Förderung von unkonventionellen Methodiken für z.B. personalisierte Hochdurchsatz-Arzneimitteltests oder Untersuchungen von neurodegenerativen Erkrankungen.

Preface

This cumulative thesis is based on seven first- and four co-authored publications which were referred to in the main text by their corresponding Roman numerals I to VII and VIII to XI, respectively. The first-authored publications contain the main results and their key aspects were summarized in the results section. Results from the co-authored papers were included when they completed the narrative of the thesis. The gist of the thesis was written to be understood by a generally informed reader. However, certain statements might only be accessible to informed readers since some terminology was used without detailed explanations to keep the results concise. Further, the experimental details were in general not explicitly discussed in this thesis but can be found in the original manuscripts or their corresponding supporting information, which were attached in the appendix of the document.

First-authored manuscripts:

I Harberts, J.; Kusch, M.; O'Sullivan, J.; Zierold, R.; Blick, R. H., **A temperature-controlled patch clamp platform demonstrated on Jurkat T lymphocytes and human induced pluripotent stem cell-derived neurons**. *Bioengineering* 2020, 7(2), 46. [1]

II Harberts, J.; Zierold, R.; Fendler, C.; Koitmäe, A.; Bayat, P.; Fernandez-Cuesta, I.; Loers, G.; Diercks, B.-P.; Fliegert, R.; Guse, A. H.; Ronning, C.; Otnes, G.; Borgström, M.; Blick, R. H., **Culturing and patch clamping of Jurkat T cells and neurons on Al_2O_3 coated nanowire arrays of altered morphology**. *RSC Adv.* 2019, 9(20), 11194–11201. [2]

III Harberts, J.; Bours, K.; Siegmund, M.; Hedrich, C.; Glatza, M.; Schöler, H. R.; Haferkamp, U.; Pless, O.; Zierold, R., Blick, R. H., **Culturing human iPSC-derived neural progenitor cells on nanowire arrays: mapping the impact of nanowire length and array pitch on proliferation, viability, and membrane deformation**. *Nanoscale* 2021, 13(47), 20052–20066. [3]

IV Harberts, J.; Haferkamp, U.; Haugg, S.; Fendler, C.; Lam, D.; Zierold, R.; Pless, O.; Blick, R. H., **Interfacing human induced pluripotent stem cell-derived neurons with designed nanowire arrays as a future platform for medical applications**. *Biomater. Sci.* 2020, 8(9), 2434–2446. [4]

V Harberts, J.; Siegmund, M.; Schnelle, M.; Zhang, T.; Lei, Y.; Yu, L.; Zierold, R.; Blick, R. H., **Robust neuronal differentiation of human iPSC-derived neural progenitor cells cultured on densely-spaced spiky silicon nanowire arrays**. *Sci. Rep.* 2021, 11(1), 18819. [5]

VI Harberts, J.; Siegmund, M.; Hedrich, C.; Kim, W.; Fontcuberta i Morral, A.; Zierold, R.; Blick, R. H., **Generation of human iPSC-derived neurons on nanowire arrays featuring varying lengths, pitches, and diameters**. *Adv. Mater. Interfaces* 2022, 9(24), 2200806. [6]

VII Harberts, J.; Fendler, C.; Teuber, J.; Siegmund, M.; Silva, A.; Rieck, N.; Wolpert, M.; Zierold, R.; Blick, R. H., **Toward brain-on-a-chip: human induced pluripotent stem cell-derived guided neuronal networks in tailor-made 3D nanoprinted microscaffolds**. *ACS Nano* 2020, 14(10), 13091–13102. [7]

Co-authored manuscripts:

VIII Fendler, C.; Harberts, J.; Rafeldt, L.; Loers, G.; Zierold, R.; Blick, R. H., **Neurite guidance and neuro-caging on steps and grooves in 2.5 dimensions**. *Nanoscale Adv.* 2020, 2(11), 5192–5200. [8]

IX   Koitmäe, A.; Harberts, J.; Loers, G.; Müller, M.; Bausch, C. S.; Sonnenberg, D.; Heyn, C.; Zierold, R.; Hansen, W.; Blick, R. H., **Approaching integrated hybrid neural circuits: axon guiding on optically active semiconductor microtube arrays**. *Adv. Mater. Interfaces* 2016, 3(24), 1600746. [9]

X   Koitmäe, A.; Müller, M.; Bausch, C. S.; Harberts, J.; Hansen, W.; Loers, G.; Blick, R. H., **Designer neural networks with embedded semiconductor microtube arrays**. *Langmuir* 2018, 34(4), 1528–1534. [10]

XI   Fendler, C.; Denker, C.; Harberts, J.; Bayat, P.; Zierold, R.; Loers, G.; Münzenberg, M.; Blick, R. H., **Microscaffolds by direct laser writing for neurite guidance leading to tailor-made neuronal networks**. *Adv. Biosys.* 2019, 3(5), 1800329. [11]

The author's contributions

First-authored manuscripts:

I   J.H. and M.K. contributed equally. M.K. built the device and conducted the measurements. J.H. and M.K. wrote the manuscript. J.H. and J.O. conducted the cell culturing. J.H., R.Z., and R.H.B. conceived the study, supervised the project, and assisted in data evaluation and manuscript finalization. All authors conducted a final proofreading. All authors have read and agreed to the published version of the manuscript.

II   Patch clamping, fluorescent imaging, data analysis, and manuscript writing: J.H., cell culture: J.H., C.F., A.K., animal preparation: G.L, T cell preparation: B.-P.D., R.F., A.H.G., SEM/FIB imaging: J.H., I.F.C., P.B., ZnO NW preparation: C.R., InP NW preparation: G.O., M.B., ALD: R.Z., supervision: R.Z., R.H.B.

III   J.H., K.B., M.S. conducted cell culture. J.H., K.B., M.S. conducted epifluorescence microscopy imaging. U.H., O.P. helped with smNPC characterization. J.H. conducted confocal microscopy imaging. J.H., C.H. prepared the NW substrates. J.H., K.B. analyzed the data. J.H. wrote the manuscript. J.H., R.Z. conceptualized the study. R.Z., R.H.B. supervised the study. J.H., K.B., M.S., R.Z., M.G., H.R.S. revised the manuscript. R.Z., R.H.B. acquired funding. All authors conducted proofreading and approved the manuscript.

IV   J.H. and U.H. contributed equally. J.H. performed the confocal microscopy imaging, scanning electron microscopy imaging with focused ion beam milling, patch clamp measurements and data analysis. U.H., D.L. developed the cell culture protocols. U.H. performed the cell culture, immunocytochemistry, flow cytometry, and differential gene expression analysis. J.H., S.H., R.Z. prepared the NW substrates. C.F. performed the critical point drying. J.H., U.H., O.P. wrote the manuscript. O.P., R.H.B. supervised the study. R.H.B. provided funding and general support. All authors conducted proofreading and approved the manuscript.

V   Cell culture: J.H. supported by M.Si. and M.Sc.; SEM/FIB imaging: J.H.; IF imaging: J.H.; nanowire array preparation: T.Z., Y.L.; conceptualization: J.H., R.Z., L.Y., and R.H.B.; writing–original draft preparation: J.H.; writing–review and editing: J.H., M.Si., R.Z.; funding acquisition: L.Y., R.H.B. All authors reviewed the manuscript.

VI   Si NW preparation, cell culture, immunofluorescence and confocal microscopy imaging, patch clamping, data analysis, manuscript writing: J.H., GaAs NW preparation: W.K., A.F.iM., and J.H., assistance in cell culture: M.S., ALD: J.H., C.H., and R.Z., conceptualization: J.H., funding: A.F.iM., R.Z., and R.H.B.

VII   J.H. and C.F. contributed equally. C.F. designed and fabricated the microscaffolds supported by M.S. J.H. performed the patch clamp measurements and SEM/FIB imaging. J.H. and N.R. performed confocal microscopy for network analysis. J.H. and M.W. conducted immunofluorescence imaging. J.H. supervised the cell culture supported by N.R., A.S., J.T., and M.S. A.S. performed control viability assays. R.Z. performed ALD. J.H. and C.F. analyzed data. J.H. wrote the manuscript. R.Z., C.F., and R.H.B. revised the manuscript. R.Z. and R.H.B. supervised the study. All authors have given approval to the final version of the manuscript.

Co-authored manuscripts:

VIII   C.F. and L.R. produced the substrates and conducted the analysis of the culturing results. C.F. and <u>J.H.</u> cultivated the neurons. G.L. prepared the murine cerebella. C.F., <u>J.H.</u>, and R.Z. wrote the manuscript. C.F and R.H.B. conceived the study. R.Z. and R.H.B. supervised the project. R.H.B. assisted in manuscript finalization. All authors significantly contributed to the scientific discussion during data evaluation and manuscript preparation. All authors conducted a final proofreading.

IX   Cell preparation, cultivation, imaging, axon detection: A.K., sample preparation: M.M., PLL printing: <u>J.H.</u>, installation of the photoluminescence setup under supervision of A.K.: <u>J.H.</u>, photoluminescence measurements and writing of the manuscript: A.K., tube design: C.S.B., animal preparation: G.L., wafer preparation: R.Z., D.S., C.H., W.H., supervision: R.H.B.

X   Sample preparation: A.K, M.M., manuscript writing, cell preparation, cultivation: A.K., cell imaging: M.M., A.K., SEM imaging: M.M., PLL printing: M.M. with support of <u>J.H.</u>, patch clamping: <u>J.H.</u>, animal preparation: G.L., tube design: C.S.B., wafer preparation: W.H., supervision: R.H.B.; A.K. and M.M. contributed equally.

XI   Sample design/fabrication: C.F., C.D., M.M., manuscript writing: C.F., cell culture: C.F., <u>J.H.</u>, animal preparation: G.L., SEM/FIB imaging: C.F., P.B., patch clamping: C.F., <u>J.H.</u>, atomic layer deposition: R.Z., computer-generated imagery: <u>J.H.</u>, supervision: R.H.B.

Abbreviations and acronyms

2D	two-dimensional
2.5D	two-and-a-half-dimensional
2PP	two-photon polymerization
3D	three-dimensional
AHP	afterhyperpolarization
ALD	atomic layer deposition
AP	action potential
AraC	cytosine arabinoside
BoC	brain-on-a-chip
Ca	calcein
CAD	computer-aided design
CLSM	confocal laser scanning microscopy
D	diameter
DBSCAN	density-based spatial clustering of applications with noise
DIV	days *in vitro*
DLW	direct laser writing
DNA	deoxyribonucleic acid
EBL	electron-beam lithography
ED	electroplating
EDX	energy-dispersive X-ray spectroscopy
EP	electroporation
ESC	embryonic stem cell
FIB	focused ion beam
GRIN1	glutamate ionotropic receptor N-methyl-D-aspartate type subunit 1
GUV	giant unilamellar vesicle
HD	high-density
hESC	human embryonic stem cell
hiDN	human iPSC-derived dopaminergic neuron
hiGN	human iPSC-derived glutamatergic neuron
hiNPC	human iPSC-derived neural progenitor cell
hiPSC	human induced pluripotent stem cell
ICC	immunocytochemistry
iPSC	induced pluripotent stem cell
IR	input resistance
L	length
LD	low-density
MAP2	microtubule-associated protein 2
MC	membrane capacitance
MEA	microelectrode array
mPN	murine primary neuron
MSC	mesenchymal stem cell

MTC	membrane time constant
NC	nanocup
NeuN	neuronal nuclei
NP	nanoparticle
NPC	neural progenitor cell
NS	nanostraw
NW	nanowire
OM	original manuscript
P	pitch
PDL	poly-D-lysine
PDMS	polydimethylsiloxane
PEG	polyethylene glycol
PI	propidium iodide
PLL	poly-L-lysine
PLO	poly-L-ornithine
PVD	physical vapor deposition
qRT-PCR	quantitative real-time polymerase chain reaction
RIE	reactive ion etching
RMP	resting membrane potential
RNA	ribonucleic acid
RP	refractory period
RT	room temperature
SEM	scanning electron microscopy
sEPSC	spontaneous excitatory postsynaptic current
SI	supporting information
T cell	Jurkat cell/human T lymphocyte
TH	tyrosine hydroxylase
UV	ultraviolet
VLS	vapor-liquid-solid

Contents

Motivation and scope

Overcoming the boundaries between traditional practice in physics, chemistry, and biology might be a key factor to push life sciences to unrivaled dimensions.[12–14] Advances in micro- and nanofabrication allow for engineering biological metamaterials, which are considered promising candidates, e.g., to support biomedical translation, to fabricate minimal invasive nanoelectronics, or to be utilized as nanotools in neuroscience and regenerative medicine.[15–20] Based on that mindset, this work employed central elements from the natural sciences to merge some of their unique features into hybrid cell/micro-nano systems for testing their applicability for future medical applications (Figure 1.1). Specifically, human induced pluripotent stem cell (iPSC)-derived neurons were cultivated on various types of nanowire (NW) arrays, i.e., high-aspect-ratio nanostructures, as well as inside three-dimensional (3D) scaffolds and investigated by *in vitro* experiments (e.g., patch clamping). Note, the motives for choosing these three constituents will be further elaborated on in the subsequent sections. One focus of this work was to ensure the preservation of the differentiation outcome including neuronal functionality despite potential modulation of the intracellular signaling during the growth elicited by the sophisticated substrate topographies.[21] Here, strong interactions between the cells and the artificial substrates might substantially alter the outcome of the stem-cell protocols originally established in regular Petri dishes.[22]

Both NW arrays and 3D microscaffolds used as cell culture substrates play an increasingly important role in interrogating cells on molecular and cellular levels, and in bridging the gap between conventional planar cell cultures and live tissue by mimicking natural cell environments, respectively.[23–27] Currently, the experiments in the respective fields are still being dominated by ordinary cell lines such as HEK293 and HeLa cells or rodent neurons for reasons elaborated later.[28–31] The impact of NW arrays and 3D scaffolds on medical applications such as drug screenings and neurodegenerative disease studies might, however, be significantly improved by employing the *right* type of cells, namely, cells derived from human iPSCs.[32,33] One of the major advantages of employing human iPSCs is, for example, the avoidance of high clinical failure rates from the animal model to the human physiology.[34,35] Especially neurons derived from human iPSCs—which were employed in this thesis—are of keen interest as they resemble a crucial building block for recreating human brain-like tissues *in vitro* in order to study, for instance,
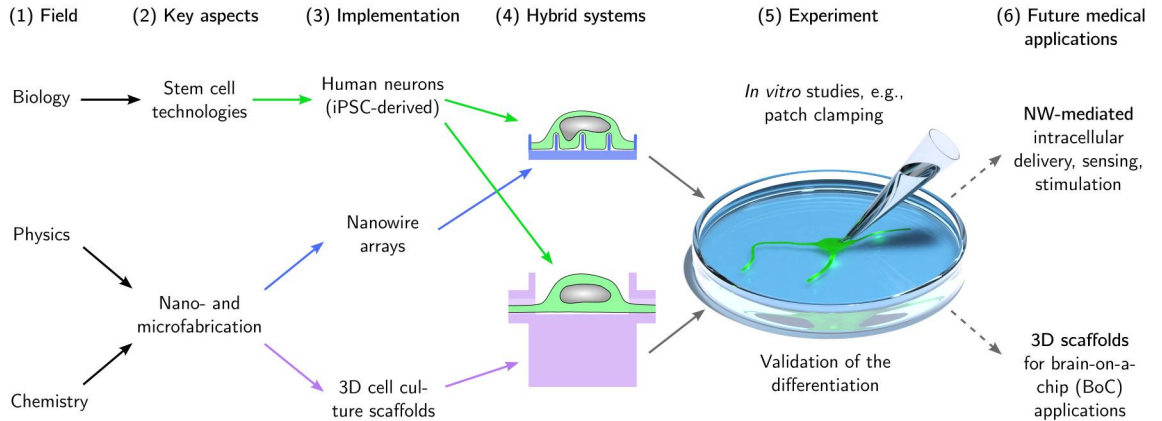

Figure 1.1 – Motivation and scope of the work. Unique features from biology, physics, and chemistry (1) such as stem cell technologies and nano-/microfabrication techniques (2) were employed to merge human iPSC-derived neurons with NW arrays and 3D cell culture scaffolds (3) into hybrid systems (4) to test in *in vitro* studies (5) their potential for future medical applications (6). Not published.

pathophysiological conditions including Parkinson's or Alzheimer's disease.[36–38] To exemplify potential applications of the utilized hybrid systems in human iPSC research: appropriately designed NW arrays are capable to induce cellular reprogramming, to enhance differentiation (mesenchymal stem cells), or to enable electrical recordings in neuronal cells.[39] Complementary, 3D cell culture scaffolds are considered to facilitate the development of iPSC-derived brain organoids and microfluidic brain-on-a-chip (BoC) devices for preclinical nanomedicine.[40–42]

The analysis of the cell cultivation on the artificial substrates was conducted predominantly by the patch clamp technique whose quantitative, temporal, and spatial resolution is essentially still unmatched.[43] For that reason, investigating the neuronal differentiation of human iPSCs cultured on NW arrays and inside 3D scaffolds not only by immunocytochemistry (ICC) but also by patch clamping to obtain evidence of functional electrophysiology is indispensable. Note, particularly dense/encapsulated 3D systems become increasingly challenging to be investigated with conventional techniques such as epifluorescence microscopy or patch clamping.[44,45] However, ordinary experimental methods—including the here mainly used patch clamp technique—can be made applicable by transiently reducing the size and complexity of the neuronal network for proof-of-concept studies by employing neuronal guiding techniques combined with tailor-made microscaffolds. One potent tool to fabricate such microscaffolds for biological applications is direct laser writing (DLW) *via* two-photon polymerization (2PP), which allows for freely recreating computer-aided design (CAD) drafts with feature sizes down to 150 nm.[46–49]

In the following chapter, more details regarding integral aspects of the work such as the applications of NW arrays, the principles of neuronal guiding for BoC applications, the advantages and challenges of iPSC culture, and the techniques used for sample preparation will be given.

— 2 —

Background

In this chapter, the background regarding the different aspects of the thesis will be elaborated. First, this will cover a detailed presentation of the applications feasible with NW arrays as well as approaches to guide and control neuronal growth including cell culture in 3D. Subsequently, the advantages of human cells derived from iPSCs will be highlighted. Also, the main technique for verifying the outcome of the differentiations, namely, the patch clamp technique, will be introduced. Lastly, the general procedures for the NW array fabrication and the principle of DLW will be presented.

NW arrays used as cell culture substrates can elicit profoundly diverse types of interactions between the cell and the substrate (Figure 2.1). Naturally, the type of interaction might have a strong impact on the overgrowing cells and, likewise, define the range of later applications associated with the NW arrays.[50] The settling regimes can alter from a fakir-like state on a bed-of-nails (Figure 2.1a) to encapsulating states including nucleus deformations (panels b–d) depending on the array characteristics such as the array density and the lengths of the NWs. A model to predict the settling regimes depending on the mean array density (i.e., array pitch (P)), NW length (L), and NW diameter (D) was devised by Buch-Månson *et al.*[51] In general, a fakir-like resting state is favored in case of a high array density, long NWs, and thin NWs. Correspondingly, the encapsulating states are more likely for low array densities, short NWs, and thick NWs. The NW length and diameter, however, are less pivotal for the settling regimes compared to the array density. Thus, depending on the array densities, the NW arrays used in this thesis will be rated high-density (HD) if a fakir-like state is expected and low-density (LD) if NW encapsulation is likely. Note, the arrangement of the NWs within the array, namely, ordered or random, is irrelevant. The NW length plays of course an important role in the degree of cell indentation. In the case of short NWs primarily the cell membrane is deformed (Figure 2.1b). The cell's nucleus, however, is also being deformed if the NWs are in the dimension of the cell's height (panel c). If the NW lengths exceed the cell size, the cell is likely to be no longer in contact with the bottom of the substrate (panel d). Extremely thin NWs might even pierce through the entire soma.[52] The strong interaction between the cells and the NWs can have an impact on cellular growth and moreover, renders possible a multitude of applications such as biosensing to examine cells.[53–61] Specifically, variations in the array densities, NW lengths, and NW diameters have been
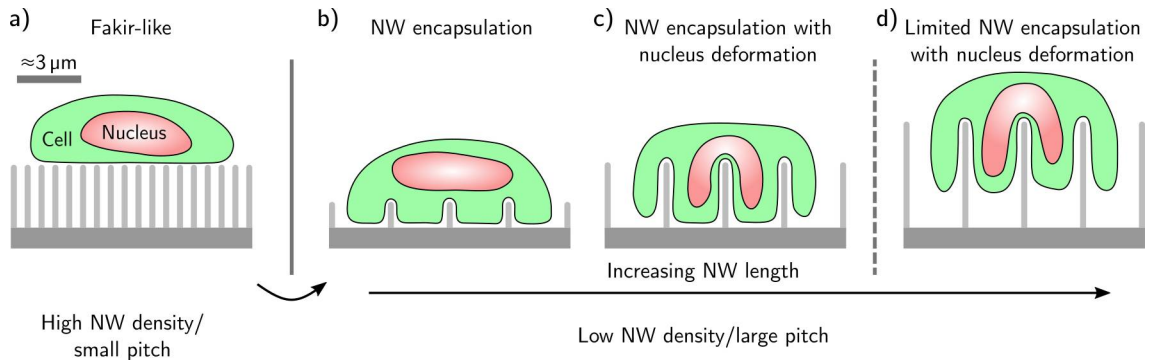

Figure 2.1 – **Illustration of typical settling regimes of cells cultured on NW arrays with varying characteristics such as array pitch and NW length. a)** Cells cultured on high-density (HD) NW arrays rest in a fakir-like state on a bed-of-nails. **b)** Using low-density (LD) NW arrays, the cell encapsulated the NWs. **c)** With increasing NW length, the NWs begin to interact with the cell's nucleus. **d)** Once the NW lengths exceed the cell's dimension, contact with the bottom of the substrate becomes unlikely. Adapted from publication III.

shown to influence viability, movement, proliferation, adhesion, morphology, and spreading of overgrowing cells.[62–81] Moreover, NW arrays were used to measure mechanical cell properties,[82–85] to interact with the cell's nucleus,[86,87] to reorganize actin,[88] to stimulate the mechanotransduction machinery,[89] or to direct cell polarization such as outgrowth and branching of neurites.[90–99] Among passive functions, the arrays can also have an executing function by either being functionalized themselves or being used to improve other experiments: the former is distinguished by enhancing cell transfection, cell activation, or the delivery of drugs and other payloads such as nanoparticles (NPs)—partly by hollow NWs, which also can be used for cell sampling.[100–123] The latter can be characterized, for example, in the form of a modified electrode surface of microelectrode arrays (MEAs) to improve electrochemical coupling between external electrodes and the cell for advanced sensing and stimulation.[124–137] Ultimately, photoelectrochemical properties of NWs—either in arrays or free-standing, i.e., detached from the substrate—can be used to modulate neuronal or cardiac activity *in vitro* or as retina implants.[138–141] Transparent NW arrays, fabricated, for instance, by embedding the NWs into a translucent polymer, can in addition facilitate optical imaging of living cells.[142] The substantial variety of potential applications thus renders devices that implement NW arrays promising candidates for next-generation biomedical instruments and nano-enabled neuronal interfaces.[143–147] Yet, the applicability of cultivating human iPSC-derived neurons on NW arrays needs to be verified since the outcome of the delicate culturing protocols for obtaining these neurons might be altered by, for instance, topography-induced intracellular signaling and gene regulation like it has been observed for the growth and differentiation of, e.g., mesenchymal stem cells (MSCs) and embryonic stem cells (ESCs).[148–156] Nevertheless, material cues are also considered to be potent regulators of epigenetics and general stem cell function and might thus have a substantial positive implication on the human iPSC culture.[157]

Guiding of neuronal networks inside cell culture scaffolds including cell adhesion and movement can be achieved by employing directing principles such as chemotaxis, topotaxis, and their respective tropisms.[158,159] Figure 2.2 illustrates three examples of neuronal guiding in either 2D, 2.5D, or 3D. In 2D (panel a/a′), a planar substrate can be modified with adhesion-promoting amino acids such as poly-D-lysine (PDL), poly-L-lysine (PLL), and poly-L-ornithine (PLO), or repellent substances such as polyethylene glycol (PEG) to control adhesion and growth just by chemical cues.[160–164] While the surface
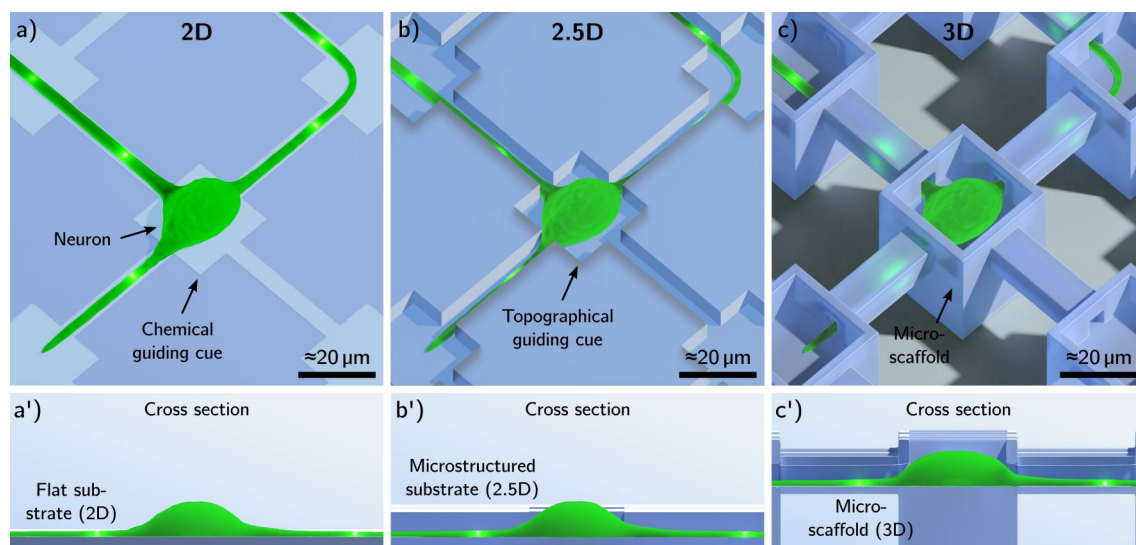

Figure 2.2 – Exemplification of neuronal guiding in 2D, 2.5D, and 3D. a) Planar substrate micropatterned with chemical cues (e.g., PDL) to control adhesion and growth in 2D by chemotaxis. **b)** Trenches prepared by, e.g., reactive ion etching (RIE) in 2.5D to induce topotaxis *via* contact guiding. **c)** Microprinted scaffold prepared, for example, by DLW to bridge the gap between 2.5D and 3D. **a′–c′)** Respective cross-sectional view of the upper panels. Not published.

chemistry is important for the adhesion[165,166] and usually sufficient to guide on planar surfaces by micropatterning,[167–169] the guiding efficiency can be substantially amplified by employing not only chemical but also topographical guiding cues at which the dominating guiding stimulus is often evoked by the topographical conditions.[170–175] Topographical cues, for example, can be introduced by cavities to hold the cells and by narrow trenches to guide the neurites (Figure 2.2b,b′). In addition to such confinements in neurocages, groves, and microchannels,[176–190] guiding was achieved by guidance barriers,[191–195] (functionalized) microstructures,[196,197] or microtube arrays.[198–200] While considerable progress to create designer neuronal networks was accomplished with such devices, the networks are restricted to 2D and 2.5D, respectively. Nevertheless, 3D cell culture being closer to natural biological tissue might be crucial for drug discovery by potentially offering more efficient and cost-effective preclinical screenings.[201–203] Both scaffold-free and scaffold-assisted approaches are used in the field, but notably, techniques without a scaffold such as hanging-drop culture lack structural support and the opportunity to control the outgrowth of the network.[204] To offer at least structural support—but yet without guiding capabilities—and to mimic the extracellular matrix, materials such as hydrogels, fibrinogen, and cellulose nanofibrils were used to create aerogels or suchlike porous structures.[205–209] Also polydimethylsiloxane (PDMS) lattices or graphene foam and even micropillar-based scaffolds were made use of to improve neuronal cell culture.[210–213] In general, changes with regard to, e.g., viability, proliferation, and gene expression were observed with cells cultured in the 3D scaffolds.[214–216] Although the scaffolds have a beneficial impact on the cell culture *per se*, guiding of neuronal networks within the structures is not feasible since the structures lack defined guiding cues—predominantly because of the microscopic scale of the feature details and the self-assembly nature of the fabrication techniques.[217] Yet, in the context of designing defined 3D neuronal networks for, e.g., BoC applications, the capability of the scaffold to control the neuronal growth is essential. As stated in the motivation section, DLW should be considered one of the future tools to fabricate biocompatible 3D microscaffolds with guiding capabilities. Figure 2.2c and c′ illustrate an example of a scaffold design where elevated cavities are interlinked with freestanding microchannels. So far, 3D DLW scaffolds consisting of microtowers or woodpile structures have been presented in the literature but, in fact, without guiding capabilities.[218–220] At least, selective adhesion within pole-like scaffolds was achieved by employing a two-component polymer system featuring adhesive and repellent surface characteristics, respectively.[221] To achieve comprehensive guiding also in the DLW scaffolds, the reasonable approach in 3D is to employ the guiding strategies well-established in 2D/2.5D such as cavities and microchannels. In addition, the microfluidic character of such design chimes in excellently with microfluidic approaches to study cells and to build blood–brain barriers and BoC devices.[222–228]

Brain-on-a-chip (BoC) is a continuative approach of organ-on-a-chip, which essentially aims for creating physiological *in vitro* microenvironments of, e.g., lungs, hearts, or livers on a single chip for advanced preclinical studies such as drug screenings.[229–239] Recreating the brain is a particular challenge due to the enormous complexity, for example, in terms of chemistry, neuronal wiring, or phenomenons and functions such as synchronicity and memory, respectively.[240,241] The clinical need for physiological brain models, however, is beyond dispute as they not only would help to understand the function of the brain but would equally facilitate improved neurodegenerative disease studies.[242–245] Initial and also more recent approaches for BoC used 2D microfluidic systems, for example, to test neurites, myelination, network formation, and regeneration after axotomy.[246–251] However, studies with 2D cell cultures lack the cytoarchitecture and cell–cell interactions naturally found in *in vivo* tissue, and thus, data collected from cultures with 3D cross-talk between different cells, e.g., regarding synaptogenesis, might be more relevant for understanding neuronal networks and their function.[252] As mentioned earlier, 3D cultures can be generated both scaffold-free and scaffold-assisted. Scaffold-free cultures to generate, for instance, human iPSC-derived brain organoids—introduced in the following paragraph—indeed fail to offer control of the formation of the neuronal networks, but such organoids were demonstrated to be valuable for

studying neurodegenerative diseases such as Huntington's or Parkinson's.[253] In this context, confined structures and microfluidics might even highlight the preclinical impact by improving the handling and reproducibility of organoid cultures.[254] One additional major challenge lies in the limited accessibility of a scaffold-free 3D culture in terms of, e.g., electrophysiology, which would thus require the implementation of electronics, for instance, by flexible 3D MEAs.[255,256] The 3D DLW scaffolds presented in this thesis reflect a promising intermediate step between conventional 2D culture and intricate organoid culture that excels by facilitating neuronal guiding and accessibility of individual cells for quantitative patch clamp measurements. The application of human neurons obtained by neuronal differentiation of iPSCs is in this context a prerequisite to resemble the nature of a human brain at its best.[257]

Human iPSC-derived cells are considered to be key players in the context of advancing high-throughput drug or toxicity screenings and neurodegenerative disease studies, in particular, by enabling human (patient-specific) *in vitro* models without limitations in cell availability.[258–262] The fundamental restriction in the availability of primary human cells is hereby overcome by the underlying procedure of sampling, reprogramming, and differentiation into any cells as illustrated in Figure 2.3 and specified later. The procedure was initially published in 2006 by Takahashi *et al.* and awarded a Nobel prize in 2012.[263,264] Especially, the differentiation into human neurons for studying neurodegenerative diseases such as Alzheimer's or Parkinson's is of keen interest since adequate cell models otherwise scarcely exist.[265–267] The problem in neuronal cell culture is that mature neurons no longer proliferate, which makes maintaining a neuronal cell culture virtually impossible—not to mention that gaining samples of primary human neurons would be beyond the means for obvious reasons.[268] Primary neurons could be obtained from animals such as rodents but suchlike conceptualized studies often suffer from errors during the translation from the animal model to the human physiology.[34,35,269,270]. Human neuron-like cells have been generated for a long time, e.g., from neuronal tumors, but these cells frequently show significant physiological alterations compared to the cell type they were obtained from.[271] Human embryonic stem cells (hESCs) resembled the next historical improvement for deriving human cells in the Petri dish.[272] Their use, however, raises sharp ethical and political controversies since the creation of such ESCs requires the destruction of the human embryo.[273] For that reason, the generation and cultivation of hESCs is either highly restricted or entirely prohibited in most of the world's countries.[274] Creating human iPSCs (hiPSCs), in contrast, only requires an initial cell sample obtained by a harmless skin biopsy from the proband (Figure 2.3a).[275] Subsequently, the dermal fibroblasts are reprogrammed into iPSCs using retroviral vectors according to the original procedure developed by Takahashi *et al.* (Figure 2.3b). In
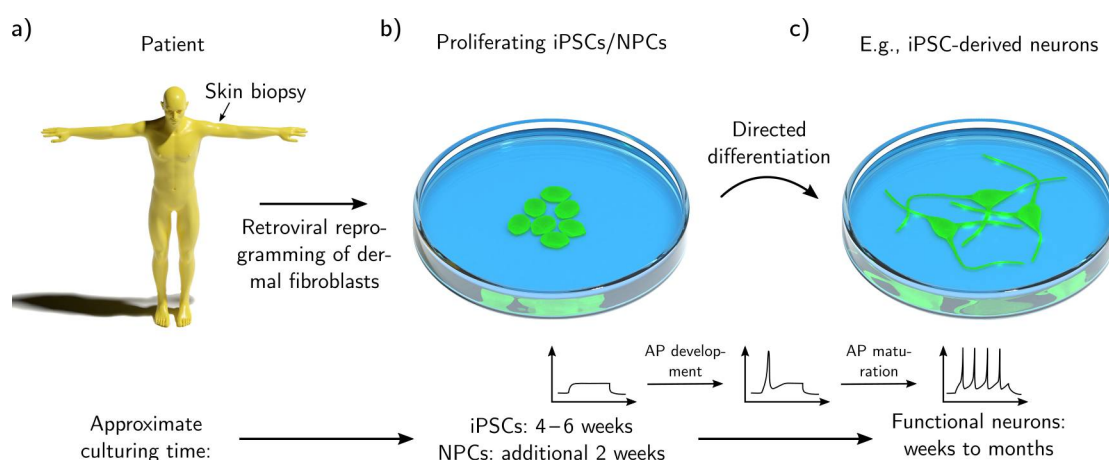

Figure 2.3 – **Simplified scheme of the generation of iPSC-derived neurons including the approximate cultivation periods. a)** Skin biopsy of a patient to obtain the initial patient-specific cell sample. **b)** Reprogramming of dermal fibroblasts using retroviral vectors to generate colonies of iPSCs that can be transformed into neural progenitor cells (NPCs) after embryoid body harvesting and clonal expansion. **c)** Final neuronal differentiation into mature human iPSC-derived neurons showing trains of action potentials (APs). Not published.

this work, not the hiPSCs themselves were used to differentiate the neurons from, but instead, hiPSCs in an intermediate multipotent neuronal differentiation state were utilized—namely, neural progenitor cells (NPCs). One substantial benefit of employing such predifferentiated NPCs to generate the neurons is accentuated by the significantly reduced total cultivation time required to reach mature neurons (weeks instead of months). Remarkably, the NPCs still have the ability to proliferate, which ensures having an infinite stock of cells. Moreover, these cells can also be frozen to enable long-term storage and thawed later for further experiments. To derive the NPCs from the iPSCs, neuronal differentiation is initiated, which results in embryoid bodies (neural rosettes) that are manually picked and split multiple times to generate pure NPC cultures. The NPCs can be maintained for several passages using specific NPC cell culture media, which suspend neuronal maturation and minimize spontaneous neuronal differentiation. Typically, the iPSC reprogramming and generation of NPCs with its manifold steps of culturing require up to months of delicate cell handling.[276] Note, particular steps of the procedure vary among the multitude of specific protocols. In general, final neuronal maturation is initiated by replacing the differentiation-inhibiting NPC medium with growth media that contain directing neuronal growth factors such as brain-derived or glial-derived neurotrophic factors (BDNF/GDNF) (Figure 2.3c).[277–280] The glutamatergic or dopaminergic phenotype can be promoted, for instance, by supplemental small molecules such as cyclopamine or purmorphamine.[281,282] Noteworthy, the functional neuronal maturation including the proper firing of action potential (AP) trains instead of only single spikes requires a few weeks up to several months depending on the culturing protocol.[283,284] In this work, 2–4 weeks of differentiation were conducted to obtain functional neurons growing as individual cells. Pioneering advances in the understanding of stem cell behavior and sophisticated control of the biological microenvironments even allow for the cultivation of iPSC-derived organoids, which characterize self-organized miniaturized model systems of organs.[285] State-of-the-art protocols facilitate not only the generation of internal organs such as liver or lung but also brain organoids for human disease studies.[286–291] As briefly stated in the beginning and to be elaborated in more detail in the 'Future perspectives' chapter, organoid cultures have their own particular challenges at which microfluidic platforms and 3D microscaffolds might further improve the impact of organoid models in stem cell biology, for instance, by enabling mimicking neurovascular systems or 3D electrophysiological readout.[292–296] In this work, the electrophysiological readout to test the iPSC-derived cells for, e.g., neuronal differentiation by recordings of characteristic APs is enabled by the patch clamp technique.

The patch clamp technique allows for testing electrophysiological properties (i.e., electrical properties of cells) such as currents and potentials across the cell membrane by employing a thin glass pipette to establish an indirect electrochemical contact with the cell interior (Figure 2.4a).[297] The technique was initially described by Sakman and Neher in 1976 by showing recordings of single-channel currents in frog muscle fibers and in 1991 their work was rewarded with the Nobel prize.[298] Specifically, the currents and potentials are recorded using an electrode placed inside a glass pipette that is filled with an electrolyte similar to the intracellular fluid (pipette solution) and a ground electrode placed in an electrolyte similar to the extracellular fluid (bath solution). Crucial for low-noise measurements is an electrical seal between the pipette and the cell membrane in the gigaohm range—also called 'gigaseal' or 'tight seal' (Figure 2.4b).[299] The gigaseal is usually established by attaching the pipette instantaneously to the membrane without any additional movement or subsequent repositioning of the pipette since this would contaminate the orifice of the pipette with membrane patches or even damage the cell. The immediate attachment is in general only achieved by following a strict routine where at first, a positive pressure is applied to the pipette in order to cause an outflow of the pipette solution (Figure 2.4c). Then, the pipette is brought extremely close to the cell whereas the outflow of the fluid slightly indents the cell membrane preventing unintentional contact with the cell (1.). Subsequently, the gigaseal is formed by changing the positive pressure into a mild suction and the membrane juts out toward the pipette
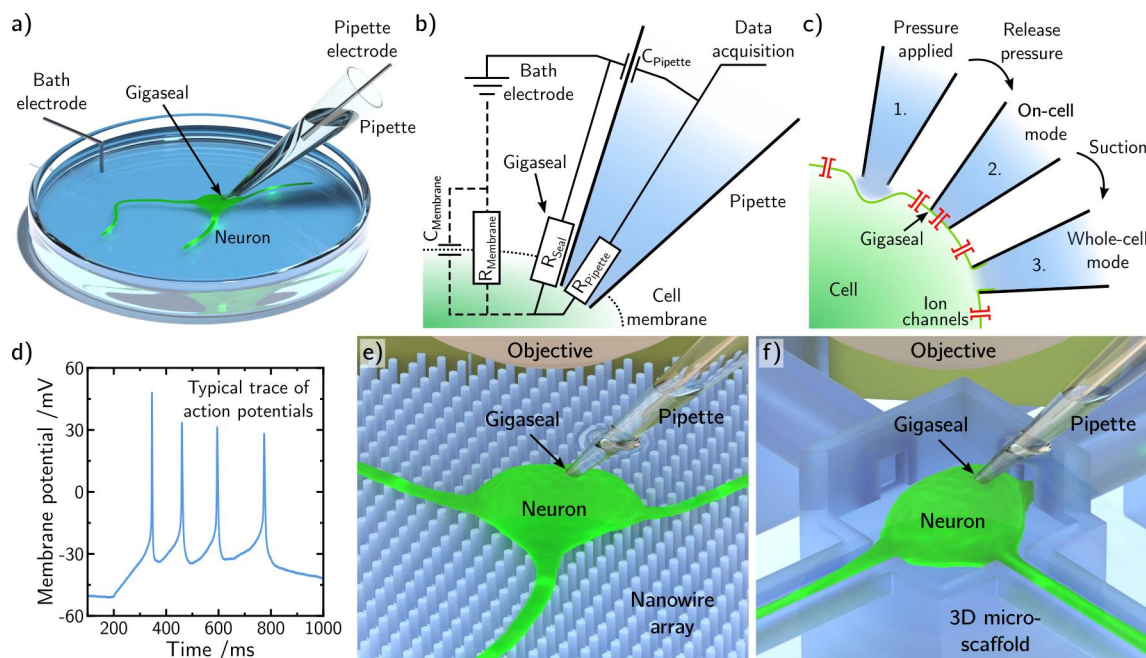
Figure 2.4 – **Schematic diagram of the patch clamp procedure including illustrations of patch clamping of neurons cultured on top of NW arrays and within 3D microscaffolds. a)** Illustration of the patch clamp routine: The pipette is in contact with the cell (gigaseal) to enable an electrochemical connection between the bath electrode and the pipette electrode. **b)** Electrical configuration of the patch clamp technique used for measuring currents and potentials across the cell membrane. **c)** Illustration of the patch pipette approaching the cell. A positive pressure causes an outflow of the pipette solution and prevents unintentional contact between pipette and cell (1.). The release of the pressure elicits the on-cell mode, where individual ion channels are measurable (2.). By applying a pulse of suction the membrane patch inside the pipette orifice ruptures creating the whole-cell mode (3.) and the ion channels in the entire membrane are now recorded. **d)** Exemplary trace of an AP train. **e)** Illustration of patch clamping a neuron that is cultivated on a NW array. **f)** Illustration of a neuron cultivated and patch clamped inside a 3D microscaffold. Note, the scaffold is partly cut open to enable highlighting the cell. Not published.

orifice (2.). Note, the success rates for establishing gigaseals strongly depend on the right ensemble of experimental details such as the shape/size of the pipette, the choice of patch clamp solutions, or the cell type/batch. Nevertheless, the proportion of successful seals can reach about 90% in a well-running patch clamp experiment. The configuration after establishing the gigaseal is called on-cell mode and facilitates the examination of individual ion channels. In this thesis, however, all experiments were conducted in whole-cell mode, which measures currents and voltages across the entire cell membrane (3.). The whole-cell mode is obtained by a short pulse of suction that ruptures the membrane patch at the pipette opening.[300] Measurements were conducted in both voltage- and current-clamp mode, which either fixate the voltage or current to measure currents and voltages, respectively.[301] The voltage-clamp mode was used, for example, to determine gating characteristics of voltage-gated ion channels, to measure characteristic membrane currents, or to detect postsynaptic events.[302] The current-clamp mode was used, for instance, to determine resting membrane potentials or to record APs (Figure 2.4d).[303] In the main part of the thesis, electrophysiological measurements were performed on cells that were cultivated on either NW arrays (Figure 2.4e) or in 3D microscaffolds (Figure 2.4f). One key aspect with regard to the NW arrays was to demonstrate that the cells being cultivated on such substrates maintain their electrophysiological properties, i.e., for example, their identical neuronal differentiation state, despite the challenging substrate topography. The focus with regard to the microscaffolds was to enable the formation of tailor-made neuronal networks that then also show network activity. The respective substrates were fabricated by top-down/bottom-up approaches (NW arrays) and DLW *via* 2PP (3D microscaffolds) briefly described in the following paragraphs.

The preparation of the NW arrays used in this thesis was carried out either in a top-down or bottom-up approach and both paradigms are well described in the literature (Figure 2.5a and b).[304] Specifically,
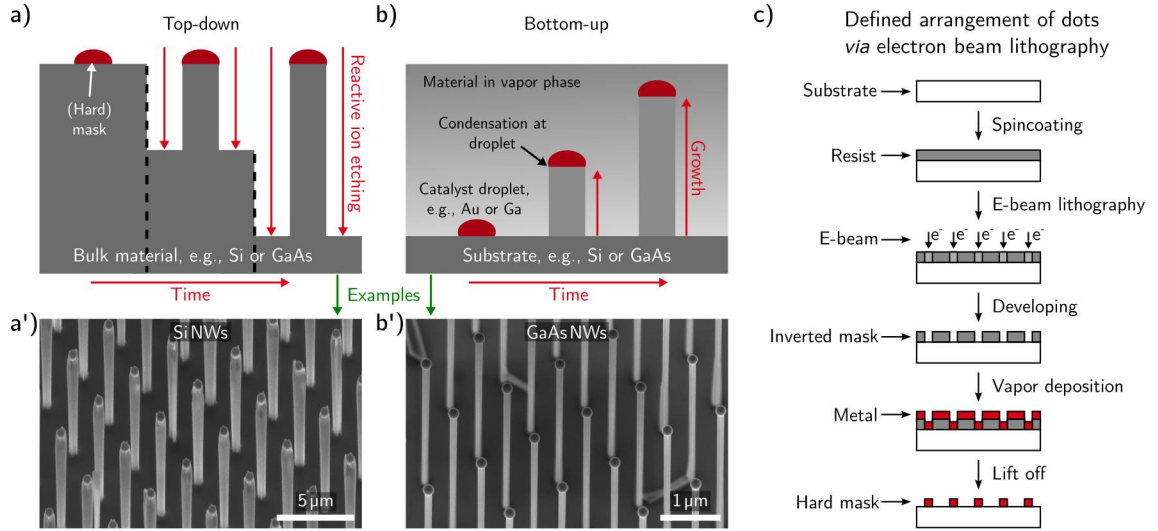
Figure 2.5 – **NW fabrication via top-down and bottom-up approaches including patterning procedure. a)** Schematic of the top-down approach. A (hard) mask is used to shield the plain substrate while with time unprotected areas are stripped *via* reactive ion etching (RIE). **a')** Example of a NW array prepared with the top-down approach (Si). Tilt: 45° (corrected). **b)** Schematic of the bottom-up approach. Material in the vapor phase condensates at the catalyst droplet causing material deposition under the catalyst droplet while with time elevating the very one simultaneously. **b')** Example of a NW array prepared with the bottom-up approach (GaAs). Tilt: 20°. Recorded by W. Kim. **c)** Exemplary schematic of a patterning routine using electron-beam lithography (EBL). Not published.

the top-down approach describes the procedure which starts with a (hard) masked bulk material that is then selectively etched away (Figure 2.5a). To fabricate NWs, the mask consists of circles whose diameters define the NW diameters whereas the etching time controls the NW lengths. The prerequisite for transferring the mask adequately to the bulk material is the application of an anisotropic etching technique such as reactive ion etching (RIE).[305] This dry etching technology uses a chemically reactive plasma created by a radio-frequency electric field. The electric field is arranged perpendicularly to the substrate creating a fundamental directionality of the RIE process by accelerating the reactive ions likewise perpendicularly toward the surface of the material. However, the final etching behavior, e.g., wall slope, undercut, etch depth, and surface roughness, depends on a multitude of processing parameters such as gas composition, chamber pressure, material, doping, and mask design, to name a few.[306–309] With an appropriate ensemble of settings, the etching profiles show almost vertical walls suitable for NW fabrication (Figure 2.5a′). In doing so, NW arrays prepared by RIE have been obtained, for example, from Si, Ge, GaAs, or GaN substrates.[310–313] The alternative bottom-up approach to fabricate NWs uses a catalyst droplet to locally deposit material on the substrate, i.e., to literally grow the NWs (Figure 2.5b). The material in the vapor phase adsorbs to the liquid catalyst droplet and then, supersaturation in the alloy droplet initiates the epitaxial crystallization of solid material at the surface of the substrate—also known as vapor-liquid-solid (VLS) mechanism by referencing the respective states of matter.[314] The bottom-up approach *via* VLS growth has been used to fabricate NW arrays, for instance, from materials such as GaAs, GaN, InP, ZnO, and Si using catalysts such as Ga, Ni, and Au (Figure 2.5b′).[315–319] The NW diameter is tunable by the catalyst droplet size and growth parameters such as the chamber pressure and eutectic composition.[320,321] The length of the NWs depends on the growth time whereas the growth direction is usually biased by the crystal orientation of the growth substrate.[322] By dynamically changing the ambient conditions during the NW growth, fundamental characteristics along the axial orientation such as the doping or—if the catalyst is part of the NW material, e.g., Ga for GaAs NWs—the diameter are adjustable.[315,323] For either approach, the array density is determined by the layout of the mask's circles and the catalyst droplets, respectively. To arrange these, preceding lithography steps using, for instance, electron-beam lithography (EBL) are required.[324] A typical routine to structure a substrate is illustrated in Figure 2.5c. First, the substrate is spin-coated with a thin layer of e-beam resist. The

patterns are then written with EBL and subsequently developed. A metal, e.g., Cr as a hard mask or Au as a catalyst, is deposited by physical vapor deposition (PVD) and after the lift-off, a grid of circle structures remains on the substrate. The sample is then further processed either by RIE or VLS growth. Note, if a defined arrangement of the NWs is not required, the circle structures might be prepared by self-assembly processes such as dewetting of thin metal films.[325]

The preparation of the 3D microscaffolds was conducted by direct laser writing (DLW), which sequentially exposes a resin with a scanning laser (Figure 2.6a). The resin is being cross-linked only in the focal spot of the scanning laser by employing two-photon polymerization (2PP). The application of such a multi-photon process, which has been theorized already in the 1930s by Göppert-Mayer,[327] is crucial as it prevents the cross-linking of the resin by single-photon polymerization in the expanded beam before and after the focal spot. Fundamentally, the DLW technique is based on the non-linear probability of multi-photon processes to polymerize the resin depending on the number of photons per volume,[328] i.e., the 2PP-rate (R_{2PP}) has a quadratic dependency on the laser power P:

$$R_{2PP} = \frac{\delta}{2} \frac{l}{A} C P^2, \tag{2.1}$$

with the 2-photon cross section δ, the focus volume l/A, the molar concentration C, and a $1/2$ normalization to consider the need for two photons.[329] For that reason, the probability for polymerization outside the focus, which contains low photon densities, is vanishingly small and the resin is only being polymerized at the focal spot with the highest spatial compression of the photons (Figure 2.6b).[330] The complex theory behind 2PP might be approached by a full quantum mechanical description based on the second-order perturbation theory.[331] However, a more graphical explanation is given by considering a transition from the ground state E_0 to an excited state E_1 by means of a virtual state V (Figure 2.6c).[332] The virtual state is created by a non-resonant interaction between the photons and the molecule, and its short lifetime of about 10^{-15} s is defined by Heisenberg's time-energy uncertainty relation.[333] To enable multi-photon absorption, the second photon needs to be absorbed within the lifetime of the virtual state, which results in 2-photon cross sections in the order of only 10^{-48} to 10^{-50} cm^{4}s/photon.[334,335] Due to the small cross section, considerable polymerization rates are only feasible with extremely high photon fluxes. Experimentally, this is achieved by employing pulsed lasers instead of continuous lasers to make use of temporal compression of the photons (Figure 2.6d). In this work, a Nanoscribe GT2 was used equipped with a 50–150 mW pulsed laser (780 nm) with a pulse length of 100–200 fs and a repetition rate of 80 MHz.[336]

The next chapter will be committed to the results selected from the main publications I to VII and the co-authored publications VIII to XI. Moreover, a preceding section is added to summarize the types of cells, NW arrays, and microscaffolds that have been used in the studies.
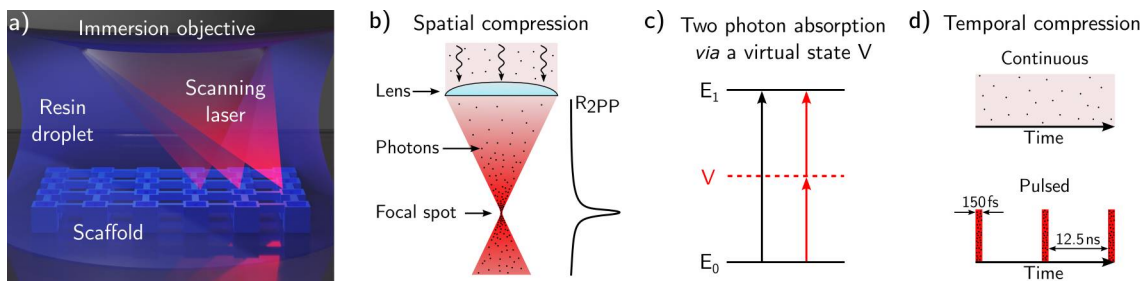

Figure 2.6 – **3D microscaffold fabrication using direct laser writing (DLW) by means of two-photon polymerization (2PP). a)** Illustration of the DLW process using a focused laser beam (red) to write the scaffold within the resin droplet (blue). **b)** Spatial compression: illustration of the photon density at the focal spot of the laser and the respective polymerization rate R_{2PP}. **c)** Schematic of the energy states (E_i) used in sequential photon absorption compared to simultaneous photon absorption, i.e., 2PP in the resin, *via* a virtual state V. **d)** Temporal compression: comparison of the photon density in a constant wave laser and a pulsed laser with the same laser power. b, d) adapted from Spangenberg *et al.*[326]

— 3 —

Cells cultivated on NW arrays and inside 3D microscaffolds

Hybrid systems that combine biological cells with micro- and nanostructured materials were analyzed in the context of this PhD thesis. Specifically, two different topics were investigated—namely, NW arrays to enhance the interaction of the cells with the substrate and topographical confinements in the form of channels and cavities to guide cellular growth. The experiments undertaken cover a broad spectrum of methods and techniques, which range from initial micro- and nanoprocessing for preparing the cell culture substrates to the final cultivation and examination of the cells growing on these substrates. The subset of results presented in this manuscript focuses on the electrophysiology and growth of the cells cultured on the micro- and nanostructures. Important results beyond the electrophysiology, e.g., immunofluorescence stainings have been included in cases where they help to understand the gist of the thesis or to complete the main narrative. The utilized experimental techniques are briefly described at first appearance and important details are highlighted, but for the sake of readability, comprehensive specifications such as dye concentrations are not provided here. The same argument applies to the sample preparation and the cell culture protocols, which are also not further stated in the next sections. Naturally, precise experimental information such as the sample fabrication, the compositions of the growth media, the dye concentration, or the used patch clamp solutions can be found in full in the original manuscripts (OMs) or their supporting information (SI) being attached in the appendix.

To outline the selected results: First, general electrophysiological studies are presented. In this context, a temperature-controlled microscope inset for the patch clamp setup was developed to enable recordings at physiological temperatures. Secondly, the culturing of cells on NW arrays with altering characteristics showing functional electrophysiology is demonstrated. Finally, 2D and 3D scaffolds for tailor-made neuronal networks are introduced and network activity is indicated by patch clamp recordings.

Five different types of cells were used in the experiments. Note, so far, only cells derived from human iPSCs were introduced. However, some results were collected with a cell line and primary rodent cells, respectively. Thus, the utilized cells fundamentally differ in function and origin, which are both briefly described in the next paragraphs. Specifically, Jurkat cells/human T lymphocytes (T cells), murine primary neurons (mPNs), human iPSC-derived neural progenitor cells (hiNPCs), human iPSC-derived glutamatergic neurons (hiGNs), and human iPSC-derived dopaminergic neurons (hiDNs) were employed. A comparison of the morphology of the five cell types is compiled in Figure 3.1 and important data such as the biological origin and the culturing periods are summarized in Table 3.1.
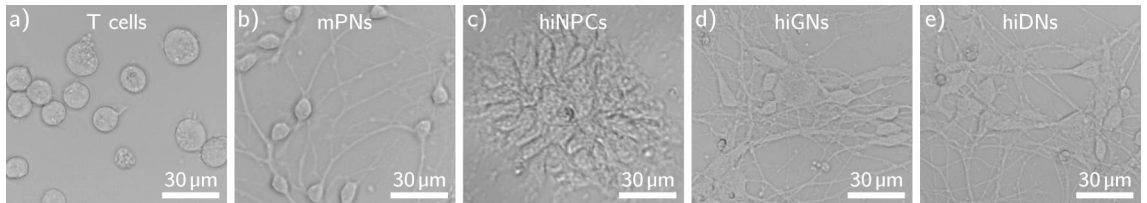

Figure 3.1 – Bright-field microscopy images of the utilized cell types to visualize size and morphology. a) Jurkat cells/human T lymphocytes (T cells) feature a simple roundish shape and large cell diameters of about 15 μm. **b)** Murine primary neurons (mPNs) are smaller with respect to the cell soma. **c)** Human iPSC-derived neural progenitor cells (hiNPCs) grow on very dense cell clusters. **d)** Human iPSC-derived glutamatergic neurons (hiGNs) and **e)** human iPSC-derived dopaminergic neurons (hiDNs) develop a more complex morphology with similar sizes of the somata compared to the murine primary neurons (mPNs). Not published.

Table 3.1 – Overview of the cells used for the experiments. [†]The cultivation period refers to the total cultivation period until the cell is mature enough for the experiment. For T cells and hiNPCs, no value is given since the cells do not require to mature, however, as they continuously proliferate the experiment has to be timed with the passaging routine. [‡]The adhesion period refers to the time required to grow on the final substrate until the experiment can be conducted. Note, the proportions of the cultivation period and the adhesion period of the hiDNs vary significantly depending on the reviewed publication. The particular values are specified in the respective sections.

General notation	Type	Souce	Origin	Host	Cultivation period[†]	Adhesion period[‡]	Abbreviation
Jurkat cells	T lymphocyte	cell line	blood	human	n/a	15–30 min	T cells
Cerebellar granule cells	glutamatergic	primary	cerebellum	mouse	4–10 days	4–10 days	mPNs
iPSC-derived hiNPCs	neuronal progenitor	iPSC-derived	skin	human	n/a	1 h–4 days	hiNPCs
iPSC-derived neurons	glutamatergic	iPSC-derived	fetal skin	human	4 weeks	2 weeks	hiGNs
iPSC-derived neurons	dopaminergic	iPSC-derived	skin	human	2–3 weeks	1–15 days	hiDNs

The Jurkat cells are an immortalized cell line of human T lymphocytes (T cells) obtained from a leukemia patient in the 1970s and since then routinely used to study T cell signaling, for example, in the context of immune responses including diseases such as HIV.[337] As a part of the immune system, T cells are located in the blood system and have a simple spherical shape (Figure 3.1a). Compared to primary T cells,[338] Jurkat cells are comparatively big with diameters of about 15 μm. The simple shape and the large size make them ideal candidates to practice the patch clamp technique. Moreover, the cell culture protocol is extremely simple as the cell suspension just needs to be diluted with a standard cell culture medium every 2–3 days.[339] Since T cells are not adherently growing cells they need to be attached to the respective substrates using adhesive coatings such as PDL or PLL in order to conduct patch clamp measurements.[340] However, the adhesion procedure only requires a few minutes.

The mPNs used herein were obtained from 6–7 days old mice, which were bred at the Center for Molecular Neurobiology Hamburg (ZMNH) of the University Medical Center Hamburg (UKE). Dissected cerebellar were provided and then in-house processed until dissociated cerebellar granule cells were obtained. The cells were then cultured for about one week according to a previously described protocol by Loers *et al.*[342] During that time, the neurons mature further and neuronal networks are formed (Figure 3.1b). Note, the enhanced complexity of the neuronal morphology and also the significantly smaller size of the somata make it more challenging to patch clamp these cells. However, since the majority of the cerebellum consists of granule cells,[343] the cell culture results in a quite pure ensemble of neuronal cells and the selection of cells for the patch clamp experiment is simplified. The homogeneity of the cell culture can be maintained for several days as long as, e.g., cytosine arabinoside (AraC) is used to suppress the proliferation of other cells such as astrocytes.[344]

The hiNPCs, hiGNs, and hiDNs (Figure 3.1c–e) originate from two independent protocols describing the hiNPC generation including the neuronal differentiation promoting a dopaminergic phenotype as well as the generation of another type of hiNPCs, which were used for the differentiation favoring a glutamatergic phenotype, respectively.[276,277] Note, the latter type of hiNPCs was not used in this thesis since only the derived hiDNs—obtained from a collaborator—were used (discussed later). The neural progenitors still proliferate but are already preprogrammed to become neuronal cells. As a result, mature

Table 3.2 – Types of NW arrays that were used for the cell culture. Materials indicated with a [†] were uniformly coated with biocompatible Al_2O_3 by atomic layer deposition (ALD) to avoid a potential influence of the surface chemistry within the same study.[341] The NWs were either prepared by a top-down approach using reactive ion etching (RIE) or a bottom-up approach using epitaxial growth (EG). Note, the epitaxial growth was done by collaborators: [1]Linke group, Lund University, [2]Ronning group, Jena University, [3]Yu Group, Nanjing University, [4]Fontcuberta i Morral Group, école polytechnique fédérale de Lausanne.

Material	Arrangement	Prep. method	Length /μm	Diameter /nm	Pitch /μm	Density /NWs×100 μm²	Cells used	Coating	Publication
InP[†]	Hexagonal	EG[1]	2	180	0.5	460	T cells, mPNs	PDL+lam.	II
ZnO[†]	Random	EG[2]	3	70–180	0.3	1300	T cells, mPNs	PDL+lam.	II
Si	Rectangular	RIE	1.5, 3, 5	700	1, 3, 5, 10	100, 11.1, 4, 1	hiNPCs	Matrigel	III
Si₃N₄[†]	Hex., Rect.	RIE	1.2	250	1.8, 4	31, 6	hiGNs	PLO+lam.	IV
Si₃N₄[†]	Random	RIE	1.2	200–400	1.8	31	hiGNs	PLO+lam.	IV
Si	Random	EG[3]	1	30–100	0.44	600	hiDNs	Matrigel	V
Si[†]	Rectangular	RIE	1, 3, 5	270–1070	1, 3, 5	100, 11.1, 4	hiDNs	Matrigel	VI
GaAs[†]	Rectangular	EG[4]	2, 4.5	250–600	1, 3, 5	100, 11.1, 4	hiDNs	Matrigel	VI

Table 3.3 – **Types of cell culture substrates/scaffolds that were used to guide neuronal growth.** Materials were uniformly coated with biocompatible Al_2O_3 or parylene C, respectively, to avoid a potential impact of the surface chemistry.[341,345]

Material	Passivation layer	Dimension	Guiding cues	Preparation method	Coating	Type of cells	Publication
Glass	Al_2O_3	2D	PDL	PDL-printing	PDL + lam.	mPNs	VIII
Si	parylene C	2.5D	trenches	RIE	PDL + lam.	mPNs	VIII
InAlGaAs	parylene C	2.5D	microtubes	lattice mismatch	PLL	mPNs	IX
InAlGaAs	parylene C	2.5D	microtubes	lattice mismatch	PLL	mPNs	X
IP-DIP	Al_2O_3	3D	microscaffold	DLW	PDL + lam.	mPNs	XI
IP-DIP	Al_2O_3	3D	microscaffold	DLW	PLL + lam.	hiDNs	VII

neurons are generated within only a few weeks instead of months since time-consuming steps such as cell reprogramming and harvesting of neural rosettes are skipped. Still, culturing of the iPSC-derived cells remains to be both time-consuming and challenging. First of all, the hiNPCs have to be passaged every 4–6 days. Moreover, the differentiating cells also require a further reseeding step and need, in addition, various types of culturing media depending on the state of the differentiation. Since all cultivation stages are constantly running, depending on each other, and need to be conducted strictly to the protocols to maintain reproducibility and comparability of the trials, the planning as well as the coordination of experiments running in parallel can reach any level of complexity. For patch clamping, the hiGNs and hiDNs were the most difficult ones because stem cell differentiation never results in perfectly pure cultures of neurons and suitable cells must be selected by, e.g., morphology and size. Note, the hiGNs—only used in publication IV—were cultured in collaboration with the Fraunhofer Institute (IME/ITMP, Screening-Port) based on previously published work.[278–280] The initial cell culture including seeding onto the NW samples was conducted in the Fraunhofer laboratories. Afterward, the samples were transferred back to the Center for Hybrid Nanostructures (CHyN) for the final maturing and the experiments conducted. The hiDNs, however, were cultivated entirely in-house and the reproduction of the differentiation protocol was established specifically in the framework of this PhD thesis. In addition to the cells described above, human neurons differentiated from SH-SY5Y cells generated from a neuroblastoma were patched during the PhD period.[346] But since they were not applied to any micro- or nanostructured materials these cells are not further discussed. For the sake of completeness, the hiNPCs were in fact only used for, e.g., proliferation studies on the NW arrays but not for any patch clamp experiments since their immature differentiation state would not yet allow for expressing distinct features of neuronal functionality such as the firing of APs.[347]

The micro- or nanostructured cell culture substrates featured, on the one hand, different types of NW arrays with altered array pitches, NW lengths, and NW diameters, and, on the other hand, different topographical constraints such as trenches and 3D scaffolds to direct the cellular growth. The specific type of substrate is introduced in detail in the corresponding section. However, respective anticipatory tabular listings of the NWs arrays and scaffolds are compiled in Tables 3.2 and 3.3.

In the next subsection—before presenting any experiments on the micro- or nanostructured substrates—a more general patch clamp study, namely, a comparison of electrophysiological properties measured at both physiological and room temperature (RT) will be presented. One focus of this study was to test the custom-built temperature control. Hence, the measurements were conducted simply on regular glass coverslips.

3.0.1 Patch clamping at physiological temperatures (Publication I)

In general, patch clamping at just RT is a widely disseminated standard in the electrophysiology community.[348] However, RT does not represent the natural physiological body temperature of mammals of about 37 °C and literature is reporting repeatedly, for instance, on the temperature sensitivity of ligand- or voltage-gated ion channels.[349–351] Although the T cells, mPNs, and hiDNs used herein were, in fact, already successfully patch clamped at RT elsewhere,[277,352,353] a temperature control for the patch

clamp setup was developed to test for a potential benefit of an environment closer to a physiological one. In contrast to commercially available temperature controls, the custom-built device is rather affordable and also can easily be adapted to different setup configurations. After construction, the temperature controller was tested using T cells and hiDNs. Figure 3.2a displays an image of the microscope inset during a patch clamp procedure. The inset consists of a Peltier element, which creates a temperature gradient between two copper plates. A passive heatsink is attached to the bottom plate to dissipate the thermal energy generated from the Peltier element (either heat or cold). The upper plate holds a 35 mm Petri dish containing the cells. A temperature sensor is dipped into the bath solution to read the water temperature and a thin tube is adding fluid to replace evaporating bath solution during long-term experiments. Another temperature sensor is built into the upper copper plate. Two thermometers were installed since the built-in sensor responded faster to temperature changes because of direct thermal coupling and thus allowed for more precise temperature control. Nevertheless, the bath thermometer is required to calibrate the offset between the temperature of the plate and the actual temperature of the bath solution. The control electronics including the switches, potentiometers, and connectors to choose the heating/cooling mode, to set the temperature, and to connect the peripherals (power supply, Peltier element, thermometers) are mounted in a custom-made 3D-printed case (Figure 3.2b). Further details regarding the design, the operation modes, and the electrical circuit can be found in the OM.

The controller is designed to enable both heating and cooling of the platform. On the one hand, heating is of course required to reach physiological temperatures. On the other hand, cooling down of the cells can be used to slow down temperature-dependent processes that are too fast for standard detection methods and thus enables resolving recordings beyond the amplifier's time resolution.[354] The temperature controller was able to operate at temperatures from 15 °C to 60 °C (Figure 3.2c). The upper and lower limits were primarily defined by the utilized power supply, which delivered 3 A, and by the passive heatsink. If necessary, both limits could easily be extended by using a power supply that is able to deliver more current and/or applying a more efficient thermal coupling of the lower copper plate by, e.g., a water cooling system. Nevertheless, the employed components were by all means sufficient to reach physiological temperatures of about 37 °C. Eventually, the final experiments were conducted at 36 °C, which is close to the natural body temperatures but still offers a 1 °C safety zone to avoid pyrexia. Such temperature was reached in less than 5 minutes and stable within approx. ±0.25 °C (Figure 3.2d).
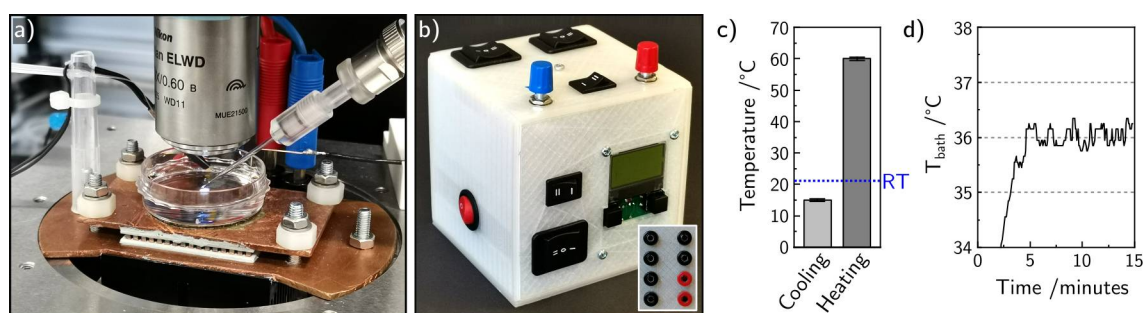

Figure 3.2 – **Patch clamp temperature control including controller and characterization of the cooling/heating capabilities.** **a)** Image of the temperature-controlled microscope inset for the patch clamp setup. A Peltier element is positioned between two copper plates to create a temperature gradient in between. The bottom plate is equipped with a passive heatsink to dissipate produced thermal energy. The upper plate holds the 35 mm Petri dish with the cells. A temperature sensor is dipped into the patch clamp solution and a thin tube is adding fluid to compensate for evaporation during long-term measurements. **b)** Case for the control electronics incl. switches, potentiometers, and connectors (inset) to choose the heating/cooling mode, to set the temperature, and to connect the power supply, the Peltier element, and the thermometers, respectively. **c)** Temperatures reached for cooling and heating, respectively. Error bar is ±0.25 °C. **d)** Exemplary trace of the temperature depending on the time with a set-point of 36 °C. The final temperature is reached without overshoot in less than five minutes and stable within approx. ±0.25 °C. Adapted from publication I.

The T cells and the hiDNs were tested for diverse electrophysiological characteristics such as the opening of voltage-gated ion channels and the capability to fire APs, respectively. Figure 3.3a displays an exemplary trace of APs recorded from a neuron at 36 °C in which the APs were stimulated by a small current injection to depolarize the cell above the threshold potential. Note, also at RT, the neurons were able to release APs. A direct comparison, however, of the maximal frequency and amplitude of the APs revealed that the mean maximal frequency of about 36 Hz at 36 °C was almost twice as high compared to RT (20 Hz) whereas the mean amplitude of the APs was reduced from 80.8 to 54.2 mV (Figure 3.3b). In general, these values are appropriate amplitudes for APs measured on human iPSC-derived neurons.[355,356] The higher AP frequency at 36 °C can be explained by faster gating sodium and potassium ion channels, which was described for other cells in the literature.[357,358] These ion channels form the crucial elements of the AP dynamics and a faster response allows for a more rapid sequence of depolarization and repolarization of the cell. That also explains the smaller amplitude of the APs since the compensating ion flux for repolarization begins earlier and the peak heights of the APs are lowered. The literature regarding the temperature dependency of APs is not consistent as for rodent neurons, for example, both temperature dependency as well as insensitivity were reported.[359,360] For the T cells, the gating potentials of the potassium ion channels were determined to be -22.7 mV at 36 °C and -24.4 mV at RT (Figure 3.3c). In general, such values are in accordance with the literature,[361] and a fundamental change with respect to an altered temperature was not expected since the channels are voltage-gated. Next, the membrane time constants (MTCs) and the membrane capacitances (MCs) were identified (Figure 3.3d and e). For the MTCs, an increase from 5.7 to 9.7 ms and from 21.5 to 29.3 ms for T cells and neurons, respectively, was observed. The MCs were basically not affected by the temperature, which is reasonable since no gating dynamics are involved. In fact, the capacitance primarily depends on the membrane area, which does not change with temperature.[362]

The temperature control for the patch clamp setup makes it possible to conduct the experiments at, for instance, physiological temperatures. However, the results with regard to the temperature-dependency were mixed, which is in a way consistent with the literature also reporting on inconsistent behavior of electrophysiological properties such as a two-way temperature correlation regarding firing frequencies of APs.[363] Hence, it is important to keep in mind that the comparison of absolute values should be done carefully if the patch clamp measurements were done at different temperatures. In any case, a direct comparison of biological studies is often virtually impossible anyways since identical cell culture protocols are rarely employed, especially, in the case of iPSC-derived cells. Thus, differences in electrophysiology should only be accentuated if they were at least measured at similar temperatures. Nevertheless, the patch clamp measurements presented in the following sections were all conducted at RT since concomitant difficulties outweighed potential advantages. The hypothetical benefits of establishing physiological temperatures during the patch clamp measurements were in no adequate relation to the effort required
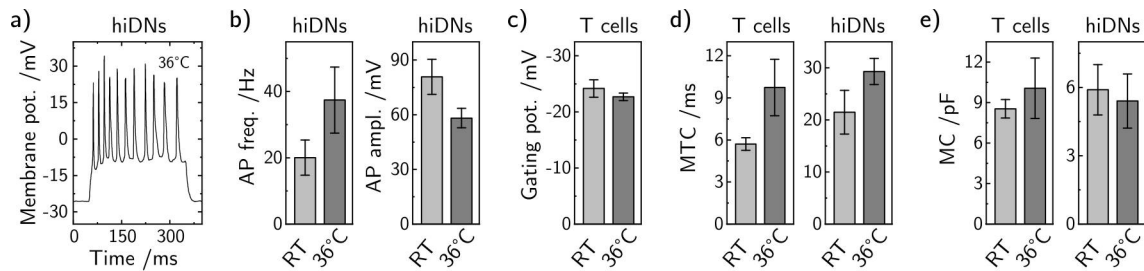

Figure 3.3 – Comparison of electrophysiological measurements on T cells and hiDNs at RT and 36 °C. a) Exemplary trace of APs recorded at 36 °C from a hiDN. b) Maximal frequency and amplitude of the AP trains reached at RT and 36 °C. c) Gating potentials of potassium ion channels of T cells at RT and 36 °C. d) Membrane capacitances (MCs) of T cells and hiDNs at RT and 36 °C. e) Membrane time constants (MTCs) of T cells and hiDNs at RT and 36 °C. The error bars are standard deviations (SDs). n = 7–11. Adapted from publication I.

to handle the additional susceptibility to noise, the need to compensate for increased evaporation of the bath fluid, and the thermal expansion-dependent shifts of the sample.[364] Thus, patch clamping of the cells on the micro- and nano-structured substrates at RT instead of physiological temperatures was considered appropriate. The next chapter presents the initial results of electrophysiologically intact T cells and mPNs cultured on ordered InP and randomly distributed ZnO NW arrays.

3.1 Studies using NW arrays

The herein presented studies on cells interfaced with NW arrays started with T cells and mPNs cultured on HD InP and ZnO NW arrays. During the course of the PhD studies, hiGNs and hiDNs were employed and the differentiation was tested on various types of NW arrays with varying characteristics, such as the array densities or the NW lengths and shapes.

Albeit cells cultured on NW arrays have been investigated in many ways—for example, in terms of viability, proliferation, or movement, to name a few—their electrophysiology has been examined rather rarely. One trivial reason might be that the patch clamp technique, although delivering unmatched high-quality data and in principle well-established, is not quite widespread among bio-laboratories, presumably, due to the high labor requirements, the complex experimental procedure, and the comparatively low screening throughput.[365] Even when patch clamp setups are available in well-appointed bio-institutes, so are these setups often installed in inverted configurations designed for regular transparent dishes. Consequently, such inverted setups are not suitable for inherently opaque substrates such as the NW arrays. By being restricted to upright-oriented patch clamp setups, the scarce options to conduct electrophysiological studies are further reduced, which is, as mentioned, reflected in the marginal number of patch clamp studies of cells cultured on NW arrays. Note, the setup used in this thesis was explicitly built by me for patch clamping cells on NW arrays (Master's thesis).[366] Another but yet important reason for the limited number of patch clamp studies in the field might be a fundamental restriction of applying the patch clamp technique to cells cultured on NW arrays. Specifically, the NW array's spiky character might substantially damage the cells during the sealing procedure. To remind the reader, attaching the patch pipette to the cell membrane goes along with inflicting a certain amount of unavoidable mechanical stress against the cell. For that reason, it was not clear in the beginning whether the spiky topography of the NW arrays might prevent successful patch clamping in the first place. The work presented here now shows that electrophysiological readout of cells cultured on NW arrays *via* patch clamping is feasible. Needless to say, however, the general patch clamp routine was rendered more difficult, for example, due to varying visibility of the cells depending on the array characteristics (e.g., HD arrays appear very dark) and—of course—the increased requirement to approach the cell with great care to prevent damages during establishing the gigaseal.

3.1.1 Intact electrophysiology of T cells and mPNs cultured on NW arrays   (Publication II)

In this section, the growth and electrophysiology of T cells and mPNs cultured on HD NW arrays with altering morphology were tested. Specifically, well-arranged InP NW arrays (Figure 3.4a) and randomly distributed ZnO NW arrays (Figure 3.4b) were used as cell culture substrates. The arranged growth of the InP wires was defined *via* nanoimprint lithography, which created hexagonal patterns of gold droplets to serve as catalysts during the epitaxial growth process.[367] The nanoimprint lithography not only allows for defining the diameter of the seed particles but also ensures a uniform size, which results in identical NW geometries, namely, length and diameter. Herein, the diameter was 180 nm, the length was 2 μm and the pitch was 500 nm. The ZnO NWs were fabricated in a self-catalytic and self-assembled epitaxial growth process resulting in a randomized arrangement with an average pitch of 300 nm with NW diameters of 70
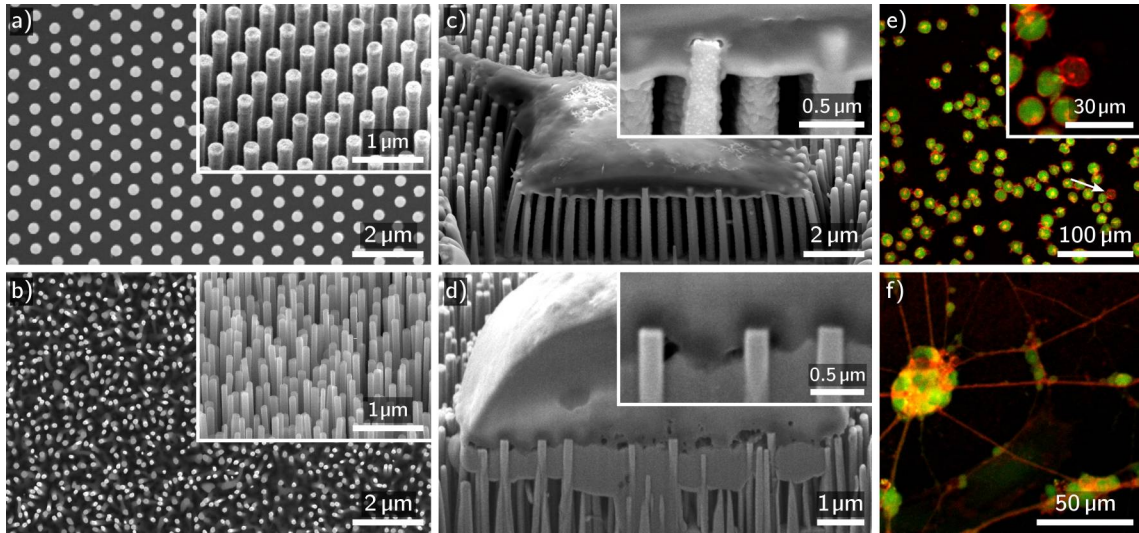
Figure 3.4 – **Imaging of T cells and mPNs cultured on NW arrays. a)** Top-view scanning electron microscopy (SEM) image of the ordered InP NW array. The pitch is 500 nm, the NW diameter is 180 nm, and the length is 2 µm. Inset: 40° tilt. **b)** Top-view SEM image of the randomly arranged ZnO NW array. The average pitch is about 300 nm, the NW diameters range from 70 to 180 nm, and the length is approx. 3 µm. Inset: 40° tilt. **c)** Cross-sectional SEM image of a neuron cultured on ordered InP NWs prepared with focused ion beam (FIB) milling. The cell is just in contact with the very NW tip. **d)** Cross-sectional SEM image of a T cell cultured on randomly arranged ZnO NWs prepared with FIB milling. The cell is just in contact with the very NW tip. **e)** Epifluorescence microscopy image of calcein (Ca)- (green) and membrane-stained (red) T cells cultured on ordered InP NWs. Inset: close-up of none Ca-labeled cell. **f)** Epifluorescence microscopy image of Ca- (green) and membrane-stained (red) neurons cultured on randomly arranged ZnO NWs. Adapted from publication II.

to 180 nm and slightly varying NW lengths (about 3 µm).[368] The utilized array pitches result in densities of more than 400 NWs/100 µm^2, which corresponds to a HD in the field.[55] The samples were passivated with Al_2O_3 to avoid the potential influence of the material of the NWs and to ensure biocompatibility.[369] Moreover, untreated ZnO was found to be chemically unstable during long-term culture at ph 7.4 of the cell culture medium, which is in accordance with the literature.[370]

The hybrid interface and cell viability were tested by cross-sectional scanning electron microscopy (SEM) imaging (Figure 3.4c,d) and fluorescent microscopy (Figure 3.4e,f), respectively. Details will be discussed below. To enhance the adhesion of the T cells and mPNs to the NW arrays, the samples were coated with PDL.[340] In addition, substrates used for the mPNs were also treated with laminin to promote neuronal growth.[371] The T cells adhered for about 15 min to the NW arrays whereas the mPNs were cultivated for 6–7 days on the NWs. Due to the HD character of the employed NW arrays, the cells were expected to grow in a fakir-like state on NWs.[51] Such a settling regime on a bed-of-nails was confirmed for both T cells and mPNs on the ordered InP and the random ZnO NWs arrays by cross-sectional SEM imaging prepared by focused ion beam (FIB) milling (examples in Figure 3.4c and d, others in the OM).[372] The insets with corresponding close-ups emphasized that only the very NW tips were in contact with the cells and heavy deformations of the membrane were absent. This type of cell/NW interface is in accordance with the literature where cells on HD NW arrays were inspected by cross-sectional imaging.[102,373] In a next step, viability assays of the cells cultured on both types of substrates were prepared in which all cells were labeled in red by an unspecific membrane strain and viable cells were then identified in green by using Ca (examples in Figure 3.4e,f, others in the OM). Ca labels only viable cells since only these still contain the esterases to transform the non-fluorescent acetomethoxy derivate of calcein (calcein-AM) into fluorescent Ca.[374] Note, Thermofisher just refers to a 'viability indicator' in their ready-to-use staining kit.[375] The proportion of viable cells was semi-manually determined using the cell counter plugin in ImageJ/Fiji.[376,377] The viability of the T cells was almost 100% on all types of substrates (Figure 3.5a). In general, high viability of cancer-cell lines is normal and thus the results are in

accordance with the literature.[378] Worth mentioning, determining the cell viability right after adhesion might have even further increased the proportion of viable cells because of the selective nature of the adhesion process in which necrotic cells and cell debris would not actively attach to the PDL-coated surface of the NWs. The viabilities of the neurons after one week of culturing were $65.4 \pm 4.5\%$ and $66.5 \pm 4.4\%$ on the NW substrates and $73.9 \pm 3.6\%$ and $72.9 \pm 6.2\%$ on the control substrates (Figure 3.5b). In general, such viabilities are in line with the literature.[342] The slightly reduced viability on the NW arrays can be explained by the challenging substrate topography. The type of HD NW array, however, does not play any role in cell viability.

The electrophysiological integrity of the cells cultured on the NW arrays was finally tested in terms of cell-specific ion channel activity/responses and basic membrane characteristics such as the resting membrane potential (RMP) and the MC. For T cells the gating properties of voltage-gated ion channels were tested by applying voltage ramps from -60 to $+10\,\mathrm{mV}$ with a slope of $80\,\mathrm{mV}/100\,\mathrm{ms}$ while measuring the ionic membrane currents through the cell membrane (Figure 3.5c). The increase of the ionic current at about $-30\,\mathrm{mV}$ originates from the gating of the voltage-gated ion channels, which significantly increases the conductivity of the membrane allowing for higher membrane currents. In general, no fundamental differences between the traces recorded on NW arrays and control samples were observed and thus state the equivalence of the substrates. Furthermore, such gating potentials are normal for Jurkat cells/human T lymphocytes and can be assigned to voltage-gated potassium channels.[361] The mPNs cultured on the NW arrays were tested for the capability to release APs to verify that the neurons are functional and able to process neuronal information. Here, equal quality of the NW substrates to culture the neurons was proven by recordings of AP trains during a current injection with amplitudes between 45 and $85\,\mathrm{mV}$ and firing rates of approx. $27\,\mathrm{Hz}$ (Figure 3.5d). Additionally, the measured values are in agreement with the literature.[379,380] For both cell types, also basic membrane parameters were determined (OM). For T cells measured on all types of substrates, the RMPs and MCs ranged from $-53.4 \pm 2.9\,\mathrm{mV}$ to $-56.6 \pm 8.9\,\mathrm{mV}$, and from $8.0 \pm 1.7\,\mathrm{pF}$ to $10.6 \pm 2.5\,\mathrm{pF}$, respectively (n = 5). For neurons, the RMPs and MCs were between $-55.9 \pm 7.2\,\mathrm{mV}$ and $-58.1 \pm 4.9\,\mathrm{mV}$, and $3.7 \pm 1.0\,\mathrm{pF}$ and $4.7 \pm 0.8\,\mathrm{pF}$ (n = 5). Within the groups, no statistically significant deviations were found, which demonstrates that the substrates have no critical impact on the cells and their growth (Welch's t-test with a 95% confidence interval). Also, these results match the literature.[379,381–385] To briefly conclude, the T cells and mPNs rested in a fakir-like state on the NW arrays only interacting with the very NW tips. For both cell types, no detrimental impact on the cell viability while being cultured on NWs was observed. Moreover, the patch clamp measurements
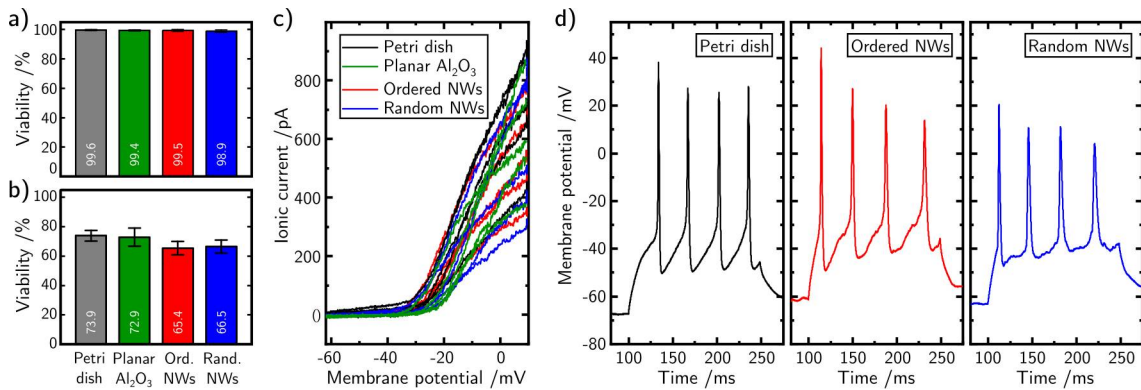

Figure 3.5 – **Viability and electrophysiology of T cells and mPNs cultured on NW arrays. a)** Bar chart of the viability of T cells cultured on NW and control substrates. **b)** Bar chart of the viability of neurons cultured on NW and control substrates. Error bars are SDs. **c)** Recordings of the membrane currents of T cells cultured on NW and control substrates during the application of voltage ramps from -60 to $+10\,\mathrm{mV}$ with a slope of $80\,\mathrm{mV}/100\,\mathrm{ms}$. The increase in current at about $-30\,\mathrm{mV}$ indicates the gating of the voltage-gated ion channels. **d)** Exemplary traces of APs recorded of neurons cultured on planar Al_2O_3 and NW substrates. The amplitudes of the APs were between 45 and $85\,\mathrm{mV}$ with firing rates of approx. $27\,\mathrm{Hz}$. n = 5. Adapted from publication II.

demonstrated that the electrophysiological parameters were maintained independent of an ordered or random arrangement of the NW arrays. Finally, the results also confirmed, that the patch clamp technique is a suitable tool to determine electrophysiological properties of cells on NW arrays despite applying some mechanical stress during the sealing procedure. This crucial outcome was then also the starting point for further studies.

In the following sections, cells derived from human iPSCs were employed for the studies. First, the results of culturing the hiNPCs on various types of NW arrays will be summarized. Subsequently, the analysis of the terminal differentiation of NPCs into hiGNs and hiDNs, respectively, while being cultivated on NW arrays with varying geometrical characteristics will be presented.

3.1.2 Proliferation and survival of hiNPCs cultured on NW arrays (Publication III)

The general feasibility to cultivate the hiNPCs on the NW arrays is a prerequisite for the overarching objective of a further differentiation of these cells toward functional neurons while being cultured on these substrates. For that reason, the proliferation and viability of the hiNPCs were investigated on various types of NW arrays. These NW arrays featured array pitches of 1, 3, 5, and 10 μm (P1, P3, P3, P10) combined with NW lengths of 1.5, 3, and 5 μm (L1.5, L3, L5) (Figure 3.6). The utilized pitches result in array densities of 100, 11.1, 4, and 1 NWs/100 μm², respectively. Both pitch and length encase array characteristics frequently used in the field.[55] Also, these parameters cover sufficiently diverse parameters to expect changing settling regimes from a fakir-like state to a complete encapsulation of the NWs. In the following paragraphs, a pitch of 1 μm is referred to as HD, the larger pitches are classified as low(er)-density (LD). The NWs were prepared in a top-down approach from plain silicon using RIE. The utilized chromium hard mask featured dots with a diameter of 700 nm and was defined by EBL. The NW lengths were controlled by the RIE time. The application of RIE to fabricate NW arrays has been reported before, but often only shorter NWs of about 1 μm were produced.[386] Usually, longer NWs are prepared in a multi-step deep RIE (DRIE) process.[387,388]

The proliferation and viability of the hiNPCs cultured on the NW arrays were assessed by quantifying the number of viable cells right after adhesion (after about 1 h, referred to as 0 days *in vitro* (DIV)) and the following four consecutive days (1–4 DIV). The cells were identified using cell-permeant Hoechst 33342, which labels the deoxyribonucleic acid (DNA) in the cell's nucleus (examples of 0 and 4 DIV in Figure 3.7a and b). Additionally, viable and dead cells were indicated using Ca (green) and propidium iodide (PI) (red), respectively (Figure 3.7c, example of 4 DIV). Similar to Hoechst, PI also binds to the DNA but it is not permeant to viable cells and thus only stains dead cells. Using the 'CellProfiler' software,[389] cells were initially identified using the Hoechst channel and sorted into viable and dead cells by reading the Ca and PI channels. The numbers of viable cells were determined 0–4 DIV for all types of NW arrays and compared to planar controls (0, 3, and 4 DIV in Figure 3.7d, 1 and
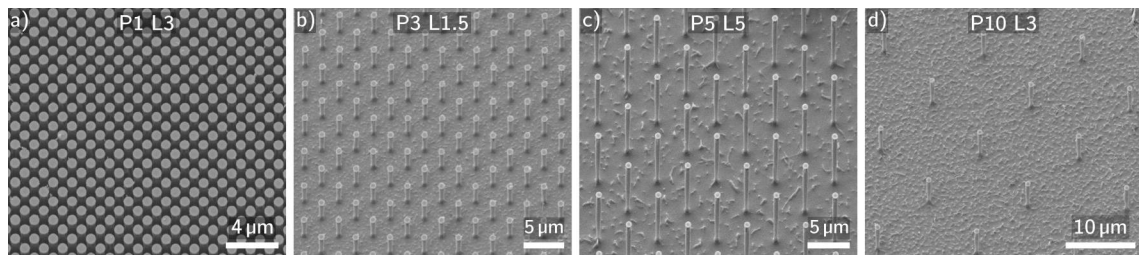

Figure 3.6 – Exemplary SEM images of Si NW arrays used for the hiNPC cell culture. The NW arrays with array pitches (P) of 1, 3, 5, and 10 μm and NW lengths (L) of 1.5, 3, and 5 μm were produced in a top-down approach using RIE. The utilized pitches result in array densities of 100, 11.1, 4, and 1 NWs/100 μm², respectively. **a)** Pitch of 1 μm and length of 3 μm. **b)** Pitch of 3 μm and length of 1.5 μm. **c)** Pitch of 5 μm and length of 5 μm. **d)** Pitch of 10 μm and length of 3 μm. Adapted from publication III.
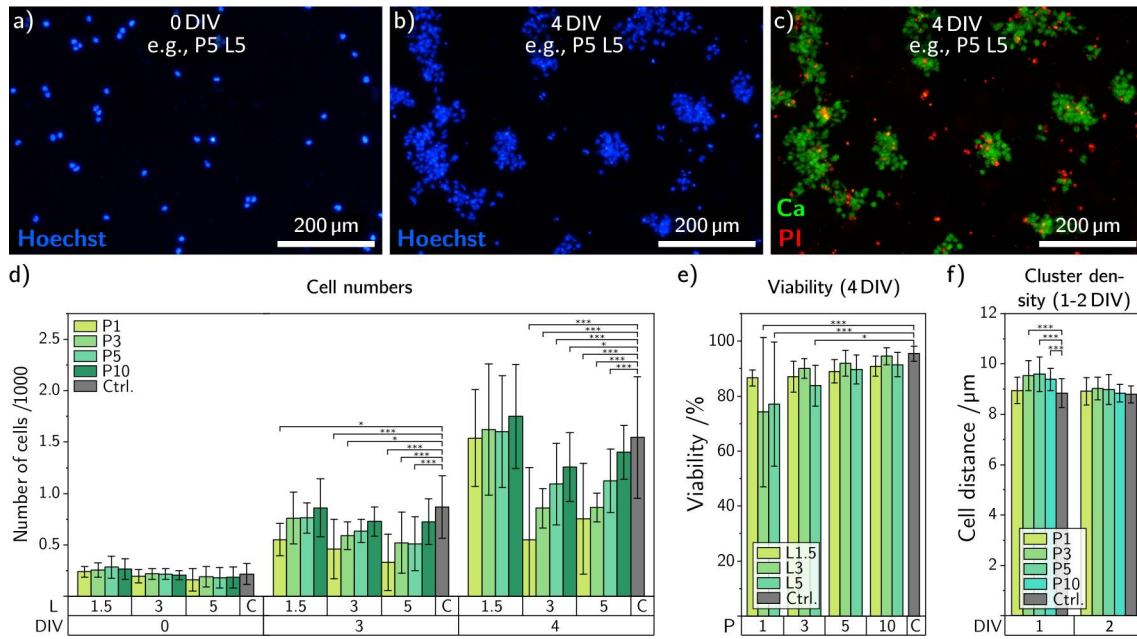
Figure 3.7 – **Proliferation and viability of hiNPCs on altered NW arrays. a, b)** Exemplary micrographs of Hoechst-stained hiNPCs (blue) cultured on NW arrays imaged directly after adhesion (0 DIV) and 4 DIV, respectively. **c)** Exemplary merged micrograph of Ca- (green) and propidium iodide (PI)-stained (red) hiNPCs cultured on NW arrays imaged after 4 DIV. **d)** Number of viable cells cultured on NW arrays and controls from 0, 3, and 4 DIV. **e)** Viability of cells cultured on NW arrays after 4 DIV. **f)** Cluster density of cells cultured on NW arrays after 1 and 2 DIV. n(images) ≥ 15. Control: Si. Error bars are SDs. Indicated significances were calculated using an ANOVA analysis with post-hoc Tukey's test and labeled as follows: *$\alpha = 0.05$, **$\alpha = 0.01$, ***$\alpha = 0.001$. Adapted from publication III.

2 DIV in the OM, control was plain silicon being equal to glass (SI)). Three basic statements could be made based on the results. First, L1.5 NW arrays had no influence on the cell numbers after 4 DIV. Second, there was scarcely a difference between L3 and L5 samples. Third, with increasing array density in the case of the L3 and L5 NWs, the number of cells decreased. The first and the second observation were consistent in themselves, but the third one raised some questions after closer inspection: For LD NW arrays (P≥3), i.e., encapsulating regimes, the results were reasonable since more indentations per cell were induced with increasing array density. The higher number of indentations went along with a larger impact on the proliferation—a phenomenon, which is in accordance with the literature.[70,75,390] For the HD NW arrays (P1), however, i.e., the fakir-like regime, the reduced cell numbers were contra-intuitive since cells in a fakir-like would not be influenced by any indentations. Moreover, this is, for example, also in direct contrast to other work showing that HD arrays can even enhance the proliferation of murine neural stem cells.[155] To highlight another contradiction, the L1.5 P1 samples showed normal cell numbers, which means that within the P1 group of samples, the NW lengths had a decisive impact. The perceived inconsistencies were attributed to particular interactions between the cells and the NW arrays, which were further elaborated by SEM and confocal laser scanning microscopy (CLSM) presented in the next paragraph. Nevertheless, more data were extracted from the Hoechst/Ca/PI images and are discussed first. The cell viability was tracked also on five consecutive days and the final viability after 4 DIV is presented in Figure 3.7e. In general, viabilities of more than 85% were observed and only dropped below 80% for the HD NW arrays (P1 L3 and P1 L5) in which case also reduced proliferation was found. A neglectable influence of the NWs on the viability is overall in agreement with the literature.[53,62,391–393] However, universal conclusions were difficult to draw since factors such as cell type, culturing time, NW length, or array pitch sometimes play decisive roles. For instance, Bonde *et al.* showed that HEK293 cells showed lower viability when cultured on NW arrays in settling regimes in which the NWs were partly or fully encapsulated by the cell.[71] Yet in fakir-like settling states, viability should not be affected.[394] As mentioned before, this case will be inspected in more detail later. The spreading and movement of the

cells on the NW arrays were investigated by determining the distances between individual cells. First, a *density-based spatial clustering of applications with noise* (DBSCAN) algorithm was used to determine the proportion of cells in cell clusters (OM).[395] The proportion of cells belonging to clusters increased from about 25% to 75% within one day and plateaued at about 90% after 4 DIV. In general, clusters are formed by movement and cell division. Since the cell numbers hardly increased between 0 and 1 DIV, initial clusters were predominantly caused by migration. In the proportion of cells in clusters, however, no differences were found. In contrast, the quantification of the distances between individual cells in clusters using ImageJ/Fiji showed that the average distance was slightly yet significantly larger on LD arrays than on HD arrays and control after 1 DIV (Figure 3.7f). This observation allowed for the conclusion that migration was hindered at low array densities, which is also reported in the literature.[75,153,396,397] Normal movement on HD NW arrays is in accordance with the literature as well.[74,398] The differences disappeared the day after since proliferation started to outplay migration. Next, the inconsistent cell numbers on the HD NW arrays (P1) were further investigated by characterizing the cell/NW interface.

The interaction between the cells and the NWs was analyzed by additional imaging to address the remaining open question of the reduced proliferation on the HD NW arrays. Initially, the samples were examined *via* SEM imaging, which showed that hiNPCs cultured on P1 NW arrays repeatedly formed narrow extensions along the array axes while growing in a fakir-like state (Figure 3.8a–c). Note, the elongations appeared independent of the NW lengths. In a next step, staining of *f-actin* with phalloidin revealed that these extrusions were part of the cytoskeleton (Figure 3.8d). The ability of well-ordered NW arrays to generate guiding forces to polarize cells or to direct neurite growth is described in the literature.[91,93–96,98,172,399] In these publications, several parameters were tuned, but in the end, the array pitch was found to be decisive whereas guiding occurs only in between two thresholds: for extremely small pitches, cells consider the surface homogeneous without any directing forces; for substantially large pitches, the cells are not able to reach the next NW and thus guiding is also not possible. Despite
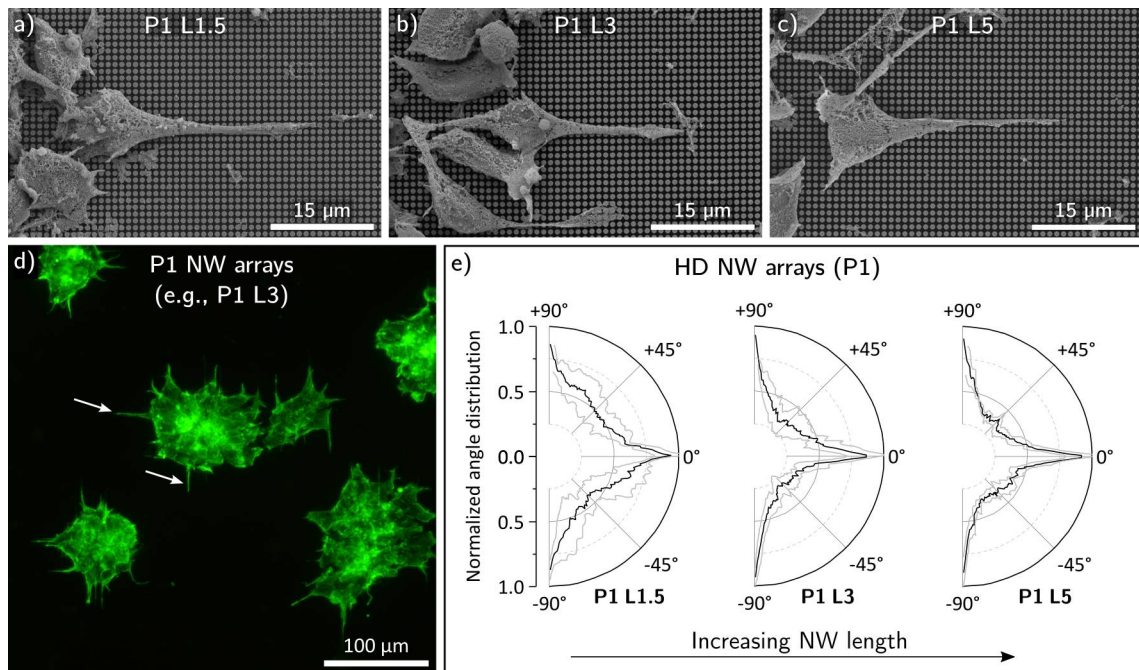

Figure 3.8 – **Alignment of the cytoskeleton along the NW axes of HD NW arrays (P1). a–c)** Exemplary SEM images of a hiNPC with elongation along a NW axis using P1 L1.5, P1 L3, and P1 L5 NW arrays. **d)** Exemplary epifluorescence microscopy image of cells cultured on HD NW arrays with the cytoskeleton stained by phalloidin (green). The arrows point to examples of the elongations. **e)** Quantification of the angular orientations of the elongations formed by cells cultured on HD NW arrays sorted by lengths (L1.5, L3, and L5). The gray lines indicate the SDs. The peaks at ±90° and 0° were less distinct for L1.5 NW arrays. Adapted from publication III.

many studies reporting this phenomenon, a direct comparison of the threshold values, however, was only possible with Bucaro *et al.* as they at least used comparable array pitches (0.8 to 5 µm with fixed 5 µm length). They determined a window for guiding from 1.25 µm to 3.5 µm, which is in contrast with the results found here, i.e., guiding at a pitch of 1 µm. Anyhow, the impact on, for instance, proliferation and viability, was not tested in Bucaro *et al.* but the potential need for such studies was explicitly mentioned. The findings here suggested, that the reorganization of the cytoskeleton also changed the normal cell dynamics and interfered with regular proliferation.[400,401] So far, the mere visual inspection of the SEM and phalloidin images did not explain the normal cell numbers on L1.5 P1 samples since the elongations were found in all three types of P1 NW arrays. A difference between the P1 samples was found, however, by comparing the normalized angle distributions of the elongations determined with the OrientationJ plugin ImageJ/Fiji (Figure 3.8e). All samples showed indeed clear peaks at 0 and ±90° corresponding to the array axes but for the L1.5 samples, the minima were less distinct of about 0.5 compared to approx. 0.25 for the longer NWs (L3, L5). Hence, the guiding forces on arrays with the shortest NWs must have been less. To detect potential differences in the interaction of the cells with the NWs, high-resolution 3D images were reconstructed from z-stacks prepared by CLSM (Figure 3.9a and b, green: cytoskeleton/phalloidin, red: nuclei/DRAQ5, purple: NW tips). Note, the main panels show the
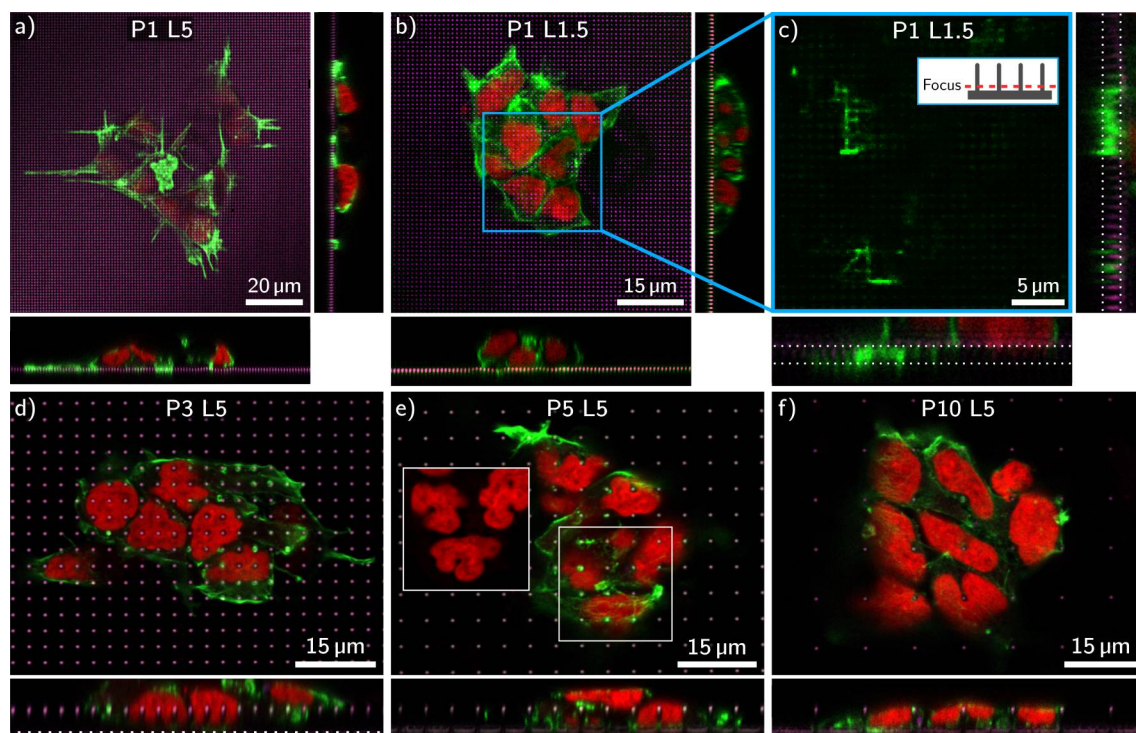
Figure 3.9 – **CLSM imaging of the cytoskeleton for determining the settling states.** The cytoskeleton/*f-actin* was stained with phalloidin (green), the nuclei were labeled with DRAQ5 (red), and the reflections of the NW tips appeared in purple. Note, the nuclei were stained with DRAQ5 (ex/em 647/681 nm) merely because the confocal microscope does not support ultraviolet (UV) excitation required for Hoechst. **a)** Exemplary image of a cell cluster cultured on HD NW arrays with long wires with focus on the NW tips. Main panel: top view. Adherent panels: cross sections along the NW tips. The cells were just in contact with the NW tips. **b)** Exemplary image of a cell cluster cultured on HD NW arrays with short wires with focus on the NW tips. Main panel: top view. Adherent panels: cross sections along the NW tips. The cells rested on the NW tips but the same image area with the focus on the NW bottom (panel **c)**) showed that the cells also interacted with the substrate bottom. The cross sections were positioned between the NWs and the positions of the NW tips and the substrate bottom were indicated with dashed lines. **d)** Exemplary image of a cell cluster cultured on NW arrays with a pitch of 3 µm and 5 µm long wires with focus on the NW tips. The NWs were partly encapsulated and the nuclei were poked multiple times. **e)** Exemplary image of a cell cluster cultured on NW arrays with a pitch of 5 µm and 5 µm long wires with focus on the NW tips. The NWs were completely encapsulated and the nuclei were deeply indented by the NWs or squeezed/deformed (inset). **f)** Exemplary image of a cell cluster cultured on NW arrays with a pitch of 10 µm and 5 µm long wires with focus on the NW tips. Even though the nuclei would smoothly fit between the NWs, still some nuclei were severely indented. Adapted from publication III.

x-y plane with the focus on the NW tips and the attached panels display the corresponding cross sections along the rows of NWs. Initially, the cross sections along the NWs drew a similar picture of a fakir-like state for the cells cultured on P1 NW arrays with either long (shown here: L5) or short (L1.5) NWs. However, when focused on the substrate bottom it became clear that for L1.5 NWs the cells were also in contact with the bottom (Figure 3.9c). The cross sections now prepared *between* the NWs emphasized that part of the cytoskeleton was between the NWs (side panels of Figure 3.9c). Worth mentioning, the position of the tips was indicated by the dotted line since they do not appear when focused between the NWs. To emphasize the results, the proliferation on the P1 NW arrays was normal since the cells rested in a mixed state on the arrays responsible for a less prominent alignment of the cytoskeleton, i.e., less auxiliary stress. Finally, the cells were also imaged on all the other types of substrates and particularly impressive configurations, namely, P3 L5, P5 L5, and P10 L5 samples, in which the cells underwent heavy deformations (Figure 3.9d–f). Specifically, for a pitch of 3 μm, the cells settled in an intermediate state on the NWs partly encapsulating the nanostructures (Figure 3.9d). Noteworthy, each of the nuclei was impaled by multiple NWs. Using a pitch of 5 μm, the NWs were completely encapsulated and also the nuclei were deeply indented. Moreover, the nuclei were squeezed and deformed by the NWs as shown in the inset only containing the DRAQ5 color channel (Figure 3.9e). Even with a pitch of 10 μm, some nuclei were indented although the nuclei would have smoothly fit between the NWs (Figure 3.9f). A strong interaction between the nucleus and the NWs was described before.[70,402,403] For shorter wires, similar effects were observed but the deformations were less distinct (OM). The general trends of the hiNPCs favoring a fakir-like settling state for small array pitches and long NWs as well as preferring NW encapsulation for large array pitches and short NWs are in good agreement with the literature.[51,74,95] Concludingly, it is remarkable that the hiNPCs overall maintained their viability—particularly on samples containing the longest NWs (L5). Moreover, the strong interaction of the NW and the nucleus might offer the opportunity to use the NW substrates prospectively for future applications such as gene transfection or biomolecule delivery.[102,107,404]

Next, the differentiation of hiNPCs into functional neurons while being cultured on multiple types of NW arrays was investigated. Initially, the neuronal differentiation was tested on several types of NW arrays featuring only short NWs (about 1 μm) in order to start with rather conservative NW array topographies. In the following section, the generation of hiGNs from hiNPCs cultured on short Si_3N_4 NW arrays was tested and is presented in the next section.

3.1.3 Interfacing hiGNs with silicon nitride NW arrays (Publication IV)

The differentiation toward hiGNs was tested on multiple types of Si_3N_4 NW arrays (Figure 3.10a–e). Specifically, two different densities of approx. 31 NWs/100 μm² (HD) and 6 NWs/100 μm² (LD), a NW length of 1.2 μm, and altering array arrangements featuring random, hexagonal, and rectangular patterns were used. The NW arrays were prepared using RIE similar to the previous chapter. The mask of random arrays was prepared in a de-wetting process of a thin gold film deposited by sputtering. The ordered arrays were defined with EBL. The differentiation of the hiNPCs into hiGNs was initiated in conventional multi well-plates and the cells were cultured like that for two weeks. The pre-differentiated cells were detached and transferred to the NW sample in order to mature for another two weeks—thus four weeks of differentiation in total—until imaging and measurements were conducted. To remind the reader, the cell culture was started in the Fraunhofer Institute (IME/ITMP, ScreeningPort) and the samples/cells were transferred back to the CHyN a few days before the experiments. Note, the glutamatergic phenotype of the culturing protocol was verified in the Fraunhofer Institute from control samples using quantitative real-time polymerase chain reaction (qRT-PCR) showing an up-regulation of genes of the glutamatergic system, e.g., GRIN1 (glutamate ionotropic receptor N-methyl-D-aspartate type subunit 1) (OM).
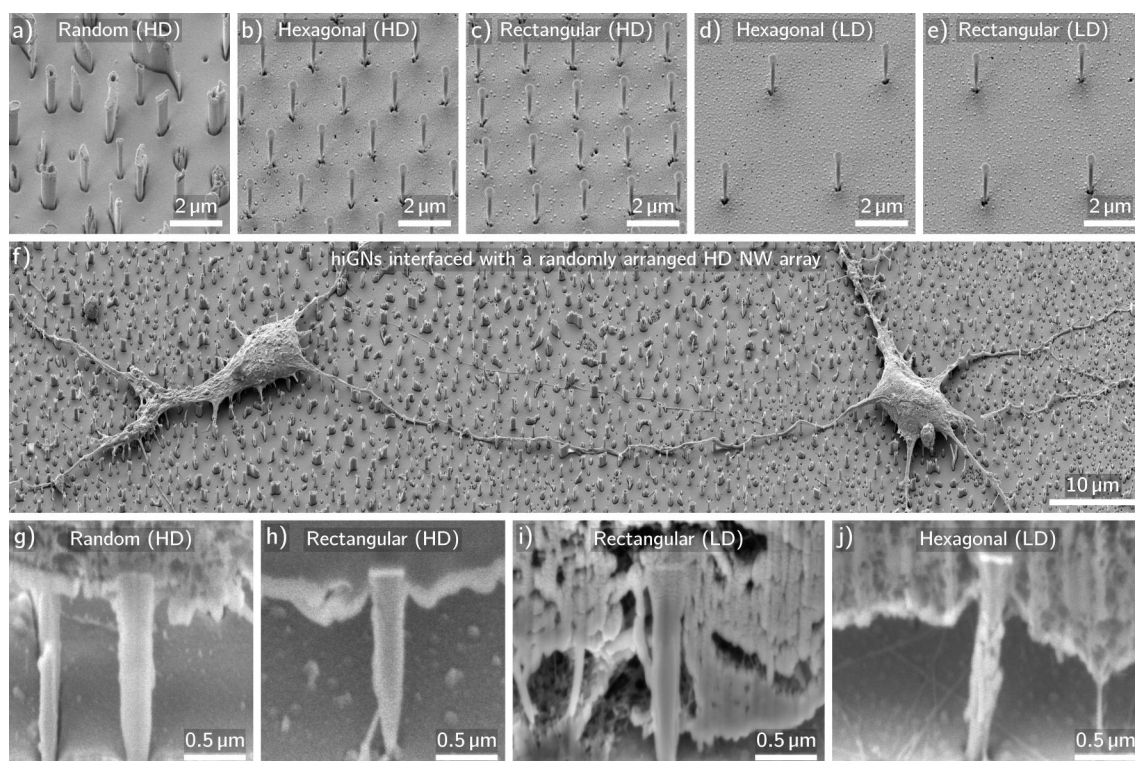
Figure 3.10 – **SEM images of the utilized Si_3N_4 NW arrays and the cell/NW interface prepared by FIB milling. a–e)** SEM images of Si_3N_4 NW arrays with random, hexagonal, and rectangular arrangements with array densities of about $31\,NWs/100\,\mu m^2$ (HD) and $6\,NWs/100\,\mu m^2$ (LD). The pitches of the ordered arrays were 1.8 and $4\,\mu m$, respectively. The NW lengths were approx. $1.2\,\mu m$. Tilt was 45° (corrected). **f)** Exemplary SEM image of hiGNs cultured on random Si_3N_4 NW arrays. Tilt was 45° (corrected). Not published. **g–j)** Exemplary cross-sectional SEM images prepared by FIB milling. Using HD NW arrays, the cell rested on the NW tips and with LDs, the NWs were either completely or partly encapsulated by the cell (others: OM). Tilt was 54° (corrected). Adapted from publication IV.

The neuronal growth and the settling regimes were investigated by SEM (example in Figure 3.10f), CLSM (OM), and cross sections prepared by FIB milling (Figure 3.10g–j). Specifically, exemplary cross sections of random, rectangular, and hexagonal arrangements at HD and LD are shown (others in the OM). In the case of HD arrays, the cells rested in a fakir-like state in the NW tips (panels g and h) whereas, for LD arrays, the NWs were entirely or partly encapsulated (panels i and j). The respective settling states were reconfirmed with CLSM (OM). Both regimes of a fakir-like state and NW encapsulation for HD and LD NW arrays match the literature.[52,402,405] In addition, guiding of the neurites was observed by CLSM when the ordered HD NW arrays, which has been reported in other work as well.[94,172,406] Next, the viability of the cells was tested by Ca and PI staining and the results confirmed that the viability of the neurons is maintained compared to planar control after two weeks of culturing on the NW arrays (OM). Unimpaired viability is in good agreement with the previous results and the literature.[71]

The electrophysiology of the hiGNs was tested on all types of NW arrays by the patch clamp technique (Figure 3.11a). Here, the neurons showed excellent firing of APs proving not only the functionality of the neurons but also the mature state (Figure 3.11b). Note, immature neurons, i.e., neurons in an early stage of neuronal development would either be incapable to fire APs or only release single spikes.[407] The overall mean height of the APs was $93.6 \pm 14.3\,mV$ (Figure 3.11c) and showed no statistically significant variations to the controls (ANOVA with post-hoc Tukey's test). Such amplitudes of the APs correspond to a notably distinct characteristic of the spikes compared to the literature.[277,280,284,355,356,408,409] In a next step, the accurate interplay of the sodium and the potassium ion channels was confirmed by measurements of the membrane currents, which showed the characteristic early-inward currents (negative peaks) and late-outward currents (positive, constant), respectively (Figure 3.11d, here HD/LD hexagonal, others in the OM).[279] Basic electrophysiological parameters such as the RMP, MC, input
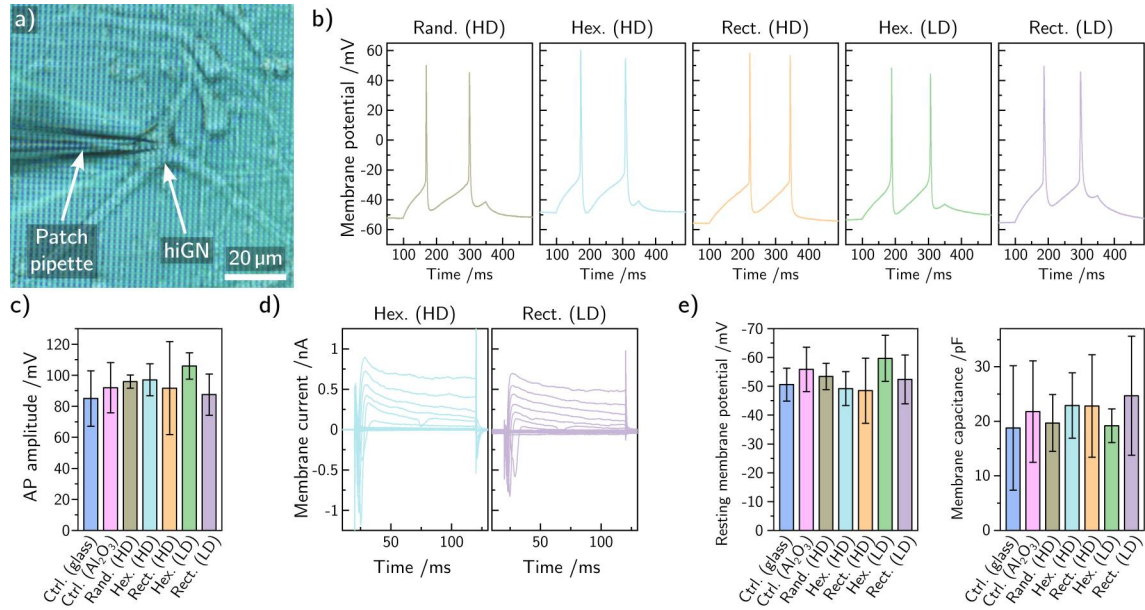
Figure 3.11 – **Electrophysiology of hiGNs cultured on Si₃N₄ NW arrays. a)** Exemplary bright-field image of the patch clamping procedure taken with the patch clamp microscope. **b)** Exemplary traces of APs recorded on control and different NW arrays (controls in the OM). **c)** Quantification of the AP heights recorded on controls and NW arrays measured peak to peak. **d)** Exemplary traces of early-inward (negative peaks, sodium) and late-outward (positive, potassium) currents recorded on HD and LD NW arrays (hex. and rect. arrangement, respectively, others: OM). Voltage steps from -70 mV to $+30$ mV were applied. Others in the OM. **e)** Bar charts of RMPs and MCs recorded on controls and NW arrays. Error bars are SDs. No statistical significances were determined (ANOVA with post-hoc Tukey's test, $\alpha = 0.05$). n = 6–9. Adapted from publication IV.

resistance (IR), and MTC were determined, which revealed no statistically significant deviations between control and NW substrates (Figure 3.11e, IR and MTC in the OM). Since no deviations were found only the overall means are compared to the literature: The RMPs were normal to above-average for mature neurons (-52.8 ± 7.4 mV).[277,280,355,356,409,410] The MCs were in average 21.4 ± 7.9 pF and comparable to other studies.[277,284,356,410] From similar MCs one also can conclude that the cellular outgrowth is equal since the capacitance directly scales with the surface area of the membrane.[411] The average IRs of 1.9 ± 0.7 GΩ were appropriate,[280,284,355,356,409] and the same applied for the MTCs of 42.2 ± 12.2 ms.[412,413]

In summary, the electrophysiological characterization stated an excellent condition of the hiGNs and emphasizes that the differentiation is robust toward the substrate's topography. This work resembles a crucial step for employing human iPSC-derived dopaminergic neurons in future studies with functionalized NWs arrays. In the next two sections, the differentiation into a different type of human iPSC-derived neurons was tested with various types of NW arrays in order to extend the versatility of potential applications in stem cell research. Specifically, the respective protocol generates predominantly dopaminergic instead of glutamatergic neurons and the neuronal differentiation was first examined using short spiky Si NW arrays.

3.1.4 Robust differentiation toward hiDNs on spiky silicon NW arrays   (Publication V)

The generation of hiDNs was tested here on spiky Si NW arrays (Figure 3.12a). The NWs were fabricated using a self-assembled growth process, which caused a random distribution and a random angle orientation.[319,414] The average NW length was about 1 µm and the NWs featured a gradually tapered shape with a narrow tip of approx. 30 nm. The array density was about 600 NWs/100 µm². This value corresponds to a very high NW density compared to the other NW substrates used in this manuscript and the NW arrays used in the field.[51] Initially, the neuronal outgrowth was inspected *via* SEM (Figure 3.12b). The observed formation of a distinct neuronal network on the NWs and the growth in both single cells
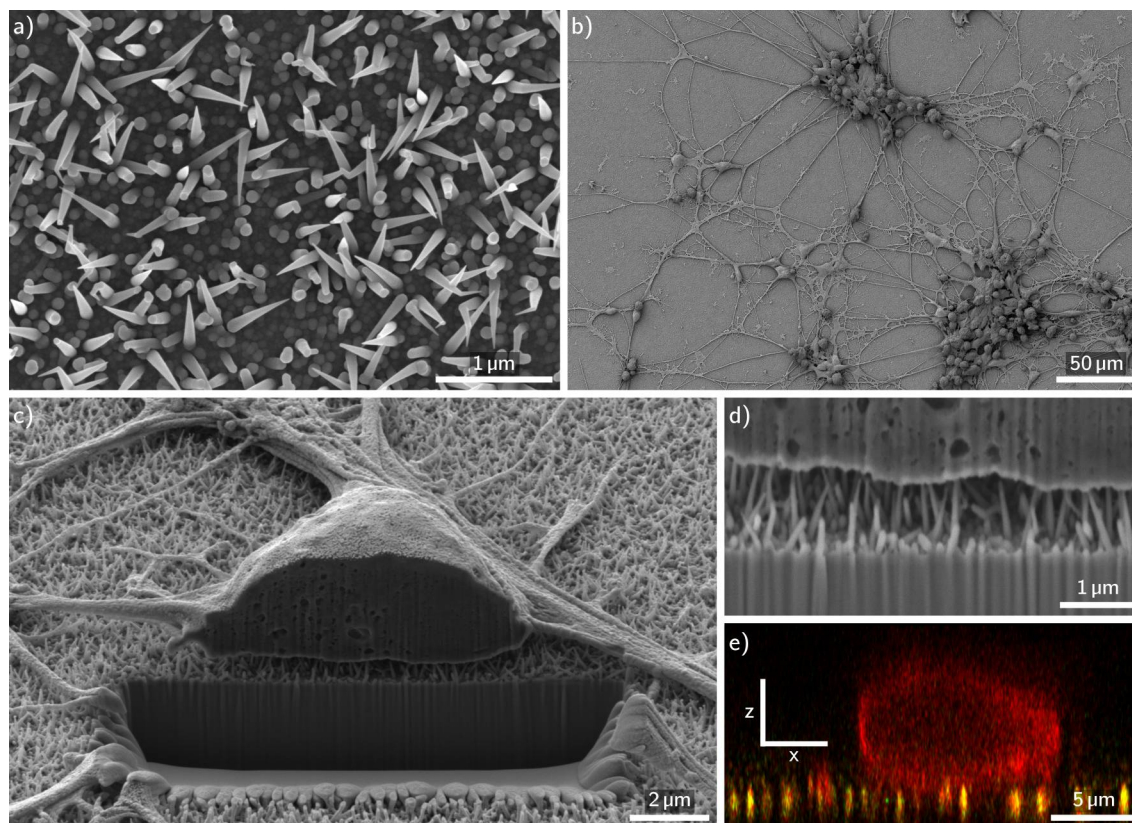
Figure 3.12 – **Images of hiDNs cultured on spiky Si NWs. a)** Top-view SEM image of spiky Si NWs. The average length is about 1 µm and the density is approx. 600 NWs/100 µm². **b)** Top-view SEM image of neurons cultured on the spiky NWs. **c)** Cross-sectional SEM image prepared *via* FIB milling. Tilt is 54°. **d)** Close-up view of the NW/cell interface also shown in panel c. The cell was hovering about 1 µm—the NW length—above the bottom of the substrate. Tilt is 54° (corrected). **e)** Cross-sectional CLSM image of a cell (membrane: red) cultured on NWs (yellow). The cell membrane was in close contact with the NWs. Adapted from publication V.

and cell clusters with multiple neurites per cell is comparable to other studies.[68,394] Cross-sectional SEM imaging prepared with FIB milling revealed that the cells rest in a fakir-like state on the NW arrays (Figure 3.12c). Note, the cell hovered about 1 µm—the length of the NWs—above the substrate's bottom and was only in contact with the very NW tips (Figure 3.12d). This type of interaction is similar to other reports using HD NW arrays.[373] CLSM confirmed the close contact between the cell membrane (red) and the NWs (yellow) (Figure 3.12e). The close contact between the cell and the NWs in combination with the conical shape of the NWs potentially facilitates in future experiments the delivery of biological payloads or cell transfection, which has been demonstrated in the literature already using basic cell lines or MSCs.[104,112]

Immunofluorescence microscopy was used to study the cellular outgrowth on the NW substrates in terms of proliferation, viability, spreading, and neuronal differentiation (Figure 3.13). Note, the differentiation was—similarly to the previous section—initiated in regular multi-well plates but here only for six days. Then, the cells were transferred to the NW arrays for further maturing of the neurons (additional 15 DIV). This reseeding procedure is a regular step in the original protocol.[277] To track the development of the cell culture, the samples were fixed 1, 7, 11, and 15 DIV after seeding onto the NW arrays for subsequent imaging. First, the nuclei were labeled with Hoechst (Figure 3.13a and b, examples of 1 and 15 DIV). Visual inspection of the images revealed that with culturing time the substrates were covered more densely with cells. The cell numbers were then determined from the Hoechst-stained images using CellProfiler showing that the initial cell number (about 500 cells per analyzed image) quadrupled to approx. 2000 cells within 11 days at which a plateau was reached (Figure 3.13c). The increase of cell numbers was to be expected since the differentiation from proliferating hiNPCs to post-mitotic neurons
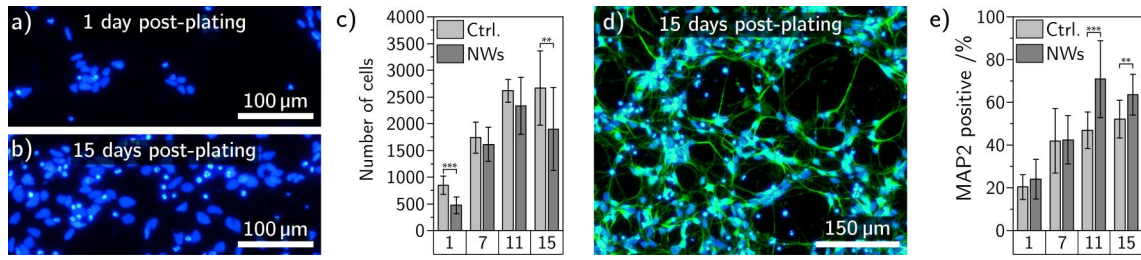
Figure 3.13 – Immunofluorescence microscopy of hiDNs cultured on spiky Si NWs and quantification of the differentiation efficiency. a, b) Hoechst-stained nuclei of neurons cultured on Si NWs 1 and 15 days post-plating. **c)** Quantification of the cell numbers 1, 7, 11, and 15 days post-plating on NW substrates compared to planar control (glass). **d)** Microtubule-associated protein 2 (MAP2)-stained neurons (green) with Hoechst counterstain (blue) cultured on Si NWs 15 days post-plating. **e)** Quantification of microtubule-associated protein 2 (MAP2)-positive cells cultured on Si NWs 1, 7, 11, and 15 days post-plating compared to planar control. Error bars are the standard deviations Indicated significances were calculated using a Mann-Whitney U test and P values were labeled as follows: *P = 0.05, **P = 0.01, ***P = 0.001. Adapted from publication V.

is a gradual process that requires time to develop. Notably, the final cell numbers on the NWs were in mean smaller (about 2000 vs. 2500 cells). In general, reduced cell numbers on NW arrays are in accordance with the literature reporting on reduced proliferation on HD NW arrays.[73] The analysis of the cell colonies revealed that the proportion of single cells, which do not belong to clusters was significantly increased on the NW arrays (e.g., 35% vs. 13% one day post-plating, OM). Since cell movement is one reason for cluster formation the larger amount of single cells on the NW arrays implied that the cell movement was impaired by the NWs. Reduced cell mobility on NW arrays has been reported before.[75] The cell viability of about 55% was maintained on the NWs, which is also in accordance with the literature in which densely spaced NW arrays had no detrimental impact on the cell viability.[71] The differentiation yields were determined by ICC using microtubule-associated protein 2 (MAP2) antibodies to label neuron-specific cytoskeletal proteins (Figure 3.13d). Quantification of the MAP2-positive cells 1, 7, 11, and 15 days post-plating showed, that the proportion of neurons increased from about 20% to up to 60% (Figure 3.13e). Remarkably, the yield of the neuronal differentiation was higher after 11 and 15 DIV when cultured on NW substrates compared to planar control (about 50%). A potential reason for the higher percentage in neurons on the NW arrays is the slightly reduced proliferation of the remaining hiNPCs, i.e., the generation of new undifferentiated cells. To emphasize, the NW arrays not only represented an equivalent growth substrate but also had a supportive effect on increasing the proportion of differentiated cells. The assertive influence of NW arrays on cell differentiation has been described before, for example, with human embryonic stem cells toward definitive endoderm or neuron-like differentiation of mesenchymal stem cells.[153,154] The quality of the NW substrates being employed for neuronal differentiation was moreover reflected in the similar neurite lengths of about 80 μm per cell (SI). The formation of focal adhesions was comparable to the controls (SI), which is in agreement with the literature showing no influence in the case of HD NW arrays.[74]

The electrophysiological state of the hiDNs was examined using the patch clamp technique (Figure 3.14). Basic parameters such as the RMP and MC of neurons cultured on the NW arrays were -51 ± 6.1 mV and 11.1 ± 4.7 pF, respectively, comparable to the control and to other human iPSC-derived neurons (OM).[277,356,409] Proper interplay of the sodium and potassium ion channels was confirmed by adequate early-inward and late-outward currents (Figure 3.14a). The corresponding peak currents normalized to the MCs plotted against the applied voltage of the voltage steps showed dependencies similar to control and literature.[277,415] Functionality of the neurons was testified by measurements of APs showing trains of spikes (Figure 3.14c). Analysis of the kinetics of the APs approves similar characteristics compared to the control and literature (Figure 3.14d).[280,355,409,412,416] Specifically, the AP amplitude was 67.0 ± 8.6 mV, the AP threshold was -20.4 ± 4.0 mV, the afterhyperpolarization (AHP) was 15.1 ± 5.9 mV, and the AP duration was 3.3 ± 0.8 ms.
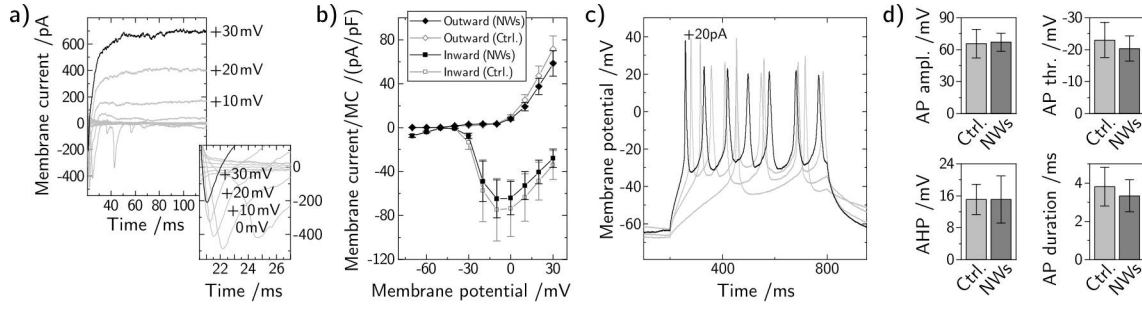
Figure 3.14 – Electrophysiological analysis of hiDNs cultured on spiky Si NWs. a) Exemplary traces of early-inward and late-outward currents recorded on neurons cultured on NWs. Voltage-steps from −70 to +30 mV with 10 mV intervals were applied. Inset: Zoom onto the early-inward currents. **b)** Plot of the peak inward/outward currents normalized to the MC depending of the applied voltage. The error bars are SDs. **c)** Exemplary traces of AP trains recorded from a neuron cultured on NWs. Currents from 5 to 20 pA in 5 pA steps were applied. **d)** Analysis of the kinetics of the APs: AP amplitude from threshold to peak (AP ampl.), AP threshold (AP thr.), afterhyperpolarization (AHP, undershoot after AP), and full-width half maximum of the APs (AP duration). Control: glass. No statistical significances were found (Mann-Whitney U test: all $P > 0.05$). n(NWs) = 7, n(ctrl.) = 10. Error bars are SDs. Adapted from publication V.

So far, the differentiation toward neurons while being cultured on NW arrays was tested only with rather short NWs of about 1 µm. In the next section, the neuronal differentiation was tested across a wide range of array characteristics including up to 5 µm long NWs. Overall, 18 different combinations of NW length, array pitch, and NW diameter were employed.

3.1.5 Neuronal differentiation on 18 different types of NW arrays (Publication VI)

In this section, the neuronal differentiation toward hiDNs was tested with a set of NW arrays whose specifications were significantly varied. The tests with the hiNPCs showed already (section 3.1.2), that long NWs (L ≥ 3 µm) were able to deform the cell and its nucleus significantly, yet, the hiNPCs showed no fundamental alterations after four days of cultivation. The differentiation toward hiDNs, however, requires significantly more time on the NW arrays, namely, at least eight days. Specifically, the six-days predifferentiated cells were seeded onto the NW arrays and differentiated for another eight days to reach a mature neuronal state (two weeks in total). The temporally longer cultivation on the NW arrays while strongly interacting with the NW arrays might—after all—have an influence on the differentiation toward neurons. For that reason, the generation of neurons was tested with NW arrays featuring varying degrees of expected impact on the cells such as the number and depth of the indentations elicited by the NWs.

The NW arrays used in this section featured lengths of 1, 3, and 5 µm (L1, L3, L5), array pitches of 1, 3, and 5 µm (P1, P3, P3), and diameters of thin (D−, 270–600 nm) and thick (D+, 590–1070 nm) character (Figure 3.15). The NW arrays were fabricated from Si in a top-down process *via* RIE. The top-down approach was used because it allows for large-scale fabrication of the NW array with high reproducibility. In contrast, bottom-up approaches using, for instance, VLS growth often suffer from defects such as missing or askew NWs.[417–419] Yet, a defect-free nature of the NW arrays was crucial to study their potential impact on the neuronal differentiation systematically. Missing NWs in P5 NW arrays, for example, would appear as P10 to individual cells—or even as flat if the cell is located in between the NWs—and thus such defects would distort the results. However, VLS grown NWs have also advantages such as improved surface states, fewer materials defects, and the feasibility to add functionality by integrating hetero-junctions by varying the doping during the growth, e.g., to build NW solar cells for stimulating overgrowing cells.[420–423] For that reason, the feasibility to generate neurons on NW arrays fabricated in such a bottom-up approach was also tested and verified with different types of VLS grown GaAs NW arrays (SI). Nevertheless, the comprehensive study was then conducted with NW arrays prepared by the more reliable top-down approach using RIE masked by chromium circles defined by EBL.
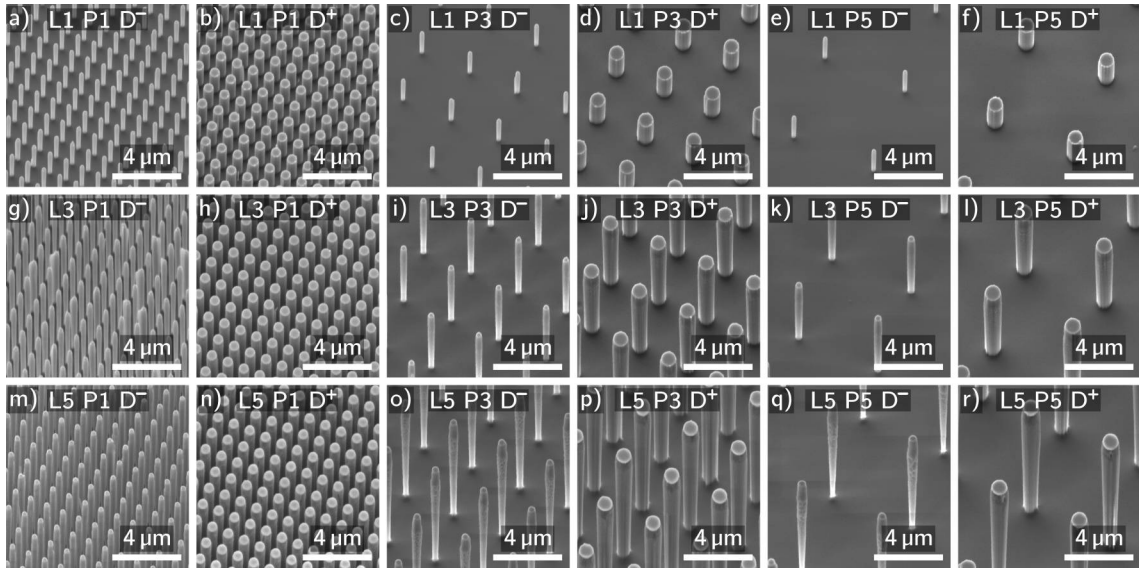
Figure 3.15 – **Compilation of SEM images of the utilized Si NW arrays featuring altering lengths, pitches, and diameters.** The lengths of the NWs were 1, 3, and 5 µm (L1, L3, L5). The array pitches (L) were 1, 3, and 5 µm (P1, P3, P3). The diameters for the *thin* type (D$^-$) were between 270 and 600 nm depending on the length and pitch (longer NWs and larger pitches required larger diameters to be compatible with the RIE processing). The *thick* type (D$^+$) was about 600 nm in diameter for P1 NW arrays and approx. 1000 nm for the P3/P5 NW arrays. Adapted from publication VI.

The used diameters of the circles for D$^-$ NWs were the minimal value that was compatible with the RIE process (approx. 270–600 nm). Specifically, longer wires (L3, L5) and larger pitches (P3, P5) required gradually increased diameters to compensate for the occurring tapering toward the base of the NWs (clearly visible in Figure 3.15o and q). For D$^+$ NW arrays the diameter was arbitrarily set to a rather large value of approx. 1000 nm. Note, for P1 D$^+$ NW arrays, the diameter was only about 600 nm to balance the spacing and the diameter of the NWs. The used lengths and pitches are similar to values frequently found in the literature.[55] The D$^-$ diameters achieved by RIE cover rather the upper range of NW diameters used in the field—especially for the L5 NW arrays. Thinner NWs used for cell culture are usually prepared by epitaxial growth, which allows for diameters even below the three-digit nm range.[424,425] However, for, e.g., solar cell applications diameters of around 300–400 nm can be appropriate.[426–428] Employing even thicker NWs (D$^+$) extends the universality of the study since, for example, also NWs with a diameter of about 1 µm influence cell spread or facilitate cell transfection.[429,430] Moreover, such larger diameters fill to some extent the gap between NW and micropillar arrays used in cell culture.[431–434]

The interaction of the neurons with the NW arrays was investigated using CLSM using MAP2 (green) and DRAQ5 (red) (Figure 3.16). The compilation illustrates the three typically observed setting states, namely, fakir-like (panel c), intermediate (panel f), and encapsulating (panel h) predominantly depending on the array pitches P1, P3, and P5. Thus, the cells followed in general the rules modeled by Buch-Månson *et al.* for the settling regimes to favor the fakir-like state for HD arrays and the encapsulating state for LD arrays.[51] However, peculiarities depending on the NW diameter were observed and are discussed as follows: Thin (D$^-$) NWs were more likely to be enwrapped by the cell causing, for example, intermediate states using L1 P1 NW arrays (Figure 3.16a). Note, for rather short NWs the nuclei are usually unaffected. Also, in the case of L1/3 P3 NW arrays with D$^-$ diameters the cells were more likely to encapsulate the NWs (Figure 3.16b,d). In contrast, P3 NW arrays with D$^+$ diameters favored fakir-like or intermediate regimes (Figure 3.16e). This contradictive observation might be explained by the effective NW spacing (i.e., pitch minus diameter) falling below the threshold for NW encapsulation. A comparable phenomenon has been described in the literature in which for a constant pitch of 1 µm and a NW length of 500 nm the cells encapsulated NWs featuring a diameter of <200 nm but were fakir-like for
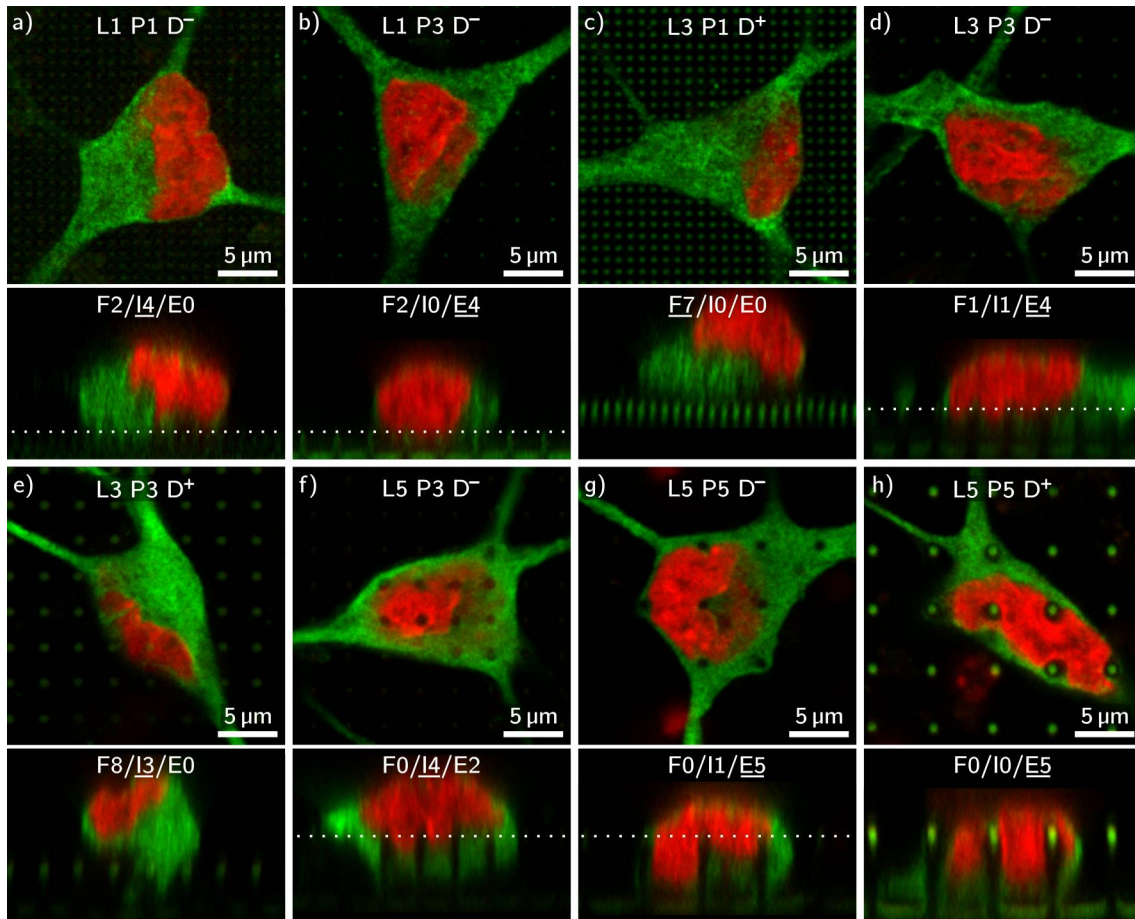
Figure 3.16 – Exemplary CLSM images of hiDNs cultivated on Si NW arrays sorted by length, pitch, and diameter. The neurons were labeled with MAP2 (green) and DRAQ5 (red, nuclei). The main panels show the top views whereas the panels below contain the corresponding cross-sectional views. The numbers indicate the quantity of the imaged cells found in a fakir-like (F), intermediate (I), and encapsulating (E) state. Note, the shown states are underlined. The subset of images exemplifies the interactions observed (all other images in the OM). Overall, small pitches (P1) favored fakir-like states (e.g., panel c) and larger pitches (P5) encapsulating states (e.g., panel h). In the encapsulating regime, long NWs (L5) caused massive deformations of the nuclei. Thin NWs (D⁻) were more likely to be enwrapped by the cells (e.g., panel a and d). Adapted from publication VI.

500 nm thick NWs due to the decreased effective array pitch (500 vs 800 nm).[402] This might also explain the occurring intermediate states instead of only fakir-like states in the case of the L1 P1 D⁻ NW arrays. Using the longest NWs (L5), the cells were exposed to the strongest deformations of the somata and nuclei (Figure 3.16f–h). However, L3 P3 D⁻ NW arrays mostly elicited intermediate regimes unable to enwrap the entire NWs (Figure 3.16f). To briefly conclude, the general behavior of the cells throughout the samples is in accordance to other literature in which HD NW arrays elicited fakir-like states whereas LD NW arrays caused encapsulating states.[71,102,373,435] Noteworthy, in direct comparison to the previous tests with the hiNPCs cultured on NW arrays, the differentiated neurons were more likely to favor a fakir-like state at similar specifications of the NW arrays. The inspection of individual cells *via* CLSM showed already that neurons were generated on all types of NW arrays. In a next step, epifluorescent ICC imaging was used to quantify the overall differentiation rates across the entire arrays to test whether the massive deformations have an impact on the overall outcome of the neuronal differentiation.

ICC was used to study the proportion of neurons in the cell culture (Figure 3.17). In comparison to the previous study, ICC was conducted not only with MAP2 but also with neuronal nuclei (NeuN) and tyrosine hydroxylase (TH) to broaden the neuronal characterization (examples shown in Figure 3.17a and b, respectively, others in the SI). NeuN binds to a neuron-specific nuclear protein and is frequently used in the stem-cell community to specify neuronal differentiation.[436,437] TH is an enzyme that is
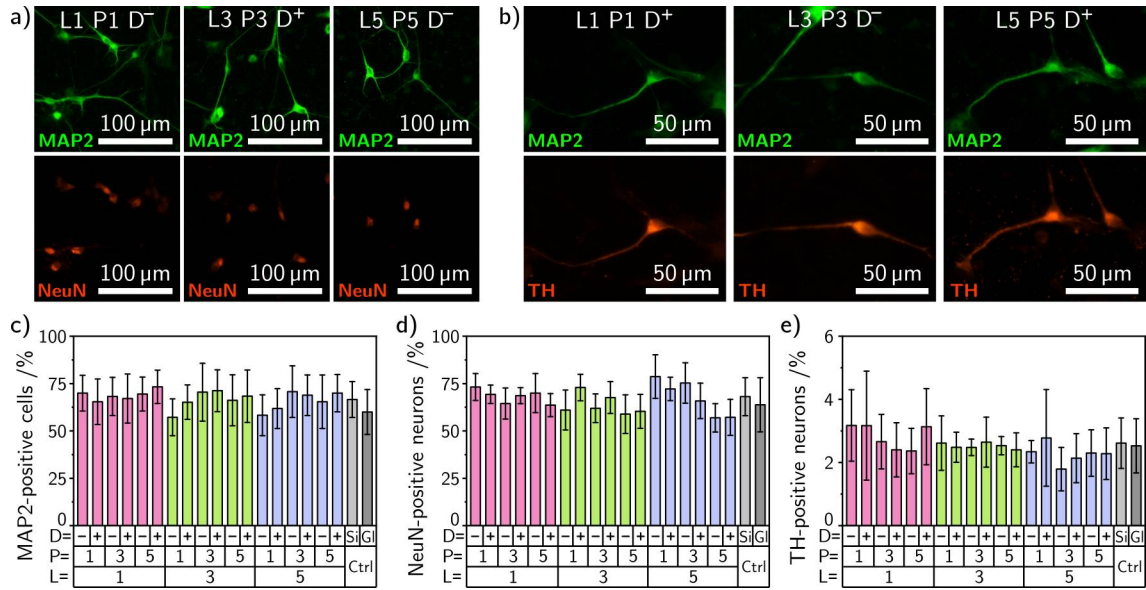
Figure 3.17 – **ICC stainings and analyses of MAP2-, NeuN-, and TH-positive hiDNs. a)** Examples of MAP2- (green) and NeuN-positive (red) cells (others: SI). **b)** Examples of MAP2- (green) and TH-positive (red) cells (others: SI). **c)** Proportion of MAP2-positive cells. **d)** Proportion of MAP2/NeuN double-positive cells. **e)** Proportion of MAP2/TH double-positive cells. No statistically significant deviations from the controls (ANOVA with post-hoc Tukey's test, $\alpha = 0.05$). controls: Si, glass. n(images) = 7. Error bars are SDs. Adapted from publication VI.

involved in the catalyzation of L-DOPA, a precursor of dopamine, and is used to indicate a dopaminergic phenotype of neurons.[438–440] The quantification of the MAP2 stainings showed that about 65% of the cells cultivated on the NW arrays were MAP2-positive, which was comparable to the controls on plain Si and glass (Figure 3.17c). Similar proportions of MAP2-positive cells are reported in the literature using regular well plates.[441] About 65% of the cells cultured on the NW arrays were, in addition, double-positive regarding MAP2/NeuN comparable to the controls and the literature (Figure 3.17d).[409] Moreover, on all types of NW substrates also MAP2/TH double-positive cells were observed (approx. 2.5%, similar to the controls) indicating the differentiation toward a dopaminergic phenotype (Figure 3.17e). Notably, the proportion of TH-positive neurons was rather small but TH being a rather later neuronal marker—for example, a significant TH upregulation after 20 days of differentiation was reported in Gilmozzi *et al.*—the referred values here are appropriate as literature also reports on single-digit proportions for even longer cultured cells (30 DIV).[442] Note, dead cells were excluded from the analysis by discriminating the bright nuclei, i.e, apoptotic cells, in the Hoechst channel (about 50% dead cells, SI). Overall, the given ICC values reflect rather normal yields compared to the literature but in fact, it is remarkable that the NW arrays have virtually no impact on the yields of the differentiation although fundamental changes in the interaction regimes were observed. Consequentially, the cultivation of the hiDNs on NW arrays with the intention to use such substrates in future applications with functionalized NWs including varying geometrical specifications for, e.g., optimized electrical coupling is outright feasible. In a next step, the equality of the NW arrays regarding the development of neuronal functionality was tested using the patch clamping technique.

The electrophysiology of the hiDNs was especially tested by verifying their functionality, i.e., the capability to fire trains of APs (Figure 3.18a). Notably, APs were recorded on all types of NW arrays (traces of the controls in the SI). The quantification of the AP amplitudes showed regardless of the type of NW arrays mean values of about 70 mV, which was comparable to the controls and is also in good agreement with the literature (Figure 3.18b).[284,356,416] The AP thresholds and AP widths were in average approx. −25 mV and 3.6 ms, respectively (Figure 3.18c and d). Again, the findings on the NW arrays were comparable to the controls and also in accordance with the literature.[284,356,416] The RMPs of the neurons

were abound $-50\,\mathrm{mV}$, which was comparable to the controls and other studies (Figure 3.18e).[284,356,416] The average MCs were about $12\,\mathrm{pF}$ and comparable to the controls (Figure 3.18f). Such values of the MCs are similar to other publications.[284,356,416] Lastly, the early-inward and late-outward currents were measured (Figure 3.18g, example from P1L1D$^-$, others in the SI). The peak currents were normalized
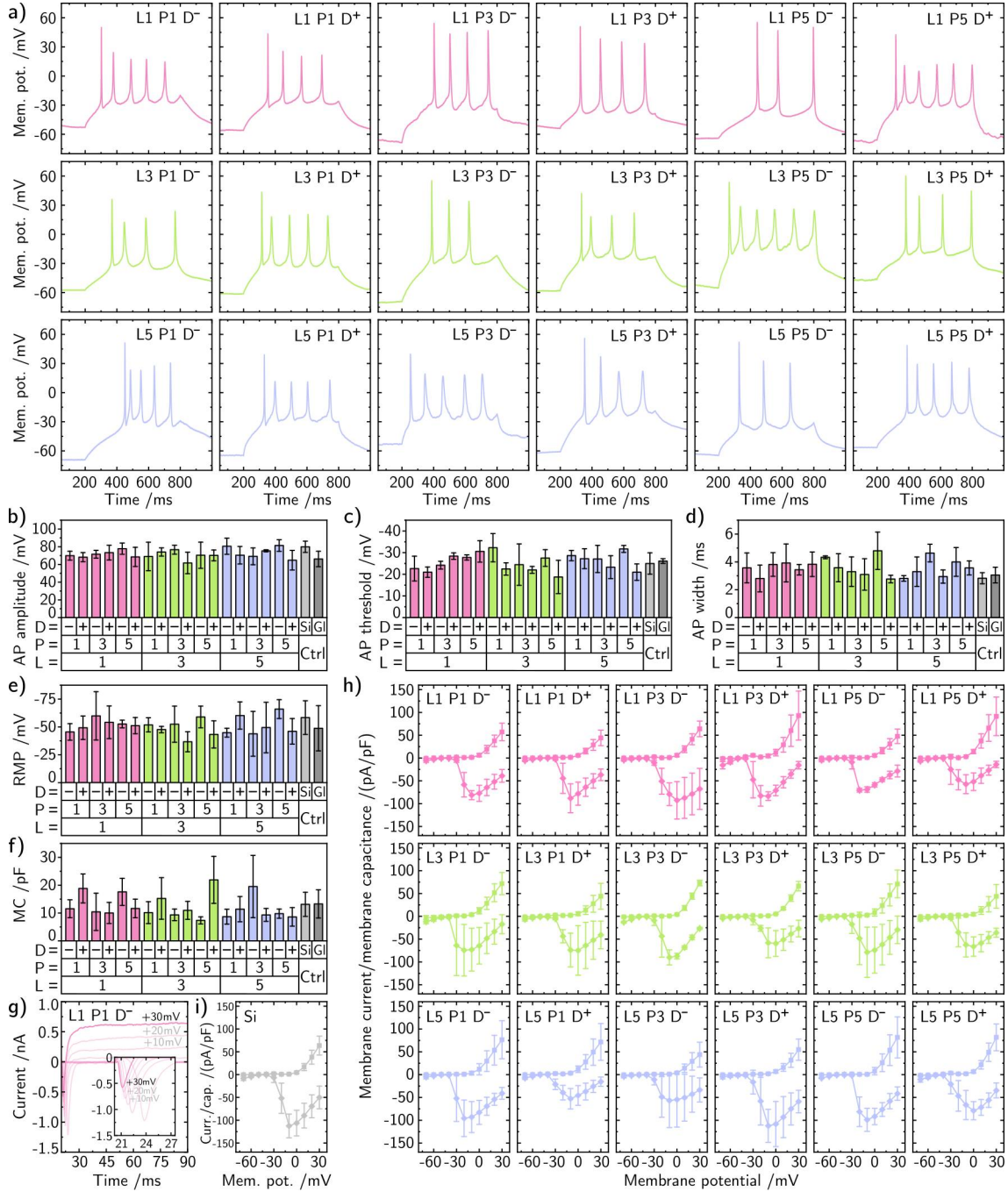

Figure 3.18 – **AP traces recorded from hiDNs cultured on NW arrays with an extensive variation of the array specifications including analyses. a)** Compilation of AP traces recorded from neurons cultivated on the respective NW arrays. **b)** Analysis of the AP amplitude. **c)** Analysis of the AP threshold. **d)** Analysis of the AP width. **e)** Analysis of the RMPs. **f)** Analysis of the MCs. No statistically significant deviations compared to the controls (ANOVA with post-hoc Tukey's test, $\alpha = 0.05$) **g)** Example of the in- and outward currents (here: L1 P1 D$^-$, all other traces in the OM/SI). Inset: Zoom-in of inward currents. **h)** Compilation of normalized voltage-current dependencies of the peak in- and outward currents of hiDNs generated on the NW arrays. Diamond: inward, square: outward. **i)** Normalized voltage-current dependencies of the peak in- and outward currents for Si control (glass in the SI). Diamond: inward, square: outward. No statistically significant deviations from the controls (ANOVA with post-hoc Tukey's test, $\alpha = 0.05$). Controls: Si, glass. n(analyzed cells) $= 4, 6, 3, 4, 4, 3, 3, 6, 2, 2, 3, 5, 3, 6, 4, 3, 4, 5, 7, 7$. Error bars are SDs. Adapted from publication VI.

to the MCs and plotted against the applied potential (Figure 3.18h, Si: panel i, glass: SI). The overall character of the peak current-voltage dependency was similar on all substrates. Moreover, such normalized currents are similar to the literature.[277,415] Concludingly, also the functional development of hiDNs was equal on all types of NW arrays despite the tremendous differences in the hiDN/NW interactions highlighting again the potential to employ the hiDNs in future applications with NW arrays.

To briefly recapitulate the NW/cell section, the reliable generation of hiGNs and hiDNs while being cultured on the NW arrays is an excellent stepping stone for employing further functionalized NW arrays in future applications such as neural interfaces or regenerative medicine.[443–445] The next section will deal with creating defined neuronal networks using both chemical and topographical guiding cues to control cell adhesion and neurite growth for being prospectively employed in BoC applications.

3.2 Studies using cell culture scaffolds

The initial experiments regarding guided neuronal growth were conducted using mPNs. These studies began with basic experiments with patterned surface coatings (2D) and subsequently, the intricacy of the substrates gradually advanced by employing 2.5D and 3D microstructuring. Finally, the closing studies were conducted with hiDNs cultivated in 3D microscaffolds.

3.2.1 Neurite guiding of mPNs in 2D, 2.5D, and 3D   (Publications VIII, IX, X, and XI)

In this section, a brief summary of work to achieve neurite guiding in 2D, 2.5D, and 3D using mPNs is presented. Both chemical and topographical guiding cues were used and a set of different approaches has been compiled in Figure 3.19.

Chemical cues were tested first to direct the settling and growth of mPNs on flat substrates just patterned with a surface modification, namely, a laterally structured PDL coating (Figure 3.19a). The neurons adhered predominantly to the areas covered with PDL indicated by the dash-lined circles. Overall, the promoting effect of PDL to create defined neuronal networks is in accordance with the literature that used PDL or similar amino acids such as PLL.[160,161,446–448] The strong directional guiding by PDL was confirmed by the neurites mostly growing either directly or diagonally to the neighboring PDL spots despite gaps of about 50 μm. Larger distances of, for example, about 150 μm, however, were no longer bridged (OM). The relevance of the inter-spacing to connect or separate cells with surface coatings is known in literature[162] and the findings here are in good agreement with work from Petrelli *et al.*, which reports a critical distance of about 60 μm.[449]

Topographical guiding cues for basic path finding of the neurites were tested next. Trenches with step heights of 3, 6, and 9 μm were prepared with RIE to elicit growth along the edges. As a result, neurites were well controlled by wall heights of 9 μm (3.19b), but less or not at all with 6 or 3 μm high edges, respectively (OM). Thresholds to overcome barriers are known in literature and have been linked to the size of the growth cone as shown by Li *et al.* for cortical neurons (10–11 μm).[171] Partial orientation of the neurites along steps with a height of 6 μm (OM) is also in agreement with the literature that reports on a similar form of contact guiding.[30,173,450,451] To further constrain the neuronal growth, microtubes horizontally lying on a substrate were employed at which the somata were positioned at the entrances of the microtubes (Figure 3.19c) and the neurites were growing through the tubes (Figure 3.19d). By arranging such microtubes in arrays and covering the intersections with, e.g., PLL (Figure 3.19e), controlled neuronal networks with neurons settling at the crossings and neurites growing through the microtubes were created (Figure 3.19f). The potential to use microtube arrays to guide neurons has also been shown in other studies.[199,200] The functionality of the mPNs cultured on microtube arrays was tested by patch clamp measurements (Figure 3.19g), which proved the capability to fire APs (Fig-
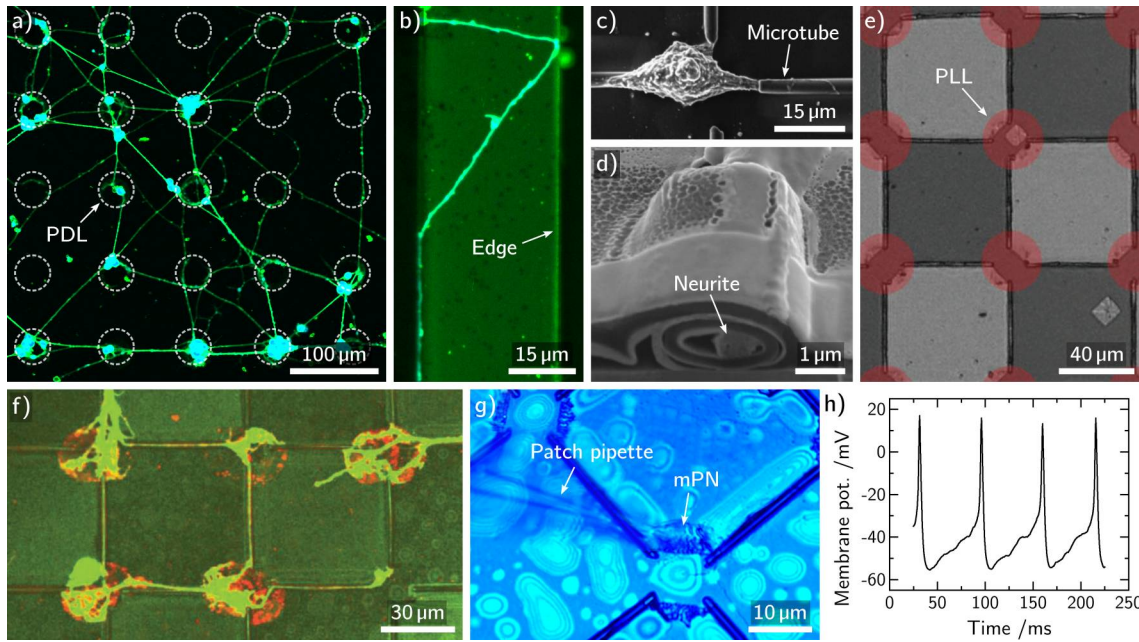
Figure 3.19 – **Neurite guiding of mPNs in 2D and 2.5D by chemical and topographical guiding cues. a)** Fluorescent microscopy image of neurons (green) growing on a PDL–micropatterned glass chip (2D). Dots with PDL were prepared using a customizable ink-jet printer (Dimatix DMP-2831, Fujifilm) and are indicated by circles. Neurons settled on the surface-modified areas and neurites grew predominantly to the next neighboring dots (horizontally, vertically, and diagonally). **b)** CLSM image of a neurite (green) trapped by steps with a 9 µm height difference (indicated by dark/bright background) prepared by RIE (2.5D). **c)** SEM image of neuronal guiding by physical confinement with microtubes (diameter: 3 µm) where the neurites grew through the microtubes (cross-sectional image prepared with FIB milling shown in panel **d)**). **e)** SEM image of the microtubes arrangement with points of intersection surface-modified with PLL. **f)** Fluorescent microscopy image of neurons (yellow) settling on the intersections and neurites growing through the microtubes. **g)** Widefield microscopy image of a neuron cultured on a sample with arranged microtubes and being patch clamped. **h)** Exemplary trace of APs recorded from a cell cultured on a sample with arranged microtubes. Adapted from publications VIII, IX, and X.

ure 3.19h). Strategies to create functional neuronal networks in 2D and 2.5D were elaborated here so far, but the utilized techniques for sample fabrication are fundamentally limited to producing flat networks. Nevertheless, 3D microscaffolds are required for controlling neuronal growth also in the third dimension in order to tackle fundamental challenges in neuroscience such as a better understanding of the function of the—three-dimensional—human brain.[452] One promising approach to micro-engineer such 3D cell culture scaffolds is to use DLW since the technique allows for micro-engineering such scaffolds with the required precision of the feature details.[453]

3D microscaffolds prepared by DLW (Nanoscribe) were used to transfer the planar neuronal networks into the third dimension by means of arrays of individual towers with cavities to hold the cells connected by freestanding microchannels to guide the neurites (Figure 3.20a). The rendered image shows a segment of the scaffold with 3×3 towers to illustrate the dimensions. Specifically, the towers with heights of 45, 55, and 65 µm were spaced by 25 µm and featured a cavity on the top with a size of 20×20×10 µm³ (W×D×H). Note, the final 3D-printed microscaffold then consisted of 10×10 towers (image section in Figure 3.20b, entire scaffold: OM). The entrances to the microchannels featured an orifice diameter of a few micrometers similar to the microtubes shown earlier (Figure 3.20c). The neurons (red) rested inside the cavities and the neurites grew into the microchannel (example in Figure 3.20d). Cross-sectional SEM imaging gave insight into the microchannels used for neurite guiding and illustrated that the neurites (red) grew in the corners of the channels—a result of contact guidance (Figure 3.20e). The controlled adhesion of the cells into the cavities and improved guiding properties of the scaffold were both achieved by a site-specific coating of the scaffold interior with PDL. Precise coating of the scaffold was done using a pipette filled with PDL, which was brought in contact with a wall of a cavity—capillary forces then distributed the solution into the entire structure (video in the SI). Additionally, neuronal growth was enhanced with a complementary
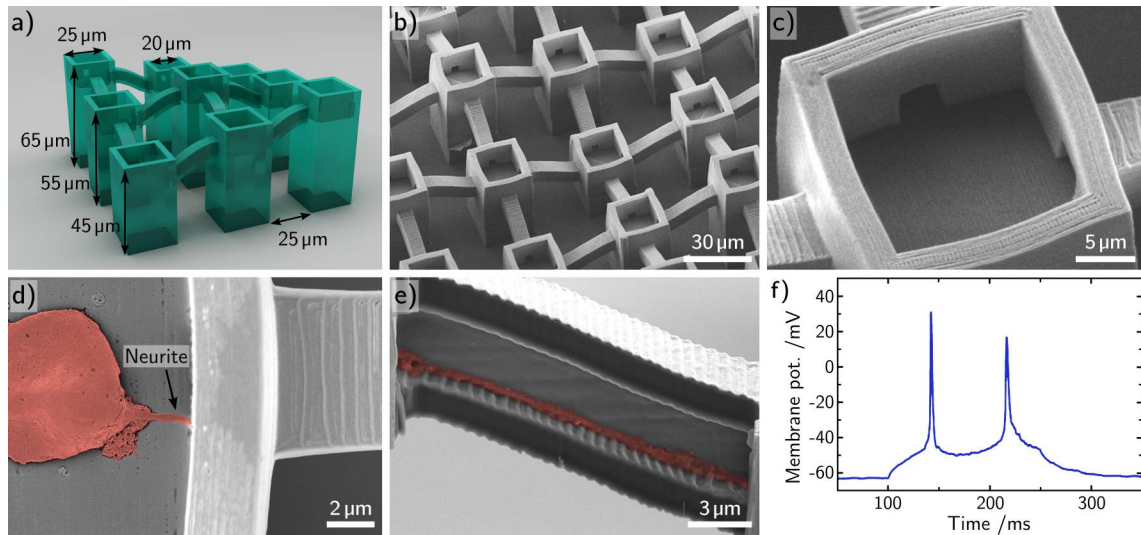
Figure 3.20 – **3D microprinted scaffolds prepared by DLW for culturing of mPNs with defined neuronal networks. a)** Rendered image of a section (3×3 towers) from the CAD file used for DLW to visualize the scales (the final scaffold was 10×10 towers): Towers with heights of 45, 55, and 65 µm were spaced by 25 µm and featured a cavity on the top with a size of 20×20×10 µm³ (W×D×H). The elevated cavities were connected by free-standing microchannels with a channel diameter a few micrometers similar to the microtubes shown earlier. **b)** SEM image of the 3D-printed microscaffold. **c)** SEM image of a single cavity within the 3D scaffold also highlighting the entrance of a channel. **d)** Close-up top view SEM of a neuron (red) located in a cavity with a neurite entering the microchannel. **e)** Cross-sectional SEM image of the microchannels prepared by FIB milling showing a neurite (red) growing in the corner of the channel. **f)** Exemplary trace of APs recorded from a neuron growing in the microscaffold. Adapted from publication XI.

unspecific laminin coating. The functionality of the neurons cultured inside the microscaffolds was proven with recordings of APs (Figure 3.20f).

Finally, the DLW 3D microscaffolds were applied to the hiDNs. In that context, the analysis of the neuronal growth inside the scaffold was intensified and measurements of synaptic currents by patch clamping even indicate activity of the neuronal networks—the results are presented in the next section.

3.2.2 Human iPSC-derived neuronal networks in 3D-printed microscaffolds (Publication VII)

The DLW 3D microscaffold used for culturing the hiDNs maintained the fundamental design used in the previous study (Figure 3.21a). Specifically, arrays of elevated cavities to hold the cells with dimensions of 20×20×10 µm³ (W×D×H) connected by free-standing microchannels to guide the neurites with a channel length of 25 µm and a cross section of 4×5 µm² (W×H) were used. The mean shrinkage of the scaffold after developing the resin (IP-DIP) was between 3 and 16% depending on the inspected features of the scaffold (min: tower height, max: channel interior), which is normal for the resin (OM).[454] In general, the major scaffold specifications were sustained, yet detail changes were made to the scaffold design as follows: The total scaffold size was reduced to 4×6 towers in order to fit into both a single write field of the laser writer (Nanoscribe) and the field of view of the patch clamp setup. Additionally, the heights of the towers were reduced to a fixed value of 30 µm to reduce the fabrication time on the one hand, and on the other hand, to facilitate the patch clamping and imaging procedure by finding all cells at the same focus plane. The hiDNs (red) grew reliably inside the microscaffolds (green) and the neurites stretched across several cavities and microchannels (Figure 3.21b). Note, the scaffolds were coated similarly to the previous description with PLL (specific) as well as laminin (unspecific) and two-week-old mature hiDNs were reseeded onto the scaffolds. The analysis of the neurite growth revealed that within 3 DIV of culturing inside the scaffold neurite lengths of more than 400 µm were reached (OM). The influence of contact guidance on the cellular growth was also observed with the hiDNs shown by cross-sectional views prepared by CLSM (Figure 3.21c–e, positions of the slices indicated in panel b).[173] Bot the soma and
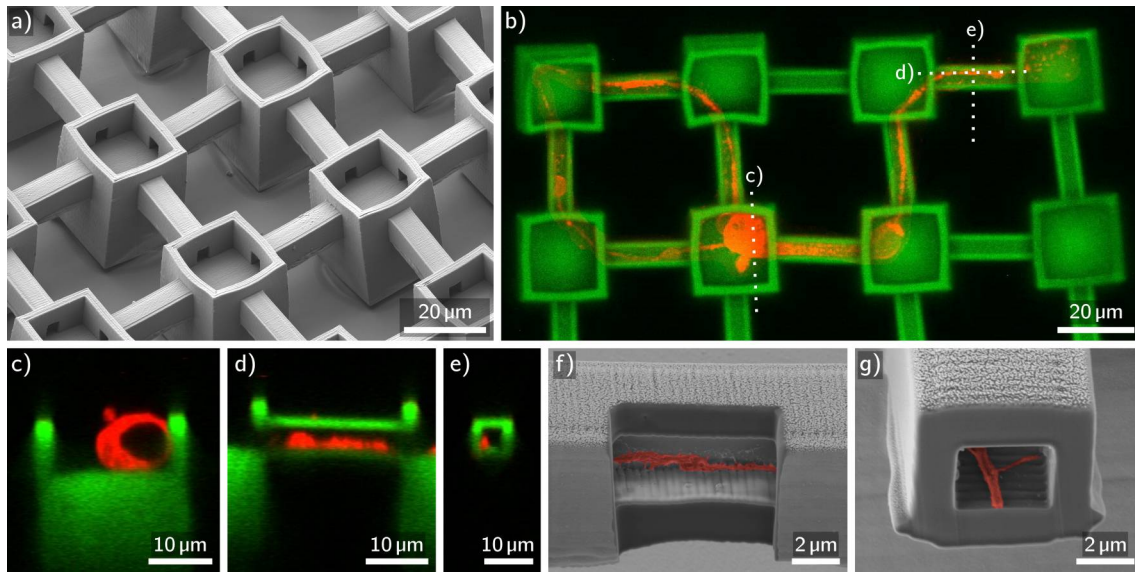
Figure 3.21 – **3D microprinted scaffolds for culturing of hiDNs with guided neuronal networks. a)** Tilted SEM image of the DLW microscaffold. Towers with cavities to hold the cells are connected by free-standing microchannels to the directly neighboring microtowers. **b)** Exemplary CLSM image of neurons (red, membrane stain) settling in the microcavities (green) and neurites growing through the microchannels of the scaffold. The image was produced from a down-projection of the slices in z-direction. The dotted lines indicate the positions of the cross sections shown in the panels c, d, and e. **c)** Cross section of a neuron settling in a microcavity. **d,e)** Cross section of a neurite growing through the microchannel (longitudinal and transverse cut, respectively). **f,g)** Cross-sectional SEM image prepared with FIB milling of a neurite growing through a microchannel (longitudinal and transverse cut, respectively). Adapted from publication VII.

the neurites were located close to the walls and corners of the cavity and the microchannel, respectively. The predilection of the neurites for growing along the corners of the microchannels was also confirmed with cross-sectional SEM imaging (Figure 3.21f, green: neurite). Sometimes, however, neurites changed the side of the microchannel (Figure 3.21g). The growth direction of the neurites after entering another cavity was linked to a form of random walk since the probability of a neurite picking a straight-ahead or deflected microchannel was matching the angle probability of the corresponding microchannel (OM). That is in agreement with the literature showing that contact-guided neuronal growth around corners featuring more than 84° is rather unlikely.[183] The integrity of the hiDNs cultured in the scaffold was not only shown by viability assays using Ca and PI (about 77%, OM) and ICC (positive for MAP2 and TH, SI) but also—and more importantly—by patch clamp measurements.

The functionality of the neurons and indicators of network activity were both confirmed by patch clamp measurements (Figure 3.22). The electrophysiological characterization of the hiDNs covered basic membrane properties, APs dynamics, characteristic membrane currents, and synaptic activity by means of spontaneous excitatory postsynaptic currents (sEPSCs). To illustrate the patch clamp experiment in the microscaffold, Figure 3.22a exemplarily displays a patch pipette (blue) being attached to a neuron (green) resting in a cavity. The measured RMPs and MCs were $-54.9 \pm 4.9\,\mathrm{mV}$ and $8.1 \pm 1.5\,\mathrm{pF}$, respectively—similar to planar control and in agreement with the literature (OM).[280,355,356,416,455] From the MCs the average neurite length was roughly estimated: assuming a mean neurite diameter of $1\,\mathrm{\mu m}$, spherical somata with a diameter of $10\,\mathrm{\mu m}$, and a specific membrane conductance of $0.9\,\mathrm{pA/cm^2}$,[456] the estimated average neurite length per neuron was $180\,\mathrm{\mu m}$, which matches the neurite analysis *via* microscopy (OM). The hiDNs growing inside the microscaffold showed mature recordings of APs (Figure 3.22b). The kinetics of the APs in terms of AP height ($69.5 \pm 6.0\,\mathrm{mV}$), AP threshold ($-25.4 \pm 2.5\,\mathrm{mV}$), AHP ($16.1 \pm 3.4\,\mathrm{mV}$), and AP duration ($4.4 \pm 0.5\,\mathrm{ms}$) were similar to the control and are in accordance with other human iPSC-derived neurons (Figure 3.22c).[280,355,409,412,416] Also, the characteristic early-inward and late-outward currents of the sodium and potassium ion channels (peak currents normal-
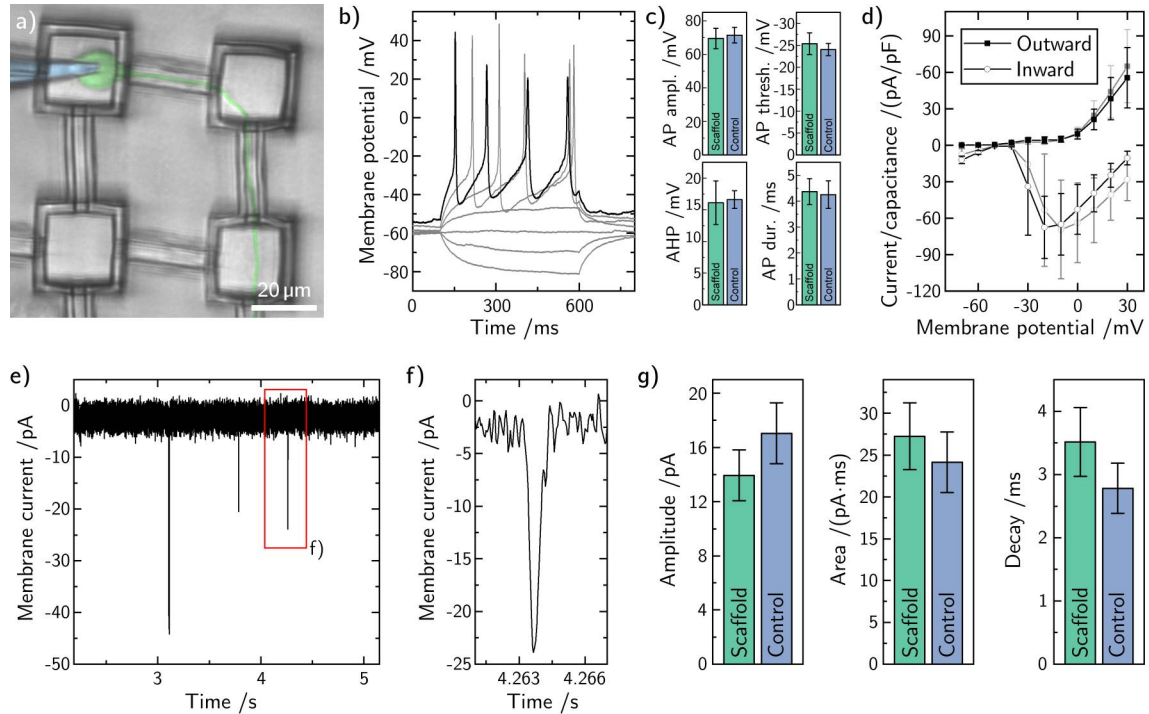
Figure 3.22 – **Functional electrophysiology of hiDNs cultured in microprinted 3D scaffolds. a)** Exemplary widefield microscopy image of the patch clamp routine where the pipette (blue) was in contact with the cell (green). **b)** Examples of traces with APs recorded from a neuron cultured in the microscaffold. **c)** Quantification of the AP kinetics recorded in scaffolds compared to recordings on planar control. Error bars are standard errors of means (SEOMs). **d)** Peak early-inward and late-outward currents normalized to the MC plotted against the applied membrane potential (black) compared to control (gray). Error bars are SDs. n(measured cells) = 6–9. **e)** Exemplary trace of spontaneous excitatory postsynaptic currents (sEPSCs) recorded from a neuron cultured in a microscaffold. **f)** Zoom into a single sEPSC event highlighted by the red rectangular in panel e. **g)** Quantification of the kinetics of the sEPSCs in terms of amplitude, area, and decay time constant. n(events) = 28–70. Controls: glass. The error bars are SEOMs. No statistically significant deviances (ANOVA with post hoc Tukey's test, $\alpha = 0.05$). Adapted from publication VII.

ized to the MCs) were similar to the control and the literature (Figure 3.22d).[277,415] Finally, functional synaptogenesis—the formation of synapses between neurons—was demonstrated by measurements of sEPSCs (Figure 3.22e, negative current spikes). Note, the formation of synapses is a prerequisite for developing network activity and is essential for neuronal function.[284] Thus, the existence of such synaptic events was an indicator of potential network activity. The analysis of the individual events (Figure 3.22f) testified similar kinetics in terms of amplitude, area, and decay (Figure 3.22g). In particular, the mean amplitude was $13.9 \pm 1.9\,\mathrm{mV}$, the area was $27.2 \pm 4.0\,\mathrm{pA \cdot ms}$, and the decay time constant was $3.5 \pm 0.5\,\mathrm{ms}$, which is in line with other human iPSC-derived neurons.[409,455]

Two more scaffolds with more complex network topologies were either tested with cells or conceptionally elaborated (Figure 3.23). A sophisticated scaffold consisting of towers with cavities at four different elevations was prepared (Figure 3.23a). The cavities were highly interconnected by contorted microchannels to bridge the different altitudes. The neuronal growth was tested with the hiDNs where CLSM showed the capability of the cells to grow from one cavity to other ones located at different heights (Figure 3.23b–f). Specifically, neurites were able to cross the entire scaffold diagonally (panel b) while going up and down again (cross section in panel c). The neurons also grew from the very bottom cavity to the highest tower (Figure 3.23d–f). The ability of the neurons to reach remote cavities at altering elevation by steep and twisted microchannels allows for hypothesizing future designs using stackable 2D elements (Figure 3.23g).[457,458] One element would consist of a grid of cavities (panel h) that would connect to the next element with cross-linking channels (panel i, connection highlighted in red). The elements would be
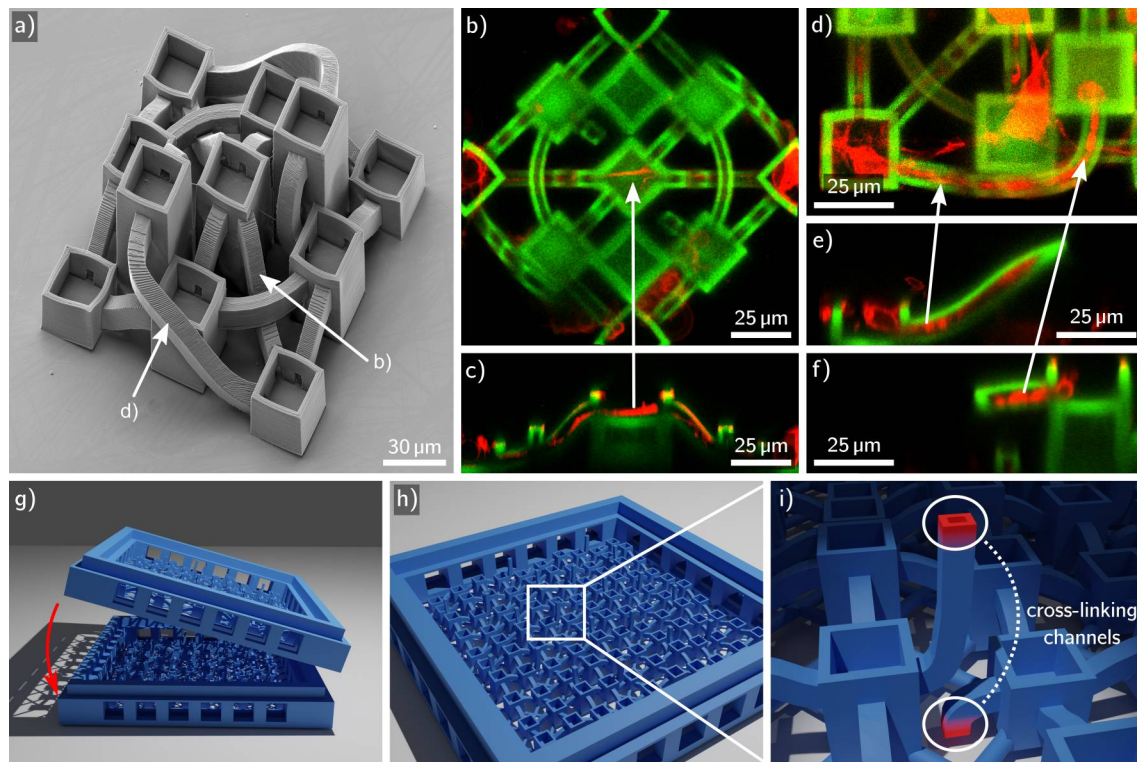
Figure 3.23 – **Established/potential designs of the microscaffold with more complex network topologies. a)** SEM image of a microscaffold with four different heights of the towers connected by contorted microchannels that reach even from the lowest to the highest cavity. The arrows indicate the positions of the images shown in the next panels. **b–f)** Examples of hiDNs (red) cultured in the scaffolds with complex channel arrangement (green) demonstrating that the cells were able to grow between cavities of different heights. **g–i)** CAD sketch of a concept to stack multiple scaffolds after cell seeding. The individual platforms (panel h) have cross-linking channels (panel i, red endpoints) to connect the respective parts. Adapted from publication VII.

assembled after cell seeding using a micromanipulator—the general feasibility to handle the scaffolds in such a manner was tested with regular manual tweezers (SI).

Another fundamental upgrade of the microprinted scaffolds would be individually addressable microelectrodes placed in each cavity to analyze the signaling in the neuronal networks in more detail. An approach using localized electroplating (ED) to create electrical circuits inside the scaffold is presented in the concluding 'future perspectives' chapter. In addition, that chapter compiles a broader outline of how the capabilities of the NWs arrays and the microscaffolds could be utilized in the future to address current research appropriately based on the findings obtained in this thesis. Nevertheless, before giving future perspectives based on the presented work, the next chapter will first summarize the selected results.

— 4 —

Summary

The cultivation of human iPSC-derived neurons was tested and verified on various types of NW arrays and inside 3D-printed cell culture scaffolds. Being cultured on these artificial substrates, the cells were analyzed, for example, in terms of viability, functionality, and/or network formation. By employing human iPSC-derived neurons, this thesis not only addressed the present absence of such advanced cells in the respective fields but might also open up new paths for next-generation stem-cell research and therapies.[459]

Throughout this thesis, multiple initial experiment-specific aspects such as the used cells, the nature of the substrates, or the measurement techniques used for collecting first insights were refined as a prerequisite for achieving the final results (Figure 4.1, discussed later in detail). One particular focus of this work was the preservation of the neuronal differentiation outcome and the formation of tailor-made neuronal networks in the face of the challenging and artificial growth environments. The functional electrophysiological character of the neurons was investigated by the patch clamp technique. Key results of this thesis are the equal generation of human iPSC-derived neurons cultured on various types of NW arrays compared to planar controls and the indicated network activity of the neuronal networks grown inside the 3D scaffolds. Among the utilized NW arrays, especially the generation of functional neurons on NW arrays with long NWs (e.g., 5 µm) and large pitches (e.g., 5 µm) is remarkable since such specifications maximized the topographical stress, i.e., the extent of the NW-associated indentations. Inside the 3D scaffolds, tailor-made neuronal networks were formed by the human iPSC-derived neurons. The growth was analyzed by CLSM and the functionality of the neurons was likewise demonstrated by patch clamp recordings. Particularly, the synaptogenesis was shown by measurements of sEPSCs, which in turn indicate network activity. The overall progress is briefly elaborated on in the following paragraphs.

The NW arrays were changed in the studies in terms of density, arrangement, shape, length, and diameter to cover a broadly based set of NW arrays (Figure 4.1a). Note, the initial experiments testing the influence on T cells and mPN culture were only performed on slightly altered HD NW arrays. Then, the comprehensive investigation of culturing human iPSC-derivatives (e.g., NPCs and neurons) on NW arrays was conducted using more profoundly changed array characteristics such as a variation of the array density, the NW shape, or the NW lengths. Specifically, the neuronal differentiation was similar to control for NW arrays featuring short NWs (about 1 µm) with altering array arrangements (random, rectangular, hexagonal) including different array pitches (1.8, 4 µm), on short spiky HD NWs arrays, and on another set of 18 different types of NW arrays sweeping the combinations of three lengths (up to 5 µm), three pitches, and two diameter ranges.

The scaffolds—or more generally spoken the substrates with guiding capabilities—advanced from plain 2D substrates to sophisticated 3D scaffolds (Figure 4.1b). The 2D samples featured patterned surface modifications using amino acids such as PDL or PLL to enhance adhesion and guiding. The 2.5D substrates added topographical guiding cues such as trenches, tubes, and cages to further constrain the neuronal outgrowth. By employing DLW, both chemical and topographical guiding cues were translated into 3D.

The cell culture was commenced with a cell line (T cells) being easy to maintain and to handle (Figure 4.1c). The cells allowed for basic tests, e.g., the evaluation of the patch clamp procedure on the NW arrays. However, not being neuronal, the T cells naturally could not serve, for example, for the investigation of neuronal networks. Primary cerebellar granule cells from mice were the initial source for
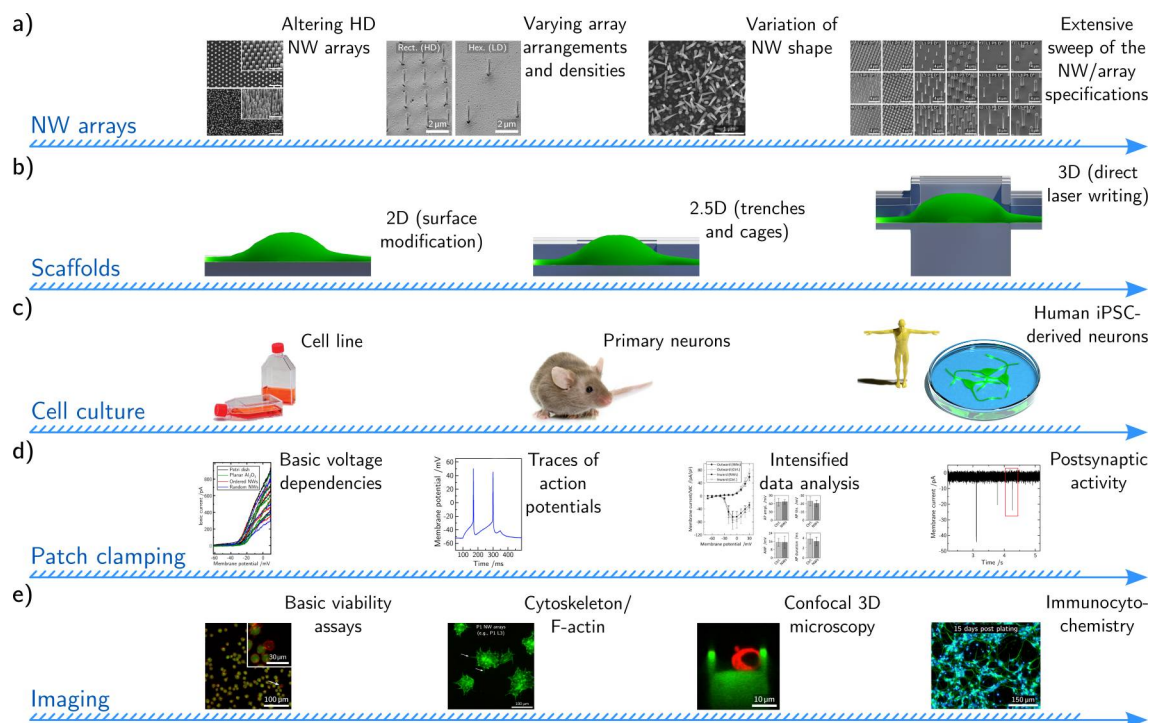
Figure 4.1 – **Summarizing figure of the experiments, cell culture, and types of micro- and nanostructured cell culture substrates. a)** The first NW arrays covered only a few changes in the geometrical specifications whereas finally, universal sweeps of the array characteristics were conducted. **b)** Neurite guiding shaped up from elemental guiding in 2D toward complex cell culture scaffolds in 3D. **c)** The cell culture changed from basic cell lines to the culture of human iPSC-derived neurons. **d)** The patch clamp methods evolved from basic voltage-clamp measurements of voltage-gated ion channels toward measurements of APs and postsynaptic currents. **e))** Imaging started with ordinary viability assays and ended up in high-resolution confocal 3D microscopy visualization and ICC stainings.

neurons. To increase the relevance of the experiments from the medical point of view, the cell culture was changed to neurons derived from human iPSCs as they would allow for, e.g., patient-specific studies and thus are considered a potent tool in regenerative medicine.[460] Note, so far, human iPSC-derived neurons were scarcely—if not never—used in similar settings before.

Patch clamping—still being considered the gold standard for electrophysiological measurements—began in this thesis with fundamental measurements such as basic voltage dependencies of membrane currents or membrane potentials using non-neuronal cells (Figure 4.1d).[461] Then, neurons allowed for the recording of APs stimulated by a current injection. In the course of time, more sophisticated protocols such as the measurement of early-inward and late-outward currents including intensified data analyses of the overall collected traces were established. Finally, the synaptic activity of the neurons was shown by recordings of sEPSCs. The comprehensive electrophysiological analysis allowed for an adequate evaluation of the neuronal differentiation and comparison to the literature.

Imaging of the cells on the substrates was a cornerstone for studying the cellular growth (Figure 4.1e). Viability assays using Ca and PI were employed to verify the fundamental integrity of the cells. The interactions with the substrates were investigated, for instance, by imaging the cytoskeleton or focal adhesions. CLSM allowed for 3D imaging prepared from stacked image planes, e.g., to locate the neurons inside the microscaffolds. In the end, the neuronal differentiation was in addition to the functional analysis also studied by ICC—a standard complementary tool in cytology.[462] The neuronal state was tested, for example, with MAP2 or NeuN. Moreover, ICC labeling was used to specify the phenotype of the neurons (e.g., TH for a dopaminergic characteristic). The next chapter will present selected preliminary results and elaborate future perspectives of potential follow-up experiments based on the results shown in this thesis.

$$— 5 —$$

Future perspectives

In this section, I want to briefly present preliminary results of ongoing work that emerged from the findings that are already published. Furthermore, I would like to map out potential future experiments that would use the obtained insights to proceed with the respective projects meaningfully. Five routes to continue the experimental work—two relating to the NW arrays and three in matters of the neuronal guiding, respectively—should be considered: 1. NW-assisted delivery of payloads, 2. electrical sensing or stimulation by exploiting the enhanced coupling between the NW and the cell, 3. the establishment of self-stimulating neuronal ring-oscillators, 4. the design of neuronal networks with actual three-dimensional network topology, and 5. the implementation of individually addressable microelectrodes into the cavities of the scaffold.

Delivery of biological payloads using NW arrays was, for example, demonstrated with porous Si nanoneedles that modulated endocytosis—the cellular process of internalizing external substances by membrane encapsulation.[112] The nanostructures facilitated the formation of vesicular structures at NW sites, which enhanced, e.g., the uptake of biomolecular markers of endocytosis and short-stranded ribonucleic acids (RNAs).[463] The spiky Si NWs used in publication V could be a good starting point as they featured a similar tapered shape although the length would be reduced compared to the referenced work (about $2.5\,\mu m$). However, the pertinence of the NW length was not further elaborated. Note, the vesicular structures were not agglomerated at the NW tip as one might expect. In any case, the functionalization of the NWs would require steps of plasma and UV light treatment followed by loading the cargo *via* incubating the samples immersed in the solution with, e.g., biomarkers. At this point, it is crucial to know that the feasibility to load the material with cargo depends on multiple factors, such as pore size and charge of the substrate, which must match the size and charge of the cargo. Likely, the requirements for, e.g., the porosity of the NW materials used herein are not fulfilled in their present form but might be achieved with intermediate processing steps such as electrochemical etching.[464] Nevertheless, two other bottlenecks might reduce the usability of porous Si, in particular, and cargo delivery with porous materials, in general, in the context of stem cell differentiation. First, porous Si is considered biodegradable meaning that the samples might degrade over time depending on the porosity and the physiological conditions.[465,466] Moreover, literature reports that the cargoes are essentially released within $24\,h$ as soon as the solution to load the substrate is removed.[109] Thus, the period of sample erosion and cargo release might be disproportional to the time required to differentiate the stem cells. For a one-time delivery right after sell seeding, however, porous Si might be sufficient. Yet, preferable would be materials that are chemically stable for weeks, which might be given, for example, by porous TiO_2, Mn_2O_3, or In_2O_3 already used for NW fabrication (no data given regarding long-term stability in cell culture media).[467–470] Also, a mechanism to temporally control the release of the cargo would greatly improve the value of the NW device. Better dosage control would be provided using arrays of hollow NWs—so-called nanostraws (NSs)—which allow for the injection of payloads controlled by temporarily rupturing the membrane *via* electroporation (EP).[106,113,114,471–475] Usually, such NSs are embedded into a thin membrane (approx. $15\,\mu m$ of thickness) that separates a reservoir containing the fluid with cargo from the cell culture medium. The EP is then triggered by a potential across this membrane. Although this approach holds advantages such as timing control and exchangeability of the cargo-laden solution, drawbacks are, for instance, the fragility of the membranes and the collective triggering of all NSs at once. A potential alternative strategy to embark on might be

the employment of arrayed 'nanocups' (NCs) shown in Figure 5.1a. The NCs were prepared with RIE using a hard mask that is too thin to endure the entire etching procedure. As a result, the interior of the NW is being etched away while a shell that predominantly consists of fluorine—a component of one of the etching gases—remained, which was determined *via* energy-dispersive X-ray spectroscopy (EDX). The precise mechanism, however, was not yet confirmed. The cross-sectional SEM imaging illustrates the core/shell structure (Figure 5.1b, yellow: shell, blue: Si, green: inner part). The cup could hold a defined volume of cargo-laden solution, which is applied to the NC, for example, by immersion into the respective fluid. Subsequently, the excessive solution is rinsed away. Non-permeable payloads could even just be added to the cell suspension and fluid outside the cups would be washed out after cell adhesion by a medium exchange. Nevertheless, permeable payloads or other drugs that must not be in contact with the cells during seeding need to be laden beforehand. One of the challenges might be the necessity to seal the cups containing the payload until the cell is covering the orifice. Noteworthy, other studies show that in the case of smaller tube dimensions (less than 500 nm in diameter) the diffusion from the tube reservoirs into the medium was negligible and sealing the cups was not needed at all.[476] Larger NCs might, however, might need a mechanism to block the cup orifices. A conceivable approach would be to close the cups with a lipid bilayer—also used to seal small pores—by applying giant unilamellar vesicles (GUVs), which are also capable of enwrapping entire NWs.[477–479] EP would allow for opening the covering membrane. Further, electrical pre-structuring of the silicon wafer could enable addressing the NWs individually to precisely administer the payload to a particular cell.

Electrical stimulation and sensing by the NWs would be feasible in a twofold manner: First, the NWs can be used to enhance the electrical coupling between conventional planar MEAs and the cell by encapsulating the 3D electrodes.[130,480] Such modified electrodes facilitate long-term measurements and enhance, for example, the signal-to-noise ratio or reduce the required currents to activate individual neurons by increasing the seal resistance.[125,134,481–485] Advanced underlying circuitry even allows for individually addressing single NWs to increase the spatial resolution below the cellular scale.[131] Moreover, NWs allow for EP not available with planar electrodes to further increase the sensitivity.[486] Beside utilizing the NWs as the final element to link external amplifiers to the cells, the NWs can directly stimulate the cells electrically when *p-n* junctions are integrated to form miniature solar cells either free-standing or in arrays.[138,139,141,487–489] Such solar cell NW arrays can be built with either radial or axial arrangement of the *p-n* junctions.[317,490–492] The optical absorption characteristics depend, on the
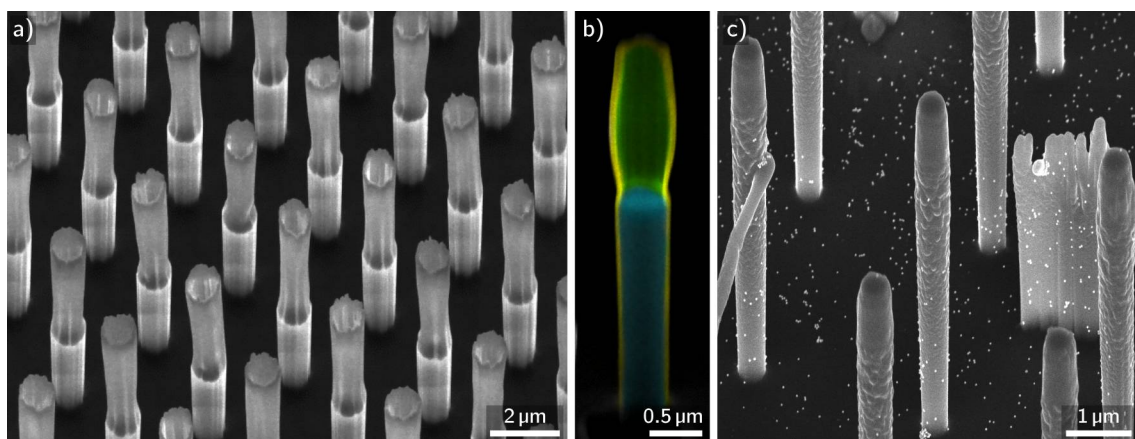

Figure 5.1 – Potential approaches to functionalize the NW arrays. a) SEM image of NWs featuring NCs at the NW tips to be filled with a cargo-laden fluid. **b)** Cross-sectional SEM image of a NW with NC. The walls were false-colored in yellow, Si in blue, and the inner part in green. The shell predominantly consisted of fluorine confirmed with EDX. **c)** Exemplary SEM image of TiO passivated NWs speckled with Au NPs to enhance the photocatalytic properties. The Au NPs have a mean diameter of 50 nm and were deposited by spin coating. Note, defective samples showing, for example, faulty RIE were used for the preliminary tests. Not published.

one hand, on intrinsic material properties such as the band gaps but, on the other hand, also on the array geometry such as array pitch, NW length, and NW diameter.[493] In the preliminary tests with mPNs cultured on high-efficient HD InP NW solar cells featuring axial *p-n* junctions,[317] no stimulation of the cells was observed (my Master's thesis).[366] Presumably, the electrical coupling was insufficient due to the small contact area between the NWs and the cells in the fakir-like settling state caused by the small array pitch. By the presented mapping of the settling regimes of the human iPSC-derived cells, the optimal array characteristics for the solar cell application can now be chosen under the condition that the cells encapsulate the individual NWs to maximize the electrochemical coupling. Instead of the integration of *p-n* junctions into the NWs, photoactive properties can also be achieved by employing the electrolyte character of the growth medium and materials with photocatalytic/photoelectrochemical properties such as TiO_2.[494,495] Note, the typically poor conversion efficiency of untreated plain TiO_2 can be significantly improved by nanostructuring with NW arrays—as used here for the cell culture—to create a larger surface area and, moreover, by plasmonic enhancement with coatings such as gold NPs.[496–499] To stimulate cells, literature reports that such Au-decorated TiO_2 NW arrays were, for example, used to stimulate a response of the optic nerve in blind mice.[140] In preliminary tests, the already prepared Si NW arrays were coated with TiO_2 using atomic layer deposition (ALD) and equipped with Au NPs *via* spin coating (Figure 5.1b). The plasmon-enhanced photocatalysis to generate photocurrents might then stimulate overgrowing neurons. Future experiments would also involve the mapping of the stimulation efficiency not only depending on the NW array characteristics such as array pitch, and NW length and diameter, but also in relation to the size and density of the Au NPs and thickness of the TiO_2 layer.

Self-stimulating neuronal ring oscillators could be employed to study neuronal autapse, namely, the formation of synaptic connections between the neurite with its own entity.[502] A potential scaffold to introduce such a neuronal ring oscillator is shown in Figure 5.2a—the concept and motivation will be described in the following. From the physics point of view, a neuron that is linked to itself and thus features a synaptic feedback loop can be considered a neuronal oscillator.[503] The biological function is rather unclear but simulations indicate that autapses can help to synchronize neuronal networks,[504–507] to generate bursting patterns,[508–510] to control short-term memory storage,[511] or even to enhance self-adaptation after injury,[512] each depending on the loop characteristics such as delay time or coupling strength. Especially, understanding the influence of autapses on neural oscillations and on long- and short-ranged synchrony is of particular interest because of their implications for theories of human consciousness,[513] and their impact in the context of major brain disorders such as schizophrenia, epilepsy, and autism spectrum disorders.[514–516] As already indicated by the large number of published simulations, the experimental implementation of neuronal networks with defined autapses is difficult to access.[517] The idea of employing ring scaffolds to elicit autapse formation was already pursued in a study from 2012 using hydrogel rings and individually cultivated rat neurons but actual autapses were not shown.[518] However, the authors emphasized the potential of ring structures for autapse studies. One of the problems of employing a hydrogel for guiding the neuronal growth might have been the insufficient precision of the neurite guiding back to the soma. Hence, ring scaffolds with improved guiding capabilities prepared, e.g., by RIE or DLW, that hold individual neurons and then accurately compel the neurites to be linked back to the initial neuron again could be a promising starting point for future experiments. In the previously shown example (Figure 5.2a), precise ring structures with increasing channel lengths representing varying delays of the feedback loops were prepared using EBL and RIE. The different rings were convoluted to increase the yield and were arrayed multiple times to maximize the number of ring oscillators per one cell seeding. Furthermore, two cavities per ring were used to increase the chance to find a neuron inside the structure after random cell adhesion. Note, the sample contained thousands of structures making specific coating disproportionate. One peculiar case could be studied with the ring structures, namely, in which the time required for the AP to propagate along the neurite before reaching the neuron again is larger than the
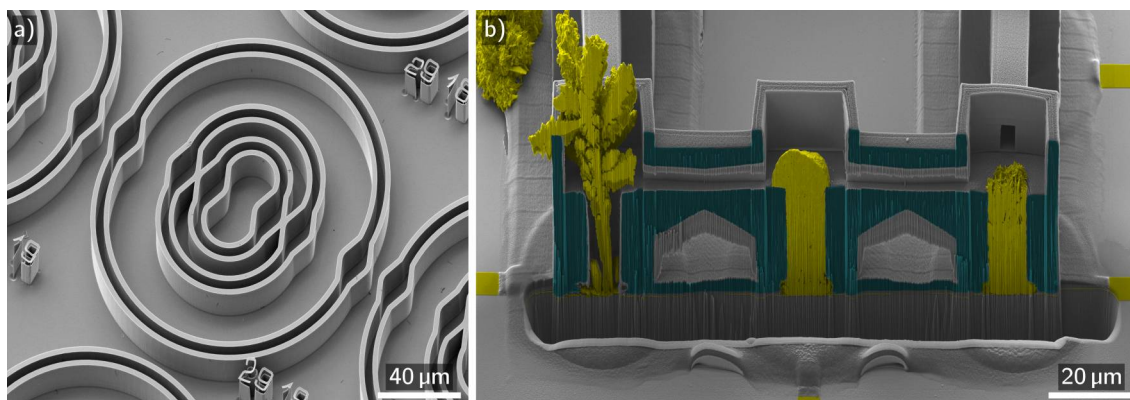
Figure 5.2 – **Potential approaches to improve the microscaffolds for future applications. a)** SEM image of ring structures that might be used to create biological ring oscillators mediated by self-stimulation. The ring structures featured two cavities as well as altering channel lengths. Note, the rings with different circumferences were convoluted to increase the yield. Each convolution was arrayed multiple times to maximize the number of oscillators per chip to be used per one cell seeding. **b)** Cross-sectional SEM image of a 3D scaffold (sectional area: green) with integrated circuitry (gold: yellow). The scaffold was printed onto a custom-built MEA and each tower was equipped with a vertical channel that was aligned with the electrodes from the MEA. The channels were filled with Au by ED. From left to right, the deposition rate was reduced, which resulted in different textures of the gold surface in the cavity. Adapted from supervised Bachelor's (Dat Nguyen) and Master's (Malte Siegmund) theses.[500,501]

refractory period (RP)—the time period in which it is impossible or difficult to elicit another AP.[268] The duration of the RP of neurons can be estimated by the AP length (few ms) with suppressed excitability including the AHP phase (up to several 10 ms) featuring decreasingly hindered capability to fire APs again. Another delay is caused by the diffusion-limited signaling of the synapses, which can add another few ms of delay time.[519,520] The propagation speeds of APs in unmyelinated neurites typically range from about 0.2 to 0.8 m/s.[521–523] As a result, the minimal neurite length for exceeding, e.g., a RP of 15 ms while assuming a propagation velocity of 0.2 m/s must be 3 mm. Preliminary tests with the hiDNs showed, that fibers with a length of more than 1 mm are formed within 1–2 days post-plating giving the reason to believe that neurites might become long enough to fulfill the length criterion (*cf.* Bachelor's thesis of Dat Nguyen).[500] In principle, such scaffolds to elicit autapses could be fabricated in 3D using DLW. However, tests showed that developing extremely long microchannels is not trivial. The removal of the resin completely out of the channels became intricate and damages caused by shrinking added up. Moreover, it is not clear whether the neurites would obtain enough cell culture medium, i.e., vital nutrients, in such long channels to properly grow. The preparation of open trenches by EBL and RIE does not suffer from the aforementioned issues and in addition, duly scales with the required dimensions. Nevertheless, DLW scaffolds are crucial for leaping up to the third dimension.

3D network topologies were already conceptualized in the closing section of the selected results chapter on page 38 (Figure 3.23). To briefly accentuate, DLW is an outstanding tool to create any kind of scaffold shape to cultivate cells in 3D. In comparison to other scaffolds, for example, built from PMEDSAH, fibrin hydrogel, micropillars, or microfibrous chitin-alginate to culture human iPSCs in 3D,[524–527] DLW excels by offering the opportunity to recreate scaffolds with the suitability to guide neuronal growth. The tests with small scaffolds featuring actual 3D network topology showed that the hiDNs grew with ease through steep twisted microchannels allowing for the construction of stackable platforms that would be connected by such demanding channels. Employing spatially confining cell culture substrates might be one of the key factors to bring *in vitro* experiments to the next level and crucial for a BoC approach that would require 3D scaffolds.[242,257,528] Such tailor-made 3D scaffolds not only allow for adding, e.g., vascular systems to larger organoid cultures to provide nutrients,[40,529–531] but also might create a potent tool to investigate neuronal activity in predefined circuits in the context of electrophysiology and drug screenings.[532–534] However, in order to significantly increase the use of the scaffolds for neuronal network studies with advanced

network topologies, the number of cells to be analyzed in parallel must be substantially scaled up—a requirement that patch clamping fails to fulfill. A promising approach is the integration of conventional MEA technology in the scaffolds contemplated in the next paragraph.

Individually addressable readout of the cells located in the cavities might be achieved by the implementation of auxiliary circuitry (Figure 5.2b, green: scaffold, yellow: integrated circuits). The scaffold was printed onto a custom-made MEA chip and the hollow towers of the scaffold were filled with gold by ED (*cf.* Master's thesis of Malte Siegmund).[501] Note, the deposition rate influenced the quality of the electrode surface, which could be used to optimize the coupling between cell and electrode.[535] Ultimately, the electrode surface could even be improved by adding NWs or other nanostructures such as mushroom-shaped electrodes.[536,537] Employing (commercially available) MEAs to be subsequently structured, for example, with cavities, trenches, or channels built from PDMS or glass to influence the cellular growth and/or the network formation was demonstrated in the literature already.[538–541] However, the recordings were only conducted from 2D as the measured cells still needed to be in contact with the flat surface of the initial MEA. By extending the planar electrodes into the scaffold, the network topology would no longer be restricted to one level. The custom-made MEA used here is built to be compatible with commercially available amplifiers such as the ME2100 system from Multichannel Systems, which is able to both stimulate and sense with up to 256 channels. By fabricating the MEAs from scratch, the very substrate is freely configurable to be optimized for writing the 3D scaffolds—for example, by defining the size and arrangement of the electrodes as well as the positions of the alignment markers. Purchasable MEAs devices, for instance, from Multichannel Systems, might be an option for DLW as well—either directly or after some modifications such as an adhesion layer to ensure proper attachment of the scaffold—yet, their geometrical specifications might be suboptimal and naturally, they would lack handy features such as alignment markers for the DLW processing. CMOS-based MEA devices such as the BioCam4096 (3Brain) have other limitations as they do not fit by default into the DLW machine due to the attached well and, moreover, its CMOS sensor might even be damaged during the DLW by the high energies of the pulsed laser. Nevertheless, to conclude the 3D custom-built MEA approach, 3D scaffolds with fully addressable circuitry for sensing and stimulation might be one of the key technologies for BoC and organoid studies and complement or even replace other techniques such as mesh nanoelectronics, which lack, for example, cellular resolution.[45,295]

— A —

Appendix

The appendix contains the original manuscripts I to XI including the supporting information as printed by the publisher. However, the documents were reduced to 120 DPI and highly compressed to keep the overall file size of this document within the limit of the University's guidelines. Additional note: For the manuscripts VII and XI, supporting movie material is available on the publisher's website.

A.1 Publication I

A temperature-controlled patch clamp platform demonstrated on Jurkat T lymphocytes and human induced pluripotent stem cell-derived neurons

Jann Harberts, Max Kusch, John O'Sullivan, Robert Zierold, and Robert H. Blick

(11 + 1 pages)

bioengineering

Article

A Temperature-Controlled Patch Clamp Platform Demonstrated on Jurkat T Lymphocytes and Human Induced Pluripotent Stem Cell-Derived Neurons

Jann Harberts [1,†] , **Max Kusch** [1,†] , **John O'Sullivan** [1,2] , **Robert Zierold** [1,*] and
Robert H. Blick [1,3]

1 Center for Hybrid Nanostructures, Universität Hamburg, Luruper Chaussee 149, 22761 Hamburg, Germany;
   jann.harberts@chyn.uni-hamburg.de (J.H.); max.kusch@gmx.de (M.K.); john.o'sullivan.16@ucl.ac.uk (J.O.);
   rblick@chyn.uni-hamburg.de (R.H.B.)
2 Department of Physics and Astronomy, University College London, London WC1E 6BT, UK
3 Material Science and Engineering, College of Engineering, University of Wisconsin-Madison, Madison,
   WI 53706, USA
* Correspondence: rzierold@chyn.uni-hamburg.de
† These authors contributed equally.

check for
updates

Abstract: Though patch clamping at room temperature is a widely disseminated standard procedure in the electrophysiological community, it does not represent the biological system in mammals at around 37 °C. In order to better mimic the natural environment in electrophysiological studies, we present a custom-built, temperature-controlled patch clamp platform for upright microscopes, which can easily be adapted to any upright patch clamp setup independently, whether commercially available or home built. Our setup can both cool and heat the platform having only small temperature variations of less than 0.5 °C. We demonstrate our setup with patch clamp measurements at 36 °C on Jurkat T lymphocytes and human induced pluripotent stem cell-derived neurons. Passive membrane parameters and characteristic electrophysiological properties, such as the gating properties of voltage-gated ion channels and the firing of action potentials, are compared to measurements at room temperature. We observe that many processes that are not explicitly considered as temperature dependent show changes with temperature. Thus, we believe in the need of a temperature control in patch clamp measurements if improved physiological conditions are required. Furthermore, we advise researchers to only compare electrophysiological results directly that have been measured at similar temperatures since small variations in cellular properties might be caused by temperature alterations.

Keywords: patch clamping; Jurkat cells; human induced pluripotent stem cell-derived neurons; temperature control; electrophysiology

1. Introduction

In 1780, Luigi Galvani set the cornerstone for modern electrophysiology by accidentally discovering electrical processes within living creatures as electrical currents evoked the movement of frog legs [1]. Two centuries later—in 1976—Neher and Sakmann made a Nobel's prize-winning breakthrough when they improved the sensitivity of their measurements to such an extent that they were able to measure currents from individual ion channels [2]. Since then, Neher and Sakmann's patch clamping technique added numerous valuable aspects to our understanding of biological matter and contributed in thousands of publications [3,4]. Today, we know that our entire nervous system is based on the transmission of electrical as well as chemical signals on a single-cell scale, and patch clamping helped fundamentally in understanding the role of many different ion channels in the context of physiological

and pathophysiological functions [5–7]. In particular, Na^+, K^+, and Ca^{2+} voltage-gated ion channels play an important role in the nervous system, and the accurate apprehension of the electrical signaling could even render a direct connection between the nervous system and a computer [8,9]. To address high throughput applications such as drug screening, automated patch clamping and planar patch clamping represent useful extensions to the conventional technique [10–12]. However, manual patch clamping is not replaceable at all, since flexibility and data quality are unmatched [13]. In addition, in vivo (automated) patch clamping offers the opportunity to study electrophysiology in living animals—a setting as close as it can get to nature—but such applications are even more challenging due to more complex setups and low giga-seal probabilities [14,15]. For obvious ethical reasons, in vivo patch clamping in humans is out of the question. Thus, patch clamp studies involving the human organism are limited to in vitro experiments with human cell lines or cells derived from human stem cells. However, many experiments to determine electrophysiological properties of suchlike human cells are performed at room temperature (RT) [16–22]. Thus, all electrophysiological processes within these studies operate significantly below the natural body temperature of about 37 °C. It is worth noting that many biological processes inside the animal's/human's body are temperature dependent, and organs like the brain are extremely sensitive to temperature fluctuations; for instance, a core body temperature of about 20 °C would quickly lead to death [23,24]. A patch clamp setup allowing for electrophysiological measurements at controlled temperatures would be of great interest to researchers in order to shed light onto temperature depending cell processes and functions [25]. Unfortunately, commercially available setups from well-established companies, such as "ALA Scientific Instruments" or "Multichannel Systems", are quite expensive and specific for their dedicated patch clamp platforms. Herein, we present a low-cost, low-tech approach—feasible for everybody and adaptable to every setup independently, whether commercially bought or in-house built—for controlling the temperature of biological samples during patch clamp measurements. In this work, we initially describe the construction details of the microscope inset as well as the corresponding temperature controller. Furthermore, we demonstrate the practical implementation with electrophysiological measurements on Jurkat T lymphocytes (T cells) and human induced pluripotent stem cell-derived neurons (neurons). Aside from basic electrophysiological properties, we compare specific characteristics such as the voltage gating of voltage-gated ion channels and firing of action potentials at RT and 36 °C. Here, we found small influences on non-specifically temperature depending processes confirming the potential need of a temperature control in patch clamp measurements if best biological conditions are required. Furthermore, researchers should only compare their data to the results measured at same temperatures if differences are highlighted compared to literature.

2. Materials and Methods

2.1. Cell Culture

The T cells were cultured in RPMI 1640+GlutaMAX™-I medium (Gibco) with 25 mM 4-(2-hydroxyethyl)-1-piperazineethanesulfonic acid (HEPES), 7.5% new-born calf serum and 1.2% (*w/v*) penicillin/streptomycin in T75 cell culture flasks at 37 °C and 5% CO_2 in air. The cell suspension was diluted with fresh medium every 2-3 days to keep the cell concentration between 0.3×10^6 and 1.2×10^6 cells/mL [26].

The neurons were cultured and differentiated based on the protocol in Reinhardt et al. [27]. Human small molecule neural progenitor cells (smNPCs) were provided in frozen vials from the Max Planck Institute for molecular biomedicine in Muenster, Germany. Further cell culture was conducted on-site. smNPCs were maintained in basic medium (50:50 DMEM/F12:Neurobasal, 1:100 Penicillin/Streptomycin/Glutamine, 1:100 B27 supplement without vitamin A, 1:200 N2 supplement, Life Technologies, Carlsbad, CA, USA) and was supplemented with ascorbic acid (AA, 100 µM, Sigma Aldrich, St. Louis, MO, USA), smoothened agonist (SAG, 0.5 µM, Biomol, Hamburg, Germany), and CHIR (CHIR 99021, 3 µM, Axon MedChem, Groningen, Netherlands). smNPCs were split close to

confluency (every 4–5 days) in a ratio of 1:10–1:20. Differentiation into midbrain-dopaminergic neurons (mDANs) was initiated by changing the smNPC growth medium to patterning medium (basic medium supplemented with 100 μM AA, 0.5 μM SAG, 1 ng/mL glial-derived neurotrophic factor (GDNF), and 1 ng/mL brain-derived neurotrophic factor (BDNF), PeproTech, Rocky Hill, NJ, USA). After 6 days, the growth medium was adjusted to maturation medium (basic medium supplemented with 100 μM AA, 2 ng/mL GDNF, 2 ng/mL BDNF, 1 ng/mL transforming growth factor-β3 (TGF-ß3, PeproTech), and 100 μM dibutyryl cyclic-AMP (dbcAMP, Sigma Aldrich)) and the cells differentiated for at least 8 more days (14 in total). The patch clamp measurements were performed after 2–3 weeks after initiation of the differentiation procedure. The cells were kept in a humidified incubator at 37 °C and 5% CO_2. The growth media were replaced by fresh ones every 2–3 days. All cells were cultured on Matrigel coated 6-well plates and transferred to 35 mm Petri dishes one to two days before the measurements. For passaging/splitting/transferring cells, cells were detached using Accutase$^®$ for 10–15 min at 37 °C, centrifuged and subsequently resuspended in the corresponding cell culture medium.

Ethics approval: Jurkat T lymphocytes: cell line, no approval required. Human induced pluripotent stem cell-derived neurons: All experiments were conducted in accordance with the ethical statement in Reinhardt et al. [27].

2.2. Patch Clamp Setup

The temperature-controlled inset was installed in a patch clamp setup consisting of a Nikon Eclipse FN1 upright microscope equipped with a non-immersion objective with an extra-long working distance of 11 mm (Nikon CFI TU Plan EPI ELWD 50× N.A. 0.60/W.D. 11.00 mm). Signals were recorded with a HEKA EPC 10 USB patch clamp amplifier using a HEKA red star headstage. The data was processed with a Bessel low pass filter at 2.9 kHz. All measurements were performed with identically fabricated patch pipettes. The borosilicate glass capillary blanks (GB150T-8P, Science Products) were pulled with a Sutter Instrument P-2000 pipette puller (program: three rows with heat = 430, 420, 450; filament = 5, 5, 5; velocity = 70, 70, 70; delay = 200, 200, 200; pull = 0, 0, 0) and subsequently heat polished (CPM-2, ALA Scientific Instruments). The diameter of the pipette tip was about 950 nm, which resulted in resistances of 3–5 MΩ. Pipettes with similar properties prepared with a different pipette puller would be suitable as well. Pipette capacitance and series resistance were automatically compensated.

2.3. Electrophysiology

The patch clamp solutions for the T cells were adapted from Partida-Sanchez et al. [28]. The pipette solution consisted of 140 mM KCl, 2 mM $MgCl_2$, 1 mM $CaCl_2$ and 2.5 mM ethylene glycol tetraacetic acid (EGTA) and is buffered with 10 mM 4-(2-hydroxyethyl)-1-piperazi-neethanesulfonic acid (HEPES). The pH was adjusted to 7.3 with KOH. The bath solution consisted of 140 mM NaCl, 5 mM KCl, 2 mM $MgCl_2$, 2 mM $CaCl_2$, 5 mM glucose and was buffered with 10 mM HEPES, adjusted to pH 7.4 with NaOH.

For neurons, the patch clamp measurements were performed using a bath solution consisting of 140 mM NaCl, 2.4 mM KCl, 1.3 mM $MgCl_2$, 2.5 mM $CaCl_2$, 10 mM HEPES and 10 mM D-glucose. The pH-value was adjusted to 7.4 using NaOH. The corresponding pipette solution consisted of 125 mM potassium-gluconate, 10 mM NaCl, 1 mM EGTA, 4 mM MgATP, 10 mM HEPES and 10 mM D-glucose. The pH-value was adjusted to 7.4 using NaOH [27].

Resting membrane potential was measured at zero holding current. Membrane capacitance was determined from the patch clamp software. Membrane time constant was identified by an exponential fit of the membrane potential after a small hyperpolarization. The voltage gating of the T cells was measured by applying a voltage-ramp with a slope of 80 mV/100 ms and determined by the voltage-level showing an increasing membrane current. Action potentials were evoked by stepwise current injections. The data collected at RT and 36 °C originates from at least two independent patch clamp sessions for each cell type. The data was analyzed using C++ programming language. The plots

were prepared with Origin (v. 2018). The error bars are the standard error of mean if not stated otherwise. Statistical analysis via ANOVA with post hoc Turkey's test is given in the supporting materials (*cf.* Table S1).

3. Construction of the Temperature-Controlled Patch Clamp Inset

The detached microscope inset is shown in Figure 1a. The central component is a Peltier element (1). It is sandwiched between a lower (2) and an upper (3) copper plate to create a temperature gradient between these copper plates. Conventional thermal paste is used to increase the heat transfer and four screws firmly press the components together. The copper disc (4) on top of the upper plate is designed in such a way, that it fits into the bottom of a standard 35 mm Petri dish to ensure maximum heat transfer between cell sample and the upper copper plate. A thermometer T_1 is integrated into the copper disc in order to monitor the temperature next to the Petri dish. The copper disc and the thermometer are held in place by solder, which ensures good thermal connection between the thermometer and the upper plate. The Peltier element is contacted via banana plugs P+ and P−, and the thermometer is connected by two inner connectors ($C_{1,2}$). Though our sample holder is designed primarily to adjust the temperature above RT, it also allows for the cooling of the bath solution temperature below RT. This feature is, for instance, useful during patch clamp measurements to slow down temperature-dependent processes that are too fast for the standard detection methods and thus enables to resolve recordings beyond the amplifiers time resolution [29]. When the inset is used for cooling below RT, an additional heat sink (5) is required, because the Peltier element has to transport heat from the upper to the lower plate. The performance of this heat transfer process depends mainly on the ability of the lower plate to dissipate the transported heat to the environment. In order to support heating and cooling, two separate controllers for the Peltier element have been used. However, when only the heating of the samples is intended, no heatsink is necessary.
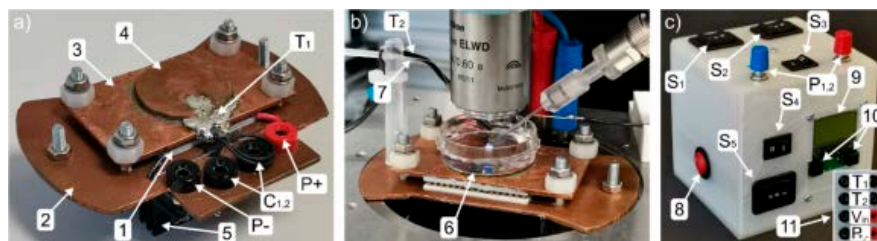

Figure 1. (**a**) Temperature-controlled sample holder: the sample holder consists mainly of a Peltier element (1), fixed between a lower copper plate (2) and an upper copper plate (3), including a copper disc (4), to fit a 35 mm Petri dish. A heat sink (5) is mounted to the lower plate and a thermometer, T_1, soldered to the copper disc. The Peltier element is electrically connected via P+ and P−. The thermometer is contacted with the two connectors, $C_{1,2}$. (**b**) Sample holder inside the patch clamp setup: The bottom plate fits into the microscope table, which has enough space underneath to accommodate the heatsink. Thermometer T_2 is used to monitor the temperature of the bath solution inside a 35 mm Petri dish (6). Attached to thermometer T_2 is the feed line (7) of the fluid compensation system. (**c**) 3D printed housing for the controller parts: power switch (8), switches S_1, S_2, and S_3, potentiometers P_1 and P_2, display (9), buttons to change display settings (10), connectors on the backside (11).

In this study, we designed the lower plate to fit into the microscope platform of a Nikon FN1 microscope shown in Figure 1b. From the backside, the thermometer, T_1, and the Peltier element are connected. A second thermometer, T_2, is dipping into the bath solution inside the 35 mm Petri dish (6) to monitor its temperature directly. The different configurations regarding the use of T_1 and T_2 are described in the results section later on. In order to compensate for the evaporation of the bath solution in long-term measurements, an automated syringe pump (Aladdin AL-1000) connected through a rubber hose to a thin plastic tube (7) hanging into the bath solution has been used. The necessary refill

rates using distilled water have been determined to be 250 and 750 μL/h at RT and 36 °C, respectively, and perfusion was applied using a small continuous flow.

    Both controllers for heating and cooling, a display to read out the thermometers, two potentiometers to regulate the temperature, and several switches to choose the operation modes have been built into a 3D printed housing shown in Figure 1c. The functions of the switches are explained in combination with the circuit description in below. The connectors for the power supply, the Peltier element, and the thermometers are placed on the backside. Detailed specifications of the utilized parts can be found at the end of this study, and the 3D model of the housing is made freely accessible online (IEEE dataport, http://dx.doi.org/10.21227/zj2v-9c32). The electrical circuit to connect all parts is shown at full length in Figure 2. The upper blue box displays the electronics inside the 3D printed housing. Both microcontrollers, to drive the Peltier element for heating and cooling, feature their own potentiometer ($P_{1,2}$) to set the target temperature. The electrical circuit design allows for the use of thermometer T_1 for feedback to the controller and the second thermometer, T_2, to show the bath temperature on the display. Since both thermometers have to be connected to a microcontroller in order to work properly, both controllers are permanently turned on. Switches S_1, S_2 as well as S_3 are used to change between heating and cooling mode. The switch S_4 can be used to connect thermometer T_2 instead of T_1 to the currently used microcontroller. Last, switch S_5 is used to select thermometer T_1 or T_2 to be shown on the display. The lower dash-lined box contains the parts of the patch clamp inset with the Peltier element and the thermometers T_1 and T_2. Note, the capacitors $C_{1,2}$ and the resistor R_1 form a low-pass filter. It reduces the electromagnetic noise of the microcontrollers that would otherwise disturb the sensitive patch clamp measurements. A small remaining noise in the measurements is removed in data post-processing with a digital filter. Furthermore, the resistor R_1 also limits the current through the Peltier element to keep the voltage constantly above the minimum of 10 V needed to operate the microcontrollers. Despite the additional resistor, the Peltier element still used more than 1 A of current, which comes along with a notable power drop across the resistor R_1 leading to a significant heating of the adjacent components. Therefore, the resistor has to be cooled sufficiently and we decided to set up it outside the 3D printed housing. However, the integration of this part into a 3D printed housing can be realized by adding additional ventilation, such as a CPU cooling fan into the housing design.
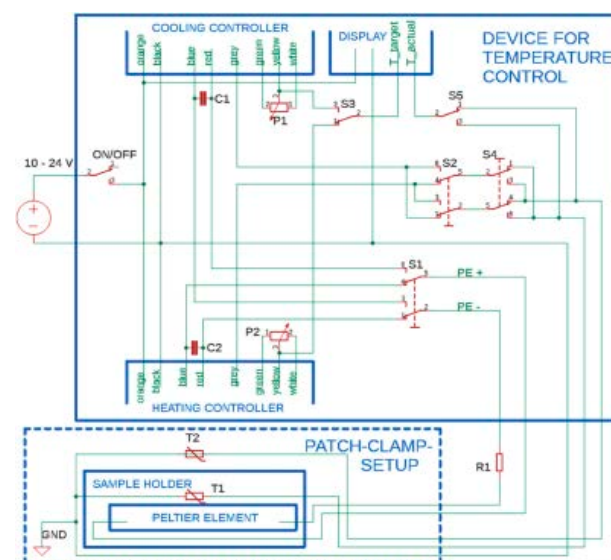

Figure 2. Top: Circuit inside 3D printed housing. Bottom: Microscope inset. P_1, P_2: Potentiometer for temperature adjustment. T_1, T_2: Thermometers. S_1, S_2, S_3: Switching between heating and cooling. S_4: Thermometer selection for the controllers. S_5: Thermometer selection for the display. R_1, $C_{1,2}$: Low-pass filter and current matching. (Appendix A).

4. Results and Discussion

At first, the maximum cooling and heating performances of the custom-made inset using bath solution in a 35 mm Petri dish have been investigated. We achieved a minimum temperature of 15 °C and a maximum temperature of 60 °C, as illustrated in Figure 3a. These upper and lower temperatures are generally limited by the maximum current output of 3 A from the power source (Laboratory PS-303D) and the capability of the passive heat sink to dissipate the produced heat and thus cool the Peltier element, respectively. Specifically, the upper limit is restricted primarily by the maximal current we used. The lower limit is especially limited at high currents due to ohmic (Joule) heating of the Peltier element itself. Here, in addition to the current induced Peltier effect, the current applied to the Peltier element also produces a considerable amount of heat. Therefore, the cooling of samples relies solely on the Peltier effect and proper heat dissipation from the bottom plate. Since only a passive heat sink has been used in our setup, symmetric cooling and heating from room temperature is not possible. However, symmetric behavior could easily be achieved by improving the cooling performance by using an active water-cooled heat sink, which then replaces the air-cooled finned heat sink.
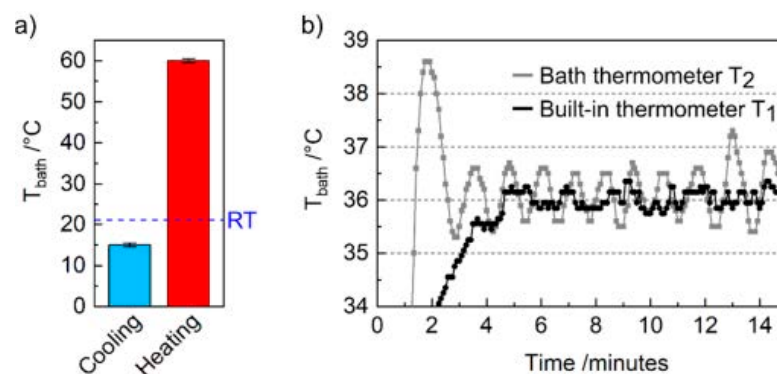
Figure 3. Regulation of the temperature in a 35 mm Petri dish. (**a**) Maximum cooling and heating capability using a 3 A power supply and a passive heat sink. Error bar is ±0.5 °C. (**b**) Temperature course of the bath solution during heating to 36 °C using the bath thermometer and the built-in thermometer as feedback line for the controller, respectively. The temperature was measured with the bath thermometer T_2.

Then, we investigated the response of the fluid temperature over time when using the built-in thermometer T_1 and the bath thermometer T_2 as feedback line for the Peltier heating. Using T_1 for feedback has been proved to be the better option for temperature control in terms of temperature stability illustrated in Figure 3b. The graph displays the time dependency of the bath solution's temperature in both configurations during heating from RT to a set point temperature of 36 °C. By utilizing the bath thermometer, an initial temperature overshoot is observable within the first three minutes (gray line), which could be critical for sensitive biological samples. In contrast, a built-in thermometer feedback leads to a smooth approach to the desired temperature (black line). Furthermore, using T_1 instead of T_2 reduces the temperature variation from about ±0.5 to ±0.25 °C. The worse response using T_2 as a loop back signal can be explained by poor heat conductivity of the plastic Petri dish, which inhibits a sufficiently quick response to temperature changes of the sample holder. Using dishes with better heat conductivity—e.g., glass or metal—would reduce the response time. It is worth noting that, when T_1 is used as a feedback thermometer during sensitive electrophysiological measurements, a calibration of the temperature offset between desired bath temperature and actual value measured at T_1 is inevitable. In our setup, we determined an offset of approx. 10 °C between T_1 and T_2. However, if small (periodic) temperature deviations of ±0.5 °C can be tolerated, a sufficient offset-free temperature control can be achieved after heating up by using S_4 to connect thermometer T_2

to the currently used microcontroller. It is worth noting that in both measurements, T_2 has been used to read out the temperature of the fluid.

Finally, we used the previously described setup to compare—as a proof of concept— the characteristic electrophysiological properties of T cells and neurons at RT and 36 °C. The latter one represents a naturally occurring biological system as it is close to the natural human body temperature while still having a 1 K safety zone to pyrexia. It is worth noting that the investigated parameters are not explicitly known as temperature dependent such as thermoreceptors [30], yet we found a noticeable influence of the temperature. The temperature was maintained using thermometer T_1 as feedback loop for the Peltier element while observing the correct temperature on the display using thermometer T_2.

First, we investigated passive membrane properties that can be determined with both cell types—namely the resting membrane potential (RMP), the membrane time constant (MTC), and the membrane capacitance (MC) shown in Figure 4a–c. The RMP increases for T cells from −41.7 to −48.1 mV and decreases for neurons from −39.2 to −29.6 mV with higher temperature. The MTCs show an increase depending on the temperature for both cell types (from 5.7 to 9.7 ms and from 21.5 to 29.3 ms), while temperature has in principle no effect on the MC of 9 and 6 pF, respectively. Formerly mentioned changes in RMP could be explained for T cells by an increased cellular activity at physiological temperatures, leading to higher RMP values. For the neurons, higher cellular activity might mean that adenosine triphosphate (ATP) is consumed faster at 36 °C compared to RT. A lack of sufficient APT could result in a lower RMP due to ATP-dependent Na^+ and K^+ pumps in neurons [31]. For the MTCs, higher temperature raises the probability of open ion channels, which would result in an increased time constant [32]. The capacitance of the membrane is defined predominantly by the surface area of the cell membrane, a measure for the cell size. Therefore, temperature and accordantly the cellular activity have no direct influence on the membrane capacitance. However, all values are still within the error in accordance with the literature [27,33–37]. Only the capacitances of the neurons differ from literature indicated by a smaller value. The reduced MC can be explained by a smaller cell surface area caused by replanting shortly before the experiments (*cf.* methods).
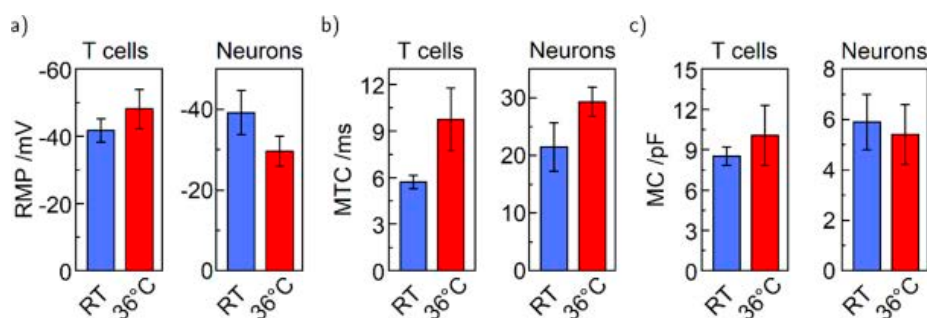

Figure 4. Basic electrophysiological properties of T cells and neurons at RT and 36 °C, respectively. (**a**) Resting membrane potential. (**b**) Membrane time constant. (**c**) Membrane capacitance. T cells: n (RT) = 11, n(36 °C) = 7. Neurons: n (RT) = 8, n (36 °C) = 7.

Second, we tested for cell specific properties in T cells and neurons. For T cells, the gating potential of voltage-gated ion channels is shown in Figure 5a. Voltage ramps from −65 to +15 mV have been applied to the cell. The threshold voltage was defined at the increase in the measured current indicating the opening of the ion channels (*cf.* Supplementary Material Figure S1). The gating potential is generally in accordance with the literature [36,38]. The small shift of the threshold from −23.3 to −25.0 mV—an earlier onset—is reasonable, since most proteins have their peak activity at physiological temperatures rather than at RT and the change in channel-conformation that leads to opening of the channels happens faster at 36 °C than at ambient temperatures [39,40]. For neurons, we tested the capability to fire action potentials (APs) after current-induced membrane depolarization to prove the proper electrophysiological function of the neurons [41]. As a result, the neurons show a characteristic

firing of APs for both RT and 36 °C [42]. An exemplary trace recorded at 36 °C is illustrated in Figure 5b. Furthermore, we can confirm a linear dependence of the firing frequency on the amount of injected current shown in Figure 5c [34,43]. Note that the maximum firing frequency of a single cell of approx. 30 Hz at 36 °C is higher compared to approx. 15 Hz at RT. This feature of higher maximal firing frequency was reproducible and goes along with a reduced AP height, summarized in Figure 5d,e. The averaged maximal firing frequency increased from 20 to 36 Hz while the corresponding height decreased from 80.8 to 54.2 mV—in general appropriate values for AP heights [20,35,44,45]. The higher frequency can be explained by faster gating ion channels again allowing for a more rapid sequence of depolarization and repolarization of the cell membrane. Note that the membrane channels at 36 °C can react faster to the ion influx during depolarization than at 20 °C; as a consequence, the repolarization takes place already at lower voltages, leading to smaller action potentials. Literature for patch clamping is not consistent since both temperature dependency and temperature insensitivity for AP frequency have been reported for rat and mouse neurons, respectively [46,47]; however, we can report on a sensitivity. Furthermore, processes in optogenetics showed sensitivity to temperature [48,49]. If one would combine patch clamping with optogenetics, our setup could offer a considerable advantage as well.
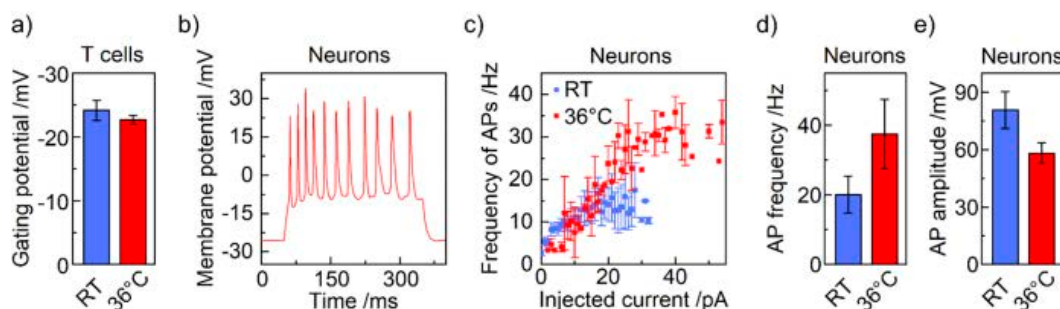
Figure 5. Specific electrophysiological properties. (**a**) Gating threshold of voltage-gated ion channels in T cells at RT and 36 °C. (**b**) Exemplary patch clamp recording of action potentials (APs) at 36 °C during current injection from 50 to 350 ms. (**c**) The firing frequency of APs depending on the injected current for RT and 36 °C of specific cells. The error bars are standard deviation. (**d**) Average maximal firing frequency of action potentials at RT and 36 °C weighted of n cells. (**e**) Average height of APs at maximal firing frequency at RT and 36 °C. T cells: n (RT) = 11, n (36 °C) = 7. Neurons: n (RT) = 8, n (36 °C) = 7.

5. Conclusions

We built an easy to adopt, custom-made, temperature-controlled patch clamp platform for upright patch clamp setups priced at approximately EUR 350 in total. The controller in our presented configuration allows for cooling to 15 °C and heating up to 60 °C limited in our configuration by the passive heat sink and the utilized 3 A power supply, respectively. Temperatures are kept steady at the adjusted values with a tolerance of maximal ±0.25 °C. Furthermore, we show the function of the setup in proof of concept measurements with Jurkat T lymphocytes and human induced pluripotent stem cell-derived neurons. We investigated both basic electrophysiological properties, such as resting membrane potential, membrane time constant, and membrane capacitance as well as cell characteristic responses such as the gating of voltage-gated ion channels and the firing of action potentials. Typically, such properties are not considered as particularly temperature dependent or literature is inconsistent in their findings. However, we found shifts of many parameters when measured at RT and 36 °C, respectively. Therefore, our results advise controlling the temperature if improved physiological conditions are required, which we can offer with our custom-built setup. Furthermore, small disparities among different studies might just be caused due to different temperatures during patch clamping, and we strongly advise considering this if results are compared directly.

Appendix A

Heating controller	Quick Ohm QC-PC-C01H-100
Cooling controller	Quick Ohm QC-PC-C01C
Peltier Element	Quick-Cool QC-127-1.4-8.5MD
Display	Quick Ohm QC-PC-D-100
Potentiometer P_1, P_2	0–10 kΩ, supplied with microcontroller
Thermometer T_1, T_2	10 kΩ NTC, supplied with microcontroller
Switches S_1, S_2, S_4	Arcolectric H1570 VB AAA 250V/AC
Switches S_3, S_5	TRU COMPONENTS TC-R13-66C-02 250 V/AC
Resistor R_1	ATE Electronics RB50 5.6 Ω 50 W 5%
Capacitors $C_{1,2}$	Yageo SE025M4700B7F-1632

References

1. Piccolino, M. Luigi Galvani and Animal Electricity: Two Centuries after the Foundation of Electrophysiology. *Trends Neurosci.* **1997**, *20*, 443–448. [CrossRef]
2. Neher, E.; Sakmann, B. Single-Channel Currents Recorded from Membrane of Denervated Frog Muscle Fibres. *Nature* **1976**, *260*, 799–802. [CrossRef] [PubMed]
3. Sakmann, B.; Neher, E. Patch Clamp Techniques for Studying Ionic Channels in Excitable Membranes. *Annu. Rev. Physiol.* **1984**, *46*, 455–472. [CrossRef] [PubMed]
4. Zhao, Y.; Inayat, S.; Dikin, D.A.; Singer, J.H.; Ruoff, R.S.; Troy, J.B. Patch Clamp Technique: Review of the Current State of the Art and Potential Contributions from Nanoengineering. *Proc. Inst. Mech. Eng. Part N. J. Nanoeng. Nanosyst.* **2008**, *222*, 1–11. [CrossRef]
5. Rubaiy, H.N. A Short Guide to Electrophysiology and Ion Channels. *J. Pharm. Pharm. Sci.* **2017**, *20*, 48. [CrossRef]
6. Kornreich, B.G. The Patch Clamp Technique: Principles and Technical Considerations. *J. Vet. Cardiol.* **2007**, *9*, 25–37. [CrossRef]
7. Chen, C.-C.; Cang, C.; Fenske, S.; Butz, E.; Chao, Y.-K.; Biel, M.; Ren, D.; Wahl-Schott, C.; Grimm, C. Patch-Clamp Technique to Characterize Ion Channels in Enlarged Individual Endolysosomes. *Nat. Protoc.* **2017**, *12*, 1639–1658. [CrossRef]
8. Armstrong, C.M.; Hille, B. Voltage-Gated Ion Channels and Electrical Excitability. *Neuron* **1998**, *20*, 371–380. [CrossRef]

9.　Wolpaw, J.R.; Birbaumer, N.; McFarland, D.J.; Pfurtscheller, G.; Vaughan, T.M. Brain–Computer Interfaces for Communication and Control. *Clin. Neurophysiol.* **2002**, *113*, 767–791. [CrossRef]

10.　Fertig, N.; Blick, R.H.; Behrends, J.C. Whole Cell Patch Clamp Recording Performed on a Planar Glass Chip. *Biophys. J.* **2002**, *82*, 3056–3062. [CrossRef]

11.　Chen, P.; Zhang, W.; Zhou, J.; Wang, P.; Xiao, L.; Yang, M. Development of Planar Patch Clamp Technology and Its Application in the Analysis of Cellular Electrophysiology. *Prog. Nat. Sci.* **2009**, *19*, 153–160. [CrossRef]

12.　Annecchino, L.A.; Schultz, S.R. Progress in Automating Patch Clamp Cellular Physiology. *Brain Neurosci. Adv.* **2018**, *2*, 239821281877656. [CrossRef] [PubMed]

13.　Yajuan, X.; Xin, L.; Zhiyuan, L. A Comparison of the Performance and Application Differences Between Manual and Automated Patch-Clamp Techniques. *Curr. Chem. Genom.* **2012**, *6*, 87–92. [CrossRef] [PubMed]

14.　Tao, C.; Zhang, G.; Xiong, Y.; Zhou, Y. Functional Dissection of Synaptic Circuits: In Vivo Patch-Clamp Recording in Neuroscience. *Front. Neural Circuits* **2015**, *9*, 23. [CrossRef]

15.　Kodandaramaiah, S.B.; Franzesi, G.T.; Chow, B.Y.; Boyden, E.S.; Forest, C.R. Automated Whole-Cell Patch-Clamp Electrophysiology of Neurons in Vivo. *Nat. Methods* **2012**, *9*, 585–587. [CrossRef]

16.　Dupuis, G.; Héroux, J.; Payet, M.D. Characterization of Ca^{2+} and K^+ Currents in the Human Jurkat T Cell Line: Effects of Phytohaemagglutinin. *J. Physiol.* **1989**, *412*, 135–154. [CrossRef]

17.　Franco-Obregón, A.; Wang, H.; Clapham, D.E. Distinct Ion Channel Classes Are Expressed on the Outer Nuclear Envelope of T- and B-Lymphocyte Cell Lines. *Biophys. J.* **2000**, *79*, 202–214. [CrossRef]

18.　Chokshi, R.; Matsushita, M.; Kozak, J.A. Sensitivity of TRPM7 Channels to Mg^{2+} Characterized in Cell-Free Patches of Jurkat T Lymphocytes. *Am. J. Physiol. Physiol.* **2012**, *302*, C1642–C1651. [CrossRef]

19.　Needham, K.; Hyakumura, T.; Gunewardene, N.; Dottori, M.; Nayagam, B.A. Electrophysiological Properties of Neurosensory Progenitors Derived from Human Embryonic Stem Cells. *Stem Cell Res.* **2014**, *12*, 241–249. [CrossRef]

20.　Khattak, S.; Brimble, E.; Zhang, W.; Zaslavsky, K.; Strong, E.; Ross, P.J.; Hendry, J.; Mital, S.; Salter, M.W.; Osborne, L.R.; et al. Human Induced Pluripotent Stem Cell Derived Neurons as a Model for Williams-Beuren Syndrome. *Mol. Brain* **2015**, *8*, 77. [CrossRef]

21.　Kikuchi, T.; Morizane, A.; Doi, D.; Magotani, H.; Onoe, H.; Hayashi, T.; Mizuma, H.; Takara, S.; Takahashi, R.; Inoue, H.; et al. Human IPS Cell-Derived Dopaminergic Neurons Function in a Primate Parkinson's Disease Model. *Nature* **2017**, *548*, 592–596. [CrossRef] [PubMed]

22.　Gunhanlar, N.; Shpak, G.; van der Kroeg, M.; Gouty-Colomer, L.A.; Munshi, S.T.; Lendemeijer, B.; Ghazvini, M.; Dupont, C.; Hoogendijk, W.J.G.; Gribnau, J.; et al. A Simplified Protocol for Differentiation of Electrophysiologically Mature Neuronal Networks from Human Induced Pluripotent Stem Cells. *Mol. Psychiatry* **2018**, *23*, 1336–1344. [CrossRef] [PubMed]

23.　Wang, H.; Wang, B.; Normoyle, K.P.; Jackson, K.; Spitler, K.; Sharrock, M.F.; Miller, C.M.; Best, C.; Llano, D.; Du, R. Brain Temperature and Its Fundamental Properties: A Review for Clinical Neuroscientists. *Front. Neurosci.* **2014**, *8*, 1–17. [CrossRef] [PubMed]

24.　Klinke, R.; Pape, H.-C.; Silbernagl, S. *Physiologie*, 5th ed.; Klinke, R., Pape, H.-C., Silbernagl, S., Eds.; Georg Thieme Verlag: Stuttgart, Germany, 2005. [CrossRef]

25.　Pape, H.-C.; Klinke, R.; Brenner, B.; Silbernagl, S. *Physiologie, 7 vollst.*; Pape, H.-C., Kurtz, A., Silbernagl, S., Eds.; Georg Thieme Verlag: Stuttgart, Germany, 2014. [CrossRef]

26.　Bausch, C.S.; Heyn, C.; Hansen, W.; Wolf, I.M.A.; Diercks, B.-P.; Guse, A.H.; Blick, R.H. Ultra-Fast Cell Counters Based on Microtubular Waveguides. *Sci. Rep.* **2017**, *7*, 41584. [CrossRef] [PubMed]

27.　Reinhardt, P.; Glatza, M.; Hemmer, K.; Tsytsyura, Y.; Thiel, C.S.; Höing, S.; Moritz, S.; Parga, J.A.; Wagner, L.; Bruder, J.M.; et al. Derivation and Expansion Using Only Small Molecules of Human Neural Progenitors for Neurodegenerative Disease Modeling. *PLoS ONE* **2013**, *8*, e59252. [CrossRef]

28.　Partida-Sanchez, S.; Gasser, A.; Fliegert, R.; Siebrands, C.C.; Dammermann, W.; Shi, G.; Mousseau, B.J.; Sumoza-Toledo, A.; Bhagat, H.; Walseth, T.F.; et al. Chemotaxis of Mouse Bone Marrow Neutrophils and Dendritic Cells Is Controlled by ADP-Ribose, the Major Product Generated by the CD38 Enzyme Reaction. *J. Immunol.* **2007**, *179*, 7827–7839. [CrossRef]

29.　Neher, E.; Sakmann, B.; Steinbach, J.H. The Extracellular Patch Clamp: A Method for Resolving Currents through Individual Open Channels in Biological Membranes. *Pfluegers Arch. Eur. J. Physiol.* **1978**, *375*, 219–228. [CrossRef]

30. Cramer, G.D.; Darby, S.A. *Clinical Anatomy of the Spine, Spinal Cord, and ANS*, 3rd ed.; Elsevier Health Sciences: London, UK, 2013.

31. Siegel, G.J. *Basic Neurochemistry*, 6th ed.; Siegel, G.J., Ed.; Lippincott Williams & Wilkins: Philadelphia, PA, USA, 1999.

32. Cesare, P.; Moriondo, A.; Vellani, V.; Mcnaughton, P.A. Ion Channels Gated by Heat. *Proc. Natl. Acad. Sci. USA* **1999**, *96*, 7658–7663. [CrossRef]

33. Cahalan, M.D.; Chandy, K.G. The Functional Network of Ion Channels in T Lymphocytes. *Immunol. Rev.* **2009**, *231*, 59–87. [CrossRef]

34. Toma, J.S.; Shettar, B.C.; Chipman, P.H.; Pinto, D.M.; Borowska, J.P.; Ichida, J.K.; Fawcett, J.P.; Zhang, Y.; Eggan, K.; Rafuse, V.F. Motoneurons Derived from Induced Pluripotent Stem Cells Develop Mature Phenotypes Typical of Endogenous Spinal Motoneurons. *J. Neurosci.* **2015**, *35*, 1291–1306. [CrossRef]

35. Moe, M.C.; Varghese, M.; Danilov, A.I.; Westerlund, U.; Ramm-Pettersen, J.; Brundin, L.; Svensson, M.; Berg-Johnsen, J.; Langmoen, I.A. Multipotent Progenitor Cells from the Adult Human Brain: Neurophysiological Differentiation to Mature Neurons. *Brain* **2005**, *128*, 2189–2199. [CrossRef] [PubMed]

36. DeCoursey, T.E.; Chandy, K.G.; Gupta, S.; Cahalan, M.D. Voltage-Dependent Ion Channels in T-Lymphocytes. *J. Neuroimmunol.* **1985**, *10*, 71–95. [CrossRef]

37. Pottosin, I.I.; Valencia-Cruz, G.; Bonales-Alatorre, E.; Shabala, S.N.; Dobrovinskaya, O.R. Methyl-β-Cyclodextrin Reversibly Alters the Gating of Lipid Rafts-Associated Kv1.3 Channels in Jurkat T Lymphocytes. *Pflügers Arch. Eur. J. Physiol.* **2007**, *454*, 235–244. [CrossRef] [PubMed]

38. Harberts, J.; Zierold, R.; Fendler, C.; Koitmäe, A.; Bayat, P.; Fernandez-Cuesta, I.; Loers, G.; Diercks, B.-P.; Fliegert, R.; Guse, A.H.; et al. Culturing and Patch Clamping of Jurkat T Cells and Neurons on Al_2O_3 Coated Nanowire Arrays of Altered Morphology. *RSC Adv.* **2019**, *9*, 11194–11201. [CrossRef]

39. Lee, S.C.; Deutsch, C. Temperature Dependence of K(+)-Channel Properties in Human T Lymphocytes. *Biophys. J.* **1990**, *57*, 49–62. [CrossRef]

40. Kimitsuki, T.; Komune, S. Temperature Enhances Activation and Inactivation Kinetics of Potassium Currents in Inner Hair Cells Isolated from Guinea-Pig Cochlea. *Clin. Exp. Otorhinolaryngol.* **2013**, *6*, 140. [CrossRef]

41. Lodish, H.F.; Berk, A.; Kaiser, C.; Krieger, M.; Bretscher, A.; Ploegh, H.L.; Amon, A.; Scott, M.P. *Molecular Cell Biology*, 7th ed.; Freeman: New York, NY, USA, 2012.

42. Koitmäe, A.; Müller, M.; Bausch, C.S.; Harberts, J.; Hansen, W.; Loers, G.; Blick, R.H. Designer Neural Networks with Embedded Semiconductor Microtube Arrays. *Langmuir* **2018**, *34*, 1528–1534. [CrossRef]

43. Djuric, U.; Cheung, A.Y.L.; Zhang, W.; Mok, R.S.; Lai, W.; Piekna, A.; Hendry, J.A.; Ross, P.J.; Pasceri, P.; Kim, D.-S.; et al. MECP2e1 Isoform Mutation Affects the Form and Function of Neurons Derived from Rett Syndrome Patient IPS Cells. *Neurobiol. Dis.* **2015**, *76*, 37–45. [CrossRef]

44. Xie, Y.; Schutte, R.J.; Ng, N.N.; Ess, K.C.; Schwartz, P.H.; O'Dowd, D.K. Reproducible and Efficient Generation of Functionally Active Neurons from Human HiPSCs for Preclinical Disease Modeling. *Stem. Cell Res.* **2018**, *26*, 84–94. [CrossRef]

45. Harberts, J.; Haferkamp, U.; Haugg, S.; Fendler, C.; Lam, D.; Zierold, R.; Pless, O.; Blick, R.H. Interfacing Human Induced Pluripotent Stem Cell-Derived Neurons with Designed Nanowire Arrays as a Future Platform for Medical Applications. *Biomater. Sci.* **2020**, *8*, 2434–2446. [CrossRef]

46. Huang, S.; Uusisaari, M.Y. Physiological Temperature during Brain Slicing Enhances the Quality of Acute Slice Preparations. *Front. Cell. Neurosci.* **2013**, *7*. [CrossRef] [PubMed]

47. Griffin, J.D.; Boulant, J.A. Temperature Effects on Membrane Potential and Input Resistance in Rat Hypothalamic Neurones. *J. Physiol.* **1995**, *488*, 407–418. [CrossRef] [PubMed]

48. Picot, A.; Dominguez, S.; Liu, C.; Chen, I.-W.; Tanese, D.; Ronzitti, E.; Berto, P.; Papagiakoumou, E.; Oron, D.; Tessier, G.; et al. Temperature Rise under Two-Photon Optogenetic Brain Stimulation. *Cell Rep.* **2018**, *24*, 1243–1253.e5. [CrossRef] [PubMed]

49. Owen, S.F.; Liu, M.H.; Kreitzer, A.C. Thermal Constraints on in Vivo Optogenetic Manipulations. *Nat. Neurosci.* **2019**, *22*, 1061–1065. [CrossRef] [PubMed]

Supporting Material

A temperature-controlled patch-clamp platform demonstrated on Jurkat T lymphocytes and human induced pluripotent stem cell-derived neurons

Jann Harberts [1, †], Max Kusch [1, †], John O'Sullivan [1, 2], Robert Zierold [1, *] and Robert H. Blick [1, 3]

[1] Center for Hybrid Nanostructures, Universität Hamburg, 22761 Hamburg, Germany

[2] Department of Physics and Astronomy, University College London, London WC1E 6BT, United Kingdom

[3] Material Science and Engineering, College of Engineering, University of Wisconsin-Madison, Madison, Wisconsin 53706, USA

[†] These authors contributed equally.

[*] Correspondence: rzierold@chyn.uni-hamburg.de
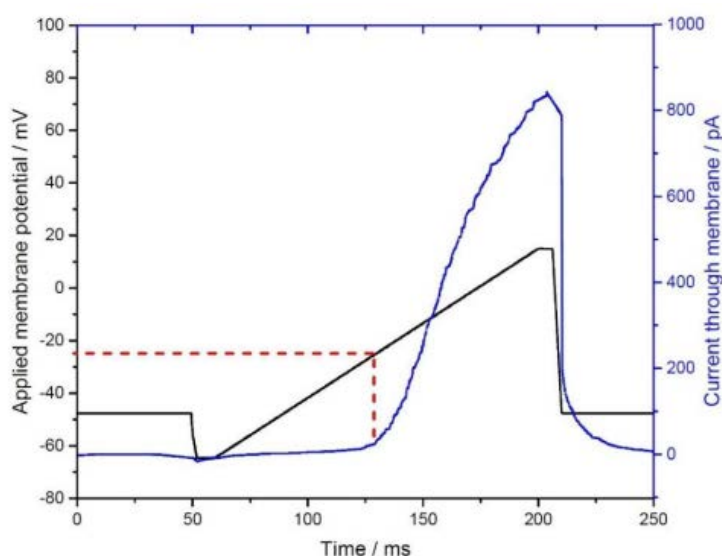
Figure S1. Illustration to describe the definition of the gating potential in T cells. Voltage ramp from -65 mV to +15 mV (black). Position/potential of the increase (red dashed) in the membrane current (blue).

Table S1: Statistical analysis of patch clamp results *via* ANOVA with post hoc Turkey's test.

Cell	Parameter	MeanDiff	SEM	q Value	Prob	Alpha	Sig	LCL	UCL
T cells	RMP	-6.37029	6.41053	1.40534	0.33515	0.35	1	-12.54202	-0.19856
	MC	1.51606	1.95361	1.09747	0.44905	0.45	1	0.00323	3.02889
	MTC	4.02522	1.67845	3.39154	0.02902	0.05	1	0.467	7.58344
	GP	1.49631	2.04625	1.03413	0.4752	0.5	1	0.08412	2.90849
Neurons	RMP	9.59087	6.81989	1.98882	0.18308	0.2	1	0.38282	18.79891
	MTC	7.82678	5.08584	2.17638	0.1478	0.15	1	0.04583	15.60773
	MC	-0.49548	1.61985	0.43258	0.76454	0.8	1	-0.91436	-0.0766
	AP freq.	17.37315	10.8821	2.25778	0.13439	0.15	1	0.72435	34.02195
	AP ampl.	-22.63455	11.44835	2.79604	0.06963	0.1	1	-42.90903	-2.36007

A.2 Publication II

Culturing and patch clamping of Jurkat T cells and neurons on Al$_2$O$_3$ coated nanowire arrays of altered morphology

Jann Harberts, Robert Zierold, Cornelius Fendler, Aune Koitmäe, Parisa Bayat, Irene Fernandez-Cuesta, Gabriele Loers, Björn-Philipp Diercks, Ralf Fliegert, Andreas H. Guse, Carsten Ronning, Gaute Otnes, Magnus Borgström, and Robert H. Blick

Author contributions: Patch clamping, fluorescent imaging, data analysis, and manuscript writing: J.H., cell culture: J.H., C.F., A.K., animal preparation: G.L, T cell preparation: B.-P.D., R.F., A.H.G., SEM/FIB imaging: J.H., I.F.C., P.B., ZnO NW preparation: C.R., InP NW preparation: G.O., M.B., ALD: R.Z., supervision: R.Z., R.H.B.

(8 + 4 pages)

Check for updates

Culturing and patch clamping of Jurkat T cells and neurons on Al₂O₃ coated nanowire arrays of altered morphology†

Jann Harberts,[a] Robert Zierold,[a] Cornelius Fendler,[a] Aune Koitmäe,[a] Parisa Bayat,[a] Irene Fernandez-Cuesta,[a] Gabriele Loers,[b] Björn-Philipp Diercks,[c] Ralf Fliegert,[c] Andreas H. Guse,[c] Carsten Ronning,[d] Gaute Otnes,[ef] Magnus Borgström[ef] and Robert H. Blick ⓘ *[ag]

Nanowire substrates play an increasingly important role for cell cultures as an approach for hybrid bio-semiconductor junctions. We investigate Jurkat T cells and neurons from mice cultured on Al₂O₃ coated ordered and randomly distributed nanowires. Cell viability was examined by life/membrane staining reporting comparable viability on planar and nanowire substrates. Imaging the hybrid interface reveals a wrapping of the cell membrane around the very nanowire tip. Patch clamp recordings show similar electrophysiological responses on each type of nanowires compared to planar control substrates. We demonstrate that the morphological characteristic of the nanowire substrate plays a subordinate role which opens up the arena for a large range of nanowire substrates in a functionalized application such as stimulation or sensing.

1 Introduction

Chemical and physical properties of surfaces and culture substrates have a significant influence on adhesion and viability of seeded dissociated cells.[1–4] Hence, nano- and micro-structured substrates lately gained increasing attention in cell biology.[5] Vertically aligned nanowires (NWs) as culturing substrate play here an important role, since variations in length, diameter, and density of the NWs influence cellular growth parameters, viability, and adhesion.[6–9] Furthermore, NW substrates can be used to support directed polarization of cells, e.g. outgrowth of axons from neurons,[10] to measure mechanical cell properties,[11] or to constrain cellular movement and spreading.[12,13] Note, compared to planar substrates, functional NWs can interact on a nanoscopic level with the cell and

the cell's membrane. Such local stimulation and interactions which cannot be realized by planar substrates allow for novel applications such as in optogenetics, as light guiding or emitting components,[14–16] for electrical sensing[17–19] as well as indirect photo current stimulation once p–n junctions are integrated,[20,21] to name a few of them. Of course, in a first step one has to prove that the cell's viability and electrophysiology are not drastically altered on NW samples compared to planar reference substrates.

Typically, cellular outgrowth and guiding experiments are analyzed with fluorescent labeling techniques as well as light microscopy primarily delivering a visual impression.[22,23] For functional measurements of cell characteristics, such as membrane capacitance, gating properties of ion channels or amplitudes of neural action potentials, to name a few of them, a more precise method—patch clamping—is required.[24–26] However, conventional inverted patch clamp setups are limited to transparent substrates and thus are not suitable for opaque semiconductor samples. Hence, a custom-built upright patch clamp setup with a long working distance objective was used in this study, which is compatible with the types of samples used herein as illustrated in Fig. 1a. The substrates consisted of ordered arrays of indium phosphide (InP) NWs with identical lengths as well as randomly distributed zinc oxide (ZnO) NWs with varying heights (cf. Fig. 1b and c). To quantify and compare the regularity and disarrangement of the NW substrates we calculated corresponding fast Fourier transforms (FFTs) of the top view SEM images. The results are shown in Fig. 1d and e. The bright spots mark the reciprocal lattice proving high accuracy of the repeating structure of the ordered NW substrate. On the contrary, absence of bright spots in the reciprocal image

[a]Center for Hybrid Nanostructures, Universität Hamburg, Luruper Chaussee 149, 22761 Hamburg, Germany. E-mail: rblick@chyn.uni-hamburg.de; Tel: +49 40 42838 1975

[b]Center for Molecular Neurobiology Hamburg, University Medical Center Hamburg-Eppendorf, Falkenried 94, 20251 Hamburg, Germany

[c]Department of Biochemistry and Molecular Cell Biology, The Calcium Signaling Group, University Medical Center Hamburg-Eppendorf, Martinistraße 52, 20251 Hamburg, Germany

[d]Institute for Solid State Physics, Friedrich-Schiller-University Jena, Helmholtzweg 3-5, 07743 Jena, Germany

[e]NanoLund, Lund University, Box 118, 22100 Lund, Sweden

[f]Solid State Physics, Lund University, Box 118, 22100 Lund, Sweden

[g]Material Science and Engineering, College of Engineering, University of Wisconsin-Madison, Madison, Wisconsin 53706, USA

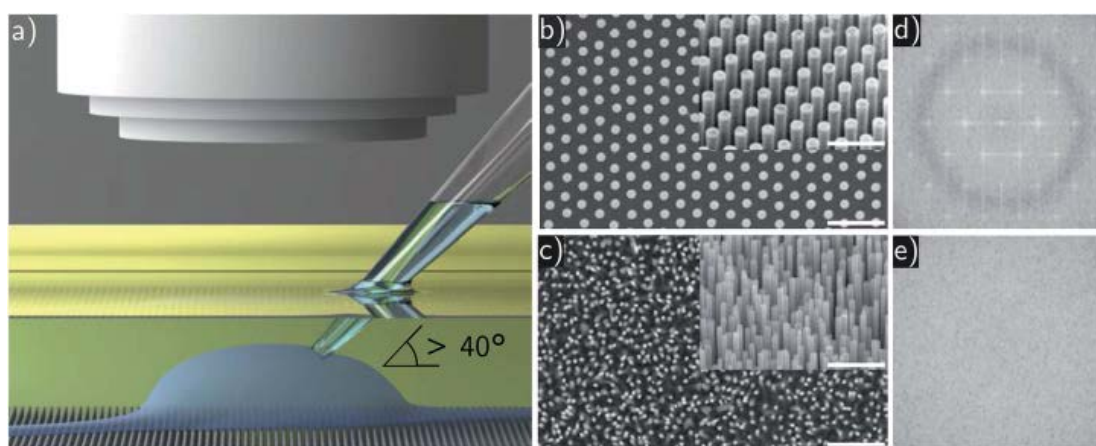† Electronic supplementary information (ESI) available. See DOI: 10.1039/c8ra05320k

Fig. 1 (a) Scheme of the upright patch clamp configuration. A non-immersion objective with extra long working distance is used. The neuron is settled on top of the NW substrate while the patch clamp pipette approaches with an angle of more than 40° between pipette and substrate. (b) A scanning electron microscope (SEM) image of the ordered pristine InP NWs: the NWs are aligned in a defined array with a pitch of 500 nm. The diameter is 180 nm with a length of 2 μm. Scale bar: 2 μm. (c) A SEM image of randomly distributed as-prepared ZnO NWs on silicon substrate. The diameters are between 70 and 180 nm, the length is about 3 μm, the average pitch is about 300 nm. Scale bar: 2 μm. Insets: angle of 40°, scale bars: 1 μm. (d) A FFT of the SEM image of ordered NWs. The bright spots mark the reciprocal lattice proving high accuracy of the repeating structure of the ordered NW substrate. (e) A FFT of the SEM image of random NWs. Absence of bright spots in the reciprocal image prove no repeating structures of the random NW substrate.

prove no repeating structures of the random NW substrate. In order to avoid any influence of the substrate's materials onto the outgrowth behavior and to study only on the geometry's impact, all substrates have been covered with a thin layer of aluminum oxide (Al_2O_3) by atomic layer deposition (ALD). A small pitch between individual NWs of less than 500 nm results for both types of samples in a high NW density. Standard Petri dishes and planar Al_2O_3 have been used as control growth substrates. We employed human T lymphocytes (Jurkat cells) and cerebellar granule cells from mice (neurons) for our studies. Considering the developed model for NW/cell interaction depending on NW density, length, and diameter in Buch-Månson et al.,[27] we expect the cells to stay on top of the NW tips, due to the high NW density. Comparable studies which combine NW arrays and patch clamping were performed with restricted areas of NWs and low NW densities.[28,29] In these configurations, the cells either adhered predominantly on areas without NWs or were wrapping around the entire NW. In our configuration, where just the NW tips carry the cells, the physical pressure of the pipette tip against the cell membrane during giga seal formation must be considered. Therefore, this undertaking also addresses the question whether spiky NW substrates are suitable for patch clamping applications without significantly damaging the cell. Our results can confirm this and show proper cell viability of both Jurkat cells and neurons independent of the NW arrangement and height distribution.

2 Methods

2.1 Nanowire preparation

The arrayed and randomly arranged NWs consisted of InP and ZnO, respectively. For the sake of comparability both types of NWs and a planar control were covered with a thin layer of

biocompatible Al_2O_3 (10–15 nm) deposited via ALD.[30] Note, for ZnO, the aluminum oxide also serves as passivation layer which is required due to chemical instability of ZnO at pH 7.4 of the cell culture medium.

The InP NWs were fabricated in an epitaxial growth process with gold droplets as seeds arranged in an array on InP(111)B substrates via nanoimprint lithography.[31] The nanoimprint technique facilitates control of the NW diameter through the seed particle size, and the regular and uniform seed particle array supports the achievement of identical NW lengths during the growth process. Here, we used a NW diameter of 180 nm, a length of 2 μm, and a pitch of 500 nm. The gold tip was removed by wet etching in a two times cycled procedure using iodine–potassium iodide solution and diluted phosphoric acid, respectively. The ZnO NWs were grown self-catalytic, self-assembled, and epitaxial on a 500 nm ZnO layer on top of silicon substrates. This process results into disordered arrays with NWs of a few micrometer length (with slight varying distribution) and diameters between 70 and 180 nm.[32] ALD was performed in a custom-built reactor utilizing trimethyl aluminum and water as precursors both kept at room temperature with a constant purge gas flow of about 25 sccm. In a typical ALD process pulse, exposure, and pump time was for both precursors 0.05 s, 30 s, and 90 s, respectively.

2.2 Cell culture

The Jurkat cells were cultured in Gibco RPMI 1640 + Gluta-MAX™-I medium with 25 mM 4-(2-hydroxyethyl)-1-piperazineethanesulfonic acid (HEPES), 7.5% new-born calf serum (NCS) and 1.2% (w/v) penicillin/streptomycin in T75 cell culture flasks at 37 °C and 5% CO_2 in air. The cell suspension was diluted with fresh medium every 2–3 days to keep the cell concentration between 0.3×10^6 and 1.2×10^6 cells per ml.

The neurons – postnatal cerebellar neurons – were derived from 6–7 days old wild-type mice (strain C57Bl6) of either sex or mice expressing GFP under the direction of the human ubiquitin C promoter (C57BL/6-Tg(UBC-GFP)30Scha/J) and were isolated as described in Loers *et al.*[33] Cell concentrations of about 2×10^5 cells per ml were used. The culture medium consisted of Neurobasal™ A, penicillin/streptomycin, bovine serum albumin, insulin, L-thyroxine, transferrin holo, sodium selenite, B-27™ supplement (see Loers *et al.*[33] for details) and 8% fetal bovine serum (Capricorn scientific, FBS Advanced). The neurons were cultured at 37 °C and 5% CO_2 in air.

Ethics approval. Jurkat cells: cell line, no approval required. Neurons: mice were kept and bred at the central animal facility of the Universitätsklinikum Hamburg-Eppendorf. Mice were kept at standard laboratory conditions with food and water supply *ad libitum* and an artificial 12 h light/dark cycle. All experiments were conducted in accordance with the German and European Community laws on protection of experimental animals, and all procedures used were approved by the responsible authorities of the State of Hamburg (Behörde für Wissenschaft und Gesundheit, Amt für Gesundheit und Verbraucherschutz, Lebensmittelsicherheit und Veterinärmedizin; animal permit number ORG 679 Morph). The manuscript was prepared following the ARRIVE guidelines for animal research.[34]

2.3 Sample preparation and cellular outgrowth

Control and NW measurements were performed in 35 mm Petri dishes (Fisher Scientific, Biolite). The plain bottom of the Petri dish was used in the control measurements. The NW substrates were sterilized in 70% ethanol and placed into the Petri dish. All substrates were coated with poly-D-lysine (PDL, mol wt 30 000–70 000, 0.1 mg ml^{-1}) in order to support cell adhesion. The coating was performed by covering the substrates with PDL for 30 min at room temperature. Subsequently, the PDL solution was removed and the samples were rinsed with deionized water and air-dried. Samples with Jurkat cells were prepared immediately prior to the measurements as described below. A droplet of cell suspension (20–30 µl) was applied to the substrate and the cells were left to adhere for 15 min in the incubator. Subsequently, the patch clamp bath solution was added. Samples for the neuron cultures were additionally coated with laminin. Here, the substrates were coated with laminin (1–2 mg ml^{-1}) for 20 min in the incubator. Subsequently, the laminin was removed and a droplet of cell suspension (20–30 µl) was applied to the substrate without drying of the remaining laminin. After an incubation period of 45–60 min at 37 °C and 5% CO_2 additional growth medium (3 ml) was added. The neurons were cultured 6–7 days *in vitro* (DIV) before the measurements. The culturing medium was renewed by two-thirds every 2–3 days with fresh medium. For imaging purposes by SEM and FIB, the samples were dried in air after a stepwise ethanol exchange.

2.4 Cell viability staining

The cell viability was tested *via* fluorescent staining and confocal microscopy. Cell somas were dyed with a cell viability indicator (Thermofisher, 496 nm/515 nm ex/em) and cell membranes were dyed with a cell membrane stain (Thermofisher, 555 nm/565 nm ex/em). Imaging was performed with a Leica TCS SP8 confocal microscope equipped with two lasers of 488 nm and 552 nm wavelength, respectively. Cell viability of the Jurkat cells was tested at the same day of transfer to the substrate and cell viability of the neurons was examined after 6 DIV of outgrowth. For staining, the growth medium was exchanged by a 1× dye mixture in Dulbecco's Phosphate-Buffered Saline (DPBS) and the cells were placed for 15 min at 37 °C and 5% CO_2 in the incubator. Subsequently, the staining solution was exchanged with a 1× background suppression dye (Thermofisher) in DPBS. With every type of substrate, 4 different areas for Jurkat cells and 6 areas for neurons were analyzed with ImageJ using the cell counter plugin.[35]

2.5 Patch clamp setup

Since the substrates for the cells were opaque, an upright patch clamp setup was utilized. In such a configuration, free space above the sample is limited generally. For this reason, the challenge was to achieve a perpendicular contact angle between the micropipette and the cell membrane, which is required for reliable giga seal forming.[36] To provide sufficient space, we used a non-immersion objective with an extra long working distance of 11 mm (Nikon CFI TU Plan EPI ELWD 50× N.A. 0.60/W.D. 11.00 mm) installed to a Nikon Eclipse FN1 upright microscope. As sketched in Fig. 1a, the angle between pipette and substrate was at least 40°, so the patch pipette approached the cell membrane in a perpendicular angle yielding high success rates for establishing giga seals. The pipette was mounted to a HEKA red star headstage and the signals were amplified with a HEKA EPC 10 USB patch clamp amplifier. The data was processed with a Bessel low-pass filter at 2.9 kHz. During patch clamping a particularly small amount of bath solution was required to minimize the surface bending of the fluid which downgrades the clear view on the sample. The probe stage carries standard 35 mm Petri dishes and a transfer of the sample was not required for any measurements. All measurements presented were performed with identically fabricated micropipettes. The borosilicate glass capillary blanks (GB150T-8P, Science Products) were pulled with a Sutter Instrument P-2000 pipette puller and subsequently heat polished (CPM-2, ALA Scientific Instruments). The diameter of the pipette tip was about 950 nm, which resulted in tip resistances of 3–5 MΩ and 7–9 MΩ depending on the different patch clamp solutions for Jurkat cells and neurons, respectively.

2.6 Electrophysiology

Different compositions of the pipette and bath solution were used for the Jurkat cells and the neurons. The patch clamp solutions for the Jurkat cells were adapted from Partida-Sanchez *et al.*[37] The pipette solution consisted of (in mM) 140KCl, 2MgCl$_2$, 1CaCl$_2$ and 2.5ethylene glycol tetraacetic acid (EGTA) and is buffered with 10 mM 4-(2-hydroxyethyl)-1-piperazineethanesulfonic acid (HEPES). The pH was adjusted to 7.3 with KOH. The bath solution consisted of (in mM) 140NaCl, 5KCl, 2MgCl$_2$, 2CaCl$_2$, 5glucose and was buffered with 10HEPES, adjusted to pH 7.4 with NaOH. The patch clamp

solutions utilized for the neurons were provided from Gall et al.[38] The pipette solution contained (in mM) 126K gluconate, 0.05CaCl$_2$, 0.15BAPTA, 4NaCl, 1MgSO$_4$, 15glucose, 5HEPES, 3MgATP, and 0.1GTP, pH adjusted to 7.2 with KOH. The bath solution was predicated on artificial cerebrospinal fluid and consisted of (in mM) 120NaCl, 2KCl, 2CaCl$_2$, 1.19MgSO$_4$, 26NaHCO$_3$, 1.18KH$_2$PO$_4$ and 11glucose, equilibrated with carbogen gas (95% O$_2$, 5% CO$_2$) to pH 7.4. All measurements were performed at room temperature. For neurons, the measurements were delayed for a few minutes after establishing the whole-cell mode to let the MgATP and GTP diffuse into the cell interior.

3   Results and discussion

We successfully cultured Jurkat cells and neurons on both ordered and randomly arranged NW arrays. After transfer and outgrowth, the cells were examined in terms of viability, interaction with the NWs and conservation of electrophysiological properties. Here, we compared the results with a twofold control on commonly used Petri dishes and additionally on planar Al$_2$O$_3$ coated substrates, because Al$_2$O$_3$ was also used to passivate the NWs.

Cell viability was tested by fluorescent life/membrane staining. For Jurkat cells, we observed high cell viabilities apparently independent of the substrate between 98.9 ± 0.8% and 99.6 ± 0.5%, as shown in Fig. 2a. The high viability can be explained by the short time period between cell transfer and measurement and a high viability of cancer cells in general. Exemplary images of stained Jurkat cells on ordered and random NWs are shown in

Fig. 2b and c, respectively. Overview images of cells on all four substrates including examples of dead Jurkat cells can be found in Fig. S1 in the ESI.† For neurons, shown in Fig. 2c, we observed cell viabilities of 73.9 ± 3.6% and 72.9 ± 6.2% on the control substrates and 65.4 ± 4.5% and 66.5 ± 4.4% on the NW substrates. The viability is comparable to the literature published in Loers et al.[33] and Koitmäe et al.[39] The decrease in total viability on NWs can be explained by a more challenging morphology of the substrate. Nevertheless, ordered and random NWs show similar results. Furthermore, exemplary images of stained neurons cultured on both types of NWs are shown in Fig. 2d and e as well as on the control substrates in Fig. S2.† Beside of vital cells, one can also observe the growth of numerous neurites on top all substrate types indicating the successful formation of a complex neural network. Corresponding top view images prepared by SEM are attached in the ESI as Fig. S3 and S4.†

In a next step, the hybrid interface between NW and cell membrane was examined by focused ion beam (FIB) (Zeiss Crossbeam 550) and SEM. Milling material with the ion beam provided insight to the interface in form of a cross section. Here, particular attention was paid to the contact area between the NW tip and the cell membrane. The compilation of the cross sections for Jurkat cells and neurons on ordered and random NWs, respectively, is shown in Fig. 3a–d. As expected from the model for NW/cell interaction mentioned in the introduction,[27] the cells stayed on the NW tips due to the high NW growth density. In particular, Fig. 3a and b illustrate the settling of Jurkat cells on each NW substrate. The insets display a close-up of the NWs and
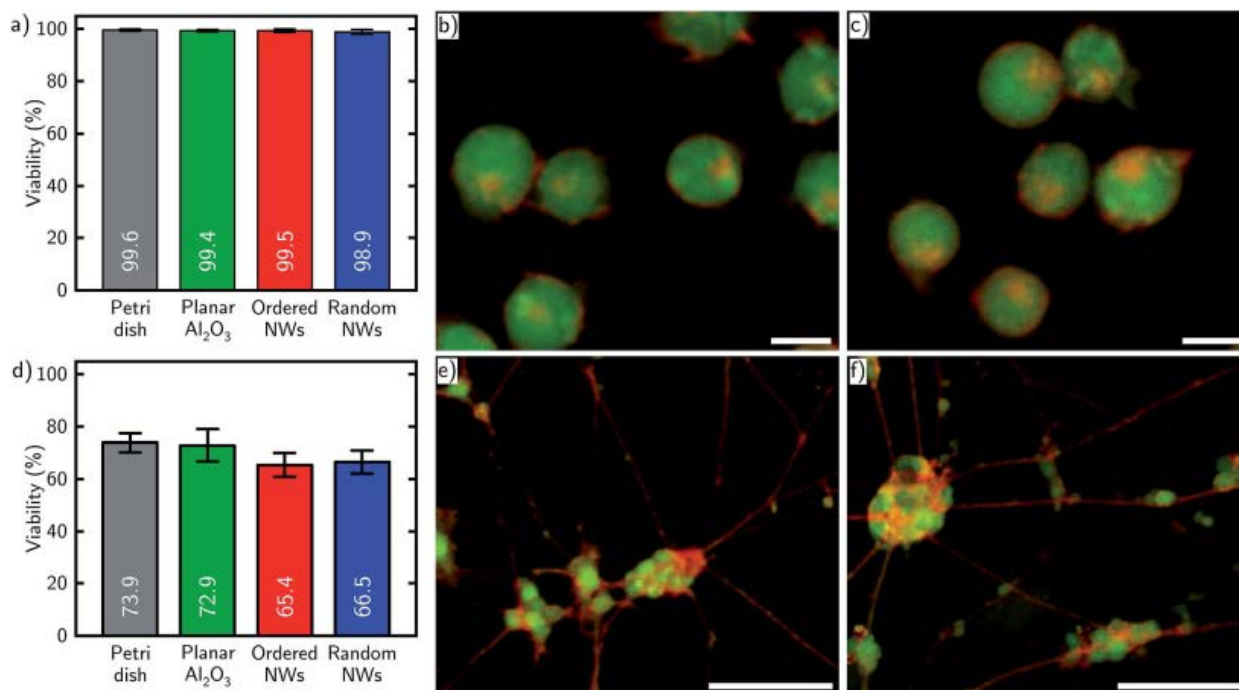

Fig. 2   Life/membrane staining results for Jurkat cells and neurons. (a) Bar chart of Jurkat cell viability settled on each substrate. (b) and (c) show stained Jurkat cells cultured on ordered and random NWs. Scale bars: 10 μm. Corresponding images on control substrates can be found in Fig. S1.† (d) Bar chart of neuron viability on each substrate. (e) and (f) show stained neurons including neurites cultured on ordered and random NWs. Scale bars: 50 μm. Corresponding images on control substrates can be found in Fig. S2.†
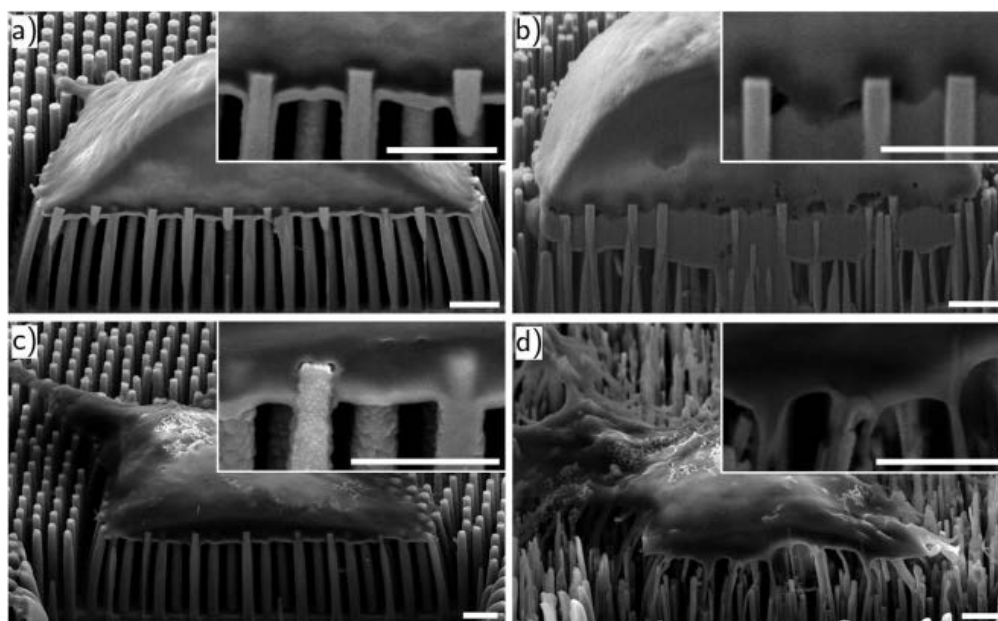
Fig. 3 SEM images of Jurkat cells on ordered (a) and randomly distributed (b) NWs as well as neurons on ordered (c) and random (d) NWs. All substrates are covered with a 10–15 nm thick layer of Al_2O_3. The cross sections were prepared via FIB. In all configurations, the cells stay on top of the NWs. Scale bars: 1 μm.

state a slight wrapping of the cell membrane around the very tip of the NW. It appears, that different diameter and arrangement of the NWs tested herein have no decisive influence on the settlement of the Jurkat cells. Similar observations can be made regarding the neuronal cells in Fig. 3c and d. Again, the neurons stay on top of the NWs and show a slight wrapping of the NW tip.

Furthermore, Fig. 3c and d also specify the statement from before regarding the growth of a neural network on top of the substrate—here: the very NW tip. Note, in both images the neurite in the top left corner of the image remains on top of the NW tips as well. Taking the confocal and SEM images into account, we want to point out that despite the "chaotic" appearance of the randomly distributed NWs, we do not observe any apparent influence of the substrate on the neurons for the ability to form neural networks.

Finally, we examined the cells on all substrates via the patch clamping technique. In order to assess the electrophysiological properties of the cells, we determined the resting membrane potential (V_{rest}), the membrane capacitance (C_{mem}), and the membrane time constant (t_{mem}). In these experiments, the membrane capacitance was directly exported by the HEKA Patchmaster software. The required data to specify the remaining parameters were obtained in a three-phased current-clamp measurement. The first section with zero current applied provided the resting potential. The second section injected a small current to the cell in order to shift the membrane potential followed by a third phase which adjusted the applied current to zero again. The exponential decay of the membrane potential toward the resting potential after zeroing the current was then characterized by the membrane time constant. For each substrate—Petri dish, planar Al_2O_3, ordered and randomly ordered NWs—five different cells were measured. The characteristic electrophysiological factors for

Jurkat cells adhered to each type of substrate are summarized in Table 1. Contemplating the measured mean values of each parameter, the resting membrane potentials range from (-53.4 ± 2.9) mV to (-56.6 ± 8.9) mV, the membrane capacitance is between (8.0 ± 1.7) pF and (10.6 ± 2.5) pF, and the time constants range from (11.4 ± 4.0) ms to (12.6 ± 4.1) ms. One can observe that the values of each parameter appear to be in the same range independent on the substrate. In order to support the intuitive interpretation, a Welch's t-test was performed for every data pair to test for statistically significant deviation. No significant deviations occurred within a 95% confidence interval (CI). All calculated t-values are listed in Table S1.† Furthermore, the experimental

Table 1 Jurkat cells: overview of the characteristic electrophysiological factors[a]

	Petri dish	Planar Al_2O_3	Ordered NWs	Random NWs
V_{rest} (mV)	-56.4 ± 4.6	-55.9 ± 6.2	-56.6 ± 8.9	-53.4 ± 2.9
C_{mem} (pF)	10.6 ± 2.5	8.1 ± 1.0	8.4 ± 1.5	8.0 ± 1.7
t_{mem} (ms)	12.6 ± 4.1	11.4 ± 4.0	11.9 ± 6.4	11.5 ± 5.4

[a] Number of cells patched on each type of substrate: $n = 5$.

Table 2 Neurons: overview of the characteristic electrophysiological factors[a]

	Petri dish	Planar Al_2O_3	Ordered NWs	Random NWs
V_{rest} (mV)	-58.1 ± 4.9	-55.9 ± 7.2	-55.9 ± 5.7	-56.8 ± 6.8
C_{mem} (pF)	4.3 ± 0.7	4.7 ± 0.8	3.7 ± 0.8	3.7 ± 1.0
t_{mem} (ms)	9.1 ± 2.9	9.5 ± 7.9	11.9 ± 3.5	15.4 ± 7.3

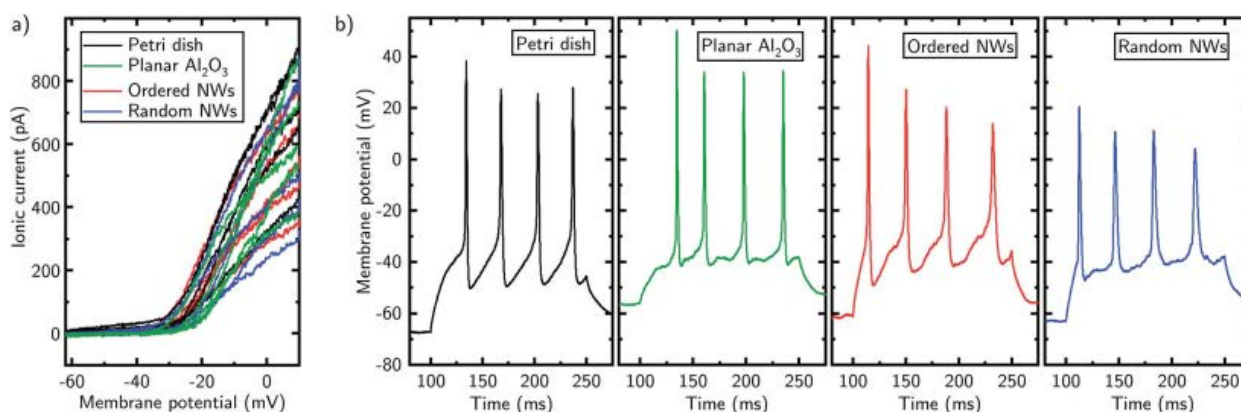[a] Number of cells patched on each type of substrate: $n = 5$.

Fig. 4 (a) Voltage–current correlation for Jurkat cells in a Petri dish (black), on planar Al_2O_3 (green), ordered (red) and random (blue) NW substrates. A voltage ramp of −60 mV to +10 mV with a slope of 80 mV/100 ms was applied to the cell. The increase of the slope of the measured current at −30 mV indicates the activation of voltage-gated ion channels. Number of cells measured on each type of substrate: $n = 5$. (b) Measurements of action potentials of neurons cultured in a Petri dish (black), on planar Al_2O_3 (green), ordered (red) and random (blue) NW substrates. The stimulation current was injected after 100 ms with a duration of 150 ms. Several actions potentials were fired.

results are in accordance with the literature.[40–42] Analogously, we proceeded with the patch clamp results from the neurons cultured on each type of substrate which are summarized in Table 2. Reviewing the minimally and maximally measured means, the resting membrane potentials range from (−55.9 ± 7.2) mV to (−58.1 ± 4.9) mV, the membrane capacitance is between (3.7 ± 1.0) pF and (4.7 ± 0.8) pF and the time constants range from (9.1 ± 2.9) ms to (15.4 ± 7.3) ms. Repeatedly, the results seem to imply no severe influence of the substrates morphology. We performed a Welch's t-test with every data pair using a 95% CI again. The t-test results for the neurons are noted in Table S2† and show no significant deviations of the electrophysiological properties between each type of substrate. Besides, the determined values are also applicable to ones in the literature.[38,43,44]

In addition to the characteristic electrophysiological parameters, we investigated cell specific ion channel activity/response for both cell types. For Jurkat cells, we studied the gating of voltage-gated potassium ion channels in voltage-clamp mode. As a result, the NW substrates have no influence on the voltage–current characteristics compared to both planar control substrates as shown in Fig. 4a. Here, voltage ramps from (−60 to +10) mV with a slope of 80 mV/100 ms were applied to the Jurkat cells while the ionic current through the cell's membrane was measured. At a membrane potential of approximately −30 mV an increased slope of the ionic current is observable. Such a gating at this voltage is also reported in literature and can be assigned to voltage-gated potassium channels in Jurkat cells.[45]

In case of the neurons, we tested for firing of action potentials. As a part of the nervous system, the capability of a neuron to fire action potentials is an important indicator of the ability to process neuronal information and hence states proper cell function. Independently of the culturing substrate, the neurons show characteristic action potentials (cf. Fig. 4b) with amplitudes between 45 mV and 85 mV and a firing rate of 27 Hz,

which is in accordance with literature.[43,46] During the experiment, a stimulus current was applied in current-clamp mode to the cell with a duration of 150 ms in order to depolarize it above the critical threshold of triggering action potentials.

4 Summary and conclusion

In summary, we cultured cells, specifically human T lymphocytes and cerebellar granule cells from mice, on a Petri dish, planar Al_2O_3, and Al_2O_3 surface-passivated ordered and randomly distributed NW substrates and show patch clamp recordings of normal electrophysiological cell activity with a custom-built upright patch clamp setup. SEM images of the NW/cell membrane interface showed that the cells investigated herein are only in contact with the NW tip. This observation is in direct contrast to any other comparable publications where patch clamp recordings have been performed, since the entire NW was wrapped by the cell's membrane due to a low NW growth density.[28,29] We showed via patch clamp recordings, that the electrophysiological properties in this configuration were conserved and fundamental cellular responses of both cell types remained intact asserting physical pressure during establishing the giga seal on spiky substrates. In detail, whilst taking into account the results from the electrophysiological characterization of the cells, the proper voltage-gating of the Jurkat cells and firing of action potentials of the neurons, we can state that the nanostructured one-dimensional NW substrate geometry in our study has no detrimental influence on the electrophysiological properties of the cell – when the cell is resting on the NW tips – compared to control experiments on planar substrates and the integrity of the cellular system is conserved. Note, our patch clamp measurements are complementary to live/dead staining analyses as well as to previous studies[9,10,47] and reveal the great potential for future investigations on the interaction of functional one-dimensional nano-sized objects with the cell
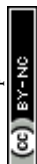
membrane, such as NW solar cells, NW electrodes, nanoscaled 1-dimensional probes or nanotubes for drug delivery, to name a few of them.

With respect to generality, we believe that characteristic cell properties of Jurkat cells and neurons may remain conserved on NW substrates independent on roughness, arrangement, and diameter of the NWs – with a substrate geometry and morphology similar to that one shown herein. Hence, this observation might pave the way to use a large variety of NW substrates in diverse applications in combination with sensitive electrophysiological patch clamp measurements. Additionally, with the predictable wrapping of the cell's membrane of the very tip of the NW leading to a point-like contact of nanostructure and cell membrane, our setup is an ideal starting point for future experiments with functionalized NWs, such as NW lasers or NW solar cells in optogenetics and sensing/stimulation experiments, respectively.

Conflicts of interest

There are no conflicts to declare.

Acknowledgements

References

1 A. S. Curtis and M. Varde, *JNCI, J. Natl. Cancer Inst.*, 1964, **33**, 15–26.

2 A. Harsch, J. Calderon, R. Timmons and G. Gross, *J. Neurosci. Methods*, 2000, **98**, 135–144.

3 Y. H. Kim, N. S. Baek, Y. H. Han, M. A. Chung and S. D. Jung, *J. Neurosci. Methods*, 2011, **202**, 38–44.

4 M. Lampin, R. Warocquier-Clérout, C. Legris, M. Degrange and M. F. Sigot-Luizard, *J. Biomed. Mater. Res.*, 1997, **36**, 99–108.

5 D. Ning, B. Duong, G. Thomas, Y. Qiao, L. Ma, Q. Wen and M. Su, *Langmuir*, 2016, **32**, 2718–2723.

6 J. Lee, B. S. Kang, B. Hicks, T. F. Chancellor Jr, B. H. Chu, H.-T. Wang, B. G. Keselowsky, F. Ren and T. P. Lele, *Biomaterials*, 2008, **29**, 3743–3749.

7 Z. Li, R. Yang, M. Yu, F. Bai, C. Li and Z. L. Wang, *J. Phys. Chem. C*, 2008, **112**, 20114–20117.

8 W. Hällström, T. Mårtensson, C. Prinz, P. Gustavsson, L. Montelius, L. Samuelson and M. Kanje, *Nano Lett.*, 2007, **7**, 2960–2965.

9 G. Piret, M.-T. Perez and C. N. Prinz, *Biomaterials*, 2013, **34**, 875–887.

10 G. Piret, M.-T. Perez and C. N. Prinz, *ACS Appl. Mater. Interfaces*, 2015, **7**, 18944–18948.

11 Z. Li, J. Song, G. Mantini, M.-Y. Lu, H. Fang, C. Falconi, L.-J. Chen and Z. L. Wang, *Nano Lett.*, 2009, **9**, 3575–3580.

12 C. N. Prinz, *J. Phys.: Condens. Matter*, 2015, **27**, 233103.

13 S. Qi, C. Yi, S. Ji, C.-C. Fong and M. Yang, *ACS Appl. Mater. Interfaces*, 2009, **1**, 30–34.

14 J. C. Johnson, H. Q. Yan, P. D. Yang and R. J. Saykally, *J. Phys. Chem. B*, 2003, **107**, 8816–8828.

15 S. Rühle, L. K. Van Vugt, H. Y. Li, N. A. Keizer, L. Kuipers and D. Vanmaekelbergh, *Nano Lett.*, 2008, **8**, 119–123.

16 C. Baratto, R. Kumar, E. Comini, G. Faglia and G. Sberveglieri, *Opt. Express*, 2015, **23**, 18937.

17 K.-Y. Lee, I. Kim, S.-E. Kim, D.-W. Jeong, J.-J. Kim, H. Rhim, J.-P. Ahn, S.-H. Park and H.-J. Choi, *Nanoscale Res. Lett.*, 2014, **9**, 56.

18 W. Kim, J. K. Ng, M. E. Kunitake, B. R. Conklin and P. Yang, *J. Am. Chem. Soc.*, 2007, **129**, 7228–7229.

19 K.-Y. Lee, S. Shim, I.-S. Kim, H. Oh, S. Kim, J.-P. Ahn, S.-H. Park, H. Rhim and H.-J. Choi, *Nanoscale Res. Lett.*, 2010, **5**, 410–415.

20 E. Garnett and P. Yang, *J. Am. Chem. Soc.*, 2008, **130**, 9224–9225.

21 J. Wallentin, N. Anttu, D. Asoli, M. Huffman, I. Aberg, M. H. Magnusson, G. Siefer, P. Fuss-Kailuweit, F. Dimroth, B. Witzigmann, H. Q. Xu, L. Samuelson, K. Deppert and M. T. Borgstrom, *Science*, 2013, **339**, 1057–1060.

22 D. J. Stephens, *Science*, 2003, **300**, 82–86.

23 S. A. Galdeen and A. J. North, in *Cell Migration, Springer Protocols*, 2011, pp. 205–222.

24 E. Neher and B. Sakmann, *Nature*, 1976, **260**, 799–802.

25 E. Neher, B. Sakmann and J. H. Steinbach, *Pflügers Arch.*, 1978, **375**, 219–228.

26 B. Sakmann, *Annu. Rev. Physiol.*, 1984, **46**, 455–472.

27 N. Buch-Månson, S. Bonde, J. Bolinsson, T. Berthing, J. Nygård and K. L. Martinez, *Adv. Funct. Mater.*, 2015, **25**, 3246–3255.

28 J. T. Robinson, M. Jorgolli, A. K. Shalek, M.-H. Yoon, R. S. Gertner and H. Park, *Nat. Nanotechnol.*, 2012, **7**, 180–184.

29 J. Abbott, T. Ye, L. Qin, M. Jorgolli, R. S. Gertner, D. Ham and H. Park, *Nat. Nanotechnol.*, 2017, **12**, 460–466.

30 D. S. Finch, T. Oreskovic, K. Ramadurai, C. F. Herrmann, S. M. George and R. L. Mahajan, *J. Biomed. Mater. Res., Part A*, 2008, **87**, 100–106.

31 G. Otnes, M. Heurlin, M. Graczyk, J. Wallentin, D. Jacobsson, A. Berg, I. Maximov and M. T. Borgström, *Nano Res.*, 2016, **9**, 2852–2861.

32 C. Borschel, S. Spindler, D. Lerose, A. Bochmann, S. H. Christiansen, S. Nietzsche, M. Oertel and C. Ronning, *Nanotechnology*, 2011, **22**, 185307.

33 G. Loers, S. Chen, M. Grumet and M. Schachner, *J. Neurochem.*, 2005, **92**, 1463–1476.

34 C. Kilkenny, W. Browne, I. Cuthill, M. Emerson and D. Altman, *J. Pharmacol. Pharmacother.*, 2010, **1**, 94.

35 S. Ebihara, K. Shirato, N. Harata and N. Akaike, *J. Physiol.*, 1995, **484**(Pt 1), 77–86.

36 A. Molleman, *Patch Clamping*, John Wiley & Sons, Ltd, Chichester, UK, 2002, pp. 1975–1977.

37 S. Partida-Sanchez, A. Gasser, R. Fliegert, C. C. Siebrands, W. Dammermann, G. Shi, B. J. Mousseau, A. Sumoza-Toledo, H. Bhagat, T. F. Walseth, A. H. Guse and F. E. Lund, *J. Immunol.*, 2007, **179**, 7827–7839.

38 D. Gall, C. Roussel, I. Susa, E. D'Angelo, P. Rossi, B. Bearzatto, M. C. Galas, D. Blum, S. Schurmans and S. N. Schiffmann, *J. Neurosci.*, 2003, **23**, 9320–9327.

39 A. Koitmäe, M. Müller, C. S. Bausch, J. Harberts, W. Hansen, G. Loers and R. H. Blick, *Langmuir*, 2018, **34**, 1528–1534.

40 M. D. Cahalan and K. G. Chandy, *Immunol. Rev.*, 2009, **231**, 59–87.

41 P. Ross, S. Garber and M. Cahalan, *Biophys. J.*, 1994, **66**, 169–178.

42 G. Dupuis, J. Héroux and M. D. Payet, *J. Physiol.*, 1989, **412**, 135–154.

43 C. Roussel, T. Erneux, S. N. Schiffmann and D. Gall, *Cell Calcium*, 2006, **39**, 455–466.

44 C. Rössert, S. Solinas, E. D'Angelo, P. Dean and J. Porrill, *Front. Cell. Neurosci.*, 2014, **8**, 1–20.

45 T. E. DeCoursey, K. G. Chandy, S. Gupta and M. D. Cahalan, *Nature*, 1984, **307**, 465–468.

46 B. P. Bean, *Nat. Rev. Neurosci.*, 2007, **8**, 451–465.

47 G. Piret, E. Galopin, Y. Coffinier, R. Boukherroub, D. Legrand and C. Slomianny, *Soft Matter*, 2011, **7**, 8642.

RSC Advances

Culturing and patch clamping of Jurkat T cells and neurons on Al$_2$O$_3$ coated nanowire arrays of altered morphology

Jann Harberts,[a] Robert Zierold,[a] Cornelius Fendler,[a] Aune Koitmäe,[a] Parisa Bayat,[a] Irene Fernandez-Cuesta,[a] Gabriele Loers,[b] Björn-Philipp Diercks,[c] Ralf Fliegert,[c] Andreas H. Guse,[c] Carsten Ronning,[d] Gaute Otnes,[ef] Magnus Borgström,[ef] and Robert H. Blick[ag‡]

[a] Center for Hybrid Nanostructures, Universität Hamburg, Luruper Chaussee 149, 22761 Hamburg, Germany
[b] Center for Molecular Neurobiology Hamburg, University Medical Center Hamburg-Eppendorf, Falkenried 94, 20251 Hamburg, Germany
[c] Department of Biochemistry and Molecular Cell Biology, The Calcium Signaling Group, University Medical Center Hamburg-Eppendorf, Martinistraße 52, 20251 Hamburg, Germany
[d] Institute for Solid State Physics, Friedrich-Schiller-University Jena, Helmholtzweg 3-5, 07743 Jena, Germany
[e] NanoLund, Lund University, Box 118, 22100 Lund, Sweden
[f] Solid State Physics, Lund University, Box 118, 22100 Lund, Sweden
[g] Material Science and Engineering, College of Engineering, University of Wisconsin-Madison, Madison, Wisconsin 53706, USA
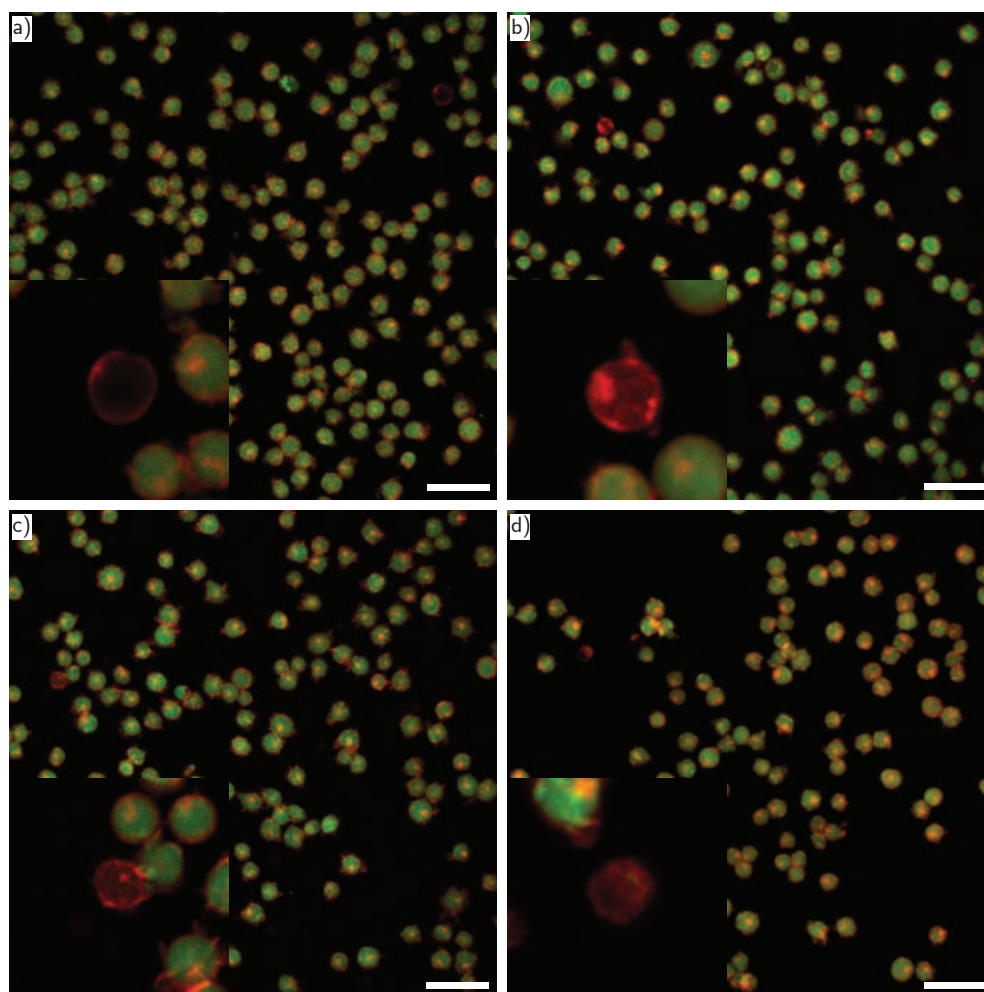‡ Tel: +49 40 42838 1975, E-mail: rblick@chyn.uni-hamburg.de

Fig. S1 Exemplary confocal microscope overview images of life/membrane (green/red) stained Jurkat cells on a) Petri dish, b) planar Al_2O_3, c) ordered and d) random NWs. The majority of the cells is viable. Insets: close-ups of dead Jurkat cells. Scale bar: 50 µm.
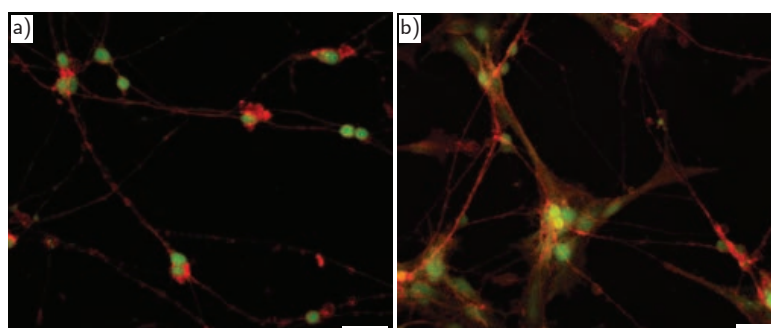

Fig. S2 Exemplary confocal microscope images of life/membrane (green/red) stained neurons on a) Petri dish and b) planar Al_2O_3. Scale bar: 25 µm.
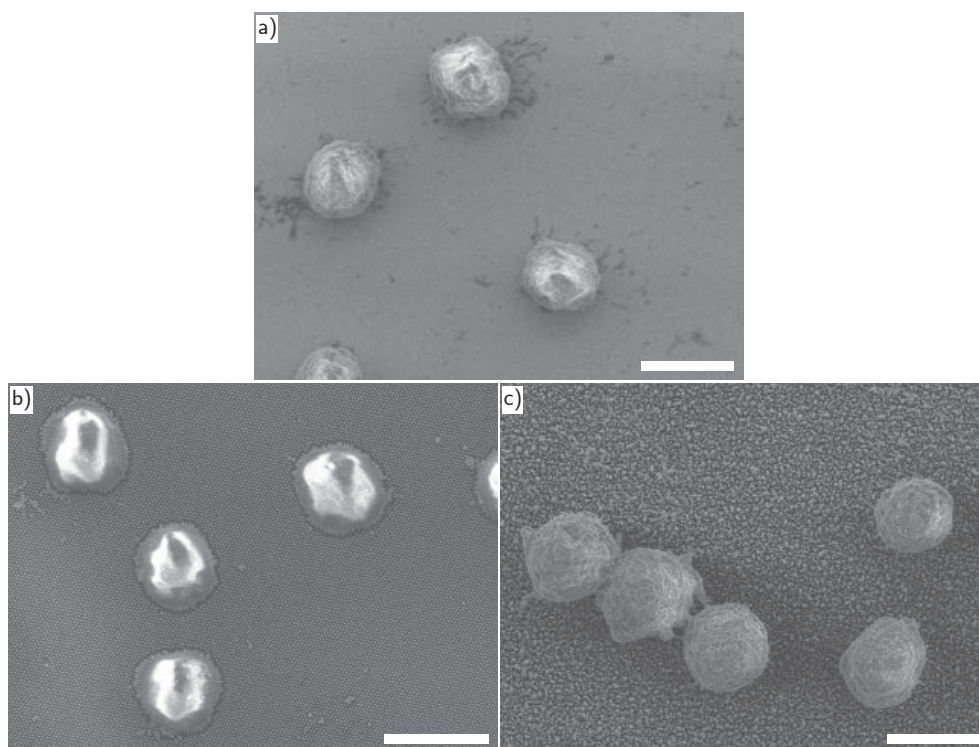
Fig. S3 Exemplary SEM image of Jurkat cells on a) planar Al_2O_3, b) ordered and c) random NWs. Scale bars: 10 μm.
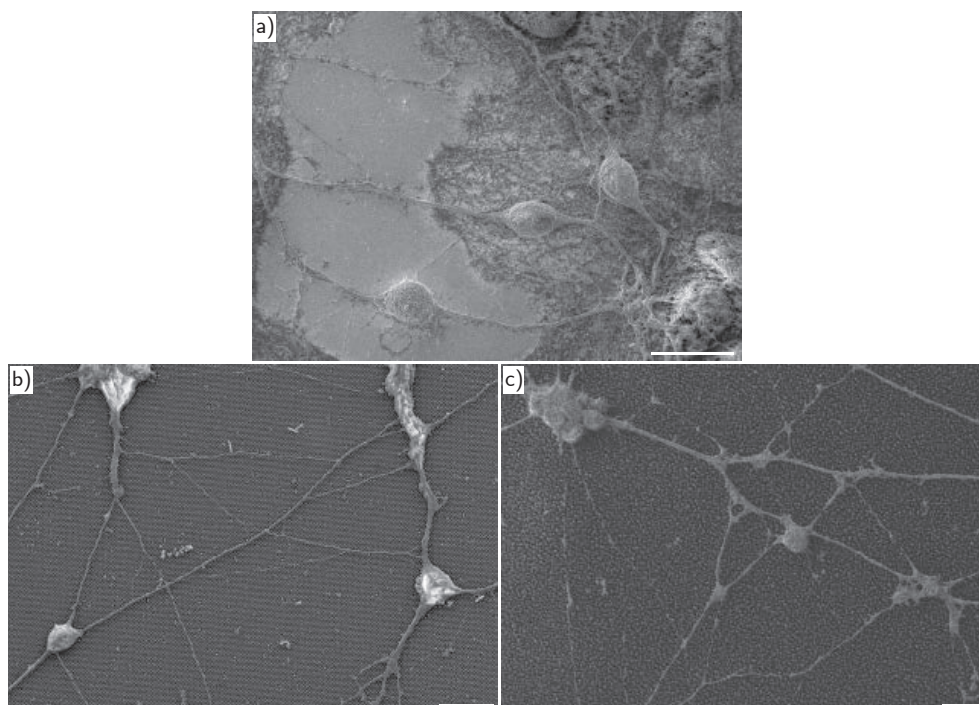

Fig. S4 Exemplary SEM image of neuronal outgrowth on a,b) planar Al_2O_3 c) ordered and d) random NWs. Scale bars: 10 μm.

Table S1 Welch's t-test results regarding electrophysiological properties of Jurkat cells cultured on each substrate with 95% confidence interval (CI).

| | NWs/Petri dish | | | | NWs/Planar Al_2O_3 | | | | Planar Al_2O_3/Petri dish | |
| | Ordered NWs | | Random NWs | | Ordered NWs | | Random NWs | | | |
	T value	95% CI	T value	95% CI	T value	95% CI	t value	95% CI	T value	95% CI
V_{rest}	0.04	2.45	-1.23	2.36	0.14	2.36	-0.82	2.45	-0.14	2.36
C_{mem}	1.69	2.36	1.92	2.36	-0.37	2.36	0.11	2.45	0.60	2.57
t_{mem}	0.21	2.36	0.36	2.36	-0.15	2.36	-0.03	2.36	0.47	2.31

Table S2 Welch's t-test results regarding electrophysiological properties of Neurons cultured on each substrate with 95% confidence interval (CI).

| | NWs/Petri dish | | | | NWs/Planar Al_2O_3 | | | | Planar Al_2O_3/Petri dish | |
| | Ordered NWs | | Random NWs | | Ordered NWs | | Random NWs | | | |
	T value	95% CI	T value	95% CI	T value	95% CI	t value	95% CI	T value	95% CI
V_{rest}	-0.65	2.31	-0.35	2.36	0.00	2.31	0.20	2.31	-0.54	2.36
C_{mem}	1.26	2.31	1.10	2.36	1.98	2.31	1.75	2.31	-0.84	2.31
t_{mem}	-1.38	2.31	-1.79	2.57	-0.62	2.45	-1.23	2.31	-0.11	2.57

A.3 Publication III

Culturing human iPSC-derived neural progenitor cells on nanowire arrays: mapping the impact of nanowire length and array pitch on proliferation, viability, and membrane deformation

Jann Harberts, Katja Bours, Malte Siegmund, Carina Hedrich, Michael Glatza, Hans R. Schöler, Undine Haferkamp, Ole Pless, Robert Zierold, and Robert H. Blick

Author contributions: J.H., K.B., M.S. conducted cell culture. J.H., K.B., M.S. conducted epifluorescence microscopy imaging. U.H., O.P. helped with smNPC characterization. J.H. conducted confocal microscopy imaging. J.H., C.H. prepared the NW substrates. J.H., K.B. analyzed the data. J.H. wrote the manuscript. J.H., R.Z. conceptualized the study. R.Z., R.H.B. supervised the study. J.H., K.B., M.S., R.Z., M.G., H.R.S. revised the manuscript. R.Z., R.H.B. acquired funding. All authors conducted proofreading and approved the manuscript.

(15 + 6 pages)

Check for updates

Culturing human iPSC-derived neural progenitor cells on nanowire arrays: mapping the impact of nanowire length and array pitch on proliferation, viability, and membrane deformation†

Jann Harberts, [ID] *[a] Katja Bours,[a] Malte Siegmund,[a] Carina Hedrich,[a]
Michael Glatza,[b] Hans R. Schöler,[b] Undine Haferkamp, [ID] [c] Ole Pless, [ID] [c]
Robert Zierold [ID] *[a] and Robert H. Blick [ID] [a,d]

Nanowire arrays used as cell culture substrates build a potent tool for advanced biological applications such as cargo delivery and biosensing. The unique topography of nanowire arrays, however, renders them a challenging growth environment for cells and explains why only basic cell lines have been employed in existing studies. Here, we present the culturing of human induced pluripotent stem cell-derived neural progenitor cells on rectangularly arranged nanowire arrays: In detail, we mapped the impact on proliferation, viability, and topography-induced membrane deformation across a multitude of array pitches (1, 3, 5, 10 μm) and nanowire lengths (1.5, 3, 5 μm). Against the intuitive expectation, a reduced proliferation was found on the arrays with the smallest array pitch of 1 μm and long NWs. Typically, cells settle in a fakir-like state on such densely-spaced nanowires and thus experience no substantial stress caused by nanowires indenting the cell membrane. However, imaging of F-actin showed a distinct reorganization of the cytoskeleton along the nanowire tips in the case of small array pitches interfering with regular proliferation. For larger pitches, the cell numbers depend on the NW lengths but proliferation generally continued although heavy deformations of the cell membrane were observed caused by the encapsulation of the nanowires. Moreover, we noticed a strong interaction of the nanowires with the nucleus in terms of squeezing and indenting. Remarkably, the cell viability is maintained at about 85% despite the massive deformation of the cells. Considering the enormous potential of human induced stem cells to study neurodegenerative diseases and the high cellular viability combined with a strong interaction with nanowire arrays, we believe that our results pave the way to apply nanowire arrays to human stem cells for future applications in stem cell research and regenerative medicine.

[a]*Center for Hybrid Nanostructures (CHyN), Universität Hamburg, Luruper Chaussee 149, 22761 Hamburg, Germany. E-mail: jann.harberts@chyn.uni-hamburg.de, robert.zierold@chyn.uni-hamburg.de*
[b]*Department of Cell and Developmental Biology, Max Planck Institute for Molecular Biomedicine, Röntgenstraße 20, 48149 Münster, Germany*
[c]*Fraunhofer Institute for Translational Medicine and Pharmacology (ITMP), ScreeningPort, Schnackenburgallee 114, 22525 Hamburg, Germany*
[d]*Material Science and Engineering, College of Engineering, University of Wisconsin-Madison, Madison, Wisconsin 53706, USA*

†Electronic supplementary information (ESI) available: Fig. S1: Comparison of cells cultured on glass control and planarly etched Si substrate. Fig. S2: Data from quantification that is not shown in the main manuscript. Fig. S3: Viable cells 1 DIV after plating. Fig. S4: SEM images of smNPCs cultured on the remaining NW substrates and on a control substrate. Fig. S5: F-actin/cytoskeleton on control substrate. Fig. S6: Exemplary anti-SOX2 stainings on all types of NW substrates and glass and Si control after 4 DIV. Fig. S7: Exemplary images of anti-NES stainings on all types of NW substrates and glass and Si control after 4 DIV. See DOI: 10.1039/d1nr04352h

Introduction

Human induced pluripotent stem cells (iPSCs) have the potential to maximize the throughput and efficacy of clinical trials and applications.[1] Many ethical and political controversies are avoided by relinquishing embryonic stem cells and the limited availability of primary human cells is overcome.[2] Moreover, iPSCs are patient-specific since the initial cell sample is commonly obtained by an ordinary skin biopsy.[3] The direct use of human cells also reduces the high failure rate of clinical translation created by differences of disease-associated pathways between human and animal cells.[4–6] Access to a multitude of human iPSC-derived cell types such as dopaminergic or glutamatergic neurons might allow for novel treatment modalities with improved pre-clinical efficacy and safety assessment.[7] Thus, human pathophysiological conditions including neurodegenerative conditions such as Alzheimer's disease or

Parkinson's disease can be explored more efficiently and potentially even be ameliorated.[8,9] Neuroscience research and clinical translation not only benefit from the feasibility to derive all major neuronal cell types but also from the progress to create more advanced cell cultures such as brain organoids or blood–brain barrier models.[10–12] Hence, iPSC technologies have profoundly changed the operation routines of basic, pre-clinical, and clinical research in neuroscience since their initial discovery in 2006.[13]

The cell culturing of these complex systems including the administration of therapeutic agents is commonly performed in regular Petri dishes or multi-well plates. However, replacing the passive surface of these dishes with an active substrate would possibly render another dimension to test or to manipulate the cells. Here, the continuous progress in micro- and nanofabrication offers novel strategies to create such functionalized biocompatible (semi-conductor) materials to be employed as cell culture substrates.[14,15]

Tailor-made substrates were published in numerous studies demonstrating their applicability but up until now primarily standard human cell lines (e.g., HEK293 or HeLa cells) or primary rodent cells were employed.[16–19] The influence of the substrate in terms of chemical and topological properties has been tested, for example, for adhesion, proliferation, viability, migration, and guidance of seeded cells.[20–26] In this context, a particular subset of substrates featuring upright arranged high aspect ratio nanostructures—so-called nanowire (NW) arrays—play an increasingly important role.[27–33]

Nanowire arrays can affect biological parameters such as cellular growth, viability, morphology, and mechanotransduction machinery,[34–39] while electrophysiological parameters are maintained.[40–43] Furthermore, NW arrays have been used to measure mechanical properties,[44–46] to interact with the cell's nucleus,[47] to constrain movement and spreading,[48–52] or to direct cell polarization such as outgrowth of neurites.[53–57] In addition to the aforementioned passive applications, functionalized NW arrays were employed to incorporate an executing role, such as drug delivery,[29,58–63] cell transfection,[64–67] electrical stimulation/sensing,[68–72] or biosensing,[73] to name a few. To address specific applications, the interaction of the cell and the NWs can be tuned by adjusting the length and diameter of the NWs and the pitch of the array.[52,74–76] Here, the settling regimes of the cells are ranging from a fakir-like state on a bed-of-nails to a complete encapsulation of the NWs. A model to estimate the regimes was developed by Buch-Månson et al.[77] Even though these NW substrates offer many advantages over conventional cell culture dishes, the application of human iPSCs on NW arrays is less prevalent. This is potentially due to the fact that the NW arrays also create a challenging topography that must be tolerated by the cells during culture. For example, material cues have been discussed to be a regulator for epigenetics and stem cell function,[78] and NW forests have been used to influence intracellular signaling, gene regulation, or basic cell differentiation.[79–83] To make use of different NW arrays for human iPSCs it is hence crucial to ensure that, e.g., proliferation and viability of the cells are maintained.

In this work, we present the cultivation of human iPSC-derived small molecule neural progenitor cells (smNPCs) on silicon (Si) NW arrays with varying lengths of 1.5, 3, and 5 μm ($L1.5$, $L3$, $L5$) and array pitches of 1, 3, 5, and 10 μm ($P1$, $P3$, $P5$, $P10$). Such array parameters cover multiple interaction regimes between cells and NWs. The proliferation and cell viability were monitored for 4 days and compared to control substrates (glass and planarly etched silicon). On substrates with $P \geq 3$, where the cells encapsulate the NWs, the cell numbers varied with the degree of topological stress, namely, the number of NWs per cell and the NW length. Remarkably, proliferation was also significantly reduced on $P1$ NW arrays (i.e., densely-packed NW arrays) at which the cells settle in a fakir-like state on a 'bed-of-nails'. In general, such a settling state is considered non-invasive compared to encapsulating settling states on NW substrates with $P \geq 3$. Imaging of F-actin showed that the cells cultured on $P1$ arrays underwent a reorganization of the cytoskeleton along the NW tips, which influenced normal cell division. However, reduced cell numbers on $P1$ arrays were only observed for $L3$ and $L5$ but not for $L1.5$. This was in agreement with further analyses that showed an intermediate settling regime for $P1$ $L1.5$ NW arrays, thus diminishing the impact on normal proliferation. In any case, on $L1.5$ NW arrays, the cell numbers after 4 days in vitro (DIV) were not only independent from the pitch and but also equal to the control. The cell viability after 4 DIV was excellent on the majority of the NW arrays with about 85% viable cells. Only on $P1$ $L3$, $P1$ $L5$, and $P3$ $L5$ substrates where the cells were either constrained to align the cytoskeleton along the NWs or deeply indented at multiple sites, viability was slightly reduced (at worst to about 75%). Three-dimensional imaging of the cells on the NW arrays showed that the cells strongly interact with NWs. Moreover, the level of NW encapsulation was defined by the NW length and array pitch. In severe appearing cases with long wires and medium array pitch, not only the cell membrane was deformed massively but also the nucleus was substantially indented or squeezed. Considering the strong interaction with the NWs and the outstanding cell viability, we believe that our results open new pathways to apply NW arrays in human stem cell biology and regenerative medicine technologies.

Results

The settling regime of cells cultured on NW arrays strongly depends on the interplay of NW length and array pitch. Specifically, the cell settling can be tuned from a fakir-like state (Fig. 1a) to complete encapsulation of the NWs (Fig. 1b–d): In the fakir-like state, the cells rest on a 'bed-of-nails' being only in contact with the very NW tips (panel a). This state is predominantly caused by high array densities, i.e., small pitches. With increasing pitch, the cells start to encapsulate the NWs (panel b). Depending on the NW length, not only the cell membrane is deformed but also the nucleus is affected when the NW length is in the order of the cell's height (panel
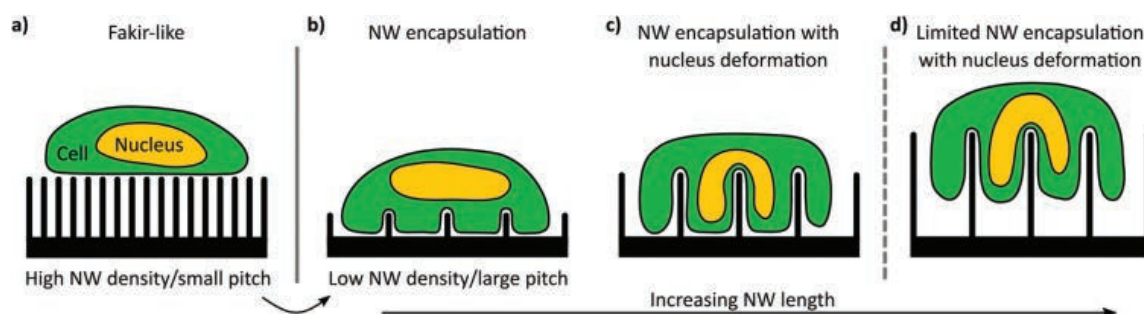
Fig. 1 Conceptualization of the cell-settling regimes that are recognized in the field. The settling regime of the cells (green) on the NWs depends on array pitch and NW length. (a) For high NW densities/small array pitches the cells are resting in a fakir-like state on a bed-of-nails merely in contact with the very NW tips. This configuration is virtually independent of the NW length. (b–d) For low NW densities/large pitches the cells encapsulate the NWs and are impaled with increasing NW length which also deforms the nucleus (yellow).

c). In the case of even longer NWs, the cells might lose contact with the bottom of the substrate creating an intermediate settling state between a fakir-like state and full encapsulation (panel d).

The design and fabrication method of the rectangularly arranged Si NW arrays is summarized in Fig. 2. To map the effect of different array pitches and NW lengths on the culturing of smNPCs, we prepared NW arrays with array pitches of 1, 3, 5, and 10 μm ($P1$, $P3$, $P5$, $P10$) combined with NW lengths of

1.5, 3, and 5 μm ($L1.5$, $L3$, $L5$) exemplarily shown in Fig. 2a. The utilized pitches result in array densities of 100, 11.1, 4, and 1 NWs per 100 μm², respectively. The NWs were produced in a top-down process via reactive ion etching (RIE) using chromium dots with a diameter of 700 nm as a hard mask. The hard mask for the array arrangement was defined by electron beam lithography on a 6 × 6 mm² area with altering pitches (Fig. 2b). The NW length was controlled by the time used for RIE per chip containing the 6 × 6 mm² patterned area (Fig. 2c).
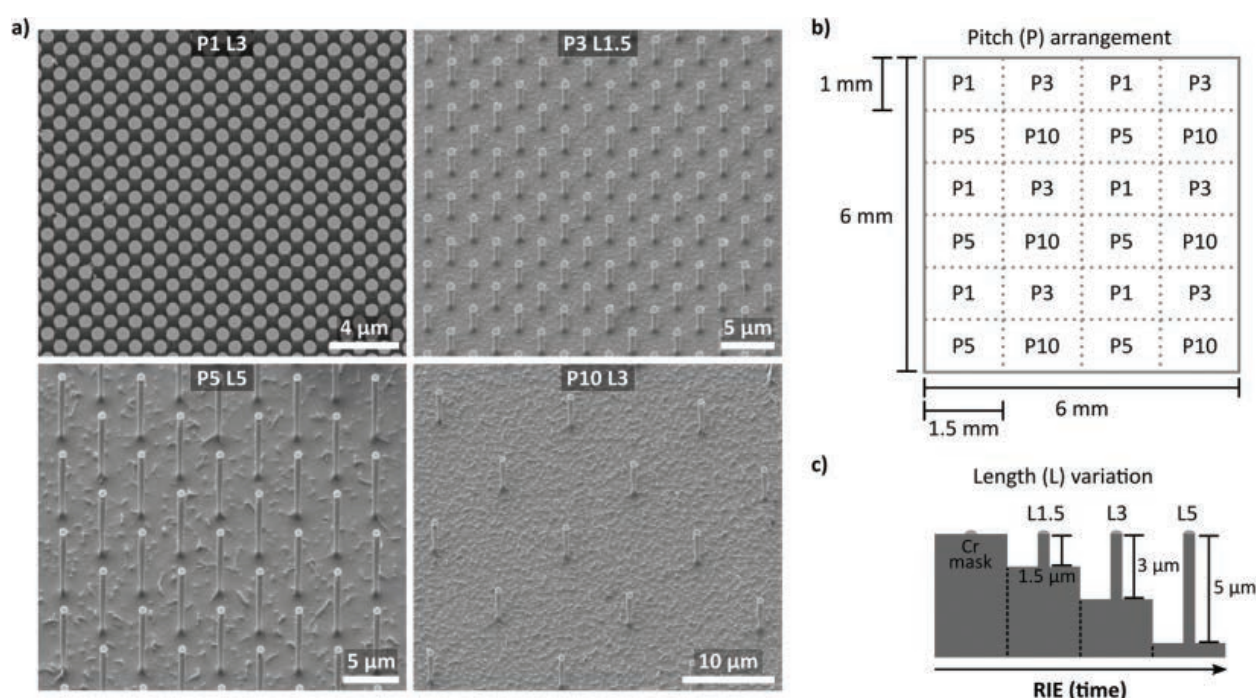

Fig. 2 Design and fabrication of the Si NW array substrates. (a) Exemplary scanning electron microscopy (SEM) images of the fabricated Si NW arrays with a rectangular pattern and array pitches of 1, 3, 5, and 10 μm ($P1$, $P3$, $P5$, $P10$) and lengths of 1.5, 3, and 5 μm ($L1.5$, $L3$, $L5$). The tilt is 45° and the images were tilt corrected. (b) The different array pitches (P) of 1, 3, 5, and 10 μm were defined by electron beam lithography and are arranged in a 6 × 6 mm² grid with 1 × 1.5 mm² areas with identical pitches. Each area with the same pitch is slightly bigger than the area imaged later on (approx. 1.3 × 0.9 mm²). The pitches result in array densities of 100, 11.1, 4, and 1 NWs per 100 μm², respectively. (c) The length (L) variation of 1.5, 3, and 5 μm was defined by the reactive ion etching (RIE) time where chromium (Cr) was used as a hard mask.

For control, areas of planarly etched Si right next to the region covered with NWs were used. Of note, cells grown here showed similar proliferation, viability, and spreading compared to controls grown on conventional glass coverslips (Fig. S1a–g†). Thus, smNPCs grown on NW arrays were compared in the following only to the Si control.

Data collection to determine the cell numbers and viability was performed on five consecutive days (0–4 DIV) using Hoechst, calcein, and propidium iodide (PI) stainings (Fig. 3). Specifically, we imaged the samples after initial cell attachment ($\geq$1 h, referred to as 0 DIV) and the following four 24 h intervals. Fig. 3a–c show examples of Hoechst-stained smNPCs cultured on NW arrays with different densities but the same NW lengths (here, e.g., $P1$ $L5$ and $P5$ $L5$) and control samples after 0, 1, and 4 DIV. Right after initial cell adhesion, the cells were found randomly distributed on the substrate as the cells sediment and allocate from the cell suspension in a random manner (panel a). After one day, the cells started to form cell clusters (Fig. 3b) and larger colonies were formed after 4 DIV on both NW arrays and control substrate (panel c). Note, solely by visual inspection, the area covered with cells appeared to be reduced using a $P1$ NW array sample. Cell viability was assayed using calcein to identify viable cells and PI to stain for dead cells (examples shown in Fig. 3d). In a next step, we quantified the images taken and determined cell numbers, viability, and spreading of the cells on all types of NW arrays from 0 to 4 days of cultivation.

The quantification of the cell numbers, viability, and spreading using an automized software-assisted image analysis are summarized in Fig. 4. Specifically, Fig. 4a displays the cell numbers for all types of NW substrates from 0–4 DIV compared to the control. Initially, about 250 cells per captured image were determined. For unaffected cells on the control samples, the cell numbers reached about 1500 cells per image on day 4. On the NW samples, the cell numbers also increased in general over time but the final number of cells after 4 DIV depended on the degree of topological stress caused by the specific type of NW array. The overall cell numbers were reduced for encapsulating regimes ($P \geq 3$) mainly with increasing number of NWs per cell ($P3$ NW arrays: $\approx$−40%, $P5$ NW arrays: $\approx$−25%, $P10$ NW arrays: $\approx$−10%) where $L5$ NW arrays decreased the cell numbers slightly more than $L3$ NW arrays. Note, $L1.5$ NW arrays showed no change in the cell numbers. Remarkably, the cell numbers for $P1$ $L3$ and $P1$ $L5$ NW arrays also showed significantly reduced values although such densely-spaced NW arrays are expected to produce a fakir-like
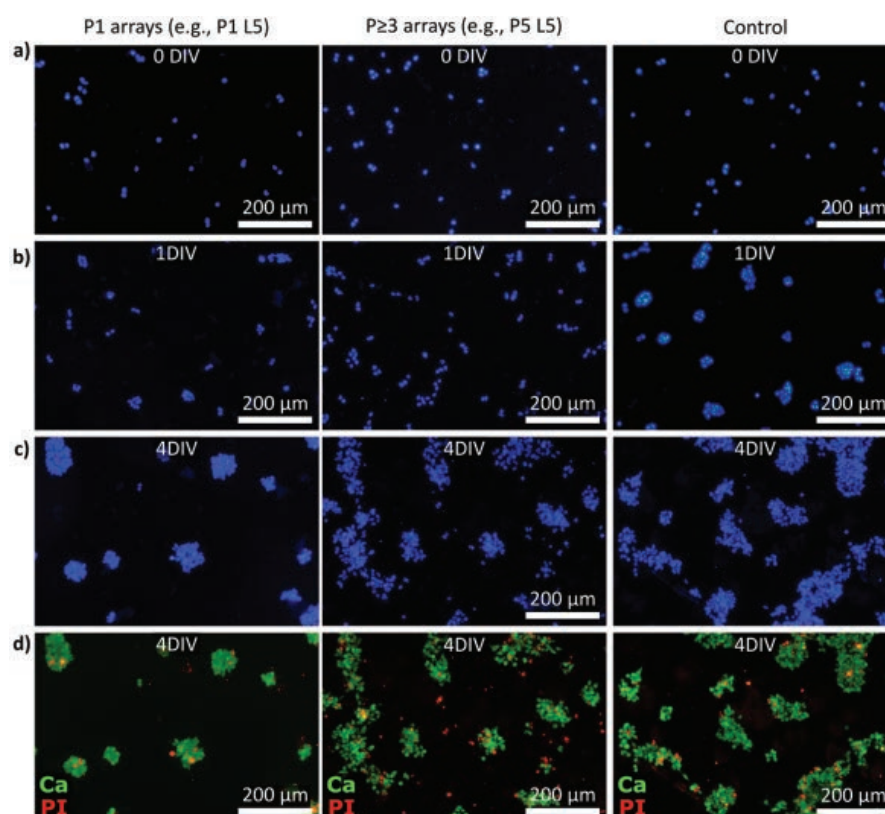

Fig. 3 Exemplary epifluorescence microscopy images of Hoechst, calcein, and propidium iodide (PI) stained smNPCs cultured on NW arrays and control after increasing days in vitro (DIV). (a–c) Exemplary Hoechst-stained smNPCs cultured on $P1$ and $P \geq 3$ NW arrays and on a control substrate right after seeding (panel a, 0 DIV) as well as after 1 and 4 DIV (panel b and c). (d) Example images of the viability assay (merged) using calcein (Ca, green) to label viable cells and PI (red) to stain dead cells (4 DIV).
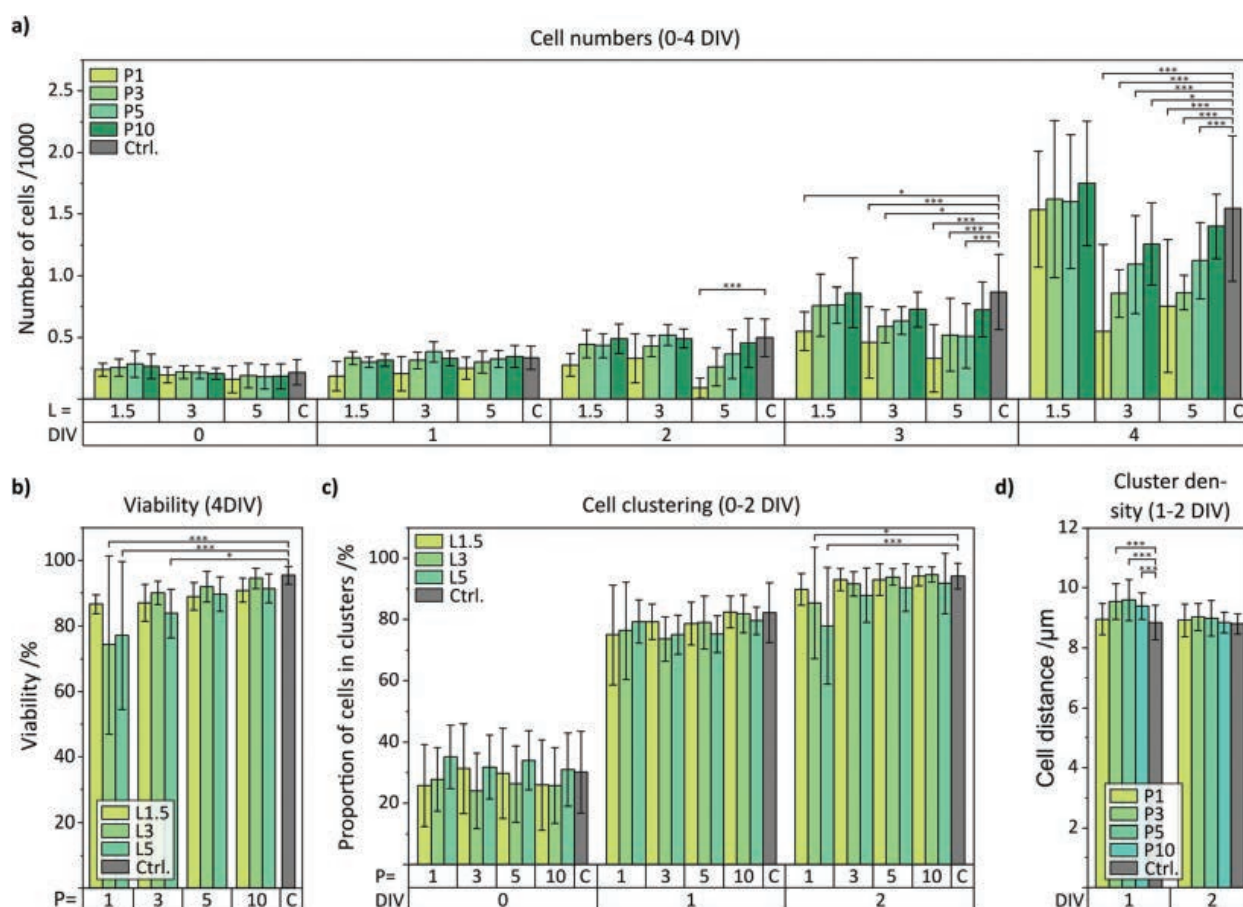
Fig. 4 Quantification of the fluorescent microscopy images in terms of proliferation, viability, and spreading of cells cultured on samples with NW arrays featuring array pitches of 1, 3, 5, and 10 μm (*P*1, *P*3, *P*5, *P*10) and NW lengths of 1.5, 3, and 5 μm (*L*1.5, *L*3, *L*5) in comparison to control (C). (a) Number of viable cells cultured on NW arrays from 0 DIV (right after seeding) up to 4 DIV. (b) Viability after 4 DIV for all NW densities and NW lengths. (c) Proportion of viable cells in clusters from 0–2 DIV for all NW densities and NW lengths. (d) Distance between viable cells in clusters for 1–2 DIV for all array pitches and combined NW lengths. Data not shown here is compiled in Fig. S2 in the ESI.† Error bars are standard deviation (SD). Indicated significances: *α = 0.05, **α = 0.01, ***α = 0.001.

settling state that is considered non-invasive. However, *P*1 *L*1.5 NW arrays showed like all *L*1.5 no change in cell numbers. The cell viabilities were quantified from the calcein and PI stainings and the final viabilities after 4 DIV are presented (Fig. 4b). For most of the NW substrates, a uniform and high cell viability of more than 85% similar to the control was found. For *P*1 *L*3, *P*1 *L*5, and *P*3 *L*5 NW arrays, however, the cell viability was reduced (at worst to about 75%) which correlates with the most prominent reduction in cell numbers on these substrates. Thus, not only the proliferation but also the viability suggests a strong interaction with the substrate. The intermediate viabilities for 0–3 DIV are shown in the ESI (Fig. S2a†). The cell clustering was analysed using a Density-Based Spatial Clustering of Applications with Noise (DBSCAN) algorithm applied to the viable cells and the bar charts of clustering and cluster density are shown in Fig. 4c and d. The proportions of cells that have been classified as part of a cell cluster with more than three cells are plotted for 0–2 DIV in

Fig. 4c (3–4 DIV: Fig. S2b†). Immediately after seeding, only 30% of the cells were located in clusters. After one day, already about 80% of the cells formed clusters until almost all cells (approx. 95%) contributed to the colonies (4 DIV). In principle, no underlying dependence of the proportion of cells in clusters could be extracted with respect to the NW characteristics. However, in the early stages between 0 and 1 DIV, the clusters must be mainly produced by cell migration instead of cell division because the cell numbers within that time hardly increased. For that reason, the spatial distance of cells in the clusters (relating to the centres of the nuclei) was quantified as shown in Fig. 4d for 1 and 2 DIV to indicate cell movement (Fig. S2c for 3–4 DIV†). After one day, the mean distance between viable cells cultured on *P*3, *P*5, and *P*10 NW arrays was slightly yet significantly increased from 8.9 μm on the control to 9.5 μm indicating that the NWs prevented the cells from moving closer together. This inhibited movement was also visible in the Hoechst-stained images in Fig. 3b for the *P*5 *L*5

NW sample at 1 DIV where cells in clusters maintain larger gaps between the cells. This phenomenon was even more pronounced when only viable cells were imaged (Fig. S3†). With time, the difference vanished since proliferation overcame movement as the driving force in cluster formation. For a pitch of 1 μm where a fakir-like settling state is likely, the movement was not impaired compared to the control.

Scanning electron microscopy (SEM) was used to study the interaction between the cells and the NW substrates (Fig. 5). In particular, Fig. 5a–c display a collection of top-view SEM images of cells cultured on $P1$ NW arrays with the lengths $L1.5$, $L3$, and $L5$. Repeatedly, smNPCs at the edge of a cluster showed distinct extensions along the x- and y-direction of the array arrangement. Remarkably, these extensions appeared on all NW substrates independent of the NW length. Hence, this observation obtained by SEM imaging did not fully correlate with the reduced proliferation on $P1$ $L3$ and $P1$ $L5$ NW arrays but normal proliferation on $P1$ $L1.5$ NW arrays. Nevertheless, on NW arrays with $P \geq 3$ ordered extensions along the array axes could not be observed as presented in the tilted SEM images in Fig. 5d–f (exemplarily for $P3$ $L3$, $P5$ $L1.5$, and $P10$ $L5$ NW arrays; images of all remaining substrates in Fig. S4†). Even though no influence of the NW array's geometry on the cell's extensions was apparent for $P \geq 3$ in the SEM images, one still was able to obtain a first impression of how the cells interact with the NWs. For example, in the case of the $P3$ $L3$ NW arrays, the cells in the outer region interacted with the NW tips but also grew between the NWs (detail in Fig. 5d). A similar interplay is seen for $P5$ $L1.5$ in the detail section of

Fig. 5e. For $P10$ $L5$, the smNPCs also interacted with the shaft of the NWs (detail image in Fig. 5f). Note, the SEM technique visualizes merely the outer face of the cells and the substrate. To gain insight into the interior of the cells and to image the deformation of the membrane and the nucleus by the NWs, a complementary fluorescent imaging technique was utilized and the results are presented later (Fig. 7 and 8).

The cytoskeleton of the smNPCs cultured on the NW arrays was imaged using confocal laser scanning microscopy (CLSM) and epifluorescent microscopy exemplarily shown in Fig. 6a–d. Here, we focused on the analysis of the cell extensions along the array axes that were previously observed by SEM imaging. The cytoskeleton was labelled with phalloidin to indicate F-actin. Specifically, Fig. 6a displays an exemplary CLSM image of a cell cluster on a $P1$ array sample (shown: $P1$ $L5$). The corresponding close-up shown in Fig. 6b illustrates that parts of the cytoskeleton were elongated in both x- and y-direction within a small area. Subsequently, widefield microscopy images were prepared of F-actin stained cells being cultured on all types of substrates (Fig. 6c and d, representative images of $P1$ and $P \geq 3$ NW arrays, e.g., $P1$ $L3$, $P3$ $L3$. Control: Fig. S5†). We determined the angles of the protrusions emerging from the cell clusters and plotted the normalized angle distribution of the occurring orientation from −90° to +90° as shown for $P1$ NW arrays and increasing NW lengths ($L1.5$, $L3$, $L5$) in Fig. 6e. All the distributions revealed peaks with amplitudes of >0.8 at angles of ±90° and 0° independent of the NW length. These angles represent the rectangular axes of the NW arrays, hence, the majority of the extensions were aligned with the orien-
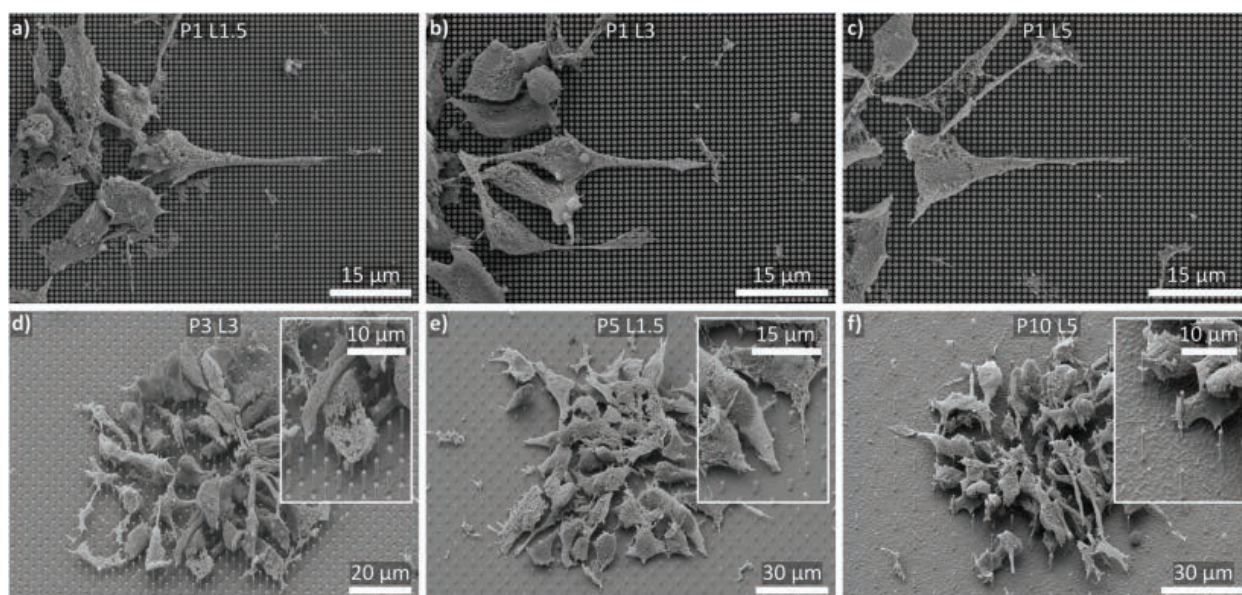

Fig. 5 SEM images of smNPCs cultured on NW arrays. (a–c) Exemplary top-views of cells cultured on $P1$ NW arrays with increasing NW lengths ($L1.5$, $L3$, $L5$). Repeatedly, the cells showed distinct elongations along the NW tips independent of the NW length. (d–f) Exemplary tilted views of cells cultured on $P \geq 3$ NW arrays with different lengths ($L3$, $L1.5$, $L5$). The cells did strongly interact with the NWs (insets) but a fundamental alignment alongside the NWs was not observed. Tilt is 45° with tilt correction. Corresponding SEM images of cells cultured on the remaining NW samples and on control substrates are shown in Fig. S4 in the ESI.†
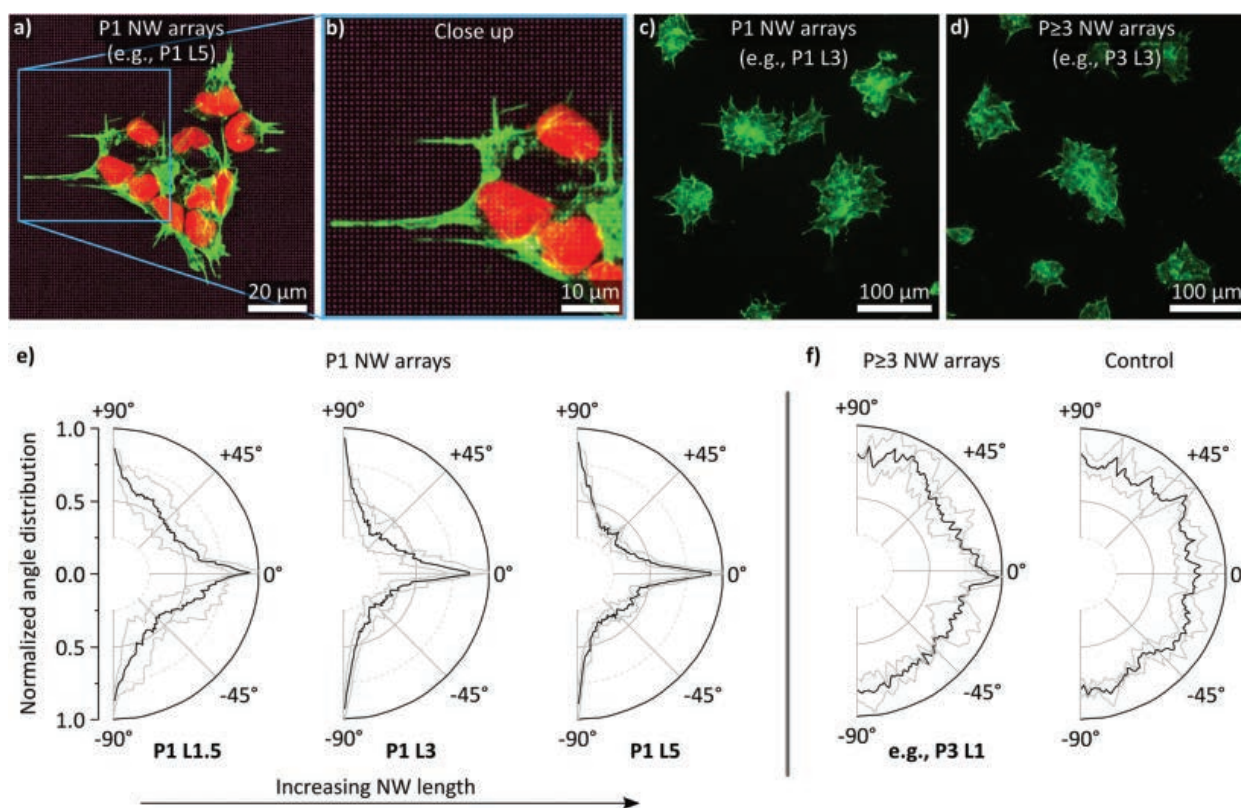
Fig. 6 Confocal laser scanning microscopy (CLSM) and epifluorescent imaging of cells cultured on NW arrays (NW tips' reflections in purple) stained with phalloidin (green) for labeling the cytoskeleton (F-actin) and quantification of angle distribution of the cellular extensions. The nuclei were stained with DRAQ5 (red). (a) Exemplary down projection of multiple *x*–*y* slices in *z*-direction prepared by high-resolution CLSM of a cell cluster cultured on *P*1 NW arrays. Cells at the border of the cluster showed multiple alignments of the cytoskeleton along the *x*- and *y*-axis of the NW array (a close-up is shown in panel b). (c and d) Exemplary epifluorescent overview images of cells cultured on *P*1 and *P* ≥ 3 NW arrays. For *P*1 NW arrays, an alignment of the cytoskeleton along the array axes was observable. A corresponding image of cells cultured on a control substrate is shown in Fig. S5 in the ESI.† (e) Angle distribution of the cellular extensions for *P*1 NW arrays and varying lengths (*L*1.5, *L*3, *L*5). The grey line indicates the standard deviation. (f) Angle distribution of the cellular extensions for *P* ≥ 3 NW arrays (representative plot, *e.g.*, *P*3 *L*1) and control substrates. The grey line indicates the standard deviation. *n* (cluster) > 50.

tation of the array. However, the values of the minima between the peaks at ±90° and 0° changed depending on the NW lengths. Specifically, for *L*3 and *L*5 NWs, distinct minima of about 0.25 were observed at angles of about ±45° which would belong to the diagonal axes of the NW array. In the case of the *L*1.5 NWs, the minima around ±45° were less pronounced and the normalized amplitudes added up to a higher value of approx. 0.5 compared to only 0.25 using *L*3 and *L*5 NWs. Taken together, cells cultured on *L*3 and *L*5 NWs combined with a *P*1 array pitch showed reduced proliferation and systematically arranged elongations of the cytoskeleton. In the case of *L*1.5 NW arrays, where proliferation was normal at a *P*1 array pitch, the effect of angle sorting was less distinct. *P* ≥ 3 NW array and control substrates showed no systematic orientation of the extensions (Fig. 6f).

The difference between *P*1 *L*1.5 and *P*1 *L* ≥ 3 NW arrays related to the interaction of the cells with the NW arrays was investigated in more detail by three-dimensional (3D) CLSM imaging. 3D reconstructions were prepared from images

recorded from varying *z*-planes (z-stacks) and then used to visualize different *x*–*y* planes and cross sections along the *z*-axis (Fig. 7). In particular, the main panel in Fig. 7a displays the example of a cell colony on a *P*1 *L* ≥ 3 NW array (*e.g.*, *P*1 *L*5) that was already shown as a down projection beforehand, but now as a single image from the *x*–*y* plane focused on the NW tips. The cross-sections (narrow panels, right/bottom) demonstrated as expected that the cells are resting in a fakir-like state on the NWs as already seen in the SEM images. A similar settling regime was observed in the case of cells cultured on *P*1 *L*1.5 NW arrays (Fig. 7b and c). The cross-sections precisely positioned along the NWs showed no detrimental difference compared to the previously shown micrographs as the cells appeared to be lying on a bed-of-nails as well. However, differences were observed when the focus was adjusted to the bottom of the NWs (Fig. 7d and e). Specifically, panel d displays a close-up of the cell cluster shown in Fig. 7b. With the focus at the base of the NWs, CLSM imaging revealed that part of the cytoskeleton was also in contact with the substrate's
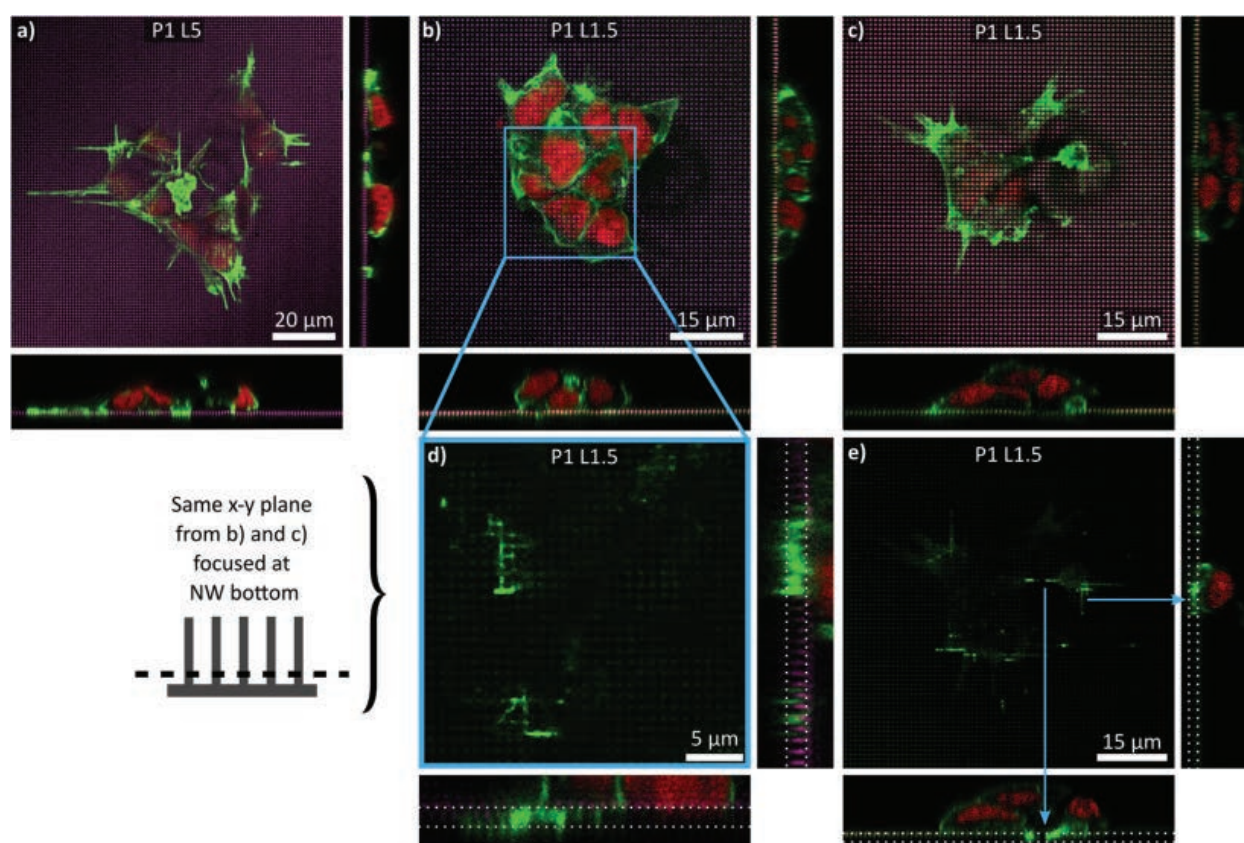
Fig. 7 Exemplary CLSM images of cells grown on $P1$ $L \geq 3$ and $P1$ $L1.5$ NW arrays stained with phalloidin (green) for the cytoskeleton (F-actin) and DRAQ5 (red) for the nuclei (NW tips' reflections in purple). The adherend panels on the side and below the main panels show the corresponding reconstructions of the cross sections (z-plane) in x- and y-direction, respectively. (a) Exemplary $x−y$ slice of cells cultured on $P1$ $L5$ NW arrays prepared by CLSM with the focus on the NW tips. The cross sections demonstrate that the cells stayed on the very NW tips. (b and c) Exemplary $x−y$ slices of cells cultured $P1$ $L1.5$ NW arrays prepared by CLSM with focus on the NW tips. Cross sections along the NW tips show that the cells were predominantly in a fakir-like settling state. Elongation along the NW tips was not pronounced. (d) Imaging the same $x−y$ plane with focus on the NW bottom reveals that the cells not only interacted with the substrate bottom but also showed alignment along the array axes in x- and y-direction (panel e). The cross sections were positioned between the NW tips and show cells that have been growing between the NWs. The z-positions of the NW tips and the substrate bottom are indicated with dotted lines as they are not visible in slices positioned between NWs of $P1$ arrays.

bottom. Cross-sections placed now between the NWs then illustrated that F-actin is found below the level of the NW tips. A similar behaviour is depicted in Fig. 7e which moreover exemplifies that the cell's extensions also aligned with the NW axes at the bottom of the substrate. To briefly conclude, for $P1$ $L1.5$ NW arrays, the cells were found to be in an intermediate state where the cells did not only rest on the NW tips but also interacted with the bottom of the substrate. Since the interaction regime differed from cells cultured on $P1$ $L3$ and $P1$ $L5$ NW arrays, the development of ordered extension was less prominent and more importantly, proliferation was apparently no longer hindered.

$P \geq 3$ NW arrays were finally imaged as well using CLSM (Fig. 8). Two fundamental statements regarding the settling regimes of the cells on the NW arrays could be made: first, with increasing NW pitch, cells were more inclined to encapsulate the NWs. Secondly, with increasing NW length a fakir-like resting state was favoured. Nonetheless, for some fixed pitches

or fixed lengths, the settling regimes of the cells on the NWs were maintained while changing the other parameter. In particular, for $L1.5$ and $L3$ NW arrays, the NWs were very likely to be encapsulated. Of course, the impact of the shortest NWs on the cells and especially the nuclei was rather small since the NW indent the cell by at most 1.5 μm which was negligible in comparison to a cell height of a few micrometres. The deformations induced by the 3 μm long wires were more distinct and thus, the interactions with the nuclei were more present. Yet, the cells did not seem to use all available means to completely avoid deformations of the nucleus. For instance, at the $P10$ $L3$ NW array, one nucleus was exactly positioned on a NW (white square) although there would have been enough free space next to the NW to avoid the very nanostructure. Instead, the nucleus was stretching down to the flat area of the substrate causing a u-shaped deformation seen in the cross-sectional panel below the main panel. For the $P3$ $L5$ NW arrays, the cells settled in an intermediate state on the NWs where
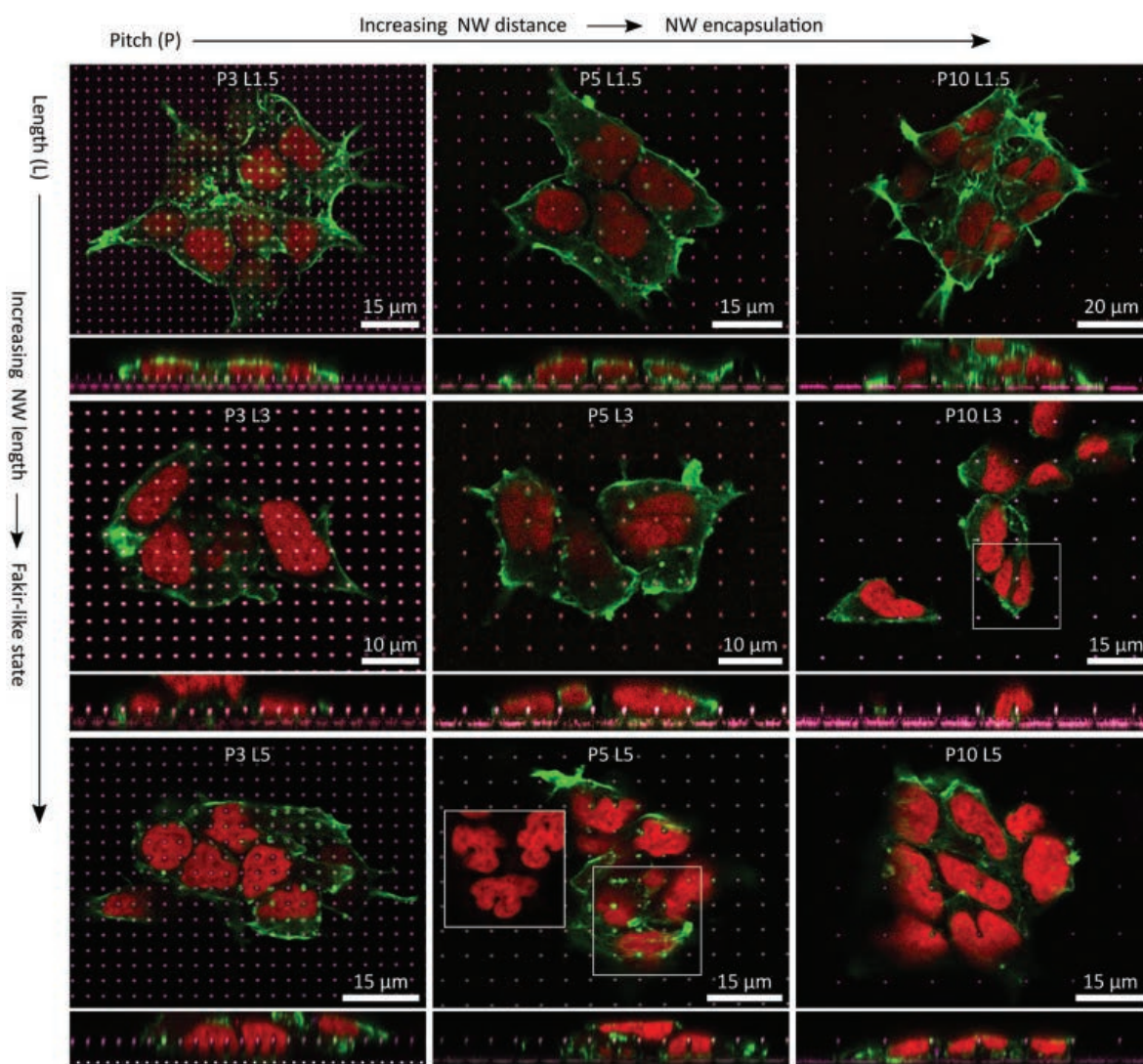
Fig. 8 Compilation of exemplary x−y and x−z planes (main and adherend lower panels, respectively) prepared from CSLM images of cells growing on $P \geq 3$ NW arrays and $L1.5$, $L3$, and $L5$ NWs. F-actin/cytoskeleton was labeled with phalloidin (green), the nuclei were labeled with DRAQ5 (red) and the NW tips' reflections appeared in purple/whitish. With increasing distance between the NWs, the cells favoured encapsulation of the NWs. With increasing NWs length, the cells began to favour a fakir-like settling state. In combinations of large pitches and long NWs, the nuclei underwent heavy deformations in terms of squeezing and indenting by the NWs.

only the top part was engulfed by the cell. Remarkably, this situation went along with heavy deformations of the nuclei where each nucleus was indented by several NWs by about 2.5 μm. Also, such strong reshaping of the nucleus occurred frequently with larger pitches where the cells encapsulated the $L5$ NWs completely. Here, the nuclei were also either indented by NWs, or strong curvatures were generated at nuclei that were squeezed by NWs or were curled around an individual NW (e.g., in the white square of the $P5$ $L5$ NW array). Especially for $P10$ NW arrays, cells could have avoided these heavy interactions of the nucleus with the NWs by resting between the NWs, but noteworthy this was not necessarily the case.

Discussion

The fabrication of Si nanostructures in a top-down approach via RIE is a well-established routine in the semiconductor community.[84] In addition, e-beam lithography is a versatile nanofabrication technique to fine-tune characteristics such as the NW spacing of highly ordered arrays and can also be operated at wafer-scale to enable mass production.[85] Reliable fabrication of highly ordered Si NW arrays using a single step RIE process has been reported before but typically shorter NWs of only about one micron are achieved.[86] Hence, we produced comparatively long nanowires of 5 μm which are usually

achieved in a multi-step deep RIE (DRIE) process.[87] In general, other (semiconductor) materials, such as optically active III–V semiconductors, could be processed by these techniques further broadening the opportunities in potential future applications, e.g., optical stimulation or read-out.[88] However, choosing Si as the essential material for the substrate not only benefits from years of experience in the microchip industry but more importantly, Si was chosen as it is considered a promising material for prospective applications such as sub-cellular bio-interfaces.[89]

The interactions of cells with NW arrays were mapped to a certain extent before, but usually fewer array parameters were altered and only basic cell lines were used. For instance, the culturing of fibroblast cells was studied using varying array densities of randomly arranged NWs but with a fixed NW length of 2 μm.[52] In the present work, we used highly ordered NW arrays with varying pitches of 1, 3, 5, and 10 μm resulting in densities of 100, 11.1, 4, and 1 NWs per 100 μm^2 and varying lengths of 1.5, 3, and 5 μm to allow for a comprehensive study. Both pitch and length cover the parameter space frequently used in the field.[33] Moreover, these characteristics encase sufficiently diverse parameter sets to expect changing settling regimes from a fakir-like state to NW encapsulation modeled by Buch-Månson et al.[77] In contrast to practically all of these studies which used basic cell lines or, e.g., primary rodents cells,[27] we employed human induced stem cell-derived neural progenitor cells in our studies. Utilizing human iPSCs as the basis for the experiments greatly improves the pertinence for neurodegenerative disease studies such as Alzheimer's disease or Parkinson's disease by enabling the use of patient-specific cells.[3,90] Feasibility to culture these patient-derived cells reliably on NW arrays would possibly render many applications such as cell transfection, bio-molecule delivery, or biosensing as demonstrated on other cells.[29,62,67,73,91–93]

Human induced stem cell-derived smNPCs were now cultured successfully on a multitude of different NW arrays. For most of the different arrays used, we can report excellent cell viability of more than 85% which was stable over a culturing period of 4 days and similar to viability in control cells. Neglectable impact on the viability of cells cultured on NW arrays is overall in accordance with the literature.[31,34,43,94,95] However, universal conclusions are difficult to draw since many factors such as cell type, culturing time, NW length, and array pitch occasionally play important roles. For example, HEK293 cells showed lower viability when cultured on nanowire arrays with a pitch of 2 μm compared to larger pitches and control.[96] Note, the HEK293 cells were in a NW encapsulating regime with partly to fully enwrapping the NWs. Interestingly, reduced viability of the smNPCs of about 75% after 4 DIV was found for the highest NW density combined with long NWs (P1 L ≥ 3). Particularly here, unchanged viability was expected since for high NW densities, the cells rest in a fakir-like state on the NWs without any deformation by the NWs.[40,97] In addition, we observed reduced cell numbers on these P1 NW arrays. SEM imaging of these particular samples

then showed that the cells form elongations along the array axes.

Imaging of F-actin revealed that the extensions along the array axes were part of the cytoskeleton. In literature, it is reported that well-ordered NW arrays can generate guiding forces to polarize cells or to direct neurite growth.[41,54–57,75,98] Many array parameters were modified in these studies, but in the end, primarily the spacing of the nanostructures was contributing decisively, and guiding only occurs within a certain range of array pitches. Nonetheless, a direct comparison can only be made with Bucaro et al. because they used comparable array pitches from 0.8 to 5 μm (but only at a fixed NW length of 5 μm) to fine-tune the polarization of human mesenchymal and rodent stem cells.[53] In contrast to our results showing polarization along the array axis with a pitch of 1 μm, polarization appeared in their experiments only with array pitches larger than 1.25 μm and smaller than 3.5 μm. Below 1.25 μm, the surface appears homogeneous to the cells; above 3.5 μm, the cells were not able to reach the next NW. Furthermore, Bucaro et al. explicitly mention that further studies are needed to elaborate whether the morphological changes correlate with proliferation since such analysis was not conducted in their work.

The proliferation as a function of time was investigated here by determining the cell numbers on five consecutive days. As already mentioned in the discussion, we observed fewer cells on the P1 NW arrays with L ≥ 3 NWs. In general, reduced viability and proliferation of cells cultured on densely-spaced NW arrays (fakir-like state) are in contrast to literature. For example, Yan et al. demonstrated that proliferation and viability of murine neural stem cells can be improved using high-density but randomly distributed NW arrays.[99] Hence, we assume in the case of the ordered arrays that particularly the reorganization of F-actin at the elongations along the defined array axes interfered with normal proliferation by changing the dynamics of the cytoskeleton.[100,101] For the shorter wires, proliferation was normal, since the settling regime changed to an intermediate state and thus the stress on the cytoskeleton was generated to an endurable extent. On samples with larger array pitches (P ≥ 3) and longer NWs (L ≥ 3), namely, encapsulating states, we also found fewer cells. Reduced proliferation on such NW arrays with encapsulation of individual NWs is reasonable due to the challenging topology and is in accordance with the literature.[37,50,102] Other studies moreover described actin reorganization at encapsulated nanostructures using osteosarcoma cells which we yet did not spot in the vicinity of the NWs.[103] For the shortest NWs (L1.5), we identified normal proliferation independent of the pitch. Although it has been demonstrated that even short NWs can have a negative impact on proliferation,[50] usually nanostructures of about 1 μm show no detrimental influence.[67,93] The reduced mobility of cells that encapsulate NWs is in good accordance with literature[30,37,81,104] whereas mobility is not influenced in a fakir-like regime.[52,105]

The interaction of the cells with NWs was imaged for all pitches and lengths. The fundamental behavior that shorter nanowires/larger array pitches favor NW encapsulation and

longer wires/smaller array pitches encourage a fakir-like regime is in accordance with the literature.[52,75,77] Deformation of the nucleus by the nanostructures was also reported when using, for example, fibroblasts or mesenchymal stem cells.[50,74,106] Considering the severe deformations of not only the cell but also the nucleus, it is remarkable that the cells maintained their viability even in the case of the longest NWs. The close interaction between the NW and the nucleus might offer the opportunity to use the NW substrates for gene transduction or biomolecule delivery.[59,66,107] We believe that the employment of human induced stem cell-derived neural progenitors not only allows for advanced patient-specific neurodegenerative disease studies or pharmacological drug screenings,[108] but also that our findings are an excellent starting point to establish a more advanced cell type for next-generation biological metamaterials featuring high aspect ratio nanostructures.[109]

Summary and conclusions

The cultivation of human induced stem cells and their derivatives on NW arrays to investigate cellular characteristics is still underrepresented in the field. One potential reason is the challenging topography of such substrates in combination with the demanding nature of stem cell culture. In this work, we show that human iPSC-derived neural progenitor cells can be successfully cultured on ordered Si NW arrays featuring a wide range of NW lengths (1.5 to 5 μm) and array pitches (1 to 10 μm). In general, the cells maintained the ability to proliferate on the NW arrays albeit the overall cell numbers varied in correlation with the topological difficulty, e.g., long NWs. A special case was found for high-density NW arrays, where we observed a reorganization of the cytoskeleton along the array axes which interfered with normal proliferation. We mapped the interaction of the human smNPCs with the NWs and found that in some configurations the cells encapsulated the NWs completely. Moreover, in these cases, the NWs strongly interacted with the nuclei. Remarkably, despite the heavy deformations of the cells, the viability was essentially unimpaired. Thus, we are convinced that our results are a promising starting point to apply human neural progenitor cells to nanowire arrays for future applications in stem cell research and regenerative medicine.

Materials and methods

Nanowire fabrication

The NWs were fabricated in a top-down process with reactive ion etching (RIE) using a chromium hard mask. The mask was predefined via electron-beam lithography (Raith Voyager e-beam lithography system) in a 90 nm thick layer of positive photoresists (PMMA, AllResist, AR-P 671.02). Circles with 700 nm diameter were defined in a rectangular arrangement with pitches of 1, 3, 5, and 10 μm. After developing (1:3 MIBK:IPA, 2.7% H_2O for 30 s and IPA for 30 s), a 65 nm thick layer of chromium was deposited in a physical vapor deposition (PVD) process. The samples were etched with an inductively coupled plasma (ICP)-RIE (Sentech SI500) using 200 W ICP power, 50 W RF power, 2 Pa pressure, 25 sccm SF_6, 50 sccm C_4F_8 at 0 °C electrode temperature. The etch rate was about 300 nm min^{-1}. To remove residues from the RIE procedure, the samples were processed with a KOH dip for a few seconds at 40 °C. To ease handling, the substrates were glued with polydimethylsiloxane (PDMS, SYLGARD® 184 Elastomer Kit, Dow Corning) to 12 × 12 mm^2 glass coverslips. For cell culture, the samples were placed in a well of a 12-well plate, sterilized in 70% ethanol for 5 min, and coated with Matrigel® (1 ml per well, cf. section 'cell culture'). After cell culture and data collection, samples were cleaned with Terg-a-zyme® (10 mg ml^{-1}) for 30 min at 37 °C for reuse purposes.

Cell culture

The smNPCs used in this study were derived from human iPSCs as previously described by Reinhardt et al.[110] All experiments were conducted in accordance with the ethical statement in Reinhardt et al.[110] The generated smNPCs were then cultivated in a 1:1 mixture of DMEM/F12 and Neurobasal medium supplemented with 1% penicillin/streptomycin/glutamine (100×), 1% B27 supplement without vitamin A (50×), 0.5% N2 supplement (100×) (Life Technologies, Carlsbad, CA, USA), 100 μM ascorbic acid (Sigma-Aldrich, St Louis, MO, USA), 0.5 μM smoothened agonist (Biomol, Hamburg, Germany), 3 μM CHIR 99021 (Axon MedChem, Groningen, Netherlands) in a humidified atmosphere at 37 °C and 5% CO_2. The medium was exchanged every 2–3 days. Cells were kept in Matrigel-coated 6-well plates and split in a ratio of 1:10 to 1:20 every 4–5 days close to confluency using Accutase® (Sigma-Aldrich). Coating with Matrigel (Corning 354263, stored in a 1:5 dilution at −20 °C and additionally diluted 1:30 for application, diluted in KnockOut DMEM, Life Technologies) was performed with 1.5 mL per well overnight at room temperature or for 1 h at 37 °C. Per well of the 12-well plate which contained the samples, 125k cells were seeded. The preservation of the neural progenitor cell (NPC) state after 4 days of culturing on the NW arrays was verified using NPC markers (SOX2 and NES (nestin), protocol in the ESI†) and the recordings for NW and control samples are shown in Fig. S6 (SOX2) and Fig. S7 (NES) in the ESI.†

Cell viability

The cells were stained with calcein (0.5 μM, acetoxymethyl esters (calcein-AM), ex/em: 495/515 nm, Thermo Fisher Scientific, Waltham, MA, USA) to identify viable cells and with propidium iodide (PI, 10 μM, Sigma-Aldrich, ex/em: 535/617 nm) to indicate dead cells. Counterstain was Hoechst 33342 (5 mg mL^{-1} in H_2O, ex/em 361/497 nm). Samples were washed with Dulbecco's phosphate-buffered saline (PBS) and staining was performed with calcein-AM, PI, and Hoechst diluted in PBS for 15 min at 37 °C and 5% CO_2 in the incubator. Subsequently, the samples were rinsed three times prior to

imaging (Nikon Eclipse FN1 microscope with a 10× objective and DSRi2 camera). Data were collected in three independent experiments with each 5–6 images per combination of NW length and array pitch. Control was collected from planarly etched silicon wafer without NWs next to the NW arrays. Note, that proliferation, viability, and spreading on the etched Si were similar compared to control on conventional glass coverslips as shown in the ESI (Fig. S1†). Image size was 1282 × 853 μm^2.

Confocal laser scanning microscopy

A Leica TCS SP8 microscope in upright configuration equipped with 488 and 638 nm wavelength laser sources was used for confocal scanning laser microscopy. Cells were stained with phalloidin (ActinGreen™ 488 ReadyProbes™ Reagent, ex/em: 495/518 nm Thermo Fisher Scientific, Massachusetts, USA) and DRAQ5 (DRAQ5 fluorescent probe, ex/em: 647/681 nm, Thermo Fisher Scientific). Samples were rinsed with PBS, fixed with 4% formaldehyde in PBS for 10 min at room temperature (RT), and rinsed three times with PBS. Cells were permeabilized and blocked with 3% bovine serum albumin (BSA), 0.1% Tween 20, and 0.1% Triton X-100 in PBS for 45 min at RT. Staining with phalloidin (2 drops per mL) and DRAQ5 (1 : 1000) in PBS with 0.1% BSA was performed in the dark for 1 h at RT. Samples were washed three times with 0.05% Tween 20 in PBS in the dark for 5 min at RT. For imaging, the samples were transferred from the 12-well plate onto a microscope slide and covered with a precision glass cover slide to use the water immersion objectives. Z-stacks were recorded with a slicing step size of 172 nm and analysed using Leica LAS X Core software.

Scanning electron microscopy

SEM images were prepared with a Crossbeam 550 from Zeiss. For this purpose, the cells were rinsed with PBS and fixed with 4% formaldehyde in PBS for 10 min at RT. The solution was exchanged with deionized water followed by dehydration in a step-wise ethanol exchange. Subsequently, the cells were critical point dried (Tousimis Autosamdri-815) and sputter-coated with a 20 nm gold layer to avoid charging effects.

Image and data analysis

Cells were identified in the Hoechst counterstain channel and cross-correlated to viable and dead cells in the calcein and PI channel, respectively, with CellProfiler 4.1.3.[111] Images of identified viable cells were exported in order to analyse clustering with ImageJ/Fiji[112] using the 'SSIDC Cluster Indicator' in the BioVoxxel toolbox.[113] Distances of cells in clusters were determined with the 'nearest neighbour distances' plugin for ImageJ/Fiji. Orientations of the extensions were quantified with OrientationJ in ImageJ/Fiji. Data were processed and plots were prepared with Origin (v.2021). Statistical analysis was done by an ANOVA analysis with a *post-hoc* Tukey's test using the 'paired comparison plot' application. Differences were considered significant for α = 0.05, α = 0.01, and α = 0.001. For publication, the images were optimized in contrast and brightness.

Author contributions

JH, KB, MS conducted cell culture. JH, KB, MS conducted epifluorescence microscopy imaging. UH, OP helped with smNPC characterization. JH conducted confocal microscopy imaging. JH, CH prepared the NW substrates. JH, KB analysed the data. JH wrote the manuscript. JH, RZ conceptualized the study. RZ, RHB supervised the study. JH, KB, MS, RZ, MG, HRS revised the manuscript. RZ, RHB acquired funding. All authors conducted proofreading and approved the manuscript.

Conflicts of interest

There are no conflicts to declare.

Acknowledgements

References

1 J. Deinsberger, D. Reisinger and B. Weber, *NPJ Regen. Med.*, 2020, **5**, 15.

2 B. Lo and L. Parham, *Endocr. Rev.*, 2009, **30**, 204–213.

3 Y. Li, H. V. Nguyen and S. H. Tsang, *Methods Mol. Biol.*, 2015, **1353**, 77–88.

4 M. Dragunow, *Nat. Rev. Drug Discovery*, 2008, **7**, 659–666.

5 J. Seok, H. S. Warren, A. G. Cuenca, M. N. Mindrinos, H. V. Baker, W. Xu, D. R. Richards, G. P. McDonald-Smith, H. Gao, L. Hennessy, C. C. Finnerty, C. M. López, S. Honari, E. E. Moore, J. P. Minei, J. Cuschieri, P. E. Bankey, J. L. Johnson, J. Sperry, A. B. Nathens, T. R. Billiar, M. A. West, M. G. Jeschke, M. B. Klein, R. L. Gamelli, N. S. Gibran, B. H. Brownstein, C. Miller-Graziano, S. E. Calvano, P. H. Mason, J. P. Cobb, L. G. Rahme, S. F. Lowry, R. V. Maier, L. L. Moldawer, D. N. Herndon, R. W. Davis, W. Xiao and R. G. Tompkins, *Proc. Natl. Acad. Sci. U. S. A.*, 2013, **110**, 3507–3512.

6 X. Xu, E. I. Stoyanova, A. E. Lemiesz, J. Xing, D. C. Mash and N. Heintz, *eLife*, 2018, **7**, e37551.

7 H. C. Ko and B. D. Gelb, *Stem Cells Transl. Med.*, 2014, **3**, 500–509.

8 J. A. Garcia-Leon, L. Caceres-Palomo, E. Sanchez-Mejias, M. Mejias-Ortega, C. Nuñez-Diaz, J. J. Fernandez-Valenzuela, R. Sanchez-Varo, J. C. Davila, J. Vitorica and A. Gutierrez, *Int. J. Mol. Sci.*, 2020, **21**, 6867.

9 B. Xiao, H. H. Ng, R. Takahashi and E.-K. Tan, *J. Neurol. Neurosurg. Psychiatry*, 2016, **87**, 697–702.

10 L. M. Smits, L. Reinhardt, P. Reinhardt, M. Glatza, A. S. Monzel, N. Stanslowsky, M. D. Rosato-Siri, A. Zanon, P. M. Antony, J. Bellmann, S. M. Nicklas, K. Hemmer, X. Qing, E. Berger, N. Kalmbach, M. Ehrlich, S. Bolognin, A. A. Hicks, F. Wegner, J. L. Sterneckert and J. C. Schwamborn, *npj Parkinson's Dis.*, 2019, **5**, 5.

11 A. Appelt-Menzel, S. Oerter, S. Mathew, U. Haferkamp, C. Hartmann, M. Jung, W. Neuhaus and O. Pless, *Curr. Protoc. Stem Cell Biol.*, 2020, **55**, e122.

12 M. A. Lancaster, M. Renner, C.-A. Martin, D. Wenzel, L. S. Bicknell, M. E. Hurles, T. Homfray, J. M. Penninger, A. P. Jackson and J. A. Knoblich, *Nature*, 2013, **501**, 373–379.

13 K. Takahashi and S. Yamanaka, *Cell*, 2006, **126**, 663–676.

14 M. W. Tibbitt, C. B. Rodell, J. A. Burdick and K. S. Anseth, *Proc. Natl. Acad. Sci. U. S. A.*, 2015, **112**, 14444–14451.

15 I. Armentano, L. Tarpani, F. Morena, S. Martino, L. Latterini and L. Torre, *Curr. Org. Chem.*, 2018, **22**, 1193–1204.

16 C. Leclech and C. Villard, *Front. Bioeng. Biotechnol.*, 2020, **8**, 1198.

17 C. Simitzi, A. Ranella and E. Stratakis, *Acta Biomater.*, 2017, **51**, 21–52.

18 M. Marcus, K. Baranes, M. Park, I. S. Choi, K. Kang and O. Shefi, *Adv. Healthcare Mater.*, 2017, **6**, 1700267.

19 W. Zhang, Y. Yang and B. Cui, *Curr. Opin. Solid State Mater. Sci.*, 2021, **25**, 100873.

20 M. Lampin, R. Warocquier-Clérout, C. Legris, M. Degrange and M. F. Sigot-Luizard, *J. Biomed. Mater. Res.*, 1997, **36**, 99–108.

21 Y. H. Kim, N. S. Baek, Y. H. Han, M. A. Chung and S. D. Jung, *J. Neurosci. Methods*, 2011, **202**, 38–44.

22 C. Fendler, J. Harberts, L. Rafeldt, G. Loers, R. Zierold and R. H. Blick, *Nanoscale Adv.*, 2020, **2**, 5192–5200.

23 A. Koitmäe, J. Harberts, G. Loers, M. Müller, C. S. Bausch, D. Sonnenberg, C. Heyn, R. Zierold, W. Hansen and R. H. Blick, *Adv. Mater. Interfaces*, 2016, **3**, 1600746.

24 A. Koitmäe, M. Müller, C. S. Bausch, J. Harberts, W. Hansen, G. Loers and R. H. Blick, *Langmuir*, 2018, **34**, 1528–1534.

25 C. Leclech and A. I. Barakat, *Cytoskeleton*, 2021, **78**, 284–292.

26 J. Harberts, C. Fendler, J. Teuber, M. Siegmund, A. Silva, N. Rieck, M. Wolpert, R. Zierold and R. H. Blick, *ACS Nano*, 2020, **14**, 13091–13102.

27 G. He, N. Hu, A. M. Xu, X. Li, Y. Zhao and X. Xie, *Adv. Funct. Mater.*, 2020, **30**, 1909890.

28 M. L. Khraiche and R. El Hassan, *J. Sci. Adv. Mater. Devices*, 2020, **5**, 279–294.

29 A. Tay and N. Melosh, *Acc. Chem. Res.*, 2019, **52**, 2462–2471.

30 A. F. McGuire, F. Santoro and B. Cui, *Annu. Rev. Anal. Chem.*, 2018, **11**, 101–126.

31 T. Berthing, S. Bonde, C. B. Sørensen, P. Utko, J. Nygård and K. L. Martinez, *Small*, 2011, **7**, 640–647.

32 R. Elnathan, M. Kwiat, F. Patolsky and N. H. Voelcker, *Nano Today*, 2014, **9**, 172–196.

33 S. Bonde, N. Buch-Månson, K. R. Rostgaard, T. K. Andersen, T. Berthing and K. L. Martinez, *Nanotechnology*, 2014, **25**, 362001.

34 W. Hällström, T. Mårtensson, C. Prinz, P. Gustavsson, L. Montelius, L. Samuelson and M. Kanje, *Nano Lett.*, 2007, **7**, 2960–2965.

35 Z. Li, R. Yang, M. Yu, F. Bai, C. Li and Z. L. Wang, *J. Phys. Chem. C*, 2008, **112**, 20114–20117.

36 G. Piret, M.-T. Perez and C. N. Prinz, *Biomaterials*, 2013, **34**, 875–887.

37 Z. Li, S. Kamlund, T. Ryser, M. Lard, S. Oredsson and C. N. Prinz, *J. Mater. Chem. B*, 2018, **6**, 7042–7049.

38 Z. Li, H. Persson, K. Adolfsson, S. Oredsson and C. N. Prinz, *Sci. China: Life Sci.*, 2018, **61**, 427–435.

39 C. S. Hansel, S. W. Crowder, S. Cooper, S. Gopal, M. João Pardelha da Cruz, L. de Oliveira Martins, D. Keller, S. Rothery, M. Becce, A. E. G. Cass, C. Bakal, C. Chiappini and M. M. Stevens, *ACS Nano*, 2019, **13**, 2913–2926.

40 J. Harberts, R. Zierold, C. Fendler, A. Koitmäe, P. Bayat, I. Fernandez-Cuesta, G. Loers, B.-P. Diercks, R. Fliegert, A. H. Guse, C. Ronning, G. Otnes, M. Borgström and R. H. Blick, *RSC Adv.*, 2019, **9**, 11194–11201.

41 J. Harberts, U. Haferkamp, S. Haugg, C. Fendler, D. Lam, R. Zierold, O. Pless and R. H. Blick, *Biomater. Sci.*, 2020, **8**, 2434–2446.

42 J. Harberts, M. Siegmund, M. Schnelle, T. Zhang, Y. Lei, L. Yu, R. Zierold and R. H. Blick, *Sci. Rep.*, 2021, **11**, 18819.

43 G. Tullii, F. Giona, F. Lodola, S. Bonfadini, C. Bossio, S. Varo, A. Desii, L. Criante, C. Sala, M. Pasini, C. Verpelli, F. Galeotti and M. R. Antognazza, *ACS Appl. Mater. Interfaces*, 2019, **11**, 28125–28137.

44 Z. Li, J. Song, G. Mantini, M.-Y. Lu, H. Fang, C. Falconi, L.-J. Chen and Z. L. Wang, *Nano Lett.*, 2009, **9**, 3575–3580.

45 W. Hällström, M. Lexholm, D. B. Suyatin, G. Hammarin, D. Hessman, L. Samuelson, L. Montelius, M. Kanje and C. N. Prinz, *Nano Lett.*, 2010, **10**, 782–787.

46 Z. Li, H. Persson, K. Adolfsson, L. Abariute, M. T. Borgström, D. Hessman, K. Åström, S. Oredsson and C. N. Prinz, *Nanoscale*, 2017, **9**, 19039–19044.

47 L. Hanson, W. Zhao, H.-Y. Lou, Z. C. Lin, S. W. Lee, P. Chowdary, Y. Cui and B. Cui, *Nat. Nanotechnol.*, 2015, **10**, 554–562.

48 K. S. Beckwith, S. Ullmann, J. Vinje and P. Sikorski, *Small*, 2019, **15**, 1902514.

49 S. Qi, C. Yi, S. Ji, C.-C. Fong and M. Yang, *ACS Appl. Mater. Interfaces*, 2009, **1**, 30–34.

50 H. Persson, C. Købler, K. Mølhave, L. Samuelson, J. O. Tegenfeldt, S. Oredsson and C. N. Prinz, *Small*, 2013, **9**, 4006–4016.

51 H. Persson, Z. Li, J. O. Tegenfeldt, S. Oredsson and C. N. Prinz, *Sci. Rep.*, 2015, **5**, 18535.

52 N. Buch-Månson, D.-H. Kang, D. Kim, K. E. Lee, M.-H. Yoon and K. L. Martinez, *Nanoscale*, 2017, **9**, 5517–5527.

53 M. A. Bucaro, Y. Vasquez, B. D. Hatton and J. Aizenberg, *ACS Nano*, 2012, **6**, 6222–6230.

54 F. Milos, A. Belu, D. Mayer, V. Maybeck and A. Offenhäusser, *Adv. Biol.*, 2021, **5**, 2000248.

55 V. Gautam, S. Naureen, N. Shahid, Q. Gao, Y. Wang, D. Nisbet, C. Jagadish and V. R. Daria, *Nano Lett.*, 2017, **17**, 3369–3375.

56 H. Amin, M. Dipalo, F. De Angelis and L. Berdondini, *ACS Appl. Mater. Interfaces*, 2018, **10**, 15207–15215.

57 M. Park, E. Oh, J. Seo, M.-H. Kim, H. Cho, J. Y. Choi, H. Lee and I. S. Choi, *Small*, 2016, **12**, 1148–1152.

58 J. J. VanDersarl, A. M. Xu and N. A. Melosh, *Nano Lett.*, 2012, **12**, 3881–3886.

59 Y. Wang, Y. Yang, L. Yan, S. Y. Kwok, W. Li, Z. Wang, X. Zhu, G. Zhu, W. Zhang, X. Chen and P. Shi, *Nat. Commun.*, 2014, **5**, 4466.

60 X. Xie, A. Aalipour, S. V. Gupta and N. A. Melosh, *ACS Nano*, 2015, **9**, 11667–11677.

61 C. Chiappini, J. O. Martinez, E. De Rosa, C. S. Almeida, E. Tasciotti and M. M. Stevens, *ACS Nano*, 2015, **9**, 5500–5509.

62 Y. Cao, H. Chen, R. Qiu, M. Hanna, E. Ma, M. Hjort, A. Zhang, R. S. Lewis, J. C. Wu and N. A. Melosh, *Sci. Adv.*, 2018, **4**, eaat8131.

63 S. Gopal, C. Chiappini, J. Penders, V. Leonardo, H. Seong, S. Rothery, Y. Korchev, A. Shevchuk and M. M. Stevens, *Adv. Mater.*, 2019, **31**, 1806788.

64 C. Chiappini, E. De Rosa, J. O. Martinez, X. Liu, J. Steele, M. M. Stevens and E. Tasciotti, *Nat. Mater.*, 2015, **14**, 532–539.

65 W. Kim, J. K. Ng, M. E. Kunitake, B. R. Conklin and P. Yang, *J. Am. Chem. Soc.*, 2007, **129**, 7228–7229.

66 R. Elnathan, B. Delalat, D. Brodoceanu, H. Alhmoud, F. J. Harding, K. Buehler, A. Nelson, L. Isa, T. Kraus and N. H. Voelcker, *Adv. Funct. Mater.*, 2015, **25**, 7215–7225.

67 Y. Chen, S. Aslanoglou, G. Gervinskas, H. Abdelmaksoud, N. H. Voelcker and R. Elnathan, *Small*, 2019, **15**, 1904819.

68 C. Xie, Z. Lin, L. Hanson, Y. Cui and B. Cui, *Nat. Nanotechnol.*, 2012, **7**, 185–190.

69 J. T. Robinson, M. Jorgolli, A. K. Shalek, M.-H. Yoon, R. S. Gertner and H. Park, *Nat. Nanotechnol.*, 2012, **7**, 180–184.

70 K.-Y. Lee, I. Kim, S.-E. Kim, D.-W. Jeong, J.-J. Kim, H. Rhim, J.-P. Ahn, S.-H. Park and H.-J. Choi, *Nanoscale Res. Lett.*, 2014, **9**, 56.

71 Z. C. Lin, C. Xie, Y. Osakada, Y. Cui and B. Cui, *Nat. Commun.*, 2014, **5**, 3206.

72 R. Liu, R. Chen, A. T. Elthakeb, S. H. Lee, S. Hinckley, M. L. Khraiche, J. Scott, D. Pre, Y. Hwang, A. Tanaka, Y. G. Ro, A. K. Matsushita, X. Dai, C. Soci, S. Biesmans, A. James, J. Nogan, K. L. Jungjohann, D. V. Pete, D. B. Webb, Y. Zou, A. G. Bang and S. A. Dayeh, *Nano Lett.*, 2017, **17**, 2757–2764.

73 X. Li, J. Mo, J. Fang, D. Xu, C. Yang, M. Zhang, H. Li, X. Xie, N. Hu and F. Liu, *J. Mater. Chem. B*, 2020, **8**, 7609–7632.

74 L. Hanson, Z. C. Lin, C. Xie, Y. Cui and B. Cui, *Nano Lett.*, 2012, **12**, 5815–5820.

75 N. Buch-Månson, A. Spangenberg, L. P. C. Gomez, J.-P. Malval, O. Soppera and K. L. Martinez, *Sci. Rep.*, 2017, **7**, 9247.

76 F. Santoro, W. Zhao, L.-M. Joubert, L. Duan, J. Schnitker, Y. van de Burgt, H.-Y. Lou, B. Liu, A. Salleo, L. Cui, Y. Cui and B. Cui, *ACS Nano*, 2017, **11**, 8320–8328.

77 N. Buch-Månson, S. Bonde, J. Bolinsson, T. Berthing, J. Nygård and K. L. Martinez, *Adv. Funct. Mater.*, 2015, **25**, 3246–3255.

78 S. W. Crowder, V. Leonardo, T. Whittaker, P. Papathanasiou and M. M. Stevens, *Cell Stem Cell*, 2016, **18**, 39–52.

79 H.-Y. Lou, W. Zhao, Y. Zeng and B. Cui, *Acc. Chem. Res.*, 2018, **51**, 1046–1053.

80 R. Liu and J. Ding, *ACS Appl. Mater. Interfaces*, 2020, **12**, 35799–35812.

81 H. Kim, I. Kim, H.-J. Choi, S. Y. Kim and E. G. Yang, *Nanoscale*, 2015, **7**, 17131–17138.

82 C. H. Rasmussen, P. M. Reynolds, D. R. Petersen, M. Hansson, R. M. McMeeking, M. Dufva and N. Gadegaard, *Adv. Funct. Mater.*, 2016, **26**, 815–823.

83 H. S. Kim and H. S. Yoo, *RSC Adv.*, 2015, **5**, 49508–49512.

84 H. Jansen, H. Gardeniers, M. de Boer, M. Elwenspoek and J. Fluitman, *J. Micromech. Microeng.*, 1996, **6**, 14–28.

85 Y. Chen, *Microelectron. Eng.*, 2015, **135**, 57–72.

86 Y.-J. Hung, S.-L. Lee, B. J. Thibeault and L. A. Coldren, *IEEE J. Sel. Top. Quantum Electron.*, 2011, **17**, 869–877.

87 Y. Q. Fu, A. Colli, A. Fasoli, J. K. Luo, A. J. Flewitt, A. C. Ferrari and W. I. Milne, *J. Vac. Sci. Technol., B: Microelectron. Nanometer Struct.–Process., Meas., Phenom.*, 2009, **27**, 1520.

88 F. Karouta, *J. Phys. D: Appl. Phys.*, 2014, **47**, 233501.

89 H. Acaron Ledesma and B. Tian, *J. Mater. Chem. B*, 2017, **5**, 4276–4289.

90 A. P. Reddy, J. Ravichandran and N. Carkaci-Salli, *Biochim. Biophys. Acta, Mol. Basis Dis.*, 2020, **1866**, 165506.

91 X. Xu, S. Hou, N. Wattanatorn, F. Wang, Q. Yang, C. Zhao, X. Yu, H.-R. Tseng, S. J. Jonas and P. S. Weiss, *ACS Nano*, 2018, **12**, 4503–4511.

92 M. Lard, H. Linke and C. N. Prinz, *Nanotechnology*, 2019, **30**, 214003.

93 L. Schmiderer, A. Subramaniam, K. Žemaitis, A. Bäckström, D. Yudovich, S. Soboleva, R. Galeev, C. N. Prinz, J. Larsson and M. Hjort, *Proc. Natl. Acad. Sci. U. S. A.*, 2020, **117**, 21267–21273.

94 A. K. Shalek, J. T. Gaublomme, L. Wang, N. Yosef, N. Chevrier, M. S. Andersen, J. T. Robinson, N. Pochet, D. Neuberg, R. S. Gertner, I. Amit, J. R. Brown, N. Hacohen, A. Regev, C. J. Wu and H. Park, *Nano Lett.*, 2012, **12**, 6498–6504.

95   C. N. Prinz, *J. Phys.: Condens. Matter*, 2015, **27**, 233103.

96   S. Bonde, T. Berthing, M. H. Madsen, T. K. Andersen, N. Buch-Månson, L. Guo, X. Li, F. Badique, K. Anselme, J. Nygård and K. L. Martinez, *ACS Appl. Mater. Interfaces*, 2013, **5**, 10510–10519.

97   S.-M. Kim, S. Lee, D. Kim, D.-H. Kang, K. Yang, S.-W. Cho, J. S. Lee, I. S. Choi, K. Kang and M.-H. Yoon, *Nano Res.*, 2018, **11**, 2532–2543.

98   A. Kundu, L. Micholt, S. Friedrich, D. R. Rand, C. Bartic, D. Braeken and A. Levchenko, *Lab Chip*, 2013, **13**, 3070.

99   Q. Yan, L. Fang, J. Wei, G. Xiao, M. Lv, Q. Ma, C. Liu and W. Wang, *J. Biomater. Sci., Polym. Ed.*, 2017, **28**, 1394–1407.

100 P. P. Provenzano and P. J. Keely, *J. Cell Sci.*, 2011, **124**, 1195–1205.

101 N. Bendris, B. Lemmers and J. M. Blanchard, *Cell Cycle*, 2015, **14**, 1786–1798.

102 D. Ning, B. Duong, G. Thomas, Y. Qiao, L. Ma, Q. Wen and M. Su, *Langmuir*, 2016, **32**, 2718–2723.

103 H.-Y. Lou, W. Zhao, X. Li, L. Duan, A. Powers, M. Akamatsu, F. Santoro, A. F. McGuire, Y. Cui, D. G. Drubin and B. Cui, *Proc. Natl. Acad. Sci. U. S. A.*, 2019, **116**, 23143–23151.

104 C. Xie, L. Hanson, W. Xie, Z. Lin, B. Cui and Y. Cui, *Nano Lett.*, 2010, **10**, 4020–4024.

105 F. Viela, D. Granados, A. Ayuso-Sacido and I. Rodríguez, *Adv. Funct. Mater.*, 2016, **26**, 5599–5609.

106 J. Carthew, H. H. Abdelmaksoud, M. Hodgson-Garms, S. Aslanoglou, S. Ghavamian, R. Elnathan, J. P. Spatz, J. Brugger, H. Thissen, N. H. Voelcker, V. J. Cadarso and J. E. Frith, *Adv. Sci.*, 2021, **8**, 2003186.

107 J.-A. Huang, V. Caprettini, Y. Zhao, G. Melle, N. Maccaferri, L. Deleye, X. Zambrana-Puyalto, M. Ardini, F. Tantussi, M. Dipalo and F. De Angelis, *Nano Lett.*, 2019, **19**, 722–731.

108 A. Farkhondeh, R. Li, K. Gorshkov, K. G. Chen, M. Might, S. Rodems, D. C. Lo and W. Zheng, *Drug Discovery Today*, 2019, **24**, 992–999.

109 S. G. Higgins, M. Becce, A. Belessiotis-Richards, H. Seong, J. E. Sero and M. M. Stevens, *Adv. Mater.*, 2020, **32**, 1903862.

110 P. Reinhardt, M. Glatza, K. Hemmer, Y. Tsytsyura, C. S. Thiel, S. Höing, S. Moritz, J. A. Parga, L. Wagner, J. M. Bruder, G. Wu, B. Schmid, A. Röpke, J. Klingauf, J. C. Schwamborn, T. Gasser, H. R. Schöler and J. Sterneckert, *PLoS One*, 2013, **8**, e59252.

111 C. McQuin, A. Goodman, V. Chernyshev, L. Kamentsky, B. A. Cimini, K. W. Karhohs, M. Doan, L. Ding, S. M. Rafelski, D. Thirstrup, W. Wiegraebe, S. Singh, T. Becker, J. C. Caicedo and A. E. Carpenter, *PLoS Biol.*, 2018, **16**, e2005970.

112 J. Schindelin, I. Arganda-Carreras, E. Frise, V. Kaynig, M. Longair, T. Pietzsch, S. Preibisch, C. Rueden, S. Saalfeld, B. Schmid, J.-Y. Tinevez, D. J. White, V. Hartenstein, K. Eliceiri, P. Tomancak and A. Cardona, *Nat. Methods*, 2012, **9**, 676–682.

113 J. Brocher, The BioVoxxel Image Processing and Analysis Toolbox, *EuBIAS-Conference*, 2015, Jan 5.

Supporting information

Culturing human iPSC-derived neural progenitor cells on nanowire arrays: Mapping the impact of nanowire length and array pitch on proliferation, viability, and membrane deformation

Jann Harberts,*[a] Katja Bours,[a] Malte Siegmund,[a] Carina Hedrich,[a] Michael Glatza,[b] Hans R. Schöler,[b] Undine Haferkamp,[c] Ole Pless,[c] Robert Zierold,*[a] and Robert H. Blick [a,d]

[a.] Center for Hybrid Nanostructures, Universität Hamburg, Luruper Chaussee 149, 22761 Hamburg, Germany. E-mail: jann.harberts@chyn.uni-hamburg.de, robert.zierold@chyn.uni-hamburg.de

[b.] Department of Cell and Developmental Biology, Max Planck Institute for Molecular Biomedicine, Röntgenstraße 20, 48149 Münster, Germany

[c.] Fraunhofer Institute for Translational Medicine and Pharmacology (ITMP), ScreeningPort, Schnackenburgallee 114, 22525 Hamburg, Germany

[d.] Material Science and Engineering, College of Engineering, University of Wisconsin-Madison, Madison, Wisconsin 53706, USA
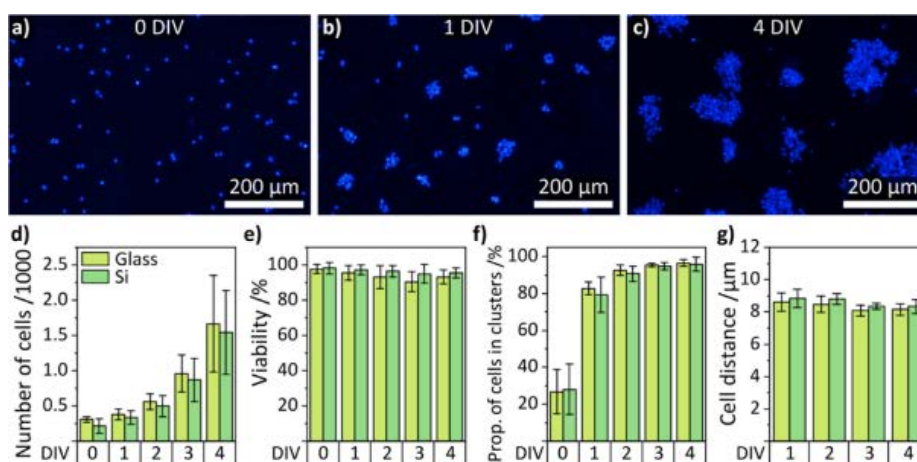
Figure S1: Comparison of cell numbers, viability, and spreading of cells cultivated on glass control and planarly etched Si substrates. a-c) Exemplary epifluorescence microscopy images of smNPCs cultured on glass substrates after 0, 1, and 4 DIV. d-g) Bar charts of the determined quantities. n ≥ 20.
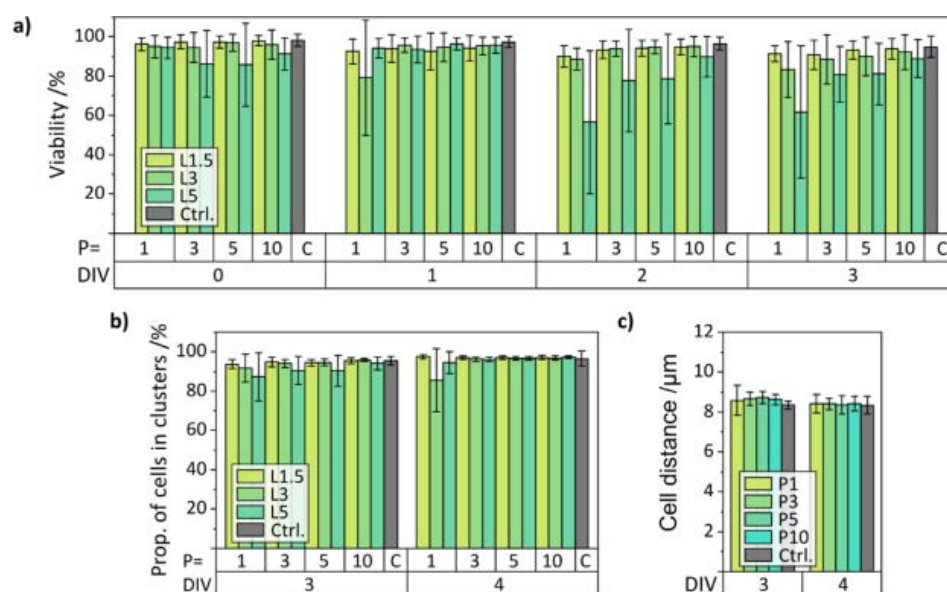
Figure S2: Data from quantification that is not shown in the main manuscript.
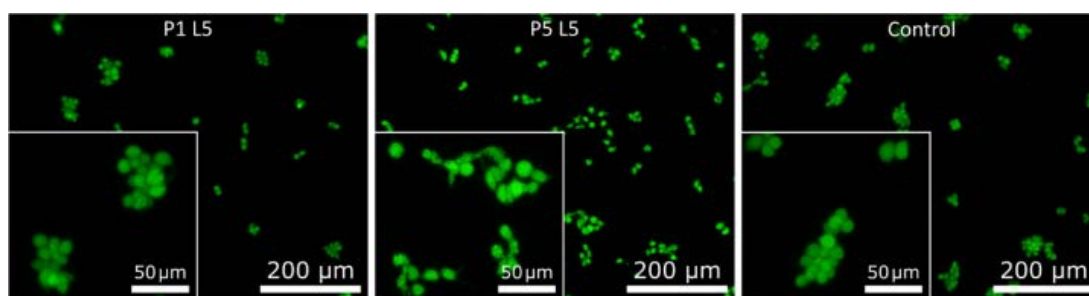

Figure S3: Viable cells 1 DIV after plating. The cells cultured on the P5 L5 NW arrays maintain larger gaps between cells that are clustered in comparison to cells cultured on the control and the P1 L5 NW sample.
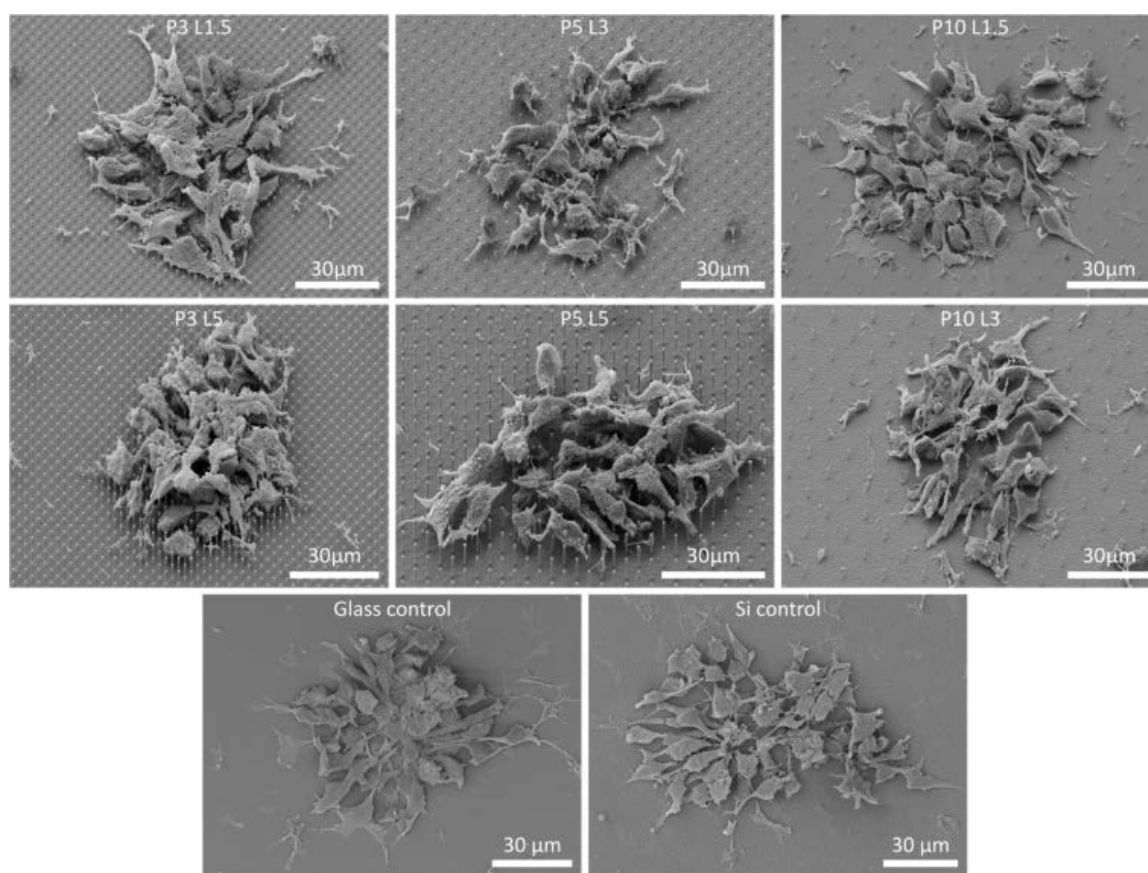
Figure S4: Collection of SEM images displaying smNPCs cultured on various NW arrays (tilt: 45°, corrected) and control samples (not shown in the main manuscript).
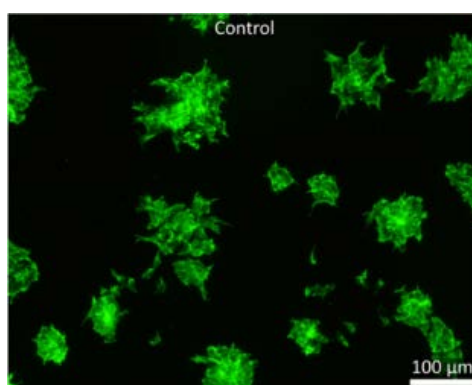

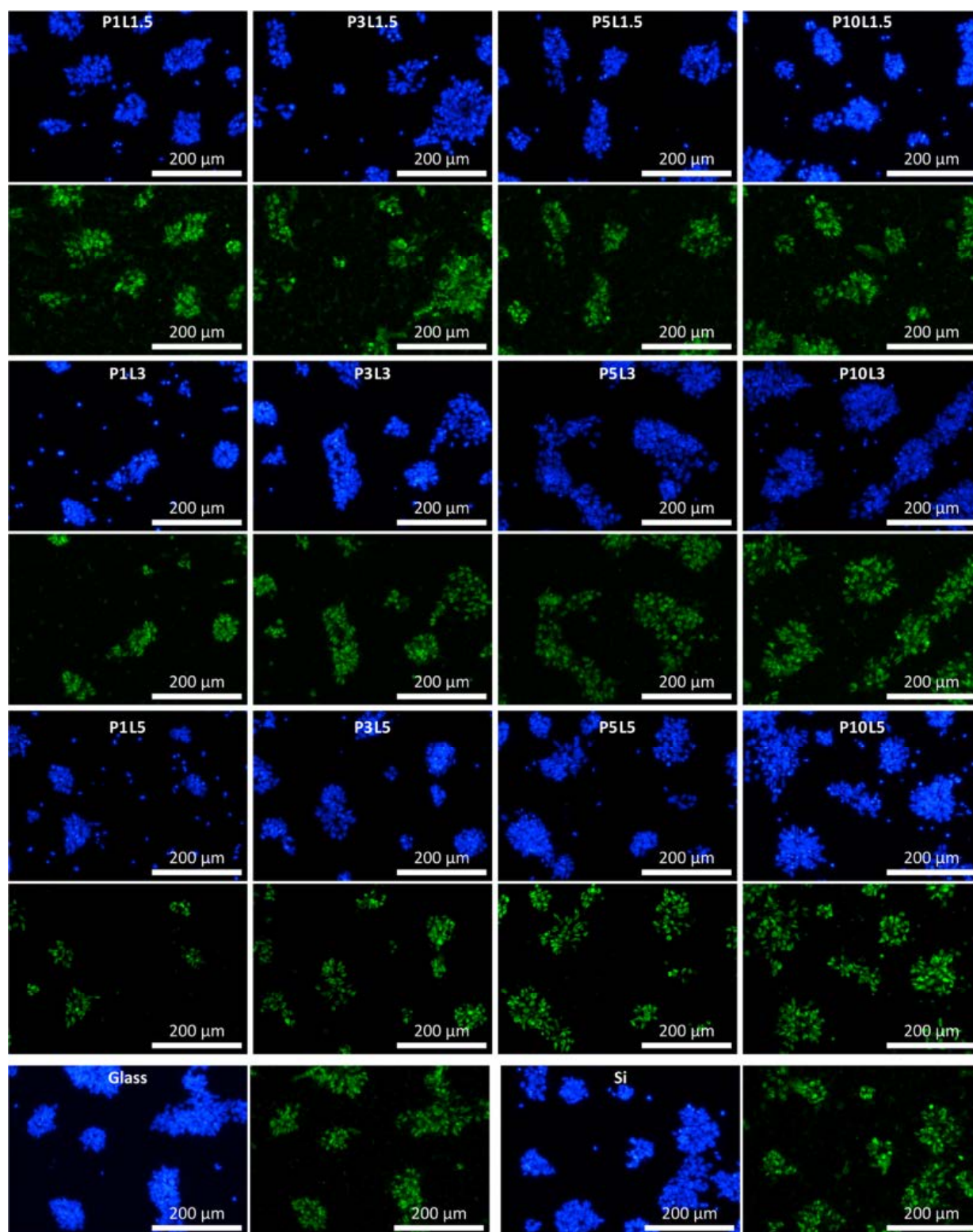Figure S5: F-actin/cytoskeleton (green) on control substrate.

Figure S6: Exemplary images of anti-SOX2 stainings on all types of NW substrates and glass and Si control after 4 DIV. Hoechst: blue, SOX2: green.
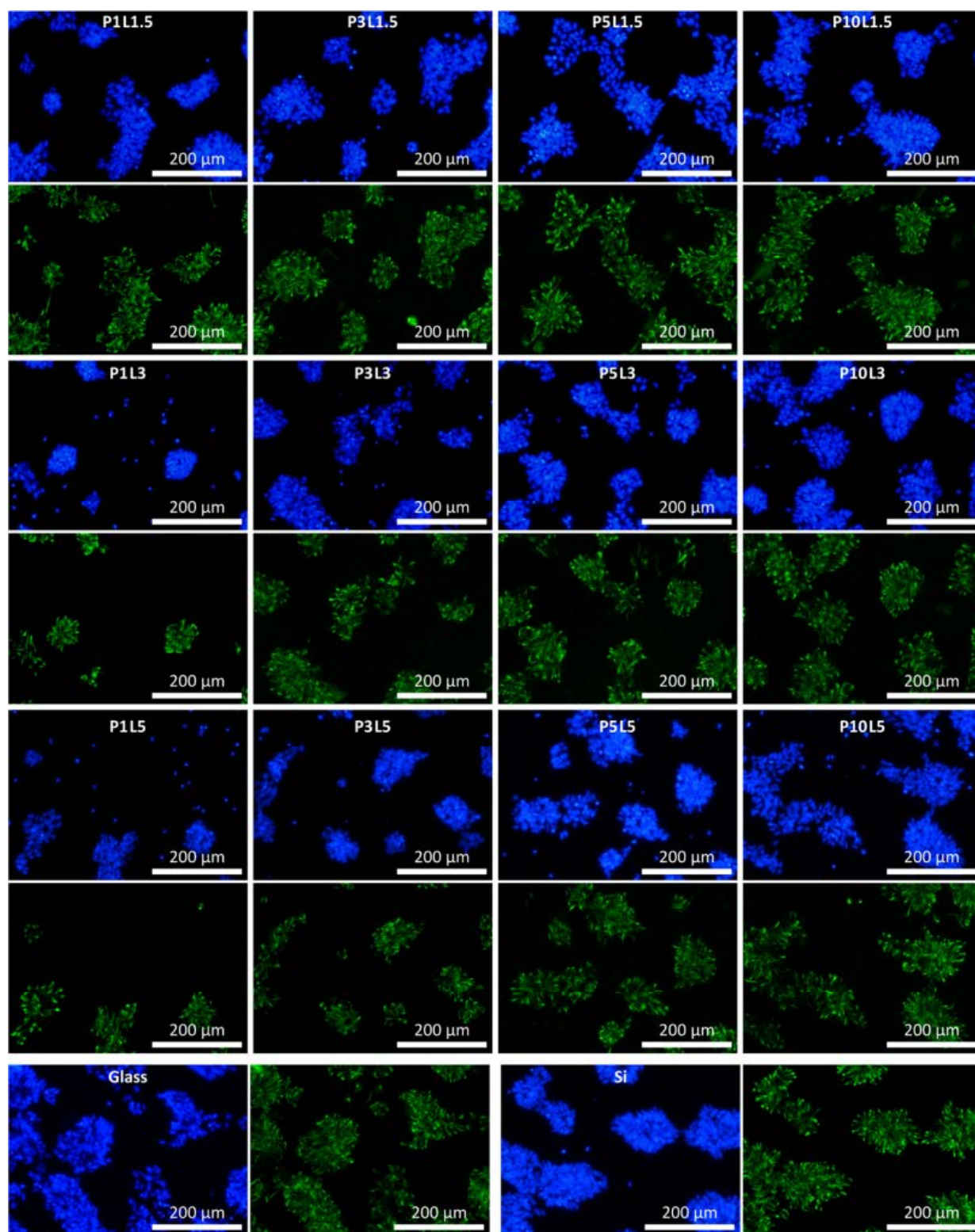
Figure S7: Exemplary images of anti-NES stainings on all types of NW substrates and glass and Si control after 4 DIV. Hoechst: blue, NES: green.

Methods—Immunocytochemistry

Samples were rinsed once with PBS (Sigma-Aldrich), fixed in formaldehyde (4% in PBS, Sigma-Aldrich) for 10 min, and again rinsed three times with PBS. Covered with PBS, samples were stored until imaging at 4 °C. Fixed cells were permeabilized and blocked for 45 min with 3% BSA (bovine serum albumin, Carl Roth, Karlsruhe, Germany), 0.1% Tween (Tween 20, Sigma-Aldrich), and 0.1% Triton-X (Triton X 100, Carl Roth) in PBS prior to incubation with anti-SOX2 or anti-NES primary antibodies (0.1% BSA, anti-SOX2: 1:300 in PBS, mouse anti-SOX2, Santa Cruz Biotechnology, Cat. No. sc-365823, anti-NES: 1:1000 in PBS, mouse anti-NES, StemCell Technologies, Cat. No. 60091) overnight at 4 °C. The cells were washed twice with PBS and incubated with Alexa fluorophore-conjugated anti-mouse secondary antibodies (0.1% BSA, Alexa 488 1:1000 in PBS, goat anti-mouse IgG-Alexa Flour 488 polyclonal antibody, Invitrogen, Cat. No. A32723) for 1 h in the dark. Stained cells were kept in the dark and washed three times with Tween (0.05% in PBS) for 5 min. The second washing step contained Hoechst 33342 as counterstain. If not further noted, all steps were conducted at room temperature.

A.4 Publication IV

Interfacing human induced pluripotent stem cell-derived neurons with designed nanowire arrays as a future platform for medical applications

Jann Harberts, Undine Haferkamp, Stefanie Haugg, Cornelius Fendler, Dennis Lam, Robert Zierold, Ole Pless, and Robert H. Blick

Author contributions: J.H. and U.H. contributed equally. J.H. performed the confocal microscopy imaging, scanning electron microscopy imaging with focused ion beam milling, patch clamp measurements and data analysis. U.H., D.L. developed the cell culture protocols. U.H. performed the cell culture, immunocytochemistry, flow cytometry, and differential gene expression analysis. J.H., S.H., R.Z. prepared the NW substrates. C.F. performed the critical point drying. J.H., U.H., O.P. wrote the manuscript. O.P., R.H.B. supervised the study. R.H.B. provided funding and general support. All authors conducted proofreading and approved the manuscript.

(13 + 3 pages)

PAPER

Check for updates

Interfacing human induced pluripotent stem cell-derived neurons with designed nanowire arrays as a future platform for medical applications†

Jann Harberts, ‡[a] Undine Haferkamp,‡[b] Stefanie Haugg,[a] Cornelius Fendler,[a] Dennis Lam,[b] Robert Zierold, *[a] Ole Pless [b] and Robert H. Blick [a,c]

Nanostructured substrates such as nanowire arrays form a powerful tool for building next-generation medical devices. So far, human pluripotent stem cell-derived neurons—a revolutionary tool for studying physiological function and modeling neurodegenerative diseases—have not been applied to such innovative substrates, due to the highly demanding nature of stem cell quality control and directed differentiation procedures to generate specialized cell types. Our study closes this gap, by presenting electrophysiologically mature human pluripotent stem cell-derived neurons on a set of nanowires in different patterns and growth densities after only four weeks of maturation—thereof 14 to 16 days on the nanowire arrays. While cell viability is maintained on all nanowire substrates, the settling regime of the cells can be controlled and tuned by the nanowire density from a fakir-like state to a complete nanowire wrapping state. Especially, full electrophysiological integrity of the neurons independent of the settling regime has been revealed by patch clamp experiments showing characteristic action potentials. Based on these results, our protocol has the potential to open new pathways in stem cell research and regenerative medicine utilizing human stem cell-derived neurons on tailor-made nanostructured substrates.

Introduction

Since their initial discovery,[1,2] human induced pluripotent stem cell (iPSC) technologies have changed the face of basic, preclinical and clinical research and application. Human iPSC-based models overcome the limited availability of primary human cells, thereby enabling the pre-clinical efficacy and safety assessment of novel treatment modalities.[3] Furthermore, iPSC-derived cell types are being utilized to study and potentially even to ameliorate various human pathophysiological conditions, including neurodegenerative diseases like Parkinson's.[4] All major brain cell types can now be differentiated from iPSCs, while increasingly complex co-culture and organoid systems are being developed to facilitate neuroscience research and clinical translation.[5,6] A comparison of disease-associated pathways between animal and human cells

is of particular importance, since species differences often contribute to failures during the development of drugs with new modes of action.[7-9]

Typically, cellular identity of human iPSC-derived cell types is characterized by the assessment of specific marker gene expression using a combination of molecular biology techniques including quantitative real-time polymerase chain reaction and immunocytochemistry.[10,11] Functionality of neurons is usually assessed by electrophysiological measurements in combination with treatment of standard compounds which block key receptors, ion channels, and transporters. By default, such characterization experiments are performed on planar Petri dishes and multiwell-plates. The continuing progress in micro- and nanostructuring of biocompatible (semiconductor-), and maybe even "active" materials[12-15] could, however, offer novel opportunities for investigating stem cell-derived cell types under artificial constraints.

So far, hybrid systems of micro- and nanostructured materials interfaced with biological cells have been used to study the influence of the substrate's chemical and physical properties on *e.g.* adhesion, proliferation, viability, and migration of seeded dissociated cells.[16-21] Especially, substrates covered with upright arranged high aspect ratio nanostructures—so-called nanowire (NW) arrays—play an increasingly important role.[22-24] Tailor-made variation in length, dia-

[a]*Center for Hybrid Nanostructures, Universität Hamburg, Luruper Chaussee 149, 22761 Hamburg, Germany. E-mail: rzierold@chyn.uni-hamburg.de*
[b]*Fraunhofer IME ScreeningPort, Schnackenburgallee 114, 22525 Hamburg, Germany*
[c]*Material Science and Engineering, College of Engineering, University of Wisconsin-Madison, Madison, Wisconsin 53706, USA*
†Electronic supplementary information (ESI) available. See DOI: 10.1039/d0bm00182a
‡These authors contributed equally.

meter, and density of the NW arrays can also influence cellular growth behavior, viability, movement, and adhesion[25–30] while maintaining electrophysiological properties.[31] In addition, NW arrays can also be used to constrain cell movement and spreading,[32–34] to measure mechanical cell properties,[35–37] to interact with the cell's nucleus,[38] or to direct cell polarization, *e.g.* outgrowth of axons.[39,40] In general, the interaction of cells with the NWs depends on the NW length, diameter as well as array density[41,42] and has been modeled in Buch-Månson *et al.*[43] Note, one can expect different cell settling regimes from a fakir-like state to a complete NW wrapping by the cell membrane depending on the NW array characteristics. More advanced, NWs can be artificially functionalized to even extend the scope of passive applications by means of an executing interaction: up to now, modified NW arrays have been used for electrical stimulation and sensing,[44–48] cell transfection,[49–51] and drug delivery.[52–57] Furthermore, integrating p–n junctions[58,59] or employing the capability of NWs to guide or to emit light[60–62] might be utilized in applications with direct photo-current stimulation[63] as well as in biosensing[64,65] and optogenetics.[66,67]

However, the referred studies utilized only conventional cancer cell lines (*e.g.* HEK293, HeLa) or primary neurons from rodents. The pertinence in the context of somatic human cells is quite limited. An exception is the work from Liu *et al.*[48] utilizing small NW electrode arrays of 8×8 NWs on an area of $32 \times 32~\mu m^2$. Specifically, cortical neurons were derived from human iPSCs based on a 65 day maturation protocol until a mature cell state with proper firing of action potentials (APs) is reached.[68] The limited array size and, much more, the long cultivation period are drawbacks, which have to be overcome. Moreover, it has been demonstrated before, that substrates featuring large scale NW forests can influence intracellular signaling[69] and cell differentiation,[70–72] which might be the case with neuronal differentiation as well.

In this work, we used a set of mm-scale tailor-made NW arrays as cell culture substrates and present a fast human iPSC differentiation protocol to obtain human iPSC-derived neurons (hiPSC-derived neurons) with mature firing of APs within only 28 to 30 days *in vitro* (DIV)—14 to 16 days of maturation on the NWs. Here, the quality of the protocol is independent of the applied NW arrays which differ in arrangement as well as spacing of the NWs. To address the predicted settling regime depending on the properties of the NW arrays, we imaged the membrane interaction with the NWs. The settling regime of the hiPSC-derived neurons can be controlled by the NW density in accordance to the model from Buch-Månson *et al.* To test the functionality of the hiPSC-derived neurons, we measured the cell viability and electrophysiological characteristics. As a result, we found no detrimental impact of the underlying NW substrate on the differentiation process and functionality of the hiPSC-derived neurons compared to planar control substrates. Particularly, the electrophysiological cell characteristics of the hiPSC-derived neurons are outstanding on all NW arrays. Featuring short culturing periods and taking into account the insensitivity to the NW lattices and densities, we propose our platform as an excellent, robust starting point for future applications using functionalized NWs in medical devices such as retina implants or neural interfaces,[73–75] to study cell intrinsic physiological or pathophysiological processes or pharmacological interventions.[76]

Results and discussion

Herein, we used silicon nitride NW arrays as culturing substrates for the hiPSC-derived neurons during the last two weeks of differentiation. All NW arrays were fabricated in a top-down approach using dry reactive ion etching (RIE) only differing in the pre-patterning procedure for the random and the ordered arrangements (*cf.* Fig. 1). Randomly distributed NWs were fabricated in a self-assembly process resulting in a NW density of about 31 NWs/100 μm², a density later referred to as high density (HD). The ordered NWs were pre-patterned with hexagonal and rectangular lattices using electron beam lithography. Both arrays were fabricated with a similar HD as well as a lower density (LD) of 6 NWs/100 μm². These densities corresponded to a pitch of about 1.8 μm and 4 μm, respectively. The NW lengths were kept constant at 1.2 μm in both approaches and were defined by the etch duration of the RIE.

The differentiation process from the human iPSC stage towards the neuronal cell fate ultimately resulting in hiPSC-
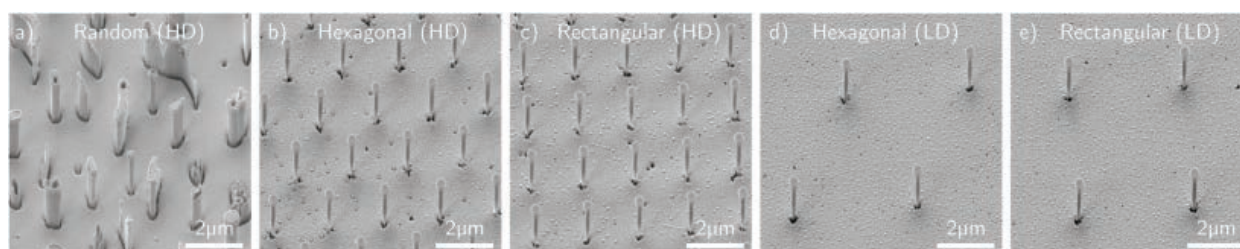

Fig. 1 Scanning electron microscopy (SEM) images of the utilized NW substrates (tilting: 45° with tilt correction). Three different NW arrangements (random, hexagonal and rectangular) and two average NW-spacings (1.8 μm and 4 μm) were used. Lengths were fixed to 1.2 μm. The pitches of 1.8 μm and 4 μm result in densities of approx. 31 NWs/100 μm² (HD – high density) and 6 NWs/100 μm² (LD – low density), respectively. (a) NWs in a self-assembled arrangement resulting in an average density of 31 NWs/100 μm². (b–c) NWs in hexagonal and rectangular-oriented HD arrays. (d–e) NWs in hexagonal and rectangular-oriented LD arrays. Overview images can be found in Fig. S1† of the supporting material.
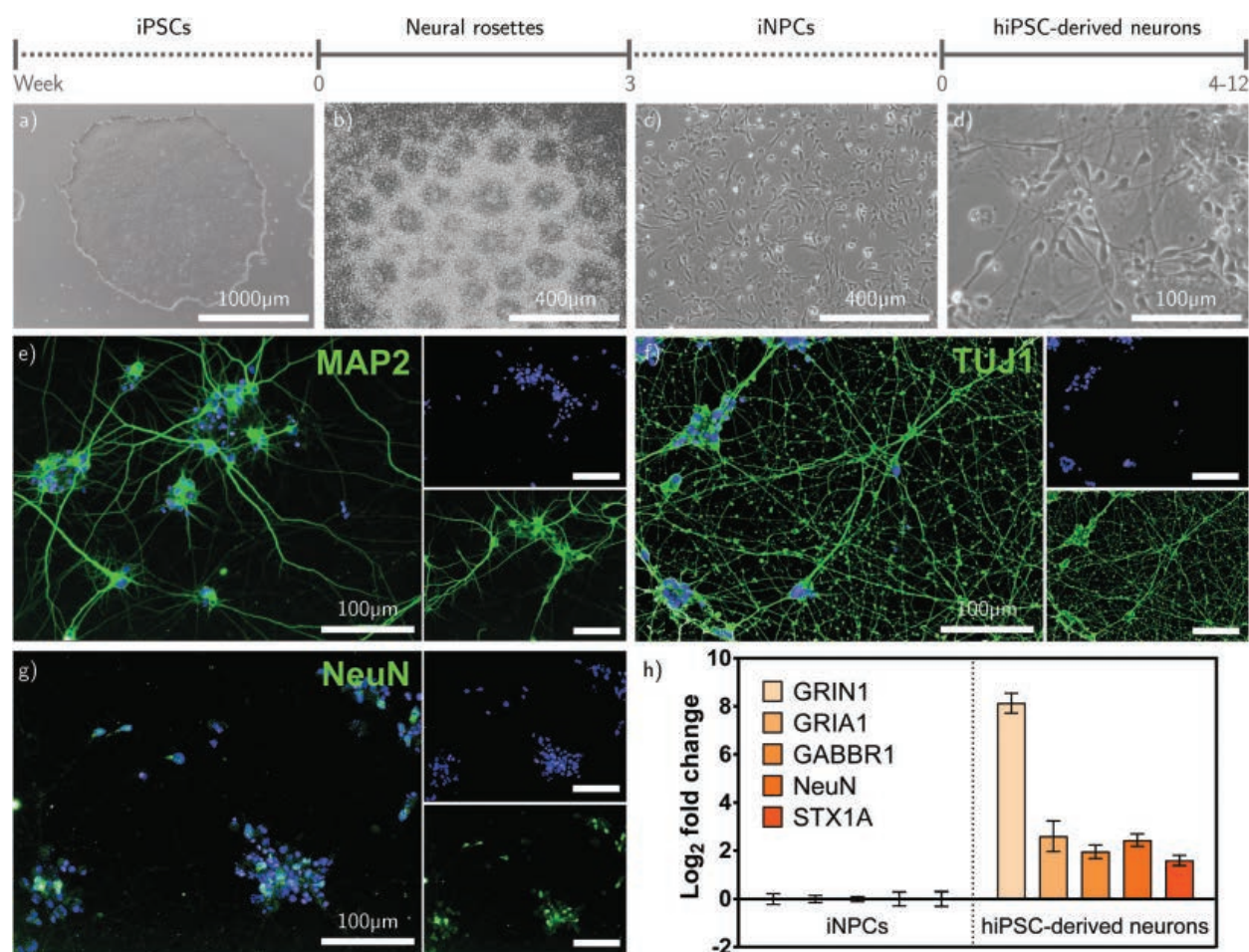
Fig. 2 Characterization of human iPSC-derived neurons (hiPSC-derived neurons). Neuronal differentiation process from (a) human iPSCs *via* (b) embryoid body formation and neural rosette selection into (c) human iPSC-derived neuronal precursor cells (iNPCs) and (d) neurons with respective timeline in weeks. (e–g) Immunofluorescence staining of characteristic neuronal marker proteins TUJ1, MAP2, NeuN. (h) Quantitative real-time PCR of iNPCs and hiPSC-derived neurons shows a strong up-regulation of genes of the glutamatergic system, *e.g.* GRIN1 (glutamate ionotropic receptor NMDA type subunit 1), indicating that the neurons have acquired a glutamatergic phenotype. Error bars indicate the standard error (SE).

derived neurons was closely monitored and the changes in morphology were confirmed by bright-field imaging (Fig. 2a–d). During the differentiation process, neural rosettes, human iPSC-derived neuronal precursor cells (iNPCs) and neurons were clearly distinguishable. As previously demonstrated,[77,78] dual inhibition of SMAD signaling pathways led to an efficient conversion of iPSCs into iNPCs, resulting in 98% Pax6, 88% Sox1 and 93% Sox2 positive cells (ESI Fig. S2†). Thus, a high-quality NPC line was generated as a starting point for neuronal differentiation, without the support of complex 3D substrates.[79] Immunocytochemistry of pan-neuronal marker proteins TUJ1, MAP2 and NeuN confirmed the neuronal phenotype (Fig. 2e–g). In addition, differential gene expression analysis (Fig. 2h) revealed a robust up-regulation of pan-neuronal transcripts (NeuN) and transcripts of the glutamatergic system (NMDA receptors (GRIN1), AMPA receptors (GRIA1)) between the iNPC and the hiPSC-derived neuron stage, suggesting that the hiPSC-derived neurons have acquired predominantly a

mature cortical glutamatergic phenotype. Nevertheless, components of the GABAergic system, *e.g.* GABA receptors (GABBR1), are also being expressed, hinting towards the presence of several neuronal subtypes in the culture. Furthermore, an upregulation of syntaxin-1A (STX1A) indicated the presence of synaptic vesicles, a prerequisite for neurotransmitter transport and release resulting in interconnectivity between pre- and post-synapse.

On the NW arrays, we first tested the fundamental integrity of the cells by viability staining and compared these results with a twofold control on standard glass coverslips and planar aluminum oxide matching the surface material of the NW substrates. As a result, the cell viability after 14–16 DIV on the substrates is neither influenced by the material under test itself nor by the substrate topology as displayed as a bar chart in Fig. 3. No statistically significant deviances after running a significance test were found (ANOVA with *post hoc* Turkey's test, alpha = 0.001, Fig. S3†). Similar insignificant influence of NW
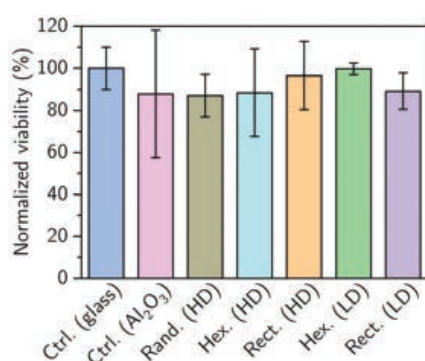
Fig. 3 Overall relative cell viability on each substrate. Error bars indicate the SE. No statistically significant deviances have been observed (Anova with *post hoc* Turkey's test, α = 0.001, *cf.* Fig. S3†).

arrays on cell viability has been demonstrated with HEK293 cells before.[80]

We went on to investigate the cellular outgrowth and the interaction of the cell membrane with the NWs by confocal microscopy.[81] Particular attention was paid to the settling regime, which is supposed to be determined by the NW density as mentioned earlier. In detail, we used confocal microscopy z-stacks to create three-dimensional images, which we discuss in this manuscript by means of x-y and x-z slices summarized in Fig. 4. The cell membrane is labeled in red and the substrate's as well as NW tips' reflections are colored in green. Tip reflections are more distinct in case of the ordered NW arrays, because the exact circular symmetrical shape of these NWs scatter the laser light source more effectively back compared to the asymmetric morphology of the randomly arranged NWs. Gaps in the reflection of the substrate mark positions of the NWs.

For high NW densities we expect a fakir-like sate,[43] meaning the cell is resting on the NWs just being in contact with the very NW tip. This configuration is precisely what is observed with the HD samples, separately discussed as follows: Fig. 4a–c illustrate the top view of cells on the three HD NW substrates focused above the NW tips as well as corresponding slices in the x–z plane across the cell soma. Note in the cross section view that the cell membrane at the soma's position is hovering approx. 1.2 μm—the NW's length—above the substrate's bottom, confirming the claim of a fakir-like state. Furthermore, we want to stress that no brighter details appear within the cell's soma, as it will be the case when the interaction state is changed to NW enwrapping for the LD NW substrates. Another feature observable in the cross sections is that a part of the cell membrane's material appears to be in contact with the bottom of the substrate. However, it is not the soma itself; this impression is caused by an axon growing between the NWs on the bottom of the substrate. This phenomenon was only observed on NW arrays with HD. To visualize this special feature, Fig. 4d–f show the identical areas from the subfigures a–c, but now focused at the NW bottom. For the random NWs we observe a random growth of the

axons. In contrast to that, for the hexagonal and rectangular arranged NWs, we observe for the axons growing between the NWs an angle of 60° and 90° fitting to the hexagonal and rectangular NW arrangement. In addition to axons growing between NWs, axons also stay on the NW tips as observed in Fig. 4a–c. For growth on the NW tips, no particular alignment with the NWs is found. In general, both phenomena of random growth on the NW tips and guiding on the substrate between the NWs are in accordance with the literature. Specifically, different guiding regimes for the neurite outgrowth on NW tips depending on NW density have been described in Bucaro *et al.*[39] However, we contrarily observe with our cells a shifted threshold for random growth towards larger NW pitches compared to the C3H10T1/2 cells in the aforementioned work. Considering the observed guided growth on the substrate between the basis of the NWs, comparable routing between micropillars has been described before using mice/rat neurons in Micholt *et al.*[82] In addition, it has been shown that NW scaffolds can support the formation of highly interconnected rodent neuronal networks.[83] Thus, we believe that our observation can be utilized to prepare 3D stacks of separated human neuronal networks mimicking the complexity of a brain in a much better way than planar structures can accomplish to date.[84–86]

Using samples with low NW densities, a different settling regime was observed as expected and is summarized in Fig. 4g–h. In the cross-sections it is obvious that the somata are resting on the substrate's bottom while the cell membrane is wrapping around the NWs. Additionally, the arrangement of the NWs appears within the somata, as apparent in the x–y slices, because the enwrapped NWs extend into the imaged plane proving our hypothesis of a membrane wrapping around the NWs. Similar results have been shown in Berthing *et al.* with HEK293 cells on NWs with 4 μm pitch.[81] In general, our observations of the cell's settling regime depending on the nanostructure features are in line with findings which employed HL-1 cells, HEK293 cells and rodent neurons.[41,42]

In order to support our conclusions drawn from the fluorescent microscopy images regarding the settling regimes, we prepared cross sections of the cell membrane/NW interface *via* focused ion beam (FIB) milling and studied them by scanning electron microscopy (SEM). The results are summarized in Fig. 5. Note, we exemplary colorized the cell interior in yellow and the NW in blue in order to guide the eye. At high NW densities, the cells are only in contact with the NW tip resulting in a fakir-like state (Fig. 5a–e). This behavior is both independent of the NW diameter for the random structure and the NW arrangement as it has been similarly observed in the confocal microscope images. Additionally, the proposed wrapping state on LD NW substrates showing a complete encapsulation of the NW by the cell membrane is confirmed (Fig. 5f and g). Moreover, in SEM, we also observed intermediate states of a partial wrapping of NWs by the cell membrane shown in Fig. 5h and i. This observation is in accordance with the confocal microscopy images where the patterns in the x–y slices in Fig. 4g and h were occasionally less distinct at a known posi-
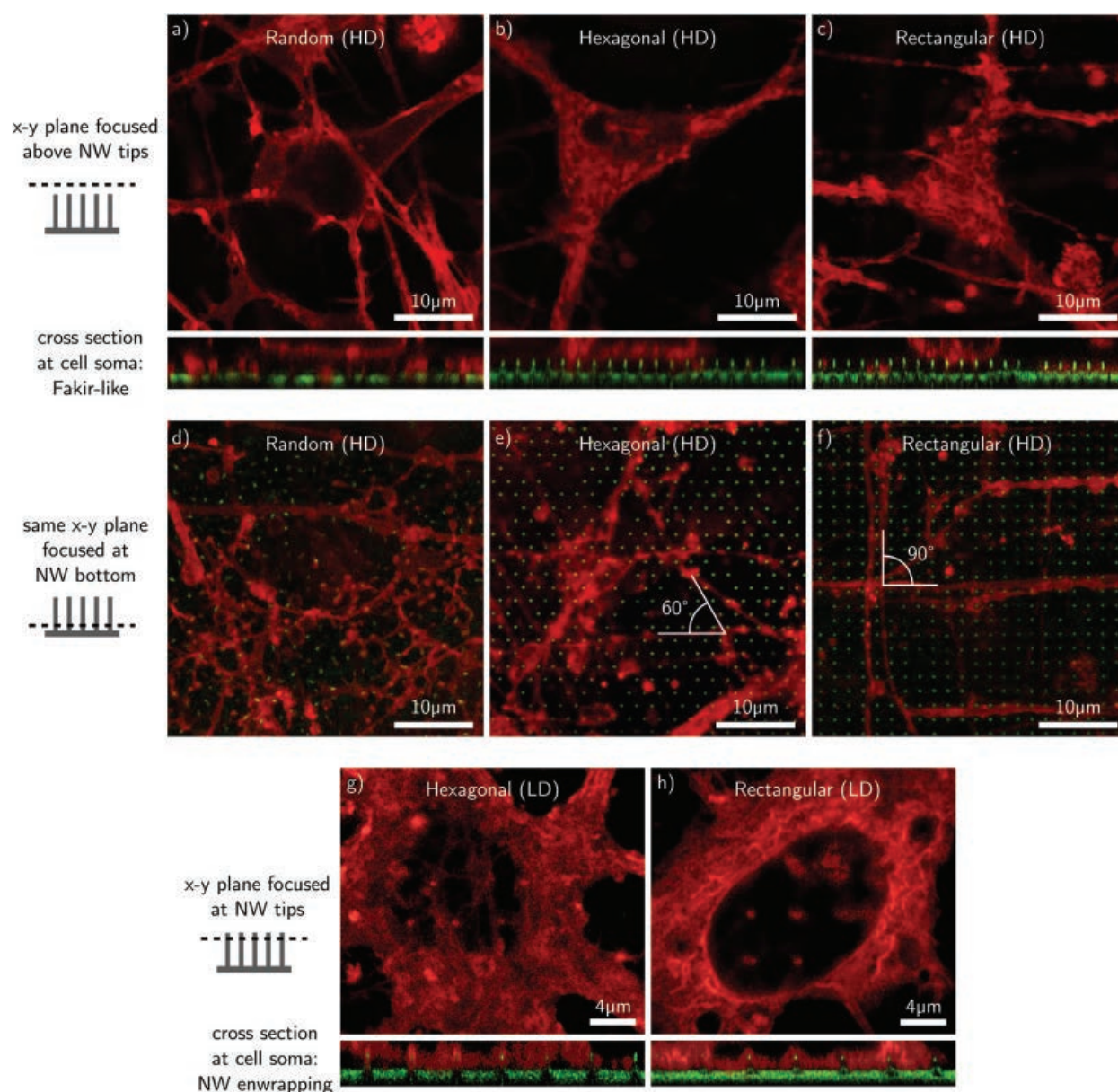
Fig. 4 Confocal microscopy images of cell somata and neurites on different NW substrates displayed as slices in the $x-y$ and $x-z$ plane of the 3D reconstructions. The cell membrane is colored in red by the staining kit; the substrate's and NW tips' reflections are displayed in green. Gaps in the substrate's reflection mark NW positions. (a–c) $x-y$ plane: cell somata imaged with focus above the NW tips. No features within the cells are observable. Cross sections: The cell somata rest on the NW tips in a fakir-like state. Red colored features between the NWs origin from axons growing on the substrate's bottom. (d–f) $x-y$ planes from same areas as before, now focused at the NW bottom. For patterned NWs, guided axon growth between NWs is observable with angles of 60° and 90° fitting to the hexagonal and rectangular NW arrangement. (g–h) Close-ups of cell somata focused at the NW tips. Brighter features appear within the cells caused by membrane wrapping around the NWs visible in the cross sections. The cells rest on the bottom of the substrate.

tion of a NW. To briefly summarize, our results of the settling states using human iPSC-derived neurons are in line with prior reports on a fakir-like cell state at HD NWs and NW enwrapping at LD NWs well matching the model from Buch-Månson *et al.*

In order to prove the neuronal integrity of the cells after 14–16 DIV on the NW substrates, we performed electrophysio-

logical studies in both current- and voltage-clamp experiments. During patch clamping, the hiPSC-derived neurons on the NW substrates can be identified feasibly as demonstrated by an image taken with the microscope camera of the patch-clamp setup shown in Fig. 6.

On the part of electrophysiology, we tested the hiPSC-derived neurons for the capability to fire APs and characteristic
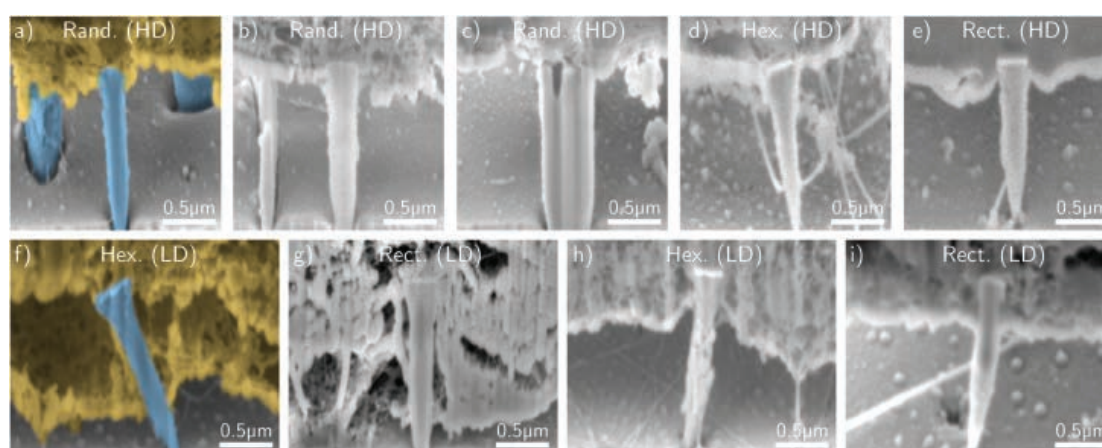
Fig. 5 SEM images of the NWs/cell membrane interface exposed by FIB milling. (a–e) Cross sections of HD NWs. The cells are carried by the NW tip. (f–i) Cross-sectional images of a LD NWs. The NWs are completely encapsulated or partially encapsulated by the cell membrane.
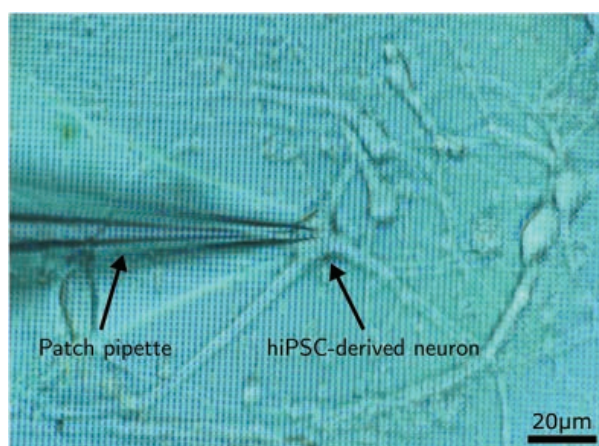

Fig. 6 Example of patch clamping on a rectangular-oriented HD nanowire substrate. Image taken with the microscope camera of the patch-clamp setup.

inward-outward currents. Proper firing of multiple APs is a distinct indicator for fully electrophysiologically mature neurons, since neurons in an early state of the development are either incapable of firing APs or only release single spikes.[87] In current-clamp, the cells show characteristic firing of APs with amplitudes of about 90 mV during a small current injection independent of the substrate used (Fig. 7, upper row). In voltage-clamp, the neurons state a proper interplay of sodium and potassium ion channels by showing the corresponding early inward-currents and late outwards-currents when voltage-steps are applied (Fig. 7, lower row).[88] Moreover, we performed statistical analysis of the AP heights and fundamental electrophysiological parameters such as resting membrane potential (RMP), membrane capacitance (MC), input resistance (IR), and membrane time constant (MTC) shown as bar charts in Fig. 8a–e. Again, no statistically significant alterations of each parameter between any of the substrates were found (Anova

with *post hoc* Turkey's test, alpha = 0.001, *cf.* Fig. S4†). Hence, we averaged the results of the particular parameters to single values and discuss these in comparison to other human neurons as follows: the AP heights were in average 93.6 ± 14.3 mV and are thereby notably distinct in amplitude.[68,89–96] The RMPs were in average −52.8 ± 7.4 mV and are normal to above-average for mature neurons.[89–93,95–97] The MCs indicating cell size[98] were in average 21.4 ± 7.9 pF. We can conclude from similar MCs, that the overall cellular outgrowth is similar on all substrates; such capacitances are comparable with the literature.[91,94,96,97] The IRs, indicating the conductivity of the entire cell membrane, were in average 1.9 ± 0.7 GΩ—an appropriate value.[92–96] The MTCs were in average 42.2 ± 12.2 ms and are also comparable to previous studies.[89,90,99,100] In summary, the electrophysiological characterization states an outstanding condition of the hiPSC-derived neurons cultured on the NW arrays and underline the robustness of the neuronal differentiation toward the substrate's morphology.

Summary

In this work, we present a protocol to interface human pluripotent stem cell-derived neurons with silicon nitride nanowire arrays which resemble future semiconductor platforms for local sensing, stimulation and drug delivery, among others. The protocol excels at a short differentiation period of only four weeks to generate fully electrophysiologically mature neurons. We fabricated Si_3N_4 nanowires with different arrangements and densities using a top-down approach. The neurons were transferred 14 DIV after initiation of the differentiation onto the nanowire substrates and the experiments for functional characterization of cells were performed after another 14–16 DIV (28–30 DIV in total after the iNPC stage). Cell viability was not negatively affected by the various nanowire substrates tested. We demonstrate a fakir-like settling state at high nanowire densities and nanowire engulfment by the cell mem-
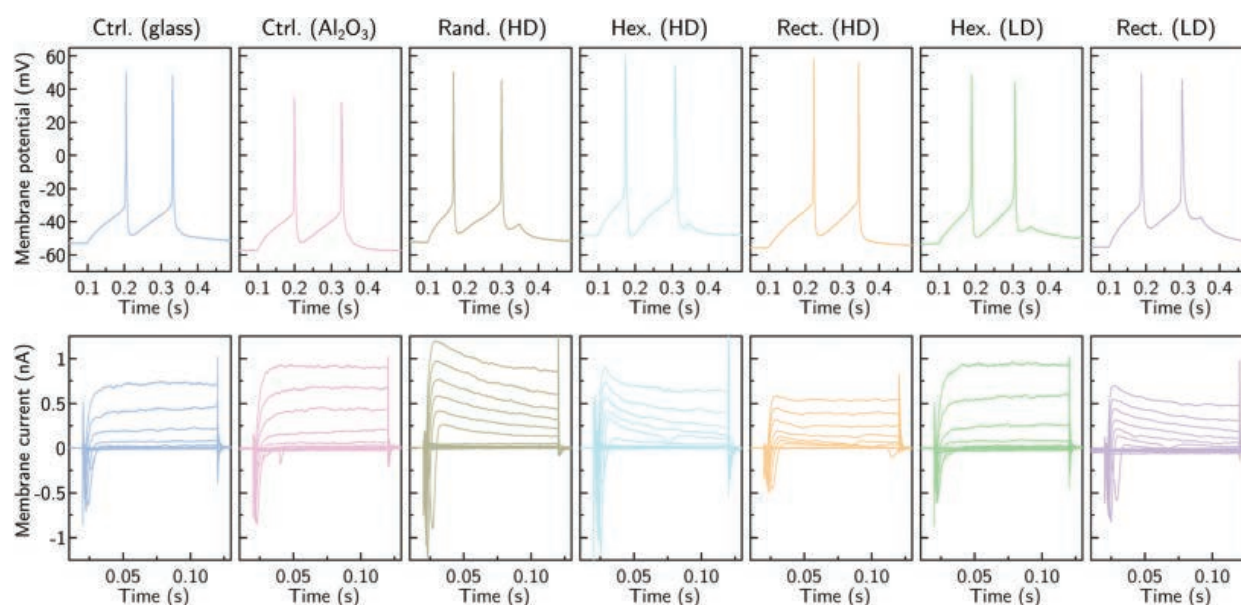
Fig. 7 Current-clamp (upper row) and voltage-clamp measurements (lower row) of the hiPSC-derived neurons on all substrate types. Upper row: Measurements of APs during current injection. On all substrates, the neurons show strong and well-shaped spikes. Lower row: Characteristic early inward-currents and late outward-currents stating a proper interplay of voltage-gated sodium and potassium ion-channels.
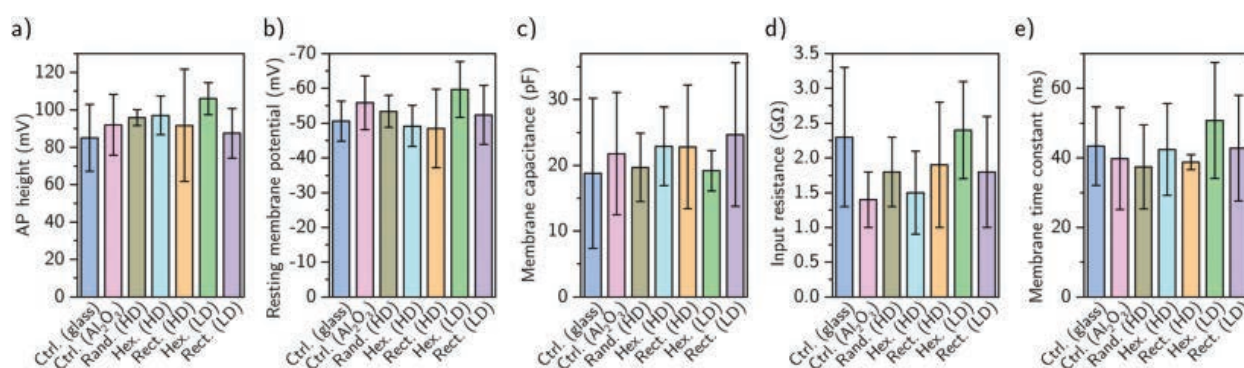

Fig. 8 Statistical comparison of fundamental electrophysiological properties such as (a) AP height, (b) resting membrane potential, (c) membrane capacitance, (d) input resistance, and (e) membrane time constant. Error bars indicate the SE. No statistically significant deviances were found between the substrates (Anova with *post hoc* Turkey's test, alpha = 0.001, *cf.* Fig. S4†). Number of measurements: control (glass) = 7, control (Al$_2$O$_3$) = 8, random (HD) = 7, hexagonal (HD) = 7, rectangular (HD) = 6, hexagonal (LD) = 8, rectangular (LD) = 9.

brane at low nanowire densities. The settling states were imaged using *z*-stacks from confocal microscopy and cross sections in scanning electron microscopy prepared with focused ion beam milling. Electrophysiological integrity was tested using patch clamp techniques and showed no statistically significant influence of the nanowire substrates. The neurons fired distinct action potentials and electrophysiological parameters such as resting membrane potential, membrane capacitance, input resistance, and membrane time constant were comparable to prior studies, which were conducted in a setting without any nanowires. In short, our protocol features short culturing periods of only 28–30 DIV and no influence of

the NW arrangement and densities on the neuronal differentiation capacity.

Conclusions and outlook

Utilizing nano and microstructured substrates for pluripotent stem cell culture just emerged in the recent years and is thus still an unexplored field. "Macroscopic" micro pillars with diameters of 10–15 μm and lengths up to 600 μm have been used as scaffolds to culture cortical progenitors which retained their multipotency and cortical identity and were able to mature

into cortical glutamatergic neurons only verified with neuronal marker β3-tubulin.[101] The fate of mesenchymal stem cells (MSCs) was guided due to increased gene expression on substrates with thin NWs with lengths of up to 25 μm.[102,103] Furthermore, short term culture (3 DIV) of MSCs showed an induced neuron-like differentiation, when cultured on silicon NWs with dimensions more comparable to this work.[104] Neural stem cells from mice showed enhanced proliferation and neuronal differentiation if cultured on high density silicon NWs.[105] Furthermore, other micro structured substrates like the polymer PMEDSAH, fibrin hydrogel or chitin-alginate 3D micro fibrous scaffolds have also been used for human pluripotent stem cells before, primarily to create more efficient substrates to generate and maintain iPSCs and neuronal progenitor cells.[79,106,107] While many of these substrates influenced the cells, we demonstrate that we can conduct the final neuronal maturation on nanostructured substrates without apparent changes of the functional electrophysiological properties. Compared to other scaffolds made from synthetic polymers and hydrogels, (semiconductor) NWs benefit from years of experience in nano/micro fabrication and the use of semiconductor materials allows for unique applications such as biosensing and optogenetics.[64–67] Using todays electron beam lithography and reactive ion etching systems designed for structuring entire wafers allows for cost-effective scalability and duplication. Other approaches to fabricate NWs like droplet-catalyzed bottom-up NW growth would also allow for NW arrays with slightly varying axial directions and NW lengths.[108,109] However, for small variations, we would expect no significant effects on neuronal maturation. Transfer of NW arrays into flexible substrates like polydimethylsiloxane (PDMS) enables the application of those in soft tissues such as the brain or the retina.[110]

Even though rodent neurons have been cultured on NWs before as introduced, employing human neurons opens up the arena for physiologically more relevant studies, as for example the glutamatergic neurons used here enable studying particular aspects of neurodegenerative diseases such as multiple sclerosis and Alzheimer's disease.[111–113] Especially the ability to study disease-associated genotype–phenotype-relationships using patient-derived cells is a unique advantage of hiPSCs.[114,115] Furthermore, we want to stress that our hiPSC-derived neurons on NW not only show the expected expression of marker proteins as in previous studies with human or rodent neurons,[101,105] but more importantly show the expected electrophysiological characteristics on a functional level. Thus, we conclude that our platform is an excellent, robust starting point for future applications paving the way to further functionalized nanowires for e.g. in vitro disease modeling and preclinical drug discovery.

Methods

Substrate fabrication

The initial substrate pieces consisted of a 1.5 μm thick Si_3N_4 layer deposited by low-pressure chemical vapor deposition (Simat Wafers, Si_3N_4, low tensile stress) on a silicon (100) wafer. The hard mask for the random structures were prepared in a self-assembly process using de-wetting of a thin gold film.[116] The initial 28 nm gold layer deposited using sputter coating was dewetted by thermal annealing in vacuum (<200 mTorr). The procedure used a heating ramp of 5 °C s^{-1}, held the temperature for 10 min at 900 °C and subsequently cooled down without additional cooling (compact RTP furnace, OTF-1200X-RTP-4, MTI Corporation). As a result, the continuous gold layer transformed into randomly distributed droplets of slightly varying diameters, which were used as hard mask for RIE. The masks for the arranged structures were prepared in a highly controlled manner via electron beam lithography (Raith Voyager e-beam lithography system). Patterned arrays of circles were written in hexagonal and rectangular arrangement into a 90 nm thick layer of positive photo resist (PMMA, AllResist AR-P 671.02). After developing, the substrate was covered with a 40 nm thick layer of chromium in a physical vapor deposition (PVD) process. A subsequent lift-off only preserves the chromium circles within the previously created holes in the resist, which were then used as a hard mask for RIE. RIE was performed with an ICP-RIE plasma etcher (Sentech SI500) using 300 W ICP power, 15 W RF power, 1 Pa pressure, 50 sccm SF_6, 70 sccm C_4F_8 and 5 sccm O_2 at 0 °C electrode temperature. Subsequently, the gold and chromium masks for the random and the ordered arrangement, respectively, were removed by wet chemical etching. Afterwards, all substrates were conformably covered by a 15 nm Al_2O_3 thin film deposited by atomic layer deposition. The control substrates consisted of standard 18 × 18 mm^2 glass coverslips and planar aluminum oxide deposited onto Si wafer pieces with native SiO_2. In order to ease the handling of the 5 × 5 mm^2 wafer pieces during imaging and patch clamping, all substrates were glued to standard 18 × 18 mm^2 glass coverslips using polydimethylsiloxane (PDMS). Every substrate was shortly treated with oxygen plasma to reduce the hydrophobicity and was then placed into a well of a 6-well plate. For culturing of cells, the substrates were sterilized in 70% ethanol for 10 min and coated with 100 μg ml^{-1} poly-L-ornithine (PLO, Sigma-Aldrich) over night at 37 °C to support cell adhesion.[117] Cellular outgrowth was enhanced using an additional 10 μg ml^{-1} laminin (Sigma-Aldrich) coating for 2 h at 37 °C.

Human iPSC culture and neuronal differentiation

All experiments were performed in accordance with the guidelines of the Christian-Albrechts-Universität zu Kiel, and experiments were approved by the ethics committee of the Christian-Albrechts-Universität zu Kiel (approval number A145/11). Informed consents were obtained from human participants of this study. For further details see Tandon et al.[118]

Human iPSCs (ZIPi013-B (Tandon et al.[118])) were maintained under feeder-free conditions on Matrigel (Corning)-coated plates in mTeSR1 medium (Stem Cell Technologies). Medium was exchanged on a daily basis and cells were passaged at 80% confluency using Gentle Cell Dissociation Reagent (Stem Cell Technologies). For neuronal induction,

iPSCs were dissociated with Accutase and seeded at a density of 3×10^6 cells per well onto AggreWell800 plates (10.000 cells per embryoid body (EB), Stem Cell Technologies) in SMADi Neural Induction Medium (SMADi NIM, Stem Cell Technologies) supplemented with 10 μM Y-27632. A daily 75% medium exchange was performed from day 1 to day 5. On day 6, EBs were harvested and plated onto Matrigel-coated plates, followed by a daily medium exchange with SMADi NIM to allow the formation of neural rosette structures within the attached EBs. On day 13, neural rosettes were manually picked and transferred to a new Matrigel-coated plate. After 4 more days in SMADi NIM, neural precursor cells were released by dissociation of the neural rosettes with Accutase and maintained for several passages at high density in Neural Progenitor Medium (Stem Cell Technologies) on Matrigel-coated plates.

Differentiation of iNPCs into neurons was performed as previous described[88,92,119] with some modifications. Among others, seeding density for neuronal induction of iNPCs was optimized for a scale-up in T75/T175 flasks suitable for screening applications. Further, neuronal differentiation medium has been modified by replacing Neurobasal (Gibco) with the Neurobasal Plus system (Gibco) in order to improve neurite outgrowth and electrophysiological maturation. Cyclopamine has been added in addition to promote a glutamatergic neuronal cell type.[120] In summary, iNPCs were seeded at a density of 5×10^4 cells per cm^2 in Neural Progenitor Medium onto PLO/laminin-coated plates. After 24 h, the medium was replaced by neural differentiation medium (day 0 of differentiation) composed of Neurobasal Plus medium (Gibco) containing 1× B27 Plus Supplement (Gibco), 1× N2 Supplement-A (Stem Cell Technologies), 1× MEM non-essential amino acids (Gibco), 1 μg ml^{-1} laminin (Sigma-Aldrich), 1 μM Dibutyryl-cAMP (Stem Cell Technologies), 10 ng ml^{-1} L-ascorbic acid (Stem Cell Technologies), 10 ng ml^{-1} brain-derived neurotrophic factor (Stem Cell Technologies) and 10 ng ml^{-1} glial-derived neurotrophic factor (Stem Cell Technologies). Half of the medium was exchanged every 2 to 3 days. To promote a glutamatergic neuronal cell type, 5 μM cyclopamine (Stem Cell Technologies) was additionally added to the medium during the first week of differentiation. In the second week, neuronal differentiation medium was supplemented with 2 μM cytosine β-D-arabinofuranoside (Sigma-Aldrich) in order to reduce proliferation of non-neuronal cells. On day 14, the cells were detached using Accutase and reseeded at a ratio of 1 : 2 onto 96-well plates for immunocytochemistry or NW substrates for confocal microscopy, viability staining as well as electrophysiological studies. Thereafter, cells were maintained in neuronal differentiation medium for another two weeks to reach a mature cell state. All further experiments were performed between 28 and 30 days after initiation of the differentiation.

Quantitative real-time polymerase chain reaction (qRT-PCR)

Cells were harvested and total RNA was extracted using the RNeasy Plus Mini Kit (Qiagen). The complementary DNA was synthesized from up to 1 μg RNA using the RevertAid H Minus First Strand cDNA Synthesis Kit (Thermo Fisher Scientific). qRT-PCR was performed with TaqMan Gene Expression Master Mix (Applied Biosystems) as a duplex reaction with a FAM-labeled TaqMan assay for the gene of interest and a VIC-labeled TaqMan assay (Applied Biosystems) for the housekeeping gene, both measured in the same well. TATA-box binding protein (TBP; Hs00427620_m1) was used as housekeeping gene and relative gene expression was determined for GRIN1 (Hs00609557_m1), GRIA1 (Hs00181348_m1), GABBR1 (Hs00559488_m1), NeuN (Hs01370654_m1) and STX1A (Hs00270282_m1) using the 7900HT Fast Real-Time PCR System (Applied Biosystems). Relative quantification was calculated according to the comparative $2^{-\Delta\Delta Ct}$ method and data are presented as log$_2$-fold difference.

Immunocytochemistry

hiPSC-derived neurons were fixated using 4% paraformaldehyde (PFA) for 10 to 15 min. After washing three times with PBS, cells were permeabilized with 0.1% Triton X-100 for 15 min. Following two washing steps, unspecific binding sites were then blocked by incubating the cells with 3% BSA and 0.1% Tween 20 (polysorbat) in phosphate-buffered saline (PBS) for 30 min. Incubation with primary antibodies diluted in blocking solution was performed overnight at 4 °C (mouse anti-MAP2 (1 : 400, Thermo Fisher Scientific Cat# 13-1500, RRID:AB_2533001), mouse anti-TUJ1 (1 : 600, Sigma-Aldrich Cat# T8578, RRID:AB_1841228), rabbit anti-NeuN (1 : 600, Abcam Cat# ab104225, RRID:AB_10711153). Cells were then washed three times with PBS and incubated with Alexa Fluor 488 secondary antibodies diluted 1 : 500 in blocking solution for 1 h at room temperature in the dark. After two additional washing steps, nuclear counterstaining was performed with 1 μg ml^{-1} Hoechst 33258 (Invitrogen). Cells were imaged using an Opera High Content Imaging System (PerkinElmer).

Cell viability and z-stacks

Confocal microscopy (Leica TCS SP8, 488 and 552 nm lasers, upright configuration) was used to quantify cell viability and to investigate the interaction between cell membrane and substrate via high-resolution z-stacks. For this purpose, the cells were fixated using 4% PFA and compartment-specific stains. The membrane was stained using a membrane stain (Thermo Fisher's neurite outgrowth staining kit (NOSK), ex/em: 555/565 nm). To quantify cell viability, a cell viability indicator (NOSK, ex/em: 496/515 nm) and propidium iodide to identify dead cells (ex/em: 535/617 nm) were used. For staining, the growth medium was removed and exchanged by dyes diluted in Dulbecco's PBS including 4% PFA. The cells were placed for 15 min at 37 °C and 5% CO$_2$ in the incubator. Subsequently, the staining solution was removed and replaced by a background suppression dye (NOSK). For imaging, the samples were transferred from the 6-well plate onto a microscope slide and covered with a coverslip to use the water immersion objectives. For every sample, at least four independent areas of 500 × 500 μm^2 were analyzed with ImageJ (smoothing-, threshold-, watershed- and analyze-particles function)[121] and data was pro-

cessed with Origin (v.2018). *z*-Stacks were processed with Fiji.[122] For publication, all images were optimized in contrast and brightness.

Flow cytometry

FoxP3 Staining Buffer Set (Miltenyi Biotec) was used for iNPC flow cytometry. Briefly, cells were dissociated with Accutase, fixed and permeabilized for 30 min on ice with Fixation/ Permeabilization solution and labeled for 30 min with the antibodies anti-Pax6-PE (1 : 10, Miltenyi Biotec Cat# 130-107-828, RRID:AB_2653166), anti-Sox1-FITC (1 : 50, Miltenyi Biotec Cat# 130-111-157, RRID:AB_2653486), anti-Sox2-FITC (1 : 10, Miltenyi Biotec Cat# 130-104-993, RRID:AB_2653499) or isotype controls REA Control (I)-FITC (1 : 10, Miltenyi Biotec Cat# 130-104-611, RRID:AB_2661677), REA Control-PE (1 : 10, Miltenyi Biotec Cat# 130-104-628, RRID:AB_2661702) diluted in Permeabilization buffer. Following the staining procedure, iNPCs were resuspended in Staining buffer (BD Biosciences) and flow cytometry was performed using a FACSCalibur (BD Biosciences).

Scanning electron microscopy

SEM was used to image the interface between cell membrane and nanowire. The cross sections were prepared *via* material milling using FIB (Zeiss Crossbeam 550). For this purpose, the cells were fixated with 4% PFA. The solution was exchanged with deionized water followed by dehydration in a step-wise ethanol exchange.[123] Subsequently, the cells were critical point dried (Tousimis Autosamdri-815) to avoid collapsing of the cells[124] and finally sputter coated with a 20 nm gold layer to avoid charging effects during imaging.

Electrophysiology

An upright patch clamp setup (Nikon Eclipse FN1) with a non-immersion objective with extra-long working distance (Nikon CFI TU Plan EPI ELWD 50× N.A. 0.60/W.D. 11.00 mm) was used to handle the opaque substrates.[31] The traces were recorded using a HEKA EPC 10 USB patch clamp amplifier and a red star headstage. The data was processed by the patch clamp software (Patch Master V2x80) with a Bessel low-pass filter at 2.9 kHz. Pipette capacitance and series-resistance were automatically compensated. For measurements, the samples were transferred to standard 35 mm Petri dishes. The bath solution consisted of (mM): NaCl 140, KCl 2.4, MgCl$_2$ 1.3, CaCl$_2$ 2.5, HEPES 10, D-glucose 10 adjusted to pH 7.4 with NaOH. The pipette solution consisted of (mM): K-gluconate 125, NaCl 10, EGTA 1, MgATP 4, HEPES 10, D-glucose 10, adjusted to pH 7.4 with KOH adapted from Reinhardt *et al.*[91] All experiments were performed at room temperature. The pipettes were fabricated from borosilicate glass capillary blanks (GB150T-8P, Science Products) using a Sutter P-2000 pipette puller and were subsequently heat polished (CPM-2, ALA Scientific Instruments). Tip diameters were approx. 950 nm resulting in resistances of 5–7 MΩ. All data was analyzed with Origin (v.2018) using a labtalk script and the integrated fitting functions. The RMP was determined by holding the cells with

zero current in current-clamp mode. The MCs were directly determined by the patch clamp amplifier software. The IR and MTC were extracted from a current-clamp experiment using a rectangular current injection of −10 pA. The IR was calculated from the increase in membrane potential during the current injection. The MTC was determined by fitting the exponential decay of the membrane potential towards the RMP after the current injection.

Author contributions

JH performed the confocal microscopy imaging, scanning electron microscopy imaging with focused ion beam milling, patch-clamp measurements and data analysis. UH, DL developed the cell culture protocols. UH performed the cell culture, immunocytochemistry, flow cytometry, and differential gene expression analysis. JH, SH, RZ prepared the NW substrates. CF performed the critical point drying. JH, UH, OP wrote the manuscript. OP, RHB supervised the study. RHB provided funding and general support. All authors conducted proofreading and approved the manuscript.

Conflicts of interest

There are no conflicts to declare.

Acknowledgements

References

1 K. Takahashi and S. Yamanaka, *Cell*, 2006, **126**, 663–676.
2 K. Takahashi, K. Tanabe, M. Ohnuki, M. Narita, T. Ichisaka, K. Tomoda and S. Yamanaka, *Cell*, 2007, **131**, 861–872.
3 H. C. Ko and B. D. Gelb, *Stem Cells Transl. Med.*, 2014, **3**, 500–509.
4 J. Takahashi, *Regener. Med.*, 2019, **14**, 93–95.
5 A. Appelt-Menzel, A. Cubukova, K. Günther, F. Edenhofer, J. Piontek, G. Krause, T. Stüber, H. Walles, W. Neuhaus and M. Metzger, *Stem Cell Rep.*, 2017, **8**, 894–906.
6 M. A. Lancaster, M. Renner, C.-A. Martin, D. Wenzel, L. S. Bicknell, M. E. Hurles, T. Homfray, J. M. Penninger, A. P. Jackson and J. A. Knoblich, *Nature*, 2013, **501**, 373–379.
7 M. Dragunow, *Nat. Rev. Drug Discovery*, 2008, 7, 659–666.
8 J. Seok, H. S. Warren, A. G. Cuenca, M. N. Mindrinos, H. V. Baker, W. Xu, D. R. Richards, G. P. McDonald-Smith,

H. Gao, L. Hennessy, C. C. Finnerty, C. M. López, S. Honari, E. E. Moore, J. P. Minei, J. Cuschieri, P. E. Bankey, J. L. Johnson, J. Sperry, A. B. Nathens, T. R. Billiar, M. A. West, M. G. Jeschke, M. B. Klein, R. L. Gamelli, N. S. Gibran, B. H. Brownstein, C. Miller-Graziano, S. E. Calvano, P. H. Mason, J. P. Cobb, L. G. Rahme, S. F. Lowry, R. V. Maier, L. L. Moldawer, D. N. Herndon, R. W. Davis, W. Xiao and R. G. Tompkins, *Proc. Natl. Acad. Sci. U. S. A.*, 2013, **110**, 3507–3512.

9 X. Xu, E. I. Stoyanova, A. E. Lemiesz, J. Xing, D. C. Mash and N. Heintz, *eLife*, 2018, **7**, e37551.

10 S. Marchenko and L. Flanagan, *J. Visualized Exp.*, 2007, (7), 267.

11 D. Ruff and P. T. Lieu, in *Methods in Molecular Biology*, 2013, vol. 997, pp. 225–236.

12 H. G. Craighead, *J. Vac. Sci. Technol., A*, 2003, **21**, S216–S221.

13 P. M. Mendes, *Chem. Soc. Rev.*, 2013, **42**, 9207.

14 M. W. Tibbitt, C. B. Rodell, J. A. Burdick and K. S. Anseth, *Proc. Natl. Acad. Sci. U. S. A.*, 2015, **112**, 14444–14451.

15 I. Armentano, L. Tarpani, F. Morena, S. Martino, L. Latterini and L. Torre, *Curr. Org. Chem.*, 2018, **22**, 1193–1204.

16 A. S. Curtis and M. Varde, *J. Natl. Cancer Inst.*, 1964, **33**, 15–26.

17 M. Lampin, R. Warocquier-Clérout, C. Legris, M. Degrange and M. F. Sigot-Luizard, *J. Biomed. Mater. Res.*, 1997, **36**, 99–108.

18 A. Harsch, J. Calderon, R. B. Timmons and G. W. Gross, *J. Neurosci. Methods*, 2000, **98**, 135–144.

19 Y. H. Kim, N. S. Baek, Y. H. Han, M. A. Chung and S. D. Jung, *J. Neurosci. Methods*, 2011, **202**, 38–44.

20 N. Li, Q. Zhang, S. Gao, Q. Song, R. Huang, L. Wang, L. Liu, J. Dai, M. Tang and G. Cheng, *Sci. Rep.*, 2013, **3**, 1604.

21 D. Ning, B. Duong, G. Thomas, Y. Qiao, L. Ma, Q. Wen and M. Su, *Langmuir*, 2016, **32**, 2718–2723.

22 T. Berthing, S. Bonde, C. B. Sørensen, P. Utko, J. Nygård and K. L. Martinez, *Small*, 2011, **7**, 640–647.

23 R. Elnathan, M. Kwiat, F. Patolsky and N. H. Voelcker, *Nano Today*, 2014, **9**, 172–196.

24 S. Bonde, N. Buch-Månson, K. R. Rostgaard, T. K. Andersen, T. Berthing and K. L. Martinez, *Nanotechnology*, 2014, **25**, 362001.

25 W. Hällström, T. Mårtensson, C. Prinz, P. Gustavsson, L. Montelius, L. Samuelson and M. Kanje, *Nano Lett.*, 2007, **7**, 2960–2965.

26 J. Lee, B. S. S. Kang, B. Hicks, T. F. Chancellor Jr., B. H. Chu, H.-T. Wang, B. G. Keselowsky, F. Ren and T. P. Lele, *Biomaterials*, 2008, **29**, 3743–3749.

27 Z. Li, R. Yang, M. Yu, F. Bai, C. Li and Z. L. Wang, *J. Phys. Chem. C*, 2008, **112**, 20114–20117.

28 G. Piret, M.-T. Perez and C. N. Prinz, *Biomaterials*, 2013, **34**, 875–887.

29 Z. Li, S. Kamlund, T. Ryser, M. Lard, S. Oredsson and C. N. Prinz, *J. Mater. Chem. B*, 2018, **6**, 7042–7049.

30 Z. Li, H. Persson, K. Adolfsson, S. Oredsson and C. N. Prinz, *Sci. China: Life Sci.*, 2018, **61**, 427–435.

31 J. Harberts, R. Zierold, C. Fendler, A. Koitmäe, P. Bayat, I. Fernandez-Cuesta, G. Loers, B.-P. Diercks, R. Fliegert, A. H. Guse, C. Ronning, G. Otnes, M. Borgström and R. H. Blick, *RSC Adv.*, 2019, **9**, 11194–11201.

32 S. Qi, C. Yi, S. Ji, C.-C. Fong and M. Yang, *ACS Appl. Mater. Interfaces*, 2009, **1**, 30–34.

33 H. Persson, Z. Li, J. O. Tegenfeldt, S. Oredsson and C. N. Prinz, *Sci. Rep.*, 2016, **5**, 18535.

34 N. Buch-Månson, D.-H. Kang, D. Kim, K. E. Lee, M.-H. Yoon and K. L. Martinez, *Nanoscale*, 2017, **9**, 5517–5527.

35 Z. Li, J. Song, G. Mantini, M.-Y. Lu, H. Fang, C. Falconi, L.-J. Chen and Z. L. Wang, *Nano Lett.*, 2009, **9**, 3575–3580.

36 W. Hällström, M. Lexholm, D. B. Suyatin, G. Hammarin, D. Hessman, L. Samuelson, L. Montelius, M. Kanje and C. N. Prinz, *Nano Lett.*, 2010, **10**, 782–787.

37 Z. Li, H. Persson, K. Adolfsson, L. Abariute, M. T. Borgström, D. Hessman, K. Åström, S. Oredsson and C. N. Prinz, *Nanoscale*, 2017, **9**, 19039–19044.

38 L. Hanson, W. Zhao, H.-Y. Lou, Z. C. Lin, S. W. Lee, P. Chowdary, Y. Cui and B. Cui, *Nat. Nanotechnol.*, 2015, **10**, 554–562.

39 M. A. Bucaro, Y. Vasquez, B. D. Hatton and J. Aizenberg, *ACS Nano*, 2012, **6**, 6222–6230.

40 G. G. Piret, M.-T. Perez and C. N. Prinz, *Appl. Mater. Interfaces*, 2015, **7**, 7–11.

41 L. Hanson, Z. C. Lin, C. Xie, Y. Cui and B. Cui, *Nano Lett.*, 2012, **12**, 5815–5820.

42 F. Santoro, W. Zhao, L.-M. Joubert, L. Duan, J. Schnitker, Y. van de Burgt, H.-Y. Lou, B. Liu, A. Salleo, L. Cui, Y. Cui and B. Cui, *ACS Nano*, 2017, **11**, 8320–8328.

43 N. Buch-Månson, S. Bonde, J. Bolinsson, T. Berthing, J. Nygård and K. L. Martinez, *Adv. Funct. Mater.*, 2015, **25**, 3246–3255.

44 C. Xie, Z. Lin, L. Hanson, Y. Cui and B. Cui, *Nat. Nanotechnol.*, 2012, **7**, 185–190.

45 J. T. Robinson, M. Jorgolli and H. Park, *Front. Neural Circuits*, 2013, **7**, 38.

46 K.-Y. Lee, I. Kim, S.-E. Kim, D.-W. Jeong, J.-J. Kim, H. Rhim, J.-P. Ahn, S.-H. Park and H.-J. Choi, *Nanoscale Res. Lett.*, 2014, **9**, 56.

47 Z. C. Lin, C. Xie, Y. Osakada, Y. Cui and B. Cui, *Nat. Commun.*, 2014, **5**, 3206.

48 R. Liu, R. Chen, A. T. Elthakeb, S. H. Lee, S. Hinckley, M. L. Khraiche, J. Scott, D. Pre, Y. Hwang, A. Tanaka, Y. G. Ro, A. K. Matsushita, X. Dai, C. Soci, S. Biesmans, A. James, J. Nogan, K. L. Jungjohann, D. V. Pete, D. B. Webb, Y. Zou, A. G. Bang and S. A. Dayeh, *Nano Lett.*, 2017, **17**, 2757–2764.

49 W. Kim, J. K. Ng, M. E. Kunitake, B. R. Conklin and P. Yang, *J. Am. Chem. Soc.*, 2007, **129**, 7228–7229.

50 R. Elnathan, B. Delalat, D. Brodoceanu, H. Alhmoud, F. J. Harding, K. Buehler, A. Nelson, L. Isa, T. Kraus and N. H. Voelcker, *Adv. Funct. Mater.*, 2015, **25**, 7215–7225.

51 Y. Chen, S. Aslanoglou, G. Gervinskas, H. Abdelmaksoud, N. H. Voelcker and R. Elnathan, *Small*, 2019, 1904819.

52 J. J. Vandersarl, A. M. Xu and N. A. Melosh, *Nano Lett.*, 2012, **12**, 3881–3886.

53 Y. Wang, Y. Yang, L. Yan, S. Y. Kwok, W. Li, Z. Wang, X. Zhu, G. Zhu, W. Zhang, X. Chen and P. Shi, *Nat. Commun.*, 2014, **5**, 4466.

54 X. Xie, A. Aalipour, S. V. Gupta and N. A. Melosh, *ACS Nano*, 2015, **9**, 11667–11677.

55 C. Chiappini, E. De Rosa, J. O. Martinez, X. Liu, J. Steele, M. M. Stevens and E. Tasciotti, *Nat. Mater.*, 2015, **14**, 532–539.

56 Y. Cao, H. Chen, R. Qiu, M. Hanna, E. Ma, M. Hjort, A. Zhang, R. S. Lewis, J. C. Wu and N. A. Melosh, *Sci. Adv.*, 2018, **4**, eaat8131.

57 S. Gopal, C. Chiappini, J. Penders, V. Leonardo, H. Seong, S. Rothery, Y. Korchev, A. Shevchuk and M. M. Stevens, *Adv. Mater.*, 2019, **31**, 1806788.

58 E. Garnett and P. Yang, *J. Am. Chem. Soc.*, 2008, **130**, 9224–9225.

59 J. Wallentin, N. Anttu, D. Asoli, M. Huffman, I. Aberg, M. H. Magnusson, G. Siefer, P. Fuss-Kailuweit, F. Dimroth, B. Witzigmann, H. Q. Xu, L. Samuelson, K. Deppert and M. T. Borgstrom, *Science*, 2013, **339**, 1057–1060.

60 J. C. Johnson, H. Q. Yan, P. D. Yang and R. J. Saykally, *J. Phys. Chem. B*, 2003, **107**, 8816–8828.

61 S. Rühle, L. K. Van Vugt, H. Y. Li, N. A. Keizer, L. Kuipers and D. Vanmaekelbergh, *Nano Lett.*, 2008, **8**, 119–123.

62 C. Baratto, R. Kumar, E. Comini, G. Faglia and G. Sberveglieri, *Opt. Express*, 2015, **23**, 18937.

63 R. Parameswaran, J. L. Carvalho-de-Souza, Y. Jiang, M. J. Burke, J. F. Zimmerman, K. Koehler, A. W. Phillips, J. Yi, E. J. Adams, F. Bezanilla and B. Tian, *Nat. Nanotechnol.*, 2018, **13**, 260–266.

64 D. Verardo, F. W. Lindberg, N. Anttu, C. S. Niman, M. Lard, A. P. Dabkowska, T. Nylander, A. Månsson, C. N. Prinz and H. Linke, *Nano Lett.*, 2018, **18**, 4796–4802.

65 M. Lard, H. Linke and C. N. Prinz, *Nanotechnology*, 2019, **30**, 214003.

66 L. Fenno, O. Yizhar and K. Deisseroth, *Annu. Rev. Neurosci.*, 2011, **34**, 389–412.

67 S. Chen, A. Z. Weitemier, X. Zeng, L. He, X. Wang, Y. Tao, A. J. Y. Huang, Y. Hashimotodani, M. Kano, H. Iwasaki, L. K. Parajuli, S. Okabe, D. B. L. Teh, A. H. All, I. Tsutsui-Kimura, K. F. Tanaka, X. Liu and T. J. McHugh, *Science*, 2018, **359**, 679–684.

68 Y. Shi, P. Kirwan, J. Smith, H. P. C. Robinson and F. J. Livesey, *Nat. Neurosci.*, 2012, **15**, 477–486.

69 H.-Y. Lou, W. Zhao, Y. Zeng and B. Cui, *Acc. Chem. Res.*, 2018, **51**, 1046–1053.

70 H. S. Kim and H. S. Yoo, *RSC Adv.*, 2015, **5**, 49508–49512.

71 Y. Tan, D. Richards, R. Xu, S. Stewart-Clark, S. K. Mani, T. K. Borg, D. R. Menick, B. Tian and Y. Mei, *Nano Lett.*, 2015, **15**, 2765–2772.

72 C. H. Rasmussen, P. M. Reynolds, D. R. Petersen, M. Hansson, R. M. McMeeking, M. Dufva and N. Gadegaard, *Adv. Funct. Mater.*, 2016, **26**, 815–823.

73 D. B. Suyatin, L. Wallman, J. Thelin, C. N. Prinz, H. Jörntell, L. Samuelson, L. Montelius and J. Schouenborg, *PLoS One*, 2013, **8**, e56673.

74 B. Roska and J.-A. Sahel, *Nature*, 2018, **557**, 359–367.

75 J. Tang, N. Qin, Y. Chong, Y. Diao, Yiliguma, Z. Wang, T. Xue, M. Jiang, J. Zhang and G. Zheng, *Nat. Commun.*, 2018, **9**, 786.

76 S. Rahong, T. Yasui, N. Kaji and Y. Baba, *Lab Chip*, 2016, **16**, 1126–1138.

77 S. M. Chambers, C. A. Fasano, E. P. Papapetrou, M. Tomishima, M. Sadelain and L. Studer, *Nat. Biotechnol.*, 2009, **27**, 275–280.

78 M. Zhang, J. Ngo, F. Pirozzi, Y.-P. Sun and A. Wynshaw-Boris, *Stem Cell Res. Ther.*, 2018, **9**, 67.

79 H. F. Lu, S.-X. Lim, M. F. Leong, K. Narayanan, R. P. K. Toh, S. Gao and A. C. A. Wan, *Biomaterials*, 2012, **33**, 9179–9187.

80 S. Bonde, T. Berthing, M. H. Madsen, T. K. Andersen, N. Buch-Månson, L. Guo, X. Li, F. Badique, K. Anselme, J. Nygård and K. L. Martinez, *ACS Appl. Mater. Interfaces*, 2013, **5**, 10510–10519.

81 T. Berthing, S. Bonde, K. R. Rostgaard, M. H. Madsen, C. B. Sørensen, J. Nygård, K. L. Martinez, C. B. Sorensen, J. Nygård and K. L. Martinez, *Nanotechnology*, 2012, **23**, 415102.

82 L. Micholt, A. Gärtner, D. Prodanov, D. Braeken, C. G. Dotti and C. Bartic, *PLoS One*, 2013, **8**, 1–14.

83 V. Gautam, S. Naureen, N. Shahid, Q. Gao, Y. Wang, D. Nisbet, C. Jagadish and V. R. Daria, *Nano Lett.*, 2017, **17**, 3369–3375.

84 A. Koitmäe, J. Harberts, G. Loers, M. Müller, C. S. Bausch, D. Sonnenberg, C. Heyn, R. Zierold, W. Hansen and R. H. Blick, *Adv. Mater. Interfaces*, 2016, **3**, 1600746.

85 A. Koitmäe, M. Müller, C. S. Bausch, J. Harberts, W. Hansen, G. Loers and R. H. Blick, *Langmuir*, 2018, **34**, 1528–1534.

86 C. Fendler, C. Denker, J. Harberts, P. Bayat, R. Zierold, G. Loers, M. Münzenberg and R. H. Blick, *Adv. Biosyst.*, 2019, **1800329**, 1800329.

87 M. Telias, M. Segal and D. Ben-Yosef, *F1000Research*, 2014, **3**, 196.

88 W.-B. Zhang, P. J. Ross, Y. Tu, Y. Wang, S. Beggs, A. S. Sengar, J. Ellis and M. W. Salter, *Sci. Rep.*, 2016, **6**, 23837.

89 M. C. Moe, M. Varghese, A. I. Danilov, U. Westerlund, J. Ramm-Pettersen, L. Brundin, M. Svensson, J. Berg-Johnsen and I. A. Langmoen, *Brain*, 2005, **128**, 2189–2199.

90 U. Westerlund, M. C. Moe, M. Varghese, J. Berg-Johnsen, M. Ohlsson, I. A. Langmoen and M. Svensson, *Exp. Cell Res.*, 2003, **289**, 378–383.

91 P. Reinhardt, M. Glatza, K. Hemmer, Y. Tsytsyura, C. S. Thiel, S. Höing, S. Moritz, J. A. Parga, L. Wagner, J. M. Bruder, G. Wu, B. Schmid, A. Röpke, J. Klingauf,

J. C. Schwamborn, T. Gasser, H. R. Schöler and J. Sterneckert, *PLoS One*, 2013, **8**, e59252.

92 U. Djuric, A. Y. L. Cheung, W. Zhang, R. S. Mok, W. Lai, A. Piekna, J. A. Hendry, P. J. Ross, P. Pasceri, D.-S. Kim, M. W. Salter and J. Ellis, *Neurobiol. Dis.*, 2015, **76**, 37–45.

93 S. Khattak, E. Brimble, W. Zhang, K. Zaslavsky, E. Strong, P. J. Ross, J. Hendry, S. Mital, M. W. Salter, L. R. Osborne and J. Ellis, *Mol. Brain*, 2015, **8**, 77.

94 R. S. Lam, F. M. Töpfer, P. G. Wood, V. Busskamp and E. Bamberg, *PLoS One*, 2017, **12**, 1–26.

95 N. Gunhanlar, G. Shpak, M. van der Kroeg, L. A. Gouty-Colomer, S. T. Munshi, B. Lendemeijer, M. Ghazvini, C. Dupont, W. J. G. Hoogendijk, J. Gribnau, F. M. S. de Vrij and S. A. Kushner, *Mol. Psychiatry*, 2018, **23**, 1336–1344.

96 Y. Xie, R. J. Schutte, N. N. Ng, K. C. Ess, P. H. Schwartz and D. K. O'Dowd, *Stem Cell Res.*, 2018, **26**, 84–94.

97 L. Coyne, M. Shan, S. A. Przyborski, R. Hirakawa and R. F. Halliwell, *Neurochem. Int.*, 2011, **59**, 404–412.

98 J. Golowasch, G. Thomas, A. L. Taylor, A. Patel, A. Pineda, C. Khalil and F. Nadim, *J. Neurophysiol.*, 2009, **102**, 2161–2175.

99 D. Prè, M. W. Nestor, A. A. Sproul, S. Jacob, P. Koppensteiner, V. Chinchalongporn, M. Zimmer, A. Yamamoto, S. A. Noggle and O. Arancio, *PLoS One*, 2014, **9**, e103418.

100 P. Koppensteiner, S. Boehm and O. Arancio, *Cell. Reprogram.*, 2014, **16**, 439–446.

101 A. Cutarelli, S. Ghio, J. Zasso, A. Speccher, G. Scarduelli, M. Roccuzzo, M. Crivellari, N. M. Pugno, S. Casarosa, M. Boscardin and L. Conti, *Cells*, 2019, **9**, 88.

102 S.-W. Kuo, H.-I. Lin, J. H.-C. Ho, Y.-R. V. Shih, H.-F. Chen, T.-J. Yen and O. K. Lee, *Biomaterials*, 2012, **33**, 5013–5022.

103 D. Liu, C. Yi, K. Wang, C.-C. Fong, Z. Wang, P. K. Lo, D. Sun and M. Yang, *ACS Appl. Mater. Interfaces*, 2013, **5**, 13295–13304.

104 H. Kim, I. Kim, H.-J. Choi, S. Y. Kim and E. G. Yang, *Nanoscale*, 2015, **7**, 17131–17138.

105 Q. Yan, L. Fang, J. Wei, G. Xiao, M. Lv, Q. Ma, C. Liu and W. Wang, *J. Biomater. Sci., Polym. Ed.*, 2017, **28**, 1394–1407.

106 L. G. Villa-Diaz, J. K. Kim, J. Lahann and P. H. Krebsbach, *Stem Cells Transl. Med.*, 2014, **3**, 1410–1417.

107 J. M. Edgar, M. Robinson and S. M. Willerth, *Acta Biomater.*, 2017, **51**, 237–245.

108 C. Borschel, S. Spindler, D. Lerose, A. Bochmann, S. H. Christiansen, S. Nietzsche, M. Oertel and C. Ronning, *Nanotechnology*, 2011, **22**, 185307.

109 P. Kasamechonchung, M. Horprathum, K. Boonpavanitchakul, N. Supaka, P. Prompinit, W. Kangwansupamonkon, A. Somboonkaew, J. Wetcharungsri, S. Pratontep, S. Porntheeraphat and A. Klamchuen, *Phys. Status Solidi*, 2015, **212**, 394–400.

110 S. Zhang, Y. Shen, H. Fang, S. Xu, J. Song and Z. L. Wang, *J. Mater. Chem.*, 2010, **20**, 10606.

111 G. M. Shankar, B. L. Bloodgood, M. Townsend, D. M. Walsh, D. J. Selkoe and B. L. Sabatini, *J. Neurosci.*, 2007, **27**, 2866–2875.

112 J. Hardy, R. Cowburn, A. Barton, G. Reynolds, E. Lofdahl, A.-M. O'Carroll, P. Wester and B. Winblad, *Neurosci. Lett.*, 1987, **73**, 77–80.

113 D. Centonze, L. Muzio, S. Rossi, F. Cavasinni, V. De Chiara, A. Bergami, A. Musella, M. D'Amelio, V. Cavallucci, A. Martorana, A. Bergamaschi, M. T. Cencioni, A. Diamantini, E. Butti, G. Comi, G. Bernardi, F. Cecconi, L. Battistini, R. Furlan and G. Martino, *J. Neurosci.*, 2009, **29**, 3442–3452.

114 A. Ochalek, B. Mihalik, H. X. Avci, A. Chandrasekaran, A. Téglási, I. Bock, M. Lo Giudice, Z. Táncos, K. Molnár, L. László, J. E. Nielsen, B. Holst, K. Freude, P. Hyttel, J. Kobolák and A. Dinnyés, *Alzheimer's Res. Ther.*, 2017, **9**, 90.

115 S. L. Sison, S. C. Vermilyea, M. E. Emborg and A. D. Ebert, *Curr. Neurol. Neurosci. Rep.*, 2018, **18**, 84.

116 C. V. Thompson, *Annu. Rev. Mater. Res.*, 2012, **42**, 399–434.

117 H. Ge, L. Tan, P. Wu, Y. Yin, X. Liu, H. Meng, G. Cui, N. Wu, J. Lin, R. Hu and H. Feng, *Sci. Rep.*, 2015, **5**, 15535.

118 R. Tandon, B. Brändl, N. Baryshnikova, A. Landshammer, L. Steenpaß, O. Keminer, O. Pless and F. J. Müller, *Stem Cell Res.*, 2018, **33**, 120–124.

119 K. J. Brennand, A. Simone, J. Jou, C. Gelboin-Burkhart, N. Tran, S. Sangar, Y. Li, Y. Mu, G. Chen, D. Yu, S. McCarthy, J. Sebat and F. H. Gage, *Nature*, 2011, **473**, 221–225.

120 S.-Y. Cao, Y. Hu, C. Chen, F. Yuan, M. Xu, Q. Li, K.-H. Fang, Y. Chen and Y. Liu, *Sci. Rep.*, 2017, **7**, 3282.

121 C. A. Schneider, W. S. Rasband and K. W. Eliceiri, *Nat. Methods*, 2012, **9**, 671–675.

122 J. Schindelin, I. Arganda-Carreras, E. Frise, V. Kaynig, M. Longair, T. Pietzsch, S. Preibisch, C. Rueden, S. Saalfeld, B. Schmid, J.-Y. Tinevez, D. J. White, V. Hartenstein, K. Eliceiri, P. Tomancak and A. Cardona, *Nat. Methods*, 2012, **9**, 676–682.

123 D. Gusnard and R. H. Kirschner, *J. Microsc.*, 1977, **110**, 51–57.

124 R. M. Albrecht, D. H. Rasmussen, C. S. Keller and R. D. Hinsdill, *J. Microsc.*, 1976, **108**, 21–29.

SUPPORTING INFORMATION

Interfacing human induced pluripotent stem cell-derived neurons with designed nanowire arrays as a future platform for medical applications

Jann Harberts, Undine Haferkamp, Stefanie Haugg, Cornelius Fendler, Dennis Lam, Robert Zierold, Ole Pless, and Robert H. Blick
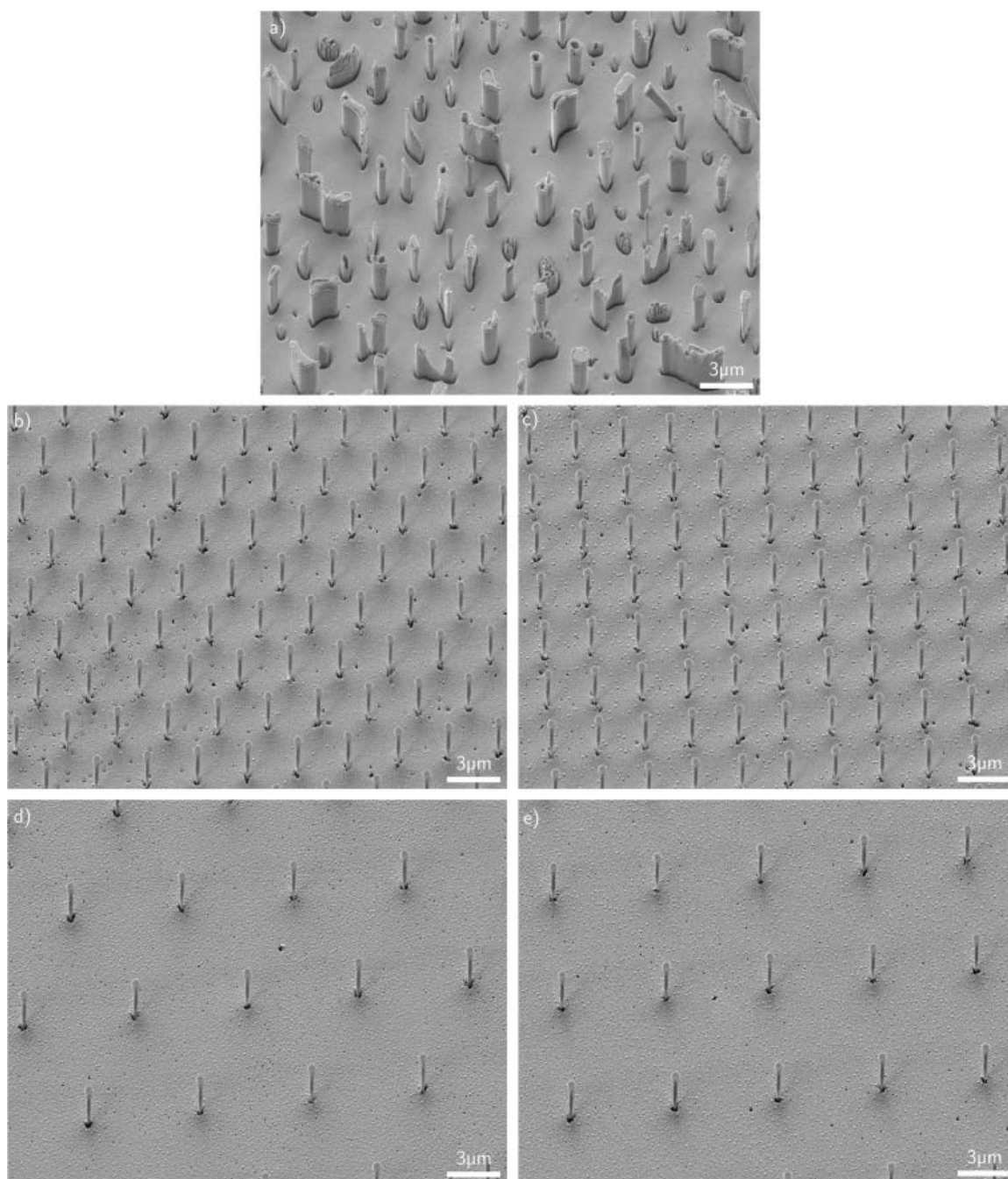
Figure S1: Sample overviews of the NW substrates. a) Random HD NWs. b) Hexagonal HD NWs. c) Rectangular HD NWs. d) Hexagonal LD NWs. e) Rectangular HD NWs.
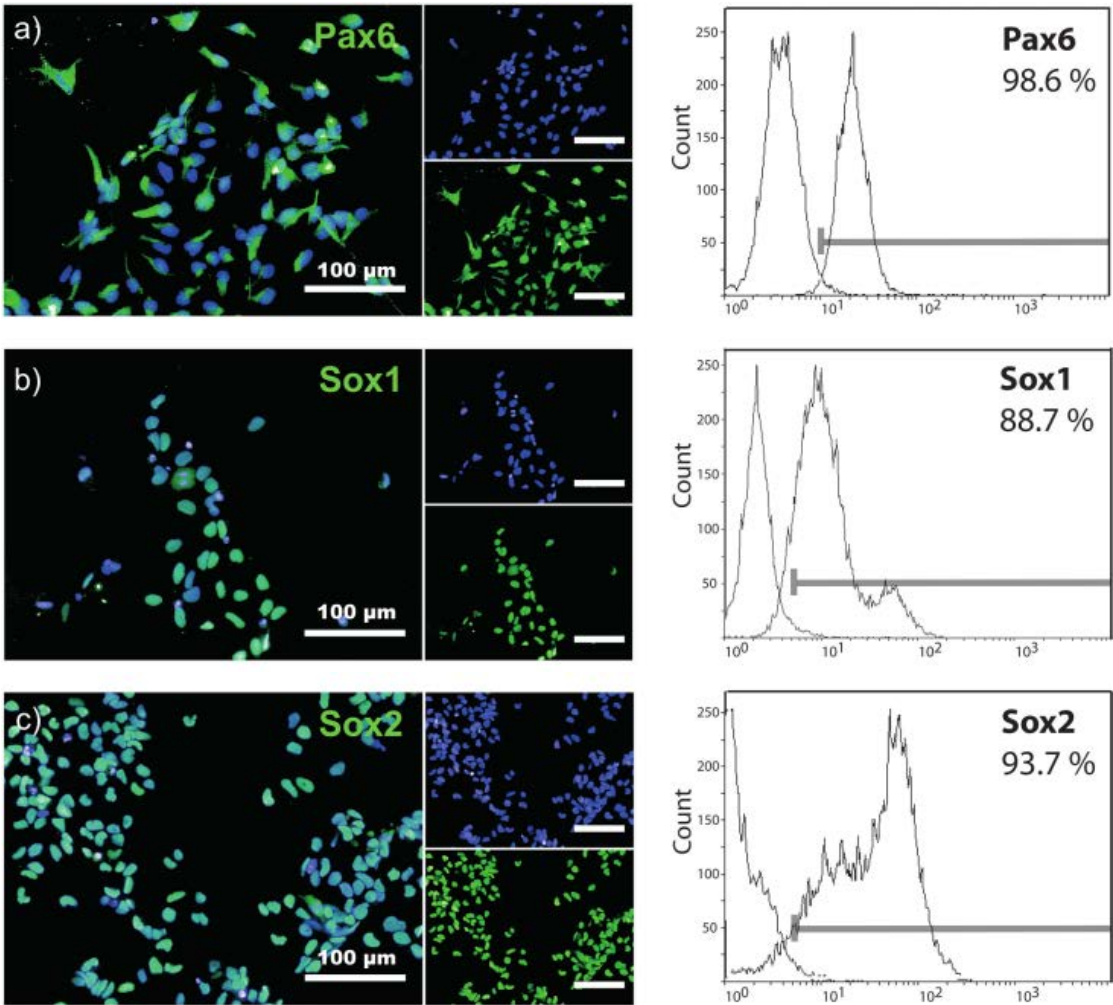
Figure S2: Characterization of human iPSC-derived neural precursor cells (iNPCs). a-c) Immunofluorescence staining and flow cytometry analysis of characteristic NPC marker proteins Pax6, Sox1 and Sox2.

Array	Type	Array	Type	MeanDiff	SEM	q Value	Prob	Alpha	Sig	LCL	UCL
Control	(Al2O3)	Control	(Glass)	-7.74477	7.18033	1.52538	0.92816	0.001	0	-42.98691	27.49737
Random	(HD)	Control	(Glass)	-8.22342	6.55472	1.77424	0.865	0.001	0	-40.39495	23.9481
Random	(HD)	Control	(Al2O3)	-0.47865	6.55472	0.10327	1	0.001	0	-32.65018	31.69287
Hexagonal	(HD)	Control	(Glass)	-7.36123	7.18033	1.44984	0.94272	0.001	0	-42.60337	27.88091
Hexagonal	(HD)	Control	(Al2O3)	0.38354	7.18033	0.07554	1	0.001	0	-34.8586	35.62568
Hexagonal	(HD)	Random	(HD)	0.86219	6.55472	0.18602	1	0.001	0	-31.30933	33.03372
Rectangular	(HD)	Control	(Glass)	-2.18024	7.18033	0.42941	0.99992	0.001	0	-37.42238	33.0619
Rectangular	(HD)	Control	(Al2O3)	5.56453	7.18033	1.09597	0.98521	0.001	0	-29.67761	40.80667
Rectangular	(HD)	Random	(HD)	6.04318	6.55472	1.30385	0.96506	0.001	0	-26.12834	38.21471
Rectangular	(HD)	Hexagonal	(HD)	5.18099	7.18033	1.02043	0.98977	0.001	0	-30.06115	40.42313
Hexagonal	(LD)	Control	(Glass)	-0.20669	7.18033	0.04071	1	0.001	0	-35.44883	35.03545
Hexagonal	(LD)	Control	(Al2O3)	7.53808	7.18033	1.48467	0.93627	0.001	0	-27.70406	42.78022
Hexagonal	(LD)	Random	(HD)	8.01674	6.55472	1.72965	0.87801	0.001	0	-24.15479	40.18826
Hexagonal	(LD)	Hexagonal	(HD)	7.15454	7.18033	1.40913	0.9497	0.001	0	-28.0876	42.39668
Hexagonal	(LD)	Rectangular	(HD)	1.97355	7.18033	0.3887	0.99996	0.001	0	-33.26859	37.21569
Rectangular	(LD)	Control	(Glass)	-6.87914	7.18033	1.35489	0.95809	0.001	0	-42.12128	28.363
Rectangular	(LD)	Control	(Al2O3)	0.86563	7.18033	0.17049	1	0.001	0	-34.37651	36.10777
Rectangular	(LD)	Random	(HD)	1.34428	6.55472	0.29004	0.99999	0.001	0	-30.82725	33.51581
Rectangular	(LD)	Hexagonal	(HD)	0.48209	7.18033	0.09495	1	0.001	0	-34.76005	35.72423
Rectangular	(LD)	Rectangular	(HD)	-4.6989	7.18033	0.92548	0.99389	0.001	0	-39.94104	30.54324
Rectangular	(LD)	Hexagonal	(LD)	-6.67246	7.18033	1.31418	0.96371	0.001	0	-41.9146	28.56969

Figure S3: ANOVA with post hoc Turkey's test of cell viability, alpha = 0.001.

Figure S4: ANOVA with post hoc Turkey's test of electrophysiological parameters, alpha = 0.001.

Array	Type	Array	Type	MeanDiff	SEM	q Value	Prob	Alpha	Sig	LCL	UCL
AP height											
Control	(Glass)	Control	(Al2O3)	-6.89821	8.06616	1.20944	0.97726	0.001	0	-42.88118	29.08475
Random	(HD)	Control	(Al2O3)	3.05893	8.06616	0.60411	0.99886	0.001	0	-32.02404	39.9419
Random	(HD)	Control	(Glass)	10.85714	8.3307	1.8431	0.84683	0.001	0	-26.30591	48.02019
Hexagonal	(HD)	Control	(Al2O3)	5.85893	8.06616	1.02723	0.96019	0.001	0	-30.12404	41.8419
Hexagonal	(HD)	Control	(Glass)	12.75714	8.3307	2.16564	0.72482	0.001	0	-24.40591	49.92019
Hexagonal	(HD)	Random	(HD)	1.9	8.3307	0.32254	0.99999	0.001	0	-35.26305	39.06305
Rectangular	(HD)	Control	(Al2O3)	-0.2125	8.41703	0.0357	1	0.001	0	-37.76067	37.33567
Rectangular	(HD)	Control	(Glass)	6.68571	8.67087	1.09044	0.9866	0.001	0	-31.99481	45.36624
Rectangular	(HD)	Random	(HD)	-4.17143	8.67087	0.68036	0.99898	0.001	0	-42.85196	34.5091
Rectangular	(HD)	Hexagonal	(HD)	-6.07143	8.67087	0.99025	0.99192	0.001	0	-44.75196	32.6091
Hexagonal	(LD)	Control	(Al2O3)	14.05	7.79266	2.5498	0.55305	0.001	0	-20.71285	48.81285
Hexagonal	(LD)	Control	(Glass)	20.94821	8.06616	3.67278	0.15122	0.001	0	-15.03475	56.93118
Hexagonal	(LD)	Random	(HD)	10.09107	8.06616	1.76923	0.86993	0.001	0	-25.8919	46.07404
Hexagonal	(LD)	Hexagonal	(HD)	8.19107	8.06616	1.43611	0.94776	0.001	0	-27.7919	44.17404
Hexagonal	(LD)	Rectangular	(HD)	14.2625	8.41703	2.39636	0.62311	0.001	0	-23.28567	51.81067
Rectangular	(LD)	Control	(Al2O3)	-4.45694	7.5731	0.8323	0.99685	0.001	0	-38.24036	29.32647
Rectangular	(LD)	Control	(Glass)	2.44127	7.85426	0.43957	0.99992	0.001	0	-32.59639	37.47893
Rectangular	(LD)	Random	(HD)	-8.41587	7.85426	1.51534	0.93318	0.001	0	-43.45353	26.62179
Rectangular	(LD)	Hexagonal	(HD)	-10.31587	7.85426	1.85744	0.84212	0.001	0	-45.35353	24.72179
Rectangular	(LD)	Rectangular	(HD)	-4.24444	8.21418	0.73075	0.99848	0.001	0	-40.88771	32.39882
Rectangular	(LD)	Hexagonal	(LD)	-18.50694	7.5731	3.45602	0.20485	0.001	0	-52.29036	15.27647
RMP											
Control	(Glass)	Control	(Al2O3)	5.20714	3.93721	1.87036	0.8378	0.001	0	-12.35664	22.77092
Random	(HD)	Control	(Al2O3)	2.49286	3.93721	0.89541	0.9953	0.001	0	-15.07092	20.05664
Random	(HD)	Control	(Glass)	-2.71429	4.06633	0.94399	0.99375	0.001	0	-20.85408	15.42551
Hexagonal	(HD)	Control	(Al2O3)	6.62143	3.93721	2.37837	0.63127	0.001	0	-10.94235	24.18521
Hexagonal	(HD)	Control	(Glass)	1.41429	4.06633	0.49187	0.99984	0.001	0	-16.72551	19.55408
Hexagonal	(HD)	Random	(HD)	4.12857	4.06633	1.43586	0.94781	0.001	0	-14.01122	22.26837
Rectangular	(HD)	Control	(Al2O3)	7.35	4.10647	2.53001	0.56209	0.001	0	-10.97778	25.67778
Rectangular	(HD)	Control	(Glass)	2.14286	4.23237	0.71602	0.99864	0.001	0	-16.73764	21.02336
Rectangular	(HD)	Random	(HD)	4.85714	4.23237	1.62298	0.90947	0.001	0	-14.02336	23.73764
Rectangular	(HD)	Hexagonal	(HD)	0.72857	4.23237	0.24345	1	0.001	0	-18.15193	19.60907
Hexagonal	(LD)	Control	(Al2O3)	-3.8875	3.8037	1.44537	0.94618	0.001	0	-20.85573	13.08073
Hexagonal	(LD)	Control	(Glass)	-9.09464	3.93721	3.26672	0.2619	0.001	0	-26.65842	8.46914
Hexagonal	(LD)	Random	(HD)	-6.38036	3.93721	2.29177	0.67012	0.001	0	-23.94414	11.18342
Hexagonal	(LD)	Hexagonal	(HD)	-10.50893	3.93721	3.77472	0.13009	0.001	0	-28.07271	7.05485
Hexagonal	(LD)	Rectangular	(HD)	-11.2375	4.10647	3.86816	0.11286	0.001	0	-29.56528	7.09028
Rectangular	(LD)	Control	(Al2O3)	3.45	3.69653	1.31989	0.96501	0.001	0	-13.04015	19.94015
Rectangular	(LD)	Control	(Glass)	-1.75714	3.83377	0.64818	0.99923	0.001	0	-18.85951	15.34522
Rectangular	(LD)	Random	(HD)	0.95714	3.83377	0.35307	0.99998	0.001	0	-16.14522	18.05951
Rectangular	(LD)	Hexagonal	(HD)	-3.17143	3.83377	1.16989	0.98077	0.001	0	-20.27379	13.93093
Rectangular	(LD)	Rectangular	(HD)	-3.9	4.00945	1.37561	0.95734	0.001	0	-21.78608	13.98608
Rectangular	(LD)	Hexagonal	(LD)	7.3375	3.69653	2.80717	0.43801	0.001	0	-9.15265	23.82765
MC											
Control	(Glass)	Control	(Al2O3)	-3.04107	4.37508	0.98301	0.99223	0.001	0	-22.55818	16.47604
Random	(HD)	Control	(Al2O3)	-2.12679	4.37508	0.68747	0.99892	0.001	0	-21.64389	17.39032
Random	(HD)	Control	(Glass)	0.91429	4.51856	0.28615	0.99999	0.001	0	-19.2429	21.07147
Hexagonal	(HD)	Control	(Al2O3)	1.13036	4.37508	0.36538	0.99997	0.001	0	-18.38675	20.64747
Hexagonal	(HD)	Control	(Glass)	4.17143	4.51856	1.30557	0.96682	0.001	0	-15.98575	24.32861
Hexagonal	(HD)	Random	(HD)	3.25714	4.51856	1.01942	0.99058	0.001	0	-16.90004	23.41433
Rectangular	(HD)	Control	(Al2O3)	0.9375	4.56538	0.29041	0.99999	0.001	0	-19.42857	21.30357
Rectangular	(HD)	Control	(Glass)	3.97857	4.70307	1.19636	0.97847	0.001	0	-17.00169	24.95883
Rectangular	(HD)	Random	(HD)	3.06429	4.70307	0.92143	0.99451	0.001	0	-17.91598	24.04455
Rectangular	(HD)	Hexagonal	(HD)	-0.19286	4.70307	0.05799	1	0.001	0	-21.17312	20.7874
Hexagonal	(LD)	Control	(Al2O3)	-2.575	4.22672	0.86157	0.99619	0.001	0	-21.43032	16.28032
Hexagonal	(LD)	Control	(Glass)	0.46607	4.37508	0.15065	1	0.001	0	-19.05104	19.98318
Hexagonal	(LD)	Random	(HD)	-0.44821	4.37508	0.14488	1	0.001	0	-19.96532	19.06889
Hexagonal	(LD)	Hexagonal	(HD)	-3.70536	4.37508	1.19773	0.97835	0.001	0	-23.22247	15.81175
Hexagonal	(LD)	Rectangular	(HD)	-3.5125	4.56538	1.08806	0.98675	0.001	0	-23.87857	16.85357
Rectangular	(LD)	Control	(Al2O3)	2.86639	4.10764	0.98687	0.99207	0.001	0	-15.45769	21.19046
Rectangular	(LD)	Control	(Glass)	5.90746	4.26014	1.96107	0.80589	0.001	0	-13.09691	24.91184
Rectangular	(LD)	Random	(HD)	4.93317	4.26014	1.65756	0.90088	0.001	0	-14.0112	23.99755
Rectangular	(LD)	Hexagonal	(HD)	1.73603	4.26014	0.5763	0.99961	0.001	0	-17.26834	20.74041
Rectangular	(LD)	Rectangular	(HD)	1.92889	4.45536	0.61227	0.99944	0.001	0	-17.94636	21.80414
Rectangular	(LD)	Hexagonal	(LD)	5.44139	4.10764	1.87341	0.83678	0.001	0	-12.88269	23.76546
IR											
Control	(Glass)	Control	(Al2O3)	0.8875	0.36622	3.4272	0.21291	0.001	0	-0.74621	2.52121
Random	(HD)	Control	(Al2O3)	0.37321	0.36622	1.44122	0.9469	0.001	0	-1.26049	2.00692
Random	(HD)	Control	(Glass)	-0.51429	0.37823	1.92292	0.81965	0.001	0	-2.20157	1.173
Hexagonal	(HD)	Control	(Al2O3)	0.07321	0.36622	0.28273	0.99999	0.001	0	-1.56049	1.70692
Hexagonal	(HD)	Control	(Glass)	-0.81429	0.37823	3.04462	0.3409	0.001	0	-2.50157	0.873
Hexagonal	(HD)	Random	(HD)	-0.3	0.37823	1.1217	0.98449	0.001	0	-1.98728	1.38728
Rectangular	(HD)	Control	(Al2O3)	0.50417	0.38215	1.86575	0.83935	0.001	0	-1.2006	2.20894
Rectangular	(HD)	Control	(Glass)	-0.38333	0.39368	1.37706	0.95712	0.001	0	-2.13951	1.37285
Rectangular	(HD)	Random	(HD)	0.13095	0.39368	0.47042	0.99988	0.001	0	-1.62523	1.88713
Rectangular	(HD)	Hexagonal	(HD)	0.43095	0.39368	1.54812	0.92644	0.001	0	-1.32523	2.18713
Hexagonal	(LD)	Control	(Al2O3)	1	0.3538	3.99717	0.09218	0.001	0	-0.57831	2.57831
Hexagonal	(LD)	Control	(Glass)	0.1125	0.36622	0.43443	0.99992	0.001	0	-1.52121	1.74621
Hexagonal	(LD)	Random	(HD)	0.62679	0.36622	2.42042	0.61217	0.001	0	-1.00692	2.26049
Hexagonal	(LD)	Hexagonal	(HD)	0.92679	0.36622	3.57891	0.17295	0.001	0	-0.70692	2.56049
Hexagonal	(LD)	Rectangular	(HD)	0.49583	0.38215	1.83491	0.8495	0.001	0	-1.20894	2.2006
Rectangular	(LD)	Control	(Al2O3)	0.39861	0.34384	1.63951	0.90542	0.001	0	-1.13523	1.93245
Rectangular	(LD)	Control	(Glass)	-0.48889	0.3566	1.93885	0.81396	0.001	0	-2.07968	1.1019
Rectangular	(LD)	Random	(HD)	0.0254	0.3566	0.10072	1	0.001	0	-1.56530	1.61618
Rectangular	(LD)	Hexagonal	(HD)	0.3254	0.3566	1.29047	0.96865	0.001	0	-1.26539	1.91618
Rectangular	(LD)	Rectangular	(HD)	-0.10556	0.37294	0.40027	0.99995	0.001	0	-1.76924	1.55813
Rectangular	(LD)	Hexagonal	(LD)	-0.60139	0.34384	2.47355	0.58792	0.001	0	-2.13523	0.93245
MTC											
Control	(Glass)	Control	(Al2O3)	3.69286	6.90064	0.75594	0.99816	0.001	0	-27.12641	34.51212
Random	(HD)	Control	(Al2O3)	-2.30429	6.90064	0.48397	0.99986	0.001	0	-33.18355	28.45498
Random	(HD)	Control	(Glass)	-6.05714	7.13521	1.20054	0.97809	0.001	0	-37.88715	25.77286
Hexagonal	(HD)	Control	(Al2O3)	2.69286	6.90064	0.55123	0.99969	0.001	0	-28.12641	33.51212
Hexagonal	(HD)	Control	(Glass)	-1	7.13521	0.1982	1	0.001	0	-32.83	30.83
Hexagonal	(HD)	Random	(HD)	5.05714	7.13521	1.00234	0.99139	0.001	0	-26.77286	36.88715
Rectangular	(HD)	Control	(Al2O3)	-0.91667	7.20915	0.17982	1	0.001	0	-33.07652	31.24310
Rectangular	(HD)	Control	(Glass)	-4.60952	7.42656	0.87778	0.99579	0.001	0	-37.73924	28.52019
Rectangular	(HD)	Random	(HD)	1.44762	7.42656	0.27566	0.99999	0.001	0	-31.6821	34.57734
Rectangular	(HD)	Hexagonal	(HD)	-3.60952	7.42656	0.68735	0.99892	0.001	0	-36.73924	29.52019
Hexagonal	(LD)	Control	(Al2O3)	11.05	6.67438	2.34135	0.64798	0.001	0	-18.72424	40.82424
Hexagonal	(LD)	Control	(Glass)	7.35714	6.90064	1.50602	0.93502	0.001	0	-23.46212	38.17641
Hexagonal	(LD)	Random	(HD)	13.41429	6.90064	2.74593	0.46472	0.001	0	-17.40498	44.23355
Hexagonal	(LD)	Hexagonal	(HD)	8.35714	6.90064	1.71073	0.88676	0.001	0	-22.46212	39.17641
Hexagonal	(LD)	Rectangular	(HD)	11.06667	7.20915	2.34749	0.64521	0.001	0	-20.19310	44.12652
Rectangular	(LD)	Control	(Al2O3)	3.09444	6.48633	0.67468	0.99903	0.001	0	-25.84092	32.02981
Rectangular	(LD)	Control	(Glass)	-0.59841	6.72714	0.1258	1	0.001	0	-30.60803	29.4112
Rectangular	(LD)	Random	(HD)	5.45873	6.72714	1.14756	0.98257	0.001	0	-24.55008	35.46834
Rectangular	(LD)	Hexagonal	(HD)	0.40159	6.72714	0.08442	1	0.001	0	-29.60803	30.4112
Rectangular	(LD)	Rectangular	(HD)	4.01111	7.03541	0.80629	0.99736	0.001	0	-27.37369	35.39592
Rectangular	(LD)	Hexagonal	(LD)	-7.95556	6.48633	1.73455	0.88007	0.001	0	-36.89092	20.97981

A.5 Publication V

Robust neuronal differentiation of human iPSC-derived neural progenitor cells cultured on densely-spaced spiky silicon nanowire arrays

Jann Harberts, Malte Siegmund, Matteo Schnelle, Ting Zhang, Yakui Lei, Linwei Yu, Robert Zierold, and Robert H. Blick

(10 + 5 pages)

scientific reports

OPEN

Robust neuronal differentiation of human iPSC-derived neural progenitor cells cultured on densely-spaced spiky silicon nanowire arrays

Jann Harberts[1✉], Malte Siegmund[1], Matteo Schnelle[1], Ting Zhang[2], Yakui Lei[2], Linwei Yu[2], Robert Zierold[1✉] & Robert H. Blick[1,3]

Nanostructured cell culture substrates featuring nanowire (NW) arrays have been applied to a variety of basic cell lines and rodent neurons to investigate cellular behavior or to stimulate cell responses. However, patient-derived human neurons—a prerequisite for studying e.g. neurodegenerative diseases efficiently—are rarely employed due to sensitive cell culture protocols and usually long culturing periods. Here, we present human patient induced pluripotent stem cell-derived neurons cultured on densely-spaced spiky silicon NW arrays (600 NWs/ 100 μm^2 with NW lengths of 1 μm) which show mature electrophysiological characteristics after only 20 days of culturing. Exemplary neuronal growth and network formation on the NW arrays are demonstrated using scanning electron microscopy and immunofluorescence microscopy. The cells and neurites rest in a fakir-like settling state on the NWs only in contact with the very NW tips shown by cross-sectional imaging of the cell/ NW interface using focused ion beam milling and confocal laser scanning microscopy. Furthermore, the NW arrays promote the cell culture by slightly increasing the share of differentiated neurons determined by the quantification of immunofluorescence microscopy images. The electrophysiological functionality of the neurons is confirmed with patch-clamp recordings showing the excellent capability to fire action potentials. We believe that the short culturing time to obtain functional human neurons generated from patient-derived neural progenitor cells and the robustness of this differentiation protocol to produce these neurons on densely-spaced spiky nanowire arrays open up new pathways for stem cell characterization and neurodegenerative disease studies.

Human induced pluripotent stem cells (iPSCs) hold a huge potential for clinical research and application since for example ethical controversies of embryonic stem cells and limited availability of primary human cells required for e.g. high-throughput drug screens are overcome[1]. Furthermore, human pathophysiological conditions including neurodegenerative diseases like Alzheimer's or Parkinson's can be studied more efficiently by patient-specific iPSCs[2]. The broad availability of human cells for drug development also reduces the high failure rate of clinical translation caused by differences of disease-associated pathways between human and animal cells[3]. At present, all major brain cell types can now be differentiated from iPSCs, and both neuroscience research and clinical translation is facilitated by increasingly complex co-cultures, organoid systems, and blood-brain barrier models[4,5]. The cellular identity of iPSC-derived cell types is usually assessed by quantitative real-time polymerase chain reaction or immunocytochemistry. Additionally, the functional state of the iPSC-derived neurons is characterized by electrophysiological measurements combined with standard compounds which block key receptors, ion channels, and transporters[6]. By default, planar Petri dishes and multiwell plates are used to perform such characterization experiments. However, novel strategies to investigate iPSC-derived cell types could be explored by employing micro- and nanostructured functionalized biocompatible (semi-conductor) materials as cell culture substrates[7,8].

[1]Center for Hybrid Nanostructures, Universität Hamburg, Luruper Chaussee 149, 22761 Hamburg, Germany. [2]School of Electronics Science and Engineering, Nanjing University, Nanjing 210093, China. [3]Material Science and Engineering, College of Engineering, University of Wisconsin-Madison, Madison, WI 53706, USA. ✉email: jann.harberts@chyn.uni-hamburg.de; robert.zierold@chyn.uni-hamburg.de

The influence of the substrate's chemical and topological properties on biological cells has been investigated for example with respect to adhesion, proliferation, viability, migration, and guiding of seeded cells[9–13]. In this context, so-called nanowire (NW) arrays which feature upright arranged high aspect ratio nanostructures play an increasingly important role[14,15]. By adjusting the length and diameter of the NWs as well as the array pitch, the interaction between cell and NWs can be tuned and different settling regimes have been modeled by Buch-Månson *et al.*[16]. Biological parameters such as cellular growth, viability, morphology, adhesion, and mechanotransduction machinery can be influenced[17–21], while electrophysiological properties are maintained[22]. Furthermore, NW arrays have been used to measure mechanical cell properties[23], to interact with the cell's nucleus[24], to constrain cell movement and spreading[25,26], or to direct cell polarization such as the outgrowth of neurites[27,28]. Apart from passive applications, NW arrays have been employed to incorporate an executing interaction such as cell transfection[29], drug delivery[30,31] as well as electrical stimulation and sensing[32]. Moreover, integrated *p-n* junctions or the capability of NWs to guide or to emit light might be used for photo-current stimulation[33,34] as well as for biosensing[35,36] and potentially in optogenetics[37].

The majority of the existing studies employ only conventional human cell lines (*e.g.* HEK293, HeLa) or primary neurons from rodents which limits the pertinence of these studies for instance to address human neurodegenerative diseases[38,39]. Indeed, Liu *et al.* were able to demonstrate, that human iPSC-derived cortical neurons can be cultured on small-scale NW arrays with an area of $32\times32\ \mu m^2$[32], but a drawback of the differentiation protocol was the requirement to culture for at least 65 days to create functional neurons. Aside from that, neuronal differentiation might be altered on large-scale NW arrays, as it has been shown that NW forests can influence intracellular signaling, gene regulation, or basic cell differentiation[40–43]. Moreover, material cues have been discussed as a potent regulator for epigenetics and stem cell function[44]. Thus, changes during terminal differentiation of human iPSCs into neurons might emerge as well on NW arrays and the very same substrate could potentially become useless for most of the promising applications introduced before. Recently, we demonstrated that human iPSC-derived neurons can be generated within 30 days even on large-scale silicon nitride NW arrays with no difference to planar control[45].

In this work, we present human iPSC-derived neurons cultured on densely-spaced spiky silicon NW arrays with electrophysiologically mature properties in less than 20 days. Additionally, the share of MAP2 positive cells is not only maintained but slightly increased by reducing the number of undifferentiated neural progenitor cells which are used as an intermediate step of the neuronal differentiation. Immunofluorescence (IF) widefield microscopy is used to quantify the cell viability and the number of progenitors and neurons. The cell/NW interface is investigated by scanning electron microscopy (SEM), focused ion beam (FIB) milling as well as confocal laser scanning microscopy (CLSM). A fakir-like interaction is revealed in which the cells only interact with the NW tips. Electrophysiological characteristics are identified with patch-clamp measurements in both current- and voltage-clamp mode and prove the functionality of the neurons. We believe that the short culturing period to generate functional human iPSC-derived neurons and the use of silicon—the standard semiconductor material—for the NW arrays make our platform a promising candidate for future large-scale and high-throughput applications such as retina implants[46] or neuronal interfaces[47] and to study pharmacological interventions and cell-intrinsic pathophysiological processes[48].

Results and discussion

A top view SEM image of the silicon NW arrays used to culture the human iPSC-derived neurons is shown in Fig. 1a. The about 1 μm long NWs feature a gradually tapered shape resulting in a spiky tip of about 30 nm. The nanostructures are randomly distributed on the substrate with a density of about 600 NWs/100 μm^2 which corresponds to a high NW density compared to other NW substrates used in the field[16]. Random arrangement and random angle orientation are caused by the self-assembling growth process[49,50]. Choosing silicon as the basic element for the substrates not only allows for accessing years of experience in nanofabrication in science and industry but also represents the promising nature of nanoscale silicon for subcellular interfaces[51].

The protocol to generate the human iPSC-derived neurons used in this study employs proliferating small molecule neural progenitor cells (smNPCs) as an intermediate differentiation step and is based on work from Reinhardt *et al.*[52]. The smNPCs are maintained in regular well plates coated with Matrigel and are pre-differentiated for 6 days before plating onto the silicon NW arrays or glass coverslips for control (both also coated with Matrigel). First, we investigated the neuronal growth on the NW samples using SEM imaging (Fig. 1b). Overall, the observed neuronal network formation is similar to literature as neurons are growing both separately and in clusters, and neurites build a dense grid in between the neurons[18,22]. The tilted close-up views in Fig. 1c,d display the soma of a neuron and a neurite growing on the NWs. Notably, the cell material is barely in contact with the substrates and only touches the very tip of the NWs. Such a fakir-like settling state on a bed-of-nails was to be expected due to the high NW density[16]. Furthermore, strong interaction with the substrate in form of multiple extensions from the cell soma has been reported before[53].

Cross-sectional images prepared by FIB milling and CLSM were used to support the previous statements regarding the cell's interaction with the substrate (Fig. 2a–e). Figure 2a displays an overview image of the neuron after FIB milling. The close-up views on the cell soma and a neurite in panel b and c clarify that the cell membrane is hovering approximately 1 μm above the substrate bottom which corresponds to the average NW length. Comparable behavior of cells cultured on high NW densities has been reported before by using FIB-SEM imaging[54]. A similar conclusion can be drawn from z-stacks prepared by CLSM imaging. Figure 2d displays a top view of a neuron cultured on a NW substrate. The cell membrane has been labeled using a membrane stain (false-colored in red). The dashed line indicates the position of the cross section in the z-x plane shown in Fig. 2e at which the cross section was prepared from a stack of images at different z-levels. The reflection of the NWs is false-colored in yellow and originates only from the NWs but not from the Matrigel as demonstrated by
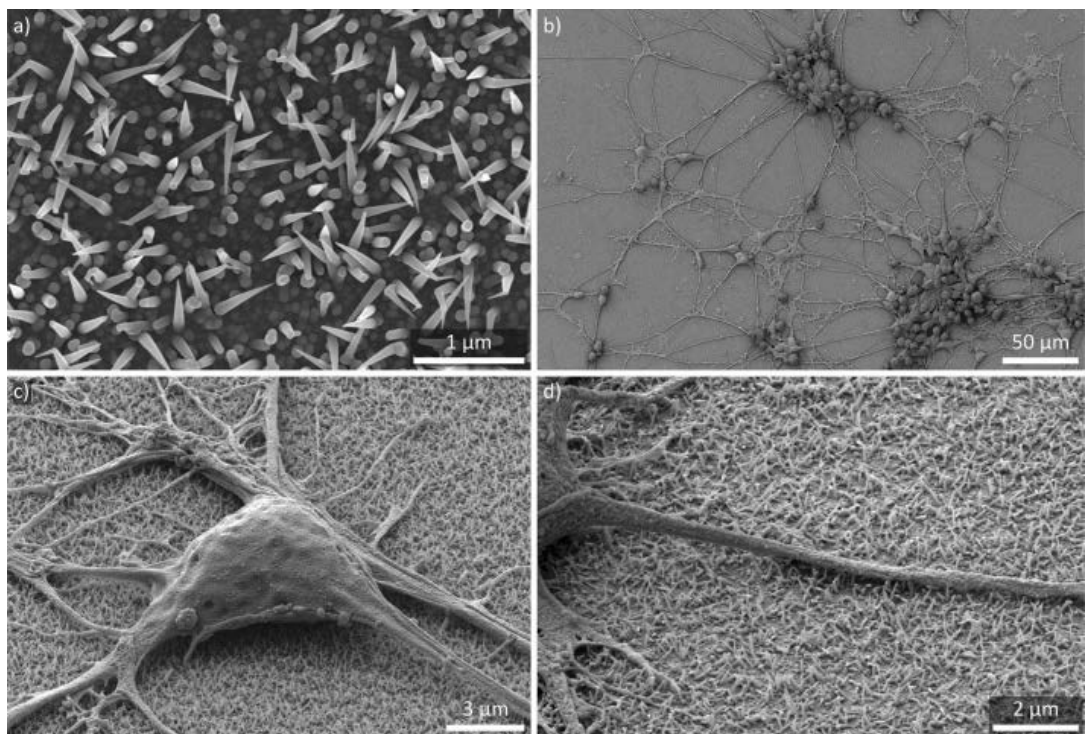
Figure 1. SEM images of a NW sample and human iPSC-derived neurons cultured on NWs. (**a**) Top view of the utilized NW substrate. The NW density is about 600 NWs/100 μm^2. The mean NW length is about 1 μm featuring a gradually tapered shape. (**b**) Top view of a neuronal network formed by human iPSC-derived neurons on a NW substrate. (**c**) Cell soma of a human iPSC-derived neuron cultured on NWs. Tilt is 54°. (**d**) Close-up view of a neurite growing on NWs. Tilt is 54°.
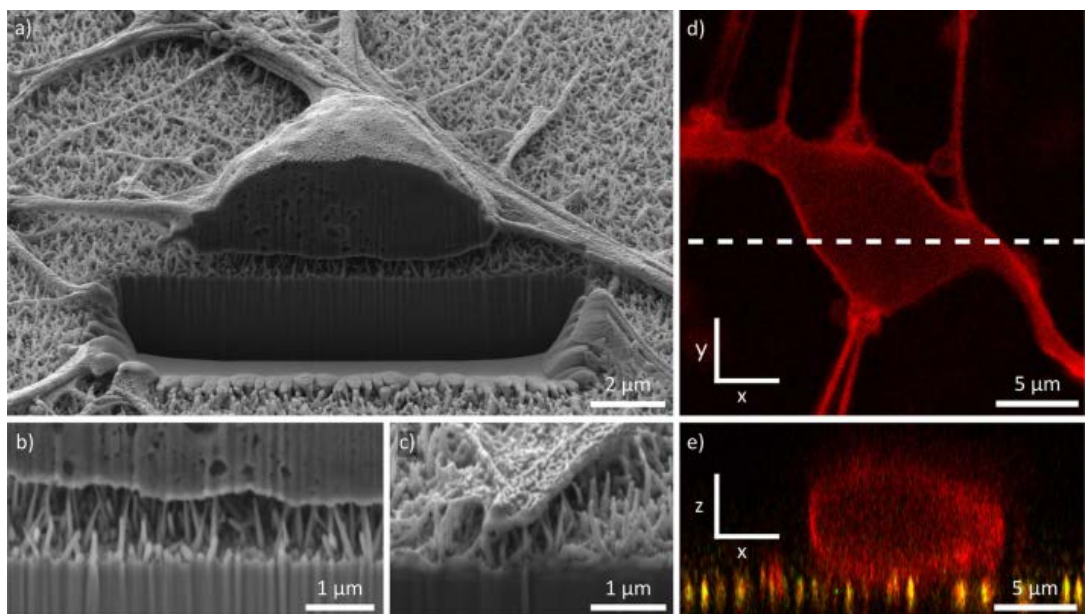

Figure 2. Cross sections prepared by FIB milling and CLSM. (**a**) Cross-sectional SEM image of the cell soma prepared by FIB milling. Tilt is 54°. (**b**, **c**) Close-up SEM images of the NW/cell membrane and NW/neurite interface, respectively. Both cell and neurite are hovering in a fakir like state on the NW tips. The distance to the substrate bottom is approx. 1 μm–the mean length of the NWs. Tilt is 54°. (**d**) Top view of the cell soma imaged via CLSM. The cell membrane is false colored in red. The dashed line indicates the position of the cross section in (**e**). (**e**) Cross section of the cell soma (red) in the x-z plane reconstructed from z-stacks prepared by CLSM. The NW tips' reflections are false colored in yellow and are in direct contact with the cell membrane.
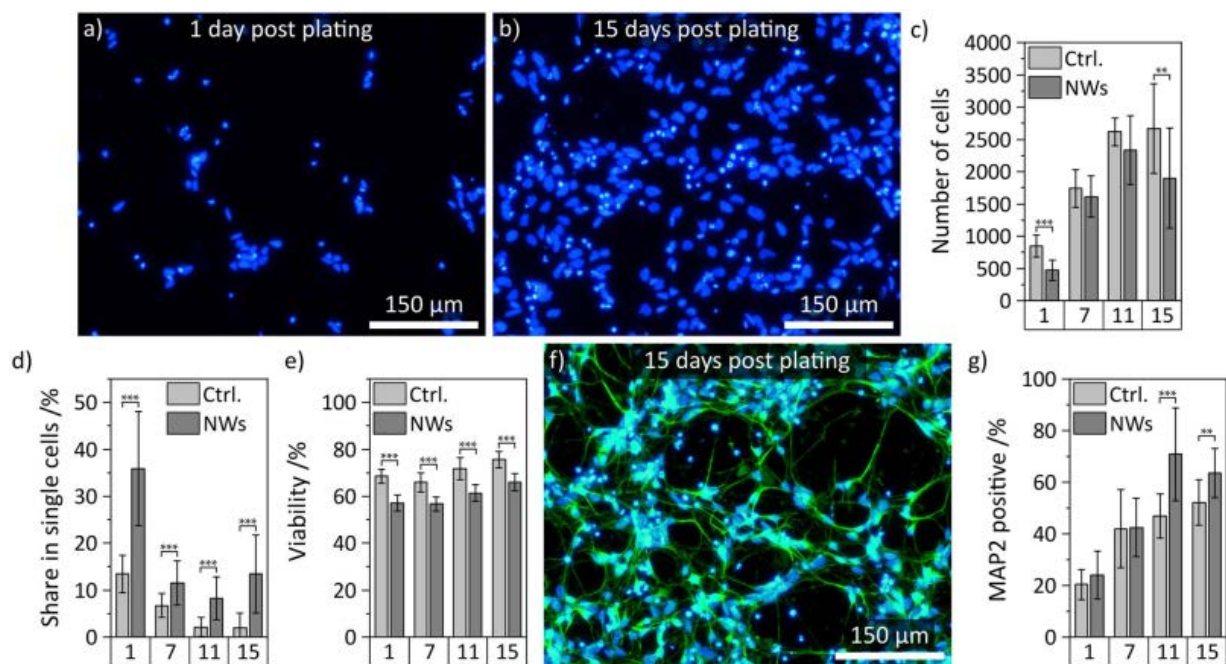
Figure 3. Analysis of cell number, cell viability and neuronal differentiation on NWs compared to planar control (1, 7, 11, and 15 days post plating). (**a**) and (**b**) Exemplary widefield microscopy images of cells 1 and 15 days post plating on NW substrates. The nuclei are labeled in blue using Hoechst 33342. (**c**) Quantification of the cell numbers per image 1, 7, 11, and 15 days after plating compared to control. (**d**) Share of cells not associated with a cell cluster of three or more cells. (**e**) Cell viability 1, 7, 11, and 15 days after plating compared to control. (**f**) Exemplary immunofluorescence image of human iPSC-derived neurons 15 days after plating. The neurons are labeled with MAP2 (green) and counterstained with Hoechst (blue). (**g**) Share in MAP2 positive cells 1, 7, 11, and 15 days after plating compared to control. All error bars are standard deviations (SDs). Statistical significances were calculated using a Mann-Whitney U test: $*P < 0.05$, $**P < 0.01$, $***P < 0.001$, *cf.* Table S1 of the supporting material.

imaging an uncoated NW sample (supporting Fig. S1). A corresponding image of a neuron on a control substrate is shown in the supporting material (Fig. S2). The cross-sectional reconstruction confirms the close contact of the cell membrane to the NWs and a fakir-like settling state which is in accordance with literature that studied cells on high-density NW arrays with CLSM[45]. Additionally, we tested for focal adhesions (FAs) to check for interactions with the substrate after long-term culture (11 days after plating). In this regard, we see no influence of the substrate compared to control which demonstrates a generally equivalent culturing environment for our human iPSC-derived neurons (Fig. S3, paxillin positive area (FAs) normalized to the area covered with cells (f-actin/cytoskeleton *via* phalloidin)) and is in agreement with literature for high NW densities[26]. Yet, cell culture substrates with Si nanoneedles have been reported to reduce the formation of FAs in short-term culture (24 h) of mesenchymal stem cells[55]. Nonetheless, the close contact between cell and NW, and the conical shape of silicon nanostructures are able to facilitate cell transfection[29] and delivery of biological payloads[30], respectively, as shown in recent work using basic cell lines and mesenchymal stem cells. We believe that comparable applications could also be adapted to our neurons to introduce new pathways in stem cell research.

In the next step, we analyzed the cellular outgrowth using (immuno-) fluorescent labeling and widefield microscopy. Six days pre-differentiated smNPCs were transferred to the NW substrates and snapshots of the neuronal development were taken 1, 7, 11, and 15 days after seeding. Figures 3a,b display exemplary images of Hoechst 33342-stained cell nuclei 1 and 15 days post plating. The total cell number increased significantly over time since terminal neuronal differentiation is a gradual process and part of the cell population is still proliferating. We quantified the increase of the cell numbers and compared the results to planar control (Fig. 3c). The number of cells approximately quadruples within 11 days until it reaches a plateau. The plateauing cell numbers on NWs are slightly smaller in comparison to the control but only the final cell number on NWs–in mean about 2000 and 2500 cells per image, respectively–is significantly different. However, a reduced cell number is overall in agreement with literature reporting on reduced cell proliferation on high-density NW arrays[25]. A visual inspection of the cell spreading on NWs compared to control depicts a considerable increase in cluster formation on control substrates (supplements: Fig. S4). Quantification of the cell clusters using a *Density-Based Spatial Clustering of Applications with Noise* (DBSCAN) algorithm validates the intuitive conclusion and shows that the share of single cells is significantly higher on NW substrates compared to control (*e.g.* about 35% and 13% at 1 DIV, respectively, Fig. 3d). One cause for cluster formation is cell movement and thus, hindered cell movement on the nanostructures is indicated by the increased share in single cells on NWs which is sustained at 7, 11, and 15 DIV. Impaired cell mobility has been described before in literature for cells cultured on NW arrays[19]. The absolute

shares of cells in clusters, however, reduce over time on both types of substrates due to continuing proliferation which generates additional cell clusters. The mean cell viability of about 60% on NW arrays is stable over time (*cf.* Fig. 3e) which is in good agreement with literature where high-density NW arrays have no detrimental effect on cell viability[17]. The slight increase in cell viability with further culturing time is reasonable since new vital cells are produced during proliferation. Compared to the control, the cell viability on NWs is lower since fewer new vital cells are produced as described earlier. In addition, we studied the neuronal differentiation of the smNPCs into neurons by IF microscopy. Figure 3f illustrates an exemplary recording of neurons 15 days post plating labeled with an anti-microtubule-associated protein 2 marker (MAP2, green) to identify neuronal phenotype and Hoechst as counterstain (blue). Similar micrographs from a control substrate and 1, 7, and 11 DIV post plating on NWs are available in the supporting material (Fig. S5). As priorly shown via SEM, an intricate neuronal network is developed on the NW arrays. Next, we determined the share of MAP2 positive vital cells 1, 7, 11, and 15 days post plating shown in Fig. 3g. Within this period, the ratio of MAP2 positive cells on NWs increases from about 20% to 60%, which is higher than on control substrates (approx. 50%). The higher percentage in neurons on NW samples could be explained by the slightly reduced proliferation of remaining smNPCs producing new undifferentiated cells. As a result, the smNPCs not only differentiate equally on NWs but also the NWs have a supportive effect to increase the share of terminally differentiated cells. Positive influence on differentiation has also been described in the literature where NW arrays enhanced differentiation *e.g.* for human embryonic stem cells toward definitive endoderm or neuron-like differentiation of mesenchymal stem cells[42,43]. Furthermore, we quantified the neuronal networks between MAP2 positive cells to evaluate the neurite health (supporting Fig. S6). The total network length per image increases from about 10 mm on day 1 to a steady value of 70 mm at days 11 and 15 where neurons cultured on NWs as well as on control show similar network sizes (panel a). Over time, the mean neurite length of individual neurites is slightly reduced on both NWs and control from about 120 μm to 80 μm (panel b) since the MAP2 positive cells become denser and neurites interlink more likely with other neurons. To conclude, even if the cell number and the viability on NW samples are slightly suppressed compared to planar control, the reduced amount of cell clusters and the larger portion of neurons renders the combination of silicon nanowire substrates with neuronal differentiation of smNPCs a promising approach for studying artificial neuronal networks.

Finally, the electrophysiology and functionality of the neurons were tested using the patch clamping technique (Fig. 4a–e). The overall healthy state of the neurons cultured on NWs is validated by stable resting membrane potentials (RMPs) of −51.4 ± 6.1 mV shown in Fig. 4a. This value is similar to the control (no statistical significance, Mann-Whitney U test: P > 0.05, *cf.* Table S2) and normal or even above average compared to other human iPSC-derived neurons[45,52,56,57]. Moreover, the cell sizes including neuronal extensions on NWs and control are equal which is indicated by consistent membrane capacitances (MCs) of 11.2 ± 3.7 pF and 11.1 ± 4.7 pF on control and NW substrates, respectively (also Fig. 4a, no statistical significance, P > 0.05, *cf.* Table S2). In addition, the MCs are in accordance with literature[56,58,59]. The accurate interplay of sodium and potassium ion channels is approved by recordings of the membrane currents at different voltages (−70 to +30 mV, 10 mV steps) which show characteristic early-inward and late-outward currents (Fig. 4b). The peak currents normalized to the MC were plotted against the applied voltage (Fig. 4c) and are comparable to the control measurements and literature[4,52,59]. Neuronal identity is confirmed by recordings of action potentials (APs) evoked by current injection shown in Fig. 4d. AP amplitude (67.0 ± 8.6 mV), AP threshold (− 20.4 ± 4.0 mV), afterhyperpolarization (AHP, 15.1 ± 5.9 mV), and AP duration (3.3 ± 0.8 ms) match the control (Fig. 4e, no statistical significance, all P > 0.05, *cf.* Table S2) and are in agreement with other human iPSC-derived neurons in literature[56,57,59].

In summary and conclusion, the human iPSC-derived neurons cultured on the densely-spaced spiky silicon NW substrates show excellent electrophysiological properties within only 20 days of differentiation despite the challenging substrate topology. The large-scale formation of neuronal networks on the NWs which is equal to control allows for novel approaches to study network properties under artificial constraints. Note, that the share of neurons is not only equal to control but even increased by 20% and thus would enhance the efficacy of future studies. The spiky shape of the nanowires renders the substrate suitable for the delivery of biomolecules or genes: such applications have already been shown using basic cell types like human umbilical vein endothelial cells (HUVECs) or human mesenchymal stem cells (hMSCs)[21,30,55] and establishing more advanced cell types in the community would help to increase the clinical impact of the field. Moreover, the broad availability of silicon and many years of experience in both science and industry make the material a great candidate for large-scale and high-throughput purposes in neurodegenerative disease studies or pharmacological drug screenings. Thus, we believe that our findings are an excellent starting point for further studies using biological metamaterials featured by high aspect ratio nanostructured surfaces[60].

Methods

Nanowire growth and sample preparation. The NW growth was previously described in Misra *et al.* and Zhang *et al.*[49,50]. In short: The NWs were grown on top of ZnO:Al coated silicon wafers. In the plasma-assisted VLS growth process, the growth of NWs is mediated by Sn nanoparticles, and the density of Sn nanoparticles can be controlled either by varying the initial thickness of the metal or by changing the parameters of H_2 plasma (to reduce the oxide layer and to form tiny catalyst droplets). Therefore, prior to loading into the PECVD chamber, Sn layers with nominal thicknesses from 1 nm to 5 nm were thermally evaporated on the substrates. Then, the Sn layers were exposed to H_2 plasma for 5 min at 180 °C, to transform them into separate Sn droplets. The chamber pressure, the RF power density and the flow rate were fixed at 600 mTorr, 50 mW/cm², and 20 sccm, respectively. Next, 6 sccm of silane (SiH_4) and 1.8 sccm of trimethylboron (1% TMB diluted in H_2) were introduced and the substrate temperature was raised to 400 °C to initiate the growth of NWs activated by the plasma, followed by a H_2 plasma etching to remove the remnant of Sn droplets. Typically, NWs grew around
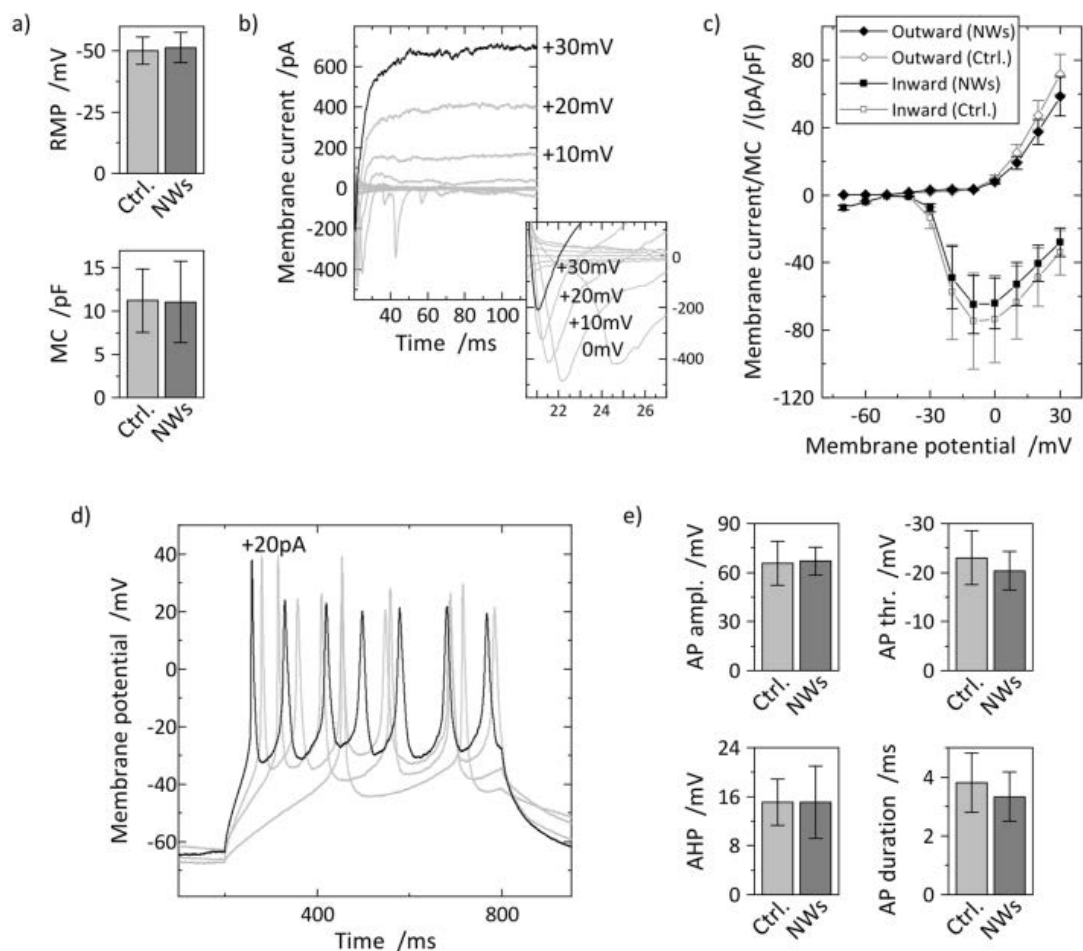
Figure 4. Electrophysiological characterization of human iPSC-derived neurons on NW substrates compared to control. (**a**) Quantification of passive membrane properties: resting membrane potential (RMP) and membrane capacitance (MC) of neurons on NWs and control. (**b**) Exemplary traces of early-inward (negative peaks) and late-outward currents (constant positive currents) of neurons cultured on NW substrates recorded in voltage-clamp mode with voltage steps of 10 mV from –70 to +30 mV. Inset: Zoom into early-inward currents. (**c**) Peak inward/outward currents normalized by MC plotted against membrane potential compared to control. (**d**) Typical action potential (AP) traces recorded from neurons on NWs. APs were stimulated by current injections from 5 to 20 pA in 5 pA steps. The firing frequency increases with increasing amplitude of the stimulus. (**e**) Analysis of the AP kinetics: AP amplitude from threshold to peak (AP ampl.), AP threshold (AP thr.), after hyperpolarization (AHP, overshoot after AP), and full width half maximum of the APs (AP duration). n(NWs) = 7, n(control) = 10, error bars are SDs, no statistical significances (Mann-Whitney U test: all P > 0.05, *cf.* Table S2 in the supporting material).

1 μm long after 15 min deposition, showing a gradually tapered shape of around 80 nm diameters at their bases and less than 30 nm at their tips. NW and control samples (glass coverslips) were treated with an oxygen plasma, sterilized in 70% ethanol, and coated overnight at room temperature or for 1 h at 37 °C with Matrigel (Corning 354263, 1:150 in Knock Out DMEM (Life Technologies)).

Cell culture. The human induced pluripotent stem cell (iPSC)-derived neurons were differentiated from human iPSC-derived small molecule neural progenitor cells (smNPCs)[52]. The neural progenitor cells were grown in basic N2/B27 medium (1:1 mixture of DMEM/F12 and Neurobasal medium, 1% penicillin/strep-tomycin/glutamine (100X), 1% B27 supplement without vitamin A (50x), 0.5% N2 supplement (100x), Life Technologies, Carlsbad, CA, USA) supplemented with 100 μM ascorbic acid (AA, Sigma-Aldrich, St. Louis, MO, USA), 0.5 μM SAG (Biomol, Hamburg, Germany), and 3 μM CHIR 99021 (Axon MedChem, Groningen, Netherlands). Differentiation was initiated by patterning medium (basic N2/B27 medium supplemented with 100 μM AA, 0.5 μM SAG, 1 ng/mL GDNF (PeproTech, Rocky Hill, NJ, USA), 1 ng/mL BDNF (PeproTech)) for 6 days and terminated in maturation medium (N2/B27 basic medium supplemented with 100 μM AA, 2 ng/mL GDNF, 2 ng/mL BDNF, 1 ng/mL transforming growth factor-β3 (TGF-β3, PeproTech), 100 μM dbcAMP (Sigma-Aldrich). The cells were kept at 37 °C with 5% CO_2 in a humidified atmosphere. 1×10^6 smNPCs were

seeded to Matrigel-coated 6-well plate wells and kept in patterning medium for 6 days in vitro (DIV). Cells were split 1:5 using accutase (Sigma-Aldrich), seeded into 12-well plates containing the NW and control samples, and cultivated in maturation medium until the experiment. SEM imaging, confocal microscopy, and patch clamping were conducted 18–20 days after initiation of the differentiation. IF imaging was performed 1, 7, 11, and 15 days after plating on the NW and control samples. Data was collected from four independent differentiations from passages 22/24 and 24/26 from two thawings of vials containing the smNPCs. Two differentiations per experiment were used.

Ethics declarations. All experiments were conducted in accordance with the ethical statement in Reinhardt *et al.*[52].

Confocal microscopy. A Leica TCS SP8 in upright configuration (488 and 552 nm wavelength laser sources) was used for confocal microscopy. Cell membranes were stained in advance with a staining kit (neurite outgrowth staining kit, ex/em: 555/565 nm, Thermo Fisher). According to the manufacturer's protocol, solutions were diluted in Dulbecco's phosphate-buffered solution (DPBS), and cells were incubated in a 1× dye mixture (4% Formaldehyde added) for 15 min at 37 °C. The z-stacks were acquired in a 1× background suppression solution with a slicing distance of 172 nm. Processing and analysis of the z-stacks were conducted with the Leica software (Leica Application Suite X, v2.0.2.15022) or ImageJ/Fiji (v1.53c, https://downloads.imagej.net/fiji/archive/20191216-2110/fiji-win64.zip). For visualization, images were optimized in contrast, brightness, and false color, if applicable.

Immunofluorescence staining. Samples were rinsed once with DPBS (Sigma-Aldrich), fixed in formaldehyde (4% in DPBS, Sigma-Aldrich) for 10 min, and again rinsed three times with DPBS. Covered with DPBS, samples were stored until imaging at 4 °C. Fixed cells were permeabilized and blocked for 45 min with 3% BSA (bovine serum albumin, Carl Roth, Karlsruhe, Germany), 0.1% Tween (Tween 20, Sigma-Aldrich), and 0.1% Triton-X (Triton X 100, Carl Roth) in DPBS prior to incubation with anti-MAP2 (microtubule-associated protein 2) primary antibodies (0.1% BSA, MAP2 1:500 in DPBS, mouse anti-MAP2 monoclonal antibody [Y113], Invitrogen, Cat. No. 13-1500) overnight at 4 °C. The cells were washed twice with DPBS and incubated with Alexa fluorophore-conjugated anti-mouse primary antibodies (0.1% BSA, Alexa 488 1:1000 in DPBS, goat anti-mouse IgG-Alexa Flour 488 polyclonal antibody, Invitrogen, Cat. No. A32723) for 1 h in the dark. Stained cells were kept in the dark and washed three times with Tween (0.05% in DPBS) for 5 min. The second washing step contained Hoechst 33342 as counterstain. If not further noted, all steps were conducted at room temperature. Per sample and point in time, 8–20 images were analyzed. The covered sample area per image size was 1282 μm × 853 μm. Images were analyzed using a custom analysis pipeline for CellProfiler 4.1.3 (https://cellprofiler-releases.s3.amazonaws.com/CellProfiler-Windows-4.1.3.exe). Hoechst images were used to identify nuclei. Vital cells were used to mask the MAP2 channel to identify marker positive cells. Images of identified vital cells were exported and clustering was analyzed using the SSIDC Cluster Indicator in the BioVoxxel toolbox in ImageJ/Fiji (v1.53c, https://downloads.imagej.net/fiji/archive/20191216-2110/fiji-win64.zip). Data was analyzed and graphs were generated with Origin (v.2021). In total, approx. 230.000 cells were analyzed.

Viability assay. Viability was estimated in the CellProfiler pipeline by discrimination of bright nuclei and medium bright nuclei after Hoechst 33342 stain for the representation of dead and living cells, respectively. The procedure results in similar values with no statically significant differences (Mann-Whitney U test) compared to a test using Calcein AM and Propodium Iodide shown in the supporting information (Fig. S7).

Scanning electron microscopy and focused ion beam milling. High-resolution images and cross sections were produced using scanning electron microscopy and focused ion beam milling with a Zeiss Crossbeam 550. Cells were prepared by fixation (4% Formaldehyde in DPBS, 10 min) and dehydration *via* a stepwise ethanol exchange. The samples were then critical point dried using Tousimis' Autosamdri-815 and a 20 nm gold layer was sputter-coated to avoid charging effects.

Electrophysiology. The patch-clamp setup consisted of an upright Nikon Eclipse FN1 microscope (objective: Nikon CFI TU Plan EPI ELWD 50× N.A. 0.60/W.D. 11.00 mm) and a HEKA EPC 10 USB patch-clamp amplifier with a red star headstage for trace recording. Patch-clamp pipettes (diameter: approx. 950 nm, resistance: 5–7 MΩ) were manufactured from borosilicate glass capillary blanks (GB150T-8P, Science Products) using a Sutter P-2000 pipette puller. Polishing was conducted with a CPM-2 microforge (ALA Scientific Instruments). Samples were rinsed three times and covered with bath solution (140 mM NaCl, 2.4 mM KCl, 1.3 mM MgCl$_2$, 2.5 mM CaCl$_2$, 10 mM 4-(2-hydroxyethyl)-1-piperazineethanesulfonic acid (HEPES), 10 mM D-glucose, pH 7.4) and pipettes were filled with pipette solution (125 mM potassium gluconate (K-gluconate), 10 mM NaCl, 1 mM Triethylene glycol diamine tetraacetic acid (EGTA), 4 mM magnesium ATP (MgATP), 10 mM HEPES, 10 mM D-glucose, pH 7.4). Patch clamping was conducted at room temperature. The Patch Master V2x80 software was used for data processing. A Bessel low-pass filter was set to 2.9 kHz and the capacitance and series-resistance were automatically compensated. Electrophysiological parameters were recorded and determined as follows. RMP: in current-clamp mode by keeping cells with zero current. MC: directly determined by the patch-clamp software. For APs, the first AP of an AP train at rheobase current was analyzed–AP height: threshold to peak. AHP: threshold to minimum after AP. AP threshold: membrane potential where the second derivative

becomes different from zero (determined with Origin). AP duration: full-width half-maximum of the AP. Number of cells analyzed: n(NWs) = 7, n(control) = 10.

References

1. Dolmetsch, R. & Geschwind, D. H. The human brain in a dish: The promise of iPSC-derived neurons. *Cell* **145**, 831–834. https://doi.org/10.1016/j.cell.2011.05.034 (2011).
2. Reddy, A. P., Ravichandran, J. & Carkaci-Salli, N. Neural regeneration therapies for Alzheimer's and Parkinson's disease-related disorders. *Biochimica et Biophysica Acta Mol. Basis Dis.* **1866**, 165506. https://doi.org/10.1016/j.bbadis.2019.06.020 (2020).
3. Leenaars, C. H. C. *et al.* Animal to human translation: a systematic scoping review of reported concordance rates. *J. Transl. Med.* **17**, 223. https://doi.org/10.1186/s12967-019-1976-2 (2019).
4. Smits, L. M. *et al.* Modeling Parkinsons disease in midbrain-like organoids. *npj Parkinsons Dis.* **5**, 5. https://doi.org/10.1038/s41531-019-0078-4 (2019).
5. Appelt-Menzel, A. *et al.* Human iPSC-derived blood-brain barrier models: Valuable tools for preclinical drug discovery and development? *Curr. Protoc. Stem Cell Biol.* **55**, e122. https://doi.org/10.1002/cpsc.122 (2020).
6. Bardy, C. *et al.* Predicting the functional states of human iPSC-derived neurons with single-cell RNA-seq and electrophysiology. *Mol. Psychiatry* **21**, 1573–1588. https://doi.org/10.1038/mp.2016.158 (2016).
7. Armentano, I. *et al.* Nanostructured biopolymer-based materials for regenerative medicine applications. *Curr. Org. Chem.* **22**, 1193–1204. https://doi.org/10.2174/1385272822666180517095551 (2018).
8. Lestrell, E., O'Brien, C. M., Elnathan, R. & Voelcker, N. H. Vertically aligned nanostructured topographies for human neural stem cell differentiation and neuronal cell interrogation. *Adv. Ther.* **2100061**, https://doi.org/10.1002/adtp.202100061 (2021).
9. Ning, D. *et al.* Mechanical and morphological analysis of cancer cells on nanostructured substrates. *Langmuir* **32**, 2718–2723. https://doi.org/10.1021/acs.langmuir.5b04469 (2016).
10. Koitmäe, A. *et al.* Approaching integrated hybrid neural circuits: Axon guiding on optically active semiconductor microtube arrays. *Adv. Mater. Interfaces* **3**, 1600746. https://doi.org/10.1002/admi.201600746 (2016).
11. Koitmäe, A. *et al.* Designer neural networks with embedded semiconductor microtube arrays. *Langmuir* **34**, 1528–1534. https://doi.org/10.1021/acs.langmuir.7b03311 (2018).
12. Fendler, C. *et al.* Neurite guidance and neuro-caging on steps and grooves in 2.5 dimensions. *Nanoscale Adv.* **2**, 5192–5200. https://doi.org/10.1039/D0NA00549E (2020).
13. Leclech, C. & Villard, C. Cellular and subcellular contact guidance on microfabricated substrates. *Front. Bioeng. Biotechnol.* **8**, 1198. https://doi.org/10.3389/fbioe.2020.551505 (2020).
14. Elnathan, R., Kwiat, M., Patolsky, F. & Voelcker, N. H. Engineering vertically aligned semiconductor nanowire arrays for applications in the life sciences. *Nano Today* **9**, 172–196. https://doi.org/10.1016/j.nantod.2014.04.001 (2014).
15. Bonde, S. *et al.* Exploring arrays of vertical one-dimensional nanostructures for cellular investigations. *Nanotechnology* **25**, 362001. https://doi.org/10.1088/0957-4484/25/36/362001 (2014).
16. Buch-Månson, N. *et al.* Towards a better prediction of cell settling on nanostructure arrays-simple means to complicated ends. *Adv. Func. Mater.* **25**, 3246–3255. https://doi.org/10.1002/adfm.201500399 (2015).
17. Bonde, S. *et al.* Tuning InAs nanowire density for HEK293 cell viability, adhesion, and morphology: Perspectives for nanowire-based biosensors. *ACS Appl. Mater. Interfaces* **5**, 10510–10519. https://doi.org/10.1021/am402070k (2013).
18. Piret, G., Perez, M.-T. & Prinz, C. N. Neurite outgrowth and synaptophysin expression of postnatal CNS neurons on GaP nanowire arrays in long-term retinal cell culture. *Biomaterials* **34**, 875–887. https://doi.org/10.1016/j.biomaterials.2012.10.042 (2013).
19. Li, Z. *et al.* Single cell analysis of proliferation and movement of cancer and normal-like cells on nanowire array substrates. *J. Mater. Chem. B* **6**, 7042–7049. https://doi.org/10.1039/C8TB02049C (2018).
20. Li, Z., Persson, H., Adolfsson, K., Oredsson, S. & Prinz, C. N. Morphology of living cells cultured on nanowire arrays with varying nanowire densities and diameters. *Sci. China Life Sci.* **61**, 427–435. https://doi.org/10.1007/s11427-017-9264-2 (2018).
21. Hansel, C. S. *et al.* Nanoneedle-mediated stimulation of cell mechanotransduction machinery. *ACS Nano* **13**, 2913–2926. https://doi.org/10.1021/acsnano.8b06998 (2019).
22. Harberts, J. *et al.* Culturing and patch clamping of Jurkat T cells and neurons on Al_2O_3 coated nanowire arrays of altered morphology. *RSC Adv.* **9**, 11194–11201. https://doi.org/10.1039/C8RA05320K (2019).
23. Li, Z. *et al.* Cellular traction forces: A useful parameter in cancer research. *Nanoscale* **9**, 19039–19044. https://doi.org/10.1039/C7NR06284B (2017).
24. Hanson, L. *et al.* Vertical nanopillars for in situ probing of nuclear mechanics in adherent cells. *Nat. Nanotechnol.* **10**, 554–562. https://doi.org/10.1038/nnano.2015.88 (2015).
25. Persson, H., Li, Z., Tegenfeldt, J. O., Oredsson, S. & Prinz, C. N. From immobilized cells to motile cells on a bed-of-nails: Effects of vertical nanowire array density on cell behaviour. *Sci. Rep.* **5**, 18535. https://doi.org/10.1038/srep18535 (2015).
26. Buch-Månson, N. *et al.* Mapping cell behavior across a wide range of vertical silicon nanocolumn densities. *Nanoscale* **9**, 5517–5527. https://doi.org/10.1039/C6NR09700F (2017).
27. Piret, G. G., Perez, M.-T. & Prinz, C. N. Support of neuronal growth over glial growth and guidance of optic nerve axons by vertical nanowire arrays. *Appl. Mater. Interfaces* **7**, 7–11. https://doi.org/10.1021/acsami.5b03798 (2015).
28. Milos, F., Belu, A., Mayer, D., Maybeck, V. & Offenhäusser, A. Polymer nanopillars induce increased paxillin adhesion assembly and promote axon growth in primary cortical neurons. *Adv. Biol.* **5**, 2000248. https://doi.org/10.1002/adbi.202000248 (2021).
29. Chen, Y. *et al.* Cellular deformations induced by conical silicon nanowire arrays facilitate gene delivery. *Small* **15**, 1904819. https://doi.org/10.1002/smll.201904819 (2019).
30. Gopal, S. *et al.* Porous silicon nanoneedles modulate endocytosis to deliver biological payloads. *Adv. Mater.* **31**, 1806788. https://doi.org/10.1002/adma.201806788 (2019).
31. Tay, A. & Melosh, N. Nanostructured materials for intracellular cargo delivery. *Acc. Chem. Res.* **52**, 2462–2471. https://doi.org/10.1021/acs.accounts.9b00272 (2019).
32. Liu, R. *et al.* High density individually addressable nanowire arrays record intracellular activity from primary rodent and human stem cell derived neurons. *Nano Lett.* **17**, 2757–2764. https://doi.org/10.1021/acs.nanolett.6b04752 (2017).
33. Parameswaran, R. *et al.* Photoelectrochemical modulation of neuronal activity with free-standing coaxial silicon nanowires. *Nat. Nanotechnol.* **13**, 260–266. https://doi.org/10.1038/s41565-017-0041-7 (2018).
34. Liu, Z. *et al.* Photoelectric cardiac pacing by flexible and degradable amorphous Si radial junction stimulators. *Adv. Healthcare Mater.* **9**, 1901342. https://doi.org/10.1002/adhm.201901342 (2020).
35. Verardo, D. *et al.* Nanowires for biosensing: Lightguiding of fluorescence as a function of diameter and wavelength. *Nano Lett.* **18**, 4796–4802. https://doi.org/10.1021/acs.nanolett.8b01360 (2018).

36. Lard, M., Linke, H. & Prinz, C. N. Biosensing using arrays of vertical semiconductor nanowires: Mechanosensing and biomarker detection. *Nanotechnology* **30**, 214003. https://doi.org/10.1088/1361-6528/ab0326 (2019).
37. Chen, S. *et al.* Near-infrared deep brain stimulation via upconversion nanoparticle-mediated optogenetics. *Science* **359**, 679–684. https://doi.org/10.1126/science.aaq1144 (2018).
38. Chiappini, C. Nanoneedle-based sensing in biological systems. *ACS Sens.* **2**, 1086–1102. https://doi.org/10.1021/acssensors.7b00350 (2017).
39. Li, X. *et al.* Vertical nanowire array-based biosensors: Device design strategies and biomedical applications. *J. Mater. Chem. B* **8**, 7609–7632. https://doi.org/10.1039/D0TB00990C (2020).
40. Lou, H.-Y., Zhao, W., Zeng, Y. & Cui, B. The role of membrane curvature in nanoscale topography-induced intracellular signaling. *Acc. Chem. Res.* **51**, 1046–1053. https://doi.org/10.1021/acs.accounts.7b00594 (2018).
41. Liu, R. & Ding, J. Chromosomal repositioning and gene regulation of cells on a micropillar array. *ACS Appl. Mater. Interfaces* **12**, 35799–35812. https://doi.org/10.1021/acsami.0c05883 (2020).
42. Kim, H., Kim, I., Choi, H.-J., Kim, S. Y. & Yang, E. G. Neuron-like differentiation of mesenchymal stem cells on silicon nanowires. *Nanoscale* **7**, 17131–17138. https://doi.org/10.1039/C5NR05787F (2015).
43. Rasmussen, C. H. *et al.* Enhanced differentiation of human embryonic stem cells toward definitive endoderm on ultrahigh aspect ratio nanopillars. *Adv. Func. Mater.* **26**, 815–823. https://doi.org/10.1002/adfm.201504204 (2016).
44. Crowder, S. W., Leonardo, V., Whittaker, T., Papathanasiou, P. & Stevens, M. M. Material cues as potent regulators of epigenetics and stem cell function. *Cell Stem Cell* **18**, 39–52. https://doi.org/10.1016/j.stem.2015.12.012 (2016).
45. Harberts, J. *et al.* Interfacing human induced pluripotent stem cell-derived neurons with designed nanowire arrays as a future platform for medical applications. *Biomater. Sci.* **8**, 2434–2446. https://doi.org/10.1039/D0BM00182A (2020).
46. Tang, J. *et al.* Nanowire arrays restore vision in blind mice. *Nat. Commun.* **9**, 786. https://doi.org/10.1038/s41467-018-03212-0 (2018).
47. Fairfield, J. A. Nanostructured materials for neural electrical interfaces. *Adv. Func. Mater.* **28**, 1701145. https://doi.org/10.1002/adfm.201701145 (2018).
48. Rahong, S., Yasui, T., Kaji, N. & Baba, Y. Recent developments in nanowires for bio-applications from molecular to cellular levels. *Lab Chip* **16**, 1126–1138. https://doi.org/10.1039/C5LC01306B (2016).
49. Misra, S., Yu, L., Foldyna, M. & Roca i Cabarrocas, P. High efficiency and stable hydrogenated amorphous silicon radial junction solar cells built on VLS-grown silicon nanowires. *Sol. Energy Mater. Sol. Cells* **118**, 90–95. https://doi.org/10.1016/j.solmat.2013.07.036 (2013).
50. Zhang, S. *et al.* Coupled boron-doping and geometry control of tin-catalyzed silicon nanowires for high performance radial junction photovoltaics. *Opt. Express* **27**, 37248. https://doi.org/10.1364/OE.27.037248 (2019).
51. Acaron Ledesma, H. & Tian, B. Nanoscale silicon for subcellular biointerfaces. *J. Mater. Chem. B* **5**, 4276–4289. https://doi.org/10.1039/C7TB00151G (2017).
52. Reinhardt, P. *et al.* Derivation and expansion using only small molecules of human neural progenitors for neurodegenerative disease modeling. *PLoS ONE* **8**, e59252. https://doi.org/10.1371/journal.pone.0059252 (2013).
53. Kim, S.-M. *et al.* Strong contact coupling of neuronal growth cones with height-controlled vertical silicon nanocolumns. *Nano Res.* **11**, 2532–2543. https://doi.org/10.1007/s12274-017-1878-7 (2018).
54. Wierzbicki, R. *et al.* Mapping the complex morphology of cell interactions with nanowire substrates using FIB-SEM. *PLoS ONE* **8**, e53307. https://doi.org/10.1371/journal.pone.0053307 (2013).
55. Seong, H. *et al.* Size-tunable nanoneedle arrays for influencing stem cell morphology, gene expression, and nuclear membrane curvature. *ACS Nano* **14**, 5371–5381. https://doi.org/10.1021/acsnano.9b08689 (2020).
56. Xie, Y. *et al.* Reproducible and efficient generation of functionally active neurons from human hiPSCs for preclinical disease modeling. *Stem Cell Res.* **26**, 84–94. https://doi.org/10.1016/j.scr.2017.12.003 (2018).
57. Gunhanlar, N. *et al.* A simplified protocol for differentiation of electrophysiologically mature neuronal networks from human induced pluripotent stem cells. *Mol. Psychiatry* **23**, 1336–1344. https://doi.org/10.1038/mp.2017.56 (2018).
58. Harberts, J., Kusch, M., O'Sullivan, J., Zierold, R. & Blick, R. H. A temperature-controlled patch clamp platform demonstrated on Jurkat T lymphocytes and human induced pluripotent stem cell-derived neurons. *Bioengineering* **7**, 46. https://doi.org/10.3390/bioengineering7020046 (2020).
59. Harberts, J. *et al.* Toward brain-on-a-chip: Human induced pluripotent stem cell-derived guided neuronal networks in tailor-made 3D nanoprinted microscaffolds. *ACS Nano* **14**, 13091–13102. https://doi.org/10.1021/acsnano.0c04640 (2020).
60. Higgins, S. G. *et al.* High-aspect-ratio nanostructured surfaces as biological metamaterials. *Adv. Mater.* **32**, 1903862. https://doi.org/10.1002/adma.201903862 (2020).

Acknowledgements

Author contributions

Cell culture: J.H. supported by M.Si. and M.Sc.; SEM/FIB imaging: J.H.; IF imaging: J.H.; nanowire array preparation: T.Z., Y.L.; conceptualization: J.H., R.Z., L.Y., and R.H.B.; writing—original draft preparation: J.H.; writing—review and editing: J.H., M.Si., R.Z.; funding acquisition: L.Y., R.H.B. All authors reviewed the manuscript.

Funding

Competing interests

The authors declare no competing interests.

Additional information

Supplementary Information The online version contains supplementary material available at https://doi.org/10.1038/s41598-021-97820-4.

Correspondence and requests for materials should be addressed to J.H. or R.Z.

Reprints and permissions information is available at www.nature.com/reprints.

Publisher's note Springer Nature remains neutral with regard to jurisdictional claims in published maps and institutional affiliations.

Supporting information

Robust neuronal differentiation of human iPSC-derived neural progenitor cells cultured on densely-spaced spiky silicon nanowire arrays

Jann Harberts [1],*, Malte Siegmund [1], Matteo Schnelle [1], Ting Zhang [2], Yakui Lei [2], Linwei Yu [2], Robert Zierold [1],* and Robert H. Blick [1,3]

[1]   Center for Hybrid Nanostructures, Universität Hamburg, Luruper Chaussee 149, 22761 Hamburg, Germany
[2]   School of Electronics Science and Engineering, Nanjing University, 210093 Nanjing, China
[3]   Material Science and Engineering, College of Engineering, University of Wisconsin-Madison, Madison, WI 53706, USA
*   Correspondence: jann.harberts@chyn.uni-hamburg.de, robert.zierold@chyn.uni-hamburg.de
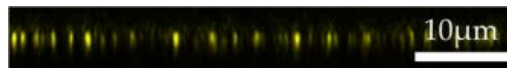
Figure S1: Cross-sectional CLSM image of silicon nanowires (yellow) without Matrigel coating.
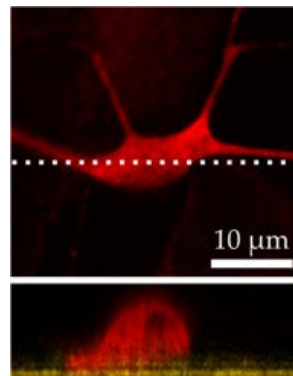
Figure S2: CLSM image including a cross section of a neuron cultured on a control substrate. The neuron appears in red, the reflection of the substrate is yellow.
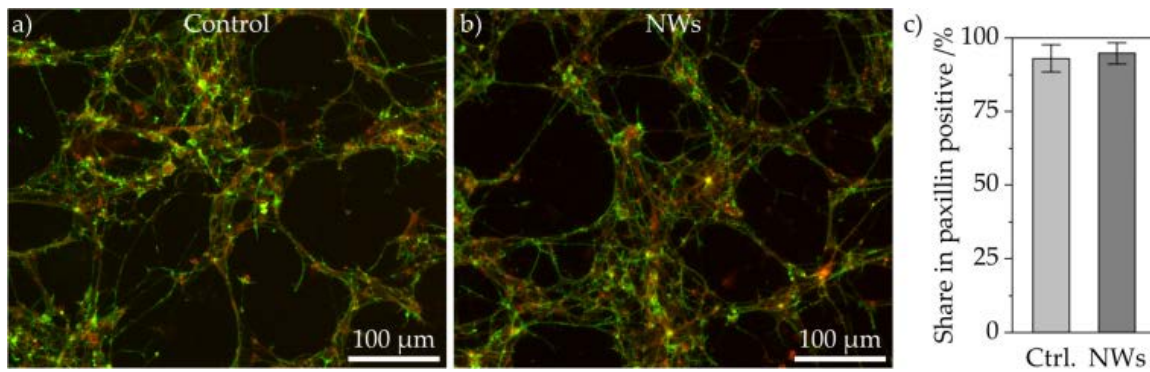
Figure S3: Comparison of f-actin/cytoskeleton (phalloidin, green) and paxillin/focal adhesions (red) of cells on NW and control substrates 11 days after plating. a) Cells on control substrate. b) Cells on NWs. c) Share in paxillin positive area in comparison with f-actin positive area. No statistical significance, Mann-Whitney U test, P > 0.05, error bars are SDs.

Samples were washed, fixated, blocked et cetera analogously to the IF staining procedure in the main manuscript. Besides, sells were stained with anti-paxillin primary antibodies (0.1% BSA, Pax 1:250 in DPBS, rabbit anti-Paxillin recombinant monoclonal Antibody [M13], Abcam, Cambridge, UK, Cat. No. ab32084) overnight at 4 °C. Samples were rinsed with DPBS two times. Secondary and Phalloidin staining was performed for 1 h in the dark with Alexa fluorophore conjugated anti-rabbit antibodies and phalloidin (0.1% BSA, Alexa 555 1:1000, PH: 2 drop /mL in DPBS, goat anti-rabbit IgG-Alexa Flour 555 polyclonal antibody, Thermo Fisher Scientific, Massachusetts, USA, Cat. No. A32732, phalloidin: ActinGreen Alexa Fluor 488 probe, Thermo Fisher Scientific, Cat. No. R37110).
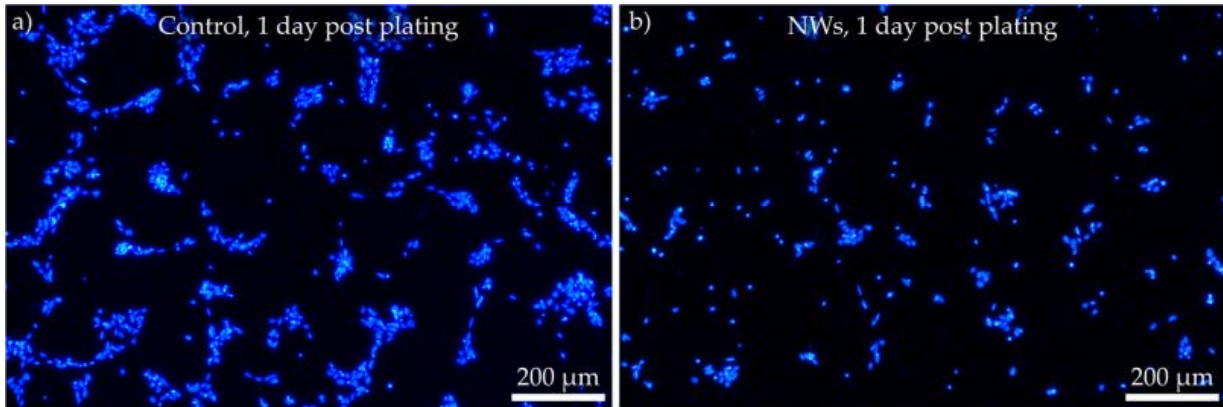
Figure S4: Exemplary images of Hoechst-stained cells (blue) on control (a) and nanowire arrays (b) one day after plating.
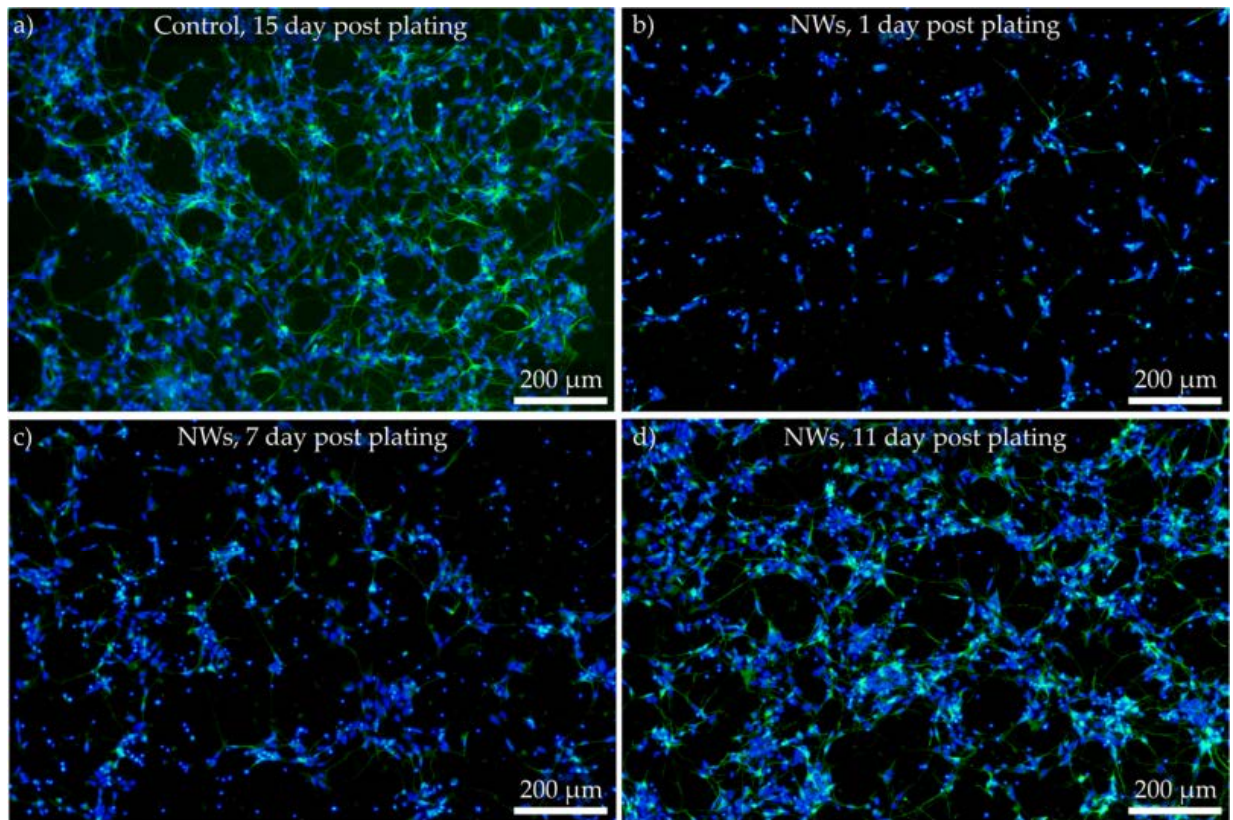
Figure S5: a) Exemplary image of neurons cultured on planar control substrate 15 days post plating labeled with anti-MAP2 (green) and Hoechst counterstain (blue). b-d) Neurons on NWs with anti-MAP2 labeling and Hoechst counterstain 1, 7, and 11 days post plating.
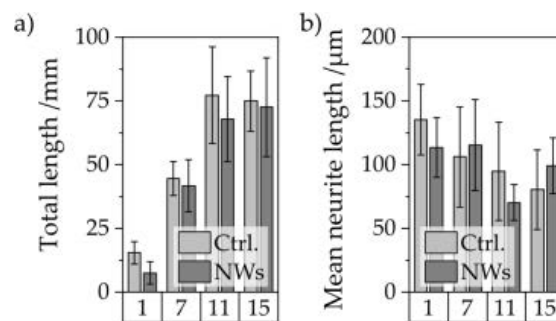
Figure S6: Total neurite length (a) and mean neurite length (b) of MAP2 positive cells determined by CellProfiler.
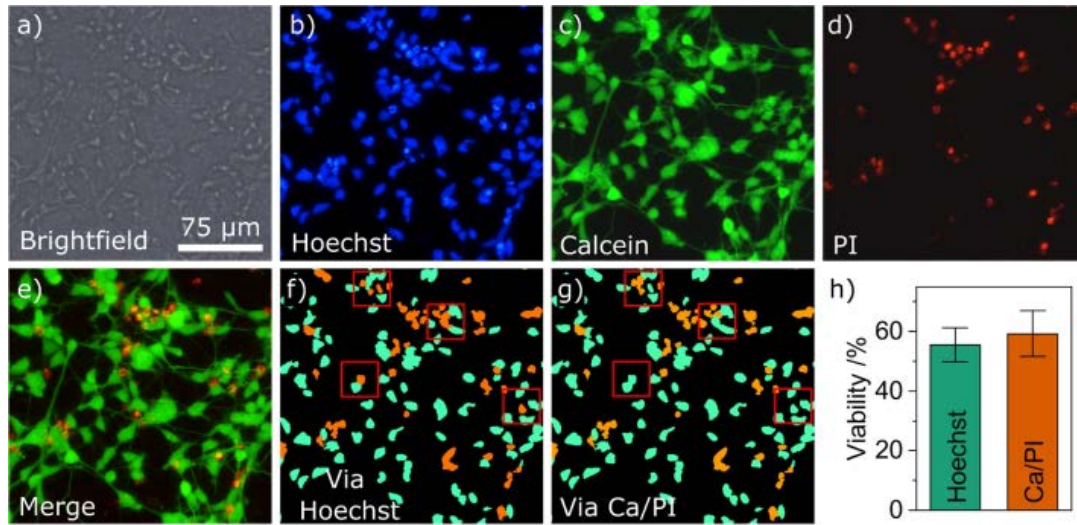
Figure S7: Comparison of estimating the viability by discrimination of vital and dead cells by brightness and by staining with Calcein and Propidium Iodide (PI). Exemplary widefield image (a) including the corresponding Hoechst (b), Calcein (c), and PI-stained (d) images including a merge (e). The analysis results from CellProfiler are compared to each other and the few differences are highlighted by red squares (f and g). The techniques deliver comparable results (55.5% vs 59.3%, bar chart in h) with no statistically significant differences (Mann-Whitney U test, P = 0.16898 > 0.05).

Table S1: Statistical significances of IF quantification in Figure 3. Mann-Whitney U test between NW and control substrates of cell number, single cells, cell viability, and MAP2 positive cells.

Parameter	Precise P	P threshold	Sig
Cell numer (1 DIV)	1.23893E-4	0.001	1
Cell numer (7 DIV)	0.33519	0.05	0
Cell numer (11 DIV)	0.07569	0.05	0
Cell numer (15 DIV)	0.00901	0.01	1
Viability (1DIV)	1.84916E-6	0.001	1
Viability (7DIV)	2.22169E-8	0.001	1
Viability (11DIV)	1.1515E-8	0.001	1
Viability (15DIV)	2.44257E-8	0.001	1
Single cells (1DIV)	1.29441E-5	0.001	1
Single cells (7DIV)	6.4152E-4	0.001	1
Single cells (11DIV)	1.51883E-5	0.001	1
Single cells (15DIV)	3.01902E-5	0.001	1
MAP2 positive (1DIV)	0.37442	0.05	0
MAP2 positive (7DIV)	0.80601	0.05	0
MAP2 positive (11DIV)	7.43885E-4	0.001	1
MAP2 positive (15DIV)	0.00103	0.01	1

Table S2: Statistical significances of electrophysiological properties in Figure 4. Mann-Whitney U test between NW and control samples of resting membrane potential, capacitance, AP amplitude, AP threshold, AHP, and AP duration.

Parameter	Precise P	P threshold	Sig
RMP	0.5362	0.05	0
MC	0.81253	0.05	0
AP amplitude	0.60088	0.05	0
AP threshold	0.19323	0.05	0
AHP	0.94138	0.05	0
AP duration	0.23879	0.05	0

A.6   Publication VI

Generation of human iPSC-derived neurons on nanowire arrays featuring varying lengths, pitches, and diameters

Jann Harberts, Malte Siegmund, Carina Hedrich, Wonjong Kim, Anna Fontcuberta i Morral, Robert Zierold, and Robert H. Blick

Author contributions: Si NW preparation, cell culture, immunofluorescence and confocal microscopy imaging, patch clamping, data analysis, manuscript writing: J.H., GaAs NW preparation: W.K., A.F.i M., and J.H., assistance in cell culture: M.S., ALD: J.H., C.H., and R.Z., conceptualization: J.H., funding: A.F.i M., R.Z., and R.H.B.

(11 + 6 pages)

RESEARCH ARTICLE

ADVANCED
MATERIALS
INTERFACES

Check for updates

www.advmatinterfaces.de

Generation of Human iPSC-Derived Neurons on Nanowire Arrays Featuring Varying Lengths, Pitches, and Diameters

Jann Harberts,* Malte Siegmund, Carina Hedrich, Wonjong Kim, Anna Fontcuberta i Morral, Robert Zierold,* and Robert H. Blick

Nanowire (NW) arrays interfaced with biological cells have been demonstrated to be potent tools for advanced applications such as sensing, stimulation, or drug delivery. Many implementations, however, have so far only been studied with rather robust basic cell models. Here, the generation of human induced pluripotent stem cell (iPSC)-derived neurons is presented on various types of NW arrays. Specifically, combinations of three NW lengths (1, 3, and 5 μm), three array pitches (1, 3, and 5 μm), and two NW diameters (thin/thick pairs, 270–600 nm/590–1070 nm) are being utilized. The cell/NW interactions range from fakir-like states to NW-encapsulating states depending on the array characteristics. The cultures show equal proportions of neuronal marker-positive cells after 8–9 days of terminal differentiation on the NW arrays (14–15 days in total) compared to planar controls. In addition, the neurons are functional with similar kinetics of the action potentials highlighting the equivalence of the NW arrays for neuronal differentiation. In the future, stem cell research and regenerative medicine might substantially benefit from further functionalized NW arrays enabling the well-established mechanisms such as NW-mediated in vitro gene editing or intracellular delivery of biomolecules to further control and/or to enhance neuronal differentiation.

1. Introduction

State-of-the-art micro- and nanofabrication techniques allow nowadays for engineering advanced biological metamaterials which are being considered promising candidates, for example, to support biomedical translation, to fabricate minimal invasive nanoelectronics, or to be utilized as nanotools in neuroscience and regenerative medicine.[1–3] In this context, vertically aligned high aspect ratio nanostructures—so-called nanowire (NW) arrays—used as cell culture substrates play an increasingly important role in establishing novel tools for interrogating and stimulating cells on molecular and cellular levels.[4–7] In recent years, studies testing the unique capabilities of NW arrays have been conducted with a variety of cell types, for instance, basic cell lines such as GPE86, HEK293, and HeLa cells, primary rodent neurons, and (mesenchymal) stem cells (MSCs), to name a few.[8,9] The impact of such studies on medical applications such as drug screenings and neurodegenerative disease studies might, however, be significantly improved by employing more sophisticated cells, namely, cells derived from human induced pluripotent stem cells (iPSCs).[10]

Human iPSC technologies have changed the way of preclinical research and application by enabling human (patient-specific) in vitro models without restrictions in cell availability.[11] Not only political and ethical controversies raised by using embryonic stem cells (ESCs) are avoided, but also all major cell types including blood-brain barrier models and brain organoids can be generated.[12,13] For studying neurodegenerative diseases such as Alzheimer's or Parkinson's, neurons derived from human iPSCs are of particular interest since adequate models are otherwise scarcely available.[14] Apart from ESCs,

J. Harberts, M. Siegmund, C. Hedrich, R. Zierold, R. H. Blick
Center for Hybrid Nanostructures (CHyN)
Universität Hamburg
Luruper Chaussee 149, 22761 Hamburg, Germany
E-mail: jann.harberts@chyn.uni-hamburg.de;
robert.zierold@chyn.uni-hamburg.de

W. Kim, A. Fontcuberta i Morral
Faculty of Engineering
Laboratory of Semiconductor Materials
Institute of Materials
École Polytechnique Fédérale de Lausanne (EPFL)
Lausanne 1015, Switzerland

A. Fontcuberta i Morral
Faculty of Basic Sciences
Institute of Physics
École Polytechnique Fédérale de Lausanne (EPFL)
Lausanne 1015, Switzerland

R. H. Blick
Material Science and Engineering
College of Engineering
University of Wisconsin-Madison
Madison, WI 53706, USA

**ADVANCED
SCIENCE NEWS**

www.advancedsciencenews.com

**ADVANCED
MATERIALS
INTERFACES**

www.advmatinterfaces.de

animal models using, for example, neurons from rodents have been employed. Corresponding studies, however, often suffer from high clinical failure rates during the translation to the human physiology and as a result, their pertinence for medical applications is typically rather limited.[15] In the same way, the existing studies demonstrating the advantages of NW arrays in cell culture but only utilizing traditional cell models might be restricted, for instance, in the context of improving neurodegenerative disease studies or pharmacological drug screenings. Nevertheless, stem cell research might substantially benefit from, e.g., improved neuronal differentiation and sophisticated neuronal cell interrogation mediated by (functionalized) NW arrays.[16]

NW arrays used as cell culture substrates elicit a strong interaction between the substrate and the cells by their unique topography.[17–19] The very interplay between both renders possible a multitude of applications such as sensing, stimulation, and drug delivery.[20–23] Passive NW arrays have been used, for example, to measure mechanical cell properties,[24] to interact with the cell's nucleus,[25] to reorganize actin,[26] to stimulate the mechanotransduction machinery,[27] or to direct cell polarization such as outgrowth and branching of neurites.[28,29] Further, the strong coupling between the cell membrane and the substrate can also help to improve electrical recording and stimulation of microelectrode arrays that have been equipped with the nanostructures.[30] Also intrinsic material features of the NWs such as photoelectrochemical properties—either in arrays or free-standing, that is, detached from the substrate—can be used to modulate neuronal or cardiac activity in vitro or as retina implants.[31,32] Another fundamental advantage of the NW arrays is the capability to support intracellular delivery by stimulated endocytosis or—in case of hollow NWs—by direct injection into the cell via electroporation.[33–35] The variety of potential applications renders NW arrays a promising element for next-generation biomedical instruments and nano-enabled neuronal interfaces.[36] However, present studies have also shown that NW arrays can influence basic cell properties such as the viability,[37] movement,[38] proliferation,[39] adhesion,[40] velocity,[41] morphology,[42] and spreading of overgrowing cells.[43] Moreover, other literature reported that the growth, gene expression, or differentiation of, for example, MSCs or ESCs can be affected when being cultured on NW arrays.[44–46] To make use of the NW array-associated advantages such as the improved electrical junction or the intracellular drug delivery, it thus is essential for the prospective applications that the neuronal differentiation of human iPSCs is maintained especially on passive NW arrays compared to planar controls. The equivalence would permit that well-established differentiation protocols tested in regular Petri dishes can be applied in the future. In previous studies, we showed the general feasibility of generating human iPSC-derived neurons on NW arrays, but the utilized substrates featured only about 1 μm long NWs.[47,48] As a result, their rather basic topographies just induced a limited amount of deformational stress toward the cells. The impact of other NW array geometries—for instance, with longer NWs—on the neuronal differentiation is still unclear and thus has been addressed in this study.

Here, we present the generation of functional human iPSC-derived neurons on NW arrays featuring multiple combinations of three different NW lengths (1, 3, and 5 μm), three different array pitches (1, 3, and 5 μm), and two different NW diameters (thin/thick pairs, 270–600 nm, 590–1070 nm) after only 14–15 days of differentiation. The extensive variation of the NW arrays characteristics went along with fundamental changes in the interaction between the neurons and the NW arrays. Specifically, the interaction regimes ranged from fakir-like states on dense NW arrays where the cells were only in contact with the very NW tips to NW-encapsulating states on sparse NW arrays where the cells enwrapped entire NWs. Severe deformations and indentations of the neurons including their nuclei were then observed particularly with 5 μm long NWs. Despite the varying interactions with the NW arrays, the proportion of neuronal marker-positive cells (MAP2, NeuN, TH) after 8–9 days of terminal differentiation on the NW arrays (14–15 days in total) was similar to planar controls. In addition, similar electrophysiological properties including the functional character of the generated neurons confirmed the quality of the neuronal differentiation on the NW arrays. By highlighting the equivalence of the culturing substrates for the neuronal differentiation, the results pave the way for enabling the unique applications of—then functionalized—NW arrays for human iPSC-derived neurons. We believe that stem cell research and regenerative medicine might substantially benefit in the future from the well-established NW array-mediated mechanisms such as in vitro gene editing or the intracellular delivery of biomolecules, for example, to further control and/or enhance neuronal differentiation.[49–52]

2. Results

The NW arrays featuring different NW lengths, array pitches, and NW diameters were prepared from plain silicon using reactive ion etching (RIE) and a hard mask of rectangularly arranged dots defined by electron beam lithography (EBL) (**Figure 1**). Specifically, three NW lengths of 1, 3, and 5 μm (L1, L3, and L5), three array pitches of 1, 3, and 5 μm (P1, P3, and P5), and two diameters (D−/D+, thin/thick pairs from 270–600 nm and 590–1070 nm diameter) were used—resulting in 18 different types of NW arrays (summarized in **Table 1**). The wide range of NW diameters within the D−/D+ categories was caused either by the nature of the RIE process or the pitch of the arrays as described in the following. The D− diameters correspond to the minimal value that was compatible with the RIE process (≈270–600 nm). Longer wires (L3 and L5) and larger pitches (P3 and P5) required gradually increased diameters to compensate for the tapering occurring toward the base of the NWs (clearly visible for L5 P3 D− and L5 P5 D−, Figure 1). For D+ NW arrays, the diameter was arbitrarily set to a rather large value of ≈1000 nm. Note, for P1 D+ NW arrays, the diameter was only about 600 nm because else the NWs essentially would have been tangent with each other and concomitant, the geometrical nature of a NW array would have been lost.

The interaction of the human iPSC-derived neurons with the NW arrays was investigated by 3D confocal laser scanning microscopy (CLSM) imaging (**Figure 2**, top-views and cross sections). Neurons (green) were identified by the neuronal marker microtubule-associated protein 2 (MAP2) and their nuclei (red) were stained with DRAQ5. Note, the NW tips'
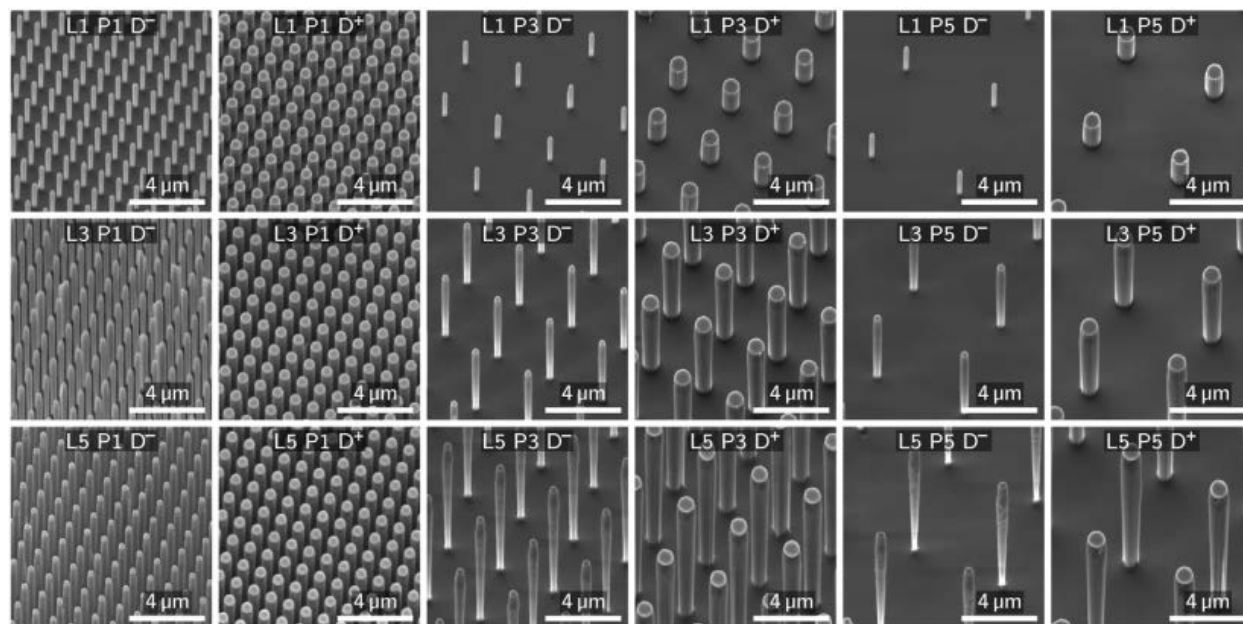
**ADVANCED
SCIENCE NEWS**
www.advancedsciencenews.com

**ADVANCED
MATERIALS
INTERFACES**
www.advmatinterfaces.de

Figure 1. Compilation of scanning electron microscopy images of the utilized Si NW arrays featuring altering lengths (L), pitches (P), and diameters (D). The lengths of the NWs were 1, 3, and 5 µm (L1, L3, and L5). The array pitches were 1, 3, and 5 µm (P1, P3, and P5). The diameters for the *thin* type (D⁻) were between 270 and 600 nm depending on the length and pitch—longer NWs and larger pitches required larger diameters to be compatible to the RIE processing. The *thick* type (D⁺) was about 600 nm in diameter for P1 NW arrays and ≈1000 nm for the P3/P5 NW arrays. Note, detailed geometrical specifications are listed in Table 1.

reflections appeared green. Overall, three interaction regimes were found, namely, fakir-like, intermediate, and encapsulating regimes. In general, the induced topographical stress on the cells (e.g., deformation of the nucleus) increased with the NW length. The specific settling regimes of the neurons were predominantly governed by the array pitch. The fakir-like states where the cells rest on a "bed-of-nails" only being in contact with the very NW tips were found for almost all P1 NW arrays. However, for L1 P1 D⁻ NW arrays, intermediate states were also observed. Note, for L3/L5 P1 D⁻ NA arrays, the neurons were fakir-like but more entanglement with the NW tips was observed. The interactions of the neurons with the P3 and P5 NW arrays were more complex. On P3 D⁻ NW arrays, to start with, the neurons often showed encapsulating settling states. However, in case of the longest NWs (L5 P3 D⁻, Figure 2) the cells were likely to lose contact to the bottom of the substrate and were thus mostly in intermediate states. In case of the corresponding D⁺ NW arrays, in contrast, the imaged cells were

more often in intermediate or even fakir-like states whereat with P3 L3 D⁺ NW arrays (Figure 2) the yield of the intermediate state was particularly low (3 of 11 imaged neurons, else fakir-like). For P5 NW arrays, the majority of the neurons completely encapsulated the NWs and were hence also in contact with the bottom of the substrate. As a result, the variation of the NW lengths using P5 NW arrays had a distinct influence on the cell/NW interface. Cells on the L1 P5 NW arrays were only scarcely visibly deformed by the short NWs. Using L3 P5 NW arrays, the NWs showed a larger impact on the somata. The nuclei, however, were usually unaffected. For L5 P5 NW arrays, in contrast, not only the somata were severely deformed but also the nuclei were indented by the NWs. The diameters of the NWs played a subordinate role for which resting state was observed. Nevertheless, the different diameters altered the amount of cell material, that is, cell membrane and nucleus, being displaced by the NWs. The analysis of cells by CSLM already showed that MAP2-positive neurons were generated on the NW arrays despite the to some extent severe appearing topographical challenges. In a next step, the overall yields of the neuronal differentiation were analyzed by additional neuronal markers.

The yields of the neuronal differentiation on the NW arrays were determined from immunocytochemistry (ICC) double-stainings and compared to planar controls (**Figure 3**). On the one hand, the cells were labeled with MAP2 and neuronal nuclei (NeuN) (Figure 3a, examples of L1 P1 D⁻, L3 P3 D⁺, and L5 P5 D⁻ NW arrays, all others and controls in Figure S1, Supporting Information) and on the other hand, with MAP2 and tyrosine hydroxylase (TH) (Figure 3b, examples of L1 P1 D⁺, L3 P3 D⁻, and L5 P5 D⁺ NW arrays, all others and controls in

Table 1. Overview of the geometry of the utilized NW arrays. The entries of the table follow the nomenclature of length (L)/pitch (P)/diameter (D) where the approximate values are given in µm/µm/nm. The diameters were measured at the thickest section of the NWs.

	P1		P3		P5	
	D⁻	D⁺	D⁻	D⁺	D⁻	D⁺
L1	1/1/270	1/1/590	1/3/280	1/3/900	1/5/280	1/5/890
L3	3/1/290	3/1/610	3/3/380	3/3/970	3/5/460	3/5/1020
L5	5/1/360	5/1/610	5/3/540	5/3/1000	5/5/600	5/5/1070

**ADVANCED
SCIENCE NEWS**

www.advancedsciencenews.com

**ADVANCED
MATERIALS
INTERFACES**
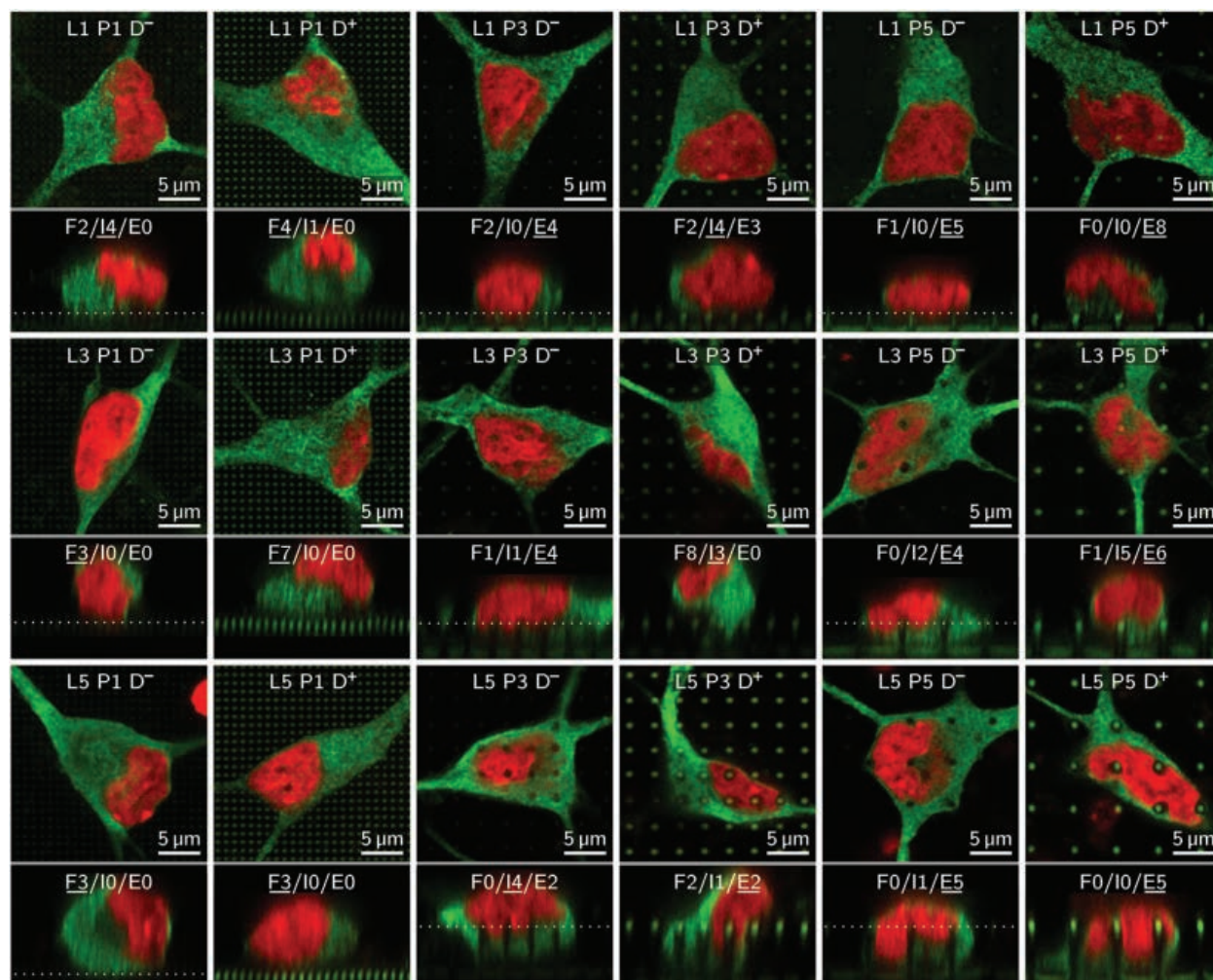
www.advmatinterfaces.de

Figure 2. Interactions of the neurons with the NW arrays depending on the NW length, array pitch, and NW diameter. Neurons were stained with MAP2 (green) and nuclei were labeled with DRAQ5 (red). The NW tips' reflections appeared in green (note, for D⁻ NW arrays, the tip reflections had substantially less intensity—to highlight the settling regimes, the NW tips were indicated in the cross sections by dotted lines). The main panels show top-views of the neurons whereas the panels below depict the corresponding cross-sectional views (z-stacks prepared by CLSM). The numbers in cross-sectional views indicate the proportion of the imaged cells which showed fakir-like (F), intermediate (I), or encapsulating (E) interaction with the NW arrays where the underlined entry is presented in the figure. P1 NW arrays mostly elicited a fakir-like resting state where the cells only interacted with the NW tips (independent of the NW length). Larger array pitches, especially P5 NW arrays, promoted the encapsulation of the NWs where with increasing NW length, the somata and nuclei were exposed to more severe deformations/indentations. Note, states were called intermediate where the cells started to enwrap the NWs but were not in contact with the bottom of the substrate. General note regarding the image composition: For the fakir-like states and the L1 NW arrays, the main panels consist of an overlay of two separate images where one is focused on the NW tips and the other in the cell. Other main panels: Only one image with focus at the NW tips.

Figure S2, Supporting Information). For quantification, cells were first identified by Hoechst-counterstaining (nuclei). Subsequently, viable cells (about 50%, Figure S3, Supporting Information) were cross-correlated to the respective ICC color channels. The proportion of MAP2-positive cells on the NW arrays was about 65% and comparable to the controls (planar Si, glass; Figure 3c). With regard to the MAP2-positive cells, that is, neurons, about 65% were also NeuN-positive (Figure 3d, similar to the controls). A smaller proportion of the neurons was also TH-positive (about 2.5%, Figure 3e, comparable to the controls). Overall, the differentiation yields on the NW arrays were similar to the planar controls. Another essential measure of the

quality of neuronal differentiation is the development of characteristic ion channels and the concomitant ability to process action potentials (APs), that is, the functionality of the neurons.

The functionality of the neurons generated on the NW arrays was tested by patch clamp measurements and compared to planar controls (**Figure 4**). The patch clamp procedure was generally feasible on the NW arrays but noteworthily, the cells' visibility on the nanostructured substrates was hindered considerably compared to the planar controls (Figure 4a, examples of L5 P1 D⁺, L1 P3 D⁻, and L3 P5 D⁺ NW arrays, controls in Figure S4a, Supporting Information). The generated neurons were functional on all types of NW arrays shown by recordings
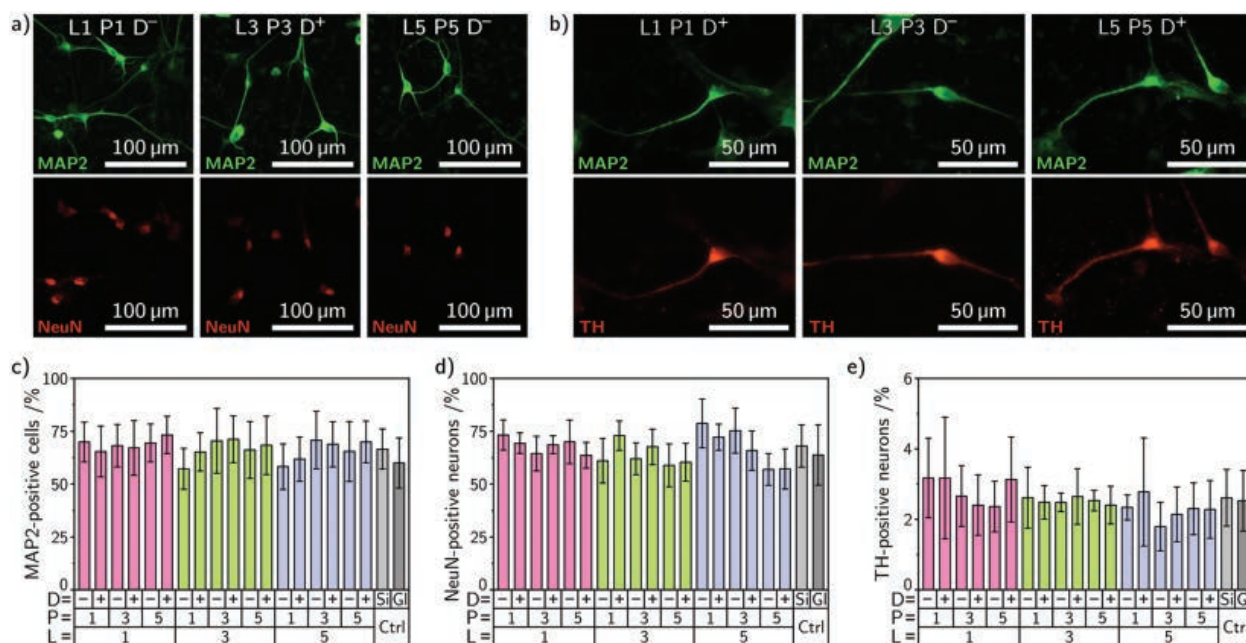
**ADVANCED
SCIENCE NEWS**
www.advancedsciencenews.com

**ADVANCED
MATERIALS
INTERFACES**
www.advmatinterfaces.de

Figure 3. ICC stainings with MAP2, NeuN, and TH. a) Exemplary ICC stainings of cells using MAP2 (green, upper panels) and NeuN (red, lower panels). Shown are L1 P1 D⁻, L3 P3 D⁺, and L5 P5 D⁻ (all others in Figure S1, Supporting Information). b) Exemplary ICC stainings of cells using MAP2 (green, upper panels) and TH (red, lower panels). Shown are L1 P1 D⁺, L3 P3 D⁻, and L5 P5 D⁺ (all others in Figure S2, Supporting Information). c) Proportion of MAP2-positive viable cells. d) Proportion of NeuN-positive neurons. e) Proportion of TH-positive neurons. No statistically significant deviations from the controls (ANOVA with post-hoc Tukey's test, $\alpha = 0.05$). n (analyzed images) = 7. Error bars are standard deviations (SDs).

of APs (Figure 4b, traces of controls in Figure S4b, Supporting Information). The amplitudes of the APs were about 70 mV and similar to the controls (Figure 4c). The AP thresholds and AP widths were ≈−25 mV and 3.6 ms, respectively, similar to the controls (Figure 4d,e). In addition to the functional analysis, we characterized further electrophysiological parameters of the neurons such as the resting membrane potentials (RMPs), membrane capacitances (MCs), and voltage-dependent membrane currents (**Figure 5**). Specifically, the RMPs and MCs were about −50 mV and 12 pF, respectively, comparable to the controls (Figure 5a). Lastly, the early-inward and late-outward currents were measured by applying voltage steps from −70 to +30 mV to the cells (Figure 5b, shown here: L1 P1 D⁻, L3 P3 D⁺, and L5 P5 D⁻, all other NW arrays in Figure S5a, Supporting Information, Si control in Figure 5d, glass in Figure S5b, Supporting Information). The recorded traces showed early negative peaks (inward currents, insets of respective panels) and late positive constant currents (outward currents) depending on the applied voltages. The peak values of the early-inward and late-outward currents normalized to cells' MCs plotted against the applied voltages showed minima of the inward currents at about 0 mV and an increase of the outward current at voltages higher than 0 mV (Figure 5c, Si in Figure 5d, glass in Figure S5c, Supporting Information).

3. Discussion

The fabrication of NW arrays by RIE in a top-down process from bulk material such as Si is well-established in the field.[53]

By defining the hard mask, that is, the array pitches and NW diameters, via EBL wafer-scale sample fabrication with high-precision is enabled.[54] In general, the utilized NW lengths and array pitches match the values frequently found in the literature.[20] The D⁻ diameters achieved by RIE rather cover the upper range of NW diameters used in the field—especially for the L5 NW arrays. Nonetheless, for applications such as solar cell NWs diameters around 300–400 nm would be acceptable.[55,56] Employing even thicker NWs (D⁺) extends the universality of the study since, for example, also NWs with a diameter of about 1 µm influence cell spreading or facilitate cell transfection.[57,58] Moreover, such larger diameters fill to some extent the gap between NW and micropillar arrays used in cell culture.[59,60] All NW arrays—with NW lengths up to 5 µm—were prepared in a single-step RIE process. Such long NWs are usually achieved in multi-step deep RIE (DRIE) processes[61] whereas NW arrays prepared by regular RIE typically reach shorter lengths of about one micron due to a critical degree of underetching.[62] The ensemble of the top-down approach via RIE and a hard mask defined by EBL ensures a high reproducibility of the NW array fabrication virtually without any defects such as missing or askew NWs which is common in bottom-up approaches.[63–65] A defect-free nature of the NW arrays, however, was crucial to study the general impact of the NW arrays on the neuronal differentiation. Single missing NWs, for example, in P5 NW arrays would appear as P10 NW arrays to individual cells—or even as a flat since the cells might fit completely in between the NWs without any further interaction. Nevertheless, we also tested the neuronal differentiation on bottom-up fabricated NW arrays since the NW growth goes
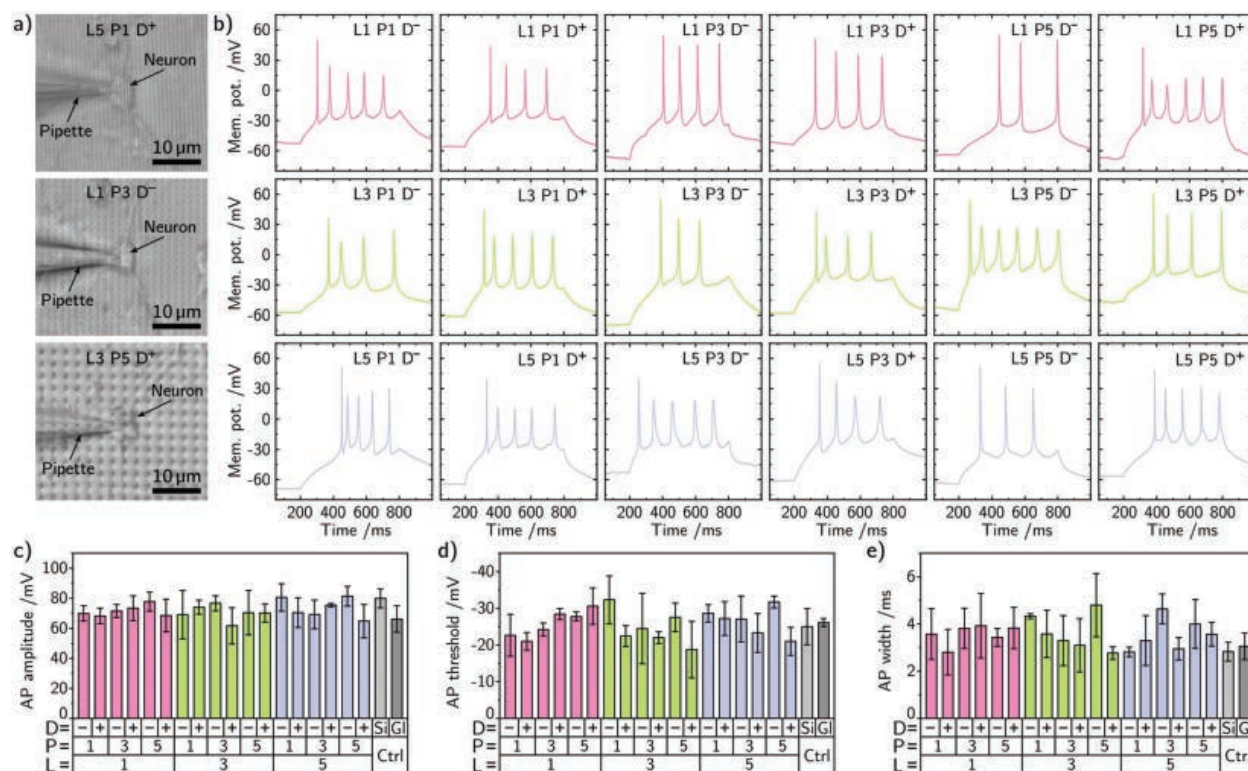
2200806 (5 of 11)

**ADVANCED
SCIENCE NEWS**

www.advancedsciencenews.com

**ADVANCED
MATERIALS
INTERFACES**

www.advmatinterfaces.de

Figure 4. Functionality of the human iPSC-derived neurons generated on the NW arrays. a) Examples of neurons patch clamped on NW arrays with different NW lengths, array pitches, and NW diameters (shown: L5 P1 D+, L1 P3 D−, and L3 P5 D+, controls: Figure S4a, Supporting Information). b) Exemplary traces of APs evoked by rheobase current for all types of NW arrays (controls: Figure S4b, Supporting Information). c) Quantification of the mean AP amplitudes. d) Quantification of the mean AP thresholds. e) Quantification of the mean AP widths. No statistically significant deviations compared to the controls (ANOVA with post-hoc Tukey's test, $\alpha = 0.05$). n (analyzed cells) = 4, 6, 3, 4, 4, 3, 3, 6, 2, 2, 3, 5, 3, 6, 4, 3, 4, 5, 7, 7, from left to right, respectively. Error bars are SDs.

along with enhanced material properties such as improved surface states, fewer material defects, and the capability to add functionality by integrating hetero-junctions by varying the doping during the growth, for example, to build NW solar cells to stimulate cells grown on top.[66,67] Specifically, we prepared L2 P3 D−, L2 P3 D+, L4.5 P1 D+, L4.5 P3 D+, and L4.5 P5 D+ GaAs NW arrays (Figure S6a, Supporting Information) and validated the generation of human iPSC-derived neurons on these NW arrays by MAP2 and NeuN stainings (Figure S6b, Supporting Information). However, employing Si for the NW fabrication—as used herein for the comprehensive analysis—is also reasonable since nanostructured Si is considered a promising material to overcome fundamental limits of current biomedical devices, for example, by enabling subcellular biointerfaces.[68]

The interface between the human iPSC-derived neurons and the NW arrays was marked by a variety of cellular settling states of which the fundamental dependency of the states with regard to the NW lengths, array pitches, and NW diameters was in accordance with a model developed in Buch–Månson et al.[69] In general, this model describes that fakir-like states are favored by cells in the case of long NWs, small array pitches, and thin diameters. In contrast, NW encapsulation is more likely for short NWs, large array pitches, and thick diameters. Overall, for P1 NW arrays, we observed the fakir-like state which is in accordance to the model and other studies with high-density

NW arrays.[43,70–72] With increasing pitch, the neurons began to encapsulate the NWs. For the P3 NW arrays, the yields for partial NW encapsulation were reduced in the case of the D+ NW arrays which is contradicotry to the expectations derived from the model. One reason might be that in the case of P3 D+ NW arrays the effective distance between the NWs (i.e., pitch minus diameter) falls below the threshold for NW encapsulation. A similar phenomenon has been observed in Hanson et al., where for a constant pitch of 1 μm and a NW length of 500 nm the cells encapsulated NWs featuring a diameter of <200 nm but were fakir-like for 500 nm thick NWs because of the decreased effective array pitch (500 vs 800 nm).[73] This also explains, why for L1 P1 D− not only fakir-like but also intermediate states were observed. For the P5 NW array, we mostly observed complete encapsulation of the NWs which is in accordance with other studies using low arrays densities.[43,74] The strong interaction of the NWs with the nuclei in the encapsulating states is also reported in the literature.[25] In direct comparison to a prior study of us with undifferentiated neural progenitor cells (NPCs)—used to generate the neurons herein—the differentiated neurons were more likely to favor the fakir-like state at similar specifications of the NW arrays.[75]

The neuronal differentiation yields on the NW arrays were analyzed after 14–15 days (8–9 on the NW arrays) of culturing by labeling neuron-specific markers such as MAP2, NeuN,
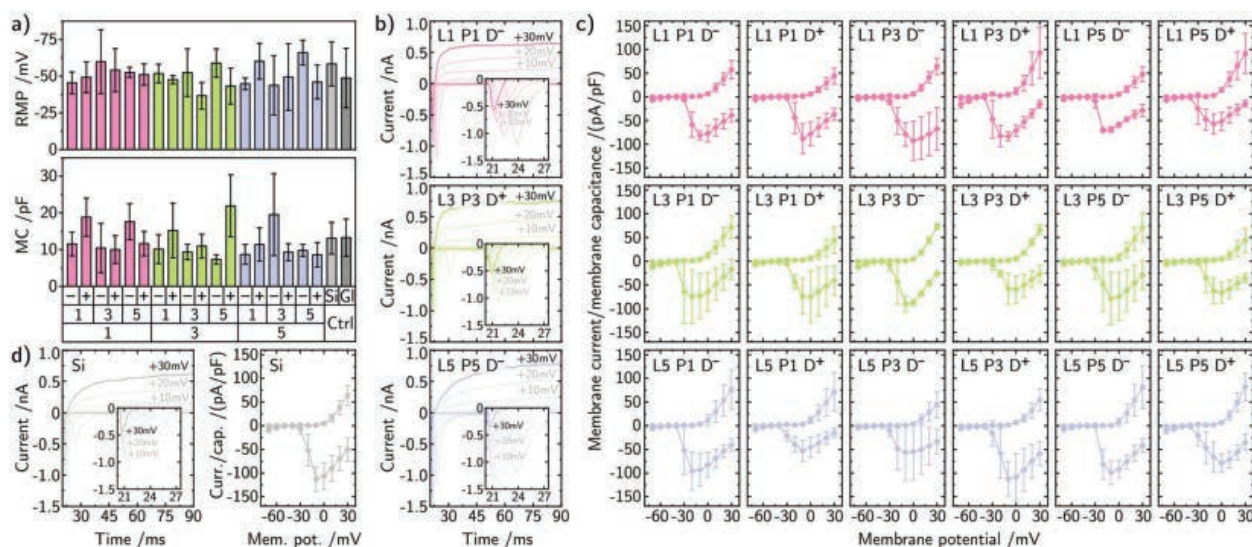
Figure 5. Additional electrophysiological analysis of the human iPSC-derived neurons cultivated on the NW arrays. a) Resting membrane potentials (RMPs) and membrane capacitances (MCs) on all types of substrates. No statistically significant deviations compared to the controls (ANOVA with post-hoc Tukey's test, $\alpha = 0.05$). b) Exemplary traces of early-inward (negative peaks) and late-outward (positive/constant) membrane currents recorded from neurons cultured on NW arrays during the application of voltage steps from −70 to +30 mV (shown here: L1 P1 D−, L3 P3 D+, and L5 P5 D−, Si control: panel (d), all other NW arrays: Figure S5a, Supporting Information, glass: Figure S5b, Supporting Information). c) Peak inward- (diamonds) and outward-currents (squares) normalized to the cells' MCs plotted against the applied voltages for all types of NW arrays (Si control: panel (d), glass: Figure S5c, Supporting Information). n (analyzed cells) = 4, 6, 3, 4, 4, 3, 3, 6, 2, 2, 3, 5, 3, 6, 4, 3, 4, 5, 7, 7, from left to right, respectively. Error bars are SDs.

and TH. About 65% of the cells cultivated on the NW arrays were positive for the postmitotic neuronal marker MAP2. Such a value is comparable to other studies conducted in regular well plates.[76] The majority of the identified neurons (≈65%) were also immunoreactive for another mature neuronal marker, namely, NeuN, similar to other studies.[77] A small fraction of neurons was also positive for TH (about 2.5%) indicating the development toward a dopaminergic phenotype. Notably, the proportion for TH was rather small but being a late marker (e.g., a significant TH upregulation after 20 days of differentiation was reported in Gilmozzi et al.) such values are normal for very young cultures as, for example, literature reports also on single-digit proportions for cells cultured even longer than here (30 days).[78] Overall, the numbers reflect normal yields for the generation of human iPSC-derived neurons but remarkably all yields were equally independent on the type of substrate, that is, the strong interaction with the NW arrays including the partly severe deformations of the somata and nuclei had no impact on the neuronal differentiation. Also, the yields compare well considering the short differentiation period of only 14–15 days versus >30 days used in other studies.[76–78] In this context, it is also striking that the neurons, in addition, were functional already. One potential reason for the fast maturation of the neurons might be the early application of DAPT (on day 6) to the maturation medium to enhance the neuronal differentiation.[79]

The electrophysiological analysis via patch clamping showed that on all types of NWs arrays the generated neurons were functional demonstrated by recordings of APs whose kinetics such as the AP amplitude, AP threshold, and AP width were similar to the planar controls. Moreover, the mean values of amplitude (about

70 mV), threshold (about −25 mV), and duration (about 3.6 ms) were comparable to other human iPSC-derived neurons.[80–84] The RMPs (about −50 mV) and MCs (about 12 pF) were not only similar to the controls but also in accordance with the literature.[80–84] Lastly, we measured the early-inward and late-outward membrane currents to test for the characteristic interplay of the sodium and potassium ion channels. Independent of the type of NW arrays, the neurons showed the typical negative peaks and constant positive currents. Here, the normalized maximum inward/outward currents plotted against the applied voltages showed similar voltage-dependencies to the controls and other studies.[79,85] Considering again the tremendous differences observed for the interface between the neurons and the NW arrays, it is remarkable that the functional maturation is equal to the controls as well as to other studies. As a result, the geometrical specifications of the NW arrays may freely be chosen to optimize both the cell/NW interface and the properties of the NW arrays in order to match prospective applications.

4. Conclusions

This study demonstrates the generation of functional human iPSC-derived neurons on NW arrays with varying geometrical specifications such as the NW length (1–5 μm), array pitch (1–5 μm), and NW diameter (270–1070 nm) within only 14–15 days of cultivation. The neuronal differentiation was equal to planar controls in terms of both neuronal markers (MAP2, NeuN, TH) and electrophysiology such as AP kinetics, RMPs, and characteristic membrane currents. Such equal outcome of the differentiation is particularly striking

**ADVANCED
SCIENCE NEWS**

www.advancedsciencenews.com

**ADVANCED
MATERIALS
INTERFACES**

www.advmatinterfaces.de

since strong interactions of the neurons with the NW arrays have been observed which were going along with altering settling states such as fakir-like states or NW-encapsulating states. The equality of the neuronal differentiation despite the topographical challenges paves the way for future applications with functionalized NW arrays and, especially, allows for tailoring the physical specifications of the NWs arrays which might facilitate advanced applications such as sensing, stimulation, or biomolecule delivery in stem cell culture.

Specific applications being invaluable in the context of stem cell technologies and based on the findings presented herein might be, for example, as follows: The neuronal differentiation of human iPSCs might be enhanced by currents/potentials directly generated from solar cell NW arrays analogously to a study by Kwon et al., where the neurogenesis of fetal stem cells benefited from electrical stimuli mediated by NW arrays externally connected to a power supply.[86] Also, therapeutic applications such as retina implants might have an advantage by employing solar cell NW arrays to precisely stimulate the respective nerve cells since the devices can be embedded into translucent polymers and tailored to be sensitive to specific wavelengths.[87] Moreover, stem cell culture might be facilitated by means of NW-mediated cell transfection to enhance, for instance, in vitro gene editing tools such as CRISPR/Cas9.[49,50] NW arrays with hollow NWs might further extend the number of suitable payloads by soluble cargoes to render possible, for example, the direct intracellular delivery of neuronal growth factors to stimulate neurogenesis.[51,52]

In conclusion, our results demonstrate the feasibility to combine human iPSC-derived neurons with NW arrays featuring a widespread compilation of geometrical characteristics to enable a likewise diversity of potential applications. Hence, we believe that stem cell research and regenerative medicine will substantially benefit in the future from further functionalized NW arrays for improved cell differentiation and interrogation.[5,16]

5. Experimental Section

Nanowire Array Preparation: The NWs arrays were fabricated from silicon wafers (Si-Mat, P/Bor <100>, 5–10 Ω·cm) in a top-down process by RIE using a chromium hard mask. The mask was predefined via EBL (Raith Voyager e-beam lithography system) in a 90 nm thick layer of positive photoresists (PMMA, AllResist, AR-P 671.02). Circles with varying diameters (from, for example, 200 nm for the L1 P1 D⁻ NW arrays, up to, for instance, 700 nm for the L5 P5 D⁺ NW arrays) were defined in a rectangular arrangement with pitches of 1, 3, and 5 µm. After developing (1:3 methyl isobutyl ketone (MIBK):isopropyl alcohol (IPA) including 2.7% H_2O for 30 s and IPA for 30 s), an about 50 nm thick layer of chromium was deposited in a physical vapor deposition (Balzer/Pfeiffer, PLS 500) process. The samples were etched with an inductively coupled plasma (ICP)-RIE (Sentech SI500) using 200 W ICP power, 50 W RF power, 2 Pa pressure, 25 sccm SF_6, and 50 sccm C_4F_8 at 0 °C electrode temperature. The etch rate was about 300 nm min⁻¹ and the etch duration was set accordingly to obtain NWs with lengths of 1, 3, and 5 µm. The NW arrays were passivated by a layer of Al_2O_3 (about 20 nm) deposited by atomic layer deposition in a custom-built system. The samples were imaged with a Crossbeam 550 (Zeiss). To ease the handling of the wafer pieces, the substrates were glued with polydimethylsiloxane (PDMS, SYLGARD 184 Elastomer Kit, Dow Corning) to 12 × 12 mm² glass coverslips. For cell culture, the samples were treated with an oxygen plasma, placed in a well of a 12-well plate, sterilized in 70% ethanol for 5 min, and

coated with Matrigel (Corning 354263, 1:150 in Knock Out DMEM, Life Technologies) over night at room temperature or 1 h at 37 °C (1 mL per well). The GaAs NW fabrication is stated in the Supporting Information.

Cell Culture: The human iPSC-derived neurons were generated from human iPSC-derived NPCs.[85] The NPCs were maintained in Matrigel-coated (1.5 mL per well) 6-well plates using basic N2/B27 medium (1:1 mixture of DMEM/F12 and Neurobasal medium, 1% penicillin/streptomycin/glutamine, 100X, 1% B27 supplement without vitamin A, 50X, 0.5% N2 supplement, 100X, Life Technologies) supplemented with 100 µM ascorbic acid (AA, Sigma-Aldrich), 0.5 µM SAG (Biomol), and 3 µM CHIR 99021 (Axon MedChem) and split ≈1:10 to about 800k cells per well of a 6-well plate every 4–5 days (detachment via accutase, Sigma-Aldrich). The neuronal differentiation of the NPCs (800k cells per well freshly seeded in 6-well plates) was initiated by changing to a patterning medium (basic N2/B27 medium supplemented with 100 µM AA, 0.5 µM SAG, 1 ng mL⁻¹ GDNF, PeproTech, 1 ng mL⁻¹ BDNF, PeproTech) for 6 days. The 6-days predifferentiated NPCs were reseeded into 12-well plates containing the NW arrays and controls. From here on, the differentiation was continued using maturation medium (N2/B27 basic medium supplemented with 100 µM AA, 2 ng mL⁻¹ GDNF, 2 ng mL⁻¹ BDNF, 1 ng mL⁻¹ TGF-β3, PeproTech, 100 µM dbcAMP, Sigma-Aldrich) for another 8–9 days. Note, at the beginning of the neuronal maturing on the NWs arrays, only a small fraction of cells was MAP2-positive (about 15% one day post-plating to the NW arrays and controls, Figure S7, Supporting Information). On day 6, also 10 µM DAPT (Biomol) was added for one day to the maturation medium.[79] The cells were kept at 37 °C with 5% CO_2 in a humidified atmosphere and culture media were replaced every 2–3 days. All experiments were conducted 14–15 days after initiation of the differentiation where for NW arrays the last 8–9 days the cells were on the very substrates. Ethics declaration: All experiments were conducted in accordance with the ethical statement in Reinhardt et al.[85]

Confocal Laser Scanning Microscopy: An upright Leica TCS SP8 confocal microscope with a HC PL APO CS2 63x/1.20 water immersion objective and 488/638 nm lasers was used to prepare the z-stacks (slicing distance: 250 nm). Neurons were stained with MAP2 (see "Immunocytochemistry") and nuclei were stained with DRAQ5 (ThermoFisher Scientific, Fluorescent Probe Solution, 5 mM, Cat. No. 62251, 1:1000 in Dulbecco's phosphate buffered saline (DPBS)) for 10 min at 37 °C. Processing and analysis of the z-stacks were conducted with the Leica LAS X Core software. For illustration, images were optimized in contrast, brightness, and false color, if applicable.

Immunocytochemistry: Samples were rinsed with DPBS, fixed in formaldehyde (4% in DPBS, Sigma-Aldrich) for 10 min, rinsed three more times with DPBS, and stored at 4 °C in DPBS until imaging. Fixed cells were permeabilized and blocked for 45 min with 3% bovine serum albumin (BSA, Carl Roth), 0.1% Tween (Tween 20, Sigma-Aldrich), and 0.1% Triton-X (Triton X 100, Carl Roth) in DPBS. Incubation with the primary antibodies (MAP2, NeuN, TH) was conducted in DPBS with 0.1% BSA overnight at 4 °C with concentrations as follows— anti-MAP2 (microtubule-associated protein 2, mouse anti-MAP2 monoclonal antibody [Y113], Invitrogen, Cat. No. 13-1500): 1:500, anti-NeuN (neuronal nuclear antigen, rabbit anti-NeuN polyclonal antibody, Abcam, Cat. No. ab104225): 1:500, anti-TH (tyrosine hydroxylase, rabbit anti-TH polyclonal antibody, Abcam, Cat. No. ab112): 1:1000. Subsequently, the cells were washed twice with DPBS and incubated with Alexa 488/555 fluorophore-conjugated anti-mouse/anti-rabbit secondary antibodies (1:1000 in DPBS with 0.1% BSA, goat anti-mouse/anti-rabbit IgG-Alexa Flour Plus 488/555 polyclonal antibody, Invitrogen, Cat. No. A32723/A32732) for 1 h in the dark. Stained cells were kept in the dark and washed three times with Tween (0.05% in DPBS) for 5 min (second washing step with Hoechst 33342 for counterstaining, 5 mg mL⁻¹ in H_2O, 1:1000). If not further noted, the steps were conducted at room temperature. Images were analyzed using a custom analysis pipeline for CellProfiler 4.2.1.[88] The Hoechst channel was used to identify nuclei. Dead cells were sorted out in the pipeline by discrimination of bright nuclei (apoptotic) and medium bright nuclei (viable).[48] Viable cells were used to mask the MAP2 channel to

identify MAP2-positive cells. The NeuN/TH channels were masked by the MAP2-positive cells to identify NeuN/TH-positive cells.

Electrophysiology: A HEKA EPC 10 USB patch-clamp amplifier with a red star headstage installed to an upright Nikon Eclipse FN1 microscope (objective: Nikon CFI TU Plan EPI ELWD 50× N.A. 0.60/W.D. 11.00 mm) was used for trace recording.[72] The patch clamp pipettes (resistance: 5–7 MΩ) were manufactured from GB150T-8P borosilicate glass capillary blanks (Science Products) using a P-2000 pipette puller (Sutter) and polished with a CPM-2 microforge (ALA Scientific Instruments). Samples were rinsed three times and subsequently covered with bath solution (140 mm NaCl, 2.4 mm KCl, 1.3 mm MgCl$_2$, 2.5 mm CaCl$_2$,10 mm 4-(2-hydroxyethyl)-1-piperazineethanesulfonic acid (HEPES), 10 mm D-glucose, pH 7.4, at room temperature) and pipettes filled with pipette solution (125 mm potassium gluconate, 10 mm NaCl, 1 mm triethylene glycol diamine tetra-acetic acid, 4 mm magnesium ATP, 10 mm HEPES, 10 mm D-glucose, pH 7.4).[85] The Patch Master V2x80 software was used for data recording including a Bessel low-pass filter set to 2.9 kHz and automatic compensation of the capacitance and series-resistance. Electrophysiological parameters were recorded and determined as follows. RMP: in current-clamp mode by keeping cells with zero current; and MC: directly determined by the patch clamp software. For APs, the first AP of an AP train at rheobase current was analyzed—namely, AP amplitude: threshold to peak; AP threshold: membrane potential where the second derivative became different from zero (determined with Origin); and AP width: full-width half-maximum of the AP.

Statistical Analysis: Confocal laser scanning microscopy imaging was conducted on 5–12 neurons per type of NW array. Immunocytochemistry data per type of NW array was collected from seven images with an area of about 1374×914 µm^2 containing in average 1035 ± 418 cells. Patch clamping was conducted on 2–7 cells per type of NW array. Origin (v.2022) was used to analyze the data using a one-way ANOVA analysis with a post-hoc Tukey's test. The graphs are presenting the means ± standard deviations. Differences were considered not statistically significant for $p > 0.05$.

Supporting Information

Supporting Information is available from the Wiley Online Library or from the author.

Acknowledgements

Conflict of Interest

The authors declare no conflict of interest.

Author Contributions

Si NW preparation, cell culture, immunofluorescence and confocal microscopy imaging, patch clamping, data analysis, and manuscript writing: J.H.; GaAs NW preparation: W.K., A.F.i M., and J.H.; assistance in cell culture: M.S.; ALD: J.H., C.H., and R.Z.; conceptualization: J.H.; funding: A.F.i M., R.Z., and R.H.B.

[1] Y. Chen, M. Alba, T. Tieu, Z. Tong, R. S. Minhas, D. Rudd, N. H. Voelcker, A. Cifuentes-Rius, R. Elnathan, *Adv. NanoBiomed Res.* **2021**, *1*, 2100002.

[2] F. Pei, B. Tian, *Adv. Funct. Mater.* **2020**, *30*, 1906210.

[3] N. P. Pampaloni, M. Giugliano, D. Scaini, L. Ballerini, R. Rauti, *Front. Neurosci.* **2019**, *12*, 953.

[4] R. Elnathan, M. Kwiat, F. Patolsky, N. H. Voelcker, *Nano Today* **2014**, *9*, 172.

[5] S. G. Higgins, M. Becce, A. Belessiotis-Richards, H. Seong, J. E. Sero, M. M. Stevens, *Adv. Mater.* **2020**, *32*, 1903862.

[6] Y. Chen, J. Wang, X. Li, N. Hu, N. H. Voelcker, X. Xie, R. Elnathan, *Adv. Mater.* **2020**, *32*, 2001668.

[7] H. Z. Yoh, Y. Chen, S. Aslanoglou, S. Wong, Z. Trifunovic, S. Crawford, E. Lestrell, C. Priest, M. Alba, H. Thissen, N. H. Voelcker, R. Elnathan, *Adv. Funct. Mater.* **2022**, *32*, 2104828.

[8] C. Chiappini, *ACS Sens.* **2017**, *2*, 1086.

[9] X. Li, J. Mo, J. Fang, D. Xu, C. Yang, M. Zhang, H. Li, X. Xie, N. Hu, F. Liu, *J. Mater. Chem. B* **2020**, *8*, 7609.

[10] R. Madonna, *Mol. Biotechnol.* **2012**, *52*, 193.

[11] D. A. Robinton, G. Q. Daley, *Nature* **2012**, *481*, 295.

[12] A. Appelt-Menzel, S. Oerter, S. Mathew, U. Haferkamp, C. Hartmann, M. Jung, W. Neuhaus, O. Pless, *Curr. Protoc. Stem Cell Biol.* **2020**, *55*, e122.

[13] M. A. Lancaster, M. Huch, *Dis. Models Mech.* **2019**, *12*, 7.

[14] A. de Rus Jacquet, H. L. Denis, F. Cicchetti, M. Alpaugh, *Mol. Psychiatry* **2021**, *26*, 2685.

[15] C. H. C. Leenaars, C. Kouwenaar, F. R. Stafleu, A. Bleich, M. Ritskes-Hoitinga, R. B. M. De Vries, F. L. B. Meijboom, *J. Transl. Med.* **2019**, *17*, 223.

[16] E. Lestrell, C. M. O'Brien, R. Elnathan, N. H. Voelcker, *Adv. Ther.* **2021**, *4*, 2100061.

[17] S. Aslanoglou, Y. Chen, V. Oorschot, Z. Trifunovic, E. Hanssen, K. Suu, N. H. Voelcker, R. Elnathan, *J. Am. Chem. Soc.* **2020**, *142*, 15649.

[18] R. Elnathan, A. W. Holle, J. Young, M. A. George, O. Heifler, A. Goychuk, E. Frey, R. Kemkemer, J. P. Spatz, A. Kosloff, F. Patolsky, N. H. Voelcker, *J. Nanobiotechnol.* **2021**, *19*, 51.

[19] H. Yoh, S. Aslanoglou, E. Lestrell, A.-R. Shokouhi, S. Belcher, H. Thissen, N. H. Voelcker, R. Elnathan, in *Semiconducting Silicon Nanowires for Biomedical Applications* (Ed: J. Coffer), Woodhead Publishing, Sawston, CA **2022**, pp. 231–278.

[20] S. Bonde, N. Buch-Månson, K. R. Rostgaard, T. K. Andersen, T. Berthing, K. L. Martinez, *Nanotechnology* **2014**, *25*, 362001.

[21] R. S. Frederiksen, E. Alarcon-Llado, P. Krogstrup, L. Bojarskaite, N. Buch-Månson, J. Bolinsson, J. Nygård, A. Fontcuberta i Morral, K. L. Martinez, *ACS Photonics* **2016**, *3*, 1208.

[22] G. He, N. Hu, A. M. Xu, X. Li, Y. Zhao, X. Xie, *Adv. Funct. Mater.* **2020**, *30*, 1909890.

[23] C. Chiappini, Y. Chen, S. Aslanoglou, A. Mariano, V. Mollo, H. Mu, E. De Rosa, G. He, E. Tasciotti, X. Xie, F. Santoro, W. Zhao, N. H. Voelcker, R. Elnathan, *Nat. Protoc.* **2021**, *16*, 4539.

[24] W. Hällström, M. Lexholm, D. B. Suyatin, G. Hammarin, D. Hessman, L. Samuelson, L. Montelius, M. Kanje, C. N. Prinz, *Nano Lett.* **2010**, *10*, 782.

[25] L. Hanson, W. Zhao, H.-Y. Lou, Z. C. Lin, S. W. Lee, P. Chowdary, Y. Cui, B. Cui, *Nat. Nanotechnol.* **2015**, *10*, 554.

[26] H.-Y. Lou, W. Zhao, X. Li, L. Duan, A. Powers, M. Akamatsu, F. Santoro, A. F. McGuire, Y. Cui, D. G. Drubin, B. Cui, *Proc. Natl. Acad. Sci. U. S. A.* **2019**, *116*, 23143.

[27] C. S. Hansel, S. W. Crowder, S. Cooper, S. Gopal, M. João Pardelha da Cruz, L. de Oliveira Martins, D. Keller, S. Rothery, M. Becce, A. E. G. Cass, C. Bakal, C. Chiappini, M. M. Stevens, *ACS Nano* **2019**, *13*, 2913.

[28] M. Park, E. Oh, J. Seo, M.-H. Kim, H. Cho, J. Y. Choi, H. Lee, I. S. Choi, *Small* **2016**, *12*, 1148.

[29] V. Gautam, S. Naureen, N. Shahid, Q. Gao, Y. Wang, D. Nisbet, C. Jagadish, V. R. Daria, *Nano Lett.* **2017**, *17*, 3369.

[30] R. Liu, J. Lee, Y. Tchoe, D. Pre, A. M. Bourhis, A. D'Antonio-Chronowska, G. Robin, S. H. Lee, Y. G. Ro, R. Vatsyayan, K. J. Tonsfeldt, L. A. Hossain, M. L. Phipps, J. Yoo, J. Nogan, J. S. Martinez, K. A. Frazer, A. G. Bang, S. A. Dayeh, *Adv. Funct. Mater.* **2022**, *32*, 2108378.

[31] R. Parameswaran, J. L. Carvalho-de Souza, Y. Jiang, M. J. Burke, J. F. Zimmerman, K. Koehler, A. W. Phillips, J. Yi, E. J. Adams, F. Bezanilla, B. Tian, *Nat. Nanotechnol.* **2018**, *13*, 260.

[32] Z. Liu, B. Wen, L. Cao, S. Zhang, Y. Lei, G. Zhao, L. Chen, J. Wang, Y. Shi, J. Xu, X. Pan, L. Yu, *Adv. Healthcare Mater.* **2020**, *9*, 1901342.

[33] A. Tay, N. Melosh, *Acc. Chem. Res.* **2019**, *52*, 2462.

[34] E. Lestrell, F. Patolsky, N. H. Voelcker, R. Elnathan, *Mater. Today* **2020**, *33*, 87.

[35] A.-R. Shokouhi, S. Aslanoglou, D. Nisbet, N. H. Voelcker, R. Elnathan, *Mater. Horiz.* **2020**, *7*, 2810.

[36] H. Acarón Ledesma, X. Li, J. L. Carvalho-de Souza, W. Wei, F. Bezanilla, B. Tian, *Nat. Nanotechnol.* **2019**, *14*, 645.

[37] W. Kim, J. K. Ng, M. E. Kunitake, B. R. Conklin, P. Yang, *J. Am. Chem. Soc.* **2007**, *129*, 7228.

[38] K. S. Beckwith, S. Ullmann, J. Vinje, P. Sikorski, *Small* **2019**, *15*, 1902514.

[39] Z. Li, S. Kamlund, T. Ryser, M. Lard, S. Oredsson, C. N. Prinz, *J. Mater. Chem. B* **2018**, *6*, 7042.

[40] J. Lee, B. Kang, B. Hicks, T. F. ChancellorJr, B. H. Chu, H.-T. Wang, B. G. Keselowsky, F. Ren, T. P. Lele, *Biomaterials* **2008**, *29*, 3743.

[41] N. Buch-Månson, D.-H. Kang, D. Kim, K. E. Lee, M.-H. Yoon, K. L. Martinez, *Nanoscale* **2017**, *9*, 5517.

[42] Z. Li, H. Persson, K. Adolfsson, S. Oredsson, C. N. Prinz, *Sci. China: Life Sci.* **2018**, *61*, 427.

[43] S. Bonde, T. Berthing, M. H. Madsen, T. K. Andersen, N. Buch-Månson, L. Guo, X. Li, F. Badique, K. Anselme, J. Nygård, K. L. Martinez, *ACS Appl. Mater. Interfaces* **2013**, *5*, 10510.

[44] H. Kim, I. Kim, H.-J. Choi, S. Y. Kim, E. G. Yang, *Nanoscale* **2015**, *7*, 17131.

[45] C. H. Rasmussen, P. M. Reynolds, D. R. Petersen, M. Hansson, R. M. McMeeking, M. Dufva, N. Gadegaard, *Adv. Funct. Mater.* **2016**, *26*, 815.

[46] H. Seong, S. G. Higgins, J. Penders, J. P. K. Armstrong, S. W. Crowder, A. C. Moore, J. E. Sero, M. Becce, M. M. Stevens, *ACS Nano* **2020**, *14*, 5371.

[47] J. Harberts, U. Haferkamp, S. Haugg, C. Fendler, D. Lam, R. Zierold, O. Pless, R. H. Blick, *Biomater. Sci.* **2020**, *8*, 2434.

[48] J. Harberts, M. Siegmund, M. Schnelle, T. Zhang, Y. Lei, L. Yu, R. Zierold, R. H. Blick, *Sci. Rep.* **2021**, *11*, 18819.

[49] Y. Chen, S. Aslanoglou, G. Gervinskas, H. Abdelmaksoud, N. H. Voelcker, R. Elnathan, *Small* **2019**, *15*, 1904819.

[50] S. Gopal, C. Chiappini, J. Penders, V. Leonardo, H. Seong, S. Rothery, Y. Korchev, A. Shevchuk, M. M. Stevens, *Adv. Mater.* **2019**, *31*, 1806788.

[51] Y. Chen, S. Aslanoglou, T. Murayama, G. Gervinskas, L. I. Fitzgerald, S. Sriram, J. Tian, A. P. R. Johnston, Y. Morikawa, K. Suu, R. Elnathan, N. H. Voelcker, *Adv. Mater.* **2020**, *32*, 2000036.

[52] E. Hebisch, M. Hjort, D. Volpati, C. N. Prinz, *Small* **2021**, *17*, 2006421.

[53] H. Jansen, H. Gardeniers, M. de Boer, M. Elwenspoek, J. Fluitman, *J. Micromech. Microeng.* **1996**, *6*, 14.

[54] Y. Chen, *Microelectron. Eng.* **2015**, *135*, 57.

[55] G. Mariani, P.-S. Wong, A. M. Katzenmeyer, F. Léonard, J. Shapiro, D. L. Huffaker, *Nano Lett.* **2011**, *11*, 2490.

[56] P. Krogstrup, H. I. Jørgensen, M. Heiss, O. Demichel, J. V. Holm, M. Aagesen, J. Nygard, A. Fontcuberta i Morral, *Nat. Photonics* **2013**, *7*, 306.

[57] X. Li, L. H. Klausen, W. Zhang, Z. Jahed, C.-T. Tsai, T. L. Li, B. Cui, **2021**, *21*, 8518.

[58] F. J. Harding, S. Surdo, B. Delalat, C. Cozzi, R. Elnathan, S. Gronthos, N. H. Voelcker, G. Barillaro, *ACS Appl. Mater. Interfaces* **2016**, *8*, 29197.

[59] X. Liu, R. Liu, B. Cao, K. Ye, S. Li, Y. Gu, Z. Pan, J. Ding, *Biomaterials* **2016**, *111*, 27.

[60] R. Liu, X. Yao, X. Liu, J. Ding, *Langmuir* **2019**, *35*, 284.

[61] Y. Q. Fu, A. Colli, A. Fasoli, J. K. Luo, A. J. Flewitt, A. C. Ferrari, W. I. Milne, *J. Vac. Sci. Technol. B Microelectron. Nanometer. Struct.* **2009**, *27*, 1520.

[62] Y.-J. Hung, S.-L. Lee, B. J. Thibeault, L. A. Coldren, *IEEE J. Sel. Top. Quantum Electron* **2011**, *17*, 869.

[63] J. Vukajlovic-Plestina, W. Kim, V. G. Dubrovski, G. Tütüncüoğlu, M. Lagier, H. Potts, M. Friedl, A. Fontcuberta i Morral, *Nano Lett.* **2017**, *17*, 4101.

[64] J. Vukajlovic-Plestina, W. Kim, L. Ghisalberti, G. Varnavides, G. Tütüncuoglu, H. Potts, M. Friedl, L. Güniat, W. C. Carter, V. G. Dubrovskii, A. Fontcuberta i Morral, *Nat. Commun.* **2019**, *10*, 869.

[65] L. Güniat, L. Ghisalberti, L. Wang, C. Dais, N. Morgan, D. Dede, W. Kim, A. Balgarkashi, J.-B. Leran, R. Minamisawa, H. Solak, C. Carter, A. Fontcuberta i Morral, *Nanoscale Horiz.* **2022**, *7*, 211.

[66] L. Güniat, P. Caroff, A. Fontcuberta i Morral, *Chem. Rev.* **2019**, *119*, 8958.

[67] W. Kim, L. Güniat, A. Fontcuberta i Morral, V. Piazza, *Appl. Phys. Rev.* **2021**, *8*, 011304.

[68] H. A. Ledesma, B. Tian, *J. Mater. Chem. B* **2017**, *5*, 4276.

[69] N. Buch-Månson, S. Bonde, J. Bolinsson, T. Berthing, J. Nygård, K. L. Martinez, *Adv. Funct. Mater.* **2015**, *25*, 3246.

[70] R. Wierzbicki, C. Købler, M. R. B. Jensen, J. Lopacińska, M. S. Schmidt, M. Skolimowski, F. Abeille, K. Qvortrup, K. Mølhave, *PLoS One* **2013**, *8*, e53307.

[71] R. Elnathan, B. Delalat, D. Brodoceanu, H. Alhmoud, F. J. Harding, K. Buehler, A. Nelson, L. Isa, T. Kraus, N. H. Voelcker, *Adv. Funct. Mater.* **2015**, *25*, 7215.

[72] J. Harberts, R. Zierold, C. Fendler, A. Koitmäe, P. Bayat, I. Fernandez-Cuesta, G. Loers, B.-P. Diercks, R. Fliegert, A. H. Guse, C. Ronning, G. Otnes, M. Borgström, R. H. Blick, *RSC Adv.* **2019**, *9*, 11194.

[73] L. Hanson, Z. C. Lin, C. Xie, Y. Cui, B. Cui, *Nano Lett.* **2012**, *12*, 5815.

**ADVANCED
SCIENCE NEWS**

www.advancedsciencenews.com

**ADVANCED
MATERIALS
INTERFACES**

www.advmatinterfaces.de

[74] X. Xie, A. M. Xu, M. R. Angle, N. Tayebi, P. Verma, N. A. Melosh, *Nano Lett.* **2013**, *13*, 6002.

[75] J. Harberts, K. Bours, M. Siegmund, C. Hedrich, M. Glatza, H. R. Schöler, U. Haferkamp, O. Pless, R. Zierold, R. H. Blick, *Nanoscale* **2021**, *13*, 20052.

[76] A. Cutarelli, V. A. Martínez-Rojas, A. Tata, I. Battistella, D. Rossi, D. Arosio, C. Musio, L. Conti, *Cells* **2021**, *10*, 1127.

[77] N. Gunhanlar, G. Shpak, M. van der Kroeg, L. A. Gouty-Colomer, S. T. Munshi, B. Lendemeijer, M. Ghazvini, C. Dupont, W. J. G. Hoogendijk, J. Gribnau, F. M. S. de Vrij, S. A. Kushner, *Mol. Psychiatry* **2018**, *23*, 1336.

[78] V. Gilmozzi, G. Gentile, D. A. Riekschnitz, M. Von Troyer, A. A. Lavdas, E. Kerschbamer, C. X. Weichenberger, M. D. Rosato-Siri, S. Casarosa, L. Conti, P. P. Pramstaller, A. A. Hicks, I. Pichler, A. Zanon, *Front. Cell Dev. Biol.* **2021**, *9*, 2013.

[79] L. M. Smits, L. Reinhardt, P. Reinhardt, M. Glatza, A. S. Monzel, N. Stanslowsky, M. D. Rosato-Siri, A. Zanon, P. M. Antony, J. Bellmann, S. M. Nicklas, K. Hemmer, X. Qing, E. Berger, N. Kalmbach, M. Ehrlich, S. Bolognin, A. A. Hicks, F. Wegner, J. L. Sterneckert, J. C. Schwamborn, *npj Parkinson's Dis.* **2019**, *5*, 5.

[80] R. S. Lam, F. M. Töpfer, P. G. Wood, V. Busskamp, E. Bamberg, *PLoS One* **2017**, *12*, e0169506.

[81] Y. Xie, R. J. Schutte, N. N. Ng, K. C. Ess, P. H. Schwartz, D. K. O'Dowd, *Stem Cell Res.* **2018**, *26*, 84.

[82] H. J. Rhee, A. H. Shaib, K. Rehbach, C. Lee, P. Seif, C. Thomas, E. Gideons, A. Guenther, T. Krutenko, M. Hebisch, M. Peitz, N. Brose, O. Brüstle, J. S. Rhee, *Cell Rep.* **2019**, *27*, 2212.

[83] J. Harberts, M. Kusch, J. O'Sullivan, R. Zierold, R. H. Blick, *Bioengineering* **2020**, *7*, 46.

[84] J. Harberts, C. Fendler, J. Teuber, M. Siegmund, A. Silva, N. Rieck, M. Wolpert, R. Zierold, R. H. Blick, *ACS Nano* **2020**, *14*, 13091.

[85] P. Reinhardt, M. Glatza, K. Hemmer, Y. Tsytsyura, C. S. Thiel, S. Höing, S. Moritz, J. A. Parga, L. Wagner, J. M. Bruder, G. Wu, B. Schmid, A. Röpke, J. Klingauf, J. C. Schwamborn, T. Gasser, H. R. Schöler, J. Sterneckert, *PLoS One* **2013**, *8*, e59252.

[86] J. Kwon, J. S. Lee, J. Lee, J. Na, J. Sung, H.-J. Lee, H. Kwak, E. Cheong, S.-W. Cho, H.-J. Choi, *Nano Lett.* **2021**, *21*, 6343.

[87] N. Tavakoli, W. Kim, T. Veeken, D. Poorten, L. Guniat, A. Rudra, A. Fontcuberta i Morral, E. Alarcon-Llado, *arXiv:2107.09465*, **2021**.

[88] D. R. Stirling, M. J. Swain-Bowden, A. M. Lucas, A. E. Carpenter, B. A. Cimini, A. Goodman, *BMC Bioinf.* **2021**, *22*, 433.

**ADVANCED
MATERIALS
INTERFACES**

Supporting Information

Generation of Human iPSC-Derived Neurons on Nanowire Arrays Featuring Varying Lengths, Pitches, and Diameters

Jann Harberts,* Malte Siegmund, Carina Hedrich, Wonjong Kim, Anna Fontcuberta i Morral, Robert Zierold,* and Robert H. Blick

Supporting information

Generation of human iPSC-derived neurons on nanowire arrays featuring varying lengths, pitches, and diameters

Jann Harberts*, Malte Siegmund, Carina Hedrich, Wonjong Kim, Anna Fontcuberta i Morral, Robert Zierold*, Robert H. Blick

J. Harberts, M. Siegmund, C. Hedrich, Dr. R. Zierold, Prof. R. H. Blick
Center for Hybrid Nanostructures (CHyN), Universität Hamburg, Luruper Chaussee 149, 22761 Hamburg, Germany.
Email Address: jann.harberts@chyn.uni-hamburg.de, robert.zierold@chyn.uni-hamburg.de

Dr. W. Kim, Prof. A. Fontcuberta i Morral
Laboratory of Semiconductor Materials, Institute of Materials, Faculty of Engineering, École Polytechnique Fédérale de Lausanne (EPFL), 1015 Lausanne, Switzerland

Prof. A. Fontcuberta i Morral
Institute of Physics, Faculty of Basic Sciences, École Polytechnique Fédérale de Lausanne (EPFL), 1015 Lausanne, Switzerland

Prof. R. H. Blick
Material Science and Engineering, College of Engineering, University of Wisconsin-Madison, Madison, Wisconsin 53706, USA
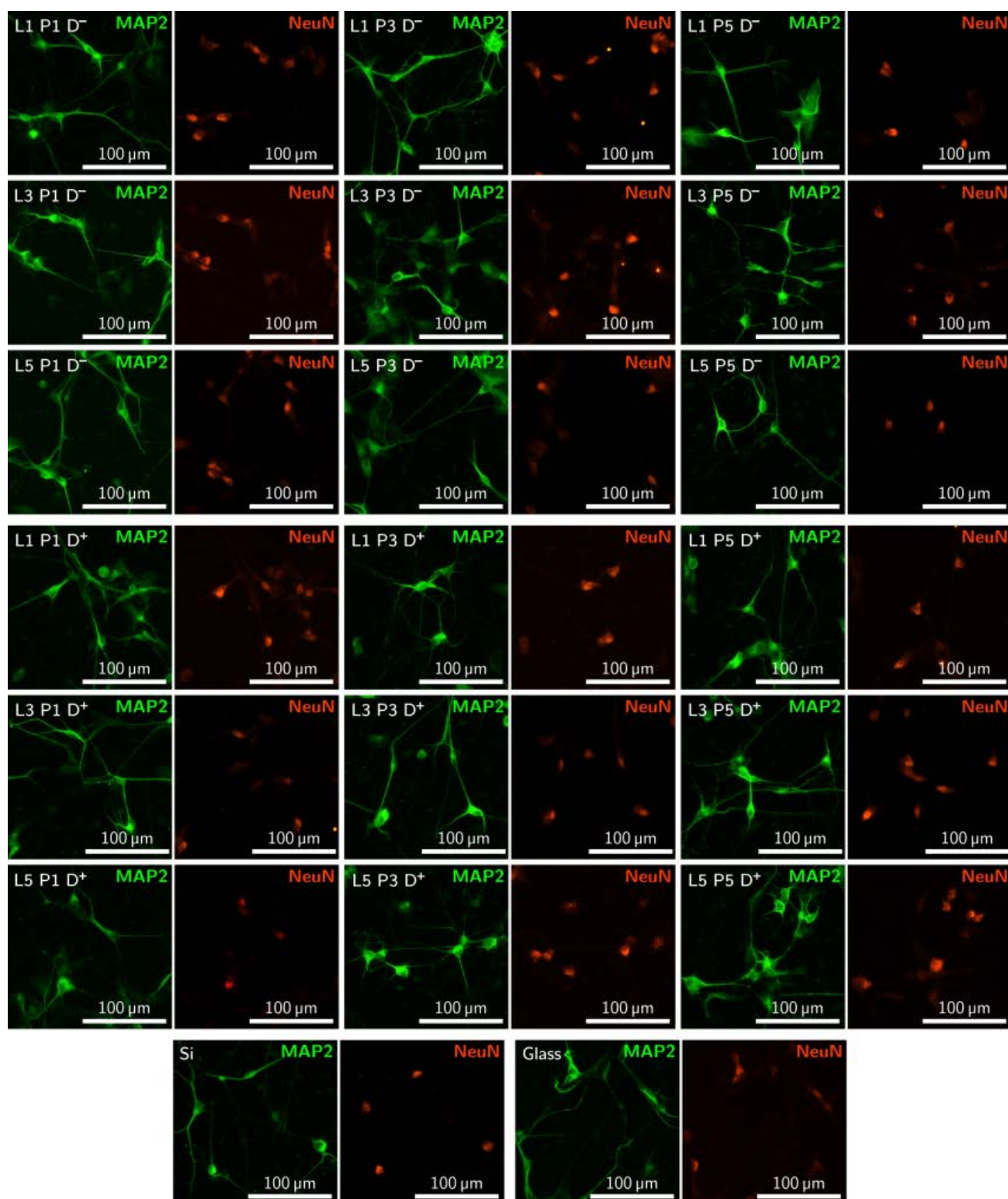
Figure S1: MAP2 and NeuN stainings. Exemplary ICC recordings of cells labeled with MAP2 (green) and NeuN (red) cultured on the NW arrays and the controls (Si and glass).
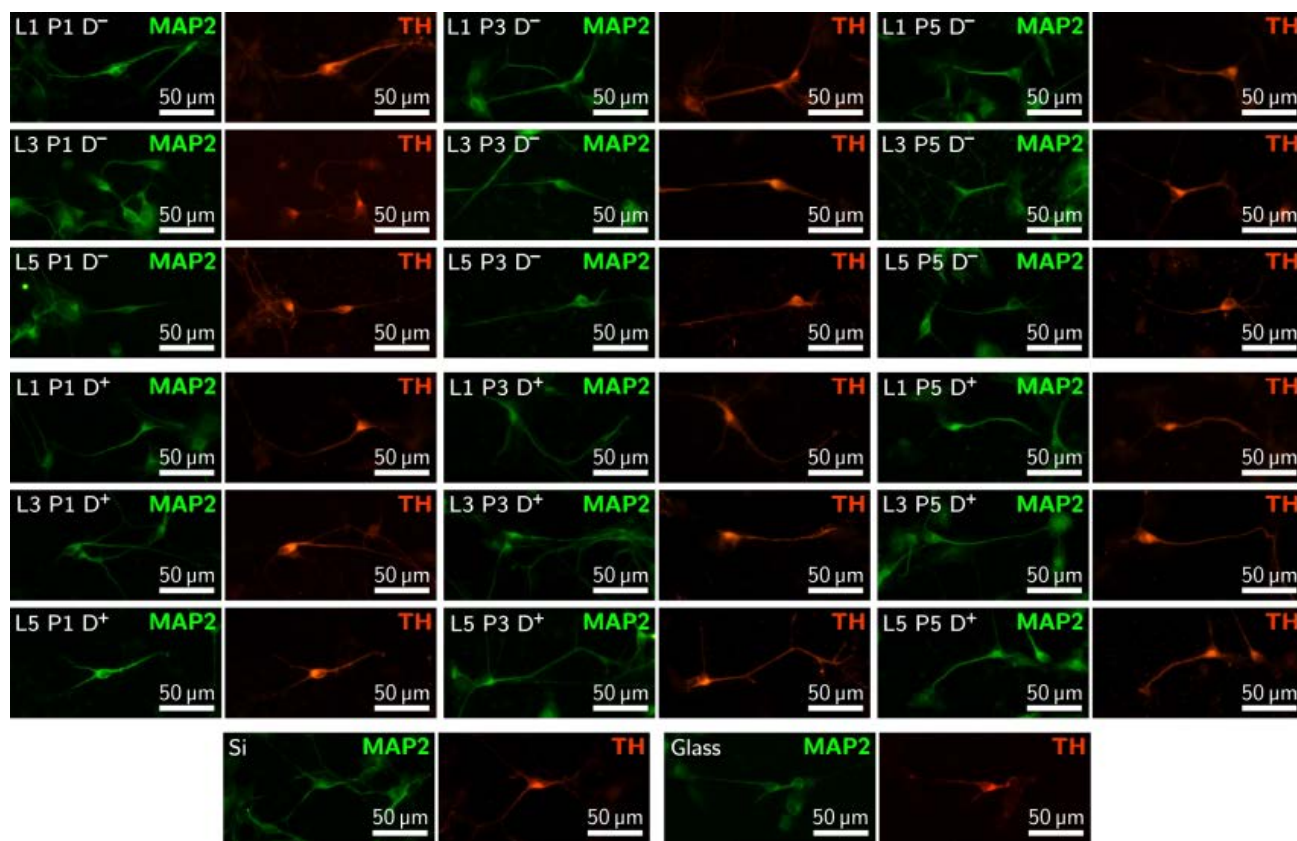
Figure S2: MAP2 and TH stainings. Exemplary ICC recordings of cells labeled with MAP2 (green) and TH (red) cultured on the NW arrays and the controls (Si and glass).
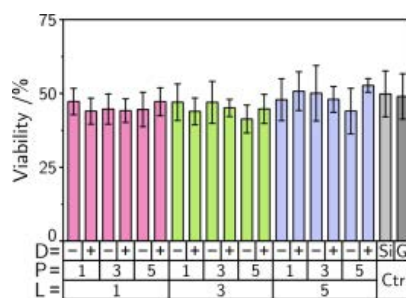
Figure S3: Viability of the cells cultured on the NW arrays and the controls. The viabilities of about 50% are reasonable for neurons after a replating procedure (Calabrese, B., Powers, R. M., Slepian, A. J., Halpain, S., *Post-differentiation Replating of Human Pluripotent Stem Cell-derived Neurons for High-content Screening of Neuritogenesis and Synapse Maturation*. J. Vis. Exp. **2019**, 150(e59305)). No statistically significant deviations in comparison to the controls (ANOVA with post-hoc Tukey's test, $\alpha = 0.05$). n(images) = 7. Error bars are SDs.
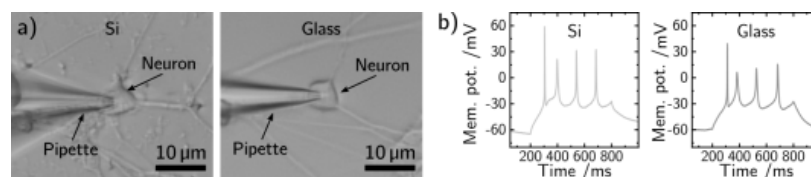
Figure S4: Exemplary images of neurons patch clamped on the control substrates (Si, glass) including traces of APs. a) Images of cells patch clamped in control substrates. **b)** Exemplary traces of APs recorded at rheobase current on Si and glass controls.
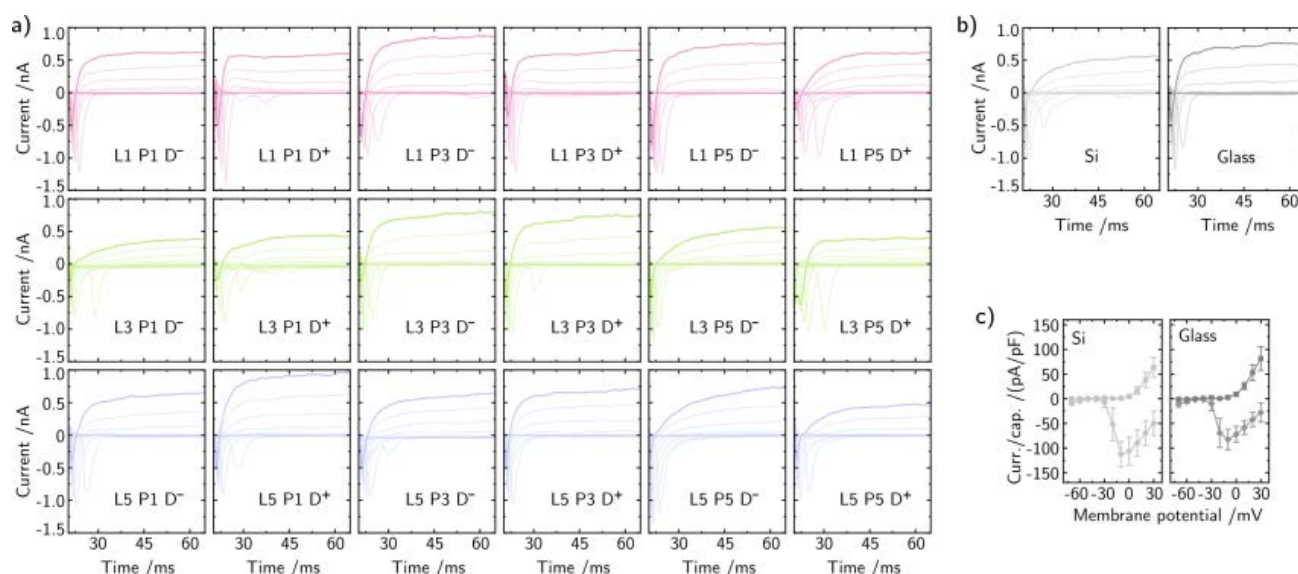
Figure S5: Electrophysiology: Control traces and completive traces on NW arrays. a) Exemplary traces of early-inward and late-outward membrane currents recorded from all types of substrates during the application of voltage steps from -70 to $+30$ mV. **b)** Corresponding membrane currents recorded from neurons on control substrates. **c)** Peak inward- and outward-currents normalized to the MCs plotted against the applied voltages for the controls (Si and glass). Error bars are SDs.
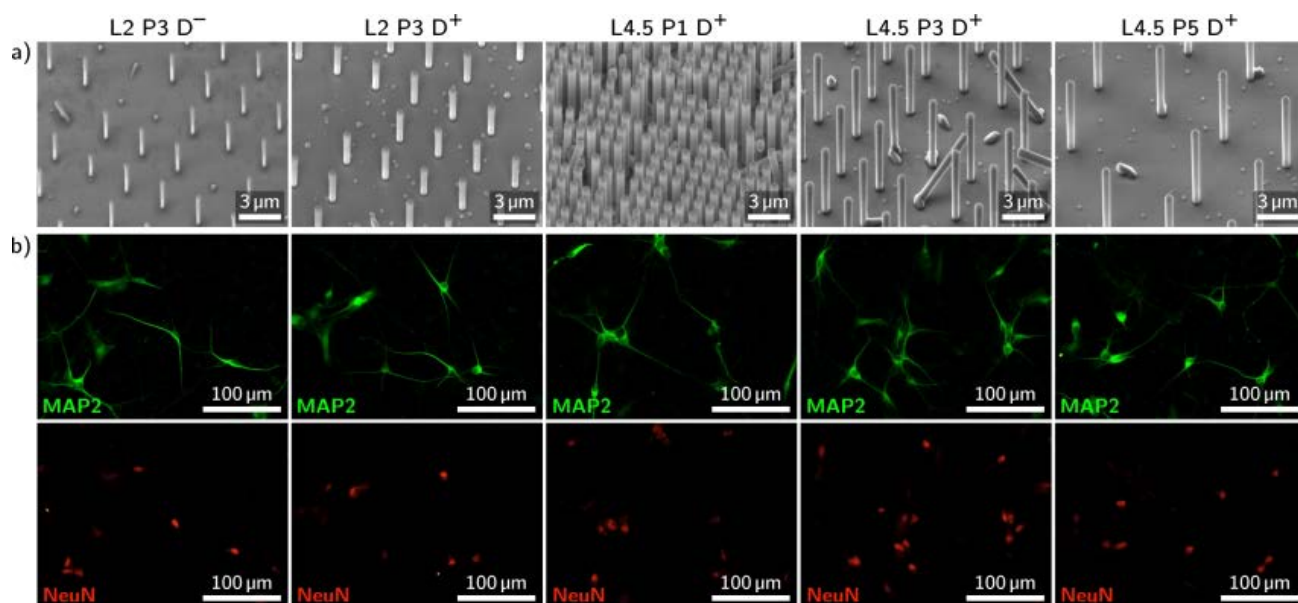
Figure S6: Examples of GaAs NW arrays including human iPSC-derived neurons generated on such NW arrays. a) Examples of GaAs NW arrays with lengths of about 2 and 4.5 μm (L2, L4.5), array pitches of 1, 3, and 5 μm (P1, P3, P5), and diameters of about 250 and 450 nm (D^-, D^+) for the L2 NW arrays, and diameters of about 600 nm (D^+) for the L4.5 NW arrays. **b)** Exemplary MAP2 (green) and NeuN (red) stainings of neurons generated on the respective NW arrays.

Fabrication of the GaAs NW arrays[1]

Thermal oxide is used as a mask to define the arrays of holes on four inch <111> P-doped Silicon wafers with a resistivity of 0.1–0.5 Ωcm. Substrates are coated with ZEP-520A resist at 8000 rpm for 1 min followed by baking at 200 °C for 5 min. This process yields a nominal resist thickness of approximately 100 nm. A VISTEC EBPG 5000+ e-beam tool operating at 100 kV was used to define the pattern. The pattern consisted of a square arrangement of holes of sizes ranging of about 65 nm; the array pitches were 1, 3, and 5 μm. The pattern is transferred on the oxide layer by a combination of wet-chemical etching based on 7:1 buffered hydrofluoric acid solution (BHF) and reactive ion etching (RIE) using SPTS APS (dielectric etcher) with CHF_3/SF_6 chemistry. After patterning, the wafers were diced into 10×10 mm^2 square chips sized for the MBE sample holder. To ensure an oxide-free surface in the holes, the chips were shortly dipped in the BHF solution prior to the introduction in the UHV chamber. All NW growth took place in DCA P600 MBE machine. The final oxide thickness before loading to machine was 10 ± 1 nm for all substrates. The prepared chips were subsequently annealed at 500 °C for 2 h in UHV to ensure a pristine surface free of water and organic molecules. The samples were then transferred to the growth chamber. There, they were degassed at 770 °C for 30 min to further remove any possible surface contaminants. In the first step, Ga was predeposited for 10 min at beam equivalent pressure (BEP) of Ga of 1.4×10^{-7} Torr (corresponding to a nominal Ga growth rate of 1.1 Å/s) by keeping the shutter opened. Once growth temperature had been reached, the As$_4$ source was opened at a beam equivalent pressure (BEP) of As$_4$ of 2×10^{-6} Torr, at a substrate temperature of 634 °C measured by pyrometer, and with 7 rpm rotation. The NW growth duration was tuned for having the targeted NW lengths. The GaAs NW arrays were—analogously to the Si NW arrays—passivated with Al$_2$O$_3$ using ALD.

[1]Adapted from: Kim, W., Dubrovskii, V. G., Vukajlovic-Plestina, J., Tütüncüoglu, G., Francaviglia, L., Güniat, L., Potts, H., Friedl, M., Leran, J. B., and Fontcuberta I Morral, A., *Bistability of Contact Angle and Its Role in Achieving Quantum-Thin Self-Assisted GaAs nanowires*, Nano Letters **2018**, 18(1), 49–57.
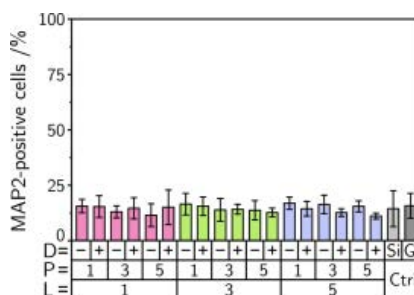

Figure S7: Proportion of MAP2-positive cells one day after plating on the NW arrays compared to controls. No statistically significant deviations in comparison to the controls (ANOVA with post-hoc Tukey's test, $\alpha = 0.05$). n(images) = 6. Error bars are SDs.

A.7 Publication VII

Toward brain-on-a-chip: human induced pluripotent stem cell-derived guided neuronal networks in tailor-made 3D nanoprinted microscaffolds

Jann Harberts, Cornelius Fendler, Jeremy Teuber, Malte Siegmund, Aaron Silva, Niklas Rieck, Merle Wolpert, Robert Zierold, and Robert H. Blick

Author contributions: J.H. and C.F. contributed equally. C.F. designed and fabricated the microscaffolds supported by M.S. J.H. performed the patch clamp measurements and SEM/FIB imaging. J.H. and N.R. performed confocal microscopy for network analysis. J.H. and M.W. conducted immunofluorescence imaging. J.H. supervised the cell culture supported by N.R., A.S., J.T., and M.S. A.S. performed control viability assays. R.Z. performed ALD. J.H. and C.F. analyzed data. J.H. wrote the manuscript. R.Z., C.F., and R.H.B. revised the manuscript. R.Z. and R.H.B. supervised the study. All authors have given approval to the final version of the manuscript.

Supporting video material is available on the publisher's website.

(12 + 5 pages)

Toward Brain-on-a-Chip: Human Induced Pluripotent Stem Cell-Derived Guided Neuronal Networks in Tailor-Made 3D Nanoprinted Microscaffolds

Jann Harberts,[⊥] Cornelius Fendler,[⊥] Jeremy Teuber, Malte Siegmund, Aaron Silva, Niklas Rieck, Merle Wolpert, Robert Zierold,* and Robert H. Blick

Cite This: *ACS Nano* 2020, 14, 13091−13102

Read Online

ACCESS | Metrics & More | Article Recommendations | Supporting Information

ABSTRACT: Brain-on-a-chip (BoC) concepts should consider three-dimensional (3D) scaffolds to mimic the 3D nature of the human brain not accessible by conventional planar cell culturing. Furthermore, the essential key to adequately address drug development for human pathophysiological diseases of the nervous system, such as Parkinson's or Alzheimer's, is to employ human induced pluripotent stem cell (iPSC)-derived neurons instead of neurons from animal models. To address both issues, we present electrophysiologically mature human iPSC-derived neurons cultured in BoC applicable microscaffolds prepared by direct laser writing. 3D nanoprinted tailor-made elevated cavities interconnected by freestanding microchannels were used to create defined neuronal networks—as a proof of concept—with two-dimensional topology. The neuronal outgrowth in these nonplanar structures was investigated, among others, in terms of neurite length, size of continuous networks, and branching behavior using z-stacks prepared by confocal microscopy and cross-sectional scanning electron microscopy images prepared by focused ion beam milling. Functionality of the human iPSC-derived neurons was demonstrated with patch clamp measurements in both current- and voltage-clamp mode. Action potentials and spontaneous excitatory postsynaptic currents—fundamental prerequisites for proper network signaling—prove full integrity of these artificial neuronal networks. Considering the network formation occurring within only a few days and the versatile nature of direct laser writing to create even more complex scaffolds for 3D network topologies, we believe that our study offers additional approaches in human disease research to mimic the complex interconnectivity of the human brain in BoC studies.

KEYWORDS: brain-on-a-chip, human induced pluripotent stem cell-derived neurons, 3D nanoprinting, 3D cell culture scaffolds, neuronal networks, patch clamping, spontaneous excitatory postsynaptic currents
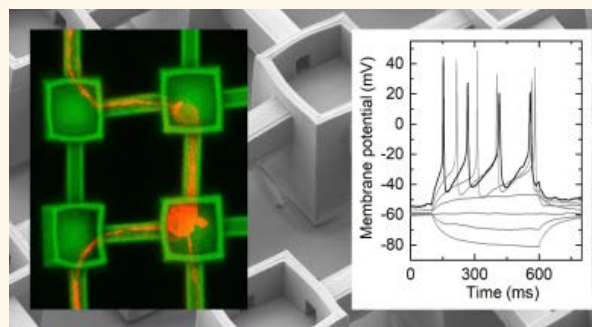
Traditional *in vitro* experiments in planar Petri dishes drastically oversimplify the complexity of *in vivo* environments, such as the human brain or spinal cord. Organ-on-a-chip has improved *in vitro* environments and led to a rise in the popularity of the complementary approach of brain-on-a-chip (BoC).[1] Initial approaches for BoC used two-dimensional (2D) microfluidic devices to separate the axon from the soma of a neuron to study the characteristics of the axon itself and the regeneration after axotomy.[2,3] Additionally, local drug treatment in the axonal region has been investigated.[4] However, the applied soft lithography techniques used limit such devices to only two dimensions that do not match the three-dimensional (3D) structure of *in vivo* environments; thereby, a demand for artificial 3D neuronal constructs exists in order to take *in vitro* experiments to the next level.[5]

The current 3D cell cultures that mimic the natural matrix use materials like fibrinogen, cellulose nanofibrils, or hydrogels to
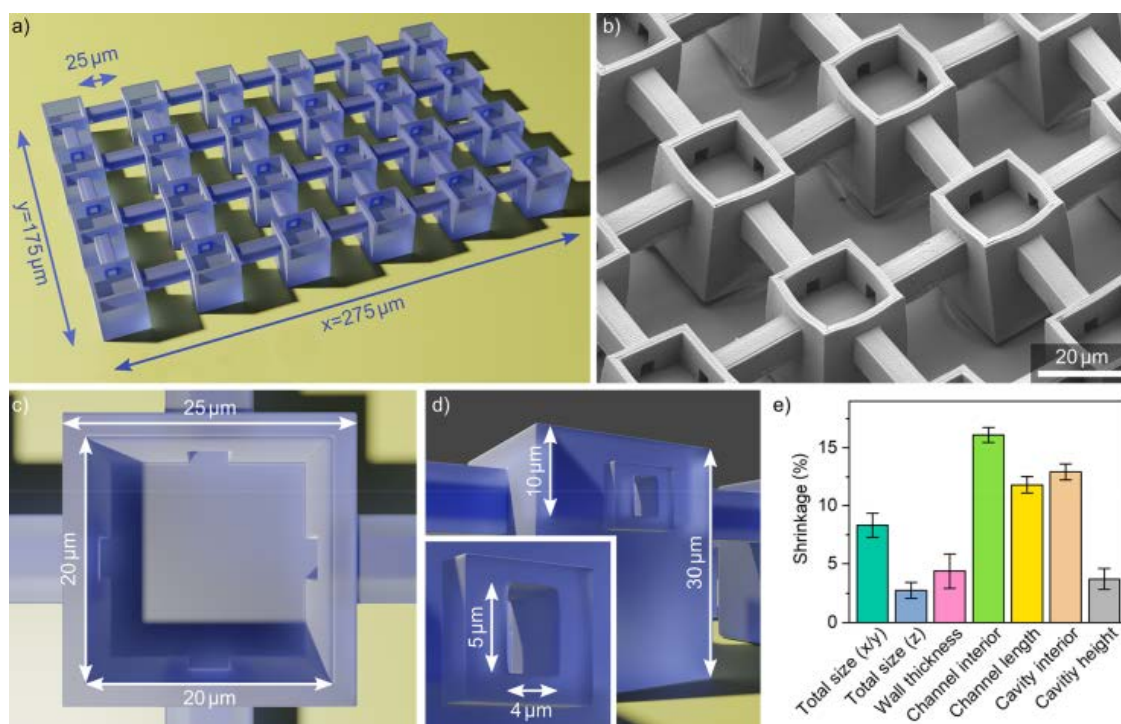
Figure 1. Description and characterization of the 3D nanoprinted (direct laser written) microscaffolds. (a) Schematic overview of the structure consisting of 4 × 6 cavities connected by freestanding microchannels to the directly neighboring cavities in the *x*- and *y*-axes. (b) Scanning electron microscopy image of the microscaffold's center. Tilt: 45°. (c) Top view of a central cavity with openings in all four directions. (d) Cross section of a microchannel. Inset: Close-up view of a microchannel's cross section. (e) Shrinkage of the direct laser written scaffold in relation to the defined feature sizes of the CAD model. *n* (scaffolds) = 5, each measured at the center and edge of the write field. Error bars are the standard error of mean.

create aerogels or suchlike porous structures.[6−8] Certainly, these scaffolds depict noteworthy progress in the field since changes in, for example, proliferation, differentiation, and gene expression have been observed by cultured cells;[9] however, they substantially lack structural features to control and manipulate neuronal network formation in a tailored fashion. A tailor-made 3D scaffold BoC that facilitates confined neuronal guiding would create a valuable tool to investigate neurons in predefined neuronal circuits for electrophysiological mechanism studies and drug screenings.[10,11]

To date, chemical and topological cues have to be used to influence neurite pathfinding within a scaffold.[12−14] The effect of chemical cues on cell adhesion, cell migration, or neuron guiding has been demonstrated with a wide variety of surface coatings such as poly-D-lysine, poly-L-lysine, poly-L-ornithine, and polyethylene glycol.[15−18] Furthermore, topological cues introduced by surface modulations of planar substrates have been studied using, for example, guidance barriers,[19−21] microtube arrays,[22−26] or confinements in neurocages, grooves, and microchannels.[2,27−34] Similar to initial 2D BoCs, standard fabrication techniques used in these studies, such as reactive ion etching, imprint/contact lithography, or laser micropatterning only operate in 2D or maximum 2.5D and are not feasible to make the leap into the "real" third dimension.[35] Technical advances in the conceptionally different technology of direct laser writing (DLW) by two-photon polymerization (2PP) now introduce previously impossible approaches to take the step from an 2D BoC toward a more natural 3D environment using CAD-designed scaffolds[36] with feature sizes down to 150 nm.[37] To date, DLW has already been used to create growth guiding

neurocages[38] in 2D as well as 3D scaffolds, such as microtowers and woodpile structures without guiding[39−41] or scaffolds with controlled cell adhesion or neurite guidance.[42,43] Hence, 2PP-DLW is a promising candidate to fabricate scaffolds for BoCs with 3D network topologies.

Employing human induced pluripotent stem cell (iPSC) technologies[44] is an additional essential key to make progress in BoC in precisely mimicking the natural structure and physiology of the human brain tissue[45] while avoiding high-failure rates of new drugs during translation from animal models.[46,47] Additionally, human iPSC-based models overcome the limited availability of primary human cells, enabling the preclinical efficacy and safety assessment of treatment modalities.[48] In fact, human iPSC-derived neurons build the cornerstone to adequately study or potentially even to ameliorate human pathophysiological conditions such as Parkinson's or Alzheimer's disease.[49,50] Moreover, neuroscience research and clinical translation are being facilitated by the development of increasingly complex co-culture and organoid systems.[51,52] Thus, human iPSC technology is fundamentally changing the strategy of basic, preclinical, and clinical research.[53]

Until now, human iPSC-derived neurons have not been applied to DLW-scaffolds; hence, the pertinence of studies using DLW is limited in the context of proving feasibility and thus addressing human pathophysiological conditions, effectively, when used in BoCs. In this work, we begin to close this gap by employing functional human iPSC-derived midbrain dopaminergic neurons in direct laser written 3D scaffolds with tailor-made neuronal network topology in 2D consisting of 24 elevated cavities connected by freestanding microchannels. Growth
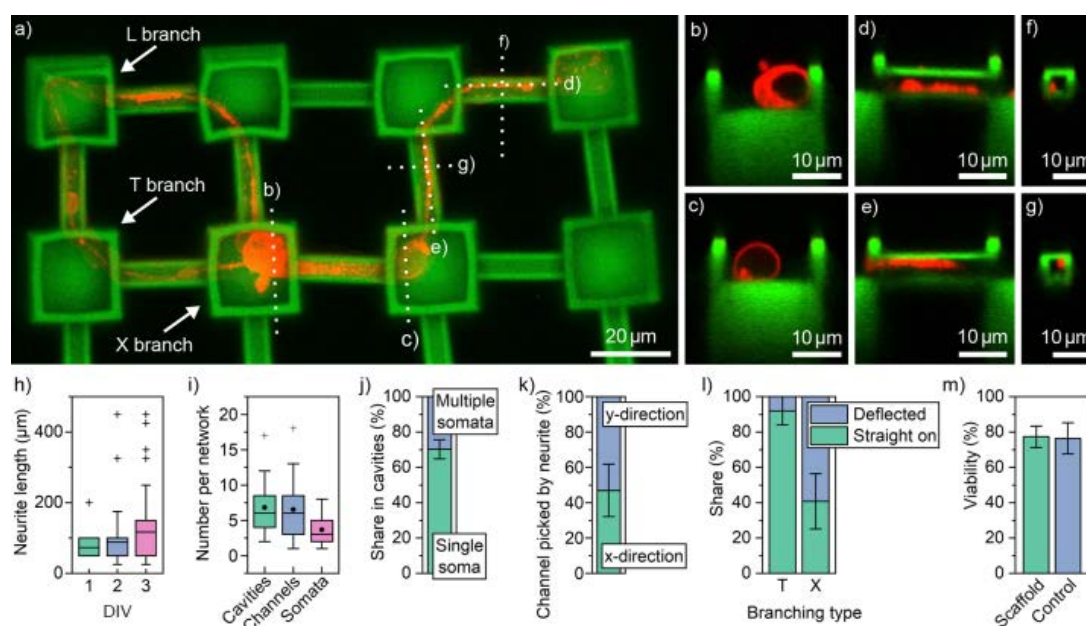
Figure 2. Visualization and characterization of the neuronal outgrowth within the microscaffolds using *z*-stacks imaged by CSLM. (a) Overview of a neuronal network (red) built by two neurons and corresponding neurites growing along the microchannels. Different branching types within the scaffold are marked by arrows. Dotted lines mark the positions of the stack slices shown in (b−g). The image was created by down projecting all *x*−*y* planes. (b, c) Cross sections of the neurons adhered to the bottom of the cavity. (d, f) Cross sections of a neurite growing on the bottom corner of the microchannel. (e, g) Cross sections of a neurite growing at the top corner of the microchannel. (h) Comparison of the neurite length of individual neurons inside the scaffold as a function of culturing time. *n* (neurites after 1, 2, 3 DIV) = 15, 56, 55. (i) Quantification of continuous networks within a scaffold containing more than two somata (*n* = 24): Number of cavities and channels involved as well as total number of somata per network. (j) Distribution of single and multiple neurons per cavity. *n* (cavities) = 273. (k) Comparison of the channel orientation picked by the neurite in *x*- and *y*-directions. *n* (branches) = 286. (l) Share of neurites growing straight on and being deflected at T and X branches, respectively. *n* (branches) = 132. (m) Cell viability during 1−4 DIV inside the scaffolds compared to planar control. *n* (scaffolds) = 172. Box plots: Boxes: 25−75% range; line: mean; whiskers: range within 1.5 IQR; and crosses: outliers. Bar charts: Error bars are standard error.

inside the microscaffolds was analyzed by *z*-stacks prepared by confocal microscopy and cross-sectional scanning electron microscopy images. With patch clamp experiments, we prove functional electrophysiological integrity of the neurons and determine electrophysiological properties such as resting membrane potentials, early inward/late-outward currents as well as kinetics of action potentials (APs). Especially, observed spontaneous excitatory postsynaptic currents (sEPSCs) indicate the presence of synaptic junctions—an important prerequisite for interneuronal communication. Thus, we propose our work to be applicable to BoC devices to build functional human neuronal networks with 3D network topologies, allowing for additional approaches to mimic the complexity of the human brain.

RESULTS AND DISCUSSION

The 3D nanoprinted (direct laser written) scaffold (Figure 1a) consists of an array of 4 × 6 cavities on top of microtowers spaced by 25 *μ*m; each cavity is connected by a microchannel to the directly neighboring cavity. Total dimensions of the CAD model are 275 *μ*m × 175 *μ*m in the *x*- and *y*-directions, respectively. The model had been adjusted to fit into a single write field of the direct laser writer (Nanoscribe) providing stitch-free scaffolds. Figure 1b displays a scanning electron microscopy image of such a scaffold. The inner part of the cavities has a width of 20 *μ*m, and the wall thickness is 2.5 *μ*m, resulting in a total width of 25 *μ*m (Figure 1c). Each cavity has a depth of 10 *μ*m and is carried by a microtower with a total height

of 30 *μ*m (Figure 1d). The microchannels have inner dimensions of 5 *μ*m in height and 4 *μ*m in width (inset in Figure 1d). Prior to cell culture experiments, we analyzed the shrinkage of the scaffold's feature sizes (Figure 1e) after writing and developing since 2PP-DLW resins usually shrink during processing. The lateral dimensions shrink by about 8%, whereas the *z*-dimension and wall thickness are less affected by the shrinkage, that is, only 3−4%. The largest discrepancy between the CAD model and real scaffold was observed at the inner dimensions of the microchannels having a total shrinkage of 16%. Consequently, the inner cross section of the channel results in an effective size of 4.3 *μ*m × 3.4 *μ*m (*H* × *W*). Channel length and cavity interior shrink by approximately 11%, whereas the cavity height shrinks less by 4%.

Dissociated dopaminergic neurons were plated onto the scaffolds in a self-assembly process (see Figure S1 for immunofluorescence stainings). To facilitate the adhesion of cells primarily inside the cavities and to support growth through the microchannels, the interior of the microscaffold is selectively coated with cell adhesive poly-L-lysine (PLL) using a PLL-filled micropipet. When the pipet tip is brought in contact with the surface of the microstructure, capillary forces distribute the solution inside the entire network. Detailed visualization of the coating process—also using food dye—can be found in the supporting material (Figure S2, Movie S1, and Movie S2). In addition to PLL, neuronal growth is generally promoted by a complementary unspecific coating of laminin.
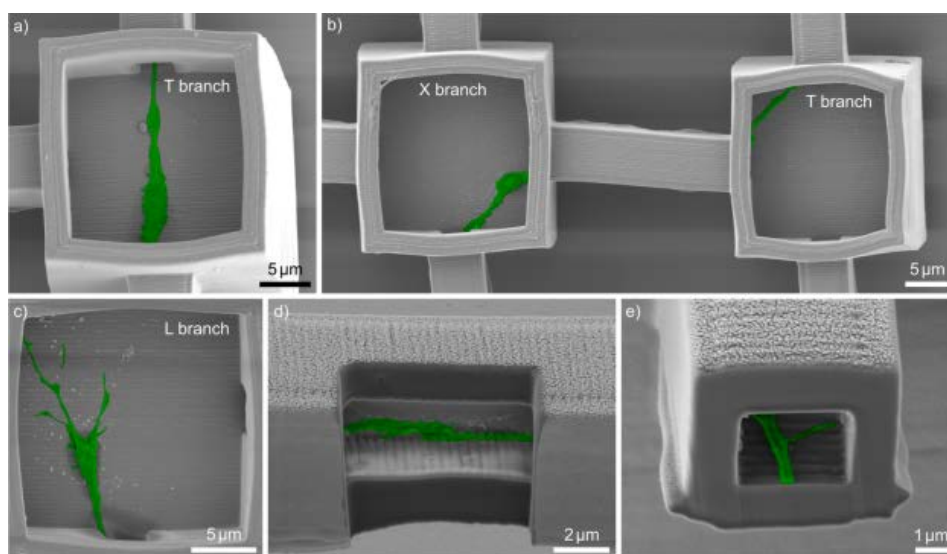
Figure 3. Scanning electron microscopy images of the neurite growth supported by cross sections prepared with focused ion beam milling. Neurites are false colored in green. (a) Top view of a neurite growing straight on in a T branch cavity. (b) Top view of a neurite being deflected at X and T branches. (c) Top view of a growth cone inside an L branch cavity. (d) Cross section along the microchannel showing a neurite growing along the bottom corner of the channel. (e) Cross section of a microchannel at a section of the channel where a neurite is in transition from the corner at which it enters the channel to the corner of the microchannel where it leaves the channel (*cf.* panel b).

The neurons used in this study were derived from human iPSCs, which differentiated at least 14 days *in vitro* (DIV) on regular Matrigel-coated well plates. Mature neurons were detached using Accutase, and the cell suspension was transferred to a well plate containing the microscaffold.

First, we analyzed the neuronal outgrowth using light microscopy and confocal scanning laser microscopy (CSLM). For the latter, the neurons were stained using the membrane stain from ThermoFisher's neurite outgrowth staining kit. A typical recording of *z*-stacks prepared by CSLM is compiled in Figure 2a−g. In detail, Figure 2a displays a top view of a typical neuronal network formed by two neurons in adjacent cavities. In this example, both neurons rest inside X branched cavities (the term X refers to four connected neighbors), and their neurites grow through microchannels passing through T (three connected neighbors) and L (two connected neighbors) branching cavities. Cross-sectional images are obtained by *z*-stacking of different image planes. The specific locations at which the selected figures in Figure 2b−g are taken, are indicated by dotted lines in the overview image Figure 2a. In detail, Figure 2b,c show the cell somata inside the cavity, which adhere to the cavity's corners to maximize the contact area to the scaffold's surface. Figure 2d,e and Figure 2f,g display cross-sectional images of neurites inside the microchannels along and across the channel orientation, respectively. Note, the neurites prefer to grow along the corners of the channel and can stick to the bottom as well as the ceiling of the microchannel.

In a following step, we analyzed the network formation by different aspects such as neurite length, continuous network scale, or branching behavior. In general, the mean neurite length of individual neurons increases from 73 to 117 μm over the time span of 1−3 DIV (Figure 2h). Especially, the number of outliers increases over time and shows maximum lengths up to 450 μm, which in turn means that up to 9 microchannels and cavities have been crossed. Furthermore, we analyzed continuous networks within a scaffold, which were defined by at least two neurons in separate cavities whose neurites overlap or cross each other within the scaffold (Figure 2i). The dimension of the networks reaches from a minimum size of just two connected neurons in neighboring cavities up to large networks, which stretch out over 17 cavities and 18 channels. On average, 3.7 neurons were involved in the formation of a continuous network. Moreover, cavities were predominantly occupied by only one neuron (Figure 2j). Continually, we examined the growth directions of the neurites. Note, the surface roughness along the *x*- and *y*-axes is slightly different due to 2PP-DL writing the scaffold line-by-line. Yet, this asymmetry of the surface roughness in *x*- and *y*-directions has no effect on lateral direction in which the neurites preferred to extend because the share of channels picked by the neurites in *x*- and *y*-directions is equal (Figure 2k). Furthermore, we quantified the turning behavior of the neurites at X and T branches (Figure 2l): For T branches, paths were only considered where the neurite had to choose between growing straight or turning, which excludes cases when neurites entered from the "bottom" of a T branch. For X branches, we observe that 59% of the neurites prefer to turn toward a channel to the side. For T branches, however, we observe that most of the neurites grew straight (92%) and turning was a lot less probably compared to X branches. Finally, we found that cells growing inside the scaffolds show a viability of about 77%, which is similar to cells cultivated on planar controls (Figure 2m).

To visually support the findings from the network analysis, a compilation of high-resolution scanning electron microscopy images of neurites inside the scaffold is shown in Figure 3. Specifically, Figure 3a,b display top views of T and X branches containing neurites growing straight and turning, respectively. The two regular cases become apparent, since neurites in the center of a channel tend to grow straight (a) and neurites at the edges are more likely to turn toward the corresponding direction (b). In addition, the growth cone displayed in Figure 3c initially turns slightly after entering the cavity. Figure 3d,e show a longitudinal and transversal cross section of the microchannel,
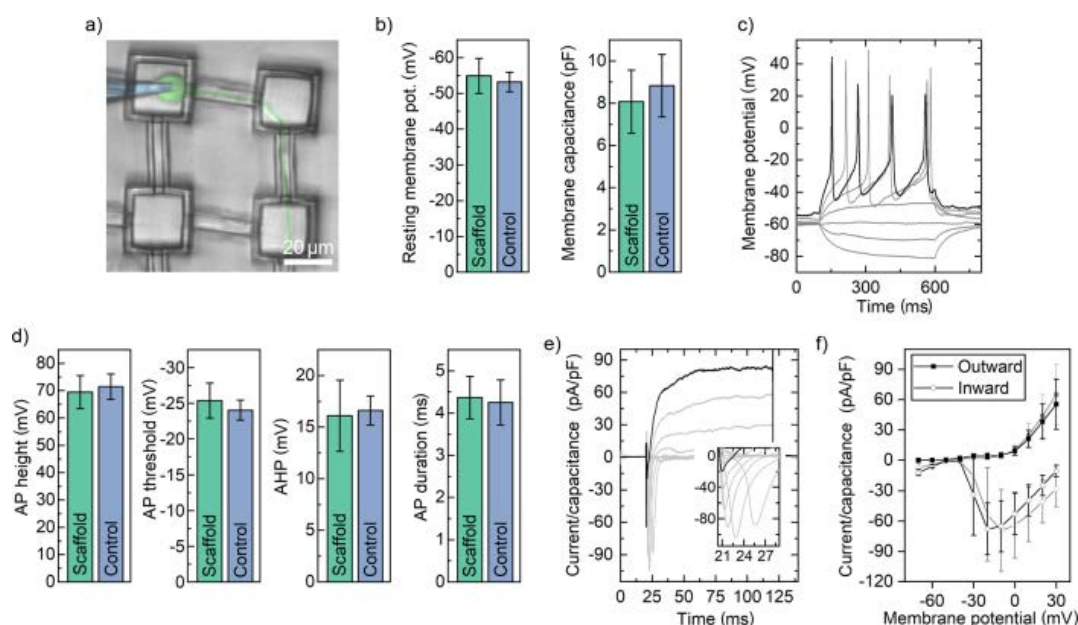
Figure 4. Electrophysiological characterization of neurons using the patch clamp technique. (a) Illustration of the patch clamp procedure while measuring a neuron grown inside the scaffold. The pipet is entering from the left (blue) and in contact with the cell (green). The neurite is growing along the L and T branch, leaving the imaged area. (b) Comparison of passive membrane properties between neurons grown inside microscaffolds ($n = 6$) and on control substrates ($n = 9$). Error bars: Standard error of mean. (c) Exemplary plot of an AP train during electrical depolarization in current-clamp mode using a current step function from −6 pA to +12 pA in 3 pA steps, where the black trace corresponds to +12 pA. (d) Quantification of the AP shape. Error bars: Standard error of mean. (e) Exemplary plot of the in- and outward currents in voltage-clamp mode using a voltage step function from −70 mV to +30 mV in 10 mV steps, where the black trace corresponds to +30 mV. (f) Current−voltage relationship of in- and outward currents inside the scaffold (black traces, $n = 6$) and control (gray traces, $n = 9$) measured on the peak and normalized to the membrane capacitance. Error bars: Standard error.
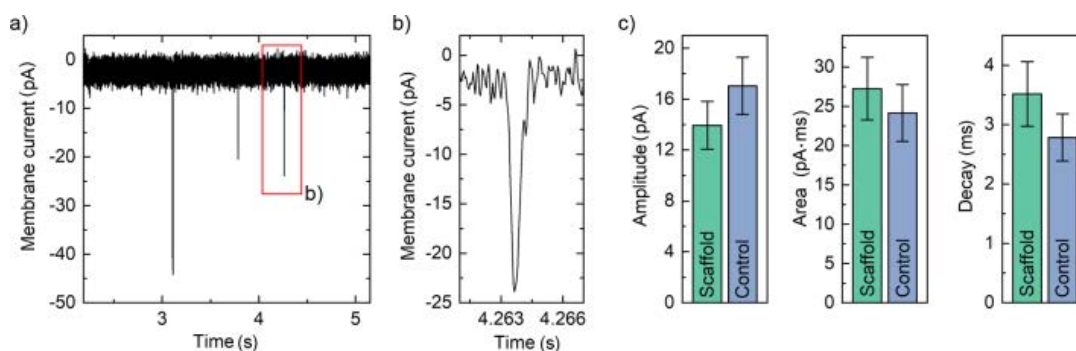

Figure 5. Characterization of sEPSCs measured on neurons inside microscaffolds. (a) Exemplary trace of postsynaptic events. (b) Zoom-in on event labeled in (a) by a red-colored box. (c) Comparison of kinetic parameters such as amplitude, area, and decay of sEPSCs measured in scaffolds ($n = 70$) compared to control ($n = 28$). Error bars: Standard error of mean.

respectively. Both cases of a neurite growing in the edge and the center of the channel are illustrated.

To test the electrophysiological integrity of the neurons inside the scaffold, we performed various types of patch clamp measurements in both current- and voltage-clamp mode. In Figure 4a, a typical patch clamp procedure is illustrated, where the patch pipet (blue) enters from the left and is in contact with the cell soma (green) located in the top left cavity. The neurite grows through the top right cavity turning downward and then leaves the picture detail through the bottom right cavity.

Passive membrane parameters of neurons measured inside the scaffold, namely, a resting membrane potential (RMP) of −54.9 ± 4.9 mV and a membrane capacitance (MC) of 8.1 ± 1.5 pF, are similar to planar control (Figure 4b) and reveal no

statistically significant deviances (ANOVA with post hoc Turkey's test, $\alpha = 0.05$, cf. Table S1). Furthermore, we analyzed APs evoked by an electrical current injection. Typical traces of APs measured from a neuron inside the cavity are displayed in Figure 4c. Injected electrical current steps were applied from −6 pA to +12 pA in 3 pA steps, where the black trace corresponds to +12 pA. The kinetics of the APs were then quantified in terms of amplitude, threshold, spike afterhyperpolarization (AHP), and duration (Figure 4d). The AP amplitude is 69.5 ± 6.0 mV, the threshold for triggering APs amounts to −25.4 ± 2.5 mV, the hyperpolarization after APs is 16.1 ± 3.4 mV, and the AP duration is determined to be 4.4 ± 0.5 ms. Again, no statistically significant deviations are found compared to the control (Table S1). Aside from these current-clamp measurements, we

performed voltage-clamp measurements to test the presence of characteristic early inward and late outward currents. Typical traces of such currents normalized to the MC—measured on a neuron in the scaffold—are shown in Figure 4e. The voltage was applied from −70 mV to +30 mV in 10 mV steps, where the black trace corresponds to +30 mV. The inset zooms in on the early inward currents. The peak currents were then plotted against the applied potentials and compared to the control (Figure 4f). Both shape and amplitude of the inward/outward voltage−current relations inside scaffolds (black) are comparable to the control (gray).

Finally, we tested the neurons inside the scaffold for spontaneous excitatory postsynaptic currents (sEPSCs). An exemplary trace of a sEPSC recording is shown in Figure 5a,b, where the latter zooms in on an individual event. We analyzed the kinetic parameters of the postsynaptic events ($n = 70$) such as amplitude, area, and decay time to be 13.9 ± 1.9 mV, 27.2 ± 4.0 (pA·ms), and 3.5 ± 0.5 ms, respectively (Figure 5c). These values are comparable to the control measurements (again, no statistically significant deviation, ANOVA with post hoc Turkey's test, $\alpha = 0.05$, cf. Table S2).

2PP-DLW is a powerful CAD-assisted tool to fabricate 3D cell culture platforms recapitulating natural features and size scales of cell environments with high precision—a prerequisite for future BoC devices.[54] In this work, we prepared an array of 4 × 6 elevated cavities connected by freestanding microchannels to hold cell somata and for neurite guiding, respectively. Conceptually, the capability of DLW to fabricate free-standing channels and elevated cavities with high grade is crucial to realize more complex scaffolds. Furthermore, scaffolds decoupled from the rigid substrate build a softer environment beneficial for soft tissue engineering concordant to hydrogels.[55] The size of 175 μm × 275 μm was optimized to fit completely in both the write field of the direct laser writer (Nanoscribe) as well as the field of view of the patch clamp setup. However, scalability in DLW fabrication is in general no issue, as it has been demonstrated already with woodpile structures[40,56,57] or 3D microscaffolds,[43] whereby fabrication time of scaffolds in mm-scale stayed in the order of hours. Note, all the materials for scaffold preparation used in such an approach are of synthetic nature and thus are free from ethical concerns. This fact is a striking advantage compared to animal-derived polymers such as collagen,[58] rendering DLW written scaffolds an ideal candidate for large-scale studies.

Compared to our earlier work on murine neurons,[43] we kept all cavities at the same height to facilitate imaging and carrying out the patch clamp measurements while keeping the network topology identical. Using Nanoscribe's IP-Dip resin, we easily achieved the necessary feature sizes of the scaffold, which compete with or even outperform prior studies that employed DLW.[39,59,60] As for many resins, IP-Dip shrinks during development. In detail, we observe a shrinkage between 3% and 16%, which is comparable to the literature for IP-Dip.[61] Since IP-Dip is not explicitly mentioned as biocompatible, we passivated the scaffolds with aluminum oxide to reliably avoid any cytotoxicity.[62−64] The complete biocompatibility of our scaffold is reflected in both cell viability and electrophysiology. Despite a small shrinkage of the scaffold, the cavity sizes and the channel diameters reliably served for soma adhesion inside the cavities and neuronal outgrowth inside the channels, as shown via confocal microscopy and scanning electron microscopy. As a matter of fact, the selective PLL coating[16] inside the scaffold and complementary laminin coating[65] substantially contribute to localized growth, as we demonstrated in prior work.[43] Inside of the microchannels, the neurites prefer to grow along the edges predominantly caused by contact guidance.[66]

The cavity's size of 20 × 20 μm^2 primarily leads to small single cells (70%) being located inside individual cavities (cell soma diameters of about 10 μm). To evaluate these findings, we applied the analysis to data used in a previous publication.[43] We found that for identical cavity dimensions, the yield rate of single cells using human iPSC-derived neurons compared to murine neurons is increased (from 70% to 40%, respectively) since the mean diameter of murine somata is smaller. Also, selectivity of 20 × 20 μm^2 sized cavities for rather small human iPSC-derived neurons is plausible since the dimensions of the cavities limit the cell sizes, which fit into an individual cavity. Albeit DLW would allow for tailor-made preparation of cavities ranging in size, larger cavities would result in a reduced number of individual neurons inside each cavity. On average, continuous networks within a scaffold were formed by 3.7 neurons, and within these networks, individual neurites crossed up to 9 cavities and microchannels. For future BOC applications, the estimation of the complexity of the neuronal network is crucial in order to model the complexity of the brain with its billions of neuronal junctions.[1] However, in this concept study, we kept the network complexity at a manageable degree for manual data analysis using low cell densities. In mean, 16% of the cavities were occupied with neurons, and the networks covered up to 75% of the scaffold. To achieve improved yields of cavities filled with neurons, the seeding density could be increased accordingly. Probably, higher seeding densities would also go along with more neurons attached elsewhere on the scaffold. Strategies using, for example, cell repellent polyethylene glycol (PEG)-functionalized PLL to coat the area without specific PLL coating could further increase settling selectivity even at high seeding densities. To avoid multiple neurons in a single cavity, one can tailor the sizes of the cavity by adjusting the CAD-file for the laser writing process.

Since DLW adds to the structure line by line, different surface topology results in the nm-scale along the x- and y-axes. Note, literature reports that surface roughness can influence adhesion and viability.[67,68] Yet, in our case, we do not observe any preferred growth direction of the neurites depending on the surface roughness, meaning that guiding by macroscopic scaffold topology and surface coating is decisive. The general pathfinding of neurites, however, differs depending on the branching type of the cavity. For X branches, 59% of the neurites turned toward a side channel. For T branches though, 92% of the neurite grew straight. In general, one can assume that after entering the cavity, the neurite most likely continues to grow straight because growing along corners in an angle of >84° is rather unlikely, as demonstrated by Renault et al.[32] On a flat surface without contact guidance, one can assume a random walk of the neurite's growth cone. For X branches, turning angles of about 0°−50° and 130°−180° would result in finding a turning channel first, which covers about 55% of the opening angle and fits well to what has been observed. For T branches, only 0°−50° turning correspond to finding a sideways laying channel first, which is about 27%. Still, this value is higher compared to our findings (8%). We believe that this discrepancy can be explained as follows: To have the option for growing straight or being deflected in a T branch, the neurite must enter the cavity from an exterior channel at the edge of the scaffold (or else they were excluded from data). To fulfill this requirement, either the neuron itself must be located in an exterior cavity or the neurite entered the outer region of the scaffold before from
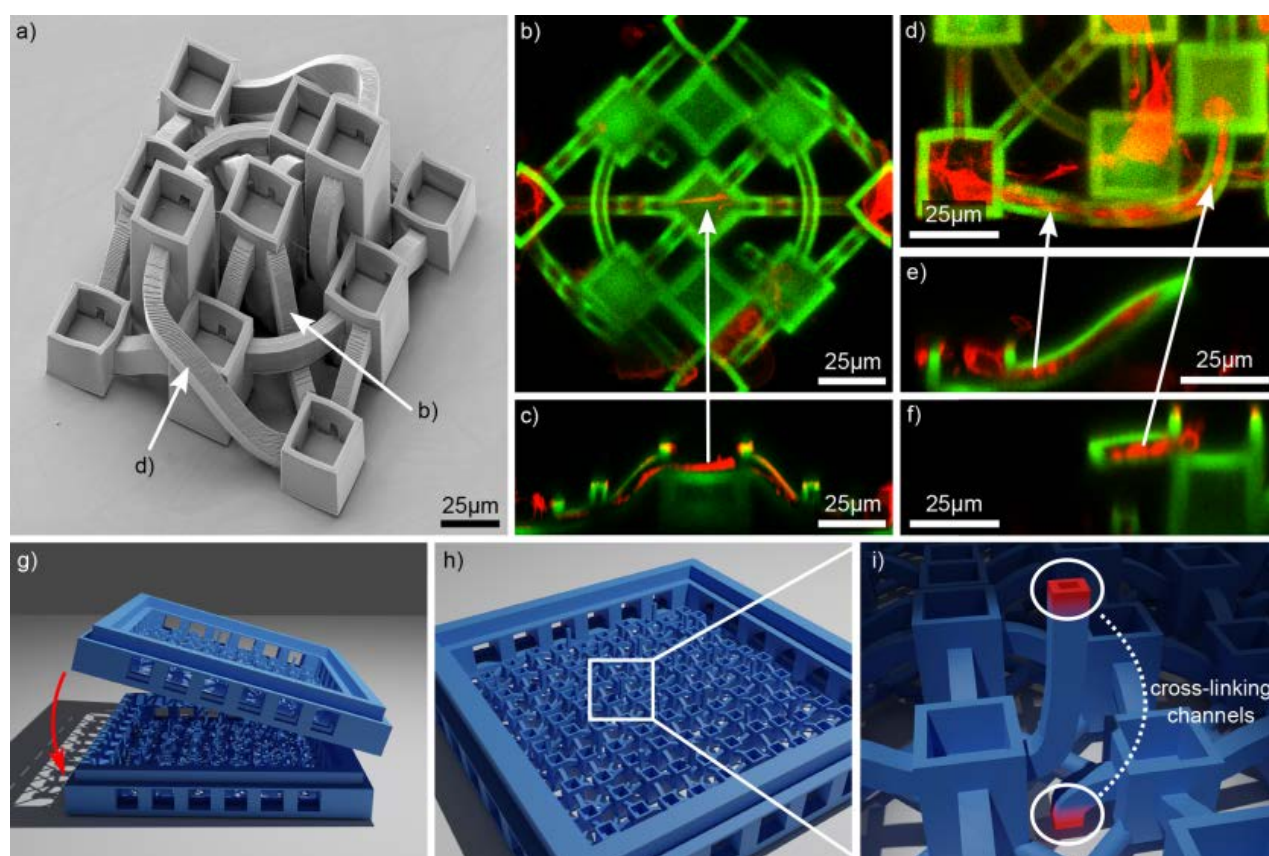
Figure 6. Potential future concepts for scaffolds with 3D network topology. (a) SEM image of a DLW print of a scaffold with cavities at four different heights connected by contorted channels ranging from cavities at the very top to bottom. **(b−f)** Projection of z-stacks and corresponding cross sections of human iPSC-derived neurons cultured in the structure shown in (a). Neurites smoothly grow to cavities at different elevations. **(g−i)** Concept of a stackable 3D scaffold: Multiple layers of planar scaffolds would be stacked after cell seeding (g). Each layer would consist of 2D networks (h) which are connected with each other by cross-linking channels (i). The joints are colored in red.

inner channels. In the latter case, the neurite is more likely to reach the outer edge of the cavities and channels first by growing straight. Due to contact guidance, the neurite then prefers to continue growing along this outer edge. In addition, neurites bend slightly toward the direction of the corner they stick to before they detach from sharp edges, as they will do while entering the cavity. This observation was also seen by Renault *et al.* and is herein visualized in a high-resolution image of the grow cone (Figure 3c). Thus, the outer edge is reached again first in the following cavity and repeats the routine leading to high probabilities to grow straight in T branches (for an example, see Figure S3).

Full functional electrophysiological integrity of the human iPSC-derived neurons inside the scaffolds was demonstrated with patch clamp measurements in both current- and voltage-clamp mode. The neurons inside scaffolds show stable RMPs (-54.9 ± 4.9 mV), which are similar or above average compared to iPSC-derived neurons.[69−73] From a MC of 8.1 ± 1.5 pF, one can roughly estimate the lengths of the neurites of the neurons patched. Assuming spherical somata with diameters of 10 μm, a mean neurite diameter of 1 μm, and a specific membrane conductance of 0.9 pF/cm^2 for neurons,[74] the average neurite length per neuron is about 180 μm, which is in accordance with our findings of the network analysis. Furthermore, comparable values of MCs for neurons originating from human iPSCs are found in literature.[72,75,76] The kinetics of the APs in terms of

amplitude (69.5 ± 6.0 mV), threshold (-25.4 ± 2.5 mV), AHP (16.1 ± 3.4 mV), and duration (4.4 ± 0.5 ms) are similar to neurons derived from human iPSCs.[69−71,77,78] Proper expression of fast-gating sodium and slow-gating potassium ion channels is shown with adequate early inward currents and late outward currents, whose normalized peak currents are in accordance with literature.[79] Furthermore, the presence of postsynaptic currents demonstrates functional synaptogenesis—the formation of synapses between neurons—a prerequisite for forming functional network activity.[80] Kinetics of the sEPSCs in terms of amplitude (13.9 ± 1.9 mV), area (27.2 ± 4.0 pA·ms), and decay (3.5 ± 0.5 ms) are in line with other human iPSC-derived neurons.[75,77]

We show that human iPSC-derived neurons form functional neuronal networks in 3D nanoprinted microscaffolds. Other studies already used nonconfining and/or random scaffolds built from PMEDSAH, fibrin hydrogel, micropillars, or microfibrous chitin-alginate as platforms to induce neuronal cells from human iPSCs.[81−84] However, our direct laser written scaffolds feature additional neurite guiding, and more importantly, functional electrophysiological analysis has been performed in contrast to the aforementioned studies. So far, other existing studies using DLW and human neurons demonstrated no or only very limited neurite guiding capabilities and no functional analysis at all. Moreover, the human neurons in these studies have been derived from human embryonic stem cells instead of human

iPSCs used in our experiments. Note, employing human embryonic stem cells raises sharp ethical and political controversies on the one hand,[85] and on the other hand, only patient-derived induced pluripotent stem cells have the unique advantage to study disease-associated genotype−phenotype relationships.[86,87]

Even though we used rather small scaffold dimensions with 2D network topology for our concept study, the versatile options of CAD-assisted DLW to fabricate intricate cell culture scaffolds[88] and the indefinite scalability of self-assembly cell plating allow us to propose our results to be applicable for scaffolds of larger scale and more complex topologies in BoC applications. Thus, we believe that our results with human iPSC-derived neurons in direct laser written scaffolds offer additional approaches to address matters regarding *in vitro* disease modeling and functional network studies.

To give a more sophisticated perspective for future designs, we created a scaffold prototype containing cavities within towers of varying heights and contorted channels, which interconnect the cavities arranged at the different levels (Figure 6a). Growth and guiding within this structure are shown in Figure 6b−f, where the neurites smoothly reach neighboring cavities at different elevations/height levels using the twisted micro-channels. Since neuronal growth in steeply curved channels is without obvious restrictions, it is reasonable to propose that such channels could be used to cross-link different layers of 2D networks. Figure 6g−i outline an approach, where stackable scaffolds (g) containing cavities and channels in 2D (h) would be used to assemble a cube-like scaffold after the cells have been seeded onto the scaffold. Several cross-linking channels (i) would then allow for interconnections between each layer of the cube scaffold. Figure S4 in the supporting material shows a comparable scaffold held by regular tweezers and demonstrates that the DLW produced scaffolds withstand the required mechanical stress to be stacked together.

CONCLUSIONS

We demonstrate that human iPSC-derived midbrain dopaminergic neurons are functional in artificial microscaffolds, which could be used in BoC applications and thereby satisfy present needs in medical research.[45] Midbrain dopaminergic neurons are an interesting candidate to build BoCs, as they control essential key functions in the brain, such as voluntary movement, reward processing, and working memory.[89] Furthermore, many disorders such as Parkinson's disease, autism, and schizophrenia are associated with malfunction of the dopaminergic system.[90]

In particular, we prepared tailor-made 3D nanoprinted microscaffolds for guided neuronal growth and employed human iPSC-derived neurons to demonstrate functional neuronal network formation within these scaffolds. Analysis of light, confocal, and scanning electron microscopy images confirm reliable network formation with guided neuronal growth, which is based on topological and chemical guiding cues. Electrophysiological integrity of neurons inside the microscaffolds is demonstrated with patch clamp measurements, whose results show no statistical deviances compared to planar control substrates. In particular, neuronal functionality was proven by the capability to fire action potentials and by recordings of spontaneous excitatory postsynaptic currents, which indicate functional synaptogenesis required for inter-cellular signaling. The application of human iPSC-derived neurons not only overcomes ethical and political controversies raised by using human embryonic stem cells but also enables patient-specific studies of disease-associated genotype−phenotype relationships. Concluding, we believe that our findings allow for additional approaches in human disease research by acting as a platform for artificial culture substrates mimicking the complexity of the human brain in, for example, BoC applications.

MATERIALS AND METHODS

Sample Preparation. The scaffolds were manufactured by two-photon polymerization direct laser writing (2PP-DLW) with a Nanoscribe Photonic Professional GT using IP-Dip resin. CAD files for structures were designed with Autodesk's AutoCAD. Scaffolds were written with 10 mm s^{-1} and 58% laser power (∼17 mW) on glass coverslips using a 63× objective. Slicing distance was 0.3 μm, hatching was 0.2 μm, and contour distance was 6 μm. The samples were developed in MR-Dev 600 for 30 min and subsequently immersed twice in isopropyl alcohol (99.9%) for 30 s. The scaffolds were uniformly passivated with 15 nm Al$_2$O$_3$ using a custom-built atomic layer deposition system in stop-mode operation heated to 95 °C utilizing trimethylaluminum and water as precursors with pulse times of 0.05 and 0.1 s, respectively. The exposure and pump times were set to 60 and 90 s for both half reactions. A constant nitrogen (6.0) flow of 20 ccm was applied during deposition. Before coating with PLL, samples were treated with atmosphere plasma at 50% power for 5 s (Femto, Diener Electronic) to increase hydrophilicity. PLL (0.01 g × L^{-1}, mol. wt. 30k−70k, Sigma-Aldrich, St. Louis, MO, USA) was selectively pipetted on the scaffold utilizing an upright patch clamp setup (poly-D-lysine would be an equivalent substitute). After coating, samples were rinsed in deionized water and sterilized in 70% ethanol for 5 min. Complete laminin coating of the scaffold (50 mg × mL^{-1}, Sigma-Aldrich) was performed directly before cell transfer for 20 min at 37 °C in a 35 mm Petri dish. Subsequently, the laminin solution was removed, 2 mL of cell culture medium was added immediately, and the sample was placed in the incubator. Mature neurons were then transferred from a 12-well plate to the 35 mm Petri dish featuring the microscaffold. For that purpose, 1 mL of cell suspension containing all neurons of a well of a 12-well plate (see Cell Culture) was gently added to 2 mL of cell culture medium already in the 35 mm Petri dish. Due to the localized cell adhesive surface treatment, the neurons settle in a self-assembly process inside the scaffold. Experiments were then conducted from 1−4 days after the transfer, depending on the trail. Samples were cleaned after the experiments for reuse purposes with Tergazyme for 20 min at 37 °C. Control experiments were conducted on glass coverslips.

Cell Culture. Human induced pluripotent stem cell-derived neurons were derived from neural progenitor cells, which still incorporate the capability to propagate. Frozen vials of small molecule neural progenitor cells (smNPCs), generated from human pluripotent stem cells according to Reinhardt *et al.*, were provided from the Max Planck Institute for Molecular Biomedicine in Muenster, Germany.[79] Further cell culture was conducted on-site. The differentiation of smNPCs into midbrain dopaminergic neurons (mDANs) is based on the protocols in Reinhard *et al.* For maintaining the smNPCs, basic medium (50:50 DMEM/F12:Neurobasal, 1:100 penicillin/streptomycin/glutamine, 1:100 B27 supplement without vitamin A, 1:200 N2 supplement, Life Technologies, Carlsbad, CA, USA) was supplemented with ascorbic acid (AA, 100 μM, Sigma-Aldrich), smoothened agonist (SAG, 0.5 μM, Biomol, Hamburg, Germany), and CHIR 99021 (3 μM, Axon MedChem, Groningen, Netherlands). smNPCs were split close to confluency (every 4−5 days) in a ratio of 1:10−1:20. To generate mDANs, approximately 1 × 10^6 smNPCs per well of a 6-well plate were seeded in patterning medium (basic medium supplemented with 100 μM AA, 0.5 μM SAG, 1 ng/mL glial-derived neurotrophic factor (GDNF) and 1 ng/mL brain-derived neurotrophic factor (BDNF), PeproTech, Rocky Hill, NJ, USA). Six days after initiating the differentiation, the cells were split 1:5—to reduce cell clustering during the differentiation—into 12-well plates containing maturation medium (basic medium supplemented with 100 μM AA, 2 ng/mL GDNF, 2 ng/mL BDNF, 1 ng/mL transforming growth factor-β3 (TGF-β3, PeproTech), and 100 μM dibutyryl cyclic-AMP (dbcAMP, Sigma-

Aldrich)) and differentiated for at least 8 more days (14 in total). Well plates were coated with Matrigel (Corning 354263, prediluted 1:5 in KnockOut DMEM (Life Technologies) and stored at −20 °C; additional dilution (1:30) in KnockOut DMEM for use, 1.5 mL per 35 mm dish/6-well, 0.75 mL per 12-well, overnight at room temperature or 1 h at 37 °C in the incubator). Cells were kept in a humidified incubator at 37 °C and 5% CO_2. Cell culture media were changed completely every 2−3 days. For passaging/splitting/transferring cells, cells were detached using Accutase for 10−15 min at 37 °C, centrifuged, and subsequently resuspended in the corresponding cell culture medium. All neurons have been differentiated for at least 14 days on Matrigel-coated well plates. They were replated in the scaffolds with such temporal advance that measurements were conducted with neurons, which then have been differentiated 15−21 days in total.

Ethics Statement. All experiments were conducted in accordance with the ethical statement in Reinhardt *et al.*[79]

Confocal Microscopy. Confocal scanning laser microscopy imaging was conducted using an upright Leica TSC SP8 confocal microscope equipped with two lasers of 488 and 552 nm wavelength. The cell membrane was stained using the membrane stain from Thermo Fisher's neurite outgrowth staining kit (A15001, ex/em: 555/565 nm), and the stain was used according to the manufacturer's instructions: Cell culture medium was exchanged by 1× dye mixture in Dulbecco's phosphate-buffered saline (DPBS) and placed for 15 min in the incubator at 37 °C. Imaging was done in 1× Thermo Fisher's background suppression in DPBS. Slicing step size of the z-stacks was 172 nm. Z-stacks were processed and analyzed using Fiji.[91] Plots were created with Origin (v. 2018, applies to all data plotted). For publication, all images were optimized in contrast as well as brightness, and/or false color coded if applicable.

Immunofluorescence Staining. Cells were stained using anti-MAP2 (microtubule-associated protein 2) and anti-TH (tyrosine hydroxylase) primary antibodies to identify the neuronal and dopaminergic phenotype, respectively. Secondary antibodies were Alexa+ fluorophores at 488 and 555 nm. Details regarding the staining procedure and materials used can be found within the figure caption of Figure S1.

Viability Assay. Viability assays were performed using calcein-AM (0.5 μM, Thermo Fisher Scientific, Waltham, MA, USA) and propidium iodide (10 μM, Sigma-Aldrich) in DPBS. Medium was exchanged by the dye solution, and the sample was placed for 15 min in the incubator at 37 °C. Before imaging, samples were rinsed with DPBS. Control samples were analyzed using ImageJ (threshold-, watershed-, and analyze-particles function).[92] Scaffolds were quantified manually.

Scanning Electron Microscopy and Focused Ion Beam Milling. High-resolution scanning electron microscopy images and cross sections created *via* focused ion beam milling were prepared using Zeiss' Crossbeam 550. Cells were fixated for 10 min with 4% paraformaldehyde in DPBS at room temperature. After dehydration using a stepwise ethanol exchange, the samples were critical point dried (Tousimis Autosamdri-815) and sputtered with 20 nm gold to reduce charging effects during imaging.

Electrophysiology. An upright patch clamp setup (Nikon Eclipse FN1) with a nonimmersion objective with extra-long working distance (Nikon CFI TU Plan EPI ELWD 50× N.A. 0.60/W.D. 11.00 mm) was used.[64] The traces were recorded using a HEKA EPC 10 USB patch clamp amplifier and a red star headstage. The data were processed by the patch clamp software (Patch Master V2x80) with a Bessel low-pass filter at 2.9 kHz. Pipet capacitance and series-resistance were automatically compensated. The bath solution consisted of (in mM): NaCl 140, KCl 2.4, $MgCl_2$ 1.3, $CaCl_2$ 2.5, HEPES 10, D-glucose 10 adjusted to pH 7.4 with NaOH. The pipet solution consisted of (in mM): K-gluconate 125, NaCl 10, EGTA 1, MgATP 4, HEPES 10, D-glucose 10, adjusted to pH 7.4 with KOH.[73] All experiments were performed at room temperature.[76] The pipets were fabricated from borosilicate glass capillary blanks (GB150T-8P, Science Products) using a Sutter P-2000 pipet puller and were subsequently heat polished (CPM-2, ALA Scientific Instruments). Tip diameters were approximately 950 nm, resulting in resistances of 5−7 MΩ. The RMP was determined by holding the cells with zero current in current-clamp mode. The MCs were directly determined by the patch clamp amplifier software. APs were characterized from the first AP of an AP train at rheobase current. AP height is defined by threshold to peak, threshold is defined by the second derivative becoming different from zero (derivative by using Origin's Savitzky−Golay smooth, polynomial order: 3, points of window: 30), AHP is threshold to minimum after AP, and AP duration is the full width half-maximum of the spike. sEPSCs were recorded at a holding potential of −70 mV and analyzed using Mini Analysis (Synaptosoft Inc.). Event detection threshold for amplitude and area was set to 5× RMS noise. RMS noise was about 1.4 pA. Patch clamp measurements were conducted 2−3 days after transfer to the scaffold.

ASSOCIATED CONTENT

Ⓢ Supporting Information

The Supporting Information is available free of charge at https://pubs.acs.org/doi/10.1021/acsnano.0c04640.

> Figure S1: Exemplary images of MAP2 (green) and TH (red) labeled neurons to affirm the dopaminergic phenotype of the neurons. Figure S2: Coating of the microscaffolds using a food dye and PLL-filled micropipet, respectively. Figure S3: Example of neurite constantly growing straight at the border of the scaffold. Figure S4: Microscaffold held by regular manual tweezers. Table S1: ANOVA analysis of resting membrane potential, capacitance, AP threshold, AP, amplitude, AHP, and AP duration. Table S2: ANOVA analysis of postsynaptic events in terms of amplitude, area, and decay (PDF)

> Movie S1: Specific coating routine with food dye (MP4)
> Movie S2: Specific coating routine with PLL (MP4)

AUTHOR INFORMATION

Corresponding Author

  Robert Zierold − *Center for Hybrid Nanostructures, Universität Hamburg, 22761 Hamburg, Germany;* ⓘ orcid.org/0000-0003-0292-0970; Email: rzierold@chyn.uni-hamburg.de

Authors

  Jann Harberts − *Center for Hybrid Nanostructures, Universität Hamburg, 22761 Hamburg, Germany*

  Cornelius Fendler − *Center for Hybrid Nanostructures, Universität Hamburg, 22761 Hamburg, Germany*

  Jeremy Teuber − *Center for Hybrid Nanostructures, Universität Hamburg, 22761 Hamburg, Germany*

  Malte Siegmund − *Center for Hybrid Nanostructures, Universität Hamburg, 22761 Hamburg, Germany*

  Aaron Silva − *Center for Hybrid Nanostructures, Universität Hamburg, 22761 Hamburg, Germany; Roy J. Carver Department of Biomedical Engineering, College of Engineering, University of Iowa, Iowa City, Iowa 52242, United States*

  Niklas Rieck − *Center for Hybrid Nanostructures, Universität Hamburg, 22761 Hamburg, Germany; School of Life Science Hamburg gGmbH, 22525 Hamburg, Germany*

  Merle Wolpert − *Center for Hybrid Nanostructures, Universität Hamburg, 22761 Hamburg, Germany; School of Life Science Hamburg gGmbH, 22525 Hamburg, Germany*

  Robert H. Blick − *Center for Hybrid Nanostructures, Universität Hamburg, 22761 Hamburg, Germany; Material Science and Engineering, College of Engineering, University of Wisconsin-Madison, Madison, Wisconsin 53706, United States*

Complete contact information is available at:
https://pubs.acs.org/10.1021/acsnano.0c04640

REFERENCES

(1) Pamies, D.; Hartung, T.; Hogberg, H. T. Biological and Medical Applications of a Brain-On-A-Chip. *Exp. Biol. Med.* **2014**, *239*, 1096−1107.

(2) Taylor, A. M.; Blurton-Jones, M.; Rhee, S. W.; Cribbs, D. H.; Cotman, C. W.; Jeon, N. L. A Microfluidic Culture Platform for CNS Axonal Injury, Regeneration and Transport. *Nat. Methods* **2005**, *2*, 599−605.

(3) Tong, Z.; Segura-Feliu, M.; Seira, O.; Homs-Corbera, A.; Del Río, J. A.; Samitier, J. A Microfluidic Neuronal Platform for Neuron Axotomy and Controlled Regenerative Studies. *RSC Adv.* **2015**, *5*, 73457−73466.

(4) Park, J.; Koito, H.; Li, J.; Han, A. Microfluidic Compartmentalized Co-Culture Platform for CNS Axon Myelination Research. *Biomed. Microdevices* **2009**, *11*, 1145−1153.

(5) Irons, H. R.; Cullen, D. K.; Shapiro, N. P.; Lambert, N. A.; Lee, R. H.; LaPlaca, M. C. Three-Dimensional Neural Constructs: A Novel Platform for Neurophysiological Investigation. *J. Neural Eng.* **2008**, *5*, 333−341.

(6) McManus, M. C.; Boland, E. D.; Simpson, D. G.; Barnes, C. P.; Bowlin, G. L. Electrospun Fibrinogen: Feasibility as a Tissue Engineering Scaffold in a Rat Cell Culture Model. *J. Biomed. Mater. Res., Part A* **2007**, *81A*, 299−309.

(7) El-Sherbiny, I. M.; Yacoub, M. H. Hydrogel Scaffolds for Tissue Engineering: Progress and Challenges. *Glob. Cardiol. Sci. Pract.* **2013**, *2013*, 38.

(8) Cai, H.; Sharma, S.; Liu, W.; Mu, W.; Liu, W.; Zhang, X.; Deng, Y. Aerogel Microspheres from Natural Cellulose Nanofibrils and Their Application as Cell Culture Scaffold. *Biomacromolecules* **2014**, *15*, 2540−2547.

(9) Ravi, M.; Paramesh, V.; Kaviya, S. R.; Anuradha, E.; Solomon, F. D. P. 3D Cell Culture Systems: Advantages and Applications. *J. Cell. Physiol.* **2015**, *230*, 16−26.

(10) Bang, S.; Na, S.; Jang, J. M.; Kim, J.; Jeon, N. L. Engineering-Aligned 3D Neural Circuit in Microfluidic Device. *Adv. Healthcare Mater.* **2016**, *5*, 159−166.

(11) Kim, S. H.; Im, S.-K.; Oh, S.-J.; Jeong, S.; Yoon, E.-S.; Lee, C. J.; Choi, N.; Hur, E.-M. Anisotropically Organized Three-Dimensional Culture Platform for Reconstruction of a Hippocampal Neural Network. *Nat. Commun.* **2017**, *8*, 14346.

(12) Kleinfeld, D.; Kahler, K.; Hockberger, P. Controlled Outgrowth of Dissociated Neurons on Patterned Substrates. *J. Neurosci.* **1988**, *8*, 4098−4120.

(13) Oliva, A. A.; James, C. D.; Kingman, C. E.; Craighead, H. G.; Banker, G. A. Patterning Axonal Guidance Molecules Using a Novel Strategy for Microcontact Printing. *Neurochem. Res.* **2003**, *28*, 1639−1648.

(14) Miller, C.; Jeftinija, S.; Mallapragada, S. Synergistic Effects of Physical and Chemical Guidance Cues on Neurite Alignment and Outgrowth on Biodegradable Polymer Substrates. *Tissue Eng.* **2002**, *8*, 367−378.

(15) Kim, Y. H.; Baek, N. S.; Han, Y. H.; Chung, M. A.; Jung, S. D. Enhancement of Neuronal Cell Adhesion by Covalent Binding of Poly-d-Lysine. *J. Neurosci. Methods* **2011**, *202*, 38−44.

(16) Wyart, C.; Ybert, C.; Bourdieu, L.; Herr, C.; Prinz, C.; Chatenay, D. Constrained Synaptic Connectivity in Functional Mammalian Neuronal Networks Grown on Patterned Surfaces. *J. Neurosci. Methods* **2002**, *117*, 123−131.

(17) Ge, H.; Yu, A.; Chen, J.; Yuan, J.; Yin, Y.; Duanmu, W.; Tan, L.; Yang, Y.; Lan, C.; Chen, W.; Feng, H.; Hu, R. Poly-L-Ornithine Enhances Migration of Neural Stem/Progenitor Cells *via* Promoting α-Actinin 4 Binding to Actin Filaments. *Sci. Rep.* **2016**, *6*, 37681.

(18) Segerer, F. J.; Röttgermann, P. J. F.; Schuster, S.; Alberola, A. P.; Zahler, S.; Rädler, J. O. Versatile Method to Generate Multiple Types of Micropatterns. *Biointerphases* **2016**, *11*, 011005.

(19) Marino, A.; Ciofani, G.; Filippeschi, C.; Pellegrino, M.; Pellegrini, M.; Orsini, P.; Pasqualetti, M.; Mattoli, V.; Mazzolai, B. Two-Photon Polymerization of Sub-Micrometric Patterned Surfaces: Investigation of Cell-Substrate Interactions and Improved Differentiation of Neuron-Like Cells. *ACS Appl. Mater. Interfaces* **2013**, *5*, 13012−13021.

(20) Kaehr, B.; Allen, R.; Javier, D. J.; Currie, J.; Shear, J. B. Guiding Neuronal Development with in *Situ* Microfabrication. *Proc. Natl. Acad. Sci. U. S. A.* **2004**, *101*, 16104−16108.

(21) Kaehr, B.; Ertaş, N.; Nielson, R.; Allen, R.; Hill, R. T.; Plenert, M.; Shear, J. B. Direct-Write Fabrication of Functional Protein Matrixes Using a Low-Cost Q-Switched Laser. *Anal. Chem.* **2006**, *78*, 3198−3202.

(22) Bausch, C. S.; Koitmäe, A.; Stava, E.; Price, A.; Resto, P. J.; Huang, Y.; Sonnenberg, D.; Stark, Y.; Heyn, C.; Williams, J. C.; Dent, E. W.; Blick, R. H. Guided Neuronal Growth on Arrays of Biofunctionalized GaAs/InGaAs Semiconductor Microtubes. *Appl. Phys. Lett.* **2013**, *103*, 173705.

(23) Froeter, P.; Huang, Y.; Cangellaris, O. V.; Huang, W.; Dent, E. W.; Gillette, M. U.; Williams, J. C.; Li, X. Toward Intelligent Synthetic Neural Circuits: Directing and Accelerating Neuron Cell Growth by Self-Rolled-up Silicon Nitride Microtube Array. *ACS Nano* **2014**, *8*, 11108−11117.

(24) Yu, M.; Huang, Y.; Ballweg, J.; Shin, H.; Huang, M.; Savage, D. E.; Lagally, M. G.; Dent, E. W.; Blick, R. H.; Williams, J. C. Semiconductor Nanomembrane Tubes: Three-Dimensional Confinement for Controlled Neurite Outgrowth. *ACS Nano* **2011**, *5*, 2447−2457.

(25) Koitmäe, A.; Harberts, J.; Loers, G.; Müller, M.; Bausch, C. S.; Sonnenberg, D.; Heyn, C.; Zierold, R.; Hansen, W.; Blick, R. H. Approaching Integrated Hybrid Neural Circuits: Axon Guiding on Optically Active Semiconductor Microtube Arrays. *Adv. Mater. Interfaces* **2016**, *3*, 1600746.

(26) Koitmäe, A.; Müller, M.; Bausch, C. S.; Harberts, J.; Hansen, W.; Loers, G.; Blick, R. H. Designer Neural Networks with Embedded Semiconductor Microtube Arrays. *Langmuir* **2018**, *34*, 1528−1534.

(27) Goldner, J. S.; Bruder, J. M.; Li, G.; Gazzola, D.; Hoffman-Kim, D. Neurite Bridging across Micropatterned Grooves. *Biomaterials* **2006**, *27*, 460−472.

(28) Scott, M. A.; Wissner-Gross, Z. D.; Yanik, M. F. Ultra-Rapid Laser Protein Micropatterning: Screening for Directed Polarization of Single Neurons. *Lab Chip* **2012**, *12*, 2265.

(29) Tooker, A.; Meng, E.; Erickson, J.; Tai, Y.-C.; Pine, J. Development of Biocompatible Parylene Neurocages. Proceedings from the *26th Annual International Conference of the IEEE Engineering in Medicine and Biology Society*, September 1−4, 2004, San Francisco, CA; IEEE: New York, 2004; Vol. 3, pp 2542−2545.

(30) Tuft, B. W.; Xu, L.; White, S. P.; Seline, A. E.; Erwood, A. M.; Hansen, M. R.; Guymon, C. A. Neural Pathfinding on Uni- and Multidirectional Photopolymerized Micropatterns. *ACS Appl. Mater. Interfaces* **2014**, *6*, 11265−11276.

(31) Li, W.; Tang, Q. Y.; Jadhav, A. D.; Narang, A.; Qian, W. X.; Shi, P.; Pang, S. W. Large-Scale Topographical Screen for Investigation of Physical Neural-Guidance Cues. *Sci. Rep.* **2015**, *5*, 8644.

(32) Renault, R.; Durand, J.-B.; Viovy, J.-L.; Villard, C. Asymmetric Axonal Edge Guidance: A New Paradigm for Building Oriented Neuronal Networks. *Lab Chip* **2016**, *16*, 2188−2191.

(33) Francisco, H.; Yellen, B. B.; Halverson, D. S.; Friedman, G.; Gallo, G. Regulation of Axon Guidance and Extension by Three-Dimensional Constraints. *Biomaterials* **2007**, *28*, 3398−3407.

(34) Fendler, C.; Harberts, J.; Rafeldt, L.; Loers, G.; Zierold, R.; Blick, R. H. Neurite Guidance and Neuro-Caging on Steps and Grooves in 2.5 Dimensions. *Nanoscale Adv.* **2020**. DOI: 10.1039/D0NA00549E

(35) Pimpin, A.; Srituravanich, W. Review on Micro- and Nano-lithography Techniques and Their Applications. *Eng. J.* **2012**, *16*, 37−56.

(36) Ovsianikov, A.; Schlie, S.; Ngezahayo, A.; Haverich, A.; Chichkov, B. N. Two-Photon Polymerization Technique for Micro-fabrication of CAD-Designed 3D Scaffolds from Commercially Available Photosensitive Materials. *J. Tissue Eng. Regener. Med.* **2007**, *1*, 443−449.

(37) Niesler, F.; Hermatschweiler, M. Two-Photon Polymerization - A Versatile Microfabrication Tool. *Laser Tech. J.* **2015**, *12*, 44−47.

(38) Turunen, S.; Käpylä, E.; Lähteenmäki, M.; Ylä-Outinen, L.; Narkilahti, S.; Kellomäki, M. Direct Laser Writing of Microstructures for the Growth Guidance of Human Pluripotent Stem Cell Derived Neuronal Cells. *Opt. Lasers Eng.* **2014**, *55*, 197−204.

(39) Turunen, S.; Joki, T.; Hiltunen, M. L.; Ihalainen, T. O.; Narkilahti, S.; Kellomäki, M. Direct Laser Writing of Tubular Microtowers for 3D Culture of Human Pluripotent Stem Cell-Derived Neuronal Cells. *ACS Appl. Mater. Interfaces* **2017**, *9*, 25717−25730.

(40) Weiß, T.; Schade, R.; Laube, T.; Berg, A.; Hildebrand, G.; Wyrwa, R.; Schnabelrauch, M.; Liefeith, K. Two-Photon Polymerization of Biocompatible Photopolymers for Microstructured 3D Biointerfaces. *Adv. Eng. Mater.* **2011**, *13*, B264−B273.

(41) Tayalia, P.; Mendonca, C. R.; Baldacchini, T.; Mooney, D. J.; Mazur, E. 3D Cell-Migration Studies Using Two-Photon Engineered Polymer Scaffolds. *Adv. Mater.* **2008**, *20*, 4494−4498.

(42) Klein, F.; Richter, B.; Striebel, T.; Franz, C. M.; von Freymann, G.; Wegener, M.; Bastmeyer, M. Two-Component Polymer Scaffolds for Controlled Three-Dimensional Cell Culture. *Adv. Mater.* **2011**, *23*, 1341−1345.

(43) Fendler, C.; Denker, C.; Harberts, J.; Bayat, P.; Zierold, R.; Loers, G.; Münzenberg, M.; Blick, R. H. Microscaffolds by Direct Laser Writing for Neurite Guidance Leading to Tailor-Made Neuronal Networks. *Adv. Biosyst.* **2019**, *3*, 1800329.

(44) Takahashi, K.; Tanabe, K.; Ohnuki, M.; Narita, M.; Ichisaka, T.; Tomoda, K.; Yamanaka, S. Induction of Pluripotent Stem Cells from Adult Human Fibroblasts by Defined Factors. *Cell* **2007**, *131*, 861−872.

(45) Bang, S.; Jeong, S.; Choi, N.; Kim, H. N. Brain-On-A-Chip: A History of Development and Future Perspective. *Biomicrofluidics* **2019**, *13*, 051301.

(46) Dragunow, M. The Adult Human Brain in Preclinical Drug Development. *Nat. Rev. Drug Discovery* **2008**, *7*, 659−666.

(47) Mak, I. W. Y.; Evaniew, N.; Ghert, M. Lost in Translation: Animal Models and Clinical Trials in Cancer Treatment. *Am. J. Transl. Res.* **2014**, *6*, 114−118.

(48) Ko, H. C.; Gelb, B. D. Concise Review: Drug Discovery in the Age of the Induced Pluripotent Stem Cell. *Stem Cells Transl. Med.* **2014**, *3*, 500−509.

(49) Takahashi, J. Preparing for First Human Trial of Induced Pluripotent Stem Cell-Derived Cells for Parkinson's Disease: An Interview with Jun Takahashi. *Regener. Med.* **2019**, *14*, 93−95.

(50) Penney, J.; Ralvenius, W. T.; Tsai, L.-H. Modeling Alzheimer's Disease with IPSC-Derived Brain Cells. *Mol. Psychiatry* **2020**, *25*, 148−167.

(51) Appelt-Menzel, A.; Cubukova, A.; Günther, K.; Edenhofer, F.; Piontek, J.; Krause, G.; Stüber, T.; Walles, H.; Neuhaus, W.; Metzger, M. Establishment of a Human Blood-Brain Barrier Co-Culture Model Mimicking the Neurovascular Unit Using Induced Pluri- and Multipotent Stem Cells. *Stem Cell Rep.* **2017**, *8*, 894−906.

(52) Lancaster, M. A.; Renner, M.; Martin, C.-A.; Wenzel, D.; Bicknell, L. S.; Hurles, M. E.; Homfray, T.; Penninger, J. M.; Jackson, A. P.; Knoblich, J. A. Cerebral Organoids Model Human Brain Development and Microcephaly. *Nature* **2013**, *501*, 373−379.

(53) Madonna, R. Human-Induced Pluripotent Stem Cells: In Quest of Clinical Applications. *Mol. Biotechnol.* **2012**, *52*, 193−203.

(54) Greiner, A. M.; Richter, B.; Bastmeyer, M. Micro-Engineered 3D Scaffolds for Cell Culture Studies. *Macromol. Biosci.* **2012**, *12*, 1301−1314.

(55) Caliari, S. R.; Burdick, J. A. A Practical Guide to Hydrogels for Cell Culture. *Nat. Methods* **2016**, *13*, 405−414.

(56) Serbin, J.; Ovsianikov, A.; Chichkov, B. Fabrication of Woodpile Structures by Two-Photon Polymerization and Investigation of Their Optical Properties. *Opt. Express* **2004**, *12*, 5221.

(57) Greiner, A. M.; Jäckel, M.; Scheiwe, A. C.; Stamow, D. R.; Autenrieth, T. J.; Lahann, J.; Franz, C. M.; Bastmeyer, M. Multifunctional Polymer Scaffolds with Adjustable Pore Size and Chemo-attractant Gradients for Studying Cell Matrix Invasion. *Biomaterials* **2014**, *35*, 611−619.

(58) Campuzano, S.; Pelling, A. E. Scaffolds for 3D Cell Culture and Cellular Agriculture Applications Derived From Non-Animal Sources. *Front. Sustain. Food Syst.* **2019**, *3*, 38.

(59) Malinauskas, M.; Danilevičius, P.; Baltriukienė, D.; Rutkauskas, M.; Žukauskas, A.; Kairytė, Ž.; Bičkauskaitė, G.; Purlys, V.; Paipulas, D.; Bukelskienė, V.; Gadonas, R. 3D Artificial Polymeric Scaffolds for Stem Cell Growth Fabricated by Femtosecond Laser. *Lith. J. Phys.* **2010**, *50*, 75−82.

(60) Melissinaki, V.; Gill, A. A.; Ortega, I.; Vamvakaki, M.; Ranella, A.; Haycock, J. W.; Fotakis, C.; Farsari, M.; Claeyssens, F. Direct Laser Writing of 3D Scaffolds for Neural Tissue Engineering Applications. *Biofabrication* **2011**, *3*, 045005.

(61) Stein, O.; Liu, Y.; Streit, J.; Campbell, J. H.; Lu, Y. F.; Aglitskiy, Y.; Petta, N. Fabrication of Low-Density Shock-Propagation Targets Using Two-Photon Polymerization. *Fusion Sci. Technol.* **2018**, *73*, 153−165.

(62) Thamaraiselvi, T. V.; Rajeswari, S. Biological Evaluation of Bioceramic Materials-A Review. *Trends Biomater. Artif. Organs* **2004**, *18*, 9−17.

(63) Finch, D. S.; Oreskovic, T.; Ramadurai, K.; Herrmann, C. F.; George, S. M.; Mahajan, R. L. Biocompatibility of Atomic Layer-Deposited Alumina Thin Films. *J. Biomed. Mater. Res., Part A* **2008**, *87A*, 100−106.

(64) Harberts, J.; Zierold, R.; Fendler, C.; Koitmäe, A.; Bayat, P.; Fernandez-Cuesta, I.; Loers, G.; Diercks, B.-P.; Fliegert, R.; Guse, A. H.; Ronning, C.; Otnes, G.; Borgström, M.; Blick, R. H. Culturing and Patch Clamping of Jurkat T Cells and Neurons on Al$_2$O$_3$ Coated Nanowire Arrays of Altered Morphology. *RSC Adv.* **2019**, *9*, 11194−11201.

(65) Evans, A. R.; Euteneuer, S.; Chavez, E.; Mullen, L. M.; Hui, E. E.; Bhatia, S. N.; Ryan, A. F. Laminin and Fibronectin Modulate Inner Ear Spiral Ganglion Neurite Outgrowth in an *in Vitro* Alternate Choice Assay. *Dev. Neurobiol.* **2007**, *67*, 1721−1730.

(66) Gomez, N.; Chen, S.; Schmidt, C. E. Polarization of Hippocampal Neurons with Competitive Surface Stimuli: Contact Guidance Cues Are Preferred over Chemical Ligands. *J. R. Soc., Interface* **2007**, *4*, 223−233.

(67) Fan, Y. W.; Cui, F. Z.; Hou, S. P.; Xu, Q. Y.; Chen, L. N.; Lee, I.-S. Culture of Neural Cells on Silicon Wafers with Nano-Scale Surface Topograph. *J. Neurosci. Methods* **2002**, *120*, 17−23.

(68) Zamani, F.; Amani-Tehran, M.; Latifi, M.; Shokrgozar, M. A. The Influence of Surface Nanoroughness of Electrospun PLGA Nano-fibrous Scaffold on Nerve Cell Adhesion and Proliferation. *J. Mater. Sci.: Mater. Med.* **2013**, *24*, 1551−1560.

(69) Djuric, U.; Cheung, A. Y. L.; Zhang, W.; Mok, R. S.; Lai, W.; Piekna, A.; Hendry, J. A.; Ross, P. J.; Pasceri, P.; Kim, D.-S.; Salter, M. W.; Ellis, J. MECP2e1 Isoform Mutation Affects the Form and Function of Neurons Derived from Rett Syndrome Patient IPS Cells. *Neurobiol. Dis.* **2015**, *76*, 37−45.

(70) Rhee, H. J.; Shaib, A. H.; Rehbach, K.; Lee, C.; Seif, P.; Thomas, C.; Gideons, E.; Guenther, A.; Krutenko, T.; Hebisch, M.; Peitz, M.; Brose, N.; Brüstle, O.; Rhee, J. S. An Autaptic Culture System for Standardized Analyses of IPSC-Derived Human Neurons. *Cell Rep.* **2019**, *27*, 2212−2228.

(71) Khattak, S.; Brimble, E.; Zhang, W.; Zaslavsky, K.; Strong, E.; Ross, P. J.; Hendry, J.; Mital, S.; Salter, M. W.; Osborne, L. R.; Ellis, J. Human Induced Pluripotent Stem Cell Derived Neurons as a Model for Williams-Beuren Syndrome. *Mol. Brain* **2015**, *8*, 77.

(72) Xie, Y.; Schutte, R. J.; Ng, N. N.; Ess, K. C.; Schwartz, P. H.; O'Dowd, D. K. Reproducible and Efficient Generation of Functionally Active Neurons from Human HiPSCs for Preclinical Disease Modeling. *Stem Cell Res.* **2018**, *26*, 84−94.

(73) Harberts, J.; Haferkamp, U.; Haugg, S.; Fendler, C.; Lam, D.; Zierold, R.; Pless, O.; Blick, R. H. Interfacing Human Induced Pluripotent Stem Cell-Derived Neurons with Designed Nanowire Arrays as a Future Platform for Medical Applications. *Biomater. Sci.* **2020**, *8*, 2434−2446.

(74) Gentet, L. J.; Stuart, G. J.; Clements, J. D. Direct Measurement of Specific Membrane Capacitance in Neurons. *Biophys. J.* **2000**, *79*, 314−320.

(75) Kang, S.; Chen, X.; Gong, S.; Yu, P.; Yau, S.; Su, Z.; Zhou, L.; Yu, J.; Pan, G.; Shi, L. Characteristic Analyses of a Neural Differentiation Model from IPSC-Derived Neuron According to Morphology, Physiology, and Global Gene Expression Pattern. *Sci. Rep.* **2017**, *7*, 12233.

(76) Harberts, J.; Kusch, M.; O'Sullivan, J.; Zierold, R.; Blick, R. H. A Temperature-Controlled Patch Clamp Platform Demonstrated on Jurkat T Lymphocytes and Human Induced Pluripotent Stem Cell-Derived Neurons. *Bioengineering* **2020**, *7*, 46.

(77) Gunhanlar, N.; Shpak, G.; van der Kroeg, M.; Gouty-Colomer, L. A.; Munshi, S. T.; Lendemeijer, B.; Ghazvini, M.; Dupont, C.; Hoogendijk, W. J. G.; Gribnau, J.; de Vrij, F. M. S.; Kushner, S. A. A Simplified Protocol for Differentiation of Electrophysiologically Mature Neuronal Networks from Human Induced Pluripotent Stem Cells. *Mol. Psychiatry* **2018**, *23*, 1336−1344.

(78) Prè, D.; Nestor, M. W.; Sproul, A. A.; Jacob, S.; Koppensteiner, P.; Chinchalongporn, V.; Zimmer, M.; Yamamoto, A.; Noggle, S. A.; Arancio, O. A Time Course Analysis of the Electrophysiological Properties of Neurons Differentiated from Human Induced Pluripotent Stem Cells (IPSCs). *PLoS One* **2014**, *9*, No. e103418.

(79) Reinhardt, P.; Glatza, M.; Hemmer, K.; Tsytsyura, Y.; Thiel, C. S.; Höing, S.; Moritz, S.; Parga, J. A.; Wagner, L.; Bruder, J. M.; Wu, G.; Schmid, B.; Röpke, A.; Klingauf, J.; Schwamborn, J. C.; Gasser, T.; Schöler, H. R.; Sterneckert, J. Derivation and Expansion Using Only Small Molecules of Human Neural Progenitors for Neurodegenerative Disease Modeling. *PLoS One* **2013**, *8*, No. e59252.

(80) Lam, R. S.; Töpfer, F. M.; Wood, P. G.; Busskamp, V.; Bamberg, E. Functional Maturation of Human Stem Cell-Derived Neurons in Long-Term Cultures. *PLoS One* **2017**, *12*, No. e0169506.

(81) Lu, H. F.; Lim, S.-X.; Leong, M. F.; Narayanan, K.; Toh, R. P. K.; Gao, S.; Wan, A. C. A. Efficient Neuronal Differentiation and Maturation of Human Pluripotent Stem Cells Encapsulated in 3D Microfibrous Scaffolds. *Biomaterials* **2012**, *33*, 9179−9187.

(82) Villa-Diaz, L. G.; Kim, J. K.; Lahann, J.; Krebsbach, P. H. Derivation and Long-Term Culture of Transgene-Free Human Induced Pluripotent Stem Cells on Synthetic Substrates. *Stem Cells Transl. Med.* **2014**, *3*, 1410−1417.

(83) Cutarelli, A.; Ghio, S.; Zasso, J.; Speccher, A.; Scarduelli, G.; Roccuzzo, M.; Crivellari, M.; Pugno, N. M.; Casarosa, S.; Boscardin, M.; Conti, L. Vertically-Aligned Functionalized Silicon Micropillars for 3D Culture of Human Pluripotent Stem Cell-Derived Cortical Progenitors. *Cells* **2020**, *9*, 88.

(84) Edgar, J. M.; Robinson, M.; Willerth, S. M. Fibrin Hydrogels Induce Mixed Dorsal/Ventral Spinal Neuron Identities during Differentiation of Human Induced Pluripotent Stem Cells. *Acta Biomater.* **2017**, *51*, 237−245.

(85) Lo, B.; Parham, L. Ethical Issues in Stem Cell Research. *Endocr. Rev.* **2009**, *30*, 204−213.

(86) Ochalek, A.; Mihalik, B.; Avci, H. X.; Chandrasekaran, A.; Téglási, A.; Bock, I.; Giudice, M. Lo; Táncos, Z.; Molnár, K.; László, L.; Nielsen, J. E.; Holst, B.; Freude, K.; Hyttel, P.; Kobolák, J.; Dinnyés, A. Neurons Derived from Sporadic Alzheimer's Disease IPSCs Reveal Elevated TAU Hyperphosphorylation, Increased Amyloid Levels, and GSK3B Activation. *Alzheimer's Res. Ther.* **2017**, *9*, 90.

(87) Sison, S. L.; Vermilyea, S. C.; Emborg, M. E.; Ebert, A. D. Using Patient-Derived Induced Pluripotent Stem Cells to Identify Parkinson's Disease-Relevant Phenotypes. *Curr. Neurol. Neurosci. Rep.* **2018**, *18*, 84.

(88) Selimis, A.; Mironov, V.; Farsari, M. Direct Laser Writing: Principles and Materials for Scaffold 3D Printing. *Microelectron. Eng.* **2015**, *132*, 83−89.

(89) Roeper, J. Dissecting the Diversity of Midbrain Dopamine Neurons. *Trends Neurosci.* **2013**, *36*, 336−342.

(90) Bissonette, G. B.; Roesch, M. R. Development and Function of the Midbrain Dopamine System: What We Know and What We Need To. *Genes, Brain Behav.* **2016**, *15*, 62−73.

(91) Schindelin, J.; Arganda-Carreras, I.; Frise, E.; Kaynig, V.; Longair, M.; Pietzsch, T.; Preibisch, S.; Rueden, C.; Saalfeld, S.; Schmid, B.; Tinevez, J.-Y.; White, D. J.; Hartenstein, V.; Eliceiri, K.; Tomancak, P.; Cardona, A. Fiji: An Open-Source Platform for Biological-Image Analysis. *Nat. Methods* **2012**, *9*, 676−682.

(92) Schneider, C. A.; Rasband, W. S.; Eliceiri, K. W. NIH Image to ImageJ: 25 Years of Image Analysis. *Nat. Methods* **2012**, *9*, 671−675.

Supporting material

Toward Brain-on-a-Chip: Human Induced Pluripotent Stem Cell-Derived Guided Neuronal Networks in Tailor-Made 3D Nanoprinted Microscaffolds

Jann Harberts,[a, ‡] Cornelius Fendler,[a ,‡] Jeremy Teuber, [a] Malte Siegmund,[a] Aaron Silva,[a,b] Niklas Rieck,[a,c] Merle Wolpert, [a,c] Robert Zierold,[a,]* and Robert H. Blick[a,d]

[a] Center for Hybrid Nanostructures, Universität Hamburg, Luruper Chaussee 149, 22761 Hamburg, Germany
[b] Roy J. Carver Department of Biomedical Engineering, College of Engineering, University of Iowa, Iowa City, Iowa 52242, United States
[c] School of Life Science Hamburg gGmbH, Schnackenburgallee 114, 22525 Hamburg, Germany
[d] Material Science and Engineering, College of Engineering, University of Wisconsin-Madison, Madison, Wisconsin 53706, United States
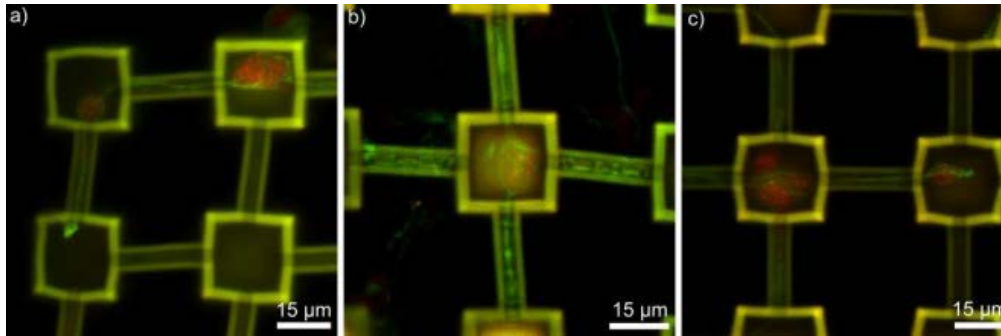
Figure S 1: Exemplary images of MAP2 (green) and TH (red) labeled neurons to affirm the dopaminergic phenotype of the neurons.

Neurons were washed with DPBS, fixated for 10 min using 4 % paraformaldehyde in DPBS at room temperature, rinsed 2 times and stored at 4 °C until further use. Cells were permeabilized and blocked for 45 min at room temperature with 3% BSA, 0.1 % Tween and 0.1 % Triton-X. Primary anti bodies (ABs) incubated over night at 4 °C using 0.1% BSA, MAP2 1:5000, TH 1:1000 (MAP2 Monoclonal Antibody (Invitrogen, Cat. No. 13-1500), Rb pAb to Tyrosine Hydroxylase (abcam, Cat. No. ab112)). Cell were washed twice with DPBS, secondary ABs incubated 1h at room temperature in the dark using 0.1% BSA and ABs 1:1000 (Goat anti-Mouse IgG (H+L), Alexa FluorTM Plus 488 (Invitrogen, Cat. No. A32723), Goat anti-Rabbit IgG (H+L), Alexa FluorTM Plus 555 (Invitrogen, Cat. No. A32732)). Cells were washed 3 times with 0.05 % Tween in DPBS for 5 min.
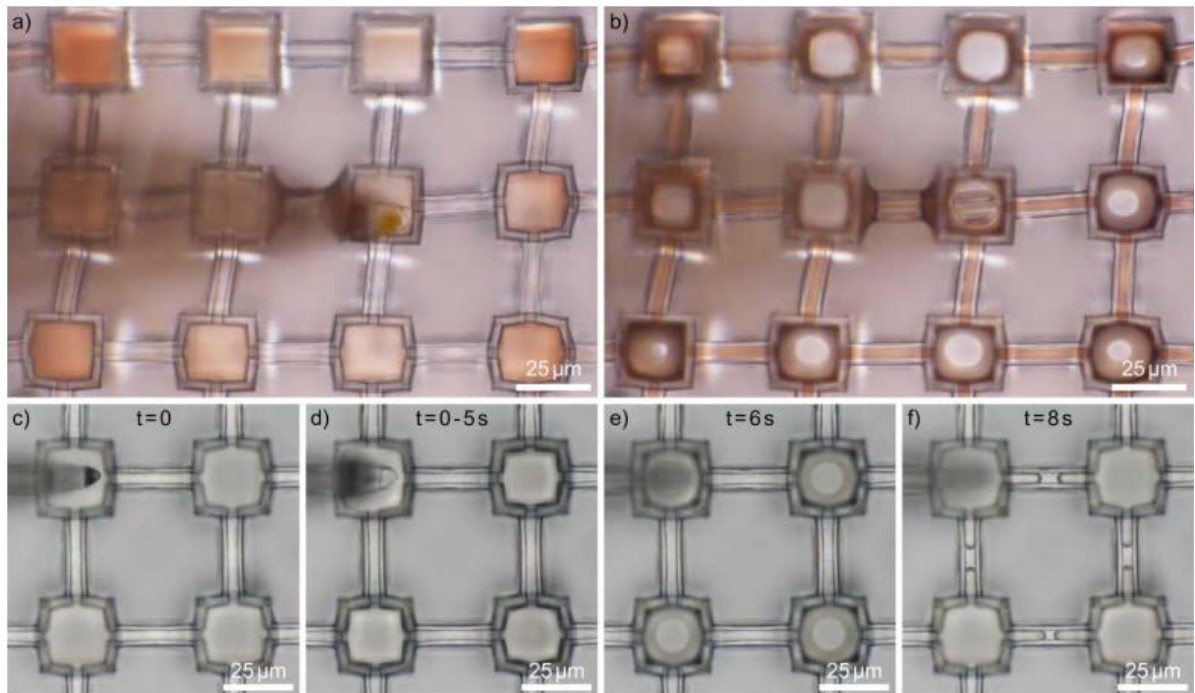
Figure S 2: Coating of the microscaffolds using a food dye and PLL-filled micropipet, respectively. The pipets enter from left. a) Cavities filled with food dye. B) The pipet is removed, and the food dye solution is drying. c) Initial pipet position inside the cavity without contact to the scaffold's surface. d) Pipet in contact with the scaffold lasting 5 s. Capillary forces cause complete filling of the scaffold. e) After removing the pipet from the surface, the scaffold dries beginning at the cavity centers. f) Subsequent drying of the channel interior after additional 2 s. All pictures are taken from video clips, which can also be found in the supporting material (Movie S1 and Movie S2). Note, that food dye was only used for visualization. Since the pipet tip easily clogs with the food dye solution, it was necessary to break the tip for coating. Also drying of the scaffold does not work properly. Using a PLL-solution, none of these problems occurred.
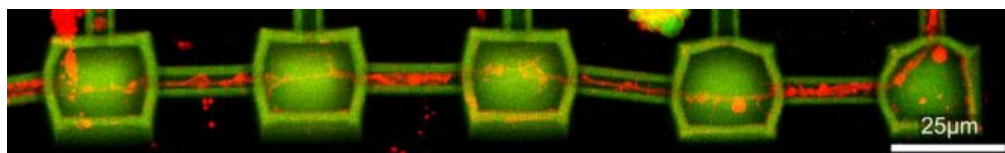
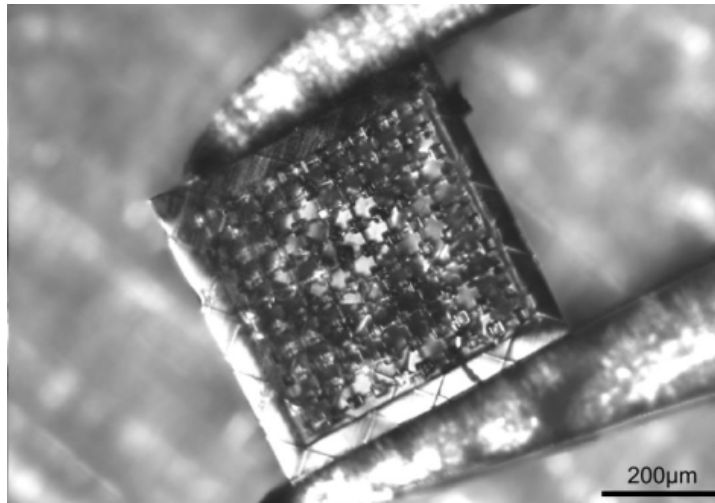**Figure S 3**: Example of neurite constantly growing straight at the border of the scaffold.

Figure S 4: Microscaffold held by regular manual tweezers.

Table S 1: ANOVA with post hoc Turkey's test between scaffold and control of resting membrane potential, capacitance, AP threshold, AP, amplitude, AHP, and AP duration, alpha = 0.05.

Parameter	MeanDiff	SEM	q Value	Prob	Alpha	Sig	LCL	UCL
RMP	1.73431	5.19116	0.47247	0.74364	0.05	0	-9.48053	12.94915
Capacitance	0.76167	2.20051	0.4895	0.73478	0.05	0	-3.99226	5.51559
AP threshold	1.33333	2.61739	0.72042	0.619	0.05	0	-4.32119	6.98786
AP amplitude	1.98333	7.50833	0.37357	0.7958	0.05	0	-14.23743	18.2041
AHP	0.52222	3.25673	0.22677	0.87507	0.05	0	-6.51353	7.55797
AP duration	-0.11667	0.77223	0.21366	0.88223	0.05	0	-1.78496	1.55163

Table S 2: ANOVA with post hoc Turkey's test between scaffold and control of post synaptic events in terms of amplitude, area, and decay, alpha = 0.05.

Parameter	MeanDiff	SEM	q Value	Prob	Alpha	Sig	LCL	UCL
Amplitude	3.09801	3.27782	1.33664	0.34696	0.05	0	-3.4084	9.60443
Area	-3.08579	6.71593	0.64979	0.64693	0.05	0	-16.41681	10.24524
Decay	-0.73321	0.8962	1.15702	0.41531	0.05	0	-2.51216	1.04573

A.8   Publication VIII

Neurite guidance and neuro-caging on steps and grooves in 2.5 dimensions

Cornelius Fendler, <u>Jann Harberts</u>, Lars Rafeldt, Gabriele Loers, Robert Zierold, and Robert H. Blick

Nanoscale Advances **2020**, 2(11), 5192–5200

Author contributions: C.F. and L.R. produced the substrates and conducted the analysis of the culturing results. C.F. and <u>J.H.</u> cultivated the neurons. G.L. prepared the murine cerebella. C.F., <u>J.H.</u>, and R.Z. wrote the manuscript. C.F. and R.H.B. conceived the study. R.Z. and R.H.B. supervised the project. R.H.B. assisted in manuscript finalization. All authors significantly contributed to the scientific discussion during data evaluation and manuscript preparation. All authors conducted a final proofreading.

(9 + 3 pages)

ROYAL SOCIETY
OF CHEMISTRY

Check for updates

Neurite guidance and neuro-caging on steps and grooves in 2.5 dimensions†

Cornelius Fendler,[a] Jann Harberts, [ID] [a] Lars Rafeldt,[a] Gabriele Loers,[b] Robert Zierold [ID] *[a] and Robert H. Blick[ac]

Directed guidance of neurites is a pre-requisite for tailor-made designs of interfaces between cells and semiconducting components. Grayscale lithography, reactive ion etching, and ultraviolet nanoimprint lithography are potent semiconductor industry-compatible techniques for a cost- and time-effective fabrication of modulated surfaces. In this work, neurite outgrowth of murine cerebellar neurons on 2.5D pathways produced with these methods is studied. Structures of micron-sized steps and grooves serve as cell culture platforms. The effects of contact guidance through topography and chemical guidance through selective poly-D-lysine coating on these platforms are analyzed. As a consequence, the herein presented fabrication approach can be utilized to cultivate and to study low-density neuronal networks in 2.5D configuration with a high degree of order.

Introduction

The ability to manipulate and direct axonal pathfinding is crucial for bioengineering defined neuronal circuits. Improved knowledge and control over axon outgrowth could lead to the development of diagnostics and cures for currently incurable and in part still poorly understood pathologies of the central nervous system such as Alzheimer's disease, multiple sclerosis or spinal cord injuries.[1] Valuable tools to study neurons are *in vitro* cell cultures on micro-patterned cell culture platforms. Specifically, axon pathfinding and neuronal outgrowth can be controlled by chemical or topographical cues or a combination of them.[2] A pioneering publication in the field of chemical guidance is the work of Kleinfeld *et al.* from 1988.[3] They showed how micropatterning of planar substrates by photolithography utilizing di- and triamines as chemical binding centers promoted local cellular adhesion and outgrowth of rodent spinal and cerebellar cells whereas monoamines, such as (3-aminopropyl)triethoxysilane—which in fact are generally used as adhesion promoter to covalently bond organic materials to oxidic surfaces—inhibited the cell adhesion. Another approach was pursued by Oliva *et al.* which used microcontact printing to define arrays of a cell adhesion molecules serving as guide for the axon's outgrowth of hippocampal neuronal cells from

embryonic rats but leaving the cell soma as well as dendrites unaffected.[4] Note, both techniques employed to define purely chemical cues, namely photolithography and contact lithography, are standard tools in semiconductor and microelectronic industry for decades. On the other hand, topographical cues (partially in combination with chemically induced guidance) have been investigated to tailor neuronal outgrowth. A plethora of surface modulated or 2.5-dimensional (2.5D) structures have been utilized to act as culture platforms for guided neurite outgrowth, including variations in nanoscale surface topography,[5] guidance barriers,[6,7] 3D confinement in neuro-cages, grooves and channels,[8-15] microtube arrays,[16-20] nanowires,[21] and nano- or micropillars.[22-26] The synthesis of such tailor-made neurite guiding platforms has been motivated for their application in drug screening, scaffolding of artificial tissue, axon-specific testing of growth direction, modeling the myelin formation, and gaining insight into regeneration processes occurring after a severe injury of the spinal cord.[27-30] Moreover, in recent years, brain-on-a-chip devices have aroused interest of the research community as pedant to organ-of-a-chip approaches. The latter ones not only focus on neuronal cells but also investigate other cells of the human body, such as liver, lung, or the skin in artificial devices.[31-33]

On the one hand, the progress in micro- and nano-structuring within the last decades allows for the synthesis of complex cell culturing substrates with tunnels and tubes being far beyond a simple surface structuring. As an example, arrays of self-rolled-up microtubes—upon release of intrinsic strain in their multilayer thin film architecture by selective etching of a sacrificial layer—or 3D-printed free-standing hollow channels by 2-photon-polymerization lithography can serve as artificial substrates for neurite guidance and confinement. However, the

[a] Center for Hybrid Nanostructures (CHyN), Universität Hamburg, 22761 Hamburg, Germany. E-mail: rzierold@physik.uni-hamburg.de

[b] Center for Molecular Neurobiology Hamburg (ZMNH), University Medical Center Hamburg-Eppendorf (UKE), Hamburg 20251, Germany

[c] Material Science and Engineering, College of Engineering, University of Wisconsin-Madison, Madison, Wisconsin 53706, USA

fabrication of complex surfaces geometries with the aforementioned procedures is time-consuming, expensive, not scalable, and hence economically not feasible for large-scale production as needed for *e.g.* drug screening experiments. Other techniques qualified for scalable applications, however, such as fibrinogen, cellulose nanofibrils, or hydrogels have been applied as cell culture substrates already but lack of structural features to manipulate neuronal outgrowth at will.[34–36]

On the other hand, substrates with tailor-made surface geometries for cell cultivation, can be prepared by making use of well-established methods in microelectronic industry, such as photolithography, microcontact printing, imprint lithography, dry- and wet-etching processes, physical and chemical vapor depositions methods to name a few of them. Moreover, such fabrication routes only make use of materials of synthetic nature and are thus free from ethical concerns and of general interest in the field.[37] In future, ethical concerns could be further minimized by the application of induced stem cell-derived neurons which have been demonstrated to be cultivatable on microstructured substrates as well.[38,39]

In this work, we combine established technologies, namely grayscale lithography (GSL) and ultraviolet nano-imprint lithography (UV-NIL) with reactive ion etching (RIE) to prepare readily reproducible and cost-effective modulated surfaces. The topographical features of the platforms are specifically designed to study contact guidance during neuronal network formation. Cellular network orientation and neurite outgrowth pathways of murine cerebellar granular cells (MCGCs) through grooves and over micron-sized edges with varying heights are analyzed herein. In detail, lithographically structured steps inside of grooves introduce 2.5D modulation in a substrate to further enhance the complexity of the outgrowth pathways. Parylene C (ParC) and alumina (Al_2O_3) surface coatings are applied by chemical vapor deposition (CVD) and atomic layer deposition (ALD), respectively, before culturing for improved cell adhesion and viability.[40–47] Furthermore, a spatially localized poly-D-lysine (PDL) coating is utilized to improve the selectivity of soma adhesion and neurite outgrowth paths.[3,48,49] Moreover, additional laminin coating promotes neurite outgrowth and neuron viability.[50]

Results and discussion

Contact guidance at steps and in grooves

One approach to tailor the neuron outgrowth is to introduce morphological traces, which serve as guide for the growth cone. Fig. 1 shows neurons cultivated on step structures produced by GSL. The height difference between adjacent steps is 2 μm with a total of four different heights (see also Fig. S1†). Vital neuronal networks have developed on the substrates as displayed by confocal laser scanning microscopy (CLSM) images (Fig. 1a–c). A tendency to settle on lower levels on the structure rather than on the top steps is observable: 32% of the cells are seeded in the pits, 34% on the lower steps, 27% on the higher steps, and 8% on the top steps. The overall cell density on the displayed substrate is (648 ± 114) cells per cm^2. Note, the pits and top steps each make up 1/6 of the total surface area, while lower and higher steps each

make up 1/3. Consequently, the measured cell density is highest in the pits with (1086 ± 264) cells per cm^2. Neuronal network formation over the entire substrate surface shows that the steps do not present an insurmountable barrier for neurite outgrowth. However, the outgrowth is significantly influenced by the topography and many neurites are oriented in the direction of the step edges. The majority of neurite trajectories is oriented within an angle of ±15° towards the step edge direction (Fig. 1d).

Further insight into the network geometry is provided by scanning electron microscopy (SEM) analysis of the same culture. Most neurites are oriented along the step edge direction for a large portion of their paths (Fig. 1e). Many thin neurites as well as neurite bundles with small impinging angles are guided and deflected by step edges (Fig. 1f and g). However, once steps are crossed, neurites are predominantly not deflected. In detail, the majority of observed neurites that cross multiple steps both upwards and downwards without deflection have a trajectory over 60° relative to the step edges (Fig. 1h and i).

In contrast to GSL-produced steps, structures produced by a combination of RIE with subsequent UV-NIL reveal sharp, well defined edges with 90° angles. Thus, such structures are ideally suited to assess neurite pathfinding along competing growth options when exposed to barriers of different heights. Three different cases are observed on steps of 3 μm, 6 μm, and 9 μm height (Fig. 2). At 3 μm steps, the orientation of neurites in the network is statistically random with neurites freely extending over the steps. On 6 μm steps, neurites in networks have a predominant orientation along the edges of the steps and somata are mostly settled on lower steps and in pits. However, cross-linkage across the top steps is sufficient for network connections between the pits. Noteworthy, neurites of single or only a few neurons are switching between perpendicular and parallel orientation along the step edges. On 9 μm steps, no network formation across the steps is observed. Neurites are completely deflected when approaching a lower step edge, which leads to confinement in the pits and guidance along the step edge direction.

Li *et al.* reported a threshold height of 10–11 μm for cortical cell cultures in crossing and turning on steps coated with PDL.[51] The authors explicitly noticed that the threshold is of the same magnitude as the growth cone dimension of cortical neurons. Hence, the results indicate that the size of the growth cone is also the defining factor for the threshold for MCGCs in crossing steps. When encountering a step of larger vertical dimensions than its dimension, the cone would need to turn in a 90° angle to cross onto the next step while turning in plane offer alternative pathways with smaller bending angles. Thus, neurites are entrapped by vertical walls of 9 μm. When encountering smaller steps, the bending angle needed to extend onto the next plane is reduced which in turn increases the likelihood of crossing.

The orientation of neurites perpendicular to 6 μm steps for low density cell cultures may be explained by the presence of topography as single guidance cues in the absence of other cells nearby. When the growth cone senses an edge, it can either align with the edge or continue its trajectory across the edge to sense for the next cue. The closest way to the next cue in form of the next step edge is directly 90° across the step. This form of perpendicular contact
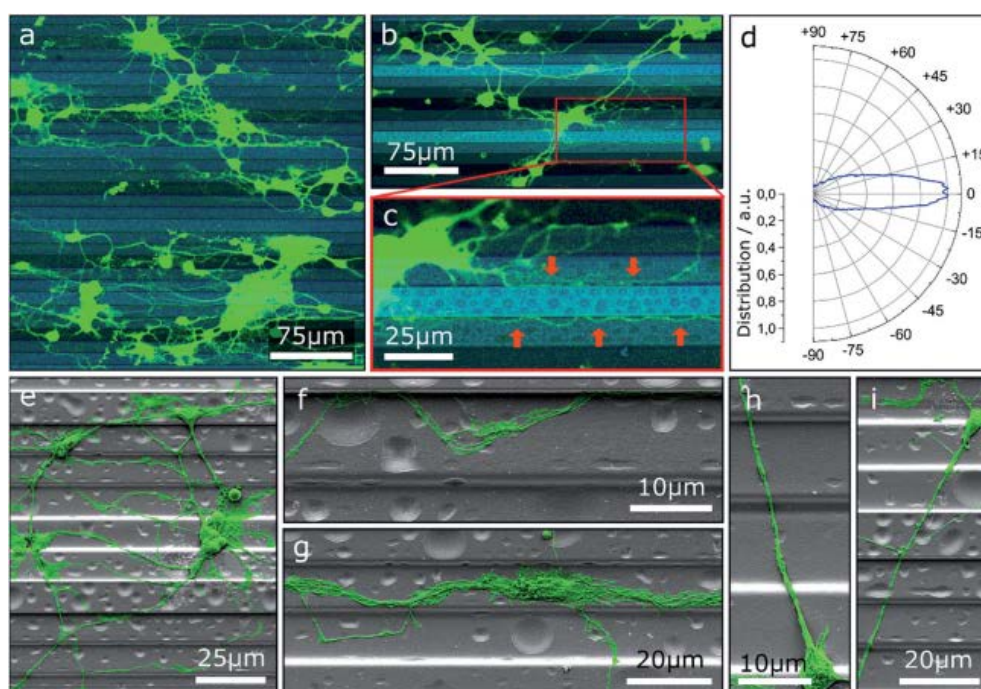
Fig. 1 (a–c) CLSM images of MCGCs cultured on ParC coated step structures produced by GSL at 4 DIV. Brightness of the steps correlates with the height: light and dark correspond to top steps and bottom pits, respectively. Red arrows point to neurites guided along edges. (d) Circular histogram of the normed distribution of neurite orientations in (a) relative to the step edges. (e–i) False-colored scanning electron microscopy (SEM) images of neurons on step-structures after 4 DIV.

guidance has previously been observed on grooves of sub-micron dimensions and on radial neurite bundles.[52–54]

One possibility to introduce an additional degree of order to neuronal networks cultivated on step structures is the addition of further topographical contact guidance. To this end, chessboard structures of cavities connected by channels with integrated steps produced by GSL were utilized as cell culture platforms for MCGCs. The height difference between consecutive steps is 2 μm as in the first scenario. Since neurites are trapped in the channel, we observe, in agreement with our previous results, no deflection at the steps because the angle of approaching the step is larger than 60°. Two neurons in adjacent cavities are shown in Fig. 3a. Neurites in the displayed channels show exemplary behavior for pathfinding observed on

all of these investigated substrates. Specifically, neurites originating from cell somata that are settled in cavities are mostly extended towards the channels. Over a certain distance, the neurites are guided over the steps along the bottom of the channels (1). At some point, typically after crossing one of the top-level steps, the neurites attach to the channel wall and do not follow the steps back downwards (2) pointing to morphological guidance at the corner. Therefore, some neurites subsequently leave the channels. However, in the displayed case the main trajectory remains inside the channel and leads back down onto the channel bottom. In contrast, other neurites leave the channel after crossing the channel bottom towards the other edge when approaching a higher step level (3) indicating that the growth cone fumbles in a preferred forward direction.
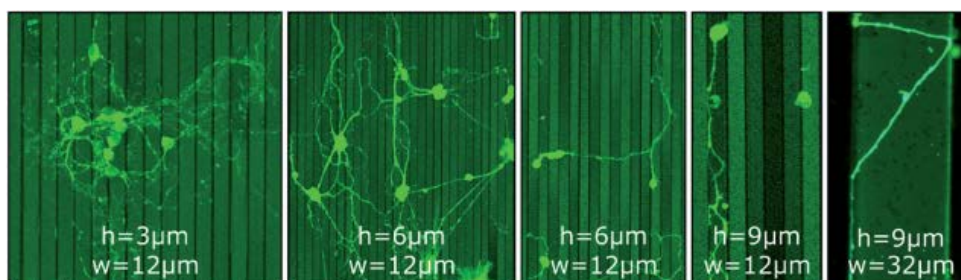

Fig. 2 CLSM images of MCGCs at 10–11 DIV on steps of varied height ($h = 3$ μm, 6 μm and 9 μm) and width ($w = 12$ μm and 32 μm) produced by RIE. All substrates have been coated with ParC and PDL.
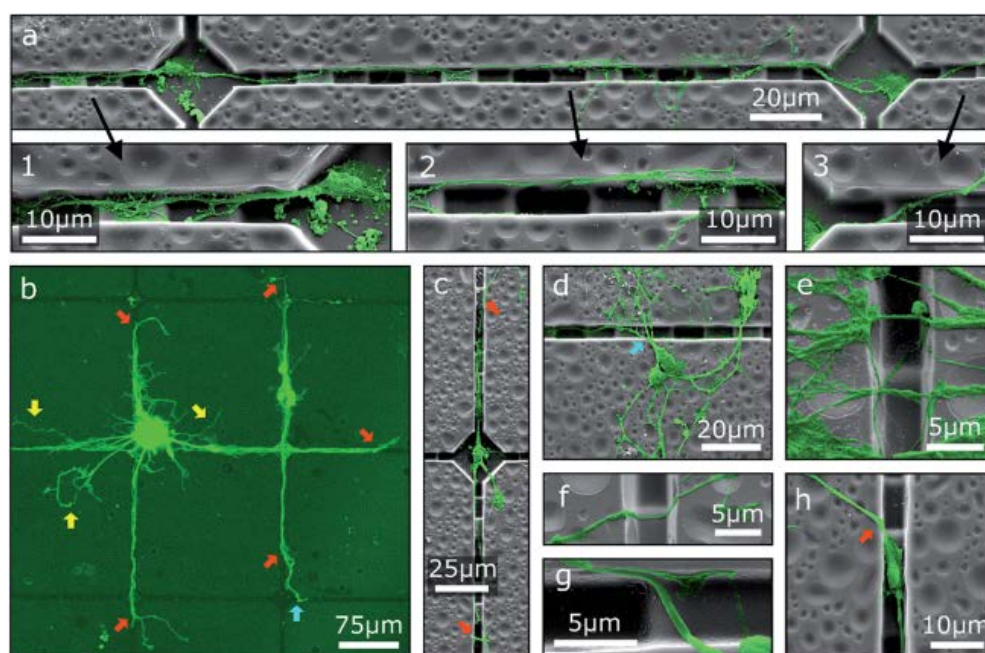
Fig. 3   False-colored SEM images and a CLSM image of MCGCs on chessboard structures produced by GSL after 6 DIV. (a) Two connected neurons. Three magnified areas of interest show (1) guidance along the bottom of a channel, (2) guidance on the sidewall of a channel, and (3) a neurite pathway exiting a channel. (b) Red arrows indicate spots, where neurites leave the channels. Yellow arrows indicate neurites, that are not guided. Blue arrows indicate re-entering of neurites into channels. Neurites originating from a cell cluster and somata that are settled on top of channels. (c–h) Examples of neurites exiting, entering, and crossing channels.

The overall guidance effect of the channels is showcased in Fig. 3b. Most neurites originating from a cell cluster settled near a cavity as well as the neurites of somata settled on the top rim of a channel are extended into the channels. Guided neurites are apparently longer than neurites without contact guidance, which may indicate an acceleration of the neurite outgrowth through contact guidance in the channels similar to the effect shown for neurites inside of tubes.[17] Nearly all observed neurites leave the channels at some point—predominantly at the highest step—and extend onto the substrate surface without 2.5D structuring. Note, observed neurites of somata settled inside of cavities typically exit the channels before reaching an adjacent cavity (Fig. 3c) indicating that the chosen distance between two cavities is too large to define connected neuronal networks when steps are introduced in the outgrowth path.

While neurite guidance along the channels is observed in the cases described above, a majority of the somata is unspecifically settled on the flat surface (Fig. 3d). Accidentally, single neurites from these somata are extended into the channels, but a large part of the neuronal networks is formed on the surface without modulation. Neurites of these networks, especially in case of neurite bundles, build suspended bridges over the channels (Fig. 3e) or extend down on one side wall and up on the other side wall without changing the trajectory (Fig. 3f and g). This observation again points to the fact of a preferred forward direction of the outgrowth by the growth cone. In a special case, some small somata are settled inside of a channel. Neurites can then be extended into the channels as well as onto the flat surface; no specific preference has been found in this case (Fig. 3h).

In intermediate summary, our observations show that steps and walls produced by GSL are sensed by the growth cone. The effect is not strong enough to reliably build ordered 2.5D networks on the structured surfaces, but some neuron caging and neurite guidance is given. The path chosen by neurites after encountering the border of a step or a channel is dependent on the angle of approach. At large angles, neurites tend to cross steps and channels without change of trajectory. At small angles, they tend to follow the step edge direction or channel. This behavior is analogous to stripe 'tracking', observed for neurites encountering stripes of fixed chemical guidance cues laminin and fibronectin.[55] High probability of neurites exiting the channels at some point can be attributed to frequent directional changes of the trajectories induced by the step structure inside the channels. Neurites have previously been shown to cross boundaries more often on surfaces with multi-directional patterns than neurites on unidirectional patterns.[13] The observation of longer neurites when extended through channels fits previous findings where axons on anisotropic patterns where significantly longer than axons on flat surfaces.[14]

Chemical guidance by poly-D-lysine

In the previous sections only contact guidance at steps and corners has been investigated. Note, the culture substrates have been uniformly coated by a PDL layer. However, selective adhesion coating can support contact guidance along the

surface topography. The effect of selective surface coating with PDL on MCGCs was first tested on flat substrates without contact guidance to evaluate the impact as chemical guidance factor. The neurons were cultivated on glass substrates with an Al_2O_3 surface coating. Droplets of PDL solution were printed in a pattern of circles with approx. 36 μm diameter. Confocal microscope images of cultured cells for circles printed every 90 μm are shown in Fig. 4a–c. 89 ± 5% of all somata are settled directly on or are attached to circular areas covered with PDL. A network of neurites spans between the circles. In the rare case of somata that are located between circles, their neurites are directly extended to the nearest circles. Within the coated areas, a higher number of somata and neurites are attached and extended on the outer rim than in the center.

The results indicate a very strong PDL reliance of cell attachment and migration of somata on the substrate. Cell adhesion near the edges of circles indicates an uneven distribution of PDL residue in the rings, likely due to the so-called coffee-ring effect, known to occur in ink-jet printing of polymers.[56] During neurite outgrowth, PDL clearly functions as a guidance cue. Orientational analysis of the neurite growth directions in case of PDL droplets with 90 μm periodicity (Fig. 4d and e) reveals that the simple quadratic pattern is sufficient to introduce a certain order to the network: dominant neurite orientation towards 0° and ±45°. Spreading of most neurites between nearest and second-nearest circles (Fig. 4f) results in preferred directions either parallel or diagonal to the printed pattern.

In contrast, Fig. 4g–i show close-ups of cultured neurons on/in circles printed with the same amount of PDL—same diameter—but every 190 μm where nearly all cellular material is attached at the PDL spots. Neurites of vital cells are exclusively extended inside the boundaries of the coated area. This result indicates that the minimal distance between two PDL circles of 154 μm (edge-to-edge) exceeds the maximal distance neurites of MCGCs span without attractive chemical guidance cues. When the distance between PDL-covered areas is too large, neurites retract and start sensing in a different direction. As a result, no neuronal networks can be formed over PDL coating with large distance spacing.

Combination of contact and chemical guidance

Based on the results of the first section, chessboard structures of cavities and channels with steps were produced by RIE as well as UV-NIL (see Fig. S2†) and were cultivated with MCGCs to obtain ordered 2.5D neuronal networks. But this time, PDL was not coated onto the entire surface, instead PDL was specifically and spatially applied to enhance the selectivity of cell adhesion only locally. First, PDL was coated with a materials printer targeted to the cavities. Note, it is reasonable to assume that droplets with PDL solution spread through the channels through capillary forces before evaporation of the solvent, leading to PDL coating that is homogenously distributed in the modulated area.[46] Using this surface treatment, guidance in the confined area is achieved and a neuronal network spans through the channels and cavities (Fig. 5a). However, neuronal
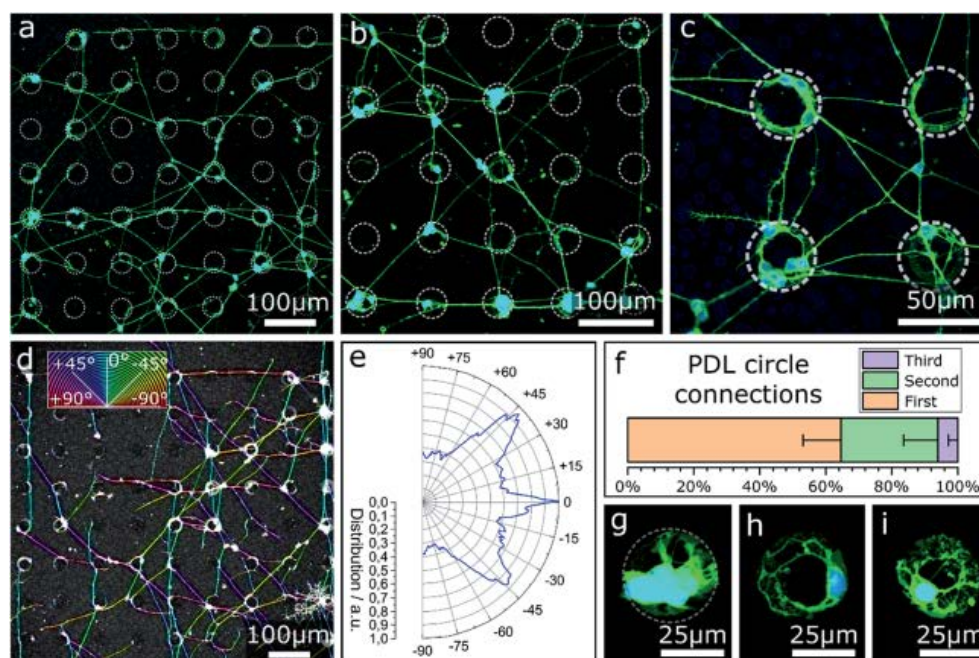

Fig. 4 CLSM images and orientation analysis of neurons cultured on PDL circles with diameters of approx. 36 μm printed on an Al_2O_3 surface (7 DIV). (a–c) Circles printed in a pattern of 90 μm periodicity and an average distance between two circles of 54 μm. (d) Color-coded confocal image of neurons cultured on PDL circles in a pattern of 90 μm. Coloration of neurites corresponds to the neurite direction relative to the pattern. (e) Circular histogram of the normed distribution of neurite orientations on the pattern. (f) Percentage share of neurite pathways between nearest (first), second nearest and third-nearest circles. (g–i) Circles printed in a pattern of 190 μm and an average distance between two circles of 154 μm.

somata are mostly not settled in the cavities, but on top of the substrate's surface or in the channels themselves. Most likely, droplets of PDL solution aimed at the cavities were deposited onto the channels due to the insufficient accuracy of the stage alignment. As a result, somata are settled in the channels and neurites are spread on straight lines across the surface of the sample (Fig. 5b). Second, and in contrast, utilizing a pipette mounted at a micromanipulator to inject PDL into cavities and channels with the same design results in neuronal networks with somata exclusively attached to the cavities and with several neurites that spread through the channels and along the bottom of the cavities (Fig. 5c and d). Some neurites are partially guided along the top edges of the channels and cavities. When clusters of several cells are settled in cavities, some neurites are spread across the surface towards different cavities (Fig. 5e). This design was tested with step heights between 2 μm and 10 μm. Overall, neuronal networks in RIE-etched structures in combination with chemical cues have a high degree of order and can be used to successfully guide neuron outgrowth along 2.5D pathways for step heights of 4 μm and below. In accordance to the findings on step structures in the first section, step heights above 6 μm hinder neurite elongation; the observed neurite guidance in those cases occurs mostly for clusters along the top edge. Within this section we showed how the combination of chemical cues for guidance with contact guidance in channels can be employed to build neuronal networks in 2.5D.

Our conclusive experiments revealed that spatially controlled chemical cue application, sharp edges, and step heights above 6 μm are needed for optimum guidance.

Conclusion

We utilized grayscale lithography, reactive ion etching, and ultraviolet nanoimprint lithography to fabricate rapidly reproducible and cost-efficient cell culture platforms with well-defined 2.5D topography on the micron scale. Murine cerebellar granule cells were successfully cultivated on these substrates and formed low-density neuronal networks. Neurites were extended on 2.5D pathways. Vertical walls with certain height and sharp 90° edges confined neurite extension in a defined space on the bottom plane. The critical step height for neurite caging has been determined to be larger than 6 μm. However, every change in the trajectory raised the probability of neurites extending alongside walls and exiting the well-defined channels over the top edge. Selective chemical coating determines potential cell adhesion spots and areas of neurite outgrowth predominantly to the coated areas. Coated cavities act as efficient neuro-cages. Thus, with a combination of chemical and topographical guidance, ordered 2.5D neuronal networks have been successfully generated and maintained. Our results of guided neuronal outgrowth experiments on 2.5D structures prepared by semiconductor industry compatible techniques might pave the way to artificial
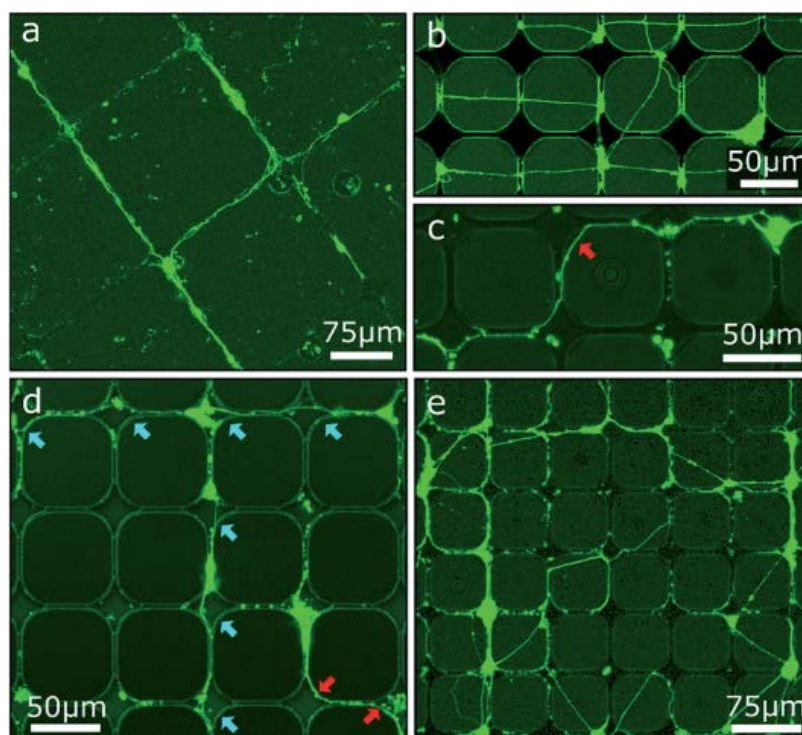

Fig. 5 CLSM images of MCGCs at 6–8 DIV on chessboard structures produced by RIE and UV-NIL. (a) Cavities of 10 μm depth and steps in channels of 5 μm height coated with PDL with a materials printer. (b–e) Cavities of 14 μm depth and steps in channels of 4 μm height. PDL coated by a material printer (b) and with a micromanipulator (c–e). Red arrows indicate neurites guided at the top edge of cavities. Blue arrows indicate neurites at the bottom of cavities.

microstructured cell culture substrates and might form the stepping stone for linking tailor-made semiconductor devices with neuronal cell cultures.

Methods

Grayscale lithography

Glass wafers were dehydrated at 200 °C for 10 min. AZ4562 photoresist (MicroResist) was deposited via spin coating at 2000 rpm for 30 s to get 10 μm thick layers and the wafers were kept on level ground at room temperature (RT) for 10 min. Optimal prebake time was 1 min at 60 °C and ramped up to 100 °C for 10 min. After GSL, the samples were developed in AZ826 MIF (metal ion free; MicroResist) for 3.5–6 min, depending on structure depth. Optical GSL was carried out using a DWL66+ laser writer (Heidelberg Instruments) equipped with a 363 nm Ar^+ laser (max. 360 mW). Grayscale files were prepared with AutoCAD (AutoDesk).

Reactive ion etching

Photomasks were produced with the DWL66+ laser writer using prefabricated photo mask blanks (G Materials) metalized with Cr and coated with 530 nm MICROPOSIT S1800 photoresist (MicroChem). The respective exposure patterns were prepared with AutoCAD. The wafers were heated to 115 °C for 50 s for postbake and developed in AZ826 MIF for 3.5 min. In preparation for RIE, Si wafers were spin coated with LOR5A at 4000 rpm and AZ4562 for 30 s at 4000 rpm. Prebake time was 1 min at 60 °C, ramped up to 100 °C for 6 min. Transferring the desired structures into the resist through contact lithography, the coated wafers were exposed for 15 s with 13 mW cm^{-1} of 365 nm UV light using an MJB4 mask aligner (Süss MicroTec). Substrates (silicon, $\langle 100 \rangle$ ±0.5°, Czochralski grown, Sie- gertWafer) were treated in a Si 500 inductively-coupled plasma (ICP)-RIE plasma etcher (Sentech). The gaseous mixture con- sisted of 50 standard cubic centimeters per minute (sccm) SF_6 feed gas, 70 sccm C_4F_8 for sputtering and 5 sccm O_2 for glow discharge. The stage temperature was set to 0 °C, ICP power was set to 400 W and radio frequency was set to 15 Hz with a chamber pressure of 1.02 bar. Subsequently, photoresist was removed with acetone in an ultrasonic bath.

UV nanoimprint lithography

UV-NIL was utilized for the duplication of structures previously produced by RIE. These structures served as master stamps for the UV-NIL production. The master stamps were covered with a layer of fluorosilane (1H,1H,2H,2H-perfluorodecyltrichlorosilane, 96%, Alfa Aesar) as anti-adhesive coating by CVD. The stamps were first cleansed by sonication in acetone and isopropyl alcohol (IPA), followed by 2 min of ozone exposure in a UV/ozone cleaner (UVO Cleaner Model 144AX Series, Jelight Company). Following ozone treatment, CVD of fluorosilane was performed in a Vacutherm vacuum oven (Fisher Scientific) for 30 min at 80 °C and 0.4 bar. Common glass coverslips (20 mm, #1, CarlRoth) were utilized as resin substrates. The substrates were cleansed and exposed to ozone plasma for dehydration analogous to the stamps.

OrmoPrime® 08 (MicroResist) was applied as adhesion layer through spin coating for 1 min at 4000 rpm and hardbaked on a hotplate for 5 min at 150 °C. OrmoStamp (MicroResist), a poly- mer with glass-like properties and high UV-NIL resolution, was used as resist. Single droplets were positioned centrally on the stamps, before glass substrates were placed on top without additional pressure. UV-curing was performed in an MJB4 mask aligner for 2 min with 13 mW cm^{-1} of 365 nm UV light. The resulting negatives of the original master stamps function as replica stamps in a second UV-NIL step with identical parameters, which produces the substrates utilized as cell culturing platforms.

Surface coatings

Alumina. Al_2O_3 was deposited by ALD utilizing trimethyla- luminum $[Al(CH_3)_3]$ and water as precursors in a custom-built ALD system. On planar control substrates, a layer thickness of 15 nm was determined by spectral ellipsometry.

Parylene C. ParC was coated on cell culture substrates by CVD in a SCS Lab-coater® 2 (Speciality Coating Systems). In previous experiments with 0.7 g ParC all surfaces of structures, including interior surfaces of microtubes, were coated with a layer of approx. 130 nm thickness.[20] For this work, 0.5 g were used for coating.

Poly-D-lysine. Regardless of the PDL deposition method, all substrates were treated with ozone plasma at 3.5–5 W for 3–5 s in a plasma system (Femto, Diener Electronic) in advance to increase the hydrophilicity of the surface.

For nonspecific PDL coating onto the entire surface of the culture platform a droplet of approx. 100 μl cm^{-2} PDL solution (0.01 g l^{-1}, mol wt 30–70k, Sigma Aldrich) was pipetted onto the substrates. Resting time was at least 30 min. After removing the PDL solution, the substrates were cleansed with DI water (18.2 MΩ cm) two or three times to remove excess PDL molecules.

Patterns of PDL were printed utilizing a Dimatix Materials printer DMP-2831 (Fujifilm) with 16 nozzle cartridges that eject 1 pl droplets of liquid. Piezo-element voltage was set to 20–25 V, with a jetting frequency of 2.5 kHz. The temperature of the nozzle chamber as well as the sample holder was set to 21 °C. The distance between write head and substrate was set to 600 μm. The viscosity of PDL solution, estimated based on droplet velocity and piezo-element voltage, is approximately 13 cP.

A custom-built upright patch clamp setup was utilized for site-specific PDL coating in cavities and grooves. The setup consists of a microscope, an objective with a large working distance, a micromanipulator and freshly prepared glass pipettes with openings of down to <1 μm.

Laminin. Right before cultivation, all substrates were addi- tionally coated with laminin by incubation with laminin solu- tion (10 μg ml^{-1}) for 20 min.

Cell culture

The substrates were cultivated with wild type murine cerebellar granule cells. All mice were 6–7 days old at the time of extrac- tion. A detailed description of the isolation process has been previously given by Loers et al.[57] Culture medium was

Neurobasal A (Thermo Fisher Scientific) supplemented with penicillin/streptomycin (1%), bovine serum albumin (1%), insulin (10 μg ml^{-1}), L-thyroxine (4 nM), transferrin holo (100 μg ml^{-1}), sodium selenite (30 nM) (all Sigma Aldrich), fetal bovine serum (6%, Capricorn Scientific – FBS Advanced) and Gibco B-27 (50×, Thermo Fisher Scientific). Cell concentration was adjusted to 2×10^5 cells per ml. Cells were plated in droplets of approx. 100 μl cm^{-2} suspension and left to settle for 1 h at 37 °C and 5% CO_2 in the incubator. Afterwards, 3 ml cell medium was added per 35 mm Petri dish (Fisher Scientific, Biolite). Cytosine arabinoside (3 μM) was added after 24 h. Medium was renewed after 2 DIV and subsequently every 2–3 days.

Animals

C57BL/6 mice were bred at the animal facility of the University Medical Center Hamburg-Eppendorf and maintained at 22 °C on a 12 h light/12 h dark cycle and provided with food and water *ad libitum*. All experiments were conducted with mice of either sex and in accordance with the German and European Community laws on protection of experimental animals. Procedures used were approved by the responsible committee of The State of Hamburg (permission no. Org_679). Experiments were carried out and the manuscript was prepared following the ARRIVE guidelines for animal research.

Confocal laser scanning microscopy

For CLSM, neurons were stained using Neurite Outgrowth Staining Kit (Invitrogen, Thermo Fisher). Growth medium was removed and the substrates were treated with 1× dye mixture in Hank's Balanced Salt Solution (HBSS) or Dulbecco's Phosphate-Buffered Saline (DPBS) for 15 min at 37 °C and 5% CO_2. Imaging was performed with a Leica TCS SP8 confocal microscope (excitation at 488 nm and 552 nm wavelength; detection between 494–530 nm and 558–610 nm). Rendering of images to 2D stacks was performed using Leica LAS X software or the Fuji distribution of ImageJ.[58,59] The OrientationJ plugin in ImageJ was used for directional analysis of neurite orientation.[60,61]

Scanning electron microscopy

In preparation for SEM, cells were fixated and dried by exposure to paraformaldehyde in HBSS (4%) for 20 min at 37 °C. Substrates were rinsed three times with purified water and successively submerged in 10%, 25%, 50%, 75% and 99.5% v/v ethanol absolute (VWR Chemicals) solution for 10 min each. Subsequently, the substrates were either air dried or critically point dried for optimal preservation (Autosamdri-815 Series A, Tousimis). Substrates were stored under vacuum in a desiccator until further use. All substrates were coated with approx. 30 nm Au by sputter coating (K550 Emitech Sputter Coater) before SEM imaging (Zeiss Crossbeam 550).

Author contributions

C. F. and L. R. produced the substrates and conducted the analysis of the culturing results. C. F. and J. H. cultivated the neurons. G. L. prepared the murine cerebella. C. F., J. H. and R.

Z. wrote the manuscript. C. F and R. B. conceived the study. R. Z. and R. B. supervised the project. R. B. assisted in manuscript finalization. All authors significantly contributed to the scientific discussion during data evaluation and manuscript preparation. All authors conducted a final proof reading.

Conflicts of interest

There are no conflicts to declare.

Acknowledgements

References

1 K. Franze, P. A. Janmey and J. Guck, *Annu. Rev. Biomed. Eng.*, 2013, **15**, 227–251.

2 C. Miller, S. Jeftinija and S. Mallapragada, *Tissue Eng.*, 2002, **8**, 367–378.

3 D. Kleinfeld, K. Kahler and P. Hockberger, *J. Neurosci.*, 1988, **8**, 4098–4120.

4 A. A. Oliva, C. D. James, C. E. Kingman, H. G. Craighead and G. A. Banker, *Neurochem. Res.*, 2003, **28**, 1639–1648.

5 Y. W. Fan, F. Z. Cui, S. P. Hou, Q. Y. Xu, L. N. Chen and I.-S. Lee, *J. Neurosci. Methods*, 2002, **120**, 17–23.

6 A. Marino, G. Ciofani, C. Filippeschi, M. Pellegrino, M. Pellegrini, P. Orsini, M. Pasqualetti, V. Mattoli and B. Mazzolai, *ACS Appl. Mater. Interfaces*, 2013, **5**, 13012–13021.

7 B. Kaehr, R. Allen, D. J. Javier, J. Currie and J. B. Shear, *Proc. Natl. Acad. Sci. U. S. A.*, 2004, **101**, 16104–16108.

8 S. Turunen, E. Käpylä, M. Lähteenmäki, L. Ylä-Outinen, S. Narkilahti and M. Kellomäki, *Optic Laser. Eng.*, 2014, **55**, 197–204.

9 J. S. Goldner, J. M. Bruder, G. Li, D. Gazzola and D. Hoffman-Kim, *Biomaterials*, 2006, **27**, 460–472.

10 A. M. Taylor, M. Blurton-Jones, S. W. Rhee, D. H. Cribbs, C. W. Cotman and N. L. Jeon, *Nat. Methods*, 2005, **2**, 599–605.

11 M. A. Scott, Z. D. Wissner-Gross and M. F. Yanik, *Lab Chip*, 2012, **12**, 2265.

12 A. Tooker, E. Meng, J. Erickson, Y.-C. Tai and J. Pine, in *The 26th Annual International Conference of the IEEE Engineering in Medicine and Biology Society*, IEEE, 2004, vol. 3, pp. 2542–2545.

13 B. W. Tuft, L. Xu, S. P. White, A. E. Seline, A. M. Erwood, M. R. Hansen and C. A. Guymon, *ACS Appl. Mater. Interfaces*, 2014, **6**, 11265–11276.

14 W. Li, Q. Y. Tang, A. D. Jadhav, A. Narang, W. X. Qian, P. Shi and S. W. Pang, *Sci. Rep.*, 2015, **5**, 8644.

15 R. Renault, J.-B. Durand, J.-L. Viovy and C. Villard, *Lab Chip*, 2016, **16**, 2188–2191.

16 C. S. Bausch, A. Koitmäe, E. Stava, A. Price, P. J. Resto, Y. Huang, D. Sonnenberg, Y. Stark, C. Heyn, J. C. Williams, E. W. Dent and R. H. Blick, *Appl. Phys. Lett.*, 2013, **103**, 173705.

17 P. Froeter, Y. Huang, O. V. Cangellaris, W. Huang, E. W. Dent, M. U. Gillette, J. C. Williams and X. Li, *ACS Nano*, 2014, **8**, 11108–11117.

18 M. Yu, Y. Huang, J. Ballweg, H. Shin, M. Huang, D. E. Savage, M. G. Lagally, E. W. Dent, R. H. Blick and J. C. Williams, *ACS Nano*, 2011, **5**, 2447–2457.

19 A. Koitmäe, J. Harberts, G. Loers, M. Müller, C. S. Bausch, D. Sonnenberg, C. Heyn, R. Zierold, W. Hansen and R. H. Blick, *Adv. Mater. Interfaces*, 2016, **3**, 1600746.

20 A. Koitmäe, M. Müller, C. S. Bausch, J. Harberts, W. Hansen, G. Loers and R. H. Blick, *Langmuir*, 2018, **34**, 1528–1534.

21 M. Kwiat, R. Elnathan, A. Pevzner, A. Peretz, B. Barak, H. Peretz, T. Ducobni, D. Stein, L. Mittelman, U. Ashery and F. Patolsky, *ACS Appl. Mater. Interfaces*, 2012, **4**, 3542–3549.

22 J. N. Hanson, M. J. Motala, M. L. Heien, M. Gillette, J. Sweedler and R. G. Nuzzo, *Lab Chip*, 2009, **9**, 122–131.

23 L. Micholt, A. Gärtner, D. Prodanov, D. Braeken, C. G. Dotti and C. Bartic, *PLoS One*, 2013, **8**, 1–14.

24 T. Limongi, F. Cesca, F. Gentile, R. Marotta, R. Ruffilli, A. Barberis, M. Dal Maschio, E. M. Petrini, S. Santoriello, F. Benfenati and E. Di Fabrizio, *Small*, 2013, **9**, 402–412.

25 M. Park, E. Oh, J. Seo, M.-H. Kim, H. Cho, J. Y. Choi, H. Lee and I. S. Choi, *Small*, 2016, **12**, 1148–1152.

26 H. Amin, M. Dipalo, F. De Angelis and L. Berdondini, *ACS Appl. Mater. Interfaces*, 2018, **10**, 15207–15215.

27 B. E. Kerman, H. J. Kim, K. Padmanabhan, A. Mei, S. Georges, M. S. Joens, J. A. J. Fitzpatrick, R. Jappelli, K. J. Chandross, P. August and F. H. Gage, *Development*, 2015, **142**, 2213–2225.

28 H. U. Lee, S. Nag, A. Blasiak, Y. Jin, N. Thakor and I. H. Yang, *ACS Chem. Neurosci.*, 2016, **7**, 1317–1324.

29 Z. Tong, M. Segura-Feliu, O. Seira, A. Homs-Corbera, J. A. Del Río and J. Samitier, *RSC Adv.*, 2015, **5**, 73457–73466.

30 A. M. Taylor, S. Menon and S. L. Gupton, *Lab Chip*, 2015, **15**, 2781–2789.

31 N. S. Bhise, J. Ribas, V. Manoharan, Y. S. Zhang, A. Polini, S. Massa, M. R. Dokmeci and A. Khademhosseini, *J. Controlled Release*, 2014, **190**, 82–93.

32 S. Na, M. Kang, S. Bang, D. Park, J. Kim, S. J. Sim, S. Chang and N. L. Jeon, *Technology*, 2016, **4**, 240–248.

33 S. Bang, S. Jeong, N. Choi and H. N. Kim, *Biomicrofluidics*, 2019, **13**, 051301.

34 M. C. McManus, E. D. Boland, D. G. Simpson, C. P. Barnes and G. L. Bowlin, *J. Biomed. Mater. Res., Part A*, 2007, **81A**, 299–309.

35 I. M. El-Sherbiny and M. H. Yacoub, *Glob. Cardiol. Sci. Pract.*, 2013, **2013**, 38.

36 H. Cai, S. Sharma, W. Liu, W. Mu, W. Liu, X. Zhang and Y. Deng, *Biomacromolecules*, 2014, **15**, 2540–2547.

37 S. Campuzano and A. E. Pelling, *Front. Sustain. Food Syst.*, 2019, **3**, 38.

38 A. Cutarelli, S. Ghio, J. Zasso, A. Speccher, G. Scarduelli, M. Roccuzzo, M. Crivellari, N. M. Pugno, S. Casarosa, M. Boscardin and L. Conti, *Cells*, 2019, **9**, 88.

39 J. Harberts, U. Haferkamp, S. Haugg, C. Fendler, D. Lam, R. Zierold, O. Pless and R. H. Blick, *Biomater. Sci.*, 2020, **8**, 2434–2446.

40 C. Metallo, R. D. White and B. A. Trimmer, *J. Neurosci. Methods*, 2011, **195**, 176–184.

41 E. M. Schmidt, M. J. Bak and J. S. McIntosh, *Exp. Neurol.*, 1976, **52**, 496–506.

42 T. V. Thamaraiselvi and S. Rajeswari, *Trends Biomater. Artif. Organs*, 2004, **18**(1), 9–17.

43 D. S. Finch, T. Oreskovic, K. Ramadurai, C. F. Herrmann, S. M. George and R. L. Mahajan, *J. Biomed. Mater. Res., Part A*, 2008, **87A**, 100–106.

44 M. O. Brose, R. J. Avers, M. R. Rieger and J. E. Duckworth, *J. Prosthet. Dent.*, 1989, **61**, 594–601.

45 G. Mendonça, D. B. S. Mendonça, L. G. P. Simões, A. L. Araújo, E. R. Leite, W. R. Duarte, L. F. Cooper and F. J. L. Aragão, *Int. J. Oral Maxillofac. Implants*, 2010, **24**, 205–215.

46 C. Fendler, C. Denker, J. Harberts, P. Bayat, R. Zierold, G. Loers, M. Münzenberg and R. H. Blick, *Adv. Biosyst.*, 2019, 1800329.

47 J. Harberts, R. Zierold, C. Fendler, A. Koitmäe, P. Bayat, I. Fernandez-Cuesta, G. Loers, B.-P. Diercks, R. Fliegert, A. H. Guse, C. Ronning, G. Otnes, M. Borgström and R. H. Blick, *RSC Adv.*, 2019, **9**, 11194–11201.

48 E. Yavin and Z. Yavin, *J. Cell Biol.*, 1974, **62**, 540–546.

49 D. Mazia, G. Schatten and W. Sale, *J. Cell Biol.*, 1975, **66**, 198–200.

50 D. Edgar, R. Timpl and H. Thoenen, *EMBO J.*, 1984, **3**, 1463–1468.

51 N. Li and A. Folch, *Exp. Cell Res.*, 2005, **311**, 307–316.

52 N. Nakatsuji and I. Nagata, *Cell Differ. Dev.*, 1989, **27**, 199.

53 I. Nagata, A. Kawana and N. Nakatsuji, *Development*, 1993, **117**, 401–408.

54 A. Rajnicek, S. Britland and C. McCaig, *J. Cell Sci.*, 1997, **110**(Pt 2), 2905–2913.

55 A. R. Evans, S. Euteneuer, E. Chavez, L. M. Mullen, E. E. Hui, S. N. Bhatia and A. F. Ryan, *Dev. Neurobiol.*, 2007, **67**, 1721–1730.

56 D. Soltman and V. Subramanian, *Langmuir*, 2008, **24**, 2224–2231.

57 G. Loers, S. Chen, M. Grumet and M. Schachner, *J. Neurochem.*, 2005, **92**, 1463–1476.

58 C. A. Schneider, W. S. Rasband and K. W. Eliceiri, *Nat. Methods*, 2012, **9**, 671–675.

59 J. Schindelin, I. Arganda-Carreras, E. Frise, V. Kaynig, M. Longair, T. Pietzsch, S. Preibisch, C. Rueden, S. Saalfeld, B. Schmid, J.-Y. Tinevez, D. J. White, V. Hartenstein, K. Eliceiri, P. Tomancak and A. Cardona, *Nat. Methods*, 2012, **9**, 676–682.

60 R. Rezakhaniha, A. Agianniotis, J. T. C. Schrauwen, A. Griffa, D. Sage, C. V. C. Bouten, F. N. van de Vosse, M. Unser and N. Stergiopulos, *Biomech. Model. Mechanobiol.*, 2012, **11**, 461–473.

61 Z. Püspöki, M. Storath, D. Sage and M. Unser, *Focus on Bio-Image Informatics*, Springer International Publishing, Cham, 2016, vol. 219.

Supporting material: Neurite guidance and neuro-caging on steps and grooves in 2.5 dimensions

Cornelius Fendler[a], Jann Harberts[a], Lars Rafeldt[a], Gabriele Loers[b], Robert Zierold[a*], Robert H. Blick,[a,c]

[a]Center for Hybrid Nanostructures (CHyN), Universität Hamburg, 22761 Hamburg, Germany
[b]Center for Molecular Neurobiology Hamburg (ZMNH), University Medical Center Hamburg-Eppendorf (UKE), Hamburg 20251, Germany.
[c]Material Science and Engineering, College of Engineering, University of Wisconsin-Madison, Madison, Wisconsin 53706, USA.

Substrates produced by grayscale lithography (GSL)

Cross sections of step structures in AZ4562 as result of exposure tests at 22 mW laser power are shown in Figure S1 a. Since photon absorption in the resist is a nonlinear process, exposure with linear grading leads to an exponential decrease of step height towards larger depths. If the goal is the production of complex geometries, results of an intensity test can be fed into computational calculation to convert desired features into fitting gray scale values. Correct values for simple structures without the demand for nanoscale accuracy, such as the ones described in this chapter, can be directly estimated based on the test results. An exemplary step structure created by GSL with a targeted step height of 2 µm is shown in Figure S1 b. The gray values were set to 42, 122 and 228 to reach 2 µm, 4 µm and 6 µm depths. A profile corresponding to such a step structure is shown in Figure S1 c. The profile indicates slightly rounded edges. Figure S1 d shows examples of a chessboard structures produced with GSL. The design connects cavities through channels with integrated steps of 2 µm height with each other.

Substrates produced by reactive ion etching (RIE)

A plot of RIE etch depth in dependence to process time is shown in Figure S2 a. Slight variations in the etch rate can be attributed to temperature fluctuations in the reaction chamber. The etch rate determined by linear regression of the etch depths is (9.8 ± 0.1) nm/s. To obtain multiple steps in one structure, up to three consecutive cycles of contact lithography and RIE were executed. An example of a structure resulting from two cycles is shown in Figure S2 b. Etching of channels with 10 µm gaps every 40 µm in one and overlaying continuous channels in the other cycle results in steps with the height defined by RIE in the cycle with the gaps included in the design. Figure S2 c shows multiple substrates for which the described principle was utilized to produce identical boundaries of 10 µm height defining channels that connect cavities with 2 µm – 10 µm additional depth, resulting in distinct steps at the channel entrances/exits. Isolated cavities were etched first, followed by the design including the channels. Steep sidewalls form 90 ° corners at the bottom of the structures. Slight misalignment of the exposure designs and interference patterns are visible due to limited accuracy of contact lithography with mask aligners during the second RIE circle. At high overall depth of 18 µm and 20 µm, deviations from the design increase with residues and uneven surface inside the cavities.
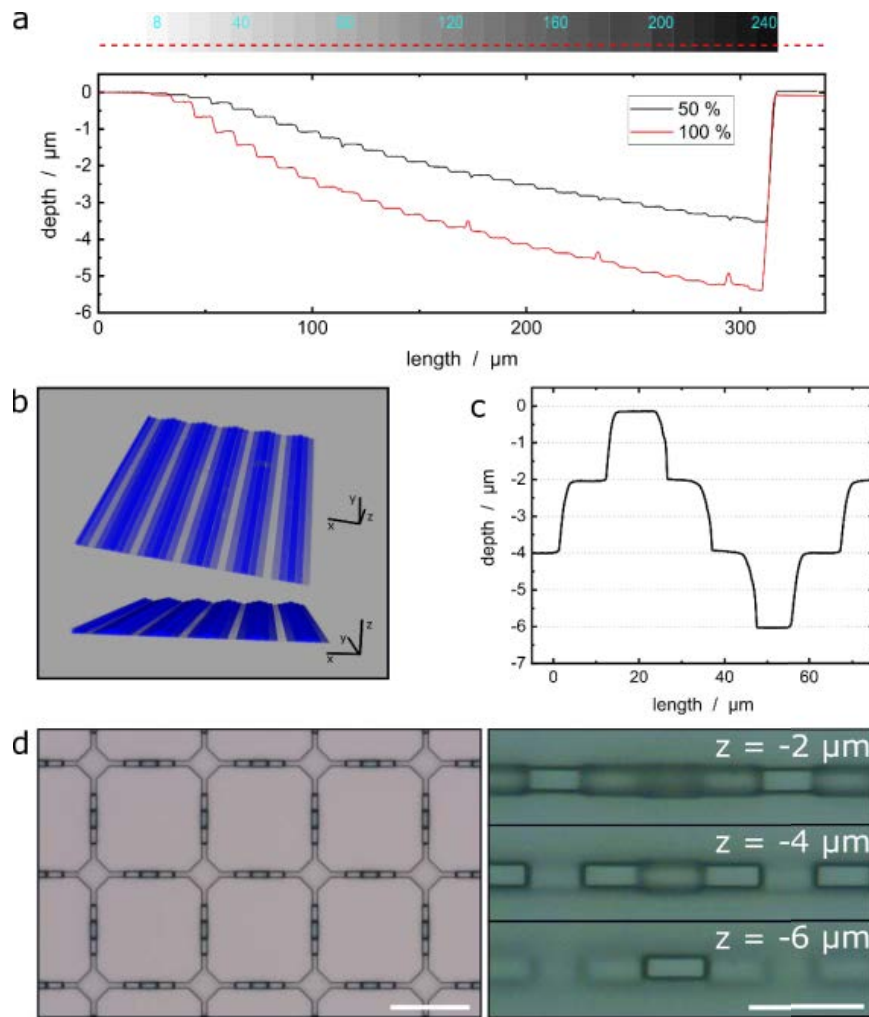
Figure S 1: Profiles and images of structures produced by GSL in AZ4562 photoresist with 22 mW laser power. The profiles were measured with a DektakXT profilometer (Bruker). (a) Results of exposure tests. A 50 % filter was installed in the beam path of the laser for the black plot in contrast to no filter for the red plot. The gray bars at the top give a top view onto the gray values of the exposure design. From left to right, the gray values increase in discrete steps of 8, which linearly correlate with the local UV laser intensity during the writing process. The red dashed line represents the profiles displayed in the plot. (b) CLSM 3D stack of the step structure. Scale: 40 μm. (c) Profile of a step structure created by exposure with alternating gray values of 0, 42, 122 and 228. (d) Brightfield images of a chessboard structure produced with the same gray values of 0, 42, 122 and 228. Cavities are connected through channels with steps. The focus of the right images is shifted by -2 μm top to bottom. Scale bars: 50 μm, 20 μm.
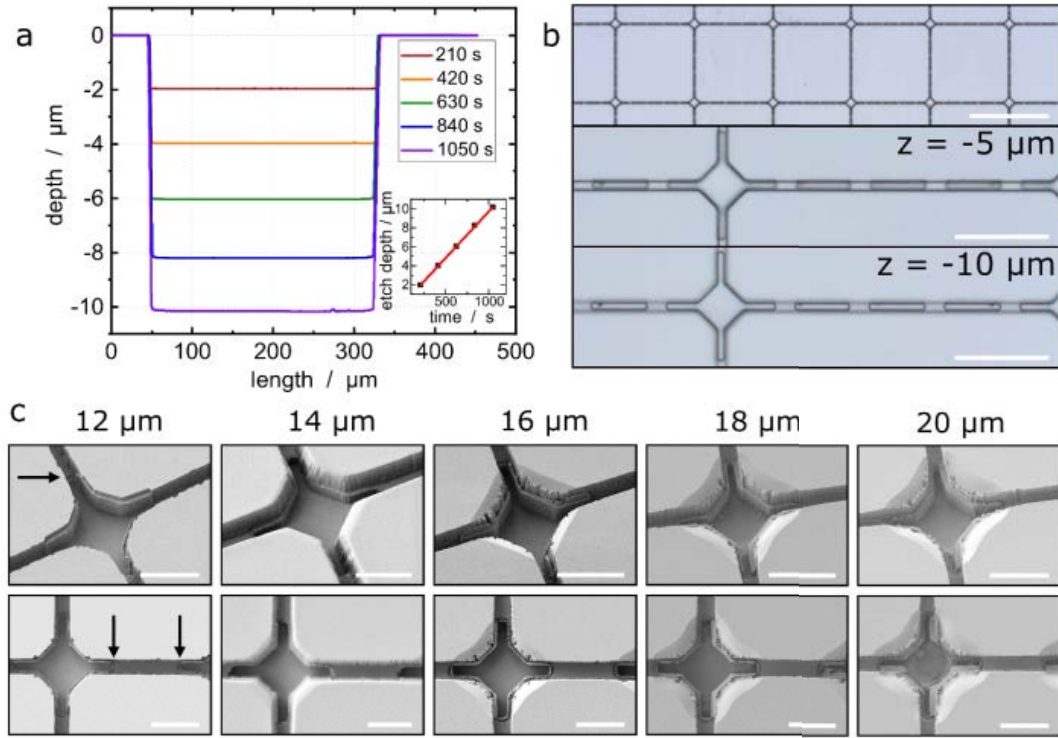
Figure S2: Profiles and images of structures produced by RIE in silicon. (a) Cross section profiles of grooves measured with a profilometer. A plot of the etch depth against time is shown in the small graph. The etch rate is (9.8 ± 0.1) nm/s. (b) Optical images of a chessboard pattern created by two consecutive etch steps. Cavities are connected through channels with steps. The focus is set to -5 μm in the middle and -10 μm in the bottom image relative to the silicon surface. Scale bars: 200 μm (top), 50 μm (middle and bottom). (c) SEM images of chessboard structures with isolated cavities with increasing depth from 12 μm to 20 μm from left to right etched in a first step and cavities connected by continuous channels with 10 μm depth edged in a second step, resulting in steps at the cavity exits accordingly (indicated for 12 μm cavities with arrows). Scale bars: 20 μm.

A.9   Publication IX

Approaching integrated hybrid neural circuits: axon guiding on optically active semiconductor microtube arrays

Aune Koitmäe, <u>Jann Harberts</u>, Gabriele Loers, Manuel Müller, Cornelius S. Bausch, David Sonnenberg, Christian Heyn, Robert Zierold, Wolfgang Hansen, and Robert H. Blick

Advanced Materials Interfaces **2016**, 3(24), 1600746

Copyright © 2016 WILEY-VCH Verlag GmbH & Co. KGaA, Weinheim.

Author contributions: Cell preparation, cultivation, imaging, axon detection: A.K., sample preparation: M.M., PLL printing: <u>J.H.</u>, installation of the photoluminescence setup under supervision of A.K.: <u>J.H.</u>, photoluminescence measurements and writing of the manuscript: A.K., tube design: C.S.B., animal preparation: G.L., wafer preparation: R.Z., D.S., C.H., W.H., supervision: R.H.B.

(6 + 3 pages)

Approaching Integrated Hybrid Neural Circuits: Axon Guiding on Optically Active Semiconductor Microtube Arrays

Aune Koitmäe,* Jann Harberts, Gabriele Loers, Manuel Müller, Cornelius S. Bausch, David Sonnenberg, Christian Heyn, Robert Zierold, Wolfgang Hansen, and Robert H. Blick

In this communication, we present a combined approach for local guided adhesion of neurons, assisted growth across a large area, and probing of synthetic neural circuits via optically active semiconductor microtubes. A quantum well, embedded in the wall of the microtube, supplies the microtube with optically active characteristic, enabling remote sensing of action potentials. The electric field caused by the alteration of the membrane potential of the axon during action potential generation propagates in the wall of the microtube, thus changing the band structure of the semiconductor and the emission wavelength (WL) of the microtube.

Improved understanding of the brain and the reasons for its misfunction, e.g., neurodegenerative disorders are of great interest for medicine and neuroscience. The challenge is to connect the disciplines of neurobiology and electronics/photonics to mimic the 3D environment of the brain while still having a highly defined system. Typically, most of the suggested devices use electrical feedback methods to detect action potentials (APs) and understand interactions in a neural network consisting of up to thousands of microelectrode arrays.[1–5] However, for over a decade, the emerging research field of optogenetics has created new promising wireless devices for neural stimulation and activation detection.[6,7] Optical detection methods have many advantages compared to using electrodes. Plane electrodes do not deliver the best signal-to-noise ratio, additionally, the branchy shape of the axons extending over large arrays of the sample does not enable to build a defined system, since the axons are passing several electrodes making the data analysis challenging. To enhance the signal-to-noise ratio, invasive electrodes are utilized[3] having the downside of damaging the cells in long term studies.

The fabrication of semiconductor microtubes is based on the growth of lattice mismatched layers.[8,9] We employ molecular beam epitaxy (MBE) to define a sequence of a sacrificial layer, a strained layer, and a top layer directly grown on a GaAs wafer, see **Figure 1**a. By using components with different lattice constants during growth, strain is formed in the multilayer. Since GaAs and AlAs have similar lattice parameters ($a_{GaAs} = 0.565$ nm and $a_{AlAs} = 0.566$ nm),[10] such a layer system would not be strained. Stress is built by adding indium to the system: Increasing the indium content increases the lattice constant linearly. In this work, a multilayer consisting of 16 nm $Al_{0.3}Ga_{0.7}As$, 4 nm GaAs, 7 nm $Al_{0.3}Ga_{0.7}As$, 15 nm $In_{0.2}Al_{0.24}Ga_{0.56}As$, and 40 nm AlAs is used. These layer thicknesses result in a tube diameter of 3 µm,[11] the same order of magnitude as the diameter of an axon.

The optically active 4 nm GaAs quantum well (QW) is located between the AlGaAs barrier layers (Figure 1b). By selective etching of the 40 nm AlAs sacrificial layer, strain is released and the tubes start rolling up (see the Supporting Information for details). Figure 1c shows a rectangular array of tubes fabricated via photolithography with a single tube length of 50 µm and diameter of 3 µm containing two windings.

Because of the toxicity of the arsenic compounds to biological materials, GaAs has to be sealed with a biocompatible material before introducing living cells to the samples. Therefore, the bottom of the GaAs wafer is coated with polydimethylsiloxane (PDMS). As a first step, microtube samples are laid on cured PDMS well. The edges of the wafer are carefully brushed with liquid PDMS (1:10). After curing out on a hotplate for 5 min at 100 °C, the bottom and the edges are coated with PDMS. The next step is coating the top of the sample with the biocompatible polymer parylene-C (Specialty Coating Systems, Labcoter 2) via chemical vapor deposition (CVD). During the CVD process, the tubes are coated from outside and inside with a 130 nm parylene-C layer.[12] This polymer shows outstanding electrical, chemical, and thermal stability and is widely used as an electrical insulator and coating for biomedical implants.[13]

The pioneering work in the field of neuron guiding on semiconductor microtube arrays by Schulze et al.[14] indicated an excellent potential for such hybrid devices. We have

Dr. A. Koitmäe, J. Harberts, M. Müller,
Dr. C. S. Bausch, Dr. D. Sonnenberg, Dr. C. Heyn,
Dr. R. Zierold, Prof. W. Hansen, Prof. R. H. Blick
Institute of Nanostructure and Solid State Physics
Universität Hamburg
Jungiusstraße 11c, Hamburg 20355, Germany
E-mail: akoitmae@physnet.uni-hamburg.de
Dr. A. Koitmäe, J. Harberts, M. Müller, Dr. C. S. Bausch,
Dr. D. Sonnenberg, Dr. R. Zierold, Prof. R. H. Blick
Center for Hybrid Nanostructures (CHYN)
Universität Hamburg
Falkenried 88, Hamburg 20251, Germany
Dr. G. Loers
Center for Molecular Neurobiology Hamburg
University Medical Center Hamburg-Eppendorf
Falkenried 94, 20251, Hamburg, Germany

ADVANCED
MATERIALS
INTERFACES
www.advmatinterfaces.de

Materials
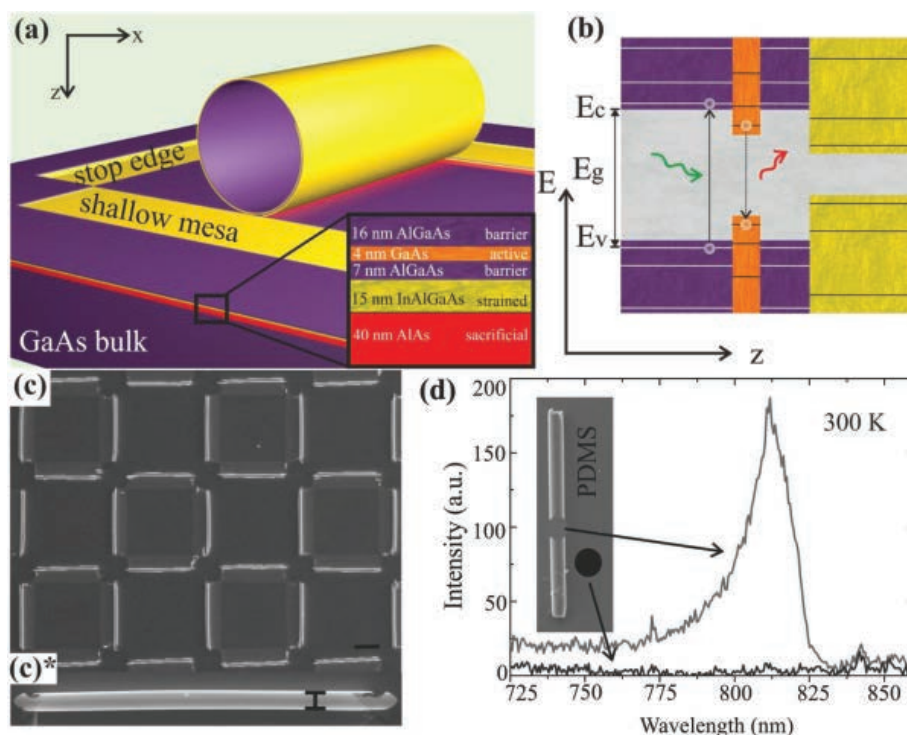Views
www.MaterialsViews.com

COMMUNICATION

Figure 1. a) A sketch of the fabrication of microtubes. The active 4 nm GaAs layer is embedded between the AlGaAs barrier layers. b) A sketch of the energy bands in the multilayer: The electrons are excited with a 552 nm laser, as a result excitons are generated relaxing in the lowest energy state of the QW and recombine via photon emission with the energy of the band gap (E_g). c) SEM image of an array of naked GaAs microtubes with a length of 50 μm and a distance between the microtubes 20 μm. c*) SEM image of an individual uncoated microtube. d) Room temperature PL spectrum of a transferred microtube. The gray curve shows emission at 818 nm which refers to the emission of a GaAs QW, the black curve refers to the PDMS substrate (scale bars (c) 20 μm and (c*) 3 μm).

shown earlier that microtubes act as geometric guides for axon outgrowth.[12,15] Axons prefer to grow along boundary surfaces[16] and can be guided into the tubes. In our earlier work (Yu et al.[15]), we focused on SiGe as a material for semiconductor microtubes and have shown excellent neuron guiding capabilities with tube diameters one order of magnitude larger than the diameters of the axons. Recently, Froeter et al.[17] reported on Si$_3$N$_4$ microtubes having diameters very similar to axons, revealing an acceleration effect on the axon outgrowth. However, the tubes of both synthesis routes were not optically active as in our approach. In our experiments, we use tailor-made tube diameters comparable with the diameters of mouse axons. By combining the topological and chemical guidance cues, 30% of the microtubes on our samples are filled with axons.

To define the adhesion areas of the neurons, the samples are selectively coated with the adhesive amino acid poly-L-lysine. **Figure 2**a shows a rectangular array of tubes. The red semitransparent circles highlight poly-L-lysine (PLL) droplets, which serve as adhesive factor for neurons.[18,19] Prior to printing the droplets of PLL on the parylene-C coated microtube samples, the samples are plasma-treated with oxygen plasma (FEMTO, diener electronic) for 1.5 s. This treatment creates a hydrophilic surface and optimizes the size of the PLL droplets to a diameter 25 μm. The deposition of the PLL arrays is undertaken using Dimatix Materials Printer (DMP-2831, Fujifilm USA)

which takes advantage of the piezoelectric inkjet technology. The delivered software enables to design a desired droplet array which is printed on the sample via nozzles having a droplet volume of about 1 pL. The distance between two microtubes (20 μm) is chosen in such a way, that the printed PLL droplets slightly overlap with the tubes' openings. This overlap is crucial to guide axons into and through the tubes since we found that their growth into the tubes is otherwise not as efficient (Figure SI1, Supporting Information).

Neuron guiding experiments are carried out with cerebellar granule neurons from mice. The so-called bipolar shape of these neurons is of advantage because there are only two neurites (which later transform to axon and dendrite) per neuron, forming a more defined system in comparison to multipolar cortical or hippocampal neurons with numerous neurites. A liquid suspension that has been optimized to obtain a cell density of 5×10^3 cells cm^{-2} is plated onto the substrate and cells are cultured for 5–21 d until axon outgrowth is determined. Figure 2b shows a synthetic neural circuit with highly controlled guiding of the axons through the tubes of a length of 50 μm, which turns out to be appropriate length for our experiments for realizing hybrid neural circuits in future. In Figure 2c, the PLL coated areas are highlighted with dashed circles, the cell bodies are located in the crossing points of the microtube's entrances and the axons grow through the microtubes forming a highly defined network.
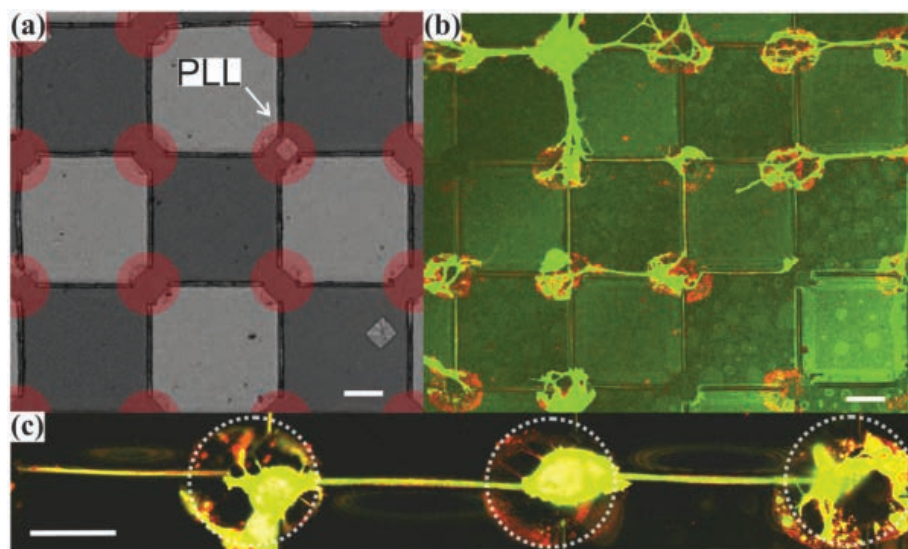
Materials
Views
www.MaterialsViews.com

ADVANCED
MATERIALS
INTERFACES
www.advmatinterfaces.de

COMMUNICATION

Figure 2. a) An optical microscope image of an array of machined microtubes. The red circles highlight the areas where PLL is microprinted to steer adhesion of the neurons. b) A confocal microscope image of synthetic neural circuit across a large area with cells cultured for 7 d. Neurons are optically labeled green and PLL shows up as red spots. c) A confocal microscope image of chemical and geometrical neuron guiding. The dashed circles highlight PLL printed areas. Scale bars in (a)–(c) are 20 μm.

For the optical characterization of the microtubes, a green (552 nm) laser, being a part of the confocal microscope Leica TSC SP8, is used. After collecting the reflected beam with a 20× objective, it is focused and directed into a spectrometer (Shamrock 303i, Andor) via broadband dielectric mirrors and collected with a charge-coupled device (CCD) (Newton CCD DU920P, Andor) camera operating in the infrared range of the spectrum.

A 2.25 eV (552 nm) green pumping laser is used to excite the electrons from the valence into the conduction band (Figure 1b, see experimental section in the Supporting Information for details). The excitation energy of the green laser exceeds the band gap energies of all semiconductor compounds and as a result of pumping, electron–hole pairs (excitons) are generated relaxing at the lowest energy state of the QW. The excitons recombine spontaneously and emit a photon corresponding to the band gap energy. Due to restrictions of the MBE, we engineered this emission WL to be 820 nm. The room temperature (RT) photoluminescence (PL) measurements are carried out on microtubes, which are transferred to a transparent glass substrate coated with a double-layer system of PDMS.[20] This transfer is essential, since (a) the interaction of GaAs substrate with the cellular materials is completely avoided and (b) the emission of the microtube–axon hybrids is more pronounced, i.e., less absorption by the semiconductor substrate.[21,22] The GaAs QW embedded in the tube's wall reveals in experiment an emission peak at 818 nm, which is in good agreement with the designed emission WL (Figure 1d). Note that RT PL measurements of such materials are extremely challenging and typically performed at low temperatures (4 K).[23,24]

To obtain more specific information about the axon placement in the tube, the tubes are milled via focused ion beam (FIB), for the first time to our knowledge, and the samples are investigated with scanning electron microscope (SEM). **Figure 3**b,c shows different magnifications of the rectangular

highlighted area of Figure 3a, where the microtube is milled perpendicularly and the cross-section clearly shows an axon in the microtube adhering tightly on the right side of the microtube's wall, which is crucial for further experiments as shown theoretically elsewhere.[25] In Figure 3c, one can distinguish between the axon, semiconductor, and polymer layers.

The confocal microscope allows high-resolution mapping of the regions of interest. For the optical probing experiments, living neurons are labeled with a green dye (Neurite Outgrowth Staining Kit, Invitrogen) which enables us to study axons in the tubes and cell viability. The dye is excited via a 552 nm green laser and the images are recorded by confocal microscopy. Although bulk GaAs is opaque in the visible regime, ≈20% of the light is transmitted due to the low semiconductor layer thickness of about 100 nm, and the labeled axons inside the tubes can be detected.[26] The conformal parylene-C coating around the tubes is transparent in the visible regime.

To confirm whether the axons truly grow through the tubes or maybe on the edges outside of the tubes, a method of intensity line plots is applied (**Figure 4**a,b). Hence, our comparative studies of the intensity carry information whether (I) a single axon, (II) an axon in the tube, or (III) an empty tube is depicted. A line plot of a single axon shows the highest intensity, while the tubes with axons inside medium intensity and empty tubes show the weakest response (Figure 4a,a*). To build a 2D neural network, the axon has to grow through the entire microtube. Therefore, our confocal microscope allows us to quantify in detail, how far into the tube an axon has grown as shown in Figure 4b,b*. The confocal image in panel (b*) clearly shows an axon 35 μm deep in the tube.

During AP propagation, the membrane potential changes generating electrical field of a magnitude of 10 mV nm^{-1}. This field propagates in the tube's wall, changes the band structure of the embedded QW,[27,28] and induces a change in the
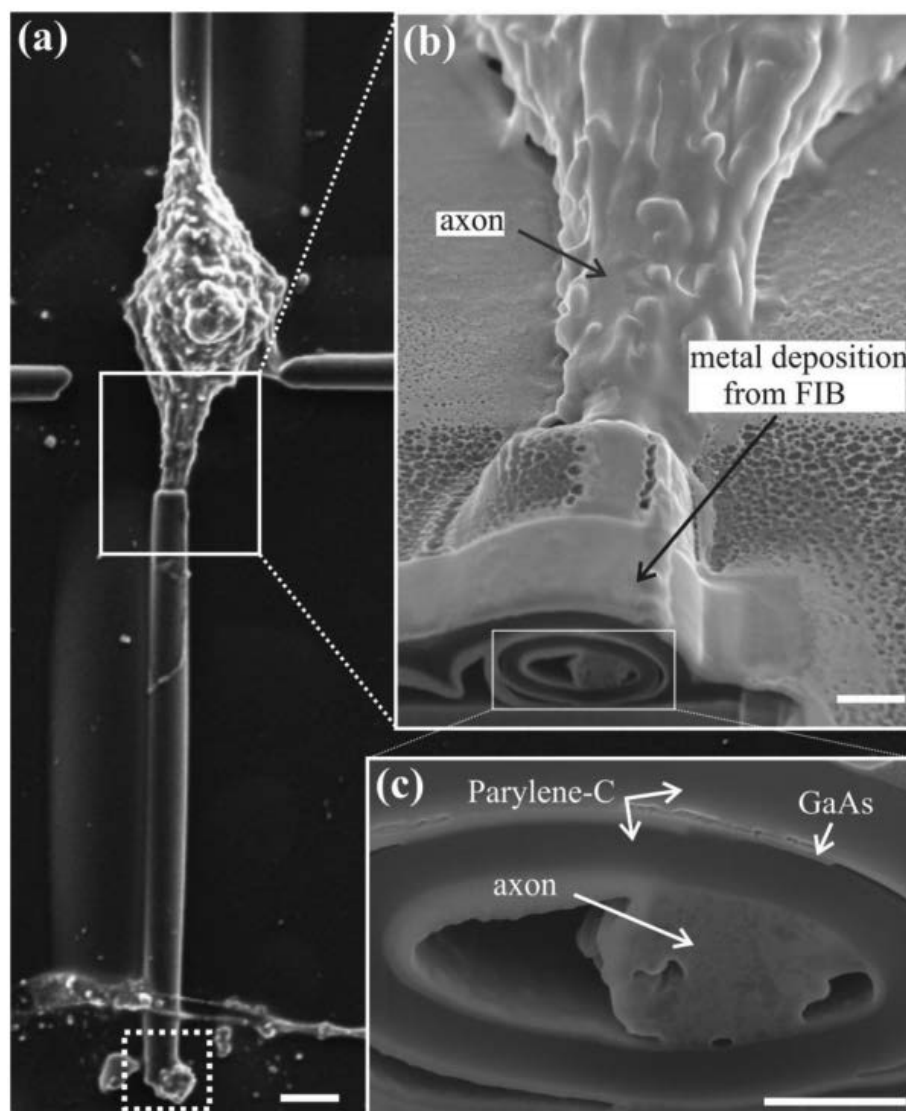
Figure 3. a) SEM image showing neurite guiding. The white labeled rectangular area shows an axon growing into the microtube. The white dashed area at the bottom highlights the end of the tube with an axon growing out of it. b) Zoom-in of the marked area in (a). The microtube has been milled with a FIB to show the axon in the tube. The tube is tightly wrapped around the axon. The bright stripe on top of the microtube marked with an arrow indicates metallic deposition, which is part of the sample preparation for FIB milling to protect the tube from demolition. c) Zoom-in of the outlined area in (b). The SEM image shows a cross-section of the parylene-coated microtube with a neurite inside. The darker circles refer to the parylene-C and the brighter area in between is the thin GaAs membrane. Scale bars 5 µm for (a), 1 µm for (b), and 500 nm for (c).

emission WL of the QW. This is typically referred to as the quantum confined Stark effect (QCSE) and can be used for wireless detection of APs.

As a proof-of-concept, we employed an "artificial axon," which is inserted into a microtube. Applied voltages of 1 and 2 V show a red-shift in the emission wavelength of the QW of 1.6 and 2.7 nm, respectively (Figure SI2b, Supporting Information). In addition, we simulate electrical fields propagating in the semiconductor membrane using COMSOL Multiphysics. A peak-to-peak voltage of $|V^{pp}_{AP}| = 150\,mV$, referring to the peak-to-peak voltage of an AP, is applied to an axisymmetric system consisting of 50 nm of electrolyte solution and semiconductor

membrane tube (SMT) embedded in boundary layer (BL) of parylene-C or TiO_2 on both sides (inset in Figure 4d). By implementing the resulting fields to the calculations of the QCSE,[29] (Figure SI2a, Supporting Information) for a 4 nm GaAs QW, we obtain the shifts in the emission WL.

Figure 4c shows the shifts as a function of BL and SMT thickness using parylene-C as coating. The highest calculated shift of 0.24 meV (0.1 nm), which can be achieved by tuning the microtube's wall system, would not be resolvable with our current setup.

The finite element simulations suggest using TiO_2 rather than parylene-C as a coating material for the microtubes since
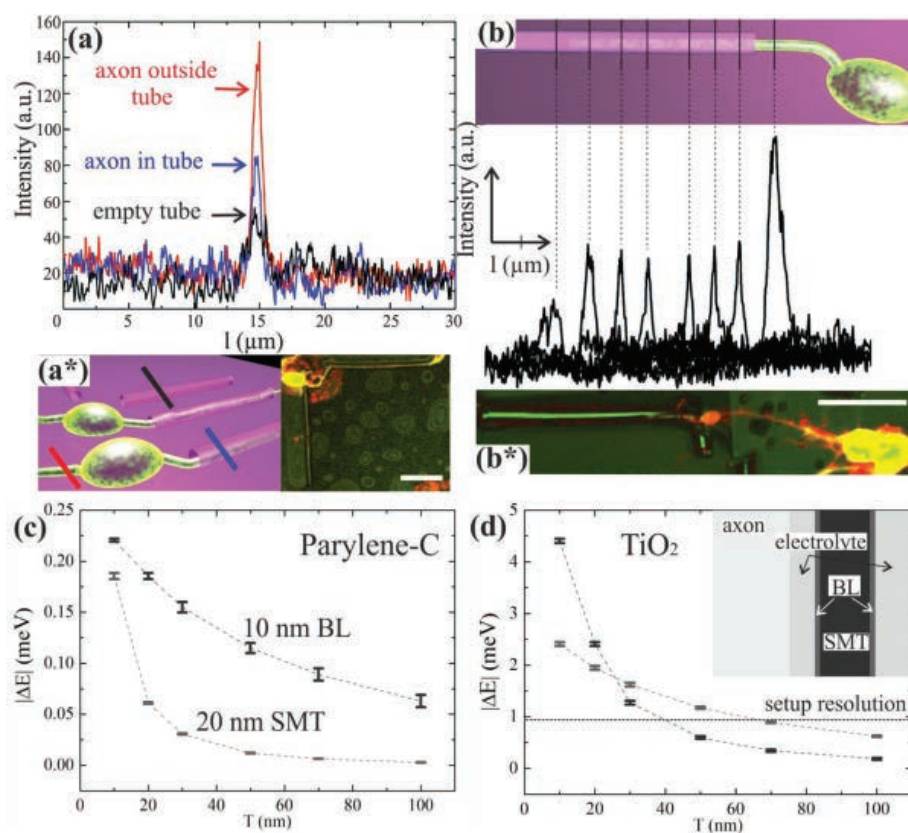
Figure 4. a) Intensity lines plotted against the distance. The red curve shows the highest intensity and refers to an axon on the semiconductor surface outside the tube. In comparison, the blue curve shows an axon in a tube and the black one refers to intensity line plot of an empty tube. a*) The corresponding sketch and confocal image to (a). b) Intensity line plots for detection of exact length of the axons inside the tubes. The labeled axon shows the highest intensity. The intensity of the axon in the tube is damped by the tube. b*) The corresponding confocal image to (b). c) Simulated QCSE using parylene-C as coating material under the influence of an applied field of $|V^{pp}_{AP}| = 150$ mV. The gray curve refers to a constant SMT thickness of 20 nm by varying the thickness of the BL. The black curve refers to a constant BL thickness of 10 nm as a function of SMT thickness. d) Simulated QCSE using TiO_2 as coating material under the influence of the same applied field showing shifts up to 4.4 meV. The black dashed curve shows the resolution of our current setup. Thus we suggest the future use of TiO_2 as coating material instead of parylene-C. Scale bars 20 µm for (a*) and (b*).

the shifts in the emission energy of the quantum well show values of about 20 times higher in comparison to parylene-C (Figure 4d). Since shifts up to 0.93 meV (0.5 nm) are resolvable with our current setup, we suggest biocompatible TiO_2[30] as coating material for the detection of real action potentials. Due to much higher relative permittivity, TiO_2 BL shows energy shifts of up to 4.4 meV (2.4 nm) (Figure 4d). Conformal deposition of TiO_2 inside the microtube can be achieved by means of atomic layer deposition based on sequential pulses of vaporous precursors[31] such as the combination of titanium isopropoxide with water.

In summary, this paper presents a combination of geometrical and chemical guidance cues resulting in a synthetic neural circuit. A detection method for axons inside optically active semiconductor microtubes with the help of intensity line plots promotes the sample mapping and creates an excellent highly defined system for further optical probing of APs and understanding the interactions between neurons. Using these optically active microtubes, APs can be detected indirectly without electrodes taking advantage of the QCSE. The sensitivity of our current device lies slightly below the resolution limit for an AP, however simulations indicate shifts up to 2.4 nm during AP propagation in the emission spectrum of the microtube for modified thicknesses of the semiconductor membrane and the coating material.

Supporting Information

Supporting Information is available from the Wiley Online Library or from the author.

Acknowledgements

COMMUNICATION

[1] D. J. Bakkum, U. Frey, M. Radivojevic, T. L. Russell, J. Müller, M. Fiscella, H. Takahashi, A. Hierlemann, *Nat. Commun.* **2013**, *4*, 2181.

[2] V. Benfenati, S. Toffanin, S. Bonetti, G. Turatti, A. Pistone, M. Chiappalone, A. Sagnella, A. Stefani, G. Generali, G. Ruani, D. Saguatti, R. Zamboni, M. Muccini, *Nat. Mater.* **2013**, *12*, 672.

[3] J. T. Robinson, M. Jorgolli, A. K. Shalek, M.-H. Yoon, R. S. Gertner, H. Park, *Nat. Nanotechnol.* **2012**, *7*, 180.

[4] M. E. Spira, A. Hai, *Nat. Nanotechnol.* **2013**, *8*, 83.

[5] Z. C. Lin, C. Xie, Y. Osakada, Y. Cui, B. Cui, *Nat. Commun.* **2014**, *5*, 3206.

[6] K. Deisseroth, *Nat. Methods* **2011**, *8*, 26.

[7] J. A. Steinbeck, S. J. Choi, A. Mrejeru, Y. Ganat, K. Deisseroth, D. Sulzer, E. V. Mosharov, L. Studer, *Nat. Biotechnol.* **2015**, *33*, 204.

[8] V. Y. Prinz, V. A. Seleznev, A. K. Gutakovsky, A. V. Chehovskiy, V. V. Preobrazhenskii, M. A. Putyato, T. A. Gavrilova, *Phys. E (Amsterdam, Neth.)* **2000**, *6*, 828.

[9] O. G. Schmidt, C. Deneke, Y. M. Manz, C. Müller, *Phys. E (Amsterdam, Neth.)* **2002**, *13*, 969.

[10] M. E. Levinshtein, M. Shur, S. Rumyantsev, *Handbook Series on Semiconductor Parameters*, World Scientific Publishing Co. Pte. Ltd., Singapore **1999**.

[11] M. Grundmann, *Appl. Phys. Lett.* **2003**, *83*, 2444.

[12] C. S. Bausch, A. Koitmäe, E. Stava, A. Price, P. J. Resto, Y. Huang, D. Sonnenberg, Y. Stark, C. Heyn, J. C. Williams, E. W. Dent, R. H. Blick, *Appl. Phys. Lett.* **2013**, *103*, 173705.

[13] R. Huang, C. Pang, Y. C. Tai, J. Emken, C. Ustun, R. Andersen, J. Burdick, *MEMS 2008 IEEE 21st Int. Conf.*, IEEE Tucson, Arizona **2008**, p. 240.

[14] S. Schulze, G. Huang, M. Krause, D. Aubyn, V. A. Bolaños Quiñones, C. K. Schmidt, Y. Mei, O. G. Schmidt, *Adv. Biomater.* **2010**, *12*, B558.

[15] M. Yu, Y. Huang, J. Ballweg, H. Shin, M. Huang, D. E. Savage, M. G. Lagally, E. W. Dent, R. H. Blick, J. C. Williams, *ACS Nano* **2011**, *5*, 2447.

[16] S. R. Hart, Y. Huang, T. Fothergill, E. W. Derek, C. Dent Lumbard, D. C. Williams, *Lab Chip* **2013**, *13*, 562.

[17] P. Froeter, Y. Huang, O. V. Cangellaris, W. Huang, E. W. Dent, M. U. Gillette, J. C. Williams, X. Li, *ACS Nano* **2014**, *8*, 11108.

[18] A. Petrelli, E. Marconi, M. Salerno, D. De Pietri Tonelli, L. Berdondini, S. Dante, *Lab Chip* **2013**, *13*, 4419.

[19] A. C. von Philipsborn, S. Lang, A. Bernard, J. Loeschinger, C. David, D. Lehnert, M. Bastmeyer, F. Bonhoeffer, *Nat. Protoc.* **2006**, *1*, 1322.

[20] A. Koitmäe, C. S. Bausch, E. Stava, D. Sonnenberg, W. Hansen, R. H. Blick, *Soft Nanosci. Lett.* **2013**, *3*, 79.

[21] S. Böttner, S. Li, J. Trommer, S. Kiravittaya, O. G. Schmidt, *Opt. Lett.* **2012**, *37*, 5136.

[22] M. H. T. Dastjerdi, M. Djavid, Z. Mi, *Appl. Phys. Lett.* **2015**, *106*, 21114.

[23] I. S. Chun, K. Bassett, A. Challa, X. Li, *Appl. Phys. Lett.* **2010**, *96*, 251106.

[24] D. S. Jiang, H. Jung, K. Ploog, *J. Appl. Phys. (Melville, NY, U.S.)* **1988**, *64*, 1371.

[25] D. Diedrich, R. H. Blick, *Appl. Phys. Lett.* **2015**, *106*, 53704.

[26] M. N. Polyanskiy, *Refractive index database*, http://refractiveindex.info/ (accessed: December 2014).

[27] D. A. B. Miller, D. S. Chemla, T. C. Damen, A. C. Gossard, W. Wiegmann, T. H. Wood, C. A. Burrus, *Phys. Rev. Lett.* **1984**, *53*, 2173.

[28] J. D. Marshall, M. J. Schnitzer, *ACS Nano* **2013**, *7*, 5.

[29] G. Bastard, E. E. Mendez, L. L. Chang, L. Esaki, *Phys. Rev. B* **1983**, *28*, 3241.

[30] W. Han, Y. D. Wang, Y. F. Zheng, *Adv. Mater. Res. (Durnten-Zurich, Switz.)* **2008**, *47*, 1438.

[31] R. Kubrin, H. S. Lee, R. Zierold, A. Yu. Petrov, R. Janssen, K. Nielsch, M. Eich, G. A. Schneider, *J. Am. Ceram. Soc.* **2012**, *95*, 2226.

**ADVANCED
MATERIALS
INTERFACES**

Supporting Information

Approaching Integrated Hybrid Neural Circuits: Axon
Guiding on Optically Active Semiconductor Microtube Arrays

Aune Koitmäe, Jann Harberts, Gabriele Loers, Manuel
Müller, Cornelius S. Bausch, David Sonnenberg, Christian
Heyn, Robert Zierold, Wolfgang Hansen, and Robert H. Blick*

Supporting Information

Approaching Integrated Hybrid Neural Circuits: Axon Guiding on Optically Active Semiconductor Microtube Arrays

Aune Koitmäe,'* Jann Harberts, Gabriele Loers, Manuel Müller, Cornelius S. Bausch, David Sonnenberg, Christian Heyn, Robert Zierold, Wolfgang Hansen, and Robert H. Blick

[*] Corresponding author

E-mail: akoitmae@physnet.uni-hamburg.de

Supporting Information

1. Fabrication of the microtubes

The rectangular arrays of microtubes are fabricated by means of photolithography defining the starting edges, shallow mesa and stop edges (Figure 1a). The starting edges are undercut with a phosphoric acid solution ($H_2O:H_2O_2:H_3PO_4$, 500:10:1), with etch rates of 1nm/s. at least 42 nm deep into the sample until reaching the sacrificial layer (AlAs). Shallow mesa and the stop edges, in contrast, are etched only 27 nm until reaching the strained InGaAs layer to ensure that the hydrofluoric acid (HF) only enters from the starting edge side. As a last step, the AlAs sacrificial layer is etched selectively with 5 % HF, thus minimizing the strain so that the tubes start rolling up.

2. Different deposition areas of PLL

The deposition area of PLL is crucial to achieve neuron guiding through the tubes. In case of coating the whole sample with PLL, the cells disperse statistically and only a few axons grow into the tubes (Figure SI1a). Printing PLL in the gaps between the tubes without any overlap with them makes the axons grow along the PLL printed areas and not into the tubes (Figure SI1b).

3. QCSE measurements on an artificial axon

To determine the magnitude of the QCSE of the QW energy levels embedded in the microtube an 'artificial axon' (tungsten needle) is inserted into a parylene-C coated microtube via a micromanipulator. The applied voltage changes the band gap characteristics of the embedded QW and induces a red shift in the emission peak of the QW (Figure SI2b).
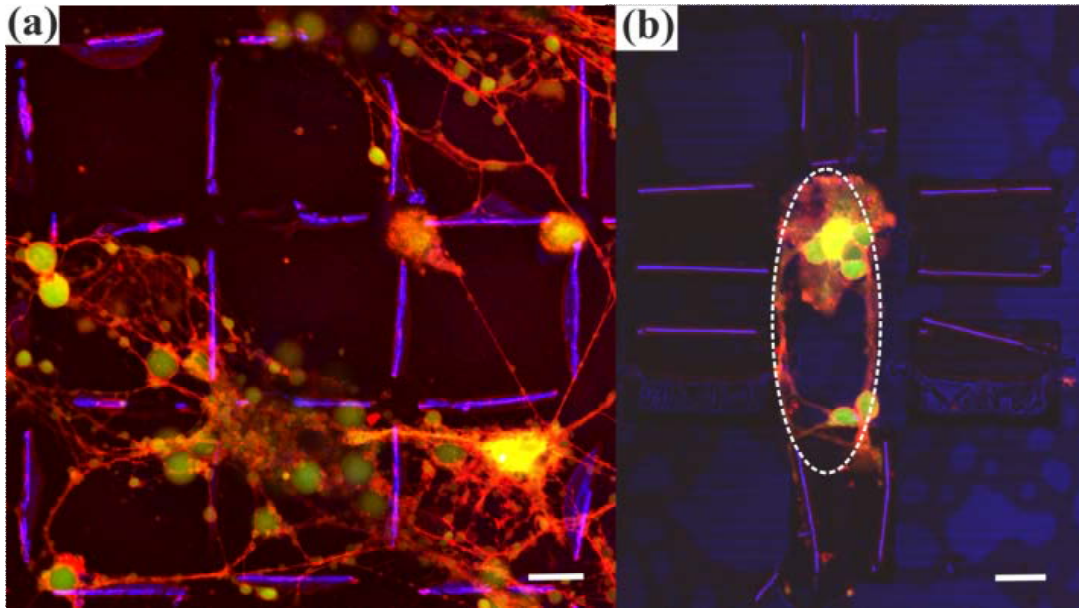
Figure SI1. (a) PLL is deposited over the whole sample. Cell bodies are labeled green and axons red. (b) The white dashed area shows the PLL printed area having no overlap with the tubes. In this case the axons only grow along the printed PLL and are not guided into the tubes. Scale bars 20 µm.
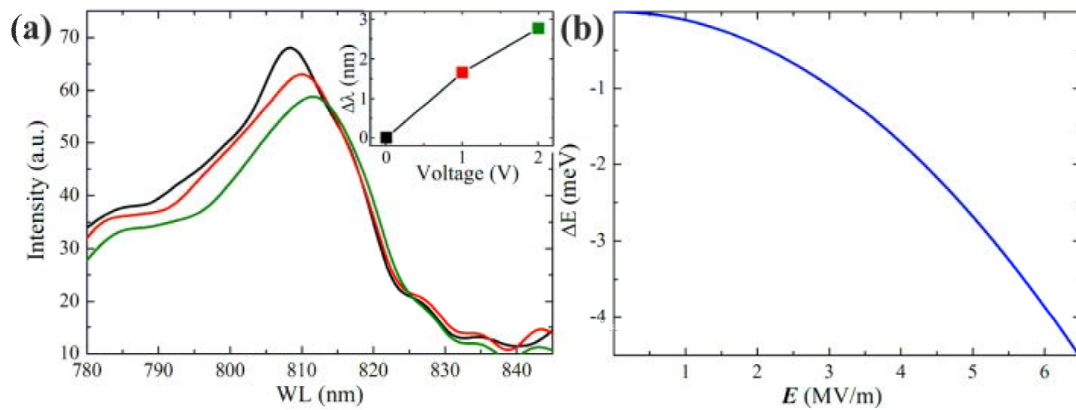

Figure SI2. (a) PL intensity plotted against the wavelength. The QCSE measurements on a microtube with an artificial axon show a red-shift in the emission of the QW. The shift is 1.7 nm and 2.6 nm for applied voltages of 1 V and 2 V respectively. Black curve refers to a bias 0 V, red curve 1 V and green curve to 2 V. The inset represents the shift in as a function of the applied voltage. (b) Calculated QCSE for a 4 nm thin GaAs QW showing quadratic dependence of the emission energy shift to the applied field. [28]Applied electric field causes a red shift in the emission energy of the QW.

A.10 Publication X

Designer neural networks with embedded semiconductor microtube arrays

Aune Koitmäe, Manuel Müller, Cornelius S. Bausch, <u>Jann Harberts</u>, Wolfgang Hansen, Gabriele Loers, and Robert H. Blick

Langmuir **2018**, 34(4), 1528–1534

Author contributions: Sample preparation: A.K, M.M., manuscript writing, cell preparation, cultivation: A.K., cell imaging: M.M., A.K., SEM imaging: M.M., PLL printing: M.M. with support of <u>J.H.</u>, patch clamping: <u>J.H.</u>, animal preparation: G.L., tube design: C.S.B., wafer preparation: W.H., supervision: R.H.B.; A.K. and M.M. contributed equally.

(7 + 8 pages)

Designer Neural Networks with Embedded Semiconductor Microtube Arrays

Aune Koitmäe,*[,†,‡,∥] Manuel Müller,[†,‡,∥] Cornelius S. Bausch,[†] Jann Harberts,[†,‡] Wolfgang Hansen,[†,‡] Gabriele Loers,[§] and Robert H. Blick[†,‡]

[†]Institute of Nanostructure and Solid State Physics (INF), University of Hamburg, Jungiusstraße 11c, Hamburg 20355, Germany

[‡]Center for Hybrid Nanostructures (CHyN), University of Hamburg, Luruper Chaussee 159, Gebäude 600, Hamburg 22761, Germany

[§]Center for Molecular Neurobiology Hamburg, University Medical Center Hamburg-Eppendorf, Falkenried 94, 20251 Hamburg, Germany

S *Supporting Information*

ABSTRACT: Here we present a designer's approach to building cellular neuronal networks based on a biocompatible negative photoresist with embedded coaxial feedthroughs made of semiconductor microtubes. The diameter of the microtubes is tailored and adjusted to the diameter of cerebellum axons having a diameter of 2−3 μm. The microtubes as well as the SU-8 layer serve as a topographical cue to the axons. Apart from the topographical guidance, we also employ chemical guidance cues enhancing neuron growth at designed spots. Therefore, the amino acid poly-L-lysine is printed in droplets of pl volume in the front of the tube entrances. Our artificial neuronal network has an extremely high yield of 85% of the somas settled at the desired locations. We complete this by basic patch-clamp measurements on single cells within the neuronal network.
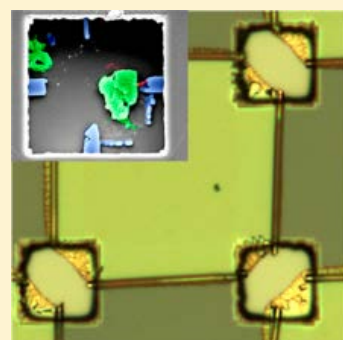
INTRODUCTION

Highly defined neural networks are the underlying base to unravel the intricate functioning of the brain, such as movement, memory, and information processing in general.[1] Axon guidance, or in a more general term pathfinding, is a self-assembly process where as a result networks for neural communication are created. In general, the target cells are found, and as a result, synapses are generated. The highly sophisticated and dynamic process of pathfinding is of prime importance since it is crucial for decoding neurodegenerative diseases such as Parkinson and Alzheimer.[2−4]

In vivo cells are surrounded by the extracellular matrix consisting of proteins. Besides offering structural and biochemical support for cells, those molecules serve as chemical cues to axons helping to find the target cell. To understand the role and the exact functions of this matrix, in vitro studies are best suited. Therefore, different compounds of the extracellular matrix are micropatterned on artificial substrates to design functionalized advanced bioelectric devices[5−7] mimicking to some degree the wiring process of the brain in a controlled environment. Often proteins such as poly-L-lysine (PLL), laminin, and fibronectin are applied, which promote neuron adhesion and axon outgrowth.[8−10] However, working toward revealing the pathfinding mechanisms, Koser et al.[11] recently reported on the mechanical influences of the environment on axon guiding. This implies that in order to decipher neural communication the mechanosensitive and topographical

aspects of the pathfinding process should be taken into account as well.

Topographical cues represent a modulation of the surface; e.g., they form grooves, ridges, and gratings.[5−13] In 2010, Schulze et al.[14] for the first time implemented semiconductor microtubes as topographical neuron guides. Axons prefer to grow along the boundary surfaces of the tubes and can be guided through the tubes. In 2011, Yu et al.[15] reported on SiGe semiconductor microtubes as excellent neuron guides.[16,17] Further studies on the guiding characteristics of the tubes were presented in following years,[18] and recently we were able to implement optically active characteristics within these microtubes, enabling the use of device concepts such as wireless detectors of neural firing.[19] The guiding characteristics of the tubes were enhanced by selectively coating the samples with PLL, which acts as a chemical guidance cue.

In this article, we combine semiconductor microtubes enhanced by a scaffold made of an SU-8 resist to form a highly effective topographical constraint strongly confining the adhesion of cells. These containers, as we named them, act as a topographical cue which we complement by micropatterning the sample with PLL as a chemical cue, increasing the yield of axons growing into the microtubes. By incorporating the

optically active characteristics into the microtubes from our previous studies, we are able to create a basis for understanding neural pathfinding. This designed network we then probe locally in a first approach via patch clamp recordings, revealing the successful integration of a neuronal network of mouse axons.

■ EXPERIMENTAL SECTION

Fabrication of the Microtubes. Figure 1 shows the fabrication of the microtubes, which is based on the principle of self-rolling of a
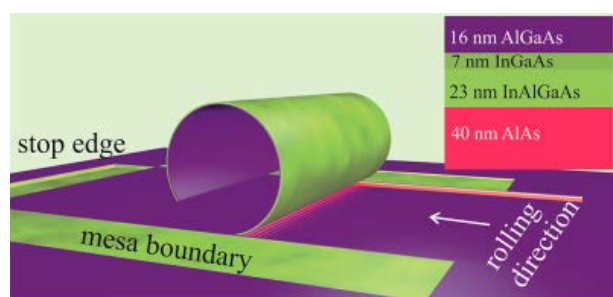

Figure 1. Sketch of the fabrication of microtubes. The microtubes are fabricated via photolithography defining starting edges, the mesa boundary, and stop edges. By selectively etching the AlAs sacrificial layer, the strain is released and the mesa starts rolling up.

strained multilayer. The diameter is tailored to be in the range of the diameter of an axon of a granule cell (1 μm). It is accomplished by tuning the layer thicknesses of the single layers, and the percentage of the components (Al, Ga, As, In) also plays a role.[20] The multilayer

implemented in this work consists of 16 nm AlGaAs, 7 nm InGaAs, and 23 nm InAlGaAs on top of an AlAs sacrificial layer separating the strained layers from the GaAs substrate. By the selective etching of the AlAs layer, the multilayer starts to roll up, and tubes with a diameter of 2.7 ± 0.1 μm are formed. A detailed description of the fabrication of the tubes can be found elsewhere.[21]

SU-8 Processing. To increase the yield of the axons growing into the tubes, the tubes are overlaid with the SU-8 negative photoresist. Because of the biocompatible characteristics, SU-8 is commonly used in various in vivo and in vitro experiments.[22−24] The design of the SU-8 layer is shown in Figure 2a, where rectangular containers in the areas of the tube openings are free of SU-8 and the rest of the sample is covered with a layer thickness ranging from 6 to 20 μm. The SU-8 layer prevents the growing of the axons along the tubes, an unwanted effect in many neuron guiding studies.[14,15]

The spin coating of SU-8 is carried out in a three-step ramp: the first step is accelerating the sample at 100 rpm/s to the desired speed, letting it spin for 2 min, and decelerating at 100 rpm/s. The spin-coating speeds were determined for the desired thicknesses in a separate step for a SU-8 GM-1075 (Gersteltec Engineering Solutions) solution with 1-methoxy-2-propanol acetate (PGMEA) in a 3:1 ratio. The small chip size of 25 mm^2 and its rectangular shape cause a non-negligible buildup of resist edge beads. We implemented a flattening process by placing a hydrophobic glass slide treated with trichloro-(1H,1H,2H,2H-perfluorooctyl)silane in a vacuum oven on the sample at the peak prebake temperature (see Figure SI2). The prebake temperature begins at 45 °C and ramps up at a rate of 5 °C/min to 95 °C for 10 to 35 min depending on the layer thickness. The chip then gets cooled to room temperature at a rate of 5 °C/min. The samples are aligned and exposed to UV light (200 mJ/cm^2), followed by the postexposure bake at a peak temperature of 95 °C for 15 to 30 min and developed with PGMEA, rinsed with isopropyl alcohol, and dried with nitrogen.
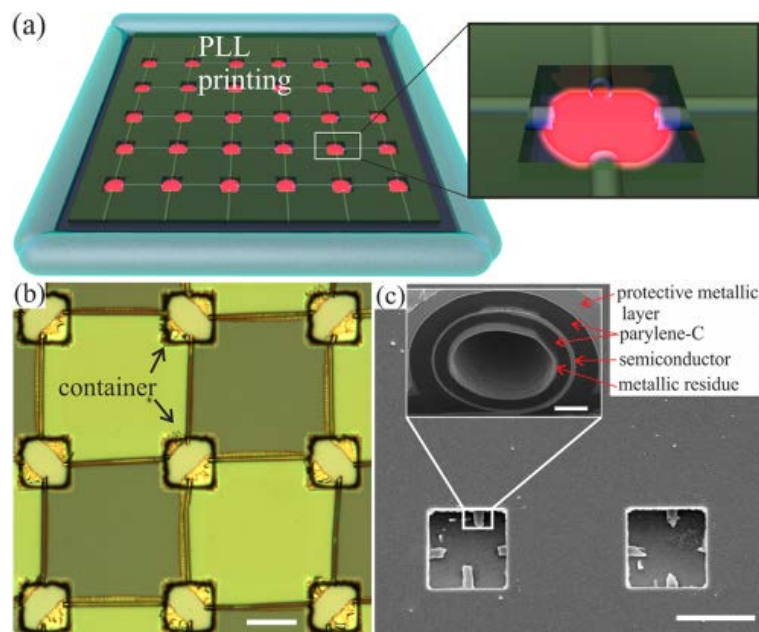

Figure 2. (a) To support the adhesion of the neurons, the containers are coated with the adhesive amino acid PLL. The zoom-in shows the overlap of the tube entrances and PLL. (b) Optical microscope image of the SU-8 superimposed microtubes. The brighter yellow-colored material in the containers is the underetched, though not rolled up, semiconductor material. It lies on the surface of the sample. The minimally wavy character is caused by the released tension due to etching. (c) SEM image of SU-8 superimposed microtubes in which the entrances of the microtubes in the containers are seen. The bottom and the sides of the sample are coated with PDMS polymer, and the top, including the microtubes from inside, are coated with parylene-C polymer. The inset shows a cross section of a focused ion-beam-milled microtube coated with parylene-C. To protect the microtube, a metallic layer was deposited on top of the tube. The brighter inner layer is the metallic residue caused by the milling. Scale bars for (b) and (c) are 25 μm, and that for the inset of (c) is 500 nm.
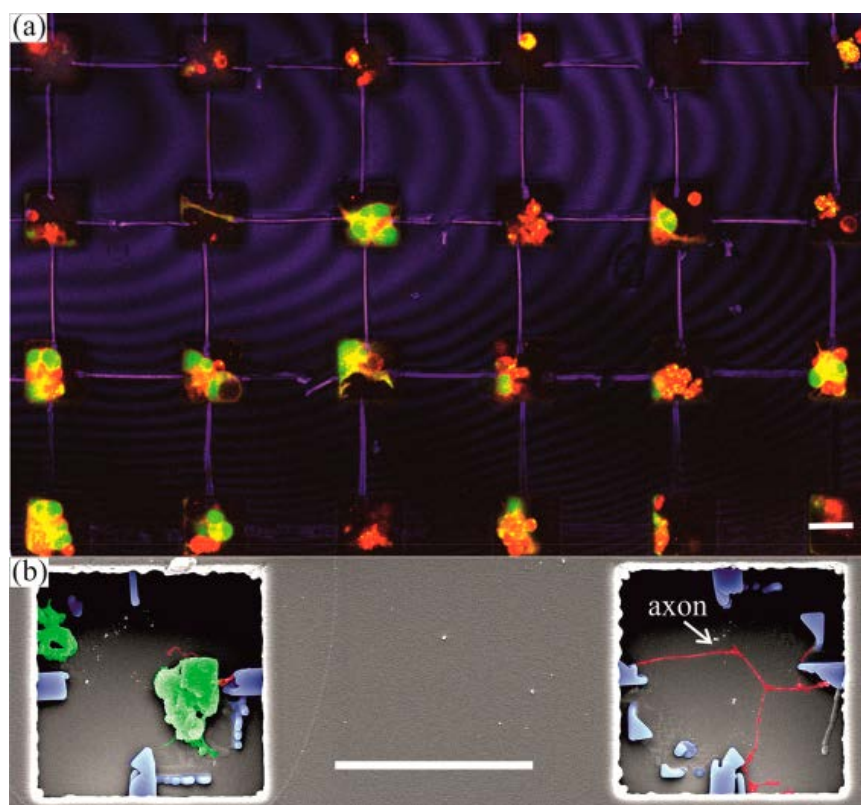
Figure 3. (a) Confocal image of a sample with cells cultured in 4DIV. Cell bodies are marked green, and cell membranes including neurites are marked red. The different shade of the microtubes indicates whether there is a neurite growing inside. The layer thickness of the PDMS is 10 μm. (b) Falsely colored SEM image of critical-point dried cells showing a neurite growing through a microtube (red). The scale bars are 20 μm for (a) and 25 μm for (b).

Coating the Samples with Parylene-C. Prior to introducing cells into the samples, the bottom and sides of the GaAs substrate are fixed in cured poly(dimethylsiloxane) (PDMS) pads whereas the top is conformally coated with biocompatible polymer parylene-C by chemical vapor deposition (Labcoater Parylene Deposition System, Specialty Coating Systems) to prevent the toxic effects of the arsenic compounds. The polymer shows outstanding electrical, chemical, and thermal stability and is widely used as an electrical insulator and coating for biomedical implants.[25] The thickness of the parylene-C layer is 130 nm. A scanning electron microscope (SEM) image of the cross section of a parylene-C-coated microtube is shown in Figure 2c.

PLL Printing. To specify the areas of cell adhesion and neurite growth, PLL (Sigma-Aldrich, mol wt 70–150 kDa, concentration 0.01%) is printed on the samples. As shown in 1975 by Mazia et al.,[26] PLL is a standard adhesion molecule for neurons that increases the cell adherence due to the interaction of the positively charged polymer and the negatively charged proteins on the cell surface. Additionally, it acts as a chemical cue for guiding neural growth.[27] We use a materials printer (Dimatix 2831 Fujifilm) to precisely microprint the samples with PLL. By treating the samples with oxygen plasma, the hydrophilic properties of the samples are improved. The resulting enlargement of the drop size on the surface increases the printed area with one ejected drop of PLL to a diameter of 30 μm on the plasma-treated sample.[28] Here, the printing pattern coincides with the container chambers of the SU-8 as shown in Figure 2a.

Neuron Preparation and Culturing. In this work, postnatal cerebellar neurons from 6- to 7-day-old mice are utilized. The cerebella are dissected and incubated with trypsin/deoxyribonuclease solution, and single cells are separated using fire-polished Pasteur pipettes. Cell concentrations of $(1 \times 10^4 – 2 \times 10^4)$ cells/cm^2 are used. The cells are incubated in culture medium consisting of Neurobasal A, penicillin streptomycin, bovine serum albumin (5%), insulin, L-thyroxine,

transferrin holo, and sodium selenite. The devices are incubated in a humidified atmosphere at 37 °C and 5% CO_2, and the neuronal outgrowth is analyzed after 3–5 days in vitro (DIV).[29]

Confocal Imaging. For the visualization of the living cells, we use a neurite outgrowth staining kit (Thermofisher) consisting of three fluorescent dyes: a cell viability indicator (495/515 ex/em), a cell membrane stain (555/565 ex/em), and a background suppression reagent. This kit enables us to visualize the cell soma and the neurites separately. The dyes are excited with blue (488 nm) and green (552 nm) lasers, which are simultaneously scanned over the sample. The results are shown in Figure 3a, where the somas are labeled green and the neurites are labeled red.

Preparation for SEM Imaging. The cells are fixed in 25% glutaraldehyde/HBSS solution, incubated for 30 min at room temperature and washed with DI water. To prepare the samples for critical-point drying (autosamdri-815), HBSS is replaced with a water/ethanol mixture with increasing ethanol content from 25 to 100%. The resolution of the SEM images is improved by sputtering the samples with a 20 nm layer of a gold–palladium alloy.

Patch Clamping. Patch clamping is a common method of probing neural activity,[30] where the voltages and currents of the cell membrane are precisely measured. The electrophysiological measurements are carried out with our upright patch-clamp setup (Nikon FN1) optimized for opaque culturing substrates where the pipet angles with respect to the sample are maximized by implementing an objective with an extra-long working distance. Figure 5a shows a sketch of the patch-clamping setup. With the help of micro-manipulators, a heat-polished glass pipet with an electrode is injected toward the cell membrane in order to form a gigaohm seal in the whole-cell mode. After the gigaohm seal is formed, a patch-clamp amplifier (HEKA EPC 10 USB Double) is used to stimulate an action potential via a current injection of 10–50 pA into the intracellular
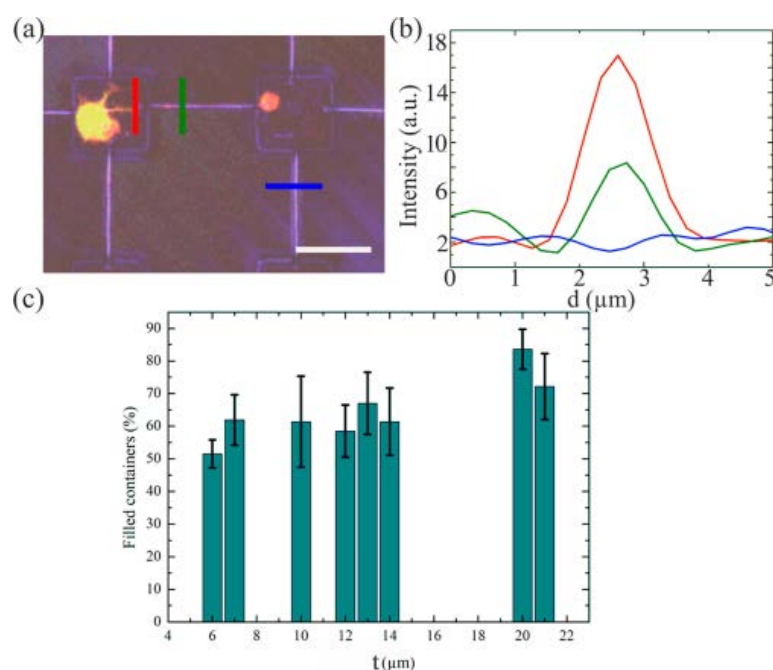
Figure 4. (a) Confocal image of neurites guided into microtubes. The red, green, and blue bars indicate the positions of the intensity line scans on the sample, and the corresponding diagram is shown in (b), differentiating among an empty microtube (blue), a neurite (red), and a tube filled with a neurite (green line). (c) Number of containers filled with neurons as a function of the thickness of the SU-8 layer. The average fill factor of the containers is about 60% for SU-8 thicknesses of up to 14 μm. Increasing the layer thickness to 20 μm increases the filling factor to an average of 80%. The scale bar for (a) is 25 μm.

electrode and record the signal (Figure 5c). Typically, the signal consists of the simultaneous opening of several ion channels causing a spiky depolarization, called the action potential.

RESULTS AND DISCUSSION

Figure 2b shows an optical microscope image of an array of SU-8-enwrapped microtubes whereas the tips of the tubes' end points are connecting different containers and the area between the crossing points of the tubes tips are free of SU-8 (see also Figure SI2). The tubes themselves have a length of 50 ± 0.2 μm and a wall thickness of 92 nm (rolled up twice). The horizontal/vertical distance between the tubes is 20 μm. The SU-8 layer thicknesses are in the range of 6–20 μm and are fabricated in this study in order to analyze the trapping characteristics of single mouse granule cells with a typical soma diameter of 10 μm (see also Figures SI5 and SI6 in Supporting Information). In Figure 2c, an SEM image of a sample is shown, where a cross section of a tube is shown in the close-up. The tube was micromilled using a focused ion beam (FIB) to confirm the conformal parylene-C coating. The semiconductor and polymere layers are clearly distinguishable in the cross-section of the tube's wall.

Figure 3a shows a confocal image with the results of neuron trapping on a sample. The somas are marked green and the neurites are marked red, and the cells are cultured in 4 DIV. The somas are trapped in rectangular containers, and the neurites are guided into the microtubes. The different shades on the confocal image of the microtube indicate whether there is a neurite growing inside. The tubes, which appear brighter, are filled with neurites. Because of the three-dimensional confinement, the tubes have an accelerative effect on axon growth. Froeter et al. claim that the growth velocity of the neuritis is enhanced 4-fold in the tubes with respect to the

growth velocity on a planar substrate.[31,32] Figure 3b shows an SEM image of a soma placed in front of the microtube and a neurite growing through the tube extending into the next container.

Although bulk GaAs and the other layer compounds are opaque in the visible regime, at layer thicknesses in the nanometer range, as used in our study, they transmit about 20% of the light[33] and the labeled neurites growing in the microtubes can be detected. SU-8 and parylene-C are transparent in the visible regime. Figure 4 presents intensity line plots to visualize whether the neurite is inside the microtube. Figure 4a shows the confocal image of a sample, superimposed with a 10 μm SU-8 layer, where each pixel of the generated image carries intensity information, and (b) shows the corresponding intensity plots. The sample is excited with a green (552 nm) laser, whereas the detection range is 562–602 nm. The red curve corresponds to fluorescent signals of a labeled neurite, the green curve corresponds to the fluorescent signal of a neurite, the signal is attenuated by the walls of the microtube, and the blue curve refers to a plane microtube. Note that the confocal image in Figure 4a is an overlay of two channels, green and red. We observe an increase in the intensity in the tubes with neurite inside (green) and are able to distinguish them from the neurites without a tube wrapping around (red) and plain tubes (blue). Using this method, the exact length of a neurite in the tube can also be extracted.[21]

A summary of the results of neuron trapping is shown in Figure 4c, where the percentage of the containers filled with neurons (either living or dead) as a function of the SU-8 thickness for a cell concentration of 1×10^4 cells/cm^2 is presented. We did not distinguish between containers filled with several cells or one cell. The graph indicates that the best yield in container filling, 85%, has a layer thickness of 20 μm. A
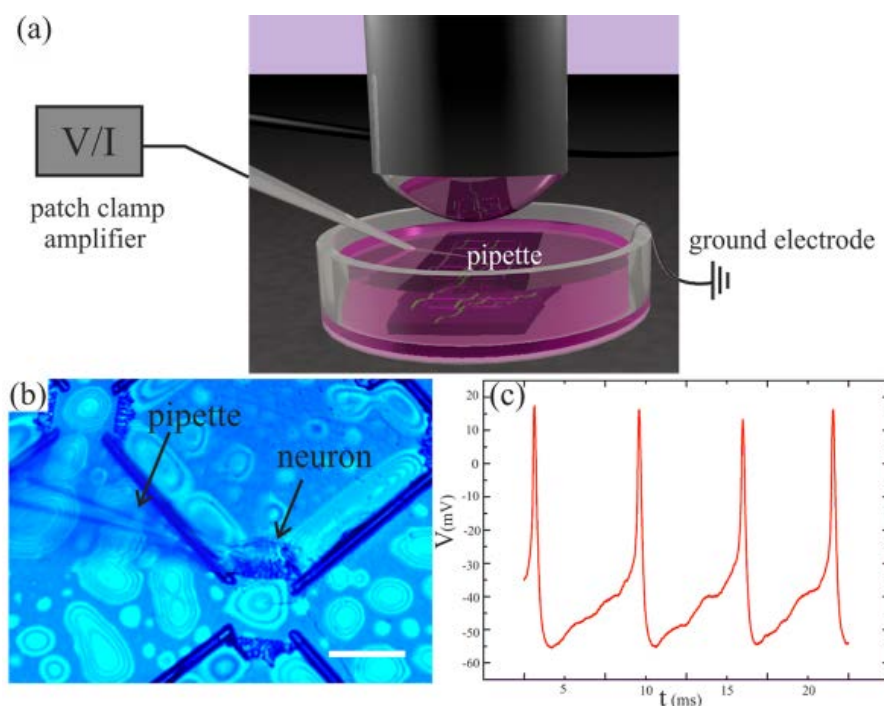
Figure 5. (a) Sketch of the patch-clamping setup: the pipet is inserted into the cell via a micromanipulator (whole cell mode), and the sensing electrode records the changing voltage caused by the opening and closing of the ion channels. An upright microscope including an objective with an extra-long working distance is implemented. (b) Light microscope image of patch-clamping of the neurons. Because of the opacity of the device, the cells are not visible with an inverted microscope. (c) Patch-clamp measurements of a neuron grown on a microtube sample showing spontaneous firing after 4 DIV. The scale bar for (b) is 10 μm.

layer thickness of 6 μm, which is also the thinnest layer, shows the lowest trapping characteristics with about 50% of containers loaded with cells. Layer thicknesses of between 6 and 20 μm show slightly higher trapping with 60% of the containers filled. The results indicate higher trapping characteristics for increasing container thicknesses. Furthermore, the number of living cells in the containers is counted. Increasing SU-8 thickness increases the percentage of living cells from about 64% for an SU-8 thickness of 6 μm to about 81% for an SU-8 thickness of 20 μm (Table SI4). In addition, the percentage of cells growing on top of the SU-8 layer is extracted. Through a combination of the SU-8 containers and the PLL printing, the number of cells on top of the samples is negligible; more information can be found in the Supporting Information in Table SI4. On 72% of the studied samples, the percentage of on-top neurons makes up <1% of the total number of neurons on the sample. On the remaining 28% of the samples, the percentage was still low with 2−3% of the total number of neurons. No correlation was noticed between the height distribution of the SU-8 layer and the percentage de/increase of the on-top neurons.

In an additional study, the number of tubes filled with neurites using the method of intensity line plots is studied in comparison to nonsuperimposed samples (coated with an identical PLL pattern as for the SU-8 superimposed samples). Even though there were more cells and cell clusters on the nonsuperimposed samples,[19] the number of neurite-filled tubes is doubled from 30 to 60% for the samples coated with SU-8 not depending on the thickness of the SU-8 layer.

Furthermore, electrophysiological measurements are carried out on neurons growing on the samples with tubes (no SU-8)

to analyze the firing potential of the cells and confirm that the cells are fully functioning on the devices (see Figure 5c). The neuron (4 DIV) is spontaneously spiking approximately every 6 ms with a spike duration of 1.2 ms per action potential.[34,35] The obtained results are recorded using a Bessel filter (all frequencies over 2.9 kHz are removed). These results are in accordance with the spiking characteristics of a typical cerebellar granule cell showing fast-spiking behavior with narrow spikes at high frequency. This behavior is mainly caused by the Kv3 voltage-gated potassium channel family since the activation of the Kv3 currents is much faster in comparison to that in other channels.[36]

■ SUMMARY AND CONCLUSIONS

In this study, we present a defined synthetic designer neural circuit with controlled characteristics for neuron trapping on 6−20 μm SU-8 layers. The microtubes array was enwrapped with an SU-8 layer to trap the neurons in front of the microtubes. The patterning with PLL promotes neurite guiding and confines the settling areas of the neurons. The best trapping results are achieved with a layer thickness of 20 μm with 85% of the containers filled with neurons. Additional patch-clamping measurements show the typical fast-spiking behavior confirming the biocompatibility of our device since the neurons spontaneously fired action potentials after 4DIV.

■ ASSOCIATED CONTENT

ⓢ Supporting Information

The Supporting Information is available free of charge on the ACS Publications website at DOI: 10.1021/acs.langmuir.7b03311.

Additional information on the removal of SU-8 edges, a tilted SEM image of the sample, and more data for the cell counting in the container (PDF)

■ AUTHOR INFORMATION

Corresponding Author
*E-mail: akoitmae@physnet.uni-hamburg.de.

ORCID
Aune Koitmäe: 0000-0003-1216-6262

Author Contributions
‖These authors contributed equally.

■ REFERENCES

(1) Andersson, H.; Berg, A. v. d. Microfabrication and microfluidics for tissue engineering: state of the art and future opportunities. *Lab Chip* **2004**, *4*, 98−103.

(2) Kuboyama, T.; Lee, Y.-A.; Nishiko, H.; Tohda, C. Inhibition of clathrin-mediated endocytosis prevents amyloid beta-induced axonal damage. *Neurobiol. Aging* **2015**, *36* (5), 1808−1819.

(3) Gomez, N.; Chen, S.; Schmidt, C. E. Polarization of hippocampal neurons with competitive surface stimuli: contact guidance cues are preferred over chemical ligands. *J. R. Soc., Interface* **2007**, *4* (13), 223−233.

(4) Van Battum, E. Y.; Brignani, S.; Pasterkamp, R. J. Axon guidance proteins in neurological disorders. *Lancet Neurol.* **2015**, *14* (5), 532−546.

(5) Britland, S.; Morgan, H.; Wojiak-Stodart, B.; Riehle, M.; Curtis, A.; Wilkinson, C. Synergistic and Hierarchical Adhesive and Topographic Guidance of BHK Cells. *Exp. Cell Res.* **1996**, *228* (2), 313−325.

(6) James, C. D.; Spence, A.; Dowell-Mesfin, N.; Hussain, R. J.; Smith, K.; Craighead, H. G.; Isaacson, M.; Shain, W.; Turner, J. Extracellular recordings from patterned neuronal networks using planar microelectrode arrays. *IEEE Trans. Biomed. Eng.* **Sept 2004**, *51* (9), 1640−1648.

(7) Kam, L.; Shain, W.; Turner, J.; Bizios, R. Axonal outgrowth of hippocampal neurons on micro-scale networks of polylysine-conjugated laminin. *Biomaterials* **2001**, *22* (10), 1049−1054.

(8) Prestwich, G. D.; Healy, K. E. Why regenerative medicine needs an extracellular matrix. *Expert Opin. Biol. Ther.* **2015**, *15* (1), 3−7.

(9) Sanes, J. R. Extracellular matrix molecules that influence neural development. *Annu. Rev. Neurosci.* **1989**, *12* (1), 491−516.

(10) Koh, H.; Yong, T.; Chan, C.; Ramakrishna, S. Enhancement of neurite outgrowth using nano-structured scaffolds coupled with laminin. *Biomaterials* **2008**, *29* (26), 3574−3582.

(11) Koser, D. E.; Thompson, A. J.; Foster, S. K.; Dwivedy, A.; Pillai, E. K.; Sheridan, G. K.; Svoboda, H.; Viana, M.; Costa, L. d. F.; Guck, J.; Holt, C. E.; Franze, K. Mechanosensing is critical for axon growth in the developing brain. *Nat. Neurosci.* **2016**, *19* (12), 1592−1598.

(12) Mahoney, M. J.; Chen, R. R.; Tan, J.; Saltzman, W. M. The influence of microchannels on neurite growth and architecture. *Biomaterials* **2005**, *26* (7), 771−778.

(13) Rajnicek, A. M.; McCaig, C. D. Guidance of CNS growth cones by substratum grooves and ridges: effects of inhibitors of the

cytoskeleton, calcium channels and signal transduction pathways. *Journal of Cell Science* **1997**, *110*, 2915−2924.

(14) Schulze, S.; Huang, G.; Krause, M.; Aubyn, D.; Bolaños Quiñones, V. A.; Schmidt, C. K.; Mei, Y.; Schmidt, O. G. Morphological Differentiation of Neurons on Microtopographic Substrates Fabricated by Rolled-Up Nanotechnology. *Adv. Eng. Mater.* **2010**, *12*, B558.

(15) Yu, M.; Huang, Y.; Ballweg, J.; Shin, H.; Huang, M.; Savage, D. E.; Lagally, M. G.; Dent, E. W.; Blick, R. H.; Williams, J. C. Semiconductor Nanomembrane Tubes: Three-Dimensional Confinement for Controlled Neurite Outgrowth. *ACS Nano* **2011**, *5*, 2447.

(16) Hart, S. R.; Huang, Y.; Fothergill, T.; Lumbard, D. C. D. E. W.; Williams, D. C. Adhesive micro-line periodicity determines guidance of axonal outgrowth. *Lab Chip* **2013**, *13*, 562−569.

(17) Zhang, Q.; Zhao, Y.; Yan, S.; Yang, Y.; Zhao, H.; Li, M.; Lu, S.; Kaplan, D. L. Preparation of uniaxial multichannel silk fibroin scaffolds for guiding primary neurons. *Acta Biomater.* **2012**, *8* (7), 2628−2638.

(18) Bausch, C. S.; Koitmäe, A.; Stava, E.; Price, A.; Resto, P. J.; Huang, Y.; Sonnenberg, D.; Stark, Y.; Heyn, C.; Williams, J. C.; Dent, E. W.; Blick, R. H. Guided neuronal growth on arrays of biofunctionalized GaAs/InGaAs semiconductor microtubes. *Appl. Phys. Lett.* **2013**, *103* (17), 173705.

(19) Koitmäe, A.; Harberts, J.; Loers, G.; Müller, M.; Bausch, C. S.; Sonnenberg, D.; Heyn, C.; Zierold, R.; Hansen, W.; Blick, R. H. Approaching Integrated Hybrid Neural Circuits: Axon Guiding on Optically Active Semiconductor Microtube Arrays. *Adv. Mater. Interfaces* **2016**, *3* (24), 1600746.

(20) Grundmann, M. Nanoscroll formation from strained layer heterostructures. *Appl. Phys. Lett.* **2003**, *83* (12), 2444−2446.

(21) Koitmäe, A.; Harberts, J.; Loers, G.; Muller, M.; Sonnenberg, D.; Heyn, C.; Hansen, W.; Blick, R. Synthetic neuronal circuits: Optically active semiconductor microtubes as remotely accessible sensors for action potentials. *Neural Engineering (NER)* **2015**, p 514, 10.1109/NER.2015.7146672.

(22) Lin, C.-H.; Lee, G.-B.; Chang, B.-W.; Chang, G.-L. A new fabrication process for ultra-thick microfluidic microstructures utilizing SU-8 photoresist. *Journal of Micromechanics and Microengineering* **2002**, *12* (5), 590.

(23) Altuna, A.; Bellistri, E.; Cid, E.; Aivar, P.; Gal, B.; Berganzo, J.; Gabriel, G.; Guimera, A.; Villa, R.; Fernandez, L. J.; Menendez de la Prida, L. SU-8 based microprobes for simultaneous neural depth recording and drug delivery in the brain. *Lab Chip* **2013**, *13*, 1422−1430.

(24) Altuna, A.; Gabriel, G.; de la Prida, L. M.; Tijero, M.; Guimerà, A.; Berganzo, J.; Salido, R.; Villa, R.; Fernandez, L. J. SU-8-based microneedles for in vitro neural applications. *J. Micromech. Microeng.* **2010**, *20* (6), 064014.

(25) Huang, G.; Bolaños Quiñnes, V. A.; Ding, F.; Kiravittaya, S.; Mei, Y.; Schmidt, O. G. Rolled-Up Optical Microcavities with Subwavelength Wall Thicknesses for Enhanced Liquid Sensing Applications. *ACS Nano* **2010**, *4* (6), 3123−3130.

(26) Mazia, D.; Schatten, G.; Sale, W. Adhesion of cells to surfaces coated with polylysine. Applications to electron microscopy. *J. Cell Biol.* **1975**, *66* (1), 198−200.

(27) Millet, L. J.; Stewart, M. E.; Nuzzo, R. G.; Gillette, M. U. Guiding neuron development with planar surface gradients of substrate cues deposited using microfluidic devices. *Lab Chip* **2010**, *10*, 1525−1535.

(28) Harberts, J. Poly-D-Lysin-Fixierung von Neuronen auf GaAs-Proben mit Hilfe von Fotolithographie und Dimatix Materials Printer.

(29) Loers, G.; Chen, S.; Grumet, M.; Schachner, M. Signal transduction pathways implicated in neural recognition molecule L1 triggered neuroprotection and neuritogenesis. *J. Neurochem.* **2005**, *92* (6), 1463−1476.

(30) Chen, R.; Canales, A.; Anikeeva, P. Neural recording and modulation technologies. *Nature Reviews Materials* **2017**, *2*, 16093.

(31) Froeter, P.; Huang, Y.; Cangellaris, O. V.; Huang, W.; Gillette, M. U.; Williams, J.; Li, X. Superior neuronal outgrowth guidance and rate enhancement using silicon nitride self-rolled-up membranes. *2015*

73rd Annual Device Research Conference (DRC), 2015, p 93, 10.1109/DRC.2015.7175571.

(32) Froeter, P.; Huang, Y.; Cangellaris, O. V.; Huang, W.; Dent, E. W.; Gillette, M. U.; Williams, J. C.; Li, X. Toward Intelligent Synthetic Neural Circuits: Directing and Accelerating Neuron Cell Growth by Self-Rolled-Up Silicon Nitride Microtube Array. *ACS Nano* **2014**, *8* (11), 11108−11117.

(33) Polyanskiy, M. N. *Refractive Index Database*; http://refractiveindex.info/, 2008−2015.

(34) Egri, C.; Ruben, P. C. Action Potentials: Generation and Propagation. *eLS* **2001**, 10.1002/9780470015902.a0000278.pub2.

(35) Xie, C.; Lin, C.; Hanson, L.; Cui, Y.; Cui, B. Intracellular recording of action potentials by nanopillar electroporation. *Nat. Nanotechnol.* **2012**, *7*, 185.

(36) Bean, B. P. The action potential in mammalian central neurons. *Nat. Rev. Neurosci.* **2007**, *8* (6), 451−465.

Designer Neural Networks with Embedded Semiconductor Microtube Arrays

Aune Koitmäe *, *Manuel Müller*, *Cornelius S. Bausch, Jann Harberts*, *Wolfgang Hansen, Gabriele Loers* , *and Robert H. Blick*

* Corresponding Author

E-Mail address: akoitmae@physnet.uni-hamburg.de

Table of content

1. Fabrication process of the devices

For better understanding the single steps of the fabrication process are listed in the Figure SI1. The whole process takes approximately three days.
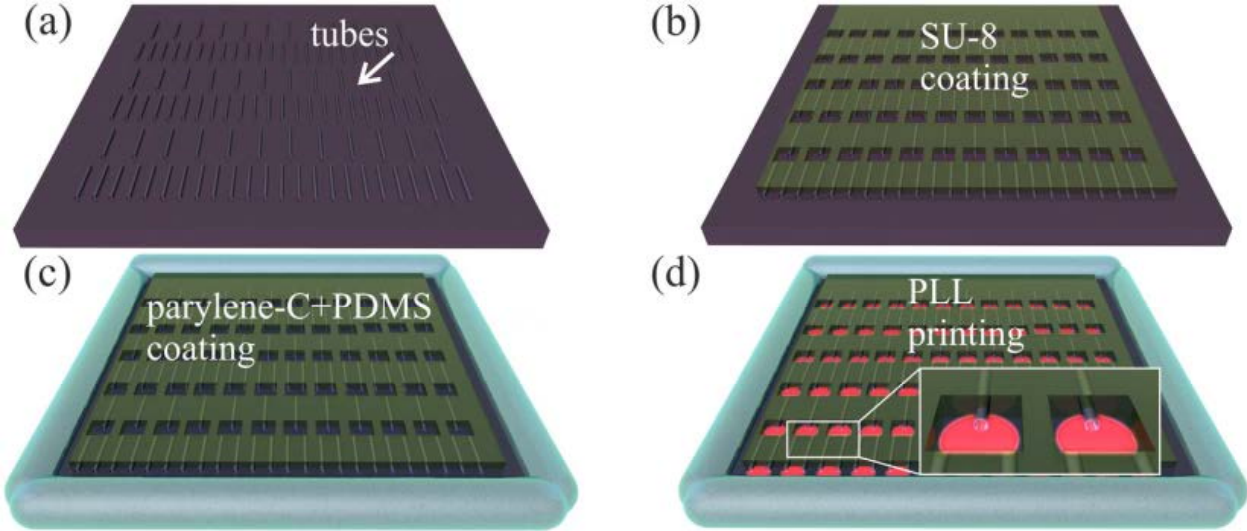

Figure SI1: (a) Step 1: Fabrication of the microtubes. (b) Step 2: The tubes are coated with SU-8. (c) Step 3: The sampes are coated with a PDMS well followed by the parylene-C coating. (d) Step 4: The samples are micro-printed with PLL.

2. Removal of SU-8 edges

The size of the implemented chips (25 mm^2) leads to an unwanted effect of resist edges, being 10 times higher than the mean thickness in the middle of the sample. To eliminate these edges, a glass slide is implemented (Figure S1(a)). The flattening process is carried out by applying a minor pressure on the glass slide with tweezers. This results in pushing the resist towards the middle of the sample and causing a non-wanted effect of creation of air bubbles on the sample (Figure S1(b)). To reduce the bubbles, SU-8 was diluted with PGME (3:1) and the prebake temperature was increased to 110°C (Figure S1(c)). The glass slide is applied during the heating process at 95°C and the temperature is cooled down immediately after reaching 110°C.
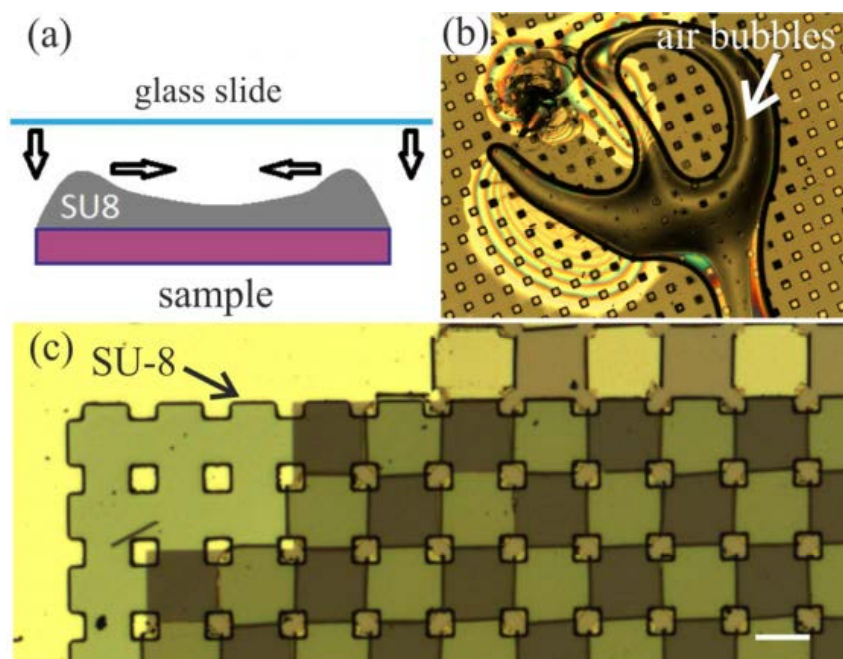
Figure SI2: (a) To reduce the SU-8 edges on the chip, a glass slide is utilized. A minor pressure using a tweezer is applied. (b) A light microscope image of the air bubbles on the sample, which appear as a result of using the glass slide. (c) A light microscope image of a sample showing the results after dilution of the SU-8 and increasing the prebake temperature to 110°C. Scale bar 50 μm.
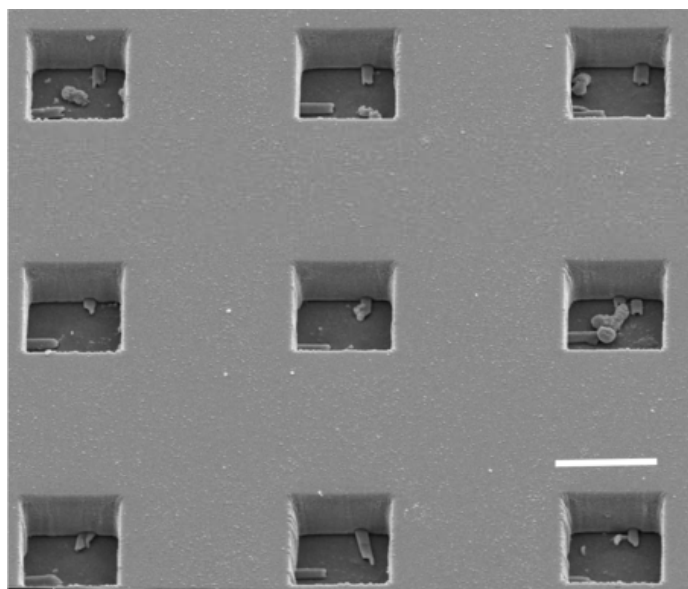
3. SEM image of a tilted sample

Figure SI3: An SEM image of SU-8 superimposed microtubes. The tubes entrances are clearly seen. The sample is tilted by 30°. Scale bar 25μm.

4. Table of cell yield in general, amount of cells out of containers and for amount of living cells

With increasing layer thickness of SU-8 the amount of living cells increases. The percentage of the cells out of containers shows no correlation with the layer thickness of the SU-8. The reason for slightly higher percentage in the case of 6 μm SU-8 layer can be the higher amount of cells introduced to the sample. We used the same volume in all of the samples, but slight differences of the number of cells can occur.

Table SI4

SU-8 thickness (μm)	% of filled containers	% of cells out of containers	% of living cells
6	**51.7**	**2.3**	**63.8**
7	**61.9**	**0.4**	**66.6**
10	**71.2**	**0**	**69.8**
13	**67.6**	**0**	**83.7**
20	**83.8**	**0.3**	**80.9**

5. Additional SEM and confocal images

In the following we would like to present some more better resolution images of the cells in the containers and also show the influence of the SU-8 thickness has to the resolution of the confocal images. With increasing layer thicknesses the resolution decreases (SI6 (b)). The reason is noise caused by the SU-8. We can achieve good resolutions for 10 µm and 12 µm SU-8 layer. For 20 µm the resolution has clearly decreased.
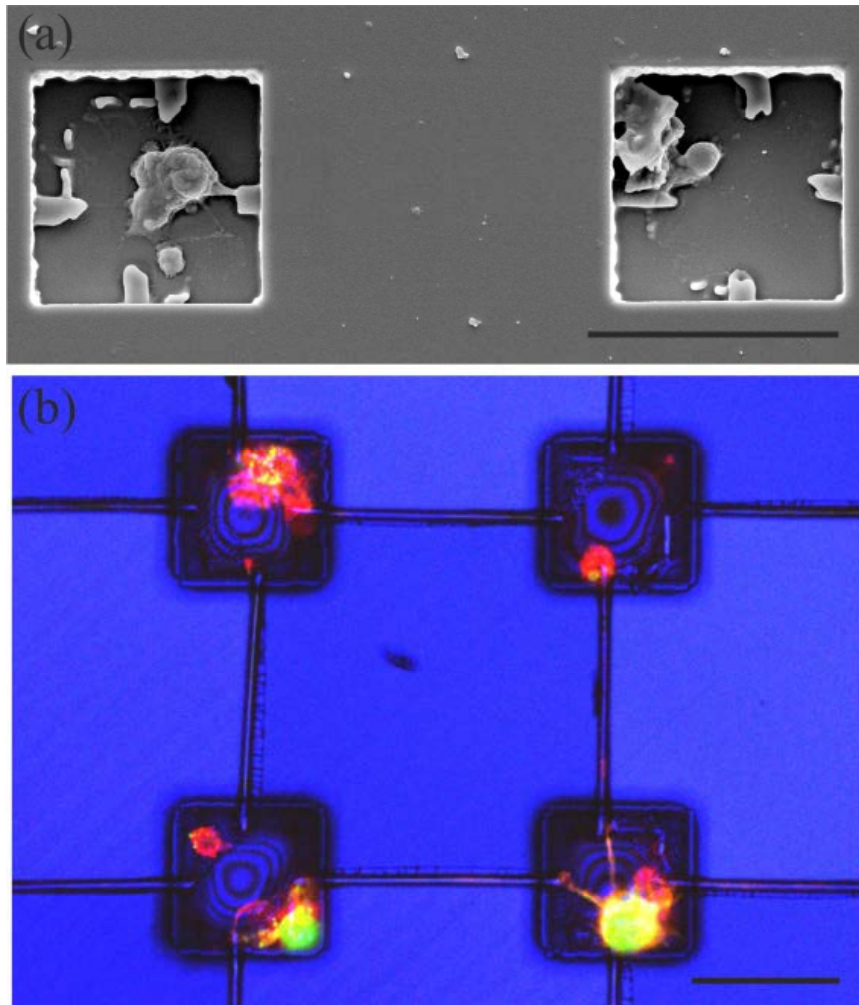
Figure SI5: (a) An SEM image of a neuron in the left container and a neurite extending in the neighboring container. The material in the right container upper left corner is presumably cell material, which is peeled off during the processing for the SEM imaging. The layer thickness of the SU-8 is 10 µm. (b) A confocal image of a sample with 10 µm SU-8. The somas are marked green and the neuritis red. One can see neurites extending from one container to the neighboring ones. The scale bars are 30 µm for (a) and 25 µm for (b).
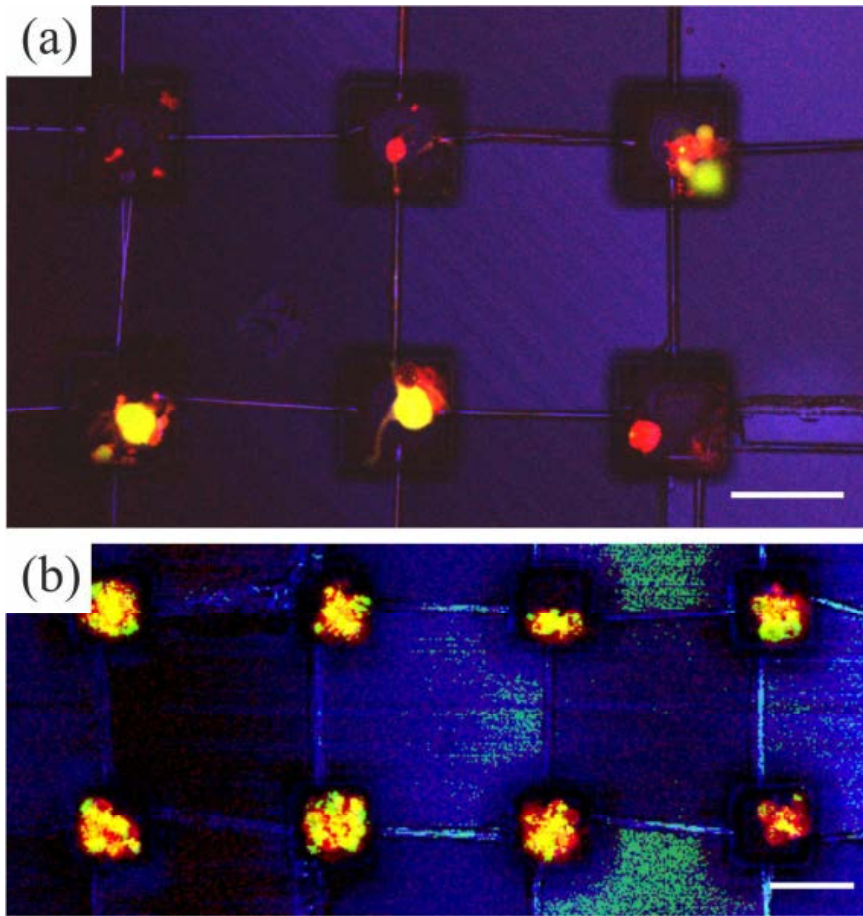
Figure SI6: (a) A confocal image of a sample with 12 µm SU-8. . The somas are marked green and the neuritis red. One can see neurites extending from one container to the neighboring ones. The tubes with axons inside show slightly different color from the empty tubes. The different color shades is the neurite filled tubes can be explained by the different position od the neurite in the tube. In case the neurite locates against the tube´s wall on the upper side of the tube, the signal coming from the neurite is higher than the signal coming from a neurite located on the ground of the tube. (b) A confocal image of a sample with 20 µm SU-8. Due to the higher thickness of the SU-8 the recorded images include more noise. The scale bars are 25 µm for both.

A.11 Publication XI

Microscaffolds by direct laser writing for neurite guidance leading to tailor-made neuronal networks

Cornelius Fendler, Christian Denker, <u>Jann Harberts</u>, Parisa Bayat, Robert Zierold, Gabriele Loers, Markus Münzenberg, and Robert H. Blick

Advanced Biosystems **2019**, 3(5), 1800329

Author contributions: Sample design/fabrication: C.F., C.D., M.M., manuscript writing: C.F., cell culture: C.F., <u>J.H.</u>, animal preparation: G.L., SEM/FIB imaging: C.F., P.B., patch clamping: C.F., <u>J.H.</u>, atomic layer deposition: R.Z., computer-generated imagery: <u>J.H.</u>, supervision: R.H.B.

Supporting video material is available on the publisher's website.

(8 + 3 pages)

FULL PAPER

Cell Culture Platforms

ADVANCED
BIOSYSTEMS

www.adv-biosys.com

Check for updates

Microscaffolds by Direct Laser Writing for Neurite Guidance Leading to Tailor-Made Neuronal Networks

Cornelius Fendler, Christian Denker, Jann Harberts, Parisa Bayat, Robert Zierold, Gabriele Loers, Markus Münzenberg, and Robert H. Blick*

While modern day integrated electronic circuits are essentially designed in a 2D fashion, the brain can be regarded as a 3D circuit. The thus enhanced connectivity enables much more complex signal processing as compared to conventional 2D circuits. Recent technological advances in the development of nano/microscale 3D structuring have led to the development of artificial neuron culturing platforms, which surpass the possibilities of classical 2D cultures. In this work, in vitro culturing of neuronal networks is demonstrated by determining predefined pathways through topological and chemical neurite guiding. Tailor-made culturing substrates of microtowers and free-standing microtubes are fabricated using direct laser writing by two-photon polymerization. The first scaffold design that allows for site-specific cell attachment and directed outgrowth of single neurites along defined paths that can be arranged freely in all dimensions, to build neuronal networks with low cell density, is presented. The neurons cultured in the scaffolds show characteristic electrophysiological properties of vital cells after 10 d in vitro. The introduced scaffold design offers a promising concept for future complex neuronal network studies on defined neuronal circuits with tailor-made design specific neurite connections beyond 2D.

1. Introduction

On 2D substrates, the mechanics of neurite formation and path finding (neuron polarization) has been widely analyzed in the past.[1–4] Various chemical cues such as fibronectin and laminin[5,6] have been applied to either attract or repel axons by affecting the cytoskeleton development of the axon growth cone.[7,8] Topological cues such as stiffness,[4] hydrophobicity,[9] and modulation of the surrounding surface, for example, through variations in roughness[10,11] or through guiding barriers[12–14] and channels,[15–20] have also been found to be effective methods to direct the neurite outgrowth on artificial substrates.

A significant drawback of classical 2D neuronal in vitro cultures is their inability to sufficiently mimic the distinct 3D connections in a nervous system.[21] Most of the standard lithography techniques are only available in 2D or 2.5D.[22] However, recent advances in micro- and nanoscale fabrication, especially direct laser writing by two-photon polymerization (2PP-DLW), now enable the construction of complex resist-based 3D substrates with feature sizes down to ≈150 nm.[23] Using 2PP-DLW, nearly any mechanically stable structure can be realized as real 3D culturing substrate consisting of a biocompatible polymer within only a few hours. 2PP-DLW has already been utilized for neuronal growth studies.[24–29] Note, while most of these applications try to mimic the natural brain environment to a certain structural degree, the adhesions spots of the cell somata and/or the direction of neurite outgrowth on 3D substrates have been statistical so far. As a first step toward 2PP-DLW application for neurite guidance, Turunen et al. used DLW in 2014 to print walls on planar glass substrates to form cavities and channels, and applied laminin with a microinjection system inside the neurocages.[27] The design lacked efficient cell confinement properties, but potential function of printed channels as neurite guides was shown.

Other approaches, which enable in vitro neuronal network growth in a 3D environment in different ways, such as synthetic hydrogel platforms,[30–32] network growth on micro beads,[21,33] polymer scaffolds fabricated by gaseous salt leaching,[34,35] or microfibrous scaffolds[36] feature only statistically oriented network growth.

Here, we present an approach for guided neuronal network growth that features single neurites specifically grown through rectangular tubes in a 3D scaffold. The design we show herein combines the tunability and the precision of a 3D design utilizing 2PP-DLW manufacturing with topologically and chemically predefined adhesion areas as well as guidance paths for

C. Fendler, J. Harberts, P. Bayat, Dr. R. Zierold, Prof. R. H. Blick
Center for Hybrid Nanostructures (CHyN)
Universität Hamburg
Luruper Chaussee 149, Hamburg 22761, Germany
E-mail: rblick@chyn.de
Dr. C. Denker, Prof. M. Münzenberg
Institute of Physics
University of Greifswald
Felix-Hausdorff-Str. 6, Greifswald 17489, Germany
Dr. G. Loers
Center for Molecular Neurobiology Hamburg (ZMNH)
University Medical Center Hamburg-Eppendorf (UKE)
Falkenried 94, Hamburg 20251, Germany

The ORCID identification number(s) for the author(s) of this article can be found under https://doi.org/10.1002/adbi.201800329.

DOI: 10.1002/adbi.201800329

ADVANCED
SCIENCE NEWS
www.advancedsciencenews.com

ADVANCED
BIOSYSTEMS
www.adv-biosys.com

controlled axon and dendrite outgrowth. The scaffolds consist of pillars with varying height, connected to each other through freestanding tubes. Murine cerebellar granule cells were cultured in cavities on top of the pillars. Site-specific cell attachment and guided neurite growth inside of the structure are shown as proof of concept for 2.5D single cell neuronal circuits and future studies on the formation of complex tailor-made in vitro neuronal networks.

2. Results and Discussion

2.1. Direct Laser Writing

The principle scaffold design is schematically sketched in **Figure 1** and consists of towers, spaced by 25 µm but connected to each other by suspended tubes. The tops of the towers, which serve as posts for the neuronal somata, have a cross section of about 20 µm, enclosed by 2.5 µm thick walls with 10 µm in height. Neighboring towers have a height difference of 10 µm and are connected to each other through freestanding tubes with a wall thickness of 1.5 µm. The design is built to resemble the configuration of myelin sheets with alternating strong confinement inside the tubes and less confinement in the cavities. Froeter et al.[19] have shown a strong guidance effect of microtubes <4.4 µm diameter with axon extension speed strongly accelerated inside the tubes for primary cortical neurons. The distance between the towers was chosen accordingly, resulting in a tube length of ≈30 µm. The cavity cross section of 20 µm was chosen so that the space is big enough for neurons to adhere at the bottom and have access to fresh culture medium by diffusion, while also being sufficiently narrow so no big cell clusters but only a few neurons fit into one cavity. The height of the cavity walls of 10 µm is chosen so that neurites on the bottom most likely stay inside the cavity, while the cell somata at the bottom are accessible for patch-clamp measurements. A minimum final tube size after development of 2 µm is chosen because the entrances need to have a certain width for the growth cone to enter the tube. At the same time, this diameter offers strong coaxial confinement for a neurite inside a tube.

Prior to printing the scaffold structure, intensity and optimization tests were performed, which lead to optimal writing conditions (**Figure 2**). Tubes with round and quadratic cross sections were investigated. For the final design, rectangular tubes were chosen. On the one hand, they have an advantage in comparison to circular tubes regarding the refraction effects in optical microscopy analysis. This fact is important for the potential of confocal analysis of neurites in the tubes. On the other hand, the rectangular form was chosen because corners and trenches have been shown to act as topological cue to neurite outgrowth.[14,15]

After development, a shrinkage of 7%, ≈50 µm in horizontal direction compared to the original CAD design, was observed. Written directly onto the solid surface of the base carrier, this effect resulted in strong tension within the polymer and partial detachment of the structure from the carrier glass. To compensate the tension and to enhance the stability of the pillar structure, a base box of 600 × 600 µm was written beforehand with IP-Dip so that the pillars are attached to a ground that shrinks exactly at the same rate and the same amount during development (**Figure 3**a). To prevent detachment of the box itself from the glass carrier, flexible spiral springs were written onto the glass surface beforehand (Figure 3a (inset)). The final structure (also IP-Dip) was coated with aluminum oxide (Al_2O_3) by atomic layer deposition (ALD) as biocompatible passivation layer.[37]

Detailed features of the scaffold structure are given in Figure 3b–f. Cross-sectional scanning electron microscopy (SEM) analysis reveals a tube diameter of 2 µm. The tubes have a well-defined shape along the entire length and show a structure of rounded steps outside and inside of the tubes. This slight modulation of the surface structure, also inside the cavities, was implemented in the 2PP-DLW process, since nanoscale roughness has previously been shown to affect cell adhesion and morphology in a positive way,[10,11] while at the same time enabling fast manufacturing of scaffolds. The close-up on the milled ceiling of a tube shows two layers of different material on top of the structure and only one layer inside the tube. The top layer is gold, deposited before imaging for improved resolution. The layer below the gold and inside of the tube is Al_2O_3, proving successful and conformal coating by ALD after lithographic scaffold preparation.

2.2. Cell Adhesion and Neurite Guiding

Cell adhesion onto the scaffold is only desired inside of the cavities on top of the pillars to allow for purely guided
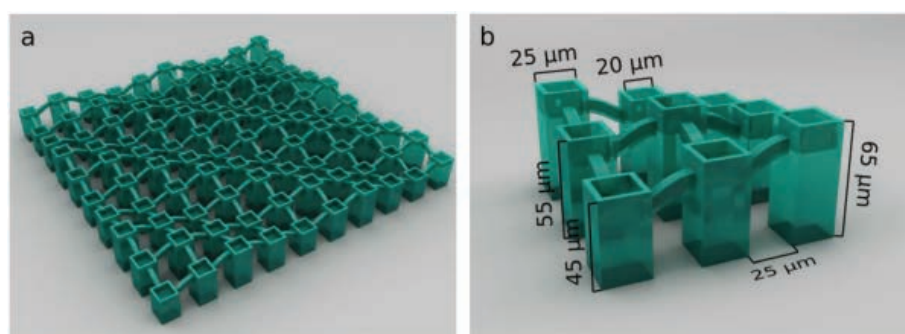

Figure 1. CAD graphics of the structure design. a) The structure consists of 10 × 10 pillars that are connected by freestanding tubes. b) Close-up on a section of the structure. The pillars are connected to direct neighbors by freestanding tubes with an internal diameter of 2 µm.
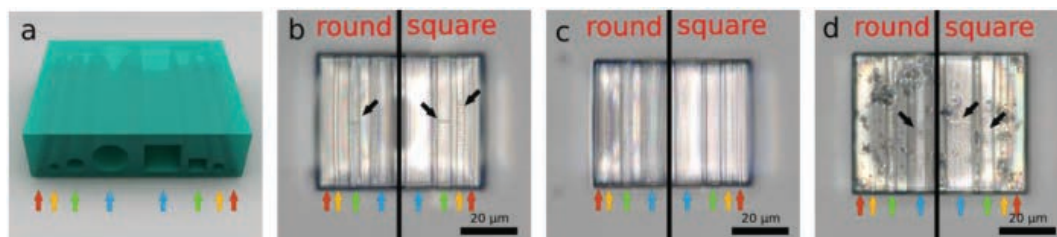
**ADVANCED
SCIENCE NEWS**
www.advancedsciencenews.com

**ADVANCED
BIOSYSTEMS**
www.adv-biosys.com

Figure 2. Schematic and light microscopy images of intensity test results on horizontal tubes in a cuboid. The test design has tubes with round (left) and quadratic (right) cross section. The arrows point to tubes of 10 µm (blue), 5 µm (green), 3 µm (yellow), and 1 µm (red) diameter. The microscopy images show a top view onto the cuboids. a) CAD graphic of the tube test. b) Already a slight variation from the optimal intensity leads to partial clogging of the 5 and 3 µm tubes (black arrows). The 1 µm tubes are completely clogged. c) At optimal laser intensity, even the 1 µm tubes have a clean shape and are unclogged. d) At too high intensity, the polymer is partially destroyed, and some tubes are clogged (black arrows).

growth within the scaffold. As a first step, we tested coating over the entire sample with poly-D-lysine (PDL) and laminin, a cell adhesion promoting polymer and a protein supporting neurite outgrowth and survival, respectively.[38,39] With this configuration, some neurons settled inside of cavities by chance (**Figure 4**a). A higher number of cells attached to the outer walls of the pillars in a randomly distributed fashion. It might be preferred by the neurons to settle on top of the
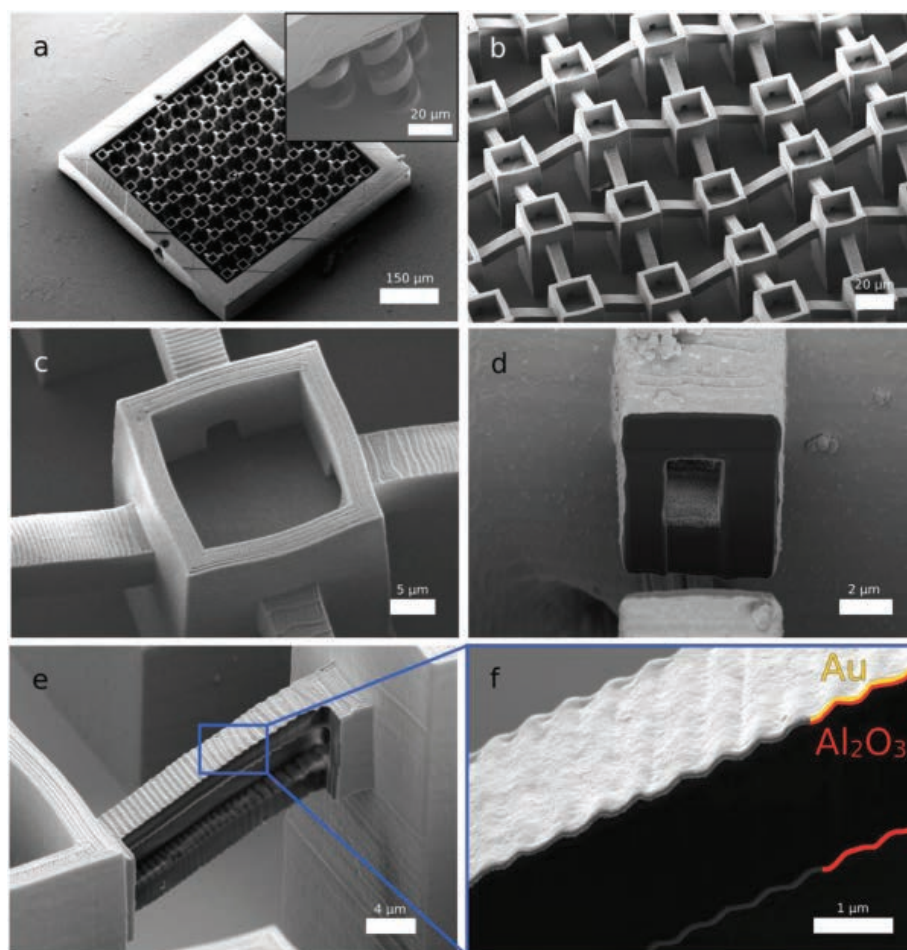

Figure 3. Scanning electron microscopy images of the structure for cell growth studies. Cross sections of tubes were obtained by milling with a gallium focused ion beam. a) The structure written inside a box. Inset: Springs, connecting the box with the carrier glass. b) Magnified image of the pillar structure. c) A pillar of medium height. The tubes on the left and back lead to higher pillars, while the tubes on the right and front go downward. d) Cross section of a milled tube. e) Side view of a milled tube. f) Side view on the ceiling of a tube. Two layers of coating material (Au and Al_2O_3) are visible on top of the polymer, while only one layer of Al_2O_3 can be resolved inside the tube.

ADVANCED
SCIENCE NEWS
www.advancedsciencenews.com
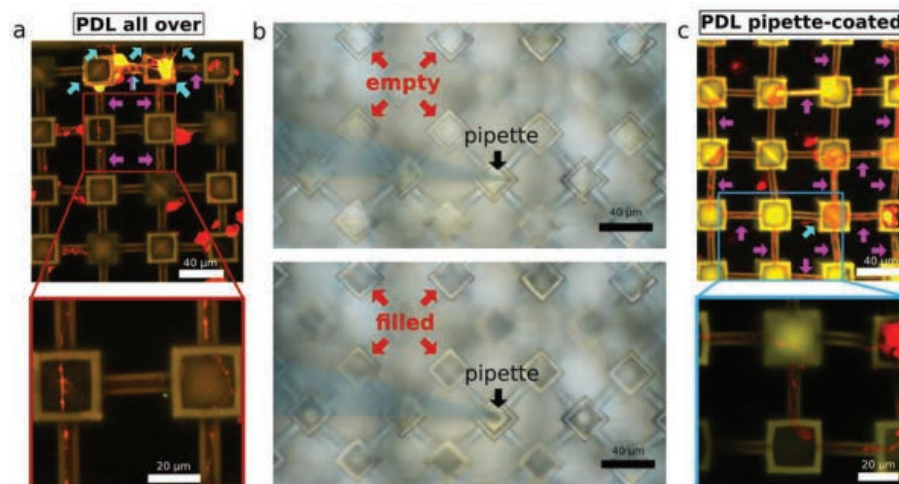
ADVANCED
BIOSYSTEMS
www.adv-biosys.com

Figure 4. a) Confocal microscopy images of cultured scaffolds with PDL coated onto the entire scaffold. Purple arrows point to neurites inside of tubes. Turquoise arrows point to neurites grown outside of the tubes. b) Optical images of the substrate during the PDL coating process (top view). The pipette is slightly colored in the images for higher visibility. Upper picture: A glass pipette filled with PDL solution carefully positioned inside one of the cavities. Lower picture: Pipette touching a corner of the cavity wall. Cavities and tubes filled with PDL solution. A clip is available in Video S1 (Supporting Information). c) Cultured scaffold with PDL coated directly into the cavities and tubes before culturing using glass pipettes (10 DIV). The ratio of neurites inside the tubes improved significantly compared to (a). Intensity differences are caused by slightly different imaging settings and use of different detectors. While (a) was detected by two HyD detectors, in (c) the range of 494–540 nm was detected with a PMT detector with gain set to ≈900.

structure due to larger surface area than inside of the scaffolds as well as more freedom to move and agglomerate. Therefore, neurite outgrowth occurred partially inside but also on top of the structure. Note, the share of neurites at the bottom of cavities extended exclusively through the tubes, indicating already at this stage the topological neuron guiding properties of the scaffold design.

To target the problem of random neurite outgrowth and to promote selective cell adhesion, PDL was coated directly into the cavities utilizing an upright patch clamp setup. A pipette filled with PDL solution and controlled by a micromanipulator was carefully brought near the pillar structure (Figure 4b, and Video S1, Supporting Information). Upon contact between the pipette and a corner of a cavity wall, the surface tension inside the pipette was broken, and the solution filled the cavity automatically without applying any pressure. All connected tubes and cavities were filled with solution by capillary forces whilst the outer part of the structure remained untreated. Because of the specific sample design, PDL solution only reached the spots where cell adhesion is desired.

Confocal images of cells cultures on scaffolds prepared as described above after 10 d in vitro (DIV) clearly reveal the effect of the coating method (Figure 4c). When PDL was systematically printed, nearly all neurons settled inside the cavities. For neuronal somata attached to the bottom of cavities, all observed neurites extended through the tubes. No neurites were observed leaving a cavity after crossing a tube. Only if clusters of neurons were attached, in rare cases single neurites from cells near the top extended over the cavity walls. The overall rate of neurons attached to the structure greatly increased, leading to the formation of cellular networks according to the paths predefined by the scaffold design (**Figure 5**). Please note, the strong effect of the side-specific PDL coating was observed even

though all samples were still completely coated with laminin before culturing, pointing to the major influence of PDL for cell adhesion.

As indicated in the close-ups in Figure 4, neurites inside of the tubes seem to stick mostly to the side walls. High-resolution SEM images of cross sections made by focused ion beam (FIB) milling reveal that the neurites actually stick to the corners, which confirms the corner's function[15,18] as topological guide for neurite outgrowth. An exemplary axon from one neuron extending through two tubes after 3 DIV is shown in **Figure 6**. Originating from the cell soma, most axons go directly in the direction of a tube. Two different settings can be observed inside the tubes: First, the axon changing the corner while crossing (Figure 6c); second, the axon sticking to one corner over the entire distance before leaving the tube (Figure 6e). Our observations strongly support the previous studies in literature which found a strong topological guidance mechanism for neurite outgrowth.[3]

2.3. Cell Viability

Note, the artificial confinement does not have any visible negative effect on the cells for the observed time of up to 14 DIV. On flat reference substrates cell clustering of most cells to groups of three or more could be observed within a few days. Despite the prevention of similar cell migration inside the tested design, neurons were vital even when seeded individually in a cavity with no soma contact to other cells. In order to further examine proper cell function, the capability of the neurons to fire action potentials was measured via patch clamp measurements in an upright setup (**Figure 7**a). The measurements were performed on single cells inside the scaffold after 10 DIV (Figure 7b).

**ADVANCED
SCIENCE NEWS**
www.advancedsciencenews.com

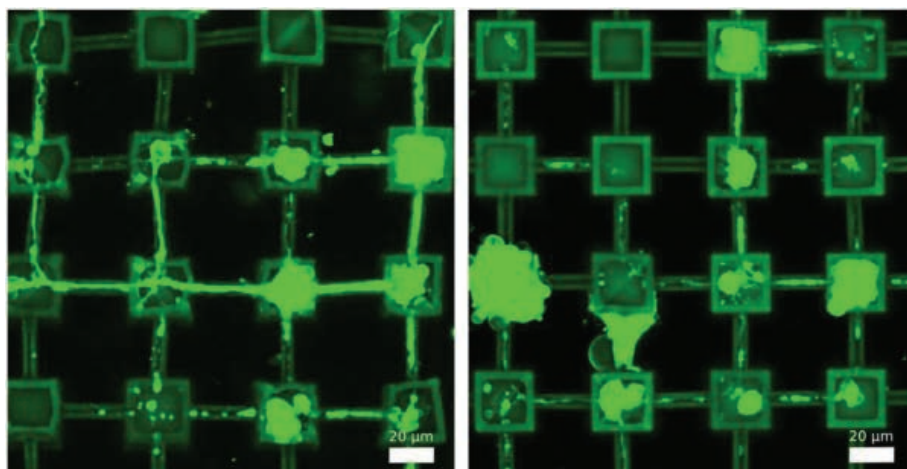**ADVANCED
BIOSYSTEMS**
www.adv-biosys.com

Figure 5. Confocal microscopy images of neurons inside of the scaffold (10 DIV). The neurites, exclusively spread through the tubes, build networks within the boundaries given by the scaffold design. In order to visualize single neurites despite strong intrinsic autofluorescence of the IP-Dip polymer, only one wavelength (552 nm) was used for excitation.

An exemplary recording is shown in comparison to a control measurement on a planar substrate in Figure 7c. Here, the contained cells show similar characteristic action potentials of vital neurons, independent of the substrate they grow on. Our results are an important indicator for proper neuronal function of nerve cells in such tailor-made scaffold designs.

3. Conclusion

In this study, we showed that 2PP-DLW can be used for the synthesis of 3D neurocages functioning as neurite guides to build neuronal networks. Therefore, a novel structure with free-standing tubes for neurite guidance to different heights between cavities was designed and successfully fabricated. Utilizing a patch-clamp setup for directed PDL coating, site-specific cell adhesion inside of cavities could be observed in culturing experiments with murine cerebellar granule cells. Furthermore, the ability of the design for neurite guidance with neurite outgrowth through the tubes was shown. The neurons inside the structure were firing action potentials at 10 DIV, with similar electrophysiological properties to neurons on control substrates.

So far, defined in vitro neuronal networks were only realized in 2D and were therefore lacking complexity. Our results present a novel scaffold structure with the ability to guide neuronal outgrowth through confinement on distinct pathways. These tubes can be designed to lead not only in plane but also truly 3D into any direction, which was not possible with any
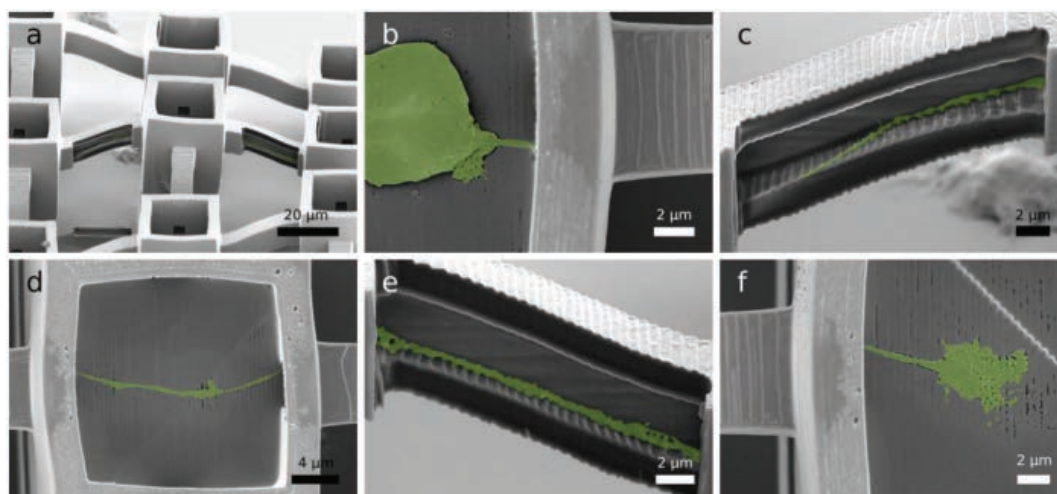

Figure 6. False-colored SEM images of an axon inside of the structure passing through two tubes after 3 DIV. Cross sections were obtained by FIB milling. a) Image of the cavities and tubes with the neuron shown in (b)–(e) inside. b) Cell soma and axon in a cavity with the axon entering a tube. c) The axon changes to the opposite side of the tube and sticks to the corner on that side before leaving the tube. d) Axon crossing one cavity and entering a tube on the opposite side. e) Axon crossing the second tube. It sticks to one corner through the whole length. f) Axon leaving the second tube, ending with its growth cone.
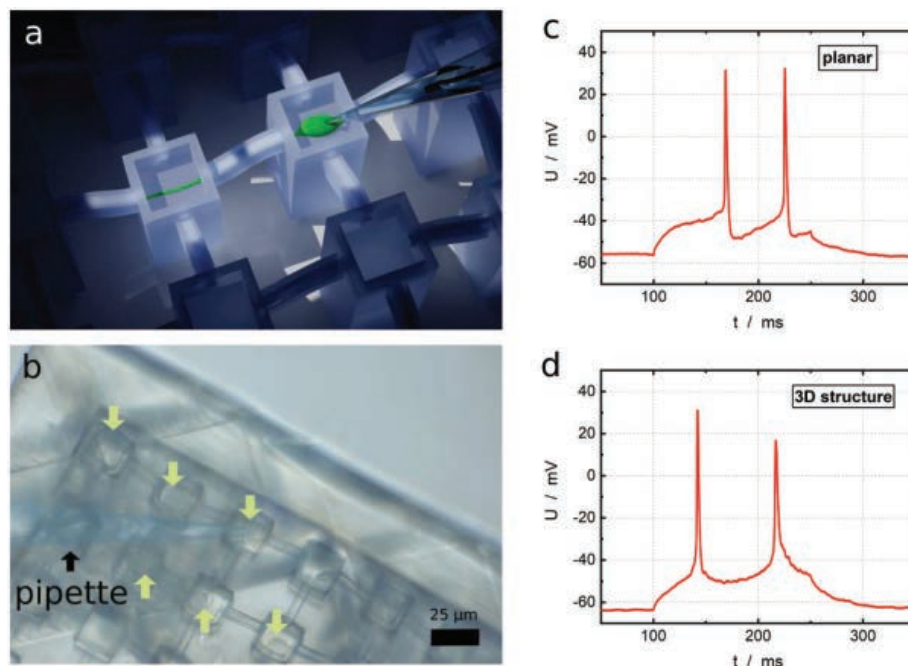
**ADVANCED
SCIENCE NEWS**
www.advancedsciencenews.com

**ADVANCED
BIOSYSTEMS**
www.adv-biosys.com

Figure 7. a) Graphic of a patched neuron in the structure. The patch pipette is in an angle of 45° to the substrate. One electrode is inside the patch pipette, the return electrode is outside of the structure in the petri dish. An objective with a distance of 4 mm is dipped into the solution from the top. b) Optical image of neurons (10 DIV) inside the structure during a patch clamp measurement. The arrows point to single cells inside the cavities. The pipette is slightly colored in the image for higher visibility. c,d) Results of electrophysiological measurements after 10 DIV. Stimulation current was injected after 100 ms for 150 ms. In (c), a single cell recording of a neuron in a planar Petri dish is drawn, while (d) shows a single cell recording inside a cavity of the structure.

other approach so far. Site-specific adhesion through chemical guiding combined with topological limitation of potential neurite growth paths in scaffolds opens completely new possibilities for in vitro neuronal circuit design. Thus, based on these results and by expanding the design, small tailor-made 2.5D networks could be realized for in-depth studies on neuronal network function and might pave the way to tailor-made neuronal networks with true 3D configuration. Cellular behavior and information transfer inside the structures could also be investigated under the influence of various pharmacological agents or different stimuli on parts of the network. Incorporating electrode arrays in the structure, similar to arrays realized on 2D neurocages in the past,[40] could enable extended long-term studies monitoring the entire network activity.

4. Experimental Section

Direct Laser Writing: 3D scaffolds were manufactured by 2PP-DLW with a Nanoscribe Photonic Professional GT. All CAD files for structures were designed with Autodesk AutoCAD. Simple $60 \times 50 \times 15$ µm³ box designs with circular and rectangular tubes embedded were used for exposure tests. The tests were performed with IP-Dip resist from Nanoscribe. All structures were written on glass slides. IP-Dip was successfully tested as potential material for culturing platforms by cultivating slides with IP-Dip boxes with wild type murine cerebellar granule cells (Figure S1, Supporting Information).

Based on the results of the exposure tests, the scaffolds for cell culturing were written with 10 mm s⁻¹ and 17 mW laser power. The

slicing distance was 0.3. Hatching and contour distance for tube structure were 0.2 with a contour count of 6. The write field was set to 141.4 µm² with 2 µm overlap. To compensate resolution differences, arising from the voxel of the polymerization threshold being ≈100 nm in *x*- and *y*-direction and 500 nm in *z*-direction, the inner tube diameter in the CAD design was set to 3 µm in horizontal and 4 µm in vertical direction. The samples were developed in MR-Dev 600 for 30 min, immersed twice in isopropyl alcohol (99.9%) for 60 s and examined with an optical microscope. Written and developed, the structure has an overall size of $480 \times 480 \times 60$ µm³.

Sample Preparation: Deposition of Al_2O_3 was carried out in a custom-built ALD system utilizing trimethylaluminum and water as precursors. A layer thickness of 15 nm was confirmed in spectral ellipsometry on planar reference substrates. Note, Al_2O_3-coated scaffolds were stable against the exposure to culture medium for several weeks without noticeable disintegration. Before further preparation all samples were treated with ozone plasma at 5 W for 3 s (Femto, Diener Electronic). PDL (0.01 g L⁻¹, mol. wt. 30k–70k, Sigma Aldrich) was selectively pipetted on the scaffold utilizing an upright patch clamp setup. Pipettes were fabricated with a pipette puller (P-2000, Shutter Instruments) out of borosilicate glass capillary blanks (GB150T-8P, Science Products). After preparation with PDL, the samples were washed with sterile deionized (DI) water three times to remove surplus PDL, carefully sterilized with 70% ethanol and exposed to UV light for 30 min. Directly before culturing, an additional coating was applied by covering the substrate for 20 min in laminin solution (1 mg mL⁻¹) at 37 °C.

Animals: C57BL/6 mice were bred at the animal facility of the University Medical Center Hamburg-Eppendorf and maintained at 22 °C on a 12 h light/12 h dark cycle and provided with food and water ad libitum. All experiments were conducted with mice of either sex and in accordance with the German and European Community laws on protection of experimental animals. Procedures used were approved

by the responsible committee of The State of Hamburg (Permission No. Org_679). Experiments were carried out and the manuscript was prepared following the ARRIVE guidelines for animal research.

Cell Cultivation: The substrates were cultivated with wild type murine cerebellar granule cells. At the time of extraction, mice were 6–7 d old. The isolation followed the description given by Loers et al.[41] The culture medium consisted of Neurobasal A (Thermo Fisher Scientific) supplemented with penicillin/streptomycin (1%), bovine serum albumin (1%), insulin (10 µg mL^{-1}), L-thyroxine (4×10^{-9} M), transferrin holo (100 µg mL^{-1}), sodium selenite (30×10^{-9} M) (all Sigma Aldrich), fetal bovine serum (6%, Capricorn Scientific – FBS Advanced), and Gibco B-27 (50×, ThermoFisher Scientific). Cell concentration was adjusted to 2×10^5 cells mL^{-1}. Droplets of 20 µm were incubated on each structure for 1 h at 37 °C and 5% CO_2 before adding 3 mL cell medium. Cell medium was changed three times a week.

Cell Imaging: For SEM imaging, neurons were fixed on the substrate beforehand. After treatment with 4% paraformaldehyde solution for 20 min at 37 °C, the substrate was rinsed three times with DI water and immersed in 10, 25, 50, 75, and 99.5% v/v ethanol solution for 10 min each. Following, the samples were air dried and stored under vacuum. Before SEM imaging, the samples were coated with ≈30 nm Au through sputter coating for improved resolution. Selected tubes of the samples were cut open by FIB milling (ZEISS Crossbeam 550).

For confocal imaging, neurons were stained beforehand with cell membrane stain (ThermoFisher, 555 nm/565 nm ex/em) and cell viability indicator (ThermoFisher, 496 nm/515 nm ex/em). Growth medium was removed, and the substrates were treated with 1× dye mixture in Dulbecco's phosphate-buffered saline (DPBS) for 15 min at 37 °C and 5% CO_2 was performed with a Leica TCS SP8 confocal microscope. Two lasers of 488 and 552 nm wavelength were used. Signals were detected with Leica HyD and photomultiplier tube (PMT) detectors adjusted to a range of 494–540 and 558–620 nm. IP-Dip has a strong intrinsic fluorescence. In order to best visualize the neurites, stained by membrane stain, the detected signal of shorter wavelength was reduced in Figure 4.

Electrophysiology: Patch clamp measurements were performed on a custom-built upright patch-clamp setup. The patch solutions were prepared according to Gall et al.[42] The bath solution consists of artificial cerebrospinal fluid supplemented with NaCl (120×10^{-3} M), NaHCO$_3$ (26×10^{-3} M), glucose (11×10^{-3} M), KCl (2×10^{-3} M), CaCl$_2$ (2×10^{-3} M), MgSO$_4$ (1.19×10^{-3} M), and KH$_2$PO$_4$ (1.18×10^{-3} M). The pipette solution contains potassium gluconate (126×10^{-3} M), glucose (15×10^{-3} M), 2-[4-(2-hydroxyethyl)piperazin-1-yl]ethanesulfonic acid (HEPES) (5×10^{-3} M), NaCl (4×10^{-3} M), MgATP (3×10^{-3} M), MgSO$_4$ (1×10^{-3} M), 1,2-bis(o-aminophenoxy)ethane-N,N,N′,N′-tetraacetic acid (BAPTA) (150×10^{-6} M), guanosine triphosphate (GTP) (100×10^{-6} M), and CaCl$_2$ (50×10^{-6} M). The pH is set to 7.2 with the addition of KOH. The bath solution was equilibrated to pH 7.4 prior to the measurements by perfusion with carbogen gas (95% O_2, 5% CO_2).

Supporting Information

Supporting Information is available from the Wiley Online Library or from the author.

Acknowledgements

Conflict of Interest

The authors declare no conflict of interest.

[1] R. W. Sperry, *Proc. Natl. Acad. Sci. USA* **1963**, *50*, 703.
[2] M. Tessier-Lavigne, C. S. Goodman, *Science* **1996**, *274*, 1123.
[3] N. Gomez, S. Chen, C. E. Schmidt, *J. R. Soc., Interface* **2007**, *4*, 223.
[4] D. E. Koser, A. J. Thompson, S. K. Foster, A. Dwivedy, E. K. Pillai, G. K. Sheridan, H. Svoboda, M. Viana, L. da F Costa, J. Guck, C. E. Holt, K. Franze, *Nat. Neurosci.* **2016**, *19*, 1592.
[5] R. W. Gundersen, *Dev. Biol.* **1987**, *121*, 423.
[6] C. Miller, S. Jeftinija, S. Mallapragada, *Tissue Eng.* **2002**, *8*, 367.
[7] L. Erskine, E. Herrera, *Dev. Biol.* **2007**, *308*, 1.
[8] D. Mortimer, T. Fothergill, Z. Pujic, L. J. Richards, G. J. Goodhill, *Trends Neurosci.* **2008**, *31*, 90.
[9] T. Limongi, F. Cesca, F. Gentile, R. Marotta, R. Ruffilli, A. Barberis, M. Dal Maschio, E. M. Petrini, S. Santoriello, F. Benfenati, E. Di Fabrizio, *Small* **2013**, *9*, 402.
[10] Y. W. Fan, F. Z. Cui, S. P. Hou, Q. Y. Xu, L. N. Chen, I. S. Lee, *J. Neurosci. Methods* **2002**, *120*, 17.
[11] F. Zamani, M. Amani-Tehran, M. Latifi, M. A. Shokrgozar, *J. Mater. Sci.: Mater. Med.* **2013**, *24*, 1551.
[12] B. Kaehr, R. Allen, D. J. Javier, J. Currie, J. B. Shear, *Proc. Natl. Acad. Sci. USA* **2004**, *101*, 16104.
[13] B. Kaehr, N. Ertas, R. Nielson, R. Allen, R. T. Hill, M. Plenert, J. B. Shear, *Anal. Chem.* **2006**, *78*, 3198.
[14] A. Marino, G. Ciofani, C. Filippeschi, M. Pellegrino, M. Pellegrini, P. Orsini, M. Pasqualetti, V. Mattoli, B. Mazzolai, *ACS Appl. Mater. Interfaces* **2013**, *5*, 13012.
[15] H. Francisco, B. B. Yellen, D. S. Halverson, G. Friedman, G. Gallo, *Biomaterials* **2007**, *28*, 3398.
[16] M. Yu, Y. Huang, J. Ballweg, H. Shin, M. Huang, D. E. Savage, M. G. Lagally, E. W. Dent, R. H. Blick, J. C. Williams, *ACS Nano* **2011**, *5*, 2447.
[17] C. S. Bausch, A. Koitmäe, E. Stava, A. Price, P. J. Resto, Y. Huang, D. Sonnenberg, Y. Stark, C. Heyn, J. C. Williams, E. W. Dent, R. H. Blick, *Appl. Phys. Lett.* **2013**, *103*, 173705.
[18] B. W. Tuft, L. Xu, S. P. White, A. E. Seline, A. M. Erwood, M. R. Hansen, C. A. Guymon, *ACS Appl. Mater. Interfaces* **2014**, *6*, 11265.
[19] P. Froeter, Y. Huang, O. V. Cangellaris, W. Huang, E. W. Dent, M. U. Gillette, J. C. Williams, X. Li, *ACS Nano* **2014**, *8*, 11108.
[20] R. Renault, J.-B. Durand, J.-L. Viovy, C. Villard, *Lab Chip* **2016**, *16*, 2188.
[21] S. Pautot, C. Wyart, E. Y. Isacoff, *Nat. Methods* **2008**, *5*, 735.
[22] A. Pimpin, W. Srituravanich, *Eng. J.* **2012**, *16*, 37.
[23] N. Anscombe, *Nat. Photonics* **2010**, *4*, 22.
[24] V. Melissinaki, A. A. Gill, I. Ortega, M. Vamvakaki, A. Ranella, J. W. Haycock, C. Fotakis, M. Farsari, F. Claeyssens, *Biofabrication* **2011**, *3*, 045005.
[25] A. M. Greiner, B. Richter, M. Bastmeyer, *Macromol. Biosci.* **2012**, *12*, 1301.
[26] E. Käpylä, D. B. Aydogan, S. Virjula, S. Vanhatupa, S. Miettinen, J. Hyttinen, M. Kellomäki, *J. Micromech. Microeng.* **2012**, *22*, 115016.
[27] S. Turunen, E. Käpylä, M. Lähteenmäki, L. Ylä-Outinen, S. Narkilahti, M. Kellomäki, *Opt. Lasers Eng.* **2014**, *55*, 197.
[28] P. S. Timashev, M. V. Vedunova, D. Guseva, E. Ponimaskin, A. Deiwick, T. A. Mishchenko, E. V. Mitroshina, A. V. Koroleva, A. S. Pimashkin, I. V. Mukhina, V. Y. Panchenko, B. N. Chichkov, V. N. Bagratashvili, *Biomed. Phys. Eng. Express* **2016**, *2*, 035001.

[29] S. Turunen, T. Joki, M. L. Hiltunen, T. O. Ihalainen, S. Narkilahti, M. Kellomäki, *ACS Appl. Mater. Interfaces* **2017**, *9*, 25717.

[30] J. N. H. Shepherd, S. T. Parker, R. F. Shepherd, M. U. Gillette, J. A. Lewis, R. G. Nuzzo, *Adv. Funct. Mater.* **2011**, *21*, 47.

[31] D. D. McKinnon, A. M. Kloxin, K. S. Anseth, *Biomater. Sci.* **2013**, *1*, 460.

[32] A. Kaneko, Y. Sankai, *PLoS One* **2014**, *9*, e102703.

[33] M. Frega, M. Tedesco, P. Massobrio, M. Pesce, S. Martinoia, *Sci. Rep.* **2015**, *4*, 5489.

[34] Y. Lai, K. Cheng, W. Kisaalita, *PLoS One* **2012**, *7*, e45074.

[35] Y. S. Nam, J. J. Yoon, T. G. Park, *J. Biomed. Mater. Res.* **2000**, *53*, 1.

[36] F. Sharifi, B. B. Patel, A. K. Dzuilko, R. Montazami, D. S. Sakaguchi, N. Hashemi, *Biomacromolecules* **2016**, *17*, 3287.

[37] D. S. Finch, T. Oreskovic, K. Ramadurai, C. F. Herrmann, S. M. George, R. L. Mahajan, *J. Biomed. Mater. Res., Part A* **2008**, *87A*, 100.

[38] D. Mazia, G. Schatten, W. Sale, *J. Cell Biol.* **1975**, *66*, 198.

[39] D. Edgar, R. Timpl, H. Thoenen, *EMBO J.* **1984**, *3*, 1463.

[40] J. Erickson, A. Tooker, Y. C. Tai, J. Pine, *J. Neurosci. Methods* **2008**, *175*, 1.

[41] G. Loers, S. Chen, M. Grumet, M. Schachner, *J. Neurochem.* **2005**, *92*, 1463.

[42] D. Gall, C. Roussel, I. Susa, E. D'Angelo, P. Rossi, B. Bearzatto, M. C. Galas, D. Blum, S. Schurmans, S. N. Schiffmann, *J. Neurosci.* **2003**, *23*, 9320.

ADVANCED BIOSYSTEMS

Supporting Information

Microscaffolds by Direct Laser Writing for Neurite Guidance Leading to Tailor-Made Neuronal Networks

Cornelius Fendler, Christian Denker, Jann Harberts, Parisa Bayat, Robert Zierold, Gabriele Loers, Markus Münzenberg, and Robert H. Blick*

WILEY-VCH

Supporting Information

Micro Scaffolds by Direct Laser Writing for Neurite Guidance Leading to Tailor-Made Neuronal Networks

Cornelius Fendler, Christian Denker, Jann Harberts, Parisa Bayat, Robert Zierold, Gabriele Loers, Markus Münzenberg, and Robert H. Blick*

Test of IP-DIP for neuron culturing

The feasibility to use the commercial photoresist IP-DIP for neuron culturing platforms created by 2PP-DLW was tested with cubic structures written on glass carriers. PDL was coated by incubating a droplet of 50 µl PDL solution (0.01 g l^{-1}, mol wt 30k - 70k, Sigma Aldrich) for 30 min at room temperature. Cell cultivation was performed according to the description given in the Experimental Section of the main script. Confocal images of stained cells are shown in Figure S1. Neurons were attached to the sides of the cubes at the interface of glass and polymer and were vital after 8 DIV. Also, the polymer was stable in culture medium. No disintegration was observed during the time of culturing.
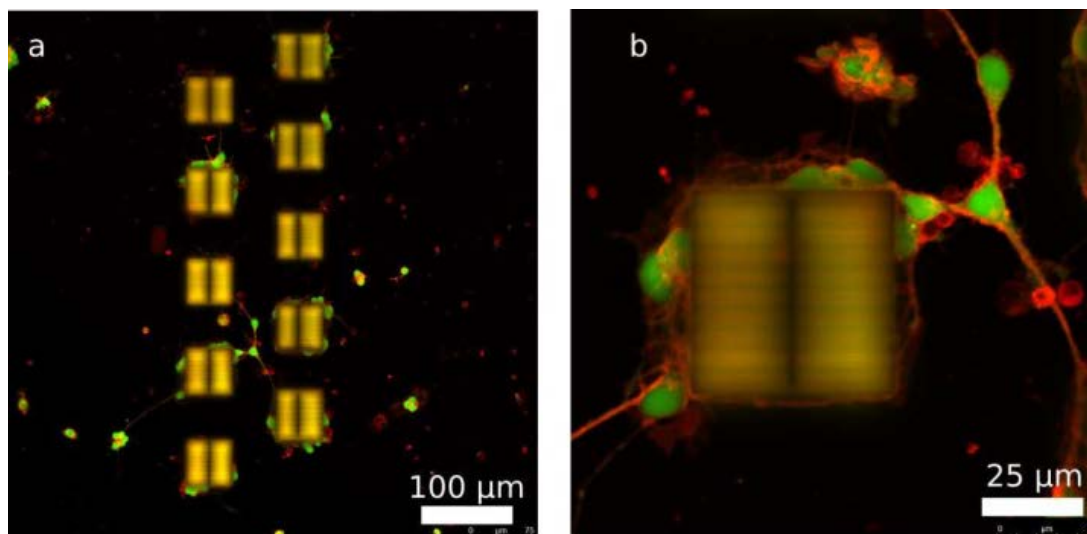
Figure S1. Confocal images of neurons cultured for 8 DIV on glass substrates with cubes written by 2PP-DLW with IP-Dip. **(a)**

Bibliography

(1) Harberts, J.; Kusch, M.; O'Sullivan, J.; Zierold, R.; Blick, R. H., 'A Temperature-Controlled Patch Clamp Platform Demonstrated on Jurkat T Lymphocytes and Human Induced Pluripotent Stem Cell-Derived Neurons', *Bioengineering* **2020**, *7*(2), 46, cited on page(s): v.

(2) Harberts, J.; Zierold, R.; Fendler, C.; Koitmäe, A., *et al.*, 'Culturing and patch clamping of Jurkat T cells and neurons on Al_2O_3 coated nanowire arrays of altered morphology', *RSC Adv.* **2019**, *9*(20), 11194–11201, cited on page(s): v.

(3) Harberts, J.; Bours, K.; Siegmund, M.; Hedrich, C., *et al.*, 'Culturing human iPSC-derived neural progenitor cells on nanowire arrays: mapping the impact of nanowire length and array pitch on proliferation, viability, and membrane deformation', *Nanoscale* **2021**, *13*(47), 20052–20066, cited on page(s): v.

(4) Harberts, J.; Haferkamp, U.; Haugg, S.; Fendler, C., *et al.*, 'Interfacing human induced pluripotent stem cell-derived neurons with designed nanowire arrays as a future platform for medical applications', *Biomater. Sci.* **2020**, *8*(9), 2434–2446, cited on page(s): v.

(5) Harberts, J.; Siegmund, M.; Schnelle, M.; Zhang, T., *et al.*, 'Robust neuronal differentiation of human iPSC-derived neural progenitor cells cultured on densely-spaced spiky silicon nanowire arrays', *Sci. Rep.* **2021**, *11*(1), 18819, cited on page(s): v.

(6) Harberts, J.; Siegmund, M.; Hedrich, C.; Kim, W., *et al.*, 'Generation of Human iPSC-Derived Neurons on Nanowire Arrays Featuring Varying Lengths, Pitches, and Diameters', *Adv. Mater. Interfaces* **2022**, *9*(24), 2200806, cited on page(s): v.

(7) Harberts, J.; Fendler, C.; Teuber, J.; Siegmund, M., *et al.*, 'Toward Brain-on-a-Chip: Human Induced Pluripotent Stem Cell-Derived Guided Neuronal Networks in Tailor-Made 3D Nanoprinted Microscaffolds', *ACS Nano* **2020**, *14*(10), 13091–13102, cited on page(s): v.

(8) Fendler, C.; Harberts, J.; Rafeldt, L.; Loers, G.; Zierold, R.; Blick, R. H., 'Neurite guidance and neuro-caging on steps and grooves in 2.5 dimensions', *Nanoscale Adv.* **2020**, *2*(11), 5192–5200, cited on page(s): v.

(9) Koitmäe, A.; Harberts, J.; Loers, G.; Müller, M., *et al.*, 'Approaching Integrated Hybrid Neural Circuits: Axon Guiding on Optically Active Semiconductor Microtube Arrays', *Adv. Mater. Interfaces* **2016**, *3*(24), 1600746, cited on page(s): vi.

(10) Koitmäe, A.; Müller, M.; Bausch, C. S.; Harberts, J., *et al.*, 'Designer Neural Networks with Embedded Semiconductor Microtube Arrays', *Langmuir* **2018**, *34*(4), 1528–1534, cited on page(s): vi.

(11) Fendler, C.; Denker, C.; Harberts, J.; Bayat, P., *et al.*, 'Microscaffolds by Direct Laser Writing for Neurite Guidance Leading to Tailor-Made Neuronal Networks', *Adv. Biosyst.* **2019**, *3*(5), 1800329, cited on page(s): vi.

(12) Craighead, H. G., 'Nanostructure science and technology: Impact and prospects for biology', *J. Vac. Sci. Technol. A Vacuum, Surfaces, Film.* **2003**, *21*(5), S216–S221, cited on page(s): 1.

(13) Wong, I. Y.; Bhatia, S. N.; Toner, M., 'Nanotechnology: emerging tools for biology and medicine', *Genes Dev.* **2013**, *27*(22), 2397–2408, cited on page(s): 1.

(14) Bayda, S.; Adeel, M.; Tuccinardi, T.; Cordani, M.; Rizzolio, F., 'The History of Nanoscience and Nanotechnology: From Chemical–Physical Applications to Nanomedicine', *Molecules* **2019**, *25*(1), 112, cited on page(s): 1.

(15) Sniadecki, N. J.; Desai, R. A.; Ruiz, S. A.; Chen, C. S., 'Nanotechnology for Cell–Substrate Interactions', *Ann. Biomed. Eng.* **2006**, *34*(1), 59–74, cited on page(s): 1.

(16) Chen, Y.; Alba, M.; Tieu, T.; Tong, Z., *et al.*, 'Engineering Micro–Nanomaterials for Biomedical Translation', *Adv. NanoBiomed Res.* **2021**, *1*(9), 2100002, cited on page(s): 1.

(17) Pei, F.; Tian, B., 'Nanoelectronics for Minimally Invasive Cellular Recordings', *Adv. Funct. Mater.* **2020**, *30*(29), 1906210, cited on page(s): 1.

(18) Pampaloni, N. P.; Giugliano, M.; Scaini, D.; Ballerini, L.; Rauti, R., 'Advances in Nano Neuroscience: From Nanomaterials to Nanotools', *Front. Neurosci.* **2019**, *12*, 953, cited on page(s): 1.

(19) Tibbitt, M. W.; Rodell, C. B.; Burdick, J. A.; Anseth, K. S., 'Progress in material design for biomedical applications', *Proc. Natl. Acad. Sci.* **2015**, *112*(47), 14444–14451, cited on page(s): 1.

(20) Armentano, I.; Tarpani, L.; Morena, F.; Martino, S.; Latterini, L.; Torre, L., 'Nanostructured Biopolymer-based Materials for Regenerative Medicine Applications', *Curr. Org. Chem.* **2018**, *22*(12), 1193–1204, cited on page(s): 1.

(21) Zhang, W.; Yang, Y.; Cui, B., 'New perspectives on the roles of nanoscale surface topography in modulating intracellular signaling', *Curr. Opin. Solid State Mater. Sci.* **2021**, *25*(1), 100873, cited on page(s): 1.

(22) Liu, X.; Wang, S., 'Three-dimensional nano-biointerface as a new platform for guiding cell fate', *Chem. Soc. Rev.* **2014**, *43*(8), 2385–2401, cited on page(s): 1.

(23) Kwak, M.; Han, L.; Chen, J. J.; Fan, R., 'Interfacing Inorganic Nanowire Arrays and Living Cells for Cellular Function Analysis', *Small* **2015**, *11*(42), 5600–5610, cited on page(s): 1.

(24) Higgins, S. G.; Becce, M.; Belessiotis-Richards, A.; Seong, H.; Sero, J. E.; Stevens, M. M., 'High-Aspect-Ratio Nanostructured Surfaces as Biological Metamaterials', *Adv. Mater.* **2020**, *32*(9), 1903862, cited on page(s): 1.

(25) Rahong, S.; Yasui, T.; Kaji, N.; Baba, Y., 'Recent developments in nanowires for bio-applications from molecular to cellular levels', *Lab Chip* **2016**, *16*(7), 1126–1138, cited on page(s): 1.

(26) Pampaloni, F.; Reynaud, E. G.; Stelzer, E. H. K., 'The third dimension bridges the gap between cell culture and live tissue', *Nat. Rev. Mol. Cell Biol.* **2007**, *8*(10), 839–845, cited on page(s): 1.

(27) Benetti, E. M.; Gunnewiek, M. K.; van Blitterswijk, C. A.; Julius Vancso, G.; Moroni, L., 'Mimicking natural cell environments: design, fabrication and application of bio-chemical gradients on polymeric biomaterial substrates', *J. Mater. Chem. B* **2016**, *4*(24), 4244–4257, cited on page(s): 1.

(28) Chiappini, C., 'Nanoneedle-Based Sensing in Biological Systems', *ACS Sensors* **2017**, *2*(8), 1086–1102, cited on page(s): 1.

(29) Simitzi, C.; Ranella, A.; Stratakis, E., 'Controlling the morphology and outgrowth of nerve and neuroglial cells: The effect of surface topography', *Acta Biomater.* **2017**, *51*, 21–52, cited on page(s): 1.

(30) Leclech, C.; Villard, C., 'Cellular and Subcellular Contact Guidance on Microfabricated Substrates', *Front. Bioeng. Biotechnol.* **2020**, *8*, 1198, cited on page(s): 1, 33.

(31) Li, X.; Mo, J.; Fang, J.; Xu, D., *et al.*, 'Vertical nanowire array-based biosensors: device design strategies and biomedical applications', *J. Mater. Chem. B* **2020**, *8*(34), 7609–7632, cited on page(s): 1.

(32) Mendes, P. M., 'Cellular nanotechnology: making biological interfaces smarter', *Chem. Soc. Rev.* **2013**, *42*(24), 9207, cited on page(s): 1.

(33) Madonna, R., 'Human-Induced Pluripotent Stem Cells: In Quest of Clinical Applications', *Mol. Biotechnol.* **2012**, *52*(2), 193–203, cited on page(s): 1.

(34) Dragunow, M., 'The adult human brain in preclinical drug development', *Nat. Rev. Drug Discov.* **2008**, *7*(8), 659–666, cited on page(s): 1, 6.

(35) Leenaars, C. H. C.; Kouwenaar, C.; Stafleu, F. R.; Bleich, A., *et al.*, 'Animal to human translation: a systematic scoping review of reported concordance rates', *J. Transl. Med.* **2019**, *17*(1), 223, cited on page(s): 1, 6.

(36) Dolmetsch, R.; Geschwind, D. H., 'The Human Brain in a Dish: The Promise of iPSC-Derived Neurons', *Cell* **2011**, *145*(6), 831–834, cited on page(s): 2.

(37) Reddy, A. P.; Ravichandran, J.; Carkaci-Salli, N., 'Neural regeneration therapies for Alzheimer's and Parkinson's disease-related disorders', *Biochim. Biophys. Acta - Mol. Basis Dis.* **2020**, *1866*(4), 165506, cited on page(s): 2.

(38) de Rus Jacquet, A.; Denis, H. L.; Cicchetti, F.; Alpaugh, M., 'Current and future applications of induced pluripotent stem cell-based models to study pathological proteins in neurodegenerative disorders', *Mol. Psychiatry* **2021**, *26*(7), 2685–2706, cited on page(s): 2.

(39) Lestrell, E.; O'Brien, C. M.; Elnathan, R.; Voelcker, N. H., 'Vertically Aligned Nanostructured Topographies for Human Neural Stem Cell Differentiation and Neuronal Cell Interrogation', *Adv. Ther.* **2021**, *4*(9), 2100061, cited on page(s): 2.

(40) Velasco, V.; Shariati, S. A.; Esfandyarpour, R., 'Microtechnology-based methods for organoid models', *Microsystems Nanoeng.* **2020**, *6*(1), 76, cited on page(s): 2, 44.

(41) Rodrigues, R. O.; Sousa, P. C.; Gaspar, J.; Bañobre-López, M.; Lima, R.; Minas, G., 'Organ-on-a-Chip: A Preclinical Microfluidic Platform for the Progress of Nanomedicine', *Small* **2020**, *16*(51), 2003517, cited on page(s): 2.

(42) Hoang, P.; Ma, Z., 'Biomaterial-guided stem cell organoid engineering for modeling development and diseases', *Acta Biomater.* **2021**, *132*, 23–36, cited on page(s): 2.

(43) Gao, J.; Liao, C.; Liu, S.; Xia, T.; Jiang, G., 'Nanotechnology: new opportunities for the development of patch-clamps', *J. Nanobiotechnology* **2021**, *19*(1), 97, cited on page(s): 2.

(44) Lee, J. M.; Lin, D.; Kim, H.-R.; Pyo, Y.-W., *et al.*, 'All-Tissue-like Multifunctional Optoelectronic Mesh for Deep-Brain Modulation and Mapping', *Nano Lett.* **2021**, *21*(7), 3184–3190, cited on page(s): 2.

(45) Forro, C.; Caron, D.; Angotzi, G.; Gallo, V., *et al.*, 'Electrophysiology Read-Out Tools for Brain-on-Chip Biotechnology', *Micromachines* **2021**, *12*(2), 124, cited on page(s): 2, 45.

(46) Nguyen, A. K.; Narayan, R. J., 'Two-photon polymerization for biological applications', *Mater. Today* **2017**, *20*(6), 314–322, cited on page(s): 2.

(47) Ovsianikov, A.; Schlie, S.; Ngezahayo, A.; Haverich, A.; Chichkov, B. N., 'Two-photon polymerization technique for microfabrication of CAD-designed 3D scaffolds from commercially available photosensitive materials', *J. Tissue Eng. Regen. Med.* **2007**, *1*(6), 443–449, cited on page(s): 2.

(48) Niesler, F.; Hermatschweiler, M., 'Two-Photon Polymerization - A Versatile Microfabrication Tool', *Laser Tech. J.* **2015**, *12*(3), 44–47, cited on page(s): 2.

(49) Agrawal, L.; Saidani, M.; Guillaud, L.; Terenzio, M., 'Development of 3D culture scaffolds for directional neuronal growth using 2-photon lithography', *Mater. Sci. Eng. C* **2021**, *131*, 112502, cited on page(s): 2.

(50) Yoh, H.; Aslanoglou, S.; Lestrell, E.; Shokouhi, A.-R., *et al.*, 'Cellular nanotechnologies: Orchestrating cellular processes by engineering silicon nanowires architectures', *Semicond. Silicon Nanowires Biomed. Appl.* Elsevier **2022**, ISBN: 978-0-12-821351-3, 231–278, cited on page(s): 3.

(51) Buch-Månson, N.; Bonde, S.; Bolinsson, J.; Berthing, T.; Nygård, J.; Martinez, K. L., 'Towards a Better Prediction of Cell Settling on Nanostructure Arrays-Simple Means to Complicated Ends', *Adv. Funct. Mater.* **2015**, *25*(21), 3246–3255, cited on page(s): 3.

(52) Berthing, T.; Bonde, S.; Rostgaard, K. R.; Madsen, M. H., *et al.*, 'Cell membrane conformation at vertical nanowire array interface revealed by fluorescence imaging', *Nanotechnology* **2012**, *23*(41), 415102, cited on page(s): 3, 24.

(53) Berthing, T.; Bonde, S.; Sørensen, C. B.; Utko, P.; Nygård, J.; Martinez, K. L., 'Intact Mammalian Cell Function on Semiconductor Nanowire Arrays: New Perspectives for Cell-Based Biosensing', *Small* **2011**, *7*(5), 640–647, cited on page(s): 3, 20.

(54) Elnathan, R.; Kwiat, M.; Patolsky, F.; Voelcker, N. H., 'Engineering vertically aligned semiconductor nanowire arrays for applications in the life sciences', *Nano Today* **2014**, *9*(2), 172–196, cited on page(s): 3.

(55) Bonde, S.; Buch-Månson, N.; Rostgaard, K. R.; Andersen, T. K.; Berthing, T.; Martinez, K. L., 'Exploring arrays of vertical one-dimensional nanostructures for cellular investigations', *Nanotechnology* **2014**, *25*(36), 362001, cited on page(s): 3.

(56) Frederiksen, R. S.; Alarcon-Llado, E.; Krogstrup, P.; Bojarskaite, L., *et al.*, 'Nanowire-Aperture Probe: Local Enhanced Fluorescence Detection for the Investigation of Live Cells at the Nanoscale', *ACS Photonics* **2016**, *3*(7), 1208–1216, cited on page(s): 3.

(57) Verardo, D.; Lindberg, F. W.; Anttu, N.; Niman, C. S., *et al.*, 'Nanowires for Biosensing: Lightguiding of Fluorescence as a Function of Diameter and Wavelength', *Nano Lett.* **2018**, *18*(8), 4796–4802, cited on page(s): 3.

(58) Lard, M.; Linke, H.; Prinz, C. N., 'Biosensing using arrays of vertical semiconductor nanowires: mechanosensing and biomarker detection', *Nanotechnology* **2019**, *30*(21), 214003, cited on page(s): 3.

(59) Schaumann, E. N.; Tian, B., 'Biological Interfaces, Modulation, and Sensing with Inorganic Nano-Bioelectronic Materials', *Small Methods* **2020**, *4*(5), 1900868, cited on page(s): 3.

(60) He, G.; Hu, N.; Xu, A. M.; Li, X.; Zhao, Y.; Xie, X., 'Nanoneedle Platforms: The Many Ways to Pierce the Cell Membrane', *Adv. Funct. Mater.* **2020**, *30*(21), 1909890, cited on page(s): 3.

(61) Li, X.; Zhang, W.; Tsai, C.-T.; Cui, B., 'Vertical nanostructures for probing live cells', *Micro Nano Syst. Biophys. Stud. Cells Small Org.* Elsevier **2021**, ISBN: 978-0-12-823990-2, 43–70, cited on page(s): 3.

(62) Hällström, W.; Mårtensson, T.; Prinz, C.; Gustavsson, P., *et al.*, 'Gallium Phosphide Nanowires as a Substrate for Cultured Neurons', *Nano Lett.* **2007**, *7*(10), 2960–2965, cited on page(s): 4, 20.

(63) Lee, J.; Kang, B. S.; Hicks, B.; Chancellor Jr., T. F., *et al.*, 'The control of cell adhesion and viability by zinc oxide nanorods', *Biomaterials* **2008**, *29*(27), 3743–3749, cited on page(s): 4.

(64) Li, Z.; Yang, R.; Yu, M.; Bai, F.; Li, C.; Wang, Z. L., 'Cellular Level Biocompatibility and Biosafety of ZnO Nanowires', *J. Phys. Chem. C* **2008**, *112*(51), 20114–20117, cited on page(s): 4.

(65) Qi, S.; Yi, C.; Ji, S.; Fong, C.-C.; Yang, M., 'Cell Adhesion and Spreading Behavior on Vertically Aligned Silicon Nanowire Arrays', *ACS Appl. Mater. Interfaces* **2009**, *1*(1), 30–34, cited on page(s): 4.

(66) Piret, G.; Galopin, E.; Coffinier, Y.; Boukherroub, R.; Legrand, D.; Slomianny, C., 'Culture of mammalian cells on patterned superhydrophilic/superhydrophobic silicon nanowire arrays', *Soft Matter* **2011**, *7*(18), 8642, cited on page(s): 4.

(67) Dinan, B.; Gallego-Perez, D.; Lee, H.; Hansford, D.; Akbar, S., 'Thermally grown TiO$_2$ nanowires to improve cell growth and proliferation on titanium based materials', *Ceram. Int.* **2013**, *39*(5), 5949–5954, cited on page(s): 4.

(68) Piret, G.; Perez, M.-T.; Prinz, C. N., 'Neurite outgrowth and synaptophysin expression of postnatal CNS neurons on GaP nanowire arrays in long-term retinal cell culture', *Biomaterials* **2013**, *34*(4), 875–887, cited on page(s): 4, 26.

(69) Piret, G.; Perez, M. T.; Prinz, C. N., 'Substrate porosity induces phenotypic alterations in retinal cells cultured on silicon nanowires', *RSC Adv.* **2014**, *4*(53), 27888–27897, cited on page(s): 4.

(70) Persson, H.; Købler, C.; Mølhave, K.; Samuelson, L., *et al.*, 'Fibroblasts Cultured on Nanowires Exhibit Low Motility, Impaired Cell Division, and DNA Damage', *Small* **2013**, *9*(23), 4006–4016, cited on page(s): 4, 20, 23.

(71) Bonde, S.; Berthing, T.; Madsen, M. H.; Andersen, T. K., *et al.*, 'Tuning InAs Nanowire Density for HEK293 Cell Viability, Adhesion, and Morphology: Perspectives for Nanowire-Based Biosensors', *ACS Appl. Mater. Interfaces* **2013**, *5*(21), 10510–10519, cited on page(s): 4.

(72) Beckwith, K. S.; Cooil, S. P.; Wells, J. W.; Sikorski, P., 'Tunable high aspect ratio polymer nanostructures for cell interfaces', *Nanoscale* **2015**, *7*(18), 8438–8450, cited on page(s): 4.

(73) Persson, H.; Li, Z.; Tegenfeldt, J. O.; Oredsson, S.; Prinz, C. N., 'From immobilized cells to motile cells on a bed-of-nails: effects of vertical nanowire array density on cell behaviour', *Sci. Rep.* **2015**, *5*(1), 18535, cited on page(s): 4, 27.

(74) Buch-Månson, N.; Kang, D.-H.; Kim, D.; Lee, K. E.; Yoon, M.-H.; Martinez, K. L., 'Mapping cell behavior across a wide range of vertical silicon nanocolumn densities', *Nanoscale* **2017**, *9*(17), 5517–5527, cited on page(s): 4.

(75) Li, Z.; Kamlund, S.; Ryser, T.; Lard, M.; Oredsson, S.; Prinz, C. N., 'Single cell analysis of proliferation and movement of cancer and normal-like cells on nanowire array substrates', *J. Mater. Chem. B* **2018**, *6*(43), 7042–7049, cited on page(s): 4.

(76) Li, Z.; Persson, H.; Adolfsson, K.; Oredsson, S.; Prinz, C. N., 'Morphology of living cells cultured on nanowire arrays with varying nanowire densities and diameters', *Sci. China Life Sci.* **2018**, *61*(4), 427–435, cited on page(s): 4.

(77) Beckwith, K. S.; Ullmann, S.; Vinje, J.; Sikorski, P., 'Influence of Nanopillar Arrays on Fibroblast Motility, Adhesion, and Migration Mechanisms', *Small* **2019**, *15*(43), 1902514, cited on page(s): 4.

(78) Seo, J.; Lanara, C.; Choi, J. Y.; Kim, J., *et al.*, 'Neuronal Migration on Silicon Microcone Arrays with Different Pitches', *Adv. Healthc. Mater.* **2021**, *10*(4), 2000583, cited on page(s): 4.

(79) Paria, D.; Convertino, A.; Raj, P.; Glunde, K.; Chen, Y.; Barman, I., 'Nanowire Assisted Mechanotyping of Cellular Metastatic Potential', *Adv. Funct. Mater.* **2021**, *31*(30), 2101638, cited on page(s): 4.

(80) Kang, D.-H.; Lee, S.; Kim, J. H.; Kim, D., *et al.*, 'Large-Area Vertical Silicon Nanocolumn Arrays for Versatile Cell Interfaces', *ACS Appl. Nano Mater.* **2021**, *4*(3), 2528–2537, cited on page(s): 4.

(81) Nouri-Goushki, M.; Angeloni, L.; Modaresifar, K.; Minneboo, M., *et al.*, '3D-Printed Submicron Patterns Reveal the Interrelation between Cell Adhesion, Cell Mechanics, and Osteogenesis', *ACS Appl. Mater. Interfaces* **2021**, *13*(29), 33767–33781, cited on page(s): 4.

(82) Li, Z.; Song, J.; Mantini, G.; Lu, M. Y., *et al.*, 'Quantifying the traction force of a single cell by aligned silicon nanowire array', *Nano Lett.* **2009**, *9*(10), 3575–3580, cited on page(s): 4.

(83) Hällström, W.; Lexholm, M.; Suyatin, D. B.; Hammarin, G., *et al.*, 'Fifteen-Piconewton Force Detection from Neural Growth Cones Using Nanowire Arrays', *Nano Lett.* **2010**, *10*(3), 782–787, cited on page(s): 4.

(84) Li, Z.; Persson, H.; Adolfsson, K.; Abariute, L., *et al.*, 'Cellular traction forces: a useful parameter in cancer research', *Nanoscale* **2017**, *9*(48), 19039–19044, cited on page(s): 4.

(85) Obenaus, A. M.; Mollica, M. Y.; Sniadecki, N. J., '(De)form and Function: Measuring Cellular Forces with Deformable Materials and Deformable Structures', *Adv. Healthc. Mater.* **2020**, *9*(8), 1901454, cited on page(s): 4.

(86) Hanson, L.; Zhao, W.; Lou, H.-Y.; Lin, Z. C., *et al.*, 'Vertical nanopillars for in situ probing of nuclear mechanics in adherent cells', *Nat. Nanotechnol.* **2015**, *10*(6), 554–562, cited on page(s): 4.

(87) Zeng, Y.; Ramani, P. D.; Gao, W.; Zhao, W., 'Revealing the heterogeneity in neuroblastoma cells via nanopillar-guided subnuclear deformation', *Nanoscale* **2022**, *14*(7), 2617–2627, cited on page(s): 4.

(88) Lou, H.-Y.; Zhao, W.; Li, X.; Duan, L., *et al.*, 'Membrane curvature underlies actin reorganization in response to nanoscale surface topography', *Proc. Natl. Acad. Sci.* **2019**, *116*(46), 23143–23151, cited on page(s): 4.

(89) Hansel, C. S.; Crowder, S. W.; Cooper, S.; Gopal, S., *et al.*, 'Nanoneedle-Mediated Stimulation of Cell Mechanotransduction Machinery', *ACS Nano* **2019**, *13*(3), 2913–2926, cited on page(s): 4.

(90) Hällström, W.; Prinz, C. N.; Suyatin, D.; Samuelson, L.; Montelius, L.; Kanje, M., 'Rectifying and Sorting of Regenerating Axons by Free-Standing Nanowire Patterns: A Highway for Nerve Fibers', *Langmuir* **2009**, *25*(8), 4343–4346, cited on page(s): 4.

(91) Bucaro, M. A.; Vasquez, Y.; Hatton, B. D.; Aizenberg, J., 'Fine-Tuning the Degree of Stem Cell Polarization and Alignment on Ordered Arrays of High-Aspect-Ratio Nanopillars', *ACS Nano* **2012**, *6*(7), 6222–6230, cited on page(s): 4, 21.

(92) Piret, G. G.; Perez, M.-T.; Prinz, C. N., 'Support of Neuronal Growth Over Glial Growth and Guidance of Optic Nerve Axons by Vertical Nanowire Arrays', *Appl. Mater. Interfaces* **2015**, *7*(34), 7–11, cited on page(s): 4.

(93) Park, M.; Oh, E.; Seo, J.; Kim, M.-H., *et al.*, 'Control over Neurite Directionality and Neurite Elongation on Anisotropic Micropillar Arrays', *Small* **2016**, *12*(9), 1148–1152, cited on page(s): 4, 21.

(94) Gautam, V.; Naureen, S.; Shahid, N.; Gao, Q., *et al.*, 'Engineering Highly Interconnected Neuronal Networks on Nanowire Scaffolds', *Nano Lett.* **2017**, *17*(6), 3369–3375, cited on page(s): 4, 21, 24.

(95) Buch-Månson, N.; Spangenberg, A.; Gomez, L. P. C.; Malval, J.-P.; Soppera, O.; Martinez, K. L., 'Rapid Prototyping of Polymeric Nanopillars by 3D Direct Laser Writing for Controlling Cell Behavior', *Sci. Rep.* **2017**, *7*(1), 9247, cited on page(s): 4, 21, 23.

(96) Amin, H.; Dipalo, M.; De Angelis, F.; Berdondini, L., 'Biofunctionalized 3D Nanopillar Arrays Fostering Cell Guidance and Promoting Synapse Stability and Neuronal Activity in Networks', *ACS Appl. Mater. Interfaces* **2018**, *10*(17), 15207–15215, cited on page(s): 4, 21.

(97) Seo, J.; Kim, J.; Joo, S.; Choi, J. Y., *et al.*, 'Nanotopography-Promoted Formation of Axon Collateral Branches of Hippocampal Neurons', *Small* **2018**, *14*(33), 1801763, cited on page(s): 4.

(98) Milos, F.; Belu, A.; Mayer, D.; Maybeck, V.; Offenhäusser, A., 'Polymer Nanopillars Induce Increased Paxillin Adhesion Assembly and Promote Axon Growth in Primary Cortical Neurons', *Adv. Biol.* **2021**, *5*(2), 2000248, cited on page(s): 4, 21.

(99) Fan, S.; Qi, L.; Li, J.; Pan, D., *et al.*, 'Guiding the Patterned Growth of Neuronal Axons and Dendrites Using Anisotropic Micropillar Scaffolds', *Adv. Healthc. Mater.* **2021**, *10*(12), 2100094, cited on page(s): 4.

(100) Kim, W.; Ng, J. K.; Kunitake, M. E.; Conklin, B. R.; Yang, P., 'Interfacing Silicon Nanowires with Mammalian Cells', *J. Am. Chem. Soc.* **2007**, *129*(23), 7228–7229, cited on page(s): 4.

(101) Xu, A. M.; Aalipour, A.; Leal-Ortiz, S.; Mekhdjian, A. H., *et al.*, 'Quantification of nanowire penetration into living cells', *Nat. Commun.* **2014**, *5*(1), 3613, cited on page(s): 4.

(102) Elnathan, R.; Delalat, B.; Brodoceanu, D.; Alhmoud, H., *et al.*, 'Maximizing Transfection Efficiency of Vertically Aligned Silicon Nanowire Arrays', *Adv. Funct. Mater.* **2015**, *25*(46), 7215–7225, cited on page(s): 4.

(103) Hou, S.; Choi, J.-s.; Chen, K.-J.; Zhang, Y., *et al.*, 'Supramolecular Nanosubstrate-Mediated Delivery for Reprogramming and Transdifferentiation of Mammalian Cells', *Small* **2015**, *11*(21), 2499–2504, cited on page(s): 4.

(104) Chen, Y.; Aslanoglou, S.; Gervinskas, G.; Abdelmaksoud, H.; Voelcker, N. H.; Elnathan, R., 'Cellular Deformations Induced by Conical Silicon Nanowire Arrays Facilitate Gene Delivery', *Small* **2019**, *15*(47), 1904819, cited on page(s): 4, 26.

(105) Shalek, A. K.; Robinson, J. T.; Karp, E. S.; Lee, J. S., *et al.*, 'Vertical silicon nanowires as a universal platform for delivering biomolecules into living cells', *Proc. Natl. Acad. Sci.* **2010**, *107*(5), 1870–1875, cited on page(s): 4.

(106) VanDersarl, J. J.; Xu, A. M.; Melosh, N. A., 'Nanostraws for Direct Fluidic Intracellular Access', *Nano Lett.* **2012**, *12*(8), 3881–3886, cited on page(s): 4, 41.

(107) Wang, Y.; Yang, Y.; Yan, L.; Kwok, S. Y., *et al.*, 'Poking cells for efficient vector-free intracellular delivery', *Nat. Commun.* **2014**, *5*(1), 4466, cited on page(s): 4, 23.

(108) Xie, X.; Aalipour, A.; Gupta, S. V.; Melosh, N. A., 'Determining the Time Window for Dynamic Nanowire Cell Penetration Processes', *ACS Nano* **2015**, *9*(12), 11667–11677, cited on page(s): 4.

(109) Chiappini, C.; De Rosa, E.; Martinez, J. O.; Liu, X., *et al.*, 'Biodegradable silicon nanoneedles delivering nucleic acids intracellularly induce localized in vivo neovascularization', *Nat. Mater.* **2015**, *14*(5), 532–539, cited on page(s): 4, 41.

(110) Chiappini, C.; Martinez, J. O.; De Rosa, E.; Almeida, C. S.; Tasciotti, E.; Stevens, M. M., 'Biodegradable Nanoneedles for Localized Delivery of Nanoparticles in Vivo: Exploring the Biointerface', *ACS Nano* **2015**, *9*(5), 5500–5509, cited on page(s): 4.

(111) Cao, Y; Chen, H; Qiu, R; Hanna, M, *et al.*, 'Universal intracellular biomolecule delivery with precise dosage control', *Sci. Adv.* **2018**, *4*(10), eaat8131, cited on page(s): 4.

(112) Gopal, S.; Chiappini, C.; Penders, J.; Leonardo, V., *et al.*, 'Porous Silicon Nanoneedles Modulate Endocytosis to Deliver Biological Payloads', *Adv. Mater.* **2019**, *31*(12), 1806788, cited on page(s): 4, 26, 41.

(113) Hebisch, E.; Hjort, M.; Volpati, D.; Prinz, C. N., 'Nanostraw-Assisted Cellular Injection of Fluorescent Nanodiamonds via Direct Membrane Opening', *Small* **2021**, *17*(7), 2006421, cited on page(s): 4, 41.

(114) Cao, Y.; Hjort, M.; Chen, H.; Birey, F., *et al.*, 'Nondestructive nanostraw intracellular sampling for longitudinal cell monitoring', *Proc. Natl. Acad. Sci. U. S. A.* **2017**, *114*(10), E1866–E1874, cited on page(s): 4, 41.

(115) Tay, A.; Melosh, N., 'Nanostructured Materials for Intracellular Cargo Delivery', *Acc. Chem. Res.* **2019**, *52*(9), 2462–2471, cited on page(s): 4.

(116) Bhingardive, V.; Le Saux, G.; Edri, A.; Porgador, A.; Schvartzman, M., 'Nanowire Based Guidance of the Morphology and Cytotoxic Activity of Natural Killer Cells', *Small* **2021**, *17*(14), 2007347, cited on page(s): 4.

(117) Bhingardive, V.; Kossover, A.; Iraqi, M.; Khand, B., *et al.*, 'Antibody-Functionalized Nanowires: A Tuner for the Activation of T Cells', *Nano Lett.* **2021**, *21*(10), 4241–4248, cited on page(s): 4.

(118) Zhu, X.; Yuen, M. F.; Yan, L.; Zhang, Z., *et al.*, 'Diamond-Nanoneedle-Array-Facilitated Intracellular Delivery and the Potential Influence on Cell Physiology', *Adv. Healthc. Mater.* **2016**, *5*(10), 1157–1168, cited on page(s): 4.

(119) Lestrell, E.; Patolsky, F.; Voelcker, N. H.; Elnathan, R., 'Engineered nano-bio interfaces for intracellular delivery and sampling: Applications, agency and artefacts', *Mater. Today* **2020**, *33*, 87–104, cited on page(s): 4.

(120) Yoh, H. Z.; Chen, Y.; Aslanoglou, S.; Wong, S., *et al.*, 'Polymeric Nanoneedle Arrays Mediate Stiffness-Independent Intracellular Delivery', *Adv. Funct. Mater.* **2022**, *32*(3), 2104828, cited on page(s): 4.

(121) Chen, Y.; Wang, J.; Li, X.; Hu, N., *et al.*, 'Emerging Roles of 1D Vertical Nanostructures in Orchestrating Immune Cell Functions', *Adv. Mater.* **2020**, *32*(40), 2001668, cited on page(s): 4.

(122) Brooks, J.; Minnick, G.; Mukherjee, P.; Jaberi, A., *et al.*, 'High Throughput and Highly Controllable Methods for In Vitro Intracellular Delivery', *Small* **2020**, *16*(51), 2004917, cited on page(s): 4.

(123) Tay, A.; Melosh, N., 'Mechanical Stimulation after Centrifuge-Free Nano-Electroporative Transfection Is Efficient and Maintains Long-Term T Cell Functionalities', *Small* **2021**, *17*(38), 2103198, cited on page(s): 4.

(124) Xie, C.; Lin, Z.; Hanson, L.; Cui, Y.; Cui, B., 'Intracellular recording of action potentials by nanopillar electroporation', *Nat. Nanotechnol.* **2012**, *7*(3), 185–190, cited on page(s): 4.

(125) Robinson, J. T.; Jorgolli, M.; Shalek, A. K.; Yoon, M.-H.; Gertner, R. S.; Park, H., 'Vertical nanowire electrode arrays as a scalable platform for intracellular interfacing to neuronal circuits', *Nat. Nanotechnol.* **2012**, *7*(3), 180–184, cited on page(s): 4, 42.

(126) Suyatin, D. B.; Wallman, L.; Thelin, J.; Prinz, C. N., *et al.*, 'Nanowire-Based Electrode for Acute In Vivo Neural Recordings in the Brain', *PLoS One* **2013**, *8*(2), e56673, cited on page(s): 4.

(127) Robinson, J. T.; Jorgolli, M.; Park, H., 'Nanowire electrodes for high-density stimulation and measurement of neural circuits', *Front. Neural Circuits* **2013**, *7*, 38, cited on page(s): 4.

(128) Lee, K.-Y.; Kim, I.; Kim, S.-E.; Jeong, D.-W., *et al.*, 'Vertical nanowire probes for intracellular signaling of living cells.' *Nanoscale Res. Lett.* **2014**, *9*(1), 56, cited on page(s): 4.

(129) Lin, Z. C.; Xie, C.; Osakada, Y.; Cui, Y.; Cui, B., 'Iridium oxide nanotube electrodes for sensitive and prolonged intracellular measurement of action potentials', *Nat. Commun.* **2014**, *5*(1), 3206, cited on page(s): 4.

(130) Santoro, F.; Dasgupta, S.; Schnitker, J.; Auth, T., *et al.*, 'Interfacing Electrogenic Cells with 3D Nanoelectrodes: Position, Shape, and Size Matter', *ACS Nano* **2014**, *8*(7), 6713–6723, cited on page(s): 4, 42.

(131) Liu, R.; Chen, R.; Elthakeb, A. T.; Lee, S. H., *et al.*, 'High Density Individually Addressable Nanowire Arrays Record Intracellular Activity from Primary Rodent and Human Stem Cell Derived Neurons', *Nano Lett.* **2017**, *17*(5), 2757–2764, cited on page(s): 4, 42.

(132) Lin, Z. C.; McGuire, A. F.; Burridge, P. W.; Matsa, E., *et al.*, 'Accurate nanoelectrode recording of human pluripotent stem cell-derived cardiomyocytes for assaying drugs and modeling disease', *Microsystems Nanoeng.* **2017**, *3*(1), 16080, cited on page(s): 4.

(133) Staufer, O.; Weber, S.; Bengtson, C. P.; Bading, H.; Rustom, A.; Spatz, J. P., 'Adhesion Stabilized en Masse Intracellular Electrical Recordings from Multicellular Assemblies', *Nano Lett.* **2019**, *19*(5), 3244–3255, cited on page(s): 4.

(134) Kwon, J.; Lee, J. S.; Lee, J.; Na, J., *et al.*, 'Vertical Nanowire Electrode Array for Enhanced Neurogenesis of Human Neural Stem Cells via Intracellular Electrical Stimulation', *Nano Lett.* **2021**, *21*(14), 6343–6351, cited on page(s): 4, 42.

(135) Mariano, A.; Lubrano, C.; Bruno, U.; Ausilio, C.; Dinger, N. B.; Santoro, F., 'Advances in Cell-Conductive Polymer Biointerfaces and Role of the Plasma Membrane', *Chem. Rev.* **2022**, *122*(4), 4552–4580, cited on page(s): 4.

(136) Jahed, Z.; Yang, Y.; Tsai, C.-T.; Foster, E. P., *et al.*, 'Nanocrown electrodes for parallel and robust intracellular recording of cardiomyocytes', *Nat. Commun.* **2022**, *13*(1), 2253, cited on page(s): 4.

(137) Liu, R.; Lee, J.; Tchoe, Y.; Pre, D., *et al.*, 'Ultra-Sharp Nanowire Arrays Natively Permeate, Record, and Stimulate Intracellular Activity in Neuronal and Cardiac Networks', *Adv. Funct. Mater.* **2022**, *32*(8), 2108378, cited on page(s): 4.

(138) Parameswaran, R.; Carvalho-de Souza, J. L.; Jiang, Y.; Burke, M. J., *et al.*, 'Photoelectrochemical modulation of neuronal activity with free-standing coaxial silicon nanowires', *Nat. Nanotechnol.* **2018**, *13*(3), 260–266, cited on page(s): 4, 42.

(139) Parameswaran, R.; Koehler, K.; Rotenberg, M. Y.; Burke, M. J., *et al.*, 'Optical stimulation of cardiac cells with a polymer-supported silicon nanowire matrix', *Proc. Natl. Acad. Sci.* **2019**, *116*(2), 413–421, cited on page(s): 4, 42.

(140) Tang, J.; Qin, N.; Chong, Y.; Diao, Y., *et al.*, 'Nanowire arrays restore vision in blind mice', *Nat. Commun.* **2018**, *9*(1), 786, cited on page(s): 4, 43.

(141) Liu, Z.; Wen, B.; Cao, L.; Zhang, S., *et al.*, 'Photoelectric Cardiac Pacing by Flexible and Degradable Amorphous Si Radial Junction Stimulators', *Adv. Healthc. Mater.* **2020**, *9*(1), 1901342, cited on page(s): 4, 42.

(142) Elnathan, R.; Holle, A. W.; Young, J.; George, M. A., *et al.*, 'Optically transparent vertical silicon nanowire arrays for live-cell imaging', *J. Nanobiotechnology* **2021**, *19*(1), 51, cited on page(s): 4.

(143) Acaron Ledesma, H.; Tian, B., 'Nanoscale silicon for subcellular biointerfaces', *J. Mater. Chem. B* **2017**, *5*(23), 4276–4289, cited on page(s): 4.

(144) Fairfield, J. A., 'Nanostructured Materials for Neural Electrical Interfaces', *Adv. Funct. Mater.* **2018**, *28*(12), 1701145, cited on page(s): 4.

(145) Acarón Ledesma, H.; Li, X.; Carvalho-de Souza, J. L.; Wei, W.; Bezanilla, F.; Tian, B., 'An atlas of nano-enabled neural interfaces', *Nat. Nanotechnol.* **2019**, *14*(7), 645–657, cited on page(s): 4.

(146) Frank, J. A.; Antonini, M.-J.; Anikeeva, P., 'Next-generation interfaces for studying neural function', *Nat. Biotechnol.* **2019**, *37*(9), 1013–1023, cited on page(s): 4.

(147) Hong, G.; Lieber, C. M., 'Novel electrode technologies for neural recordings', *Nat. Rev. Neurosci.* **2019**, *20*(6), 330–345, cited on page(s): 4.

(148) Lou, H.-Y.; Zhao, W.; Zeng, Y.; Cui, B., 'The Role of Membrane Curvature in Nanoscale Topography-Induced Intracellular Signaling', *Acc. Chem. Res.* **2018**, *51*(5), 1046–1053, cited on page(s): 4.

(149) Liu, R.; Ding, J., 'Chromosomal Repositioning and Gene Regulation of Cells on a Micropillar Array', *ACS Appl. Mater. Interfaces* **2020**, *12*(32), 35799–35812, cited on page(s): 4.

(150) Seong, H.; Higgins, S. G.; Penders, J.; Armstrong, J. P. K., *et al.*, 'Size-Tunable Nanoneedle Arrays for Influencing Stem Cell Morphology, Gene Expression, and Nuclear Membrane Curvature', *ACS Nano* **2020**, *14*(5), 5371–5381, cited on page(s): 4.

(151) Migliorini, E.; Grenci, G.; Ban, J.; Pozzato, A., *et al.*, 'Acceleration of neuronal precursors differentiation induced by substrate nanotopography', *Biotechnol. Bioeng.* **2011**, *108*(11), 2736–2746, cited on page(s): 4.

(152) Kim, H. S.; Yoo, H. S., 'Differentiation and focal adhesion of adipose-derived stem cells on nano-pillars arrays with different spacing', *RSC Adv.* **2015**, *5*(61), 49508–49512, cited on page(s): 4.

(153) Kim, H.; Kim, I.; Choi, H.-J.; Kim, S. Y.; Yang, E. G., 'Neuron-like differentiation of mesenchymal stem cells on silicon nanowires', *Nanoscale* **2015**, *7*(40), 17131–17138, cited on page(s): 4, 21, 27.

(154) Rasmussen, C. H.; Reynolds, P. M.; Petersen, D. R.; Hansson, M., *et al.*, 'Enhanced Differentiation of Human Embryonic Stem Cells Toward Definitive Endoderm on Ultrahigh Aspect Ratio Nanopillars', *Adv. Funct. Mater.* **2016**, *26*(6), 815–823, cited on page(s): 4, 27.

(155) Yan, Q.; Fang, L.; Wei, J.; Xiao, G., *et al.*, 'Silicon nanowires enhanced proliferation and neuronal differentiation of neural stem cell with vertically surface microenvironment', *J. Biomater. Sci. Polym. Ed.* **2017**, *28*(13), 1394–1407, cited on page(s): 4, 20.

(156) Raos, B.; Maddah, M.; Graham, E.; Plank, N.; Unsworth, C., 'ZnO nanowire florets promote the growth of human neurons', *Materialia* **2020**, *9*, 100577, cited on page(s): 4.

(157) Crowder, S. W.; Leonardo, V.; Whittaker, T.; Papathanasiou, P.; Stevens, M. M., 'Material Cues as Potent Regulators of Epigenetics and Stem Cell Function', *Cell Stem Cell* **2016**, *18*(1), 39–52, cited on page(s): 4.

(158) SenGupta, S.; Parent, C. A.; Bear, J. E., 'The principles of directed cell migration', *Nat. Rev. Mol. Cell Biol.* **2021**, *22*(8), 529–547, cited on page(s): 4.

(159) Tessier-Lavigne, M.; Placzek, M.; Lumsden, A. G. S.; Dodd, J.; Jessell, T. M., 'Chemotropic guidance of developing axons in the mammalian central nervous system', *Nature* **1988**, *336*(6201), 775–778, cited on page(s): 4.

(160) Kim, Y. H.; Baek, N. S.; Han, Y. H.; Chung, M. A.; Jung, S. D., 'Enhancement of neuronal cell adhesion by covalent binding of poly-d-lysine', *J. Neurosci. Methods* **2011**, *202*(1), 38–44, cited on page(s): 4, 33.

(161) Wyart, C.; Ybert, C.; Bourdieu, L.; Herr, C.; Prinz, C.; Chatenay, D., 'Constrained synaptic connectivity in functional mammalian neuronal networks grown on patterned surfaces', *J. Neurosci. Methods* **2002**, *117*(2), 123–131, cited on page(s): 4, 33.

(162) Fricke, R.; Zentis, P. D.; Rajappa, L. T.; Hofmann, B., *et al.*, 'Axon guidance of rat cortical neurons by microcontact printed gradients', *Biomaterials* **2011**, *32*(8), 2070–2076, cited on page(s): 4, 33.

(163) Ge, H.; Yu, A.; Chen, J.; Yuan, J., *et al.*, 'Poly-L-ornithine enhances migration of neural stem/progenitor cells via promoting α-Actinin 4 binding to actin filaments', *Sci. Rep.* **2016**, *6*(1), 37681, cited on page(s): 4.

(164) Segerer, F. J.; Röttgermann, P. J. F.; Schuster, S.; Alberola, A. P.; Zahler, S.; Rädler, J. O., 'A versatile method to generate multiple types of micropatterns', **2015**, *011005*, cited on page(s): 4.

(165) Joseph, G.; Orme, R. P.; Kyriacou, T.; Fricker, R. A.; Roach, P., 'Effects of Surface Chemistry Interaction on Primary Neural Stem Cell Neurosphere Responses', *ACS Omega* **2021**, *6*(30), 19901–19910, cited on page(s): 5.

(166) Milky, B.; Zabolocki, M.; Al-Bataineh, S. A.; van den Hurk, M., *et al.*, 'Long-term adherence of human brain cells in vitro is enhanced by charged amine-based plasma polymer coatings', *Stem Cell Reports* **2022**, cited on page(s): 5.

(167) Gundersen, R., 'Sensory neurite growth cone guidance by substrate adsorbed nerve growth factor', *J. Neurosci. Res.* **1985**, *13*(1-2), 199–212, cited on page(s): 5.

(168) Kleinfeld, D.; Kahler, K.; Hockberger, P., 'Controlled outgrowth of dissociated neurons on patterned substrates', *J. Neurosci.* **1988**, *8*(11), 4098–4120, cited on page(s): 5.

(169) Oliva, A. A.; James, C. D.; Kingman, C. E.; Craighead, H. G.; Banker, G. A., 'Patterning axonal guidance molecules using a novel strategy for microcontact printing.' *Neurochem. Res.* **2003**, *28*(11), 1639–48, cited on page(s): 5.

(170) Miller, C.; Jeftinija, S.; Mallapragada, S., 'Synergistic Effects of Physical and Chemical Guidance Cues on Neurite Alignment and Outgrowth on Biodegradable Polymer Substrates', *Tissue Eng.* **2002**, *8*(3), 367–378, cited on page(s): 5.

(171) Li, N.; Folch, A., 'Integration of topographical and biochemical cues by axons during growth on microfabricated 3-D substrates', *Exp. Cell Res.* **2005**, *311*(2), 307–316, cited on page(s): 5, 33.

(172) Kundu, A.; Micholt, L.; Friedrich, S.; Rand, D. R., *et al.*, 'Superimposed topographic and chemical cues synergistically guide neurite outgrowth', *Lab Chip* **2013**, *13*(15), 3070, cited on page(s): 5, 21, 24.

(173) Gomez, N.; Chen, S.; Schmidt, C. E., 'Polarization of hippocampal neurons with competitive surface stimuli: contact guidance cues are preferred over chemical ligands', *J. R. Soc. Interface* **2007**, *4*(13), 223–233, cited on page(s): 5, 33, 35.

(174) Leigh, B. L.; Truong, K.; Bartholomew, R.; Ramirez, M.; Hansen, M. R.; Guymon, C. A., 'Tuning Surface and Topographical Features to Investigate Competitive Guidance of Spiral Ganglion Neurons', *ACS Appl. Mater. Interfaces* **2017**, *9*(37), 31488–31496, cited on page(s): 5.

(175) Zou, J.; Jin, K.; Chen, T.; Li, X., 'The effects of substrate morphology by regulating pseudopods formation on cell directional alignment and migration', *J. Phys. D. Appl. Phys.* **2022**, *55*(10), 105401, cited on page(s): 5.

(176) Tooker, A.; Meng, E.; Erickson, J.; Tai, Y.-C.; Pine, J., 'Development of biocompatible parylene neurocages', *26th Annu. Int. Conf. IEEE Eng. Med. Biol. Soc.* **2004**, Vol. 3, 2542–2545, cited on page(s): 5.

(177) Goldner, J. S.; Bruder, J. M.; Li, G.; Gazzola, D.; Hoffman-Kim, D., 'Neurite bridging across micropatterned grooves', *Biomaterials* **2006**, *27*(3), 460–472, cited on page(s): 5.

(178) Francisco, H.; Yellen, B. B.; Halverson, D. S.; Friedman, G.; Gallo, G., 'Regulation of axon guidance and extension by three-dimensional constraints', *Biomaterials* **2007**, *28*(23), 3398–407, cited on page(s): 5.

(179) Scott, M. A.; Wissner-Gross, Z. D.; Yanik, M. F., 'Ultra-rapid laser protein micropatterning: screening for directed polarization of single neurons', *Lab Chip* **2012**, *12*(12), 2265, cited on page(s): 5.

(180) Tuft, B. W.; Xu, L.; White, S. P.; Seline, A. E., *et al.*, 'Neural Pathfinding on Uni- and Multidirectional Photopolymerized Micropatterns', *ACS Appl. Mater. Interfaces* **2014**, *6*(14), 11265–11276, cited on page(s): 5.

(181) Taylor, A. M.; Menon, S.; Gupton, S. L., 'Passive microfluidic chamber for long-term imaging of axon guidance in response to soluble gradients', *Lab Chip* **2015**, *15*(13), 2781–2789, cited on page(s): 5.

(182) Li, W.; Tang, Q. Y.; Jadhav, A. D.; Narang, A., *et al.*, 'Large-scale Topographical Screen for Investigation of Physical Neural-Guidance Cues', *Sci. Rep.* **2015**, *5*(1), 8644, cited on page(s): 5.

(183) Renault, R.; Durand, J.-B.; Viovy, J.-L.; Villard, C., 'Asymmetric axonal edge guidance: a new paradigm for building oriented neuronal networks', *Lab Chip* **2016**, *16*(12), 2188–2191, cited on page(s): 5, 36.

(184) Courte, J.; Renault, R.; Jan, A.; Viovy, J.-L.; Peyrin, J.-M.; Villard, C., 'Reconstruction of directed neuronal networks in a microfluidic device with asymmetric microchannels', *Methods Cell Biol.* Academic Press **2018**, Vol. 148, ISBN: 978-0-12-814284-4, 71–95, cited on page(s): 5.

(185) Holloway, P. M.; Hallinan, G. I.; Hegde, M.; Lane, S. I. R.; Deinhardt, K.; West, J., 'Asymmetric confinement for defining outgrowth directionality', *Lab Chip* **2019**, *19*(8), 1484–1489, cited on page(s): 5.

(186) Fantuzzo, J. A.; Robles, D. A.; Mirabella, V. R.; Hart, R. P.; Pang, Z. P.; Zahn, J. D., 'Development of a high-throughput arrayed neural circuitry platform using human induced neurons for drug screening applications', *Lab Chip* **2020**, *20*(6), 1140–1152, cited on page(s): 5.

(187) Terryn, J.; Welkenhuysen, M.; Krylychkina, O.; Firrincieli, A., *et al.*, 'Topographical Guidance of PSC-Derived Cortical Neurons', *J. Nanomater.* **2018**, *2018*, 1–10, cited on page(s): 5.

(188) Yurchenko, I.; Farwell, M.; Brady, D. D.; Staii, C., 'Neuronal Growth and Formation of Neuron Networks on Directional Surfaces', *Biomimetics* **2021**, *6*(2), 41, cited on page(s): 5.

(189) Lohse, M.; Thesen, M. W.; Haase, A.; Smolka, M., *et al.*, 'Novel Concept of Micro Patterned Micro Titer Plates Fabricated via UV-NIL for Automated Neuronal Cell Assay Read-Out', *Nanomaterials* **2021**, *11*(4), 902, cited on page(s): 5.

(190) Mateus, J. C.; Weaver, S.; van Swaay, D.; Renz, A. F., *et al.*, 'Nanoscale Patterning of In Vitro Neuronal Circuits', *ACS Nano* **2022**, acsnano.1c10750, cited on page(s): 5.

(191) Kaehr, B.; Allen, R.; Javier, D. J.; Currie, J.; Shear, J. B., 'Guiding neuronal development with in situ microfabrication', *Proc. Natl. Acad. Sci.* **2004**, *101*(46), 16104–16108, cited on page(s): 5.

(192) Kaehr, B.; Ertaş, N.; Nielson, R.; Allen, R., *et al.*, 'Direct-Write Fabrication of Functional Protein Matrixes Using a Low-Cost Q-Switched Laser', *Anal. Chem.* **2006**, *78*(9), 3198–3202, cited on page(s): 5.

(193) Marino, A.; Ciofani, G.; Filippeschi, C.; Pellegrino, M., *et al.*, 'Two-Photon Polymerization of Sub-micrometric Patterned Surfaces: Investigation of Cell-Substrate Interactions and Improved Differentiation of Neuron-like Cells', *ACS Appl. Mater. Interfaces* **2013**, *5*(24), 13012–13021, cited on page(s): 5.

(194) Turunen, S.; Käpylä, E.; Lähteenmäki, M.; Ylä-Outinen, L.; Narkilahti, S.; Kellomäki, M., 'Direct laser writing of microstructures for the growth guidance of human pluripotent stem cell derived neuronal cells', *Opt. Lasers Eng.* **2014**, *55*, 197–204, cited on page(s): 5.

(195) Vedaraman, S.; Perez-Tirado, A.; Haraszti, T.; Gerardo-Nava, J.; Nishiguchi, A.; De Laporte, L., 'Anisometric Microstructures to Determine Minimal Critical Physical Cues Required for Neurite Alignment', *Adv. Healthc. Mater.* **2021**, *10*(20), 2100874, cited on page(s): 5.

(196) Hanson, J. N.; Motala, M. J.; Heien, M. L.; Gillette, M.; Sweedler, J.; Nuzzo, R. G., 'Textural guidance cues for controlling process outgrowth of mammalian neurons', *Lab Chip* **2009**, *9*(1), 122–131, cited on page(s): 5.

(197) Santoro, F.; Panaitov, G.; Offenhäusser, A., 'Defined Patterns of Neuronal Networks on 3D Thiol-functionalized Microstructures', *Nano Lett.* **2014**, *14*(12), 6906–6909, cited on page(s): 5.

(198) Yu, M.; Huang, Y.; Ballweg, J.; Shin, H., *et al.*, 'Semiconductor nanomembrane tubes: Three-dimensional confinement for controlled neurite outgrowth', *ACS Nano* **2011**, *5*(4), 2447–2457, cited on page(s): 5.

(199) Bausch, C. S.; Koitmäe, A.; Stava, E.; Price, A., *et al.*, 'Guided neuronal growth on arrays of biofunctionalized GaAs/InGaAs semiconductor microtubes', *Appl. Phys. Lett.* **2013**, *103*(17), 173705, cited on page(s): 5, 33.

(200) Froeter, P.; Huang, Y.; Cangellaris, O. V.; Huang, W., *et al.*, 'Toward Intelligent Synthetic Neural Circuits: Directing and Accelerating Neuron Cell Growth by Self-Rolled-Up Silicon Nitride Microtube Array', *ACS Nano* **2014**, *8*(11), 11108–11117, cited on page(s): 5, 33.

(201) Breslin, S.; O'Driscoll, L., 'Three-dimensional cell culture: the missing link in drug discovery', *Drug Discov. Today* **2013**, *18*(5-6), 240–249, cited on page(s): 5.

(202) Li, S.; Yang, K.; Chen, X.; Zhu, X., *et al.*, 'Simultaneous 2D and 3D cell culture array for multicellular geometry, drug discovery and tumor microenvironment reconstruction', *Biofabrication* **2021**, *13*(4), 045013, cited on page(s): 5.

(203) Weißenbruch, K.; Lemma, E. D.; Hippler, M.; Bastmeyer, M., 'Micro-scaffolds as synthetic cell niches: recent advances and challenges', *Curr. Opin. Biotechnol.* **2022**, *73*, 290–299, cited on page(s): 5.

(204) Jensen, C.; Teng, Y., 'Is It Time to Start Transitioning From 2D to 3D Cell Culture?', *Front. Mol. Biosci.* **2020**, *7*, 33, cited on page(s): 5.

(205) Tibbitt, M. W.; Anseth, K. S., 'Hydrogels as extracellular matrix mimics for 3D cell culture', *Biotechnol. Bioeng.* **2009**, *103*(4), 655–663, cited on page(s): 5.

(206) McManus, M. C.; Boland, E. D.; Simpson, D. G.; Barnes, C. P.; Bowlin, G. L., 'Electrospun fibrinogen: Feasibility as a tissue engineering scaffold in a rat cell culture model', *J. Biomed. Mater. Res. Part A* **2007**, *81A*(2), 299–309, cited on page(s): 5.

(207) El-Sherbiny, I. M.; Yacoub, M. H., 'Hydrogel scaffolds for tissue engineering: Progress and challenges', *Glob. Cardiol. Sci. Pract.* **2013**, *2013*(3), 38, cited on page(s): 5.

(208) Cai, H.; Sharma, S.; Liu, W.; Mu, W., *et al.*, 'Aerogel Microspheres from Natural Cellulose Nanofibrils and Their Application as Cell Culture Scaffold', *Biomacromolecules* **2014**, *15*(7), 2540–2547, cited on page(s): 5.

(209) Liu, H.; Wang, Y.; Cui, K.; Guo, Y.; Zhang, X.; Qin, J., 'Advances in Hydrogels in Organoids and Organs-on-a-Chip', *Adv. Mater.* **2019**, *31*(50), 1902042, cited on page(s): 5.

(210) Li, S.; Severino, F. P. U.; Ban, J.; Wang, L., *et al.*, 'Improved neuron culture using scaffolds made of three-dimensional PDMS micro-lattices', *Biomed. Mater.* **2018**, *13*(3), 034105, cited on page(s): 5.

(211) Li, N.; Zhang, Q.; Gao, S.; Song, Q., *et al.*, 'Three-dimensional graphene foam as a biocompatible and conductive scaffold for neural stem cells', *Sci. Rep.* **2013**, *3*(1), 1604, cited on page(s): 5.

(212) Zhang, X.; Han, F.; Syed, A.; Bukhari, E. M., *et al.*, 'Fabrication of highly modulable fibrous 3D extracellular microenvironments', *Biomed. Microdevices* **2017**, *19*(3), 53, cited on page(s): 5.

(213) Chen, C.; Dong, X.; Fang, K.-H.; Yuan, F., *et al.*, 'Develop a 3D neurological disease model of human cortical glutamatergic neurons using micropillar-based scaffolds', *Acta Pharm. Sin. B* **2019**, *9*(3), 557–564, cited on page(s): 5.

(214) Viswanathan, P.; Ondeck, M. G.; Chirasatitsin, S.; Ngamkham, K., *et al.*, '3D surface topology guides stem cell adhesion and differentiation', *Biomaterials* **2015**, *52*(1), 140–147, cited on page(s): 5.

(215) Ravi, M.; Paramesh, V.; Kaviya, S.; Anuradha, E.; Solomon, F. P., '3D Cell Culture Systems: Advantages and Applications', *J. Cell. Physiol.* **2015**, *230*(1), 16–26, cited on page(s): 5.

(216) Wang, S.; Hashemi, S.; Stratton, S.; Arinzeh, T. L., 'The Effect of Physical Cues of Biomaterial Scaffolds on Stem Cell Behavior', *Adv. Healthc. Mater.* **2021**, *10*(3), 2001244, cited on page(s): 5.

(217) Mahumane, G. D.; Kumar, P.; du Toit, L. C.; Choonara, Y. E.; Pillay, V., '3D scaffolds for brain tissue regeneration: architectural challenges', *Biomater. Sci.* **2018**, *6*(11), 2812–2837, cited on page(s): 5.

(218) Tayalia, P.; Mendonca, C. R.; Baldacchini, T.; Mooney, D. J.; Mazur, E., '3D Cell-Migration Studies using Two-Photon Engineered Polymer Scaffolds', *Adv. Mater.* **2008**, *20*(23), 4494–4498, cited on page(s): 5.

(219) Weiß, T.; Schade, R.; Laube, T.; Berg, A., *et al.*, 'Two-Photon Polymerization of Biocompatible Photopolymers for Microstructured 3D Biointerfaces', *Adv. Eng. Mater.* **2011**, *13*(9), B264–B273, cited on page(s): 5.

(220) Turunen, S.; Joki, T.; Hiltunen, M. L.; Ihalainen, T. O.; Narkilahti, S.; Kellomäki, M., 'Direct Laser Writing of Tubular Microtowers for 3D Culture of Human Pluripotent Stem Cell-Derived Neuronal Cells', *ACS Appl. Mater. Interfaces* **2017**, *9*(31), 25717–25730, cited on page(s): 5.

(221) Klein, F.; Richter, B.; Striebel, T.; Franz, C. M., *et al.*, 'Two-Component Polymer Scaffolds for Controlled Three-Dimensional Cell Culture', *Adv. Mater.* **2011**, *23*(11), 1341–1345, cited on page(s): 5.

(222) Bang, S.; Lee, S.-R.; Ko, J.; Son, K., *et al.*, 'A Low Permeability Microfluidic Blood-Brain Barrier Platform with Direct Contact between Perfusable Vascular Network and Astrocytes', *Sci. Rep.* **2017**, *7*(1), 8083, cited on page(s): 5.

(223) Coluccio, M. L.; Perozziello, G.; Malara, N.; Parrotta, E., *et al.*, 'Microfluidic platforms for cell cultures and investigations', *Microelectron. Eng.* **2019**, *208*, 14–28, cited on page(s): 5.

(224) Ahn, S. I.; Sei, Y. J.; Park, H.-J.; Kim, J., *et al.*, 'Microengineered human blood–brain barrier platform for understanding nanoparticle transport mechanisms', *Nat. Commun.* **2020**, *11*(1), 175, cited on page(s): 5.

(225) Mofazzal Jahromi, M. A.; Abdoli, A.; Rahmanian, M.; Bardania, H., *et al.*, 'Microfluidic Brain-on-a-Chip: Perspectives for Mimicking Neural System Disorders', *Mol. Neurobiol.* **2019**, *56*(12), 8489–8512, cited on page(s): 5.

(226) Appelt-Menzel, A.; Oerter, S.; Mathew, S.; Haferkamp, U., *et al.*, 'Human iPSC-Derived Blood-Brain Barrier Models: Valuable Tools for Preclinical Drug Discovery and Development?', *Curr. Protoc. Stem Cell Biol.* **2020**, *55*(1), e122, cited on page(s): 5.

(227) Cho, A.-N.; Jin, Y.; An, Y.; Kim, J., *et al.*, 'Microfluidic device with brain extracellular matrix promotes structural and functional maturation of human brain organoids', *Nat. Commun.* **2021**, *12*(1), 4730, cited on page(s): 5.

(228) Wan, J.; Zhou, S.; Mea, H. J.; Guo, Y.; Ku, H.; Urbina, B. M., 'Emerging Roles of Microfluidics in Brain Research: From Cerebral Fluids Manipulation to Brain-on-a-Chip and Neuroelectronic Devices Engineering', *Chem. Rev.* **2022**, acs.chemrev.1c00480, cited on page(s): 5.

(229) Bhise, N. S.; Ribas, J.; Manoharan, V.; Zhang, Y. S., *et al.*, 'Organ-on-a-chip platforms for studying drug delivery systems', *J. Control. Release* **2014**, *190*, 82–93, cited on page(s): 5.

(230) Lind, J. U.; Busbee, T. A.; Valentine, A. D.; Pasqualini, F. S., *et al.*, 'Instrumented cardiac microphysiological devices via multimaterial three-dimensional printing', *Nat. Mater.* **2017**, *16*(3), 303–308, cited on page(s): 5.

(231) Zhang, B.; Korolj, A.; Lai, B. F. L.; Radisic, M., 'Advances in organ-on-a-chip engineering', *Nat. Rev. Mater.* **2018**, *3*(8), 257–278, cited on page(s): 5.

(232) Ahadian, S.; Civitarese, R.; Bannerman, D.; Mohammadi, M. H., *et al.*, 'Organ-On-A-Chip Platforms: A Convergence of Advanced Materials, Cells, and Microscale Technologies', *Adv. Healthc. Mater.* **2018**, *7*(2), 1700506, cited on page(s): 5.

(233) Cong, Y.; Han, X.; Wang, Y.; Chen, Z., *et al.*, 'Drug Toxicity Evaluation Based on Organ-on-a-chip Technology: A Review', *Micromachines* **2020**, *11*(4), 381, cited on page(s): 5.

(234) Wu, Q.; Liu, J.; Wang, X.; Feng, L., *et al.*, 'Organ-on-a-chip: recent breakthroughs and future prospects', *Biomed. Eng. Online* **2020**, *19*(1), 9, cited on page(s): 5.

(235) Quan, Y.; Sun, M.; Tan, Z.; Eijkel, J. C. T., *et al.*, 'Organ-on-a-chip: the next generation platform for risk assessment of radiobiology', *RSC Adv.* **2020**, *10*(65), 39521–39530, cited on page(s): 5.

(236) Ramadan, Q.; Zourob, M., 'Organ-on-a-chip engineering: Toward bridging the gap between lab and industry', *Biomicrofluidics* **2020**, *14*(4), 041501, cited on page(s): 5.

(237) Paloschi, V.; Sabater-Lleal, M.; Middelkamp, H.; Vivas, A., *et al.*, 'Organ-on-a-chip technology: a novel approach to investigate cardiovascular diseases', *Cardiovasc. Res.* **2021**, *117*(14), 2742–2754, cited on page(s): 5.

(238) Yong, U.; Kang, B.; Jang, J., '3D bioprinted and integrated platforms for cardiac tissue modeling and drug testing', *Essays Biochem.* **2021**, *65*(3), 545–554, cited on page(s): 5.

(239) Vunjak-Novakovic, G.; Ronaldson-Bouchard, K.; Radisic, M., 'Organs-on-a-chip models for biological research', *Cell* **2021**, *184*(18), 4597–4611, cited on page(s): 5.

(240) Bassett, D. S.; Gazzaniga, M. S., 'Understanding complexity in the human brain', *Trends Cogn. Sci.* **2011**, *15*(5), 200–209, cited on page(s): 5.

(241) Tognoli, E.; Kelso, J. A. S., 'Enlarging the scope: grasping brain complexity', *Front. Syst. Neurosci.* **2014**, *8*, 122, cited on page(s): 5.

(242) Pamies, D.; Hartung, T.; Hogberg, H. T., 'Biological and medical applications of a brain-on-a-chip', *Exp. Biol. Med.* **2014**, *239*(9), 1096–1107, cited on page(s): 5, 44.

(243) Frimat, J.-P.; Luttge, R., 'The Need for Physiological Micro-Nanofluidic Systems of the Brain', *Front. Bioeng. Biotechnol.* **2019**, *7*, 100, cited on page(s): 5.

(244) Tan, H.-Y.; Cho, H.; Lee, L. P., 'Human mini-brain models', *Nat. Biomed. Eng.* **2021**, *5*(1), 11–25, cited on page(s): 5.

(245) Holloway, P. M.; Willaime-Morawek, S.; Siow, R.; Barber, M., *et al.*, 'Advances in microfluidic in vitro systems for neurological disease modeling', *J. Neurosci. Res.* **2021**, *99*(5), 1276–1307, cited on page(s): 5.

(246) Maoz, B. M., 'Brain-on-a-Chip: Characterizing the next generation of advanced in vitro platforms for modeling the central nervous system', *APL Bioeng.* **2021**, *5*(3), 030902, cited on page(s): 5.

(247) Taylor, A. M.; Blurton-Jones, M.; Rhee, S. W.; Cribbs, D. H.; Cotman, C. W.; Jeon, N. L., 'A microfluidic culture platform for CNS axonal injury, regeneration and transport', *Nat. Methods* **2005**, *2*(8), 599–605, cited on page(s): 5.

(248) Park, J.; Koito, H.; Li, J.; Han, A., 'Microfluidic compartmentalized co-culture platform for CNS axon myelination research', *Biomed. Microdevices* **2009**, *11*(6), 1145–1153, cited on page(s): 5.

(249) Tong, Z.; Segura-Feliu, M.; Seira, O.; Homs-Corbera, A.; Del Río, J. A.; Samitier, J., 'A microfluidic neuronal platform for neuron axotomy and controlled regenerative studies', *RSC Adv.* **2015**, *5*(90), 73457–73466, cited on page(s): 5.

(250) Van de Wijdeven, R.; Ramstad, O. H.; Valderhaug, V. D.; Köllensperger, P., *et al.*, 'A novel lab-on-chip platform enabling axotomy and neuromodulation in a multi-nodal network', *Biosens. Bioelectron.* **2019**, *140*, 111329, cited on page(s): 5.

(251) Ndyabawe, K.; Cipriano, M.; Zhao, W.; Haidekker, M., *et al.*, 'Brain-on-a-Chip Device for Modeling Multiregional Networks', *ACS Biomater. Sci. Eng.* **2021**, *7*(1), 350–359, cited on page(s): 5.

(252) Paşca, S. P., 'The rise of three-dimensional human brain cultures', *Nature* **2018**, *553*(7689), 437–445, cited on page(s): 5.

(253) Bang, S.; Lee, S.; Choi, N.; Kim, H. N., 'Emerging Brain-Pathophysiology-Mimetic Platforms for Studying Neurodegenerative Diseases: Brain Organoids and Brains-on-a-Chip', *Adv. Healthc. Mater.* **2021**, *10*(12), 2002119, cited on page(s): 6.

(254) Yu, F.; Hunziker, W.; Choudhury, D., 'Engineering Microfluidic Organoid-on-a-Chip Platforms', *Micromachines* **2019**, *10*(3), 165, cited on page(s): 6.

(255) Li, Q.; Nan, K.; Le Floch, P.; Lin, Z., *et al.*, 'Cyborg Organoids: Implantation of Nanoelectronics via Organogenesis for Tissue-Wide Electrophysiology', *Nano Lett.* **2019**, *19*(8), 5781–5789, cited on page(s): 6.

(256) Soscia, D. A.; Lam, D.; Tooker, A. C.; Enright, H. A., *et al.*, 'A flexible 3-dimensional microelectrode array for in vitro brain models', *Lab Chip* **2020**, *20*(5), 901–911, cited on page(s): 6.

(257) Bang, S.; Jeong, S.; Choi, N.; Kim, H. N., 'Brain-on-a-chip: A history of development and future perspective', *Biomicrofluidics* **2019**, *13*(5), 051301, cited on page(s): 6, 44.

(258) Robinton, D. A.; Daley, G. Q., 'The promise of induced pluripotent stem cells in research and therapy', *Nature* **2012**, *481*(7381), 295–305, cited on page(s): 6.

(259) Ko, H. C.; Gelb, B. D., 'Concise Review: Drug Discovery in the Age of the Induced Pluripotent Stem Cell', *Stem Cells Transl. Med.* **2014**, *3*(4), 500–509, cited on page(s): 6.

(260) Pamies, D., 'A human brain microphysiological system derived from induced pluripotent stem cells to study neurological diseases and toxicity', *ALTEX* **2017**, *34*(3), 362–376, cited on page(s): 6.

(261) Tukker, A. M.; Wijnolts, F. M.; de Groot, A.; Westerink, R. H., 'Human iPSC-derived neuronal models for in vitro neurotoxicity assessment', *Neurotoxicology* **2018**, *67*, 215–225, cited on page(s): 6.

(262) Chang, E.-A.; Jin, S.-W.; Nam, M.-H.; Kim, S.-D., 'Human Induced Pluripotent Stem Cells : Clinical Significance and Applications in Neurologic Diseases', *J. Korean Neurosurg. Soc.* **2019**, *62*(5), 493–501, cited on page(s): 6.

(263) Takahashi, K.; Yamanaka, S., 'Induction of pluripotent stem cells from mouse embryonic and adult fibroblast cultures by defined factors.' *Cell* **2006**, *126*(4), 663–76, cited on page(s): 6.

(264) Takahashi, K.; Tanabe, K.; Ohnuki, M.; Narita, M., *et al.*, 'Induction of Pluripotent Stem Cells from Adult Human Fibroblasts by Defined Factors', *Cell* **2007**, *131*(5), 861–872, cited on page(s): 6.

(265) Penney, J.; Ralvenius, W. T.; Tsai, L.-H., 'Modeling Alzheimer's disease with iPSC-derived brain cells', *Mol. Psychiatry* **2020**, *25*(1), 148–167, cited on page(s): 6.

(266) Garcia-Leon, J. A.; Caceres-Palomo, L.; Sanchez-Mejias, E.; Mejias-Ortega, M., *et al.*, 'Human Pluripotent Stem Cell-Derived Neural Cells as a Relevant Platform for Drug Screening in Alzheimer's Disease', *Int. J. Mol. Sci.* **2020**, *21*(18), 6867, cited on page(s): 6.

(267) Sison, S. L.; Vermilyea, S. C.; Emborg, M. E.; Ebert, A. D., 'Using Patient-Derived Induced Pluripotent Stem Cells to Identify Parkinson's Disease-Relevant Phenotypes', *Curr. Neurol. Neurosci. Rep.* **2018**, *18*(12), 84, cited on page(s): 6.

(268) Purves, D.; Augustine, G. J.; Fitzpatrick, D.; Katz, L. C., *et al.*, 'Neuroscience', Sunderland (MA), Sinauer Associates **2001**, 2nd ed., ISBN: 10: 0-87893-742-0, cited on page(s): 6, 44.

(269) Mak, I. W.; Evaniew, N.; Ghert, M., 'Lost in translation: animal models and clinical trials in cancer treatment.' *Am. J. Transl. Res.* **2014**, *6*(2), 114–8, cited on page(s): 6.

(270) Dawson, T. M.; Golde, T. E.; Lagier-Tourenne, C., 'Animal models of neurodegenerative diseases', *Nat. Neurosci.* **2018**, *21*(10), 1370–1379, cited on page(s): 6.

(271) Gordon, J.; Amini, S.; White, M. K., 'General Overview of Neuronal Cell Culture', *Methods Mol. Biol.* NIH Public Access **2013**, Vol. 1078, ISBN: 978-1-62703-640-5, 1–8, cited on page(s): 6.

(272) Gepstein, L., 'Derivation and Potential Applications of Human Embryonic Stem Cells', *Circ. Res.* **2002**, *91*(10), 866–876, cited on page(s): 6.

(273) Lo, B.; Parham, L., 'Ethical Issues in Stem Cell Research', *Endocr. Rev.* **2009**, *30*(3), 204–213, cited on page(s): 6.

(274) The Witherspoon Council on Ethics and the Integrity of Science, 'Appendix E: Overview of International Human Embryonic Stem Cell Laws,' *New Atl.* **2012**, Vol. 34, cited on page(s): 6.

(275) Li, Y.; Nguyen, H. V.; Tsang, S. H., 'Skin Biopsy and Patient-Specific Stem Cell Lines.' *Methods Mol. Biol.* **2016**, *1353*(3), 77–88, cited on page(s): 6.

(276) Tandon, R.; Brändl, B.; Baryshnikova, N.; Landshammer, A., *et al.*, 'Generation of two human isogenic iPSC lines from fetal dermal fibroblasts', *Stem Cell Res.* **2018**, *33*, 120–124, cited on page(s): 7, 12.

(277) Reinhardt, P.; Glatza, M.; Hemmer, K.; Tsytsyura, Y., *et al.*, 'Derivation and Expansion Using Only Small Molecules of Human Neural Progenitors for Neurodegenerative Disease Modeling', *PLoS One* **2013**, *8*(3), e59252, cited on page(s): 7.

(278) Brennand, K. J.; Simone, A.; Jou, J.; Gelboin-Burkhart, C., *et al.*, 'Modelling schizophrenia using human induced pluripotent stem cells', *Nature* **2011**, *473*(7346), 221–225, cited on page(s): 7, 13.

(279) Zhang, W.-B.; Ross, P. J.; Tu, Y.; Wang, Y., *et al.*, 'Fyn Kinase regulates GluN2B subunit-dominant NMDA receptors in human induced pluripotent stem cell-derived neurons', *Sci. Rep.* **2016**, *6*(1), 23837, cited on page(s): 7, 13, 24.

(280) Djuric, U.; Cheung, A. Y.; Zhang, W.; Mok, R. S., *et al.*, 'MECP2e1 isoform mutation affects the form and function of neurons derived from Rett syndrome patient iPS cells', *Neurobiol. Dis.* **2015**, *76*(4), 37–45, cited on page(s): 7.

(281) Cao, S.-Y.; Hu, Y.; Chen, C.; Yuan, F., *et al.*, 'Enhanced derivation of human pluripotent stem cell-derived cortical glutamatergic neurons by a small molecule', *Sci. Rep.* **2017**, *7*(1), 3282, cited on page(s): 7.

(282) Antonov, S. A.; Novosadova, E. V., 'Current State-of-the-Art and Unresolved Problems in Using Human Induced Pluripotent Stem Cell-Derived Dopamine Neurons for Parkinson's Disease Drug Development', *Int. J. Mol. Sci.* **2021**, *22*(7), 3381, cited on page(s): 7.

(283) Bardy, C.; van den Hurk, M; Kakaradov, B.; Erwin, J. A., *et al.*, 'Predicting the functional states of human iPSC-derived neurons with single-cell RNA-seq and electrophysiology', *Mol. Psychiatry* **2016**, *21*(11), 1573–1588, cited on page(s): 7.

(284) Lam, R. S.; Töpfer, F. M.; Wood, P. G.; Busskamp, V.; Bamberg, E., 'Functional Maturation of Human Stem Cell-Derived Neurons in Long-Term Cultures', *PLoS One* **2017**, *12*(1), e0169506, cited on page(s): 7.

(285) Hofer, M.; Lutolf, M. P., 'Engineering organoids', *Nat. Rev. Mater.* **2021**, *6*(5), 402–420, cited on page(s): 7.

(286) Lancaster, M. A.; Renner, M.; Martin, C.-A.; Wenzel, D., *et al.*, 'Cerebral organoids model human brain development and microcephaly', *Nature* **2013**, *501*(7467), 373–379, cited on page(s): 7.

(287) Lancaster, M. A.; Knoblich, J. A., 'Organogenesis in a dish: Modeling development and disease using organoid technologies', *Science* **2014**, *345*(6194), 1247125, cited on page(s): 7.

(288) Sterneckert, J. L.; Reinhardt, P.; Schöler, H. R., 'Investigating human disease using stem cell models', *Nat. Rev. Genet.* **2014**, *15*(9), 625–639, cited on page(s): 7.

(289) Lancaster, M. A.; Huch, M., 'Disease modelling in human organoids', *Dis. Model. Mech.* **2019**, *12*(7), cited on page(s): 7.

(290) Kim, J.; Koo, B.-K.; Knoblich, J. A., 'Human organoids: model systems for human biology and medicine', *Nat. Rev. Mol. Cell Biol.* **2020**, *21*(10), 571–584, cited on page(s): 7.

(291) Yin, F.; Zhang, X.; Wang, L.; Wang, Y., *et al.*, 'HiPSC-derived multi-organoids-on-chip system for safety assessment of antidepressant drugs', *Lab Chip* **2021**, *21*(3), 571–581, cited on page(s): 7.

(292) Maoz, B. M.; Herland, A.; FitzGerald, E. A.; Grevesse, T., *et al.*, 'A linked organ-on-chip model of the human neurovascular unit reveals the metabolic coupling of endothelial and neuronal cells', *Nat. Biotechnol.* **2018**, *36*(9), 865–874, cited on page(s): 7.

(293) Appelt-Menzel, A.; Cubukova, A.; Günther, K.; Edenhofer, F., *et al.*, 'Establishment of a Human Blood-Brain Barrier Co-culture Model Mimicking the Neurovascular Unit Using Induced Pluri- and Multipotent Stem Cells', *Stem Cell Reports* **2017**, *8*(4), 894–906, cited on page(s): 7.

(294) Osaki, T.; Sivathanu, V.; Kamm, R. D., 'Engineered 3D vascular and neuronal networks in a microfluidic platform', *Sci. Rep.* **2018**, *8*(1), 5168, cited on page(s): 7.

(295) Passaro, A. P.; Stice, S. L., 'Electrophysiological Analysis of Brain Organoids: Current Approaches and Advancements', *Front. Neurosci.* **2021**, *14*, 1405, cited on page(s): 7, 45.

(296) Wei, Z.; Sun, T.; Shimoda, S.; Chen, Z., *et al.*, 'Bio-inspired engineering of a perfusion culture platform for guided three-dimensional nerve cell growth and differentiation', *Lab Chip* **2022**, *22*(5), 1006–1017, cited on page(s): 7.

(297) Dallas, M.; Bell, D., 'Patch Clamp Electrophysiology', Springer US **2021**, Vol. 2188, ISBN: 978-1-0716-0817-3, cited on page(s): 7.

(298) Neher, E; Sakmann, B, 'Single-channel currents recorded from membrane of denervated frog muscle fibres.' *Nature* **1976**, *260*(5554), 799–802, cited on page(s): 7.

(299) Suchyna, T. M.; Markin, V. S.; Sachs, F., 'Biophysics and Structure of the Patch and the Gigaseal', *Biophys. J.* **2009**, *97*(3), 738–747, cited on page(s): 7.

(300) Kornreich, B. G., 'The patch clamp technique: Principles and technical considerations', *J. Vet. Cardiol.* **2007**, *9*(1), 25–37, cited on page(s): 8.

(301) Rubaiy, H. N., 'A Short Guide to Electrophysiology and Ion Channels', *J. Pharm. Pharm. Sci.* **2017**, *20*(1), 48, cited on page(s): 8.

(302) Sontheimer, H.; Olsen, M. L., 'Whole-Cell Patch-Clamp Recordings', *Patch-Clamp Anal.* Humana Press **2007**, Vol. 35, ISBN: 978-1-59745-492-6, 35–68, cited on page(s): 8.

(303) Bébarová, M., 'Advances in patch clamp technique: towards higher quality and quantity', *Gen. Physiol. Biophys.* **2012**, *31*(02), 131–140, cited on page(s): 8.

(304) Hobbs, R. G.; Petkov, N.; Holmes, J. D., 'Semiconductor Nanowire Fabrication by Bottom-Up and Top-Down Paradigms', *Chem. Mater.* **2012**, *24*(11), 1975–1991, cited on page(s): 8.

(305) Huff, M., 'Recent Advances in Reactive Ion Etching and Applications of High-Aspect-Ratio Microfabrication', *Micromachines* **2021**, *12*(8), 991, cited on page(s): 9.

(306) Jansen, H.; Gardeniers, H.; de Boer, M.; Elwenspoek, M.; Fluitman, J., 'A survey on the reactive ion etching of silicon in microtechnology', *J. Micromechanics Microengineering* **1996**, *6*(1), 14–28, cited on page(s): 9.

(307) Schwartz, G. C.; Schaible, P. M., 'Reactive ion etching of silicon', *J. Vac. Sci. Technol.* **1979**, *16*(2), 410–413, cited on page(s): 9.

(308) Li, R; Lamy, Y; Besling, W. F. A.; Roozeboom, F; Sarro, P. M., 'Continuous deep reactive ion etching of tapered via holes for three-dimensional integration', *J. Micromechanics Microengineering* **2008**, *18*(12), 125023, cited on page(s): 9.

(309) Karouta, F., 'A practical approach to reactive ion etching', *J. Phys. D. Appl. Phys.* **2014**, *47*(23), 233501, cited on page(s): 9.

(310) Chang, Y.-F; Chou, Q.-R; Lin, J.-Y; Lee, C.-H., 'Fabrication of high-aspect-ratio silicon nanopillar arrays with the conventional reactive ion etching technique', *Appl. Phys. A* **2006**, *86*(2), 193–196, cited on page(s): 9.

(311) Guilloy, K.; Pauc, N.; Gassenq, A.; Calvo, V., 'High aspect ratio germanium nanowires obtained by dry etching', *MRS Adv.* **2016**, *1*(13), 875–880, cited on page(s): 9.

(312) Dhindsa, N.; Saini, S. S., 'Top-down fabricated tapered GaAs nanowires with sacrificial etching of the mask', *Nanotechnology* **2017**, *28*(23), 235301, cited on page(s): 9.

(313) Fernández-Garrido, S.; Auzelle, T.; Lähnemann, J.; Wimmer, K.; Tahraoui, A.; Brandt, O., 'Top-down fabrication of ordered arrays of GaN nanowires by selective area sublimation', *Nanoscale Adv.* **2019**, *1*(5), 1893–1900, cited on page(s): 9.

(314) Wagner, R. S.; Ellis, W. C., 'Vapor-liquid-solid mechanism of single crystal growth', *Appl. Phys. Lett.* **1964**, *4*(5), 89–90, cited on page(s): 9.

(315) Kim, W.; Dubrovskii, V. G.; Vukajlovic-Plestina, J.; Tütüncüoglu, G., *et al.*, 'Bistability of Contact Angle and Its Role in Achieving Quantum-Thin Self-Assisted GaAs nanowires', *Nano Lett.* **2018**, *18*(1), 49–57, cited on page(s): 9.

(316) Wu, K.-L.; Chou, Y.-C.; Su, C.-C.; Yang, C.-C.; Lee, W.-I.; Chou, Y.-C., 'Controlling bottom-up rapid growth of single crystalline gallium nitride nanowires on silicon', *Sci. Rep.* **2017**, *7*(1), 17942, cited on page(s): 9.

(317) Wallentin, J.; Anttu, N.; Asoli, D.; Huffman, M., *et al.*, 'InP Nanowire Array Solar Cells Achieving 13.8% Efficiency by Exceeding the Ray Optics Limit', *Science* **2013**, *339*(6123), 1057–1060, cited on page(s): 9, 42, 43.

(318) Borchers, C.; Müller, S.; Stichtenoth, D.; Schwen, D.; Ronning, C., 'Catalyst–Nanostructure Interaction in the Growth of 1-D ZnO Nanostructures', *J. Phys. Chem. B* **2006**, *110*(4), 1656–1660, cited on page(s): 9.

(319) Misra, S.; Yu, L.; Foldyna, M.; Roca i Cabarrocas, P., 'High efficiency and stable hydrogenated amorphous silicon radial junction solar cells built on VLS-grown silicon nanowires', *Sol. Energy Mater. Sol. Cells* **2013**, *118*, 90–95, cited on page(s): 9, 25.

(320) Schmidt, V; Wittemann, J. V.; Gösele, U, 'Growth, Thermodynamics, and Electrical Properties of Silicon Nanowires', *Chem. Rev.* **2010**, *110*(1), 361–388, cited on page(s): 9.

(321) Puglisi, R. A.; Bongiorno, C.; Caccamo, S.; Fazio, E., *et al.*, 'Chemical Vapor Deposition Growth of Silicon Nanowires with Diameter Smaller Than 5 nm', *ACS Omega* **2019**, *4*(19), 17967–17971, cited on page(s): 9.

(322) Wu, Y.; Cui, Y.; Huynh, L.; Barrelet, C. J.; Bell, D. C.; Lieber, C. M., 'Controlled Growth and Structures of Molecular-Scale Silicon Nanowires', *Nano Lett.* **2004**, *4*(3), 433–436, cited on page(s): 9.

(323) Pinion, C. W.; Christesen, J. D.; Cahoon, J. F., 'Understanding the vapor–liquid–solid mechanism of Si nanowire growth and doping to synthetically encode precise nanoscale morphology', *J. Mater. Chem. C* **2016**, *4*(18), 3890–3897, cited on page(s): 9.

(324) Pimpin, A.; Srituravanich, W., 'Review on Micro- and Nanolithography Techniques and their Applications', *Eng. J.* **2012**, *16*(1), 37–56, cited on page(s): 9.

(325) Gentili, D.; Foschi, G.; Valle, F.; Cavallini, M.; Biscarini, F., 'Applications of dewetting in micro and nanotechnology', *Chem. Soc. Rev.* **2012**, *41*(12), 4430, cited on page(s): 10.

(326) Spangenberg, A.; Hobeika, N.; Stehlin, F.; Pierre Malval, J., *et al.*, 'Recent Advances in Two-Photon Stereolithography', *Updat. Adv. Lithogr.* InTech **2013**, ISBN: 978-953-51-1175-7, cited on page(s): 10.

(327) Göppert-Mayer, M., 'Über Elementarakte mit zwei Quantensprüngen', *Ann. Phys.* **1931**, *401*(3), 273–294, cited on page(s): 10.

(328) Tkachenko, N. V., 'Optical Spectroscopy : Methods and Instrumentations.' Elsevier **2006**, ISBN: 0080461727, cited on page(s): 10.

(329) Fisher, W. G.; Partridge, W. P.; Dees, C.; Wachter, E. A., 'Simultaneous Two-Photon Activation of Type-I Photodynamic Therapy Agents', *Photochem. Photobiol.* **1997**, *66*(2), 141–155, cited on page(s): 10.

(330) Juodkazis, S.; Mizeikis, V.; Misawa, H., 'Three-dimensional microfabrication of materials by femtosecond lasers for photonics applications', *J. Appl. Phys.* **2009**, *106*(5), 051101, cited on page(s): 10.

(331) Bischel, W. K.; Kelly, P. J.; Rhodes, C. K., 'High-resolution Doppler-free two-photon spectroscopic studies of molecules. I. The ν_3 bands of $^{12}CH_3F$', *Phys. Rev. A* **1976**, *13*(5), 1817–1828, cited on page(s): 10.

(332) Pawlicki, M.; Collins, H. A.; Denning, R. G.; Anderson, H. L., 'Two-Photon Absorption and the Design of Two-Photon Dyes', *Angew. Chemie Int. Ed.* **2009**, *48*(18), 3244–3266, cited on page(s): 10.

(333) Moscatelli, F. A., 'A simple conceptual model for two-photon absorption', *Am. J. Phys.* **1986**, *54*(1), 52–54, cited on page(s): 10.

(334) Xu, C.; Webb, W. W., 'Measurement of two-photon excitation cross sections of molecular fluorophores with data from 690 to 1050 nm', *J. Opt. Soc. Am. B* **1996**, *13*(3), 481, cited on page(s): 10.

(335) Masters, B. R.; So, P. T., 'Antecedents of two-photon excitation laser scanning microscopy', *Microsc. Res. Tech.* **2004**, *63*(1), 3–11, cited on page(s): 10.

(336) Bunea, A.-I.; del Castillo Iniesta, N.; Droumpali, A.; Wetzel, A. E.; Engay, E.; Taboryski, R., 'Micro 3D Printing by Two-Photon Polymerization: Configurations and Parameters for the Nanoscribe System', *Micro* **2021**, *1*(2), 164–180, cited on page(s): 10.

(337) Schneider, U.; Schwenk, H.-U.; Bornkamm, G., 'Characterization of EBV-genome negative "null" and "T" cell lines derived from children with acute lymphoblastic leukemia and leukemic transformed non-Hodgkin lymphoma', *Int. J. Cancer* **1977**, *19*(5), 621–626, cited on page(s): 12.

(338) Loiko, V. A.; Ruban, G. I.; Gritsai, O. A.; Gruzdev, A. D., *et al.*, 'Morphometric model of lymphocyte as applied to scanning flow cytometry', *J. Quant. Spectrosc. Radiat. Transf.* **2006**, *102*(1), 73–84, cited on page(s): 12.

(339) Bausch, C. S.; Heyn, C.; Hansen, W.; Wolf, I. M. A., *et al.*, 'Ultra-fast cell counters based on microtubular waveguides', *Sci. Rep.* **2017**, *7*(1), 41584, cited on page(s): 12.

(340) Mazia, D.; Schatten, G.; Sale, W., 'Adhesion of cells to surfaces coated with polylysine. Applications to electron microscopy.' *J. Cell Biol.* **1975**, *66*(1), 198–200, cited on page(s): 12, 17.

(341) Denes, E.; Barrière, G.; Poli, E.; Lévêque, G., 'Alumina Biocompatibility', *J. Long. Term. Eff. Med. Implants* **2018**, *28*(1), 9–13, cited on page(s): 12, 13.

(342) Loers, G.; Chen, S.; Grumet, M.; Schachner, M., 'Signal transduction pathways implicated in neural recognition molecule L1 triggered neuroprotection and neuritogenesis', *J. Neurochem.* **2005**, *92*(6), 1463–1476, cited on page(s): 12, 18.

(343) Consalez, G. G.; Goldowitz, D.; Casoni, F.; Hawkes, R., 'Origins, Development, and Compartmentation of the Granule Cells of the Cerebellum', *Front. Neural Circuits* **2021**, *14*, cited on page(s): 12.

(344) Kaczor, P. T.; Mozrzymas, J. W., 'Key Metabolic Enzymes Underlying Astrocytic Upregulation of GABAergic Plasticity', *Front. Cell. Neurosci.* **2017**, *11*, 144, cited on page(s): 12.

(345) Golda-Cepa, M.; Engvall, K.; Hakkarainen, M.; Kotarba, A., 'Recent progress on parylene C polymer for biomedical applications: A review', *Prog. Org. Coatings* **2020**, *140*, 105493, cited on page(s): 13.

(346) Shipley, M. M.; Mangold, C. A.; Szpara, M. L., 'Differentiation of the SH-SY5Y Human Neuroblastoma Cell Line', *J. Vis. Exp.* **2016**, *108*, e53193, cited on page(s): 13.

(347) Schaarschmidt, G.; Wegner, F.; Schwarz, S. C.; Schmidt, H.; Schwarz, J., 'Characterization of Voltage-Gated Potassium Channels in Human Neural Progenitor Cells', *PLoS One* **2009**, *4*(7), e6168, cited on page(s): 13.

(348) Graham, B. A.; Brichta, A. M.; Callister, R. J., 'Recording Temperature Affects the Excitability of Mouse Superficial Dorsal Horn Neurons, In Vitro', *J. Neurophysiol.* **2008**, *99*(5), 2048–2059, cited on page(s): 13.

(349) Machu, T. K.; Dillon, G. H.; Huang, R.; Lovinger, D. M.; Leidenheimer, N. J., 'Temperature: An important experimental variable in studying PKC modulation of ligand-gated ion channels', *Brain Res.* **2006**, *1086*(1), 1–8, cited on page(s): 13.

(350) Lin, H.; Jun, I.; Woo, J. H.; Lee, M. G.; Kim, S. J.; Nam, J. H., 'Temperature-dependent increase in the calcium sensitivity and acceleration of activation of ANO6 chloride channel variants', *Sci. Rep.* **2019**, *9*(1), 6706, cited on page(s): 13.

(351) Jeon, Y. K.; Choi, S. W.; Kwon, J. W.; Woo, J., *et al.*, 'Thermosensitivity of the voltage-dependent activation of calcium homeostasis modulator 1 (calhm1) ion channel', *Biochem. Biophys. Res. Commun.* **2021**, *534*, 590–596, cited on page(s): 13.

(352) Brickley, S. G.; Aller, M. I.; Sandu, C.; Veale, E. L., *et al.*, 'TASK-3 Two-Pore Domain Potassium Channels Enable Sustained High-Frequency Firing in Cerebellar Granule Neurons', *J. Neurosci.* **2007**, *27*(35), 9329–9340, cited on page(s): 13.

(353) Partida-Sanchez, S.; Gasser, A.; Fliegert, R.; Siebrands, C. C., *et al.*, 'Chemotaxis of Mouse Bone Marrow Neutrophils and Dendritic Cells Is Controlled by ADP-Ribose, the Major Product Generated by the CD38 Enzyme Reaction', *J. Immunol.* **2007**, *179*(11), 7827–7839, cited on page(s): 13.

(354) Neher, E.; Sakmann, B.; Steinbach, J. H., 'The extracellular patch clamp: a method for resolving currents through individual open channels in biological membranes.' *Pflugers Arch.* **1978**, *375*(2), 219–28, cited on page(s): 14.

(355) Khattak, S.; Brimble, E.; Zhang, W.; Zaslavsky, K., *et al.*, 'Human induced pluripotent stem cell derived neurons as a model for Williams-Beuren syndrome', *Mol. Brain* **2015**, *8*(1), 77, cited on page(s): 15.

(356) Xie, Y.; Schutte, R. J.; Ng, N. N.; Ess, K. C.; Schwartz, P. H.; O'Dowd, D. K., 'Reproducible and efficient generation of functionally active neurons from human hiPSCs for preclinical disease modeling', *Stem Cell Res.* **2018**, *26*, 84–94, cited on page(s): 15.

(357) Collins, C. A.; Rojas, E., 'Temperature dependence of the sodium channel gating kinetics in the node of Ranvier.' *Q. J. Exp. Physiol.* **1982**, *67*(1), 41–55, cited on page(s): 15.

(358) Yang, F.; Zheng, J., 'High temperature sensitivity is intrinsic to voltage-gated potassium channels', *Elife* **2014**, *3*, e03255, cited on page(s): 15.

(359) Griffin, J. D.; Boulant, J. A., 'Temperature effects on membrane potential and input resistance in rat hypothalamic neurones.' *J. Physiol.* **1995**, *488*(2), 407–418, cited on page(s): 15.

(360) Huang, S.; Uusisaari, M. Y., 'Physiological temperature during brain slicing enhances the quality of acute slice preparations.' *Front. Cell. Neurosci.* **2013**, *7*, 48, cited on page(s): 15.

(361) DeCoursey, T.; Chandy, K.; Gupta, S.; Cahalan, M., 'Voltage-dependent ion channels in T-lymphocytes', *J. Neuroimmunol.* **1985**, *10*(1), 71–95, cited on page(s): 15, 18.

(362) Platzer, D.; Zorn-Pauly, K., 'Letter to the editor: Accurate cell capacitance determination from a single voltage step: a reminder to avoid unnecessary pitfalls', *Am. J. Physiol. Circ. Physiol.* **2016**, *311*(4), H1072–H1073, cited on page(s): 15.

(363) Buzatu, S., 'The temperature-induced changes in membrane potential.' *Riv. Biol.* **2009**, *102*(2), 199–217, cited on page(s): 15.

(364) Asteriti, S.; Cangiano, L., 'Versatile bipolar temperature controller for custom in vitro applications', *HardwareX* **2020**, *8*, e00155, cited on page(s): 16.

(365) Yajuan, X.; Xin, L.; Zhiyuan, L., 'A Comparison of the Performance and Application Differences Between Manual and Automated Patch-Clamp Techniques', *Curr. Chem. Genomics* **2012**, *6*, 87–92, cited on page(s): 16.

(366) Harberts, J., 'Installation of a Patch Clamp Setup for Action Potential Studies of Neurons Cultured on InP Nanowire Array Solar Cells', Universität Hamburg **2016**, Master's thesis, cited on page(s): 16, 43.

(367) Otnes, G.; Heurlin, M.; Graczyk, M.; Wallentin, J., *et al.*, 'Strategies to obtain pattern fidelity in nanowire growth from large-area surfaces patterned using nanoimprint lithography', *Nano Res.* **2016**, *9*(10), 2852–2861, cited on page(s): 16.

(368) Borschel, C.; Spindler, S.; Lerose, D.; Bochmann, A., *et al.*, 'Permanent bending and alignment of ZnO nanowires', *Nanotechnology* **2011**, *22*(18), 185307, cited on page(s): 17.

(369) Finch, D. S.; Oreskovic, T.; Ramadurai, K.; Herrmann, C. F.; George, S. M.; Mahajan, R. L., 'Biocompatibility of atomic layer-deposited alumina thin films', *J. Biomed. Mater. Res. Part A* **2008**, *87A*(1), 100–106, cited on page(s): 17.

(370) Senapati, V. A.; Kumar, A., 'ZnO nanoparticles dissolution, penetration and toxicity in human epidermal cells. Influence of pH', *Environ. Chem. Lett.* **2018**, *16*(3), 1129–1135, cited on page(s): 17.

(371) Luckenbill-Edds, L., 'Laminin and the mechanism of neuronal outgrowth.' *Brain Res. Brain Res. Rev.* **1997**, *23*(1-2), 1–27, cited on page(s): 17.

(372) Santoro, F.; Neumann, E.; Panaitov, G.; Offenhäusser, A., 'FIB section of cell-electrode interface: An approach for reducing curtaining effects', *Microelectron. Eng.* **2014**, *124*(April), 17–21, cited on page(s): 17.

(373) Wierzbicki, R.; Købler, C.; Jensen, M. R. B.; Lopacińska, J., *et al.*, 'Mapping the complex morphology of cell interactions with nanowire substrates using FIB-SEM.' *PLoS One* **2013**, *8*(1), e53307, cited on page(s): 17, 26, 30.

(374) Uggeri, J.; Gatti, R.; Belletti, S.; Scandroglio, R., *et al.*, 'Calcein-AM is a detector of intracellular oxidative activity', *Histochem. Cell Biol.* **2000**, *122*(5), 499–505, cited on page(s): 17.

(375) Hancock, M. K.; Kopp, L.; Kaur, N.; Hanson, B. J., 'A Facile Method for Simultaneously Measuring Neuronal Cell Viability and Neurite Outgrowth', *Curr. Chem. Genomics Transl. Med.* **2015**, *9*(1), 6–16, cited on page(s): 17.

(376) Schneider, C. A.; Rasband, W. S.; Eliceiri, K. W., 'NIH Image to ImageJ: 25 years of image analysis', *Nat. Methods* **2012**, *9*(7), 671–675, cited on page(s): 17.

(377) Schindelin, J.; Arganda-Carreras, I.; Frise, E.; Kaynig, V., *et al.*, 'Fiji: an open-source platform for biological-image analysis', *Nat. Methods* **2012**, *9*(7), 676–682, cited on page(s): 17.

(378) Nicola, M. D.; Bellucci, S.; Traversa, E.; Bellis, G. D.; Micciulla, F.; Ghibelli, L., 'Carbon nanotubes on Jurkat cells: effects on cell viability and plasma membrane potential', *J. Phys. Condens. Matter* **2008**, *20*(47), 474204, cited on page(s): 18.

(379) Roussel, C; Erneux, T; Schiffmann, S.; Gall, D, 'Modulation of neuronal excitability by intracellular calcium buffering: From spiking to bursting', *Cell Calcium* **2006**, *39*(5), 455–466, cited on page(s): 18.

(380) Bean, B. P., 'The action potential in mammalian central neurons', *Nat. Rev. Neurosci.* **2007**, *8*(6), 451–465, cited on page(s): 18.

(381) Dupuis, G.; Héroux, J; Payet, M. D., 'Characterization of Ca^{2+} and K^+ currents in the human Jurkat T cell line: effects of phyto-haemagglutinin.' *J. Physiol.* **1989**, *412*(1), 135–154, cited on page(s): 18.

(382) Ross, P.; Garber, S.; Cahalan, M., 'Membrane chloride conductance and capacitance in Jurkat T lymphocytes during osmotic swelling', *Biophys. J.* **1994**, *66*(1), 169–178, cited on page(s): 18.

(383) Cahalan, M. D.; Chandy, K. G., 'The functional network of ion channels in T lymphocytes', *Immunol. Rev.* **2009**, *231*(1), 59–87, cited on page(s): 18.

(384) Gall, D.; Roussel, C.; Susa, I.; D'Angelo, E., *et al.*, 'Altered Neuronal Excitability in Cerebellar Granule Cells of Mice Lacking Calretinin', *J. Neurosci.* **2003**, *23*(28), 9320–9327, cited on page(s): 18.

(385) Rössert, C.; Solinas, S.; D'Angelo, E.; Dean, P., *et al.*, 'Model cerebellar granule cells can faithfully transmit modulated firing rate signals', *Front. Cell. Neurosci.* **2014**, *8*(October), 1–20, cited on page(s): 18.

(386) Hung, Y.-J.; Lee, S.-L.; Thibeault, B. J.; Coldren, L. A., 'Fabrication of Highly Ordered Silicon Nanowire Arrays With Controllable Sidewall Profiles for Achieving Low-Surface Reflection', *IEEE J. Sel. Top. Quantum Electron.* **2011**, *17*(4), 869–877, cited on page(s): 19.

(387) Fu, Y. Q.; Colli, A.; Fasoli, A.; Luo, J. K., *et al.*, 'Deep reactive ion etching as a tool for nanostructure fabrication', *J. Vac. Sci. Technol. B Microelectron. Nanom. Struct.* **2009**, *27*(3), 1520, cited on page(s): 19.

(388) Allani, S.; Jupe, A.; Kappert, H.; Vogt, H., 'Fabrication of Partly Encapsulated Vertical Nanoelectrodes for an Intracellular Microelectrode Array', *2019 20th Int. Conf. Solid-State Sensors, Actuators Microsystems Eurosensors XXXIII (TRANSDUCERS EUROSENSORS XXXIII)* **2019**, 1619–1622, cited on page(s): 19.

(389) McQuin, C.; Goodman, A.; Chernyshev, V.; Kamentsky, L., *et al.*, 'CellProfiler 3.0: Next-generation image processing for biology', *PLOS Biol.* **2018**, *16*(7), e2005970, cited on page(s): 19.

(390) Ning, D.; Duong, B.; Thomas, G.; Qiao, Y., *et al.*, 'Mechanical and Morphological Analysis of Cancer Cells on Nanostructured Substrates', *Langmuir* **2016**, *32*(11), 2718–2723, cited on page(s): 20.

(391) Shalek, A. K.; Gaublomme, J. T.; Wang, L.; Yosef, N., *et al.*, 'Nanowire-Mediated Delivery Enables Functional Interrogation of Primary Immune Cells: Application to the Analysis of Chronic Lymphocytic Leukemia', *Nano Lett.* **2012**, *12*(12), 6498–6504, cited on page(s): 20.

(392) Prinz, C. N., 'Interactions between semiconductor nanowires and living cells', *J. Phys. Condens. Matter* **2015**, *27*(23), 233103, cited on page(s): 20.

(393) Tullii, G.; Giona, F.; Lodola, F.; Bonfadini, S., *et al.*, 'High-Aspect-Ratio Semiconducting Polymer Pillars for 3D Cell Cultures', *ACS Appl. Mater. Interfaces* **2019**, *11*(31), 28125–28137, cited on page(s): 20.

(394) Kim, S.-M.; Lee, S.; Kim, D.; Kang, D.-H., *et al.*, 'Strong contact coupling of neuronal growth cones with height-controlled vertical silicon nanocolumns', *Nano Res.* **2018**, *11*(5), 2532–2543, cited on page(s): 20, 26.

(395) Brocher, J., 'The BioVoxxel Image Processing and Analysis Toolbox', *EuBIAS-Conference* **2015**, *Jan 5*, cited on page(s): 21.

(396) Xie, C.; Hanson, L.; Xie, W.; Lin, Z.; Cui, B.; Cui, Y., 'Noninvasive Neuron Pinning with Nanopillar Arrays', *Nano Lett.* **2010**, *10*(10), 4020–4024, cited on page(s): 21.

(397) McGuire, A. F.; Santoro, F.; Cui, B., 'Interfacing Cells with Vertical Nanoscale Devices: Applications and Characterization', *Annu. Rev. Anal. Chem.* **2018**, *11*(1), 101–126, cited on page(s): 21.

(398) Viela, F.; Granados, D.; Ayuso-Sacido, A.; Rodríguez, I., 'Biomechanical Cell Regulation by High Aspect Ratio Nanoimprinted Pillars', *Adv. Funct. Mater.* **2016**, *26*(31), 5599–5609, cited on page(s): 21.

(399) Milos, F.; Tullii, G.; Gobbo, F.; Lodola, F., *et al.*, 'High Aspect Ratio and Light-Sensitive Micropillars Based on a Semiconducting Polymer Optically Regulate Neuronal Growth', *ACS Appl. Mater. Interfaces* **2021**, *13*(20), 23438–23451, cited on page(s): 21.

(400) Provenzano, P. P.; Keely, P. J., 'Mechanical signaling through the cytoskeleton regulates cell proliferation by coordinated focal adhesion and Rho GTPase signaling', *J. Cell Sci.* **2011**, *124*(8), 1195–1205, cited on page(s): 22.

(401) Bendris, N.; Lemmers, B.; Blanchard, J. M., 'Cell cycle, cytoskeleton dynamics and beyond: the many functions of cyclins and CDK inhibitors', *Cell Cycle* **2015**, *14*(12), 1786–1798, cited on page(s): 22.

(402) Hanson, L.; Lin, Z. C.; Xie, C.; Cui, Y.; Cui, B., 'Characterization of the Cell–Nanopillar Interface by Transmission Electron Microscopy', *Nano Lett.* **2012**, *12*(11), 5815–5820, cited on page(s): 23, 24, 30.

(403) Carthew, J.; Abdelmaksoud, H. H.; Hodgson-Garms, M.; Aslanoglou, S., *et al.*, 'Precision Surface Microtopography Regulates Cell Fate via Changes to Actomyosin Contractility and Nuclear Architecture', *Adv. Sci.* **2021**, *8*(6), 2003186, cited on page(s): 23.

(404) Huang, J.-A.; Caprettini, V.; Zhao, Y.; Melle, G., *et al.*, 'On-Demand Intracellular Delivery of Single Particles in Single Cells by 3D Hollow Nanoelectrodes', *Nano Lett.* **2019**, *19*(2), 722–731, cited on page(s): 23.

(405) Santoro, F.; Zhao, W.; Joubert, L.-M.; Duan, L., *et al.*, 'Revealing the Cell–Material Interface with Nanometer Resolution by Focused Ion Beam/Scanning Electron Microscopy', *ACS Nano* **2017**, *11*(8), 8320–8328, cited on page(s): 24.

(406) Micholt, L.; Gärtner, A.; Prodanov, D.; Braeken, D.; Dotti, C. G.; Bartic, C., 'Substrate Topography Determines Neuronal Polarization and Growth In Vitro', *PLoS One* **2013**, *8*(6), e66170, cited on page(s): 24.

(407) Telias, M.; Segal, M.; Ben-Yosef, D., 'Electrical maturation of neurons derived from human embryonic stem cells', *F1000Research* **2014**, *3*, 196, cited on page(s): 24.

(408) Shi, Y.; Kirwan, P.; Smith, J.; Robinson, H. P. C.; Livesey, F. J., 'Human cerebral cortex development from pluripotent stem cells to functional excitatory synapses', *Nat. Neurosci.* **2012**, *15*(3), 477–486, cited on page(s): 24.

(409) Gunhanlar, N.; Shpak, G.; van der Kroeg, M.; Gouty-Colomer, L. A., *et al.*, 'A simplified protocol for differentiation of electrophysiologically mature neuronal networks from human induced pluripotent stem cells', *Mol. Psychiatry* **2018**, *23*(5), 1336–1344, cited on page(s): 24.

(410) Coyne, L.; Shan, M.; Przyborski, S. A.; Hirakawa, R.; Halliwell, R. F., 'Neuropharmacological properties of neurons derived from human stem cells', *Neurochem. Int.* **2011**, *59*(3), 404–412, cited on page(s): 25.

(411) Golowasch, J.; Thomas, G.; Taylor, A. L.; Patel, A., *et al.*, 'Membrane Capacitance Measurements Revisited: Dependence of Capacitance Value on Measurement Method in Nonisopotential Neurons', *J. Neurophysiol.* **2009**, *102*(4), 2161–2175, cited on page(s): 25.

(412) Prè, D.; Nestor, M. W.; Sproul, A. A.; Jacob, S., *et al.*, 'A Time Course Analysis of the Electrophysiological Properties of Neurons Differentiated from Human Induced Pluripotent Stem Cells (iPSCs)', *PLoS One* **2014**, *9*(7), e103418, cited on page(s): 25, 27, 36.

(413) Koppensteiner, P.; Boehm, S.; Arancio, O., 'Electrophysiological Profiles of Induced Neurons Converted Directly from Adult Human Fibroblasts Indicate Incomplete Neuronal Conversion', *Cell. Reprogram.* **2014**, *16*(6), 439–446, cited on page(s): 25.

(414) Zhang, S.; Zhang, T.; Cao, L.; Liu, Z., *et al.*, 'Coupled boron-doping and geometry control of tin-catalyzed silicon nanowires for high performance radial junction photovoltaics', *Opt. Express* **2019**, *27*(26), 37248, cited on page(s): 25.

(415) Smits, L. M.; Reinhardt, L.; Reinhardt, P.; Glatza, M., *et al.*, 'Modeling Parkinson's disease in midbrain-like organoids', *npj Park. Dis.* **2019**, *5*(1), 5, cited on page(s): 27, 33, 37.

(416) Rhee, H. J.; Shaib, A. H.; Rehbach, K.; Lee, C., *et al.*, 'An Autaptic Culture System for Standardized Analyses of iPSC-Derived Human Neurons', *Cell Rep.* **2019**, *27*(7), 2212–2228.e7, cited on page(s): 27.

(417) Vukajlovic-Plestina, J.; Kim, W.; Dubrovski, V. G.; Tütüncüoğlu, G., *et al.*, 'Engineering the Size Distributions of Ordered GaAs Nanowires on Silicon', *Nano Lett.* **2017**, *17*(7), 4101–4108, cited on page(s): 28.

(418) Vukajlovic-Plestina, J.; Kim, W.; Ghisalberti, L.; Varnavides, G., *et al.*, 'Fundamental aspects to localize self-catalyzed III-V nanowires on silicon', *Nat. Commun.* **2019**, *10*(1), 869, cited on page(s): 28.

(419) Güniat, L.; Ghisalberti, L.; Wang, L.; Dais, C., *et al.*, 'GaAs nanowires on Si nanopillars: towards large scale, phase-engineered arrays', *Nanoscale Horizons* **2022**, *7*(2), 211–219, cited on page(s): 28.

(420)   Güniat, L.; Caroff, P.; Fontcuberta i Morral, A., 'Vapor Phase Growth of Semiconductor Nanowires: Key Developments and Open Questions', *Chem. Rev.* **2019**, *119*(15), 8958–8971, cited on page(s): 28.

(421)   Kim, W.; Güniat, L.; Fontcuberta i Morral, A.; Piazza, V., 'Doping challenges and pathways to industrial scalability of III–V nanowire arrays', *Appl. Phys. Rev.* **2021**, *8*(1), 011304, cited on page(s): 28.

(422)   Aberg, I.; Vescovi, G.; Asoli, D.; Naseem, U., *et al.*, 'A GaAs Nanowire Array Solar Cell With 15.3Sun', *IEEE J. Photovoltaics* **2016**, *6*(1), 185–190, cited on page(s): 28.

(423)   Yuan, X.; Pan, D.; Zhou, Y.; Zhang, X., *et al.*, 'Selective area epitaxy of III–V nanostructure arrays and networks: Growth, applications, and future directions', *Appl. Phys. Rev.* **2021**, *8*(2), 021302, cited on page(s): 28.

(424)   Fan, H. J.; Werner, P.; Zacharias, M., 'Semiconductor Nanowires: From Self-Organization to Patterned Growth', *Small* **2006**, *2*(6), 700–717, cited on page(s): 29.

(425)   Anyebe, E. A.; Kesaria, M., 'Recent advances in the Van der Waals epitaxy growth of III-V semiconductor nanowires on graphene', *Nano Sel.* **2021**, *2*(4), 688–711, cited on page(s): 29.

(426)   Mariani, G.; Wong, P.-S.; Katzenmeyer, A. M.; Léonard, F.; Shapiro, J.; Huffaker, D. L., 'Patterned Radial GaAs Nanopillar Solar Cells', *Nano Lett.* **2011**, *11*(6), 2490–2494, cited on page(s): 29.

(427)   Krogstrup, P.; Jørgensen, H. I.; Heiss, M.; Demichel, O., *et al.*, 'Single-nanowire solar cells beyond the Shockley–Queisser limit', *Nat. Photonics* **2013**, *7*(4), 306–310, cited on page(s): 29.

(428)   Mukherjee, A.; Ren, D.; Vullum, P.-E.; Huh, J.; Fimland, B.-O.; Weman, H., 'GaAs/AlGaAs Nanowire Array Solar Cell Grown on Si with Ultrahigh Power-per-Weight Ratio', *ACS Photonics* **2021**, *8*(8), 2355–2366, cited on page(s): 29.

(429)   Li, X.; Klausen, L. H.; Zhang, W.; Jahed, Z., *et al.*, 'Nanoscale Surface Topography Reduces Focal Adhesions and Cell Stiffness by Enhancing Integrin Endocytosis', *Nano Lett.* **2021**, *21*(19), 8518–8526, cited on page(s): 29.

(430)   Harding, F. J.; Surdo, S.; Delalat, B.; Cozzi, C., *et al.*, 'Ordered Silicon Pillar Arrays Prepared by Electrochemical Micromachining: Substrates for High-Efficiency Cell Transfection', *ACS Appl. Mater. Interfaces* **2016**, *8*(43), 29197–29202, cited on page(s): 29.

(431)   Liu, X.; Liu, R.; Cao, B.; Ye, K., *et al.*, 'Subcellular cell geometry on micropillars regulates stem cell differentiation', *Biomaterials* **2016**, *111*, 27–39, cited on page(s): 29.

(432)   Doolin, M. T.; Stroka, K. M., 'Integration of Mesenchymal Stem Cells into a Novel Micropillar Confinement Assay', *Tissue Eng. Part C Methods* **2019**, *25*(11), 662–676, cited on page(s): 29.

(433)   Liu, R.; Yao, X.; Liu, X.; Ding, J., 'Proliferation of Cells with Severe Nuclear Deformation on a Micropillar Array', *Langmuir* **2019**, *35*(1), 284–299, cited on page(s): 29.

(434)   Xu, Y.; Zhao, R., 'Force-sensing micropillar arrays for cell mechanics and mechanobiology', *Micro Nano Syst. Biophys. Stud. Cells Small Org.* Elsevier **2021**, ISBN: 978-0-12-823990-2, 23–42, cited on page(s): 29.

(435)   Xie, X.; Xu, A. M.; Angle, M. R.; Tayebi, N.; Verma, P.; Melosh, N. A., 'Mechanical model of vertical nanowire cell penetration', *Nano Lett.* **2013**, *13*(12), 6002–6008, cited on page(s): 30.

(436)   Mullen, R.; Buck, C.; Smith, A., 'NeuN, a neuronal specific nuclear protein in vertebrates', *Development* **1992**, *116*(1), 201–211, cited on page(s): 30.

(437)   Gusel'nikova, V. V.; Korzhevskiy, D. E., 'NeuN As a Neuronal Nuclear Antigen and Neuron Differentiation Marker', *Acta Naturae* **2015**, *7*(2), 42–47, cited on page(s): 30.

(438)   Nagatsu, T, 'Tyrosine hydroxylase: human isoforms, structure and regulation in physiology and pathology.' *Essays Biochem.* **1995**, *30*, 15–35, cited on page(s): 31.

(439)   Kaufman, S., 'Tyrosine Hydroxylase', *Adv. Enzymol. Relat. Areas Mol. Biol.* John Wiley and Sons, Ltd **2006**, Vol. 70, ISBN: 9780470123164, 103–220, cited on page(s): 31.

(440)   B. White, R.; G. Thomas, M., 'Moving Beyond Tyrosine Hydroxylase to Define Dopaminergic Neurons for Use in Cell Replacement Therapies for Parkinson's Disease', *CNS Neurol. Disord. - Drug Targets* **2012**, *11*(4), 340–349, cited on page(s): 31.

(441)   Cutarelli, A.; Martínez-Rojas, V. A.; Tata, A.; Battistella, I., *et al.*, 'A Monolayer System for the Efficient Generation of Motor Neuron Progenitors and Functional Motor Neurons from Human Pluripotent Stem Cells', *Cells* **2021**, *10*(5), 1127, cited on page(s): 31.

(442)   Gilmozzi, V.; Gentile, G.; Riekschnitz, D. A.; Von Troyer, M., *et al.*, 'Generation of hiPSC-Derived Functional Dopaminergic Neurons in Alginate-Based 3D Culture', *Front. Cell Dev. Biol.* **2021**, *9*, 2013, cited on page(s): 31.

(443)   Wu, Y.; Chen, H.; Guo, L., 'Opportunities and dilemmas of in vitro nano neural electrodes', *RSC Adv.* **2020**, *10*(1), 187–200, cited on page(s): 33.

(444)   Caprettini, V.; Chiappini, C., 'Nanoneedle devices for biomedicine', *Semicond. Silicon Nanowires Biomed. Appl.* Elsevier **2022**, ISBN: 978-0-12-821351-3, 181–206, cited on page(s): 33.

(445)   Parekh, K.; Tian, B., 'Nanostructured silicon for biological modulation', *Semicond. Silicon Nanowires Biomed. Appl.* Elsevier **2022**, ISBN: 978-0-12-821351-3, 309–326, cited on page(s): 33.

(446)   James, C.; Davis, R.; Meyer, M.; Turner, A., *et al.*, 'Aligned microcontact printing of micrometer-scale poly-L-Lysine structures for controlled growth of cultured neurons on planar microelectrode arrays', *IEEE Trans. Biomed. Eng.* **2000**, *47*(1), 17–21, cited on page(s): 33.

(447)   Fujie, T.; Desii, A.; Ventrelli, L.; Mazzolai, B.; Mattoli, V., 'Inkjet printing of protein microarrays on freestanding polymeric nanofilms for spatio-selective cell culture environment', *Biomed. Microdevices* **2012**, *14*(6), 1069–1076, cited on page(s): 33.

(448)   Wu, Y.; Wang, M.; Wang, Y.; Yang, H., *et al.*, 'A neuronal wiring platform through microridges for rationally engineered neural circuits', *APL Bioeng.* **2020**, *4*(4), 046106, cited on page(s): 33.

(449)   Petrelli, A.; Marconi, E.; Salerno, M.; De Pietri Tonelli, D.; Berdondini, L.; Dante, S., 'Nano-volume drop patterning for rapid on-chip neuronal connect-ability assays', *Lab Chip* **2013**, *13*(22), 4419, cited on page(s): 33.

(450)   Nagata, I.; Kawana, A.; Nakatsuji, N., 'Perpendicular contact guidance of CNS neuroblasts on artificial microstructures.' *Development* **1993**, *117*(1), 401–8, cited on page(s): 33.

(451)   Rajnicek, A; Britland, S.; McCaig, C, 'Contact guidance of CNS neurites on grooved quartz: influence of groove dimensions, neuronal age and cell type', *J. Cell Sci.* **1997**, *110*(23), 2905–2913, cited on page(s): 33.

(452) Pautot, S.; Wyart, C.; Isacoff, E. Y., 'Colloid-guided assembly of oriented 3D neuronal networks', *Nat. Methods* **2008**, *5*(8), 735–740, cited on page(s): 34.

(453) Greiner, A. M.; Richter, B.; Bastmeyer, M., 'Micro-Engineered 3D Scaffolds for Cell Culture Studies', *Macromol. Biosci.* **2012**, *12*(10), 1301–1314, cited on page(s): 34.

(454) Stein, O.; Liu, Y.; Streit, J.; Campbell, J. H., *et al.*, 'Fabrication of Low-Density Shock-Propagation Targets Using Two-Photon Polymerization', *Fusion Sci. Technol.* **2018**, *73*(2), 153–165, cited on page(s): 35.

(455) Kang, S.; Chen, X.; Gong, S.; Yu, P., *et al.*, 'Characteristic analyses of a neural differentiation model from iPSC-derived neuron according to morphology, physiology, and global gene expression pattern', *Sci. Rep.* **2017**, *7*(1), 12233, cited on page(s): 36, 37.

(456) Gentet, L. J.; Stuart, G. J.; Clements, J. D., 'Direct Measurement of Specific Membrane Capacitance in Neurons', *Biophys. J.* **2000**, *79*(1), 314–320, cited on page(s): 36.

(457) Larramendy, F.; Yoshida, S.; Fekete, Z.; Serien, D.; Takeuchi, S.; Paul, O., 'Stackable octahedron-based photoresist scaffold by direct laser writing for controlled three-dimensional cell networks', *2015 Transducers - 2015 18th Int. Conf. Solid-State Sensors, Actuators Microsystems* **2015**, 642–645, cited on page(s): 37.

(458) Larramendy, F.; Yoshida, S.; Maier, D.; Fekete, Z.; Takeuchi, S.; Paul, O., '3D arrays of microcages by two-photon lithography for spatial organization of living cells', *Lab Chip* **2019**, *19*(5), 875–884, cited on page(s): 37.

(459) Carthew, J.; Taylor, J. B. J.; Garcia-Cruz, M. R.; Kiaie, N., *et al.*, 'The Bumpy Road to Stem Cell Therapies: Rational Design of Surface Topographies to Dictate Stem Cell Mechanotransduction and Fate', *ACS Appl. Mater. Interfaces* **2022**, *14*(20), 23066–23101, cited on page(s): 39.

(460) Zakrzewski, W.; Dobrzyński, M.; Szymonowicz, M.; Rybak, Z., 'Stem cells: past, present, and future', *Stem Cell Res. Ther.* **2019**, *10*(1), 68, cited on page(s): 40.

(461) Obergrussberger, A.; Friis, S.; Brüggemann, A.; Fertig, N., 'Automated patch clamp in drug discovery: major breakthroughs and innovation in the last decade', *Expert Opin. Drug Discov.* **2021**, *16*(1), 1–5, cited on page(s): 40.

(462) Skoog, L.; Tani, E., 'Immunocytochemistry: an indispensable technique in routine cytology', *Cytopathology* **2011**, *22*(4), 215–229, cited on page(s): 40.

(463) Chiappini, C.; Chen, Y.; Aslanoglou, S.; Mariano, A., *et al.*, 'Tutorial: using nanoneedles for intracellular delivery', *Nat. Protoc.* **2021**, *16*(10), 4539–4563, cited on page(s): 41.

(464) Chiappini, C.; Tasciotti, E.; Fakhoury, J. R.; Fine, D., *et al.*, 'Tailored Porous Silicon Microparticles: Fabrication and Properties', *ChemPhysChem* **2010**, *11*(5), 1029–1035, cited on page(s): 41.

(465) Canham, L. T., 'Bioactive silicon structure fabrication through nanoetching techniques', *Adv. Mater.* **1995**, *7*(12), 1033–1037, cited on page(s): 41.

(466) Anderson, S. H. C.; Elliott, H.; Wallis, D. J.; Canham, L. T.; Powell, J. J., 'Dissolution of different forms of partially porous silicon wafers under simulated physiological conditions', *Phys. status solidi* **2003**, *197*(2), 331–335, cited on page(s): 41.

(467) Jiang, X.; Wang, Y.; Herricks, T.; Xia, Y., 'Ethylene glycol-mediated synthesis of metal oxide nanowires', *J. Mater. Chem.* **2004**, *14*(4), 695, cited on page(s): 41.

(468) Cai, Y.; Liu, S.; Yin, X.; Hao, Q.; Zhang, M.; Wang, T., 'Facile preparation of porous one-dimensional Mn_2O_3 nanostructures and their application as anode materials for lithium-ion batteries', *Phys. E Low-dimensional Syst. Nanostructures* **2010**, *43*(1), 70–75, cited on page(s): 41.

(469) Shim, H.-W.; Lee, D. K.; Cho, I.-S.; Hong, K. S.; Kim, D.-W., 'Facile hydrothermal synthesis of porous TiO_2 nanowire electrodes with high-rate capability for Li ion batteries', *Nanotechnology* **2010**, *21*(25), 255706, cited on page(s): 41.

(470) Ma, G.; Wang, X., 'Synthesis and Applications of One-Dimensional Porous Nanowire Arrays: A Review', *Nano* **2015**, *10*(01), 1530001, cited on page(s): 41.

(471) Xie, X.; Xu, A. M.; Leal-Ortiz, S.; Cao, Y.; Garner, C. C.; Melosh, N. A., 'Nanostraw–Electroporation System for Highly Efficient Intracellular Delivery and Transfection', *ACS Nano* **2013**, *7*(5), 4351–4358, cited on page(s): 41.

(472) Xu, A. M.; Wang, D. S.; Shieh, P.; Cao, Y.; Melosh, N. A., 'Direct Intracellular Delivery of Cell-Impermeable Probes of Protein Glycosylation by Using Nanostraws', *ChemBioChem* **2017**, *18*(7), 623–628, cited on page(s): 41.

(473) Schmiderer, L.; Subramaniam, A.; Žemaitis, K.; Bäckström, A., *et al.*, 'Efficient and nontoxic biomolecule delivery to primary human hematopoietic stem cells using nanostraws', *Proc. Natl. Acad. Sci.* **2020**, *117*(35), 21267–21273, cited on page(s): 41.

(474) Shokouhi, A.-R.; Aslanoglou, S.; Nisbet, D.; Voelcker, N. H.; Elnathan, R., 'Vertically configured nanostructure-mediated electroporation: a promising route for intracellular regulations and interrogations', *Mater. Horizons* **2020**, *7*(11), 2810–2831, cited on page(s): 41.

(475) Zhang, A.; Yao, C.; Hang, T.; Chen, M., *et al.*, 'Spin-Coating-Based Fabrication of Nanostraw Arrays for Cellular Nano-electroporation', *ACS Appl. Nano Mater.* **2022**, *5*(2), 2057–2067, cited on page(s): 41.

(476) Chen, Y.; Aslanoglou, S.; Murayama, T.; Gervinskas, G., *et al.*, 'Silicon-Nanotube-Mediated Intracellular Delivery Enables Ex Vivo Gene Editing', *Adv. Mater.* **2020**, *32*(24), 2000036, cited on page(s): 42.

(477) Kresák, S.; Hianik, T.; Naumann, R. L. C., 'Giga-seal solvent-free bilayer lipid membranes: from single nanopores to nanopore arrays', *Soft Matter* **2009**, *5*(20), 4021, cited on page(s): 42.

(478) Dabkowska, A. P.; Niman, C. S.; Piret, G.; Persson, H., *et al.*, 'Fluid and Highly Curved Model Membranes on Vertical Nanowire Arrays', *Nano Lett.* **2014**, *14*(8), 4286–4292, cited on page(s): 42.

(479) Lou, H.-Y.; Zhao, W.; Hanson, L.; Zeng, C.; Cui, Y.; Cui, B., 'Dual-Functional Lipid Coating for the Nanopillar-Based Capture of Circulating Tumor Cells with High Purity and Efficiency', *Langmuir* **2017**, *33*(4), 1097–1104, cited on page(s): 42.

(480) Khraiche, M. L.; El Hassan, R., 'Advances in three-dimensional nanostructures for intracellular recordings from electrogenic cells', *J. Sci. Adv. Mater. Devices* **2020**, *5*(3), 279–294, cited on page(s): 42.

(481) Blau, A., 'Cell adhesion promotion strategies for signal transduction enhancement in microelectrode array in vitro electrophysiology: An introductory overview and critical discussion', *Curr. Opin. Colloid Interface Sci.* **2013**, *18*(5), 481–492, cited on page(s): 42.

(482) Yoo, J.; Kwak, H.; Kwon, J.; Ha, G. E., *et al.*, 'Long-term Intracellular Recording of Optogenetically-induced Electrical Activities using Vertical Nanowire Multi Electrode Array', *Sci. Rep.* **2020**, *10*(1), 4279, cited on page(s): 42.

(483) Kwon, J.; Ko, S.; Lee, J.; Na, J., *et al.*, 'Nanoelectrode-mediated single neuron activation', *Nanoscale* **2020**, *12*(7), 4709–4718, cited on page(s): 42.

(484) Bruno, U.; Mariano, A.; Santoro, F., 'A systems theory approach to describe dynamic coupling at the cell–electrode interface', *APL Mater.* **2021**, *9*(1), 011103, cited on page(s): 42.

(485) Xu, D.; Mo, J.; Xie, X.; Hu, N., 'In-Cell Nanoelectronics: Opening the Door to Intracellular Electrophysiology', *Nano-Micro Lett.* **2021**, *13*(1), 127, cited on page(s): 42.

(486) Dipalo, M.; Caprettini, V.; Bruno, G.; Caliendo, F., *et al.*, 'Membrane Poration Mechanisms at the Cell–Nanostructure Interface', *Adv. Biosyst.* **2019**, *3*(12), 1900148, cited on page(s): 42.

(487) Olsson, T. B.; Abariute, L.; Hrachowina, L.; Barrigón, E., *et al.*, 'Photovoltaic nanowires affect human lung cell proliferation under illumination conditions', *Nanoscale* **2020**, *12*(26), 14237–14244, cited on page(s): 42.

(488) Bosse, B.; Damle, S.; Akinin, A.; Jing, Y., *et al.*, 'In Vivo Photovoltaic Performance of a Silicon Nanowire Photodiode–Based Retinal Prosthesis', *Investig. Opthalmology Vis. Sci.* **2018**, *59*(15), 5885, cited on page(s): 42.

(489) Ha, S.; Khraiche, M. L.; Akinin, A.; Jing, Y., *et al.*, 'Towards high-resolution retinal prostheses with direct optical addressing and inductive telemetry', *J. Neural Eng.* **2016**, *13*(5), 056008, cited on page(s): 42.

(490) Yao, M.; Huang, N.; Cong, S.; Chi, C.-Y., *et al.*, 'GaAs Nanowire Array Solar Cells with Axial p–i–n Junctions', *Nano Lett.* **2014**, *14*(6), 3293–3303, cited on page(s): 42.

(491) Garnett, E.; Yang, P., 'Silicon nanowire radial p-n junction solar cells.' *J. Am. Chem. Soc.* **2008**, *130*(29), 9224–5, cited on page(s): 42.

(492) Zhang, H.; Lei, Y.; Zhu, Q.; Qing, T., *et al.*, 'Nanoscale Photovoltaic Responses in 3D Radial Junction Solar Cells Revealed by High Spatial Resolution Laser Excitation Photoelectric Microscopy', *ACS Nano* **2019**, *13*(9), 10359–10365, cited on page(s): 42.

(493) Anttu, N.; Xu, H. Q., 'Efficient light management in vertical nanowire arrays for photovoltaics', *Opt. Express* **2013**, *21*(May), A558, cited on page(s): 43.

(494) Hashimoto, K.; Irie, H.; Fujishima, A., 'TiO$_2$ Photocatalysis: A Historical Overview and Future Prospects', *Jpn. J. Appl. Phys.* **2005**, *44*(12), 8269–8285, cited on page(s): 43.

(495) Nakata, K.; Fujishima, A., 'TiO$_2$ photocatalysis: Design and applications', *J. Photochem. Photobiol. C Photochem. Rev.* **2012**, *13*(3), 169–189, cited on page(s): 43.

(496) Hwang, Y. J.; Hahn, C.; Liu, B.; Yang, P., 'Photoelectrochemical Properties of TiO$_2$ Nanowire Arrays: A Study of the Dependence on Length and Atomic Layer Deposition Coating', *ACS Nano* **2012**, *6*(6), 5060–5069, cited on page(s): 43.

(497) Pu, Y.-C.; Wang, G.; Chang, K.-D.; Ling, Y., *et al.*, 'Au Nanostructure-Decorated TiO$_2$ Nanowires Exhibiting Photoactivity Across Entire UV-visible Region for Photoelectrochemical Water Splitting', *Nano Lett.* **2013**, *13*(8), 3817–3823, cited on page(s): 43.

(498) Linic, S.; Christopher, P.; Ingram, D. B., 'Plasmonic-metal nanostructures for efficient conversion of solar to chemical energy', *Nat. Mater.* **2011**, *10*(12), 911–921, cited on page(s): 43.

(499) Hou, W.; Cronin, S. B., 'A Review of Surface Plasmon Resonance-Enhanced Photocatalysis', *Adv. Funct. Mater.* **2013**, *23*(13), 1612–1619, cited on page(s): 43.

(500) Nguyen, T. D. V., 'Patch-clamp studies of hiPSC-derived neurons in 2D/3D microstructures', Universität Hamburg **2021**, Bachelor's thesis, cited on page(s): 44.

(501) Siegmund, M., 'A novel approach for cultivation and potentiometric readout of human stem cell-derived neurons on 3D structured microelectrode arrays', Universität Hamburg **2021**, Master's thesis, cited on page(s): 44, 45.

(502) Van Der Loos, H.; Glaser, E. M., 'Autapses in neocortex cerebri: synapses between a pyramidal cell's axon and its own dendrites', *Brain Res.* **1972**, *48*(C), 355–360, cited on page(s): 43.

(503) Herrmann, C. S.; Klaus, A., 'Autapse Turns Neuron Into Oscillator', *Int. J. Bifurc. Chaos* **2004**, *14*(02), 623–633, cited on page(s): 43.

(504) Dhamala, M.; Jirsa, V. K.; Ding, M., 'Enhancement of Neural Synchrony by Time Delay', *Phys. Rev. Lett.* **2004**, *92*(7), 074104, cited on page(s): 43.

(505) Ma, J.; Song, X.; Jin, W.; Wang, C., 'Autapse-induced synchronization in a coupled neuronal network', *Chaos, Solitons & Fractals* **2015**, *80*, 31–38, cited on page(s): 43.

(506) Yilmaz, E.; Ozer, M.; Baysal, V.; Perc, M., 'Autapse-induced multiple coherence resonance in single neurons and neuronal networks', *Sci. Rep.* **2016**, *6*(1), 30914, cited on page(s): 43.

(507) Protachevicz, P. R.; Iarosz, K. C.; Caldas, I. L.; Antonopoulos, C. G.; Batista, A. M.; Kurths, J., 'Influence of Autapses on Synchronization in Neural Networks With Chemical Synapses', *Front. Syst. Neurosci.* **2020**, *14*, 91, cited on page(s): 43.

(508) Qin, H.; Ma, J.; Wang, C.; Wu, Y., 'Autapse-Induced Spiral Wave in Network of Neurons under Noise', *PLoS One* **2014**, *9*(6), e100849, cited on page(s): 43.

(509) Qin, H.; Ma, J.; Wang, C.; Chu, R., 'Autapse-induced target wave, spiral wave in regular network of neurons', *Sci. China Physics, Mech. Astron.* **2014**, *57*(10), 1918–1926, cited on page(s): 43.

(510) Wang, H.; Ma, J.; Chen, Y.; Chen, Y., 'Effect of an autapse on the firing pattern transition in a bursting neuron', *Commun. Nonlinear Sci. Numer. Simul.* **2014**, *19*(9), 3242–3254, cited on page(s): 43.

(511) Seung, H. S.; Lee, D. D.; Reis, B. Y.; Tank, D. W., 'The autapse: a simple illustration of short-term analog memory storage by tuned synaptic feedback.' *J. Comput. Neurosci.* **2000**, *9*(2), 171–85, cited on page(s): 43.

(512) Wang, C.; Guo, S.; Xu, Y.; Ma, J., *et al.*, 'Formation of Autapse Connected to Neuron and Its Biological Function', *Complexity* **2017**, *2017*, 1–9, cited on page(s): 43.

(513) Valencia, A. L.; Froese, T., 'What binds us? Inter-brain neural synchronization and its implications for theories of human consciousness', *Neurosci. Conscious.* **2020**, *2020*(1), cited on page(s): 43.

(514) Uhlhaas, P. J.; Singer, W., 'Neural Synchrony in Brain Disorders: Relevance for Cognitive Dysfunctions and Pathophysiology', *Neuron* **2006**, *52*(1), 155–168, cited on page(s): 43.

(515) Timofeev, I.; Bazhenov, M.; Seigneur, J.; Sejnowski, T., 'Neuronal Synchronization and Thalamocortical Rhythms in Sleep, Wake and Epilepsy', *Jasper's Basic Mech. Epilepsies*, National Center for Biotechnology Information (US) **2012**, ISBN: 978-0199746545, cited on page(s): 43.

(516)   Uhlhaas, P. J.; Pipa, G.; Lima, B.; Melloni, L., *et al.*, 'Neural synchrony in cortical networks: history, concept and current status.' *Front. Integr. Neurosci.* **2009**, *3*, 17, cited on page(s): 43.

(517)   Fan, H.; Wang, Y.; Wang, H.; Lai, Y.-C.; Wang, X., 'Autapses promote synchronization in neuronal networks', *Sci. Rep.* **2018**, *8*(1), 580, cited on page(s): 43.

(518)   Fan, Y.; Xu, F.; Huang, G.; Lu, T. J.; Xing, W., 'Single neuron capture and axonal development in three-dimensional microscale hydrogels', *Lab Chip* **2012**, *12*(22), 4724, cited on page(s): 43.

(519)   Lodish, H.; Berk, A.; Kaiser, C.; Amon, A., *et al.*, 'Molecular cell biology', Macmillan International Higher Education **2021**, Ninth edit, ISBN: 978-1-319-38360-2, cited on page(s): 44.

(520)   Katz, B.; Miledi, R., 'The measurement of synaptic delay, and the time course of acetylcholine release at the neuromuscular junction', *Proc. R. Soc. London. Ser. B. Biol. Sci.* **1965**, *161*(985), 483–495, cited on page(s): 44.

(521)   Patolsky, F.; Timko, B. P.; Yu, G.; Fang, Y., *et al.*, 'Detection, Stimulation, and Inhibition of Neuronal Signals with High-Density Nanowire Transistor Arrays', *Science* **2006**, *313*(5790), 1100–1104, cited on page(s): 44.

(522)   Bakkum, D. J.; Frey, U.; Radivojevic, M.; Russell, T. L., *et al.*, 'Tracking axonal action potential propagation on a high-density microelectrode array across hundreds of sites', *Nat. Commun.* **2013**, *4*(1), 2181, cited on page(s): 44.

(523)   Delacour, C.; Veliev, F.; Crozes, T.; Bres, G., *et al.*, 'Neuron-Gated Silicon Nanowire Field Effect Transistors to Follow Single Spike Propagation within Neuronal Network', *Adv. Eng. Mater.* **2021**, *23*(4), 2001226, cited on page(s): 44.

(524)   Lu, H. F.; Lim, S.-X.; Leong, M. F.; Narayanan, K., *et al.*, 'Efficient neuronal differentiation and maturation of human pluripotent stem cells encapsulated in 3D microfibrous scaffolds', *Biomaterials* **2012**, *33*(36), 9179–9187, cited on page(s): 44.

(525)   Villa-Diaz, L. G.; Kim, J. K.; Lahann, J.; Krebsbach, P. H., 'Derivation and Long-Term Culture of Transgene-Free Human Induced Pluripotent Stem Cells on Synthetic Substrates', *Stem Cells Transl. Med.* **2014**, *3*(12), 1410–1417, cited on page(s): 44.

(526)   Cutarelli, A.; Ghio, S.; Zasso, J.; Speccher, A., *et al.*, 'Vertically-Aligned Functionalized Silicon Micropillars for 3D Culture of Human Pluripotent Stem Cell-Derived Cortical Progenitors', *Cells* **2019**, *9*(1), 88, cited on page(s): 44.

(527)   Edgar, J. M.; Robinson, M.; Willerth, S. M., 'Fibrin hydrogels induce mixed dorsal/ventral spinal neuron identities during differentiation of human induced pluripotent stem cells', *Acta Biomater.* **2017**, *51*, 237–245, cited on page(s): 44.

(528)   Irons, H. R.; Cullen, D. K.; Shapiro, N. P.; Lambert, N. A.; Lee, R. H.; LaPlaca, M. C., 'Three-dimensional neural constructs: a novel platform for neurophysiological investigation', *J. Neural Eng.* **2008**, *5*(3), 333–341, cited on page(s): 44.

(529)   Badekila, A. K.; Kini, S.; Jaiswal, A. K., 'Fabrication techniques of biomimetic scaffolds in three-dimensional cell culture: A review', *J. Cell. Physiol.* **2021**, *236*(2), 741–762, cited on page(s): 44.

(530)   Zhang, S.; Wan, Z.; Kamm, R. D., 'Vascularized organoids on a chip: strategies for engineering organoids with functional vasculature', *Lab Chip* **2021**, *21*(3), 473–488, cited on page(s): 44.

(531)   Bang, S.; Tahk, D.; Choi, Y. H.; Lee, S., *et al.*, '3D Microphysiological System-Inspired Scalable Vascularized Tissue Constructs for Regenerative Medicine', *Adv. Funct. Mater.* **2022**, *32*(1), 2105475, cited on page(s): 44.

(532)   Bang, S.; Na, S.; Jang, J. M.; Kim, J.; Jeon, N. L., 'Engineering-Aligned 3D Neural Circuit in Microfluidic Device', *Adv. Healthc. Mater.* **2016**, *5*(1), 159–166, cited on page(s): 44.

(533)   Kim, S. H.; Im, S.-K.; Oh, S.-J.; Jeong, S., *et al.*, 'Anisotropically organized three-dimensional culture platform for reconstruction of a hippocampal neural network', *Nat. Commun.* **2017**, *8*(1), 14346, cited on page(s): 44.

(534)   Bang, S.; Hwang, K. S.; Jeong, S.; Cho, I.-J., *et al.*, 'Engineered neural circuits for modeling brain physiology and neuropathology', *Acta Biomater.* **2021**, *132*, 379–400, cited on page(s): 44.

(535)   Kim, J.-H.; Kang, G.; Nam, Y.; Choi, Y.-K., 'Surface-modified microelectrode array with flake nanostructure for neural recording and stimulation', *Nanotechnology* **2010**, *21*(8), 085303, cited on page(s): 45.

(536)   Santoro, F.; Schnitker, J.; Panaitov, G.; Offenhäusser, A., 'On Chip Guidance and Recording of Cardiomyocytes with 3D Mushroom-Shaped Electrodes', *Nano Lett.* **2013**, *13*(11), 5379–5384, cited on page(s): 45.

(537)   Teixeira, H.; Dias, C.; Aguiar, P.; Ventura, J., 'Gold-Mushroom Microelectrode Arrays and the Quest for Intracellular-Like Recordings: Perspectives and Outlooks', *Adv. Mater. Technol.* **2021**, *6*(2), 2000770, cited on page(s): 45.

(538)   Forró, C.; Thompson-Steckel, G.; Weaver, S.; Weydert, S., *et al.*, 'Modular microstructure design to build neuronal networks of defined functional connectivity', *Biosens. Bioelectron.* **2018**, *122*, 75–87, cited on page(s): 45.

(539)   Demircan Yalcin, Y.; Bastiaens, A. J.; Frimat, J.-P.; Luttge, R., 'Long-term brain-on-chip: Multielectrode array recordings in 3D neural cell cultures', *J. Vac. Sci. Technol. B* **2021**, *39*(6), 064004, cited on page(s): 45.

(540)   Girardin, S.; Clément, B.; Ihle, S. J.; Weaver, S., *et al.*, 'Topologically controlled circuits of human iPSC-derived neurons for electrophysiology recordings', *Lab Chip* **2022**, *22*(7), 1386–1403, cited on page(s): 45.

(541)   Molina-Martínez, B.; Jentsch, L.-V.; Ersoy, F.; van der Moolen, M., *et al.*, 'A multimodal 3D neuro-microphysiological system with neurite-trapping microelectrodes', *Biofabrication* **2022**, *14*(2), 025004, cited on page(s): 45.

Acknowledgments

celebration of the Hurricane festival, and most importantly by the establishment of the greatest film club southward Australia. Thank you, Coco, Chris, Marten, and Andreas for the—as yet—197 amusing, funny, sad, frightening, and often unsettling evenings! Also, I want to thank Aune Koitmäe, Stefanie Haugg, Carina Hedrich, Parisa Bayat, Malte Siegmund, Jeremy Teuber, Manuel Müller, Katja Bours, Aaron Silva, John O'Sullivan, Niklas Rieck, Matteo Schnelle, and Merle Wolpert for being wonderful colleagues, students, interns, and/or student assistants and for directly supporting me during my PhD. Moreover, I want to express my appreciation for the cleanroom/technical staff members for the amicable yet professional cooperation.

Robert Zierold, I hope it is inherently obvious what kind of decisive impact you have had on my time as a PhD student! Neither I would have made the progress that I made nor I had maintained the motivation and positive frame of mind throughout the uncountable number of setbacks. Kudos to you for being available 24/7 during the past years to provide support, advice, and all imaginable shades of assistance. I enjoyed the happenstance that we were on the same page both professionally and personally—and with that being said—cheers and keep pedaling!

Prof. Robert H. Blick offered to my delight—after overseeing already my Bachelor's and Master's theses—to be once again my supervisor. In his group, I have been in the fortunate position to freely steer my research and to be constantly supported in doing so. The endorsement, for example, to establish the self-contained human iPSC culture in our labs led to a disruptive change in my research as it allowed for more frequent execution of experiments while significantly raising the scientific impact. Thank you very much for the opportunity to prepare my dissertation in your group, for supporting my scientific advancement, and also for promoting my academic exchange of knowledge by sending me to several conferences.

The two additional reviews of my dissertation were prepared by Prof. Wolfgang J. Parak and Prof. John A. Rogers and I want to express my gratitude for taking the time and effort to evaluate my thesis. Moreover, I want to thank Prof. Jochen Liske, Prof. Viacheslav Nikolaev, and Prof. Gabriel Bester for joining the board of examiners.

Miscellaneously, I want to thank Irmgard Flick for diligently writing the 'Fachbereich Physik' newsletter, Thomas Lichthardt including the remaining post office crew for always contacting me when frozen packages arrived, and the various funding agencies that supported my research (e.g., DFG, BMBF, Herz, Cui, DAAD, LFF).

Finally, I want to thank my family and friends for indirectly contributing to my thesis by creating a warm, stable, and comfy environment aside from work. Thank you all for making living in Hamburg as exciting and enjoyable as it was. Of course, especially you, Simon, have had an extraordinary impact on my time in Hamburg and I cheerfully look back at all the years we spent together as flatmates, students, and friends! I want to thank my siblings for being family in Hamburg and, needless to say, my parents for supporting me here while simultaneously making stays back in my hometown a pleasing and welcome change of scenery. And naturally, thank you, Olga, for enduring all the evenings that I have spent late working on the thesis!

Eidesstattliche Versicherung / Declaration on oath

Hiermit versichere ich an Eides statt, die vorliegende Dissertationsschrift selbst verfasst und keine anderen als die angegebenen Hilfsmittel und Quellen benutzt zu haben.

_____   _____
Ort, Datum   Jann Immo Harberts